

**EPR-Based Distance Measurements on  
Metal Nitroxide Model Complexes  
as well as EPR Spectroscopic  
Characterization of [Si<sub>2</sub>]-Radicals and  
Titanocene Complexes**

Andreas Meyer

Dissertation



**EPR-Based Distance Measurements on  
Metal Nitroxide Model Complexes  
as well as EPR Spectroscopic  
Characterization of [Si<sub>2</sub>]-Radicals and  
Titanocene Complexes**

Dissertation

zur  
Erlangung des Doktorgrades (Dr. rer. nat.)  
der  
Mathematisch-Naturwissenschaftlichen Fakultät  
der  
Rheinischen Friedrich-Wilhelms-Universität Bonn

Vorgelegt von

**Andreas Meyer**

aus Bonn

– Bonn 2016 –





Angefertigt mit Genehmigung der Mathematisch-Naturwissenschaftlichen Fakultät  
der Rheinischen Friedrich-Wilhelms-Universität Bonn.

Dekan:	Prof. Dr. Ulf-G. Meißner
Erster Gutachter:	Prof. Dr. Olav Schiemann
Zweiter Gutachter:	Prof. Dr. Alexander C. Filippou
Tag der Promotion:	10.03.2017
Erscheinungsjahr:	2017

## Publications

Parts of this thesis have already been published in international, peer-reviewed journals. The publications listed below are reprinted in the appendices of this work.

1. A. Meyer, J. Wiecek, G. Schnakenburg, and O. Schiemann, "The crystal structure of 4'-{4-[(2,2,5,5-tetramethyl-*N*-oxyl-3-pyrrolin-3-yl)ethynyl]-phenyl}-2,2':6',2''-terpyridine", *Acta Cryst. E* **2015**, *E71*, 870 – 874.
2. A. Meyer, G. Schnakenburg, and O. Schiemann, "Crystal structure of 4'-{4-[(2,2':6',2''-terpyridyl-4'-yl)phenyl]-ethynyl}biphenyl-4-yl-(2,2,5,5-tetramethyl-1-oxyl-3-pyrrolin-3-yl)formate benzene 2.5-solvate", *Acta Cryst. E* **2015**, *E71*, 1245 – 1249.
3. A. Meyer, G. Schnakenburg, R. Glaum, and O. Schiemann, "(Bis(terpyridine))copper(II) Tetraphenylborate: A Complex Example for the Jahn-Teller Effect", *Inorg. Chem.* **2015**, *54*, 8456 – 8464.
4. A. Meyer, D. Abdullin, G. Schnakenburg, and O. Schiemann, "Single and Double Nitroxide Labeled Bis(terpyridine)-copper(II): Influence of Orientation Selectivity and Multispin Effects on PELDOR and RIDME", *Phys. Chem. Chem. Phys.* **2016**, *18*, 9262 – 9271.
5. A. Meyer and O. Schiemann, "PELDOR and RIDME Measurements on a High-Spin Manganese(II) Bisnitroxide Model Complex", *J. Phys. Chem. A* **2016**, *120*, 3463 – 3472.
6. M. I. Arz, M. Straßmann, A. Meyer, G. Schnakenburg, O. Schiemann, and A. C. Filippou, "One-Electron Oxidation of a Disilicon(0) Compound: An Experimental and Theoretical Study of NHC-trapped [Si<sub>2</sub>]<sup>+</sup>", *Chem. Eur. J.* **2015**, *21*, 12509 – 12516.
7. M. I. Arz, G. Schnakenburg, A. Meyer, O. Schiemann, and A. C. Filippou, "The Si<sub>2</sub>H Radical supported by two *N*-Heterocyclic Carbenes", *Chem. Sci.* **2016**, *7*, 4973 – 4979.
8. D. Schwarz G. Henriques, K. Zimmer, S. Klare, A. Meyer, E. Rojo-Wiechel, M. Bauer, R. Sure, S. Grimme, O. Schiemann, R. A. Flowers, and A. Gansäuer,

"Highly Active Titanocene Catalysts for Epoxide Hydrosilylation: Synthesis, Theory, Kinetics, EPR Spectroscopy", *Angew. Chem. Int. Ed.* **2016**, *55*, 7671 – 7675.

## Abstract

Metalloproteins are a class of proteins which contain metal ions in their active site. If these metal ions carry unpaired electrons, EPR spectroscopy can be used to identify and characterize these ions or even localize them within the protein backbone. This work describes the synthesis of chemical compounds containing paramagnetic metal ions and nitroxyl radicals and their application as model compounds for EPR distance measurements in metalloproteins or other metal containing biomolecules. In addition, the detection, identification, and characterization of reactive, paramagnetic substances using EPR spectroscopy is described. Chapter 1 gives a brief introduction into both fields, emphasizing the potential and importance of EPR spectroscopy in certain fields of structural biology as well as the versatility of EPR spectroscopy as a tool for the investigation of the electronic and geometric structure of small chemical compounds. Chapter 2 introduces the basic theoretical background of EPR spectroscopy, which is needed to understand the following chapters describing the experimental results. In chapters 3 and 4, the synthesis and crystallization of nitroxide substituted terpyridine ligands and their geometrical structure are described. The terpyridine and the nitroxide subunits are separated by phenylene and ethynylene building blocks. It is found, that the phenylene-ethynylene spacers are sufficiently rigid to yield predictable distances between the terpyridine nitrogen atoms and the nitroxide substituent. Chapter 5 describes the synthesis, and the full crystallographic and spectroscopic characterization of bis(terpyridine) copper bis(tetraphenylborate). It is shown that the coordination sphere is highly plastic and exhibits temperature dependent, dynamic and static Jahn-Teller distortions. These distortions are influenced by the choice of the solvent system and affect the EPR parameters of the copper ion, which is of importance for the EPR distance measurements described in chapter 6. There, the synthesis of homo- and nominally heteroleptic copper complexes of the terpyridine ligand introduced in chapter 4 and unsubstituted terpyridine is described. The resulting complexes are then used as model systems for EPR distance measurements. Using PELDOR, it is found that the obtained time traces are distorted by orientation selection and multi-spin effects. The RIDME experiment on the other hand is not subject to these effects and provides better sensitivity. Additionally, both experiments are used to investigate the immediate coordination sphere of the copper center. It is shown that one terpyridine ligand is removed from the central copper ion in acidic solvent systems. In chapter 7,

the manganese(II) analogue of the homoleptic copper complex is used as model system for EPR distance measurements involving high-spin ions. The most striking difference between the copper and the manganese complex is the high-spin ( $S = 5/2$ ) state of the manganese ion. It is shown that orientation selection also plays a role in this system, albeit the selectivity is less pronounced than in the case of the copper system. In terms of sensitivity, RIDME is superior to PELDOR in the manganese system as well. However, RIDME suffers from the occurrence of intense artifact peaks due to higher harmonics of the dipolar frequency. The degree of ligand dissociation is estimated using PELDOR. The studies on the metal-nitroxide model systems show up difficulties in EPR distance determinations that involve metal centers and possible ways to overcome those difficulties. The obtained results will be conveyed to biological systems in future studies, where one possible application would be the introduction of manganese(II) ions into RNA molecules and the subsequent use of these ions as spin label.

The final three chapters describe the detection and characterization of reactive paramagnetic substances in their natural solvent environment. In chapter 8, the structure of a paramagnetic, *N*-heterocyclic carbene substituted disilicon radical cation containing a Si-Si multiple bond in solution is investigated. Using the  $^{29}\text{Si}$  satellites it is found that the radical is less symmetric than its Lewis formula would suggest. In chapter 9, the structure of an " $\text{Si}_2\text{H}$ " radical stabilized by *N*-heterocyclic carbenes is investigated in liquid solution. The structure of the nitrogen hyperfine coupling suggests that the hydrogen atom is localized on one silicon atom. Chapter 10 focuses on catalytically active titanocene species used for epoxide hydrosilylation. Two titanocene hydride species are identified as hydrogen atom donors. Furthermore, a titanocene alkoxide species which occurs as resting state of the catalytic cycle is identified using deuteration experiments and ENDOR spectroscopy. Taken together, chapters 8 - 10 demonstrate that EPR spectroscopy can be used to obtain detailed pictures of the electronic and geometric structure of reactive paramagnetic compounds in liquid and frozen solvent matrices.

## Contents

Part I. Introduction and Theoretical Backgrounds of Electron Paramagnetic Resonance .....	1
1. Introduction and Motivation .....	2
2. Theoretical Background of Electron Paramagnetic Resonance Spectroscopy.....	7
2.1. Electron Spins and the Spin Hamiltonian.....	7
2.1.1. Electronic and Nuclear Zeeman Effect .....	9
2.1.2. Hyperfine Coupling Interaction .....	12
2.1.3. Electron Dipolar, Zero-Field Splitting, and Exchange Interactions.....	15
2.1.4. Nuclear Quadrupole Coupling .....	24
2.2. Relaxation .....	24
2.3. Pulsed EPR Experiments .....	26
2.3.1. Spin Echo .....	26
2.3.2. Inversion Recovery .....	28
2.3.3. Electron Spin Echo Envelope Modulation .....	29
2.3.4. Electron Nuclear Double Resonance .....	30
2.3.5. Methods to Measure Electron-Electron Dipolar Coupling .....	32
2.3.6. Pulsed Electron Double Resonance.....	33
2.3.7. Relaxation Induced Dipolar Modulation Enhancement .....	42
2.3.8. The Choice of Spin Label.....	46
Part II. EPR Distance Measurements Involving Metal Centers.....	50
3. The Crystal Structure of 4'-{4-[(2,2,5,5-Tetramethyl- <i>N</i> -oxyl-3-pyrrolin-3-yl)ethynyl]-phenyl}-2,2':6',2''-terpyridine .....	51
4. Crystal Structure of 4'-{[4-(2,2':6',2''-Terpyridyl-4'-yl)phenyl]-ethynyl}biphenyl-4-yl-(2,2,5,5-tetramethyl-1-oxyl-3-pyrrolin-3-yl)formate Benzene 2.5-Solvate .....	54
5. (Bis(terpyridine))copper(II) Tetraphenylborate: A Complex Example for the Jahn–Teller Effect .	57
6. Single and Double Nitroxide Labeled Bis(terpyridine)-copper(II): Influence of Orientation Selectivity and Multispin Effects on PELDOR and RIDME.....	60
7. PELDOR and RIDME Measurements on a High-Spin Manganese(II) Bisnitroxide Model Complex	65
Part III. Characterization of [Si <sub>2</sub> ]-Radicals and Titanocene Complexes Using Electron Paramagnetic Resonance .....	68
8. One-Electron Oxidation of a Disilicon(0) Compound: An Experimental and Theoretical Study of NHC-trapped [Si <sub>2</sub> ] <sup>+</sup> .....	69
9. The Si <sub>2</sub> H Radical Supported by Two N-heterocyclic Carbenes .....	73
10. Highly Active Titanocene-Catalysts for Epoxide Hydrosilylation – Synthesis, Theory, Kinetics, EPR.....	76
11. Final Summary, Conclusions, and Outlook .....	80

<b>12. References</b> .....	84
<b>Appendices</b> .....	95





## **Part I.**

# **Introduction and Theoretical Backgrounds of Electron Paramagnetic Resonance**

## 1. Introduction and Motivation

The thesis presented in the following consists of three parts, each of which consists of several chapters. Part I gives a general introduction to the field of electron paramagnetic resonance (EPR) based distance measurements involving metal centers and the investigation of the electronic structure of paramagnetic compounds using EPR spectroscopy.

The second part of this work describes the synthesis and investigation of small chemical model systems for EPR distance measurements involving metal centers. The obtained results will be useful in future investigations in the field of structural biology, which is a rapidly evolving, interdisciplinary field of science. The relevance of biochemistry and structural biology as a part of biochemistry is best demonstrated by realizing that ten out of the fifteen latest Nobel prizes for chemistry have been awarded to scientists either working in biochemistry or developing methods especially suited for biochemical analytics.<sup>1-17</sup> One of the main concepts in biochemistry is the structure-activity relationship, which states that the function of a biomolecule is determined by its structure.<sup>18</sup> The elucidation of the structure of biomolecules is therefore of key significance in the field of biochemistry.<sup>19</sup> Analytic methods to obtain structures of biomolecules include X-ray (or neutron) crystal structure analysis,<sup>20</sup> magnetic resonance techniques like nuclear magnetic resonance (NMR)<sup>21-23</sup> and electron paramagnetic resonance (EPR),<sup>24-26</sup> Foerster resonance energy transfer (FRET),<sup>27,28</sup> electron microscopy (EM),<sup>29,30</sup> and computational methods such as homology modeling<sup>31</sup> or molecular dynamics (MD) simulations.<sup>32</sup> Of these methods, X-ray crystallography is the most successful one, followed by NMR spectroscopy.<sup>19</sup> This is also documented in the protein structural database (PDB), where 119303 structures of biological macromolecules have been deposited.<sup>33,i</sup> From these structures, 106560 and 11401 have been obtained using X-ray structure analysis and NMR spectroscopy, respectively, amounting together to almost 99% of all deposited structures. Nonetheless, other methods are required for structural biology to complement these two methods, as both of them have their drawbacks. For X-ray structure analysis, it is necessary to obtain crystals of the biomolecules. This is not always possible, for examples if the molecules contain mobile domains.<sup>19</sup> Membrane proteins represent another important class of

---

<sup>i</sup> Numbers of entries obtained by PDB queries on the 5th of June, 2016.

molecules where X-ray crystallography is less successful compared to soluble proteins. In their native environment, membrane proteins are embedded in a two-dimensional, lipophilic matrix and are therefore often insoluble in water and thus difficult to crystallize. Only 3293 of all structures (i.e. less than 3%) in the PDB belong to membrane proteins, although 30 - 40% of all expressed proteins belong to the class of membrane proteins.<sup>34</sup> Another drawback of crystallography is that the crystalline environment strongly differs from the natural environment of biomolecules. Therefore, it is not always clear whether the observed structures represent the native state of the biomolecule. Finally, many proteins have several functional states and it is often not possible to crystallize the proteins in all states. These problems do not occur in NMR spectroscopy, where biomolecules can be studied in more realistic environments, like liquid solution or even *in-cell*.<sup>35,36</sup> However, with the exception of specialized studies, NMR spectroscopy is limited to molecules having a molecular weight below 100 kDa as large molecular size leads to crowding of the NMR signals and to broadening of the NMR lines.<sup>19,37</sup> Noteworthy, NMR spectroscopy is even less successful for membrane proteins than X-ray crystallography (151 PDB entries of membrane protein structures obtained using NMR, i.e. ~1.3% of all NMR entries). EPR spectroscopy is neither limited by the size of the molecule nor does it require crystalline samples, making it complement X-ray crystallography and NMR spectroscopy as a tool to investigate the structure of membrane proteins.<sup>34,38</sup> Another class of biomolecules in which EPR offers advantages over X-ray crystallography and NMR spectroscopy are metalloproteins. The relevance of metals in biology cannot be overestimated and almost any metal has either a biological function or shows specific interaction with biomolecules, e.g. as a toxin.<sup>39,40</sup> Important examples of metals in proteins include the manganese cluster in the photosynthetic reaction center,<sup>41</sup> the iron ions which transport oxygen in hemoglobin,<sup>42</sup> the copper protein hemocyanin which has the same function in invertebrates,<sup>43</sup> the cobalt ion in vitamin B12 catalyzing redox reactions and rearrangements,<sup>44</sup> iron and nickel ions in hydrogenating enzymes,<sup>45</sup> and the iron-molybdenum centers in enzymes which reduce atmospheric nitrogen yielding ammonia.<sup>46</sup> In some cases, naturally occurring metal ions can be replaced by others, opening up the possibility to introduce metal ions with specific, desired properties into biomolecules. As an example, diamagnetic magnesium ions in ribozymes have been shown to be selectively replaceable by diamagnetic cadmium(II) and paramagnetic manganese(II) ions.<sup>47</sup> Using manganese

ions, the molecules are often found to retain or even increase their catalytic activity.<sup>47,48</sup> Metalloproteins often lose their metal ions upon crystallization so that only the structure of the *apo* form can be determined by X-ray crystallography.<sup>49</sup> If the metal ion in a metalloprotein is paramagnetic, NMR absorption lines are heavily broadened, especially for the nuclei in close proximity to the metal center.<sup>50</sup> EPR spectroscopy on the other hand is a very versatile tool for the investigation of (paramagnetic) metalloproteins. It can be used to investigate the electronic structure of the metal center and to obtain details about the geometry of the immediate coordination sphere of the metal center.<sup>25,26,40,51</sup> After introduction of spin labels,<sup>38,52,53</sup> it is also possible to obtain information about the structure of the protein backbone<sup>54</sup> or to localize the metal center within the protein.<sup>55</sup> Such insights into the structure are obtained by conducting a series of EPR experiments to determine the interspin distance between the spin label attached to different sites of the biomolecule and the paramagnetic metal center.<sup>24</sup> The EPR spectroscopic properties of metal ions complicate measurements of the interspin distance by introducing orientation selection, fast electron spin relaxation, low spectral densities, and interstate mixing between different  $m_s$  levels in the case of high-spin ( $S > 1/2$ ) metal ions.<sup>24,54</sup> Establishing suitable measurement conditions for EPR distance measurements is therefore of prime importance to obtain reliable geometrical information from such measurements, which is the central aim of the second part of this work.

The third part of this work is devoted to the detection and characterization of reactive radicals and paramagnetic, organometallic compounds using EPR spectroscopy. Owing to their paramagnetic nature, such compounds often cannot be analyzed by NMR spectroscopy, which is the standard spectroscopic method to obtain information about molecules in solution.<sup>50</sup> In contrast, EPR spectroscopy is well suited to investigate such compounds in liquid or frozen solution and provides high sensitivity and resolution at the same time.<sup>56</sup> All EPR parameters are defined by the ground and excited state wavefunctions of a given molecule, which also determine the geometric structure of this molecule.<sup>57</sup> Conversely, the EPR parameters of a molecule can be used to make deductions about its electronic and geometric structure. However, interpretation of EPR spectroscopic data can be challenging and usually requires support by other spectroscopic methods and theoretical calculation. Here, some examples are used to illustrate the applicability of EPR spectroscopy when

addressing various questions regarding the electronic and geometric structure. The first example is the investigation of the one-electron oxidation of a rhodium(I) amide complex by Büttner *et al.* The resulting paramagnetic species showed a low degree of  $g$ -anisotropy and a large hyperfine splitting caused by one nitrogen atom. These observations suggest that the newly formed spin center is localized on the amide nitrogen nucleus rather than on the rhodium ion. Thus, the species generated by one-electron oxidation is better described as a rhodium(I) aminyl in contrast to a rhodium(II) amide (Figure 1.1a).<sup>58</sup> Similar ligand centered redox processes have been observed in four subsequent single electron reduction steps for bis(terpyridine) chromium(III) whereas metal centered single electron reduction and oxidation occurs in a similarly substituted nickel(II) complex.<sup>59,60</sup> In another exemplary study presented by Maurelli *et al.*, details of the arrangement of the water ligands in the Jahn-Teller active hexaqua complex of titanium(III) have been derived by combining EPR spectroscopy and theoretical calculations.<sup>61</sup> In this study, the authors used the  $g$ -anisotropy of structural models of the hexaqua complex with different point symmetries to rule out a  $D_{2h}$  symmetric structure. The dependence of the hydrogen hyperfine coupling and the  $^{17}\text{O}$  quadrupole interaction on the orientation of the water ligands was investigated using density functional theory (DFT) calculations.

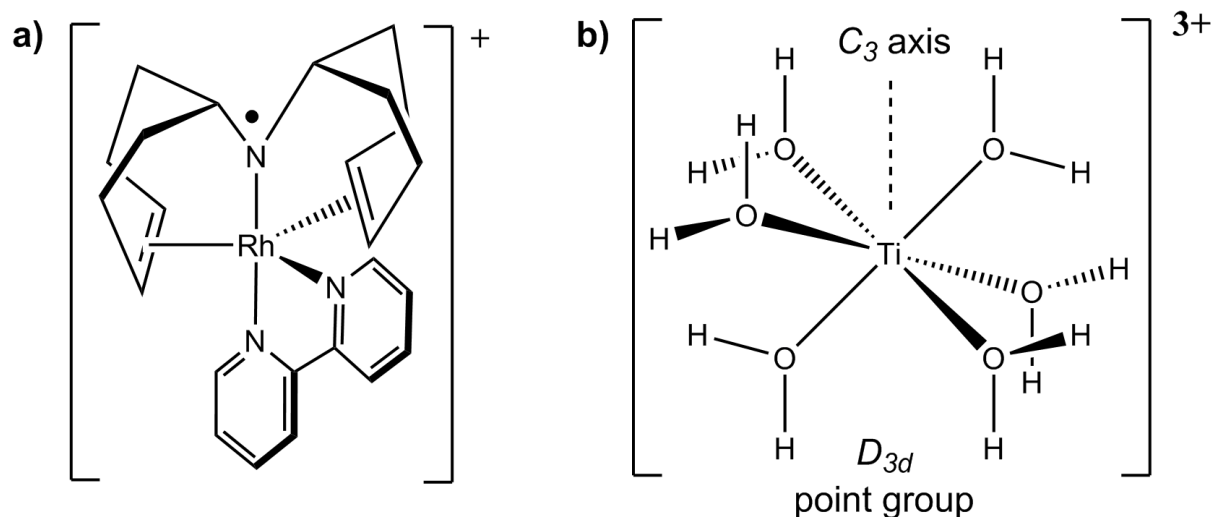


**Figure 1.1.** Examples for the use of EPR spectroscopy to elucidate the electronic and geometric structures of small, paramagnetic molecules. a) Localization of the unpaired electron on the nitrogen donor atom of the ligand in a rhodium aminyl complex.<sup>58</sup> b)  $D_{3d}$  symmetric proposal for the ground state structure of hexaquatitanium(III) obtained using ENDOR and ESEEM spectroscopy in combination with DFT calculations.<sup>61</sup>

Comparison of the theoretical hyperfine and quadrupole parameters with experimental data from electron nuclear double resonance (ENDOR) and electron spin echo envelope modulation (ESEEM) measurements revealed a  $D_{3d}$  symmetric structure as one candidate for the structure of hexaqua-titanium(III) (Figure 1.1b). X-ray crystallography would not have been well suited for this compound, as it is difficult to reliably localize hydrogen nuclei using X-ray crystallography. Maurelli *et al.* also pointed out that specific hydrogen bonding interaction between the complexes and the solvent can be investigated using EPR spectroscopy. The last example was presented by Chiesa *et al.* There, the authors have characterized the binding sites of excess electrons in magnesium oxide. Adding ammonia to the surface allowed deriving the structure of the surface spin center to great detail.<sup>62,63</sup> The occurrence of a nonet hyperfine coupling structure suggested that the excess electrons are preferably localized in corner sites having three ammonia molecules in their first coordination sphere. Using hyperfine sublevel correlation spectroscopy (HYSCORE), stabilizing proton contacts from ammonia molecules in the second coordination sphere could be detected. In the cited examples, EPR spectroscopy has been used to:

- localize unpaired electrons in compounds with known geometrical structure.
- derive details of the geometrical structure in solution where only a rough approximation of the structure was known, e.g. a coordination number and an idealized symmetry.
- localize electrons in bulk material and obtain the geometry of their immediate surroundings.

The examples clearly demonstrate the versatility of EPR spectroscopy to investigate electronic and geometric structures, which will be exploited in chapter 8 - 10 to characterize reactive silicon and titanocene species.

## 2. Theoretical Background of Electron Paramagnetic Resonance Spectroscopy

Most of the results presented in this work were obtained using electron paramagnetic resonance (EPR) spectroscopy. In order to make these results more accessible, the basic concepts and terms of EPR spectroscopy are introduced in this chapter. Furthermore, the used pulse sequences are briefly discussed. For brevity, most explanations are given on a non-formal qualitative level. For mathematical derivations and more details on the physical backgrounds, the readers are referred to the textbooks concerned with EPR spectroscopy in general<sup>56,64–67</sup> and the original publications given in the corresponding subsections. Technical aspects of the measurements<sup>67–69</sup> will not be discussed as this work is not concerned with the development of spectrometer hardware.

### 2.1. Electron Spins and the Spin Hamiltonian

EPR spectroscopy can be used to study paramagnetic substances, i.e. substances having a magnetic susceptibility  $\chi > 0$ .<sup>70</sup> Although exceptions exist,<sup>71</sup> unpaired electrons are responsible for the occurrence of paramagnetism in most substances, including all paramagnetic substances discussed in parts II and III. Brought into a magnetic field, the magnetic moments of the unpaired electrons can attain different quantum states. Transitions between two states can be achieved if the samples are subjected to irradiation having a wavelength which matches the energetic difference of the two states. This allows obtaining information about the different quantum states and can be used to deduce details of the electronic and geometric structure of the sample molecule. In continuous wave (cw) EPR spectroscopy, the EPR spectrum of a substance is obtained by subjecting the sample to continuous MW radiation. On resonance, absorption of the magnetic component of the MW radiation occurs. The obtained signal intensity is proportional to the imaginary part of the complex susceptibility of the sample.<sup>65,72</sup> This imaginary part of the magnetic susceptibility could be measured as a function of the wavelength of the radiation. However, in the standard experimental set up, the spectroscopist varies the strength of the applied magnetic field instead of the wavelength of the radiation. The results of an EPR experiment can be discussed using the quantum theory of individual electrons interacting with magnetic fields if the unpaired electrons within a sample are not strongly coupled to each other. The pioneering work in that area was conducted by

Stern and Gerlach,<sup>73</sup> Dirac,<sup>74,75</sup> van Vleck,<sup>76</sup> and others.<sup>77-81</sup> One of the results of their experiments was the discovery that every electron bears an electron spin  $s$ , giving rise to a magnetic moment  $\mu_s$ . Brought into a magnetic field, these electrons occupy one of two quantum states, corresponding to a parallel or antiparallel alignment of the magnetic moment and the magnetic field. This phenomenon is called Zeeman effect<sup>82</sup> and is the basis for all EPR experiments. Although the results were obtained for free electrons, unpaired electrons bound to a molecule can be treated in an analogous manner. As with other quantum systems, it is possible to set up a Hamiltonian operator which describes the accessible quantum states and their corresponding energies. It is usually not necessary to consider the full electronic Hamiltonian  $\mathcal{H}_{el}$  but only the part that accounts for the unpaired electron spins.<sup>83</sup> This operator is called the spin Hamiltonian  $\mathcal{H}_S$  and summarizes the interaction of the electron spins with the external magnetic field and their surroundings.<sup>56,64,65</sup>

$$\mathcal{H}_S = \mathcal{H}_{Zee,El} + \mathcal{H}_{HFC} + \mathcal{H}_{ee} + \mathcal{H}_{Zee,Nuc} + \mathcal{H}_{NQC} \quad (2-1)$$

The terms given in eq. (2-1) are sufficient to describe every spin system in this work. However, depending on the type of sample and experiment some of the terms may be omitted.<sup>64</sup> The first three terms consider the energy levels of electron spins under the influence of an external magnetic field ( $\mathcal{H}_{Zee,El}$ , Zeeman effect of the electron), a magnetic field caused by nearby nuclei possessing a nuclear spin ( $\mathcal{H}_{HFC}$ , HFC = hyperfine coupling), and a magnetic field caused by nearby electrons ( $\mathcal{H}_{ee}$ ). The HFC interaction is often described by an isotropic coupling interaction and a quasi-classical dipolar interaction between electron and nuclear spins.<sup>65</sup> The electron-electron interaction can often be described as purely dipolar interaction between magnetic moments of electrons if the electrons are separated by more than 2 nm.<sup>66</sup> In such cases, the magnitude of the interaction amounts to only a few MHz and is therefore of similar magnitude as typical HFC interactions. However, if several unpaired electrons are localized in close proximity, the interaction can be very strong leading to zero-field splitting, the treatment of which can be complicated (see chapter 2.1.3).<sup>84,85</sup> The last two terms are dealing with nuclear energy levels. Nuclear spins experience the Zeeman effect ( $\mathcal{H}_{Zee,Nuc}$ ) in analogy to electron spins. The last term  $\mathcal{H}_{NQC}$  deals with nuclear quadrupole couplings (NQC) of spins on nuclei having a quadrupolar charge distribution. Such a charge distribution only occurs for nuclei having a nuclear spin  $I > \frac{1}{2}$ . The energy splitting of the different nuclear spin states is



then affected by electric field gradients which are caused by a non-symmetric electron distribution around these nuclei. The terms given above will be briefly explained in the following subsections. Before doing so, it is sensible to consider the magnitude of the terms in eq. (2-1). For most samples presented in parts II and III, the electron Zeeman effect is the dominating interaction while all other terms are much smaller:

$$\mathcal{H}_{Zee,El} \gg \mathcal{H}_{HFC}; \mathcal{H}_{ee}; \mathcal{H}_{Zee,Nuc}; \mathcal{H}_{NQC} \quad (2-2)$$

In these cases, it is possible to treat the smaller interactions in the framework of perturbation theory, the unperturbed reference system being the electron spins in the external magnetic field. If this is not appropriate, the Hamiltonian matrix has to be diagonalized using all significant terms simultaneously.

### 2.1.1. Electronic and Nuclear Zeeman Effect

In classical electrodynamics, the interaction energy  $W$  of a magnetic moment  $\vec{\mu}$  and a magnetic field  $\vec{B}$  is given by

$$W = -\vec{\mu} \cdot \vec{B}. \quad (2-3)$$

As mentioned above, electrons possess a spin  $s$  leading to a magnetic moment  $\mu_s$ . This magnetic moment interacts with magnetic fields and can attain two possible orientations which are energetically distinct. The restriction to two orientations is a consequence of the quantum nature of the electron and contrasts with the classical interaction, in which the magnetic moment can attain any orientation with respect to the external field. To characterize the state of the electron one assigns the quantum numbers  $s$  and  $m_s$ . The two quantum numbers  $s$  and  $m_s$  are called the spin quantum number and the magnetic spin quantum number, respectively. They quantify the magnitude of the electron spin and its orientation in an external magnetic field, respectively.<sup>83</sup> For a single electron the quantum numbers are  $s = \frac{1}{2}$  and  $m_s = \frac{1}{2}$  or  $m_s = -\frac{1}{2}$ , corresponding to parallel or antiparallel orientation with respect to the external magnetic field. The magnetic moment is not fully aligned along the magnetic field but still has components perpendicular to the external field. In fact, the electron spin is said to precess around the external magnetic axis with only the component along that axis fixed. Two (or more) electrons strongly coupled to each other behave

in an analogous manner. Such a situation is met for example in high-spin metal ions. In the absence of strong zero-field splitting (see chapter 2.1.3), the electrons can then be assigned the quantum numbers  $S = s_1 + s_2 + \dots$  and  $M_s \in [-S, S]$ . As before, the quantum number  $M_s$  describes the orientation of  $S$  with respect to the external field. Importantly,  $M_s$  can only assume either integer or half-integer values, depending on whether or not  $S$  is an integer or a half-integer. Taking into account the restrictions for the magnetic quantum number, this gives rise to

$$M = 2S + 1 \quad (2-4)$$

possible orientations of the spin  $S$  in a magnetic field. The number  $M$  defined by eq. (2-4) is called the multiplicity of a given spin state. So far, only the possible orientations of the spins with respect to external fields have been considered. To calculate the magnitude of the Zeeman interaction, it is necessary to know the magnitude of the magnetic moment associated with the spin of unpaired electrons. The magnetic moment of electron spins is usually expressed in units of Bohr's magneton  $\mu_B$ , which can be seen as the quantum of magnetic moment. Based on Bohr's model of the atom, the magnitude of the magnetic moment of an electron with charge  $e$  and mass  $m_e$  moving in an atomic orbital can be calculated according to:<sup>86</sup>

$$\mu_B = \frac{\hbar e}{2m_e} = 9.274 \cdot 10^{-24} \text{ J/T}. \quad (2-5)$$

Empirically, the magnetic moment of a free electron  $\mu_{e,free}$  was found to deviate from  $\mu_B$ . This is taken into account by introducing a proportionality factor  $g_e$ :

$$\mu_{e,free} = g_e \mu_B \quad (2-6)$$

In eq. (2-6),  $g_e$  is the  $g$ -value of the free electron. An empirical factor of  $g_e = 2$  was introduced by Landé.<sup>87</sup> Later, Dirac derived the same value using relativistic quantum mechanics, thereby showing that the deviation of  $\mu_{e,free}$  from  $\mu_B$  is a relativistic effect.<sup>74,75</sup> Using a more sophisticated approach in the framework of quantum electrodynamics a value of  $g_e = 2.0023193048$  is achieved.<sup>81,88</sup> For electrons in atoms or molecules, the  $g$ -value deviates from the free electron  $g$ -value  $g_e$  owed to spin orbit coupling interactions in first or second order.<sup>56,65</sup> Strong first order  $g$ -shifts only occur for degenerate ground states or when Russell-Saunders coupling is strong (i.e. for heavy elements like lanthanides).<sup>64,65,86</sup> Therefore, first order  $g$ -shifts are not

expected to play an important role for any of the compounds presented herein and are not discussed further. The second order  $g$ -shift occurs in all spin centers and is an anisotropic property. This is represented in the  $g$ -matrix  $\bar{g}$  (also called  $g$ -tensor), whose elements can be calculated using eq. (2-7):<sup>65</sup>

$$g_{ij} = g_e - 2 \lambda_{SOC} \sum_n \frac{\langle \psi_0 | l_i | \psi_n \rangle \langle \psi_n | l_j | \psi_0 \rangle}{E_n - E_0} \quad (2-7)$$

Thus, the  $g$ -values depend on the ground and excited state wave functions  $\psi_0$  and  $\psi_n$ , on their respective energies  $E_0$  and  $E_n$  of these states and on the spin orbit coupling (SOC) constant  $\lambda_{SOC}$ . As  $\lambda_{SOC}$  depends on the effective nuclear charge to the fourth power,<sup>86,89</sup> the expected deviations from the free electron  $g$ -value are the larger the heavier the atom on which the spin density resides. The equation for the energy  $E_{Zee}$  owed to the Zeeman effect depends on the eigenstates  $|\psi\rangle$  of the system and contains  $\bar{g}$  as anisotropic proportionality factor

$$E_{Zee} = \langle \psi | \mu_B \vec{B} \bar{g} \vec{S} | \psi \rangle. \quad (2-8)$$

If the molecules rotate rapidly,<sup>56,90-93</sup> the anisotropy is averaged out and eq. (2-8) is then simplified to yield eq. (2-9)

$$E_{Zee} = \mu_B g_{iso} B_0 \cdot m_s. \quad (2-9)$$

where  $m_s$  can be replaced by  $M_s$  in the case of high-spin ( $S > 1/2$ ) compounds. The isotropic  $g$ -value  $g_{iso}$  in eq. (2-9) is the average of the principal values of  $\bar{g}$  and can be calculated using the trace operation:  $g_{iso} = \frac{1}{3} Tr(\bar{g})$ . In a standard EPR experiment using liquid samples, EPR transitions are only allowed if the EPR selection rule

$$|\Delta m_s| = 1 \quad (2-10)$$

is met, thus the resonance condition for a spin transition is

$$h\nu = \mu_B g_{iso} B_0. \quad (2-11)$$

Eqs. (2-9) and (2-11) give the Zeeman energies of the  $m_s$  states and the excitation energies for allowed EPR transitions. Additionally, it is often useful to define effective Zeeman relations. Such effective Zeeman relations can be used to relate line spacings  $\Delta B$  in multiline EPR spectra to interaction frequencies or to define effective  $g$ -values.<sup>56,94</sup> To complete this subsection, the Zeeman effect is also discussed for

nuclear spins. Although the physics are essentially identical, some differences are noteworthy. The energy of a nuclear spin state can be written as

$$E_{Zee,Nuc} = g_N \mu_N B_0 \cdot m_I. \quad (2-12)$$

The nuclear magneton  $\mu_N$  in eq. (2-12) can be obtained by replacing the electron mass  $m_e$  in eq. (2-5) by the proton mass  $m_p$ .<sup>86</sup> As  $m_p$  is ~1836 times larger than  $m_e$ , nuclear magnetic moments are three orders of magnitude smaller than electron magnetic moments. The nuclear  $g$ -factor  $g_N$  is a nuclide specific proportionality constant.<sup>86</sup> Sometimes,  $g_N \mu_N$  in eq. (2-12) is replaced by the magnetogyric ratio  $\gamma$ . Nuclear spin transitions<sup>i</sup> follow the selection rule

$$|\Delta m_I| = 1 \text{ and } |\Delta m_S| = 0. \quad (2-13)$$

In electron nuclear double resonance (ENDOR, see chapter 2.3.4), NMR and EPR transitions are combined to obtain spectra of the nuclear spin transitions. Transitions in which the magnetic quantum number of the electron spin and a nuclear spin are changed simultaneously can occur if anisotropic interactions are present and are briefly discussed in chapter 2.3.3.

### 2.1.2. Hyperfine Coupling Interaction

Unpaired electrons and nuclei with  $I \neq 0$  possess magnetic moments which give rise to dipolar magnetic fields (cf. Figure 2.1). These dipole fields lift or partially lift the degeneracy of the different  $m_S$  states (or  $m_I$  states, for nuclear spins). The different, interacting spins are said to be coupled. This coupling is called hyperfine coupling (HFC) and the coupling energy  $E_{HFC}$  for the interaction of one electron with one nucleus is given by

$$E_{HFC} = \langle \psi | \vec{S} \vec{A} \vec{I} | \psi \rangle, \quad (2-14)$$

where  $\vec{I}$  is the nuclear spin operator and  $\vec{A}$  the HFC matrix. If several magnetic nuclei and/or several independent unpaired electrons are present, all pair wise electron-nucleus interactions need to be considered in a first order treatment of the HFC interaction. The HFC matrix can be represented in a diagonal form, depending on the choice of the coordinate system.<sup>65</sup>

<sup>i</sup> These transitions are also called NMR transitions, as nuclear spin transitions are the subject of nuclear magnetic resonance (NMR) spectroscopy.

$$\overline{\overline{A}}_{\text{choice of coordinate system}} \overline{\overline{A}}_{\text{diag}} = \begin{pmatrix} A_{XX} & & \\ & A_{YY} & \\ & & A_{ZZ} \end{pmatrix} \quad (2-15)$$

The corresponding coordinate system is called the principal axes systems. In this coordinate system, the elements  $A_{JJ}$  of the HFC matrix bear upper case indices and can be identified as the hyperfine coupling constants (HFCC) observed when the magnetic field is aligned along one of these principal axes. The HFCC generally consists of two contributions:

$$A_{JJ} = a_{iso} + T_{JJ} \quad (2-16)$$

The first term in eq. (2-16) is the isotropic HFCC  $a_{iso}$  and results from a non-zero electron spin density<sup>83</sup>  $Q(0)$  at the magnetic nucleus. The isotropic HFCC is proportional to the magnitude of the magnetic moments  $g\mu_B$  and  $g_N\mu_N$  of the electron and the nucleus, respectively, and can be calculated if  $Q(0)$  is known:<sup>83</sup>

$$a_{iso} = \frac{8\pi}{3} g\mu_B g_N\mu_N \mu_0 \cdot Q(0) \quad (2-17)$$

The second term in eq. (2-16) is an element of the dipolar HFC matrix  $\overline{\overline{T}}$ . The elements of  $\overline{\overline{T}}$  can be calculated using the classical theory of magnetic dipolar interactions. The equation for the general, non-diagonal case is given by eq. (2-18):<sup>65</sup>

$$T_{ij} = \frac{\mu_0 g\mu_B g_N\mu_N}{4\pi r^5} \langle 3ij - r^2\delta_{ij} \rangle \quad (2-18)$$

In eq. (2-18),  $\mu_0$  is the magnetic permittivity of the vacuum and  $\delta_{ij}$  is Kronecker's symbol. The pointy brackets indicate that averaging over the electronic wavefunction has to be performed to calculate the elements of  $\overline{\overline{T}}$ . Anisotropic HFC interactions are averaged out if the molecule tumbles rapidly and the hyperfine splitting energy can then be calculated to first order according to eq. (2-19).<sup>65</sup>

$$E_{HFC} = a_{iso} m_I \cdot m_S, \quad (2-19)$$

In the resulting EPR spectrum,  $a_{iso}$  can then be read off from the separation between two hyperfine lines of the corresponding multiplet signal. The magnitude of the HFC interaction relative to the Zeeman interaction in different spin systems covers a wide range. As an example, for some Cu(II) complexes HFCCs of the order of 500 MHz are observed.<sup>40,95,96</sup> At a field strength of about 350 mT, which is used in most EPR

experiments, the electron Zeeman splitting is of the order of 9.5 GHz, i.e. 18 times more than the HFC interaction. This means that the hyperfine field at the unpaired electron stemming from the Cu nucleus amounts to only 18 mT for a dipolar HFCC of 500 MHz. Therefore, the electron spin is aligned along the external magnetic field and the HFC field can be treated as a small perturbation. In contrast, the nuclear Zeeman splitting of the Cu nucleus only amounts to  $\sim 4$  MHz in the same external magnetic field. Still assuming a dipolar HFCC of 500 MHz, the nuclear Zeeman splitting owed to the external field is 125 times smaller than the dipolar HFC interaction. In this case, the corresponding, dipolar HFC field at the position of the Cu nucleus originating from the unpaired electron can be calculated to amount to  $\sim 43750$  mT. Hence, from the perspective of the nucleus, the HFC field is much stronger than the external magnetic field. As a consequence, the nuclear spin is orientated along the dipolar field of the electron instead of the external magnetic field.<sup>97</sup> The second example is of practical importance and concerns nuclei which are further away from the unpaired electron. For such nuclei, the HFC field caused by the electron spin and the external field are often similar in strength. Therefore, both fields have to be added vectorially to find the quantization axis of the nuclear spin as illustrated in Figure 2.1.

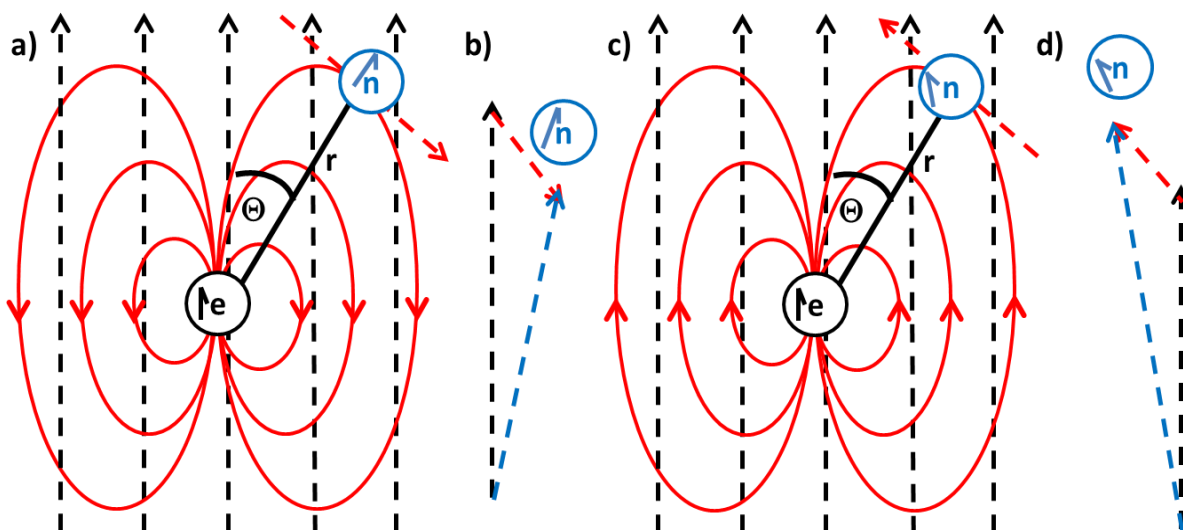


**Figure 2.1.** Orientation of the electron spin  $e$  and its dipolar field (full, red lines) in an external magnetic field (dashed, black arrows) for the (a) spin up and (c) spin down configuration. The nuclear spin  $n$  is oriented along the magnetic field resulting from both the external and the dipolar field of the electron at the nucleus. (b) and (d) illustrate how the resulting field (blue, dashed arrows) experienced by the nuclear spin is formed by vectorial addition of the external field and the dipolar field of the electron spin at the position of the nucleus (red, dashed lines).

In such a situation, changes of the electron spin orientation are accompanied by a change of the quantization axis for the nuclear spin. The realignment of this axis leads to the simultaneous occurrence of allowed ( $|m_s| = 1$  and  $|m_l| = 0$ ) and forbidden transitions ( $|m_s| = 1$  and  $|m_l| \neq 0$ ). This phenomenon is used in ESEEM experiments.<sup>65,66</sup>

### 2.1.3. Electron Dipolar, Zero-Field Splitting, and Exchange Interactions

In this subsection, the effects of electron-electron interaction are discussed. As indicated in the title of this chapter, several types of electron-electron interaction will be differentiated. The first type of interaction is the through-space dipolar interaction between two electron spins which takes place when the two spins are separated far enough so that there is negligible overlap between their spin densities. This is the case for the nitroxide and metal centered spins presented in chapters 6 and 7. There, the magnitude of the dipolar interaction amounts to less than 5 MHz, i.e.  $\sim 0.05\%$  of the microwave (MW) quantum at X-band frequency.<sup>i</sup> It is a purely dipolar magnetic interaction and hence it is described by equations similar to eqs. (2-14) and (2-18), where the nuclear spin has to be replaced by an electron spin:

$$E_{ee} = \langle \psi | \vec{S}_1 \vec{D}_{dip} \vec{S}_2 | \psi \rangle \quad (2-20)$$

$$D_{dip,ij} = \frac{\mu_0 g_1 g_2 \mu_B^2}{4\pi r^5} (3ij - r^2 \delta_{ij}). \quad (2-21)$$

Eq. (2-20) represents the general case, in which averaging over the wavefunctions occurs. Owing to the averaging procedure, it is not always possible to obtain a meaningful interspin separation from the dipolar interaction described by eqs. (2-20) and (2-21), especially if the spins are close to each other and delocalized over several atoms. However, for spins, which are confined to a small area (e.g. localization on a single atom or a bond between two atoms) and are separated far enough to prevent overlap of spin densities, the point dipole approximation is applicable. In this framework an average interspin separation  $r$  can be used and treated as the actual distance between the different electrons. In practice, it is more

---

<sup>i</sup> Normally, MW radiation of constant frequency is used in EPR spectroscopy and the resonance condition is established by varying the magnetic field [eq. (2-11)]. MW sources produce MW radiation which belongs to a certain frequency band. These bands are labelled by letters. Important MW bands often encountered in the field of EPR spectroscopy include the X-, Q-, and W-band with frequencies of approximately 9.5, 35, and 95 GHz, respectively.<sup>65,67</sup>

convenient to use the spherical coordinates  $r$ ,  $\theta$ , and  $\phi$  instead of the Cartesian coordinates  $x$ ,  $y$ , and  $z$  (Figure 2.2). Then, the operator in eq. (2-20) can be rewritten using the so-called dipolar alphabet<sup>67,72</sup>

$$\vec{S}_1 \vec{D}_{dip} \vec{S}_2 = \frac{\mu_0 g_1 g_2 \mu_B^2}{4\pi h r^3} (A + B + C + D + E + F). \quad (2-22)$$

The single terms of the dipolar alphabet are given by eqs. (2-23) - (2-28):

$$A = S_{1z} S_{2z} (1 - 3\cos^2\theta) \quad (2-23)$$

$$B = -\frac{1}{4} (S_1^+ S_2^- + S_1^- S_2^+) (1 - 3\cos^2\theta) \quad (2-24)$$

$$C = -\frac{3}{2} (S_1^+ S_{2z} + S_{1z} S_2^+) \sin\theta \cos\theta \cdot e^{-i\phi} \quad (2-25)$$

$$D = -\frac{3}{2} (S_1^- S_{2z} + S_{1z} S_2^-) \sin\theta \cos\theta \cdot e^{i\phi} \quad (2-26)$$

$$E = -\frac{3}{4} S_1^+ S_2^+ \sin^2\theta \cdot e^{-2i\phi} \quad (2-27)$$

$$F = -\frac{3}{4} S_1^- S_2^- \sin^2\theta \cdot e^{2i\phi} \quad (2-28)$$

In eqs. (2-24) - (2-28), the raising and lowering operators  $S^+$  and  $S^-$  have been introduced. These operators are defined by eqs. (2-29) and (2-30)

$$S^+ = S_x + iS_y \quad (2-29)$$

$$S^- = S_x - iS_y \quad (2-30)$$

and have the effect of raising and lowering the magnetic spin quantum number  $m_s$  by 1, respectively. The effect of each term in the dipolar alphabet may be understood by considering a two-spin system in an external magnetic field. The energy  $E$  of the two-spin system is determined by the Zeeman energy of electrons 1 and 2 ( $E_{Zee,1}$  and  $E_{Zee,2}$ , respectively) and their interaction energy  $E_{ee}$ .

$$E = E_{Zee,1} + E_{Zee,2} + E_{ee} \quad (2-31)$$

Importantly, the Zeeman terms are assumed to strongly exceed  $E_{ee}$ , which is the case for biradicals under the standard experimental conditions where MW frequencies of 9.5 GHz are used. Then, the Zeeman interaction can be considered first and the electron-electron interaction can be introduced as a perturbation to the



Zeeman operator. Taking the products of the individual spin functions  $|\alpha\rangle$  and  $|\beta\rangle$  as basis yields four basis functions  $|1\rangle - |4\rangle$ :

$$|1\rangle = |\alpha_1\alpha_2\rangle \quad (2-32)$$

$$|2\rangle = |\alpha_1\beta_2\rangle \quad (2-33)$$

$$|3\rangle = |\beta_1\alpha_2\rangle \quad (2-34)$$

$$|4\rangle = |\beta_1\beta_2\rangle \quad (2-35)$$

In this basis, the Zeeman operators of spins 1 and 2 are diagonal (see chapter 2.1.1) and give the total Zeeman energies  $E_{Zee,tot}$

$$E_{Zee,tot}(|1\rangle) = \frac{1}{2}\mu_B B_0(g_1 + g_2) \quad (2-36)$$

$$E_{Zee,tot}(|2\rangle) = \frac{1}{2}\mu_B B_0(g_1 - g_2) \quad (2-37)$$

$$E_{Zee,tot}(|3\rangle) = \frac{1}{2}\mu_B B_0(-g_1 + g_2) \quad (2-38)$$

$$E_{Zee,tot}(|4\rangle) = -\frac{1}{2}\mu_B B_0(g_1 + g_2) \quad (2-39)$$

The  $A$  term of the dipolar operator is also diagonal in this basis and yields the dipolar interaction energies to first order if all other terms of the dipolar alphabet can be ignored. This is the case for unlike spins, in which

$$\Delta E_{Zee} = |E_{Zee,tot}(|2\rangle) - E_{Zee,tot}(|3\rangle)| \gg E_{ee}. \quad (2-40)$$

Eq. (2-40) is met for the examples discussed in chapters 6 - 7. It is customary to define  $\nu_{dip}$ , which can be expressed as function of  $r$  and  $\theta$ , using spherical coordinates (Figure 2.2):

$$\nu_{dip} = \frac{\mu_0 g_1 g_2 \mu_B^2}{4\pi h r^3} (3\cos^2\theta - 1). \quad (2-41)$$

In the absence of orientational selection, measurement of the dipolar interaction according to eq. (2-41) in frozen solution<sup>i</sup> gives rise to a so-called Pake pattern if the EPR spectrum of the observed spin is not distorted by other anisotropic interactions

<sup>i</sup> In liquid solution the dipolar interaction is averaged out to zero ( $\text{Tr}(\bar{D}_{dip})=0$ ) unless the rotational motion of the spin centers is hindered.

like  $g$ -anisotropy or HFC to nearby nuclei (Figure 2.2b). The dipolar coupling frequency at  $\theta = 90^\circ$ , the so-called perpendicular orientation, can be obtained by measuring the separation  $\Delta B$  between the two singularities of the Pake pattern.  $\Delta B$  can be converted to frequency units by using  $\nu_{dip} = \frac{g\mu_B\Delta B}{h}$  in the case of coupling between two unlike  $s = \frac{1}{2}$  spins (see chapter 2.1.1). The side wings are separated by two times  $\Delta B$  and correspond to the parallel orientation, i.e.  $\theta = 0^\circ$ .

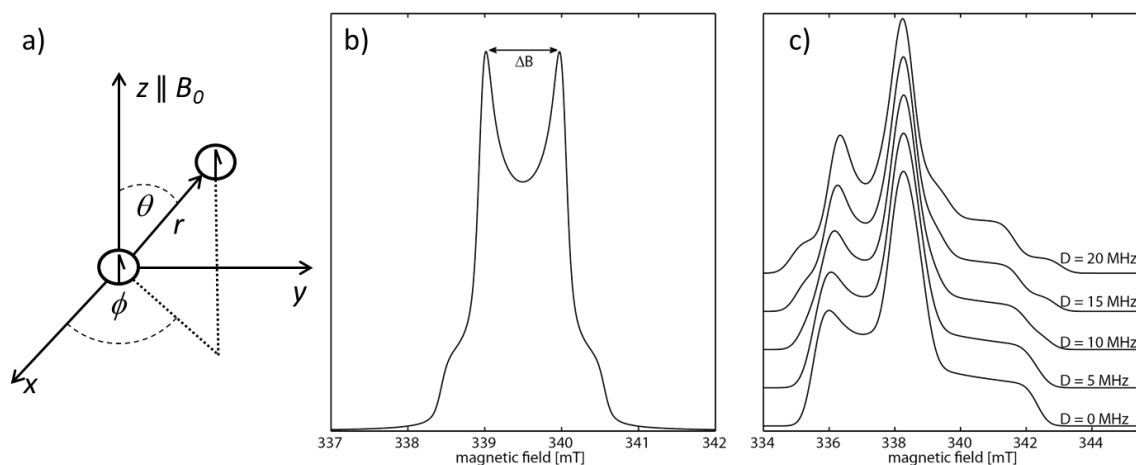


**Figure 2.2.** a) Dipolar spin-spin interaction in Cartesian coordinates ( $x, y, z$ ) or spherical coordinates ( $r, \theta, \phi$ ). b) Simulated cw EPR spectrum in the shape of a Pake pattern for a spin center which would have a single line, isotropic EPR spectrum in the absence of electron-electron interaction. c) Simulated nitroxide cw EPR spectra in the presence of dipolar electron-electron coupling of different magnitudes. Simulation parameters:  $g_{xx} = 2.095$ ;  $g_{yy} = 2.0075$ ;  $g_{zz} = 2.0025$ ;  $A_{xx} = 15$  MHz;  $A_{yy} = 15$  MHz;  $A_{zz} = 95$  MHz, linewidth  $0.65$  mT  $\approx 18.3$  MHz. The parameter  $D$  is defined in eq. (2-48).

The analysis is more complicated if the EPR spectrum is distorted by additional anisotropic interactions. Then, the EPR spectrum results from a convolution of the Pake pattern owed to the electron-electron interaction with the anisotropic EPR spectrum caused by the other anisotropic EPR parameters of the spin Hamiltonian. In such cases, an analysis of the dipolar coupling is only possible if the anisotropic electron-electron interaction is resolved and not obscured by other line broadening effects. At an interspin separation of 1 nm the frequency at the singularities of the Pake pattern amounts to  $\sim 52$  MHz. This clearly exceeds the linewidth of nitroxides (see for example chapters 6 and 7) and many other organic spin centers.<sup>98</sup> Therefore, a dipolar interaction of this magnitude leads to an additional, characteristic broadening of the EPR spectrum and can be measured using cw EPR spectroscopy for such distances. At interspin separations of  $\geq 2$  nm the dipolar interaction frequency  $\nu_{dip}$  is reduced to  $\leq 6.5$  MHz. Such small interactions are usually obscured by the

linewidth and pulsed methods have to be applied to resolve them (chapter 2.3.5).<sup>66</sup> Distances in between 1 and 2 nm represent borderline cases (also see the discussion of the  $B$  term of the dipolar alphabet given below).<sup>67,99</sup> Figure 2.2c shows simulated cw EPR spectra distorted by dipolar interactions of different magnitude. The simulations indicate that the lineshape of the EPR spectrum changes and new features like shoulders arise in the spectrum as the magnitude of the electron-electron interaction increases. The analysis of the electron-electron interaction gets more complicated in the case of electron delocalization. As already mentioned above, an effective interspin distance is used in eq. (2-41) which may be an inappropriate description of the actual interelectron distance in the case of strong electron delocalization. In such cases, the distributed dipole model can be used if the dipolar interactions occur between two delocalized spin centers which are separated far enough.<sup>100</sup> A detailed discussion concerning the applicability of different models from a theoretical viewpoint is given by Riplinger *et al.*<sup>101</sup> Riplinger's study also accounts for the occurrence of exchange interactions, which are often neglected in biradicals.<sup>i</sup>

The  $B$  term of the dipolar alphabet contains products of the raising and lowering operators. These products change the magnetic spin quantum numbers of the two spins in opposite directions and therefore connect states  $|2\rangle$  and  $|3\rangle$ . The  $B$  term is also called pseudo-secular term, since the total change of magnetic quantum numbers  $\Delta m_{s,tot}$  amounts to zero:

$$\Delta m_{s,tot} = \Delta m_{s,1} + \Delta m_{s,2} = 0. \quad (2-42)$$

The pseudo-secular term becomes important in the case of similar or like spins 1 and 2. In the case of like spins, the total Zeeman energies of states  $|2\rangle$  and  $|3\rangle$  defined by eqs. (2-37) and (2-38) are zero. Thus, the elements of the  $B$  operator can no longer be neglected, as they are of the same order as the terms of the  $A$  operator. States  $|2\rangle$  and  $|3\rangle$  are then degenerate and mix to zero-order. Appropriate zero-order wavefunctions for like spins which are diagonal in the  $A + B$  operator are

$$|2_{like}\rangle = \frac{1}{\sqrt{2}}(|2\rangle + |3\rangle) \quad (2-43)$$

---

<sup>i</sup> However, it has been pointed out by Jeschke<sup>24</sup> that the dipolar approximation appears to be more robust than predicted by Riplinger *et al.*

and

$$|3_{like}\rangle = \frac{1}{\sqrt{2}}(|2\rangle - |3\rangle). \quad (2-44)$$

These wavefunctions are identical to the singlet and triplet wavefunctions of an  $S = 1$  system.<sup>65</sup> The functions  $|1\rangle$  and  $|4\rangle$  remain unaltered. The dipolar interaction observed in the case of like spins is 50 % larger than the dipolar interaction in cases where only the  $A$  term needs to be considered.<sup>67,72</sup> Then, eq. (2-41) can be used after introducing a factor of  $3/2$ . The most complicated situation is encountered, if the operator  $B$  needs to be taken into account because the spins are unlike and eq. (2-40) does not hold. In such cases, appropriate wavefunctions have to be derived by diagonalizing the Hamiltonian matrix before the magnitude of the dipolar interaction can be calculated.<sup>72,99</sup> Jeschke and Polyhach give a value of  $\Delta E_{Zee} = 65 \text{ MHz}$  to measure interspin separation as short as 1.5 nm between nitroxide spin pairs without having to consider the pseudo-secular term  $B$  of electronic dipolar interaction operator.<sup>102</sup> However, it has been pointed out that pseudo-secular contributions might be more important for pairs of gadolinium(III) high spin centers with low zero-field splitting (ZFS, see below for a discussion).<sup>103</sup>

The dipolar operators  $C$  and  $D$  connect both the functions  $|2\rangle$  and  $|3\rangle$  with either  $|1\rangle$  or  $|4\rangle$ , respectively, while operators  $E$  and  $F$  connect  $|1\rangle$  with  $|4\rangle$ . In other words, operators  $C - F$  are off-diagonal (i.e. non-secular) in the basis given by eqs. (2-32) - (2-35)<sup>i</sup> and connect states with different Zeeman energies. Since the Zeeman energies are much larger than the electron interaction energy  $E_{ee}$ , the contributions of the non-secular terms are negligible under standard experimental conditions.<sup>67,72</sup>

The second type of electron-electron interaction will be called zero-field splitting (ZFS) and occurs in the spin Hamiltonian whenever several electrons are centered in close proximity, for example electrons in a transition metal ion. In such a situation, the electrons can no longer be treated as individual spin centers but have to be treated as a single high-spin ( $S > 1/2$ ) center. Owing to the close proximity of the electrons in a high-spin center, the ZFS is usually much larger than the dipolar interaction mentioned above (see chapter 7 for an example). Clearly, close proximity is a relative term and cannot be defined exactly. In this respect, the distinction between ZFS and the dipolar interaction is related to the situation in chemical

---

<sup>i</sup> They are also off-diagonal in the basis used for like spins.

compounds bearing two (or more) unpaired electrons. There, it is not always possible to clearly distinguish between a biradical (two spin centers, each carrying one unpaired electron, leading to purely dipolar, through-space electron-electron interaction) and a single high-spin center which carries two, strongly coupled electrons (leading to ZFS).<sup>56</sup> An example for the simultaneous occurrence of both interactions is given by Cohen *et al.*<sup>104</sup> Concerning the spin-spin interaction, it is clearly no longer possible to obtain a meaningful interspin separation  $r$  like in the point dipole model. Instead, an effective value of  $r$  can be obtained using eq. (2-20) after averaging over the electron wavefunctions.<sup>65</sup> Dipolar spin-spin interactions represent the main source of the ZFS in organic triplet molecules.<sup>56,65,105</sup> However, the ZFS arises not only from dipolar spin-spin coupling but also from spin orbit coupling.<sup>64,65</sup> If heavier elements carry the spin density, the spin orbit coupling (SOC) contribution to the ZFS becomes increasingly important. In fact, as the SOC contribution increases with the fourth power of the effective nuclear charge,<sup>86</sup> it is often treated as the main or even sole source of ZFS in transition metal complexes.<sup>64,106</sup> Although this approximation leads to satisfying results in some cases like hexaqua chromium(II/III)<sup>107</sup> or some tetrahedral Co(II) complexes,<sup>108</sup> the importance of dipolar contributions to the ZFS has been recognized for other transition metal complexes having manganese central ions in oxidation state II, III or IV.<sup>106,109–113</sup> The spin Hamiltonian of the SOC-ZFS is formally identical to eq. (2-20).

$$E_{ee} = \langle \psi | \vec{S}_1 \vec{\bar{D}}_{SOC} \vec{S}_2 | \psi \rangle \quad (2-45)$$

The SOC-ZFS can be derived along the lines of 2<sup>nd</sup> order perturbation theory similarly to the  $g$  shifts (chapter 2.1.1). Then,  $\vec{\bar{D}}_{SOC}$  is sometimes related to  $\vec{\bar{g}}$ :<sup>56,65</sup>

$$\vec{\bar{D}}_{SOC} = \frac{\lambda_{SOC}}{2} (\vec{\bar{g}} - g_e \vec{\bar{E}}) \quad (2-46)$$

In eq. (2-46),  $\vec{\bar{E}}$  is the unity matrix. As a consequence of eq. (2-46),  $\vec{\bar{D}}_{SOC}$  is in general not traceless (in contrast to  $\vec{\bar{D}}_{dip}$ ). From the above discussion it is clear that both the spin-spin and the SOC-ZFS tensors have to be considered in general, leading to a ZFS tensor  $\vec{\bar{D}}$  of

$$\vec{\bar{D}} = \vec{\bar{D}}_{SOC} + \vec{\bar{D}}_{dip}. \quad (2-47)$$

Eq. (2-46) allows to separate the SOC and the dipolar contributions to the ZFS experimentally.<sup>56,65</sup> To do so, one has to determine the  $\bar{g}$  and  $\bar{D}$  experimentally. The splitting of the EPR spectrum owed to  $g$ -anisotropy is proportional to the external magnetic field while all other terms in the spin Hamiltonian do not depend on the external field. Therefore, the  $g$ -tensor can be obtained experimentally by application of multi-frequency EPR spectroscopy. Analysis of the experimental  $\bar{g}$  using eq. (2-7) allows estimating the value of the SOC constant  $\lambda_{SOC}$ . Then, the SOC part of the zero-field splitting can be calculated using eq. (2-46). The difference between the experimental and the calculated  $\bar{D}$  is the dipolar contribution to the ZFS. However, some care must be taken in using eq. (2-46). Application of eq. (2-46) appears to be possible in some cases (see references in the books of Atherton<sup>65</sup> and Rieger<sup>56</sup> as well as the study by Sundararajan *et al.*<sup>108</sup>). However, eq. (2-46) can only be applied if spin flip transitions do not contribute to the SOC-ZFS, as has been pointed out by Neese and Solomon.<sup>114</sup> The importance of spin-flip transitions has been confirmed in later studies for various types of transition metal complexes.<sup>106,107,109–114</sup> From the discussion and the cited examples it is also clear that the ZFS has various origins and that there is no simple approach to analyse this interaction on a theoretical basis.<sup>i</sup> Aside from the origin of the ZFS, its magnitude is of great practical importance. If the magnitude of the ZFS is comparable to the used MW quantum,  $M_s$  is no longer a good quantum number as states of different  $M_s$  are mixed by the ZFS.<sup>65</sup> Furthermore, the magnitude of the ZFS exceeds the X-band MW quantum in many transition metal complexes.<sup>116,117</sup> Such complexes are EPR silent at X-band frequencies if the degeneracy of all electron spin levels in absence of an external magnetic field is lifted by the ZFS. However, this is never the case for high-spin centers with half-integer spin quantum numbers owed to the symmetry of the ZFS term in the spin Hamiltonian.<sup>65</sup> In such complexes, so-called Kramer's doublets occur. These doublet levels behave like effective  $S = 1/2$  spin levels. Nonetheless, rapid relaxation or strong linewidth broadening can obscure the EPR signals of Kramer's systems (one example is given in chapter 7). The consequences of large magnitude ZFS interactions make high frequency EPR a prerequisite for detailed experimental studies in most cases, making an experimental analysis of the ZFS very demanding.<sup>116,117</sup> Finally, the parameters  $D$  and  $E$  (in frequency units) are introduced

---

<sup>i</sup> Even for organic radicals, where the SOC contributions are often negligible, theoretical predictions of the ZFS are often disappointing.<sup>115</sup>

in eqs. (2-48) and (2-49). These parameters are related to the elements of  $\bar{D}$  in its principal axis system, i.e. in the axis system where  $\bar{D}$  is diagonal.

$$D = \frac{D_{ZZ} - \frac{1}{2}(D_{XX} + D_{YY})}{h} \quad (2-48)$$

$$E = \frac{\frac{1}{2}(D_{XX} - D_{YY})}{h} \quad (2-49)$$

The parameters  $D$  and  $E$  are conventionally used when treating ZFS interactions.

The last type of interaction is the exchange interaction. Here, only the isotropic exchange interaction is discussed briefly. Depending on the orientation of the magnetic orbitals,<sup>118–120</sup> this interaction leads to the preference of either an antiferromagnetic or ferromagnetic ordering of two or more electron spins. In other words, this interaction is the main driving force for antiparallel or parallel spin pairing. In the majority of cases, the interaction is very strong and leads to spin pairing in antiparallel fashion,<sup>84</sup> the prime examples being electron pairing in inner shells of atoms and chemical two-electron-two-center bonds.<sup>83</sup> In other cases, the interaction is very strong but leads to parallel alignment of the spins, for example high-spin states in transition metal ions. As long as the magnitude of the exchange interaction clearly exceeds the other terms in the spin Hamiltonian, it is not necessary to introduce an explicit term for the exchange interaction in the spin Hamiltonian.<sup>83</sup> In such situations, the excited spin states are not accessible thermally and it is sufficient to only consider the spin quantum number  $S$  of the ground state. However, if this interaction is of similar magnitude as the other terms in the spin Hamiltonian this leads to mixing of states of different multiplicities and heavily complicates the behavior of the spin system. When two spins are separated by saturated linkers at a distance of more than 1.5 nm, isotropic exchange interactions can usually be neglected when investigating the spin-spin interaction.<sup>102</sup> The exchange interaction will not be treated further herein, as it was not investigated in any of the examples presented below. Detailed discussions including non-isotropic exchange are given by Atherton,<sup>65</sup> Rieger,<sup>56</sup> and Bencini.<sup>84</sup>

#### 2.1.4. Nuclear Quadrupole Coupling

The nuclear quadrupole coupling (NQC) occurs for nuclei with a nuclear spin quantum number  $I > \frac{1}{2}$ . The Hamiltonian operator  $\mathcal{H}_{NQC}$  is formally identical to that of the ZFS in that two spin operators and one coupling matrix occur in  $\mathcal{H}_{NQC}$ :

$$\mathcal{H}_{NQC} = \vec{I}\bar{Q}\vec{I} \quad (2-50)$$

The quadrupole interaction tensor  $\bar{Q}$  in eq. (2-50) is traceless. The energy of the electron spin transitions is not affected by the NQC to first order, as the nuclear spin quantum number does not change in an EPR transition obeying the selection rule  $|\Delta m_s| = 1$  and  $|\Delta m_I| = 0$ .<sup>65</sup> However, the NQC can lead to the occurrence of forbidden transitions. These can be observed as satellites of the EPR spectrum in some cases.<sup>65</sup> In hyperfine EPR spectroscopies such as ESEEM or ENDOR (chapters 2.3.3 and 2.3.4), the effects of NQC can often be very clearly observed (an example is presented in chapter 10).<sup>64-66</sup> In these experiments, the transitions between nuclear spin states are probed. The energy shift of these states caused by the NQC leads to an increased number of observable nuclear spin transitions and has a large influence on their intensities as well. Occurrence of NQC complicates the interpretation of hyperfine spectra considerably. However, this interaction can be used to probe the surroundings of nitroxide spin centers, as the magnitude of the NQC is influenced by the polarity of the environment of the nitroxide.<sup>67,121</sup>

#### 2.2. Relaxation

Before any pulsed EPR experiment can be discussed, it is necessary to extend the theory developed in the previous chapters to include relaxation effects. So far, only  $\mathcal{H}_S$  has been discussed, which yields the energy levels of a microscopic system, e.g. a single spin. However, EPR experiments are conducted on macroscopic samples which contain large ensembles of spin centers. At a given temperature, such a sample has a certain degree of equilibrium magnetization which can be calculated using the energy levels predicted by the complete spin Hamiltonian [eq. (2-1)] and Boltzmann's law.<sup>122</sup> The MW irradiation used during an EPR experiment changes the magnetization of the investigated spin system. Importantly, continuous MW radiation would lead to equal population of all electron spin states (saturation) in the absence of processes which reestablish the equilibrium magnetization. Such processes are



called relaxation processes. As before, only a few important aspects of relaxation are discussed herein while more detailed and formal accounts are given by others.<sup>64–66,123</sup> First of all, magnetization along the z-axis,  $M_z$ , needs to be distinguished from magnetization in the xy-plane,  $M_{xy}$ . The equilibrium magnetization  $M_{0,z}$  along the z-axis (longitudinal) is predicted by Boltzmann's statistics, whereas magnetization in the xy-plane (transversal) amounts to zero in an equilibrium situation. Transversal magnetization can be created by application of MW radiation and is used to detect EPR signals in pulsed EPR experiments (see chapter 2.3).<sup>65</sup> Correspondingly, two different relaxation processes occur for the two types of magnetization. These processes are called longitudinal and transversal relaxation. The former reinstalls a spin state distribution which follows Boltzmann's law while the latter destroys only the magnetization in the xy-plane. Importantly, longitudinal relaxation always leads to a change of the total energy of the spin system in contrast to transversal relaxation, during which the total energy of the system is conserved.<sup>64,69,123</sup> Therefore, the spin system needs to exchange energy with the surrounding lattice (e. g. the solvent) to relax longitudinally.<sup>i</sup> This can occur via different spin phonon coupling mechanisms where the spin system interacts with its surroundings.<sup>64,66,123</sup> During transversal relaxation, the spins of the spin system interact with each other.<sup>ii</sup> The time scales on which the two relaxation processes occur are characterized by the longitudinal and transversal relaxation times  $T_1$  and  $T_2$ , respectively. Since longitudinal relaxation reestablishes the Boltzmann distribution in the spin system, in which the transversal magnetization is zero,  $T_1 \geq T_2$  always holds. If only one (apparent) relaxation process leads to relaxation, both longitudinal and transversal relaxation can be described using single exponential decay functions.<sup>65,66,123</sup> For the return to equilibrium magnetization  $M_0$  via longitudinal relaxation this yields

$$M_z = M_{0,z} \cdot \left(1 - a e^{-\frac{t}{T_1}}\right). \quad (2-51)$$

Eq. (2-51) predicts, that for times  $t \gg T_1$  the longitudinal magnetization equals the equilibrium magnetization (i.e.  $M_z = M_{0,z}$ ) as demanded at thermal equilibrium, starting from an initial magnetization of  $M_{0,z} \cdot (1 - a)$  at  $t = 0$ . The value of  $a$  is

---

<sup>i</sup> Longitudinal relaxation is also called spin lattice relaxation.

<sup>ii</sup> Transversal relaxation is also called spin-spin relaxation.

determined by the type of experiment (cf. chapter 2.3.2 and chapters 6 and 7 for examples). If only one relaxation mechanism is active, the decay of transient, transversal magnetization  $M_{xy}$  is given by

$$M_{xy} = M_{xy,ini} \cdot e^{-\frac{t}{T_2}}, \quad (2-52)$$

where  $M_{xy,ini}$  is an initial, non-equilibrium magnetization in the  $xy$ -plane, which can be created by MW pulses (see chapter 2.3 and its subchapters). In practice, single exponentials are rarely observed and instead biexponential or multiexponential behavior is encountered. Experimentally, the decay of the primary echo in dependence of the interpulse separation is used to estimate the spin-spin relaxation time  $T_2$  (see chapters 2.3.1 and 2.3.3). In most experiments however, the echo decays with the phase memory time  $T_M$  rather than with  $T_2$  (eq. (2-52) can still be applied if  $T_2$  is replaced by  $T_M$ ). The phase memory time  $T_M$  contains contributions of spectral-, spin- and instantaneous diffusion while actual spin-spin relaxation stems only from spin flip flop transitions.<sup>66,123</sup>

## 2.3. Pulsed EPR Experiments

Pulsed EPR spectroscopy offers a variety of different pulse sequences to selectively address certain terms of the spin Hamiltonian experimentally. In contrast to cw EPR spectroscopy, the response of the spin system after application of a short period of strong MW radiation is detected. The pulsed EPR experiments used for the studies in the following chapters will be discussed qualitatively. For a quantitative or semiquantitative treatment one can use the density matrix<sup>65,66,124</sup> or product operator formalism.<sup>125</sup> Both of these formalisms describe the evolution of magnetization and magnetic coherences (these are the detectable signals in the  $xy$ -plane) during an actual EPR experiment. The experimental hardware is described in the literature, useful reviews can be found in the books of Bender *et al.*<sup>68</sup> and Poole.<sup>69</sup>

### 2.3.1. Spin Echo

In EPR spectroscopy, coherent, linearly polarized MW radiation is used to induce spin state transitions. The magnetic field component  $B_1$  of the radiation is aligned perpendicular to the external magnetic field. If the magnetic field component of the MW radiation is defined to lie along the  $x$ -axis, the magnetization vector is turned

from the z-axis to the y-axis, then further on to the negative z-axis and so on. The behavior of the magnetization vector can be determined using Bloch's equations.<sup>65</sup> In pulsed EPR experiments, MW pulses can be adjusted in their length and field strength to achieve a specific flipping angle of the magnetization.<sup>65,66</sup> Specifically, a  $\pi/2$ -pulse transfers magnetization coherently from the z-axis to the xy- plane, i.e. creates a coherent state for the spin ensemble. These coherent states (in short: coherences) of the spin system can be detected as time dependent magnetization in the xy-plane. Since this magnetization is induced by the MW radiation and decays freely (without any further interaction with radiation) over time, the resulting behavior of the spin system is also called free induction decay (FID). In principle, a single pulse would be enough to create and to observe an FID as the EPR signal, which is in fact the standard experiment in nuclear magnetic resonance (NMR) spectroscopy. A consequence of the finite length of the excitation pulse is its finite width in the frequency domain which leads to the simultaneous excitation of spins with different precession frequencies.<sup>i</sup> Then, the superposition of the different precession frequencies within the spin packet excited by the finite width pulses gives rise to a modulated FID. Fourier transformation of this FID yields the transition frequencies contributing to the spin packet.<sup>125</sup> However, this kind of experiment is usually not feasible in EPR spectroscopy, since both the excitation width  $\Delta\nu_{exc}$  and the spectral width  $\Delta\nu_{spec}$  usually exceed 50 MHz in EPR experiments. Thus, the excited spin packets have a distribution of precession frequencies exceeding 50 MHz, leading to defocussing of the coherences on a time scale of 20 ns. Such short FIDs cannot be recorded owed to the spectrometer dead-time.<sup>66</sup> However, the defocussing of the FID does not stem from relaxation, which is irreversible, but from inhomogeneous broadening of the EPR transitions. Defocussing owed to inhomogeneous broadening can be reversed by application of a second pulse after an evolution period  $\tau$ . This leads to the refocussing of the coherences at time  $t = 2\tau$ . The resulting signal is called a spin echo and can be described as a back-to-back FID. Spin echoes can be formed by different pulse sequences and are the basis for most EPR experiments. The first successful spin echo EPR experiment conducted by Hahn used two  $\pi/2$ -pulses.<sup>126</sup> Another obvious choice of pulse lengths to create a two-pulse echo

---

<sup>i</sup> The time and the frequency domain are related via the Fourier transform relation.<sup>66,125</sup> Therefore, an MW pulse (or a radio frequency pulse in NMR) always excites several, different spin transitions, giving rise to a spin packet.

corresponds to flipping angles of  $\pi/2$  and  $\pi$  (Figure 2.3a). This sequence is also part of the three- and four-pulse PELDOR sequence and other EPR sequences (see chapters 2.3.2 - 2.3.4 and 2.3.6). The stimulated echo (SE) experiment is shown in Figure 2.3b. It is the basis for other EPR experiments, an important example in this work being the RIDME experiment (see chapter 2.3.7).<sup>66</sup> In the standard SE experiment, the coherence created by the first  $\pi/2$ -pulse is subjected to a second  $\pi/2$ -pulse after a period  $\tau$ , thereby creating a polarization grating along the z-axis.<sup>i</sup> A third  $\pi/2$ -pulse after a time  $T$  brings the polarization grating back into the xy-plane where it refocuses after another period  $\tau$ . The polarization grating usually decays much slower than the coherences in the xy-plane would. This allows application of further pulses between the second and third pulse.<sup>66</sup> Noteworthy, the SE sequence also creates a virtual echo (VE) at a time  $\tau$  before the third pulse, or, more precisely, the spin system behaves as if the VE was formed at time  $\tau$  before the third pulse (the VE cannot be observed directly).<sup>66,127</sup> To observe the VE, it has to be refocused by application of a fourth pulse to yield an observable, refocused virtual echo (RVE).

### 2.3.2. Inversion Recovery

The inversion recovery (IR) experiment is used to measure the spin lattice relaxation time  $T_1$  of a spin system.<sup>66</sup> The IR sequence usually consists of a  $\pi$ -pulse which is applied at a time  $T$  before a two-pulse echo sequence (Figure 2.3c). This additional pulse leads to an inversion of the magnetization  $M_z$  [meaning  $a = 2$  in eq. (2-51)]. Since the echo intensity in the two-pulse echo experiment is proportional to the magnetization  $M_z$  an echo with negative intensity is formed if relaxation during the interpulse separation  $T$  is negligible. Eq. (2-51) suggests that the echo intensity can be fitted as a function of  $T$  to obtain an estimate of the spin lattice relaxation time  $T_1$ . In practice, it is often necessary to use biexponential functions (or even higher order exponentials) to obtain a good fit. This might indicate the occurrence of several relaxation pathways.<sup>123</sup> During inversion recovery, the echo intensity of the inverted spin centers amounts to zero at a separation of  $\sim 0.7 T_1$  between the inversion pulse and the following pulse sequence. This can be used to selectively suppress signals in samples which contains several species.<sup>128,129</sup>

---

<sup>i</sup> The alignment of a spin belonging to a certain spin packet after the second pulse depends on its precession frequency. The polarization grating is a function which describes the z-component of the spin orientation in dependence on their precession frequency.<sup>66</sup>

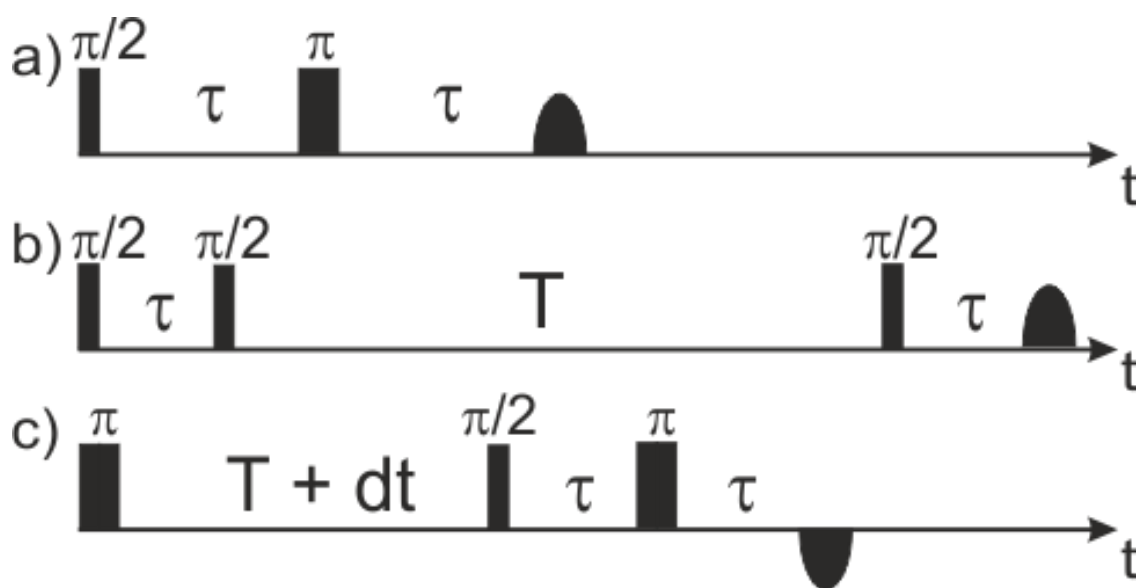


**Figure 2.3.** a) Two-pulse primary echo sequence. b) Stimulated echo sequence. c) Inversion recovery sequence, the interval  $T$  being incremented.

### 2.3.3. Electron Spin Echo Envelope Modulation

As stated above, anisotropic interactions (for example anisotropic HFC and NQC) can lead to the occurrence of forbidden electron spin transitions in which  $|\Delta m_l| \neq 0$ . Therefore, spin echoes contain contributions from coherences caused by allowed and forbidden transitions. These are phase shifted according to the difference in the respective precession frequencies and evolution times in the  $xy$ -plane. In electron spin echo envelope modulation (ESEEM) experiments, the superposition of phase shifted echoes from different coherence pathways is used to obtain a modulated echo decay curve by measuring the echo intensity as a function of the interpulse separation. The modulation frequencies are obtained by Fourier transformation of these time traces and provide information about nuclear transition frequencies.<sup>66,130,131</sup> The two basic sequences, two-pulse and three-pulse ESEEM, are identical to the echo sequences depicted in Figure 2.3a and 2.3b. In two-pulse ESEEM experiment the interval  $\tau$  is incremented to obtain a modulated time trace of the echo intensity while in three-pulse ESEEM the interval  $T$  between the second and the third pulse is incremented. The modulation is introduced by the superposition of electron spin coherences from allowed and forbidden transitions in two-pulse ESEEM. In three-pulse ESEEM, the superposition of nuclear coherences stemming from allowed and forbidden transitions after the second pulse are responsible for the occurrence of the echo modulation.<sup>66</sup> The third  $\pi/2$ -pulse in the three-pulse

experiment transfers the nuclear coherences to electron coherences, which allows observing the echo modulation. If the echo intensity is modulated by more than one nuclear frequency, the resulting time traces can often be approximately treated as product functions of individual modulation functions.<sup>66,130,131</sup> This is the case for most experiments in which the echo intensity is modulated and can lead to the occurrence of multispin effects (see chapter 6). Many modifications of these ESEEM sequences have been introduced to eliminate shortcomings of these experiments such as dead-times, to facilitate the assignment of modulation frequencies to nuclear transitions, and to suppress of certain transitions.<sup>66,128,132–134</sup> In this work, ESEEM was not primarily used to obtain information about nuclear transitions (an exception can be found in chapter 7, further examples are in the reviews<sup>25,51,135,136</sup>). Instead, two-pulse ESEEM was used to obtain  $T_M$  (see chapter 2.2, eq. (2-52) and chapters 6 and 7) while the three-pulse ESEEM sequence forms the basis for the RIDME experiment discussed in section 2.3.7. In the case of RIDME, the ESEEM modulations caused by nuclear transitions give rise to unwanted peaks in the Fourier transform and have to be suppressed to improve the data quality (chapters 6 and 7).

#### 2.3.4. Electron Nuclear Double Resonance

Electron nuclear double resonance (ENDOR) is another experiment to resolve small HFC interactions. In ENDOR, radio frequency (RF) radiation is used to excite nuclear spin transitions which affect the intensity of an electron spin transition. Usually, the field is kept constant while the RF is swept. The intensity of the electron spin transition is used to monitor the nuclear spin transitions. Here, only the echo detected Davies<sup>137</sup> and Mims<sup>138</sup> ENDOR sequences (Figure 2.4) are discussed, as these two sequences have been used in this work (chapter 10). More detailed discussions of ENDOR including some applications can be found in the literature.<sup>25,26,66</sup>

The Davies ENDOR sequence is depicted in Figure 2.4a and can be explained using Figure 2.4c. Before the first pulse, the spin states are populated according to the Boltzmann distribution (**1** in Figure 2.4c). An MW  $\pi$ -pulse inverts the population of two electron spin states leading to the situation depicted under **2** in Figure 2.4c. Then, an RF  $\pi$ -pulse is used to excite nuclear spin transitions, its frequency being swept. If its frequency matches a nuclear frequency it inverts the populations of two nuclear spin states (**3** in Figure 2.4c). The combination of the resonant MW and RF  $\pi$ -pulses thus

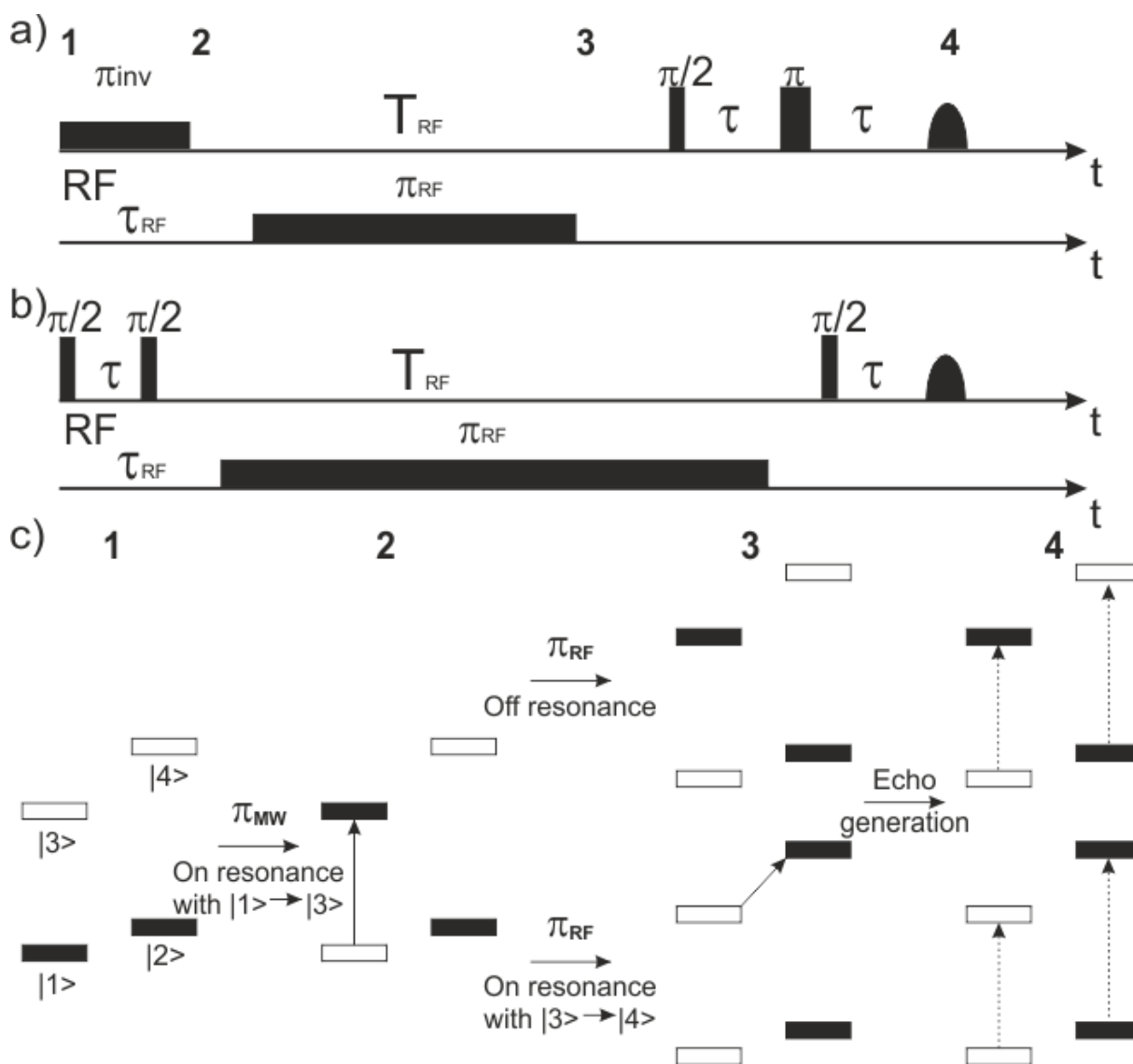


**Figure 2.4.** a) Davies ENDOR sequence. b) Mims ENDOR sequence. c) Populations of the spin states  $|1\rangle - |4\rangle$  at the times indicated in a). The dashed arrows indicate the coherences contributing to the echo formation.

leads to a double polarization transfer and ideally equalizes the population of pairs of electron spin states. Therefore, the spin packet excited by the initial MW  $\pi$ -pulse do ideally not yield an echo after the subsequent application of a two-pulse echo sequence at the same MW frequency (4 in Figure 2.4c). The double polarization transfer explained above requires the selective excitation of an electron spin transition from just one nuclear spin manifold. Therefore, the MW inversion pulse is optimally soft and selective while the echo can be generated by hard pulses. Naturally, it is easier to achieve selective pulses for large coupling constants and Davies ENDOR works well in such cases. For small coupling constants, Mims ENDOR yields better results.<sup>137</sup> In Mims ENDOR, a stimulated echo sequence is

used to generate the echo. The RF pulse is applied during the occurrence of the polarization grating between the second and the third pulse and changes the intensity of the echo if the RF pulse is on resonance with a nuclear spin transition, as the corresponding spin packets do no longer refocus in phase. This leads to a higher sensitivity of the Mims sequence, as no selective pulses have to be applied and more spin packets contribute to the echo intensity. On the other hand, this leads to the occurrence of blind spots for  $\tau = \frac{2\pi n}{a_{iso}}$  ( $n = 0, 1, 2, \dots$ ) as spin packets for which this condition applies refocus in phase after the third pulse. This blind-spot behavior is the reason why Mims ENDOR is not suited in the case of large HFCCs and the two ENDOR sequences can be used complementarily.

### 2.3.5. Methods to Measure Electron-Electron Dipolar Coupling

As outlined in chapter 2.1.3, the electron-electron interaction can be measured over several nanometers using EPR spectroscopy to deduce geometrical parameters of the investigated molecules. The accessible range of pulsed EPR lies between 2 and 10 nm<sup>66</sup> (see also chapter 2.1.3 and the following chapters) and can even be extended if special precautions are taken during sample preparation.<sup>139</sup> Such investigations of the geometric structure are not limited to paramagnetic molecules since spin bearing reporter groups (spin labels) can be introduced into diamagnetic compounds. This methodology is best developed for nitroxide spin labels in proteins and is called site directed spin labeling.<sup>140,141</sup> In the last decade, other spin labels which show different properties which are optimized for different kinds of experiments (see chapter 2.3.8 for a general discussion and chapters 6 and 7 for examples) have been introduced by several groups. Although many experiments to measure the dipolar coupling between a pair of spins separated by a certain distance are available, only those two which have been used extensively in this work will be discussed in detail. These two methods are the pulsed electron double resonance (PELDOR, also called double electron-electron resonance, DEER) and the relaxation induced modulation enhancement (RIDME) experiments. Figure 2.5 depicts some PELDOR and RIDME sequences which have been developed by various groups. The analysis of the shape of the EPR spectrum has been discussed briefly in chapter 2.1.3.<sup>99,142</sup> Other methods which will not be discussed here include double quantum



coherence (DQC),<sup>143–145</sup> single frequency techniques for refocusing dipolar couplings (SIFTER),<sup>146</sup> the 2+1 experiment,<sup>147</sup> and the analysis of the relaxation behavior.<sup>148–151</sup>

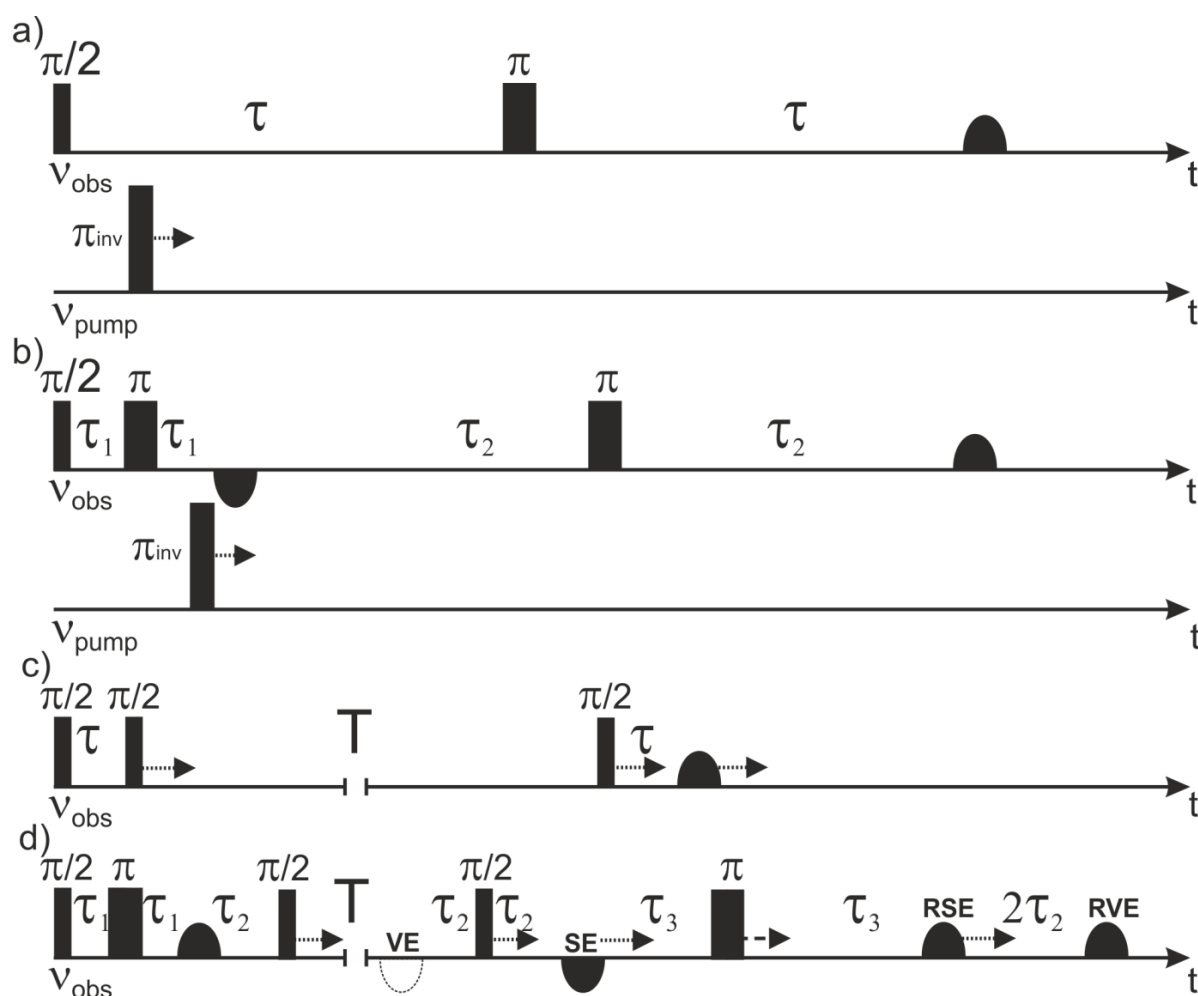


**Figure 2.5.** PELDOR and RIDME pulse sequences. a) Three-pulse PELDOR. b) Dead-time free four-pulse PELDOR. c) Three-pulse RIDME. d) Dead-time free five-pulse RIDME with the refocused stimulated and virtual echoes (RSE and RVE). The fifth pulse is only incremented when observing the RSE.

### 2.3.6. Pulsed Electron Double Resonance

In the pulsed electron double resonance (PELDOR) experiment the interspin separation between pairs of spins is measured by monitoring the effect of a spin flip of a pumped spin **B** on the echo intensity of an observer spin **A**. Spins **A** and **B** are often bound to the same molecule with an spin separation within the molecular backbone in the range of a few nanometers. The two types of spins are distinguished by applying two different MW frequencies to excite spin transitions. Figures 2.5a and 2.5b depict the three-pulse and the four-pulse PELDOR experiments.<sup>152–154</sup> The PELDOR effect can be explained most easily in the framework of the three-pulse

sequence (Figure 2.5a).<sup>152</sup> This experiment consists of a two-pulse echo sequence applied at the observer MW frequency  $\nu_A$  and an inversion pulse applied at the pump frequency  $\nu_B$  at a time  $\Delta t$  after the first pulse of the observer sequence. This pump pulse has a chance, quantified by the inversion efficiency  $\lambda$ , to reorient the **B** spins and thus change the dipolar field  $B_{dip}$  at the **A** spins. The change in orientation of the **B** spins is equivalent to a change in their magnetic quantum number  $m_{S,B}$ . The dipolar field  $B_{dip,A}$  at the location of spin **A** caused by spin **B** is related to the dipolar frequency as given in eq. (2-41) by an effective Zeeman relation:

$$B_{dip,A}(m_{S,B}) = \frac{\nu_{dip}}{g_A \mu_B / h} \approx \frac{\nu_{dip}}{2.8 \text{ MHz}} \frac{G}{\text{MHz}} m_{S,B}. \quad (2-53)$$

In eq. (2-53), a useful approximation has been introduced for organic  $s = 1/2$  radicals with  $g$  values close to  $g_e$ . In such cases, field and frequency domains are related by a factor of 2.8 MHz/G. In the PELDOR experiment, the pump pulse inverts the orientation of the spins **B** which changes the dipolar field experienced by spin **A**. Since the dipolar field is changed by the pump pulse, the coherences of the **A** spins evolve for a time  $\Delta t$  under the influence of  $B_{ext} + B_{dip,A}(m_{S,B} = \pm \frac{1}{2})$  ( $B_{ext}$  = the external magnetic field) and for a time of  $\tau - \Delta t$  under the influence of  $B_{ext} + B_{dip,A}(m_{S,B} = \mp \frac{1}{2})$  before the  $\pi$ -pulse is applied at the observer frequency  $\nu_A$ .<sup>i</sup> After the  $\pi$ -pulse at the observer frequency  $\nu_A$ , the **A** spins evolve for a time of  $\tau$  under the influence of the same dipolar field that was experienced during  $\tau - \Delta t$ . Therefore, the coherences are refocused but attain a phase shift of  $\nu_{dip}\Delta t$ . This leads to a modulation of the echo intensity with the same frequency. The function describing this modulation for **A** is called form factor  $F_n$ <sup>ii</sup> and is given by eq. (2-54) for a two-spin system.<sup>155–157</sup>

$$F_2(\Delta t) = (1 - \lambda) + \lambda P_2(\Delta t) \quad (2-54)$$

The formfactor  $F_2(\Delta t)$  in eq. (2-54) is normalized to a maximum intensity of 1 and consists of an unmodulated part having a weight of  $(1-\lambda)$  and a two-spin correlation function  $P_2$  weighted by a coefficient of  $\lambda$ .  $P_2$  is a damped cosine function and will be explained in detail when discussing the four-pulse PELDOR experiment below. The

<sup>i</sup>  $s = 1/2$  has been assumed for the **B** spins.

<sup>ii</sup> The subscript n refers to the number of coupled electron spins.

weighting factor  $\lambda$  corresponds to the chance of inverting a **B** spin which is coupled to the **A** spin used for observation. Conversely, the weight of the unmodulated part is identical to the chance of  $(1-\lambda)$  not to flip a **B** spin bound to the same molecule like an observed spin **A**. The form factor is also called the intramolecular contribution to the PELDOR signal. In addition to the intramolecular electron spin coupling, intermolecular coupling occurs. Assuming a homogenous, three-dimensional distribution of the two-spin system within the sample yields an exponential decay function for the intermolecular electron spin coupling. The resulting background decay function  $B(\Delta t)$  is given by eq. (2-55)<sup>102</sup>

$$B(\Delta t) = e^{-K\Delta t}, \quad (2-55)$$

where  $K$  is a decay constant. The complete PELDOR time trace  $V_{PELDOR}$  is given by the product of the form factor and the background decay function:

$$V_{PELDOR}(\Delta t) = F_2(\Delta t) \cdot B(\Delta t) \quad (2-56)$$

where a two-spin system has been assumed in eq. (2-56). To remove the background decay function from  $V_{PELDOR}$  one uses the fact that the pair correlation function damps out completely after a characteristic damping time  $T_{dd}$ .<sup>102</sup> Then, eq. (2-56) reduces to

$$V_{PELDOR}(\Delta t > T_{dd}) = (1 - \lambda) \cdot B(\Delta t > T_{dd}) \quad (2-57)$$

and it is possible to fit an exponential decay function to the part of the time trace where  $\Delta t > T_{dd}$  holds. Division of  $V_{PELDOR}$  by the obtained exponential decay function then yields the intramolecular part, i.e. the form factor. The form factor contains the desired information about the interspin separation. It is even possible to obtain the distribution of interspin distances. However, such a detailed analysis of PELDOR time traces is only possible if the complete form factor is available, meaning that the observation window must start at  $\Delta t = 0$  and end after all modulations have damped out. If the observation window is too short and the modulations have not damped out completely artificial broadening of the resulting distance distribution occurs. On the other hand, the initial part of the time trace is necessary to determine the experimental modulation depth. Furthermore, the shape of the initial part of the form factor is strongly affected by the distance distribution, especially in the case of broad distributions.<sup>154</sup> Achieving  $\Delta t = 0$  is not possible using the three-pulse PELDOR

experiment, as this experiment has a non-zero dead-time. Therefore, the three-pulse experiment has been replaced by the dead-time free four-pulse PELDOR experiment.<sup>153,154</sup> In this experiment, the refocused echo of a primary Hahn echo is used for observation. This allows applying the pump pulse when (or even before) the primary echo is formed. Therefore, the coherences can evolve for equal time periods before and after the refocusing pulse which eliminates the dead-time and allows recording modulated time traces starting at  $\Delta t = 0$ . The two spin correlation function  $P_2$  can then be calculated according to eq. (2-58)<sup>54</sup>

$$\lambda P_2 = \iint W(r) \lambda \cdot \cos(v_{dip}(r, \theta) \Delta t) \varepsilon(\theta) d\theta dr \quad (2-58)$$

where  $W(r)$  is the distribution of interspin distances. The dipolar coupling frequency  $v_{dip}$  is a function of the interspin distance  $r$  and the angle  $\theta$  as discussed in chapter 2.1.3 [see eq. (2-41)]. The factor  $\varepsilon(\theta)$  is a geometrical weighting factor<sup>54</sup> and is determined by the selection of orientations of the interspin vector with respect to the external magnetic field. If all orientations are equally excited by pump and observer pulses, the geometrical factor is given by  $\sin(\theta)$ :

$$\varepsilon(\theta) \xrightarrow{\text{equal excitation of all orientations}} \sin(\theta). \quad (2-59)$$

Then, the remaining factor determining the shape of the two-spin correlation function is the distance distribution  $W(r)$ . Fourier transformation of a PELDOR time trace in the absence of orientation selection gives a Pake pattern in the frequency domain (full lines in Figure 2.6). The distance distribution can be obtained by fitting the form factor using the Tikhonov regularization procedure.<sup>102,158</sup> In this procedure, the weighted sum  $G$  [eq. (2-60)] of the mean square deviation  $\rho$  between simulated and experimental time trace and the smoothness  $\eta^i$  of the time trace is minimized for different values of the regularization parameter  $\alpha$ :

$$G = \rho + \alpha \eta. \quad (2-60)$$

If eq. (2-59) does not apply, orientation selectivity has to be taken explicitly into account to fit PELDOR time traces and the Tikhonov procedure would not yield trustworthy distance distributions in such cases. Orientation selectivity effects occur if the orientation of **A** and **B** spins are correlated and at least one of the spins **A** or **B** is

---

<sup>i</sup> The smoothness  $\eta$  is proportional to the square of the second derivative of the simulated distance distribution.<sup>102</sup>

not excited equally in all orientations with respect to the external magnetic field. Such orientation selectivity effects are discussed in detail in chapter 6 and have been used to obtain further geometrical parameters relating the two spin centers **A** and **B** aside from the interspin separation  $r$ .<sup>67,159–163</sup> Figure 2.6 provides examples for PELDOR time traces and their Fourier transforms with and without orientation selection. Both time traces in Figure 2.6 have been simulated with an identical dipolar coupling frequency of  $\nu_{dip} = 3$  MHz. For the non-orientation selective case, the Fourier transform has the shape of a Pake pattern similar to the one depicted in Figure 2.2. In the case of PELDOR measurements however, the singularities are separated by two times the dipolar coupling frequency  $\nu_{dip}$ . Figure 2.6 also reveals that the time trace and the Fourier transform are heavily distorted in the orientation selective case. An interesting feature about the orientation selective data is the occurrence of pronounced peaks in the Fourier transform at  $\nu_{dip} = 3$  MHz. These peaks occur despite the severe suppression of the perpendicular orientations ( $\theta = 90^\circ$ ) in the assumed orientation selection. The reason for the occurrence of these peaks can be found by inspection of eq. (2-41) and the orientation selection given by the dashed line in Figure 2.6a. There, strong selection for orientations with an angle  $\theta \approx 35^\circ$  occurs. This angle leads to a dipolar coupling frequency of the same magnitude as for an angle  $\theta = 90^\circ$ , albeit with a different sign. As the sign of the dipolar coupling frequency is not reflected in the form factor, orientations corresponding to angles  $\theta \approx 35^\circ$  cannot be distinguished from actual perpendicular orientations (with  $\theta = 90^\circ$ ) in the Fourier transforms. It has been pointed out in an early account of orientation selection in PELDOR measurements that peaks at the dipolar coupling frequency with an apparent  $\theta$  of  $90^\circ$  are likely to occur even if orientation selectivity is present.<sup>164</sup>

Another important parameter to be considered is the sensitivity of the PELDOR experiment. The echo intensity in both the three- and the four-pulse PELDOR experiment decays with a time constant of the same order as  $T_2$  [eq. (2-52)].<sup>102</sup> Furthermore, the fraction of spins **A** contributing to the echo formation is reduced in the four-pulse experiment.<sup>102,i</sup> Therefore, the three-pulse PELDOR experiment is

---

<sup>i</sup> Generally, the more pulses are used in one sequence the lower the fraction of excited spins. The reason for that is that the excitation bandwidth for a series of pulses of a given length is lower than for a single pulse of the same length.

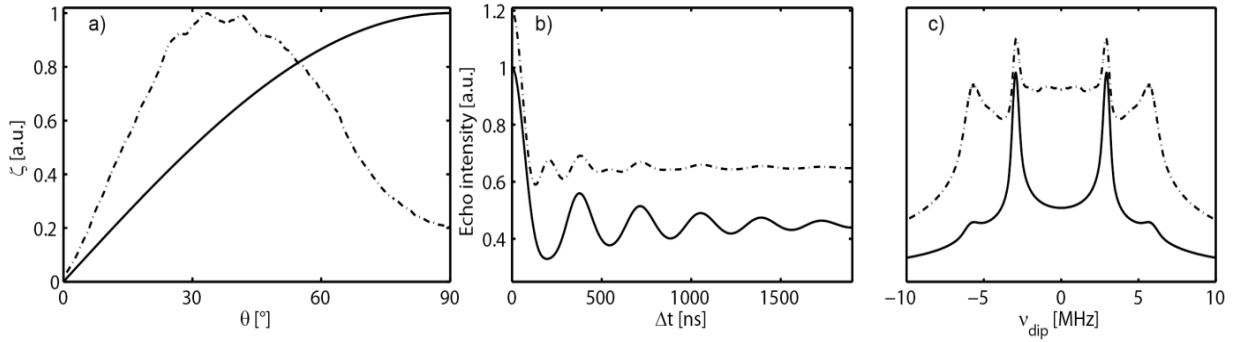


**Figure 2.6.** Simulated PELDOR data for non-orientation selective cases (full lines) and orientation selective cases (dashed dotted lines). a) Geometrical factor [eqs. (2-58) and (2-59)]. b) Normalized PELDOR time traces. The dashed dotted line has been shifted upwards for better visibility. c) Normalized Fourier transforms of the time traces shown in b), the dashed dotted line has been shifted for better visibility.

considerably more sensitive than its four-pulse pendant. If large observation windows are necessary, the DEER-Stitch experiment can be used to increase the sensitivity of PELDOR. DEER-Stitch combines both sequences by measuring the initial part of the time trace using the four-pulse sequence and a small observation window and the late parts of the time trace with the three-pulse sequence and an extended observation window.<sup>165</sup> An even more effective way to increase the sensitivity of the PELDOR experiment is to optimize the relaxation times. According to eq. (2-52), the sensitivity can be increased exponentially by increasing  $T_2$ . Normally, lower temperatures yield longer relaxation times. However, in the case of nitroxides it is observed that  $T_2$  increases strongly down to a temperature of 70 K but then stays nearly constant.<sup>102,166</sup> The spin lattice relaxation time  $T_1$  on the other hand increases upon further reduction of the temperature, which reduces the EPR signal intensity  $S$  by a factor of  $\sqrt{\frac{1}{T_1}}$  for a given number of averages of the PELDOR experiment:

$$S \sim \sqrt{\frac{1}{T_1}}. \quad (2-61)$$

Eq. (2-61) does not account for the improved magnetization achieved at lower temperatures which can be included in eq. (2-61) by introducing a factor of  $1/T$ .<sup>102,166</sup> Another factor influencing the apparent relaxation behavior of the spin center is the concentration  $c$  of the sample. At high concentrations, instantaneous diffusion strongly reduces the apparent  $T_2$  value of the spin centers.<sup>123</sup> The additional instantaneous diffusion damping factor  $D_{ID}$  of the intensity can be estimated using<sup>102</sup>

$$D_{ID} = e^{-f_{A,\pi} c N_A \frac{2\pi^2 g_A g_B \mu_0 \mu_B^2}{9\sqrt{3}} t_{seq}} \quad (2-62)$$

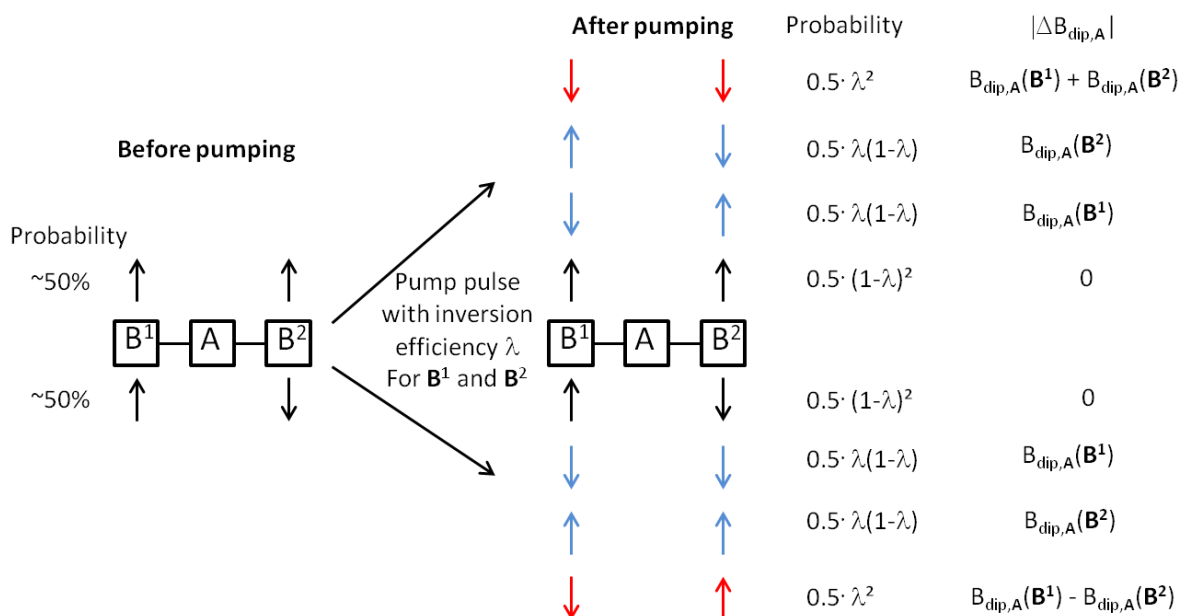
In eq. (2-62),  $f_{A,\pi}$  is the fraction of spins **A** excited by an observer  $\pi$ -pulse,  $N_A$  is Avogadro's constant and  $t_{seq}$  is the total length of the pulse sequence (i.e.  $2(\tau_1 + \tau_2)$  in the case of four-pulse PELDOR). All other variables in eq. (2-62) have been introduced before. Optimization of the relaxation times can also be achieved by choosing spin labels with suitable relaxation behavior (see chapter 2.3.8). Finally, it is possible to completely deuterate the matrix in which the spin centers are embedded (and the spin center itself, too) which usually leads to an increased apparent  $T_2$  value. The reason for this is that loss of the phase coherence is often dominated by spin diffusion mediated by nearby nuclei.<sup>64,66,123</sup> The effectiveness of such processes depends on the magnitude of the magnetic moments of these nuclei to the third power.<sup>123</sup> In the absence of fluorine nuclei, protons have by far the largest magnetic moments and are also often the most abundant nuclei in any sample. Importantly, the magnetic moment of deuterons is ~85% lower than that of protons. Thus, replacement of protons by deuterons makes spin diffusion less effective and strongly increases  $T_M$ .<sup>123,167,139</sup> Another factor which can lead to a low sensitivity of the PELDOR experiment is a low inversion efficiency  $\lambda$ . Low inversion efficiencies are expected if the width of the spectrum of the pumped spins exceeds the excitation band width of the pump pulse. Using shaped (or composite), broadband pump pulses<sup>168,169</sup> to achieve higher inversion efficiencies therefore leads to enhanced sensitivity, especially if combined with optimized, composite observer pulses.<sup>170</sup>

So far, the PELDOR experiment has only been discussed for two-spin systems. If the number of coupled spins  $N$  within a molecule is larger than two, multi-spin effects have to be considered.<sup>155-157</sup> In such a situation, any spin **A** used for observation experiences dipolar magnetic fields stemming from more than one electron within the molecule. For a three-spin system **AB<sub>2</sub>** the dipolar field present at spin **A** caused by spins **B<sup>1</sup>** and **B<sup>2</sup>** can be written as

$$B_{dip,A} = B_{dip,A}(\mathbf{B}^1, m_{s,B^1}) + B_{dip,A}(\mathbf{B}^2, m_{s,B^2}) \quad (2-63)$$

The form factor  $F_3$  for this three-spin system is determined by the coupling to both **B** spins. Multi-spin effects arise if more than one of the spins **B** in a given molecule is

reoriented by the pumping pulse. Scheme 2.1 illustrates all possible combinations for an  $\mathbf{AB}_2$  spin system, leading to different contributions to  $F_3$ .



**Scheme 2.1.** Zero, single or double spin flips at the pumped spins  $\mathbf{B}^1$  and  $\mathbf{B}^2$  and the respective probabilities of their occurrence. Before pumping, the two  $\mathbf{B}$  spins can either be aligned parallel or antiparallel with approximately equal probabilities of 50%. Only one of two possible parallel or antiparallel alignments is shown in the scheme. The pump pulse can flip no spin (black arrows after pumping), one spin (blue arrows) or both spins (red arrows). These situations correspond to the unmodulated part of the PELDOR time trace, the two spin contribution (one observer and one pumped spin) and the three spin contribution (one observer and two pumped spins), respectively. The probabilities depend on the inversion efficiency  $\lambda$  and are identical to the binomial coefficients in the case of two pumped spins (the factor of 0.5 accounts for the two possible initial spin alignments).

As apparent from scheme 2.1, the two  $\mathbf{B}$  spins can have either spin up or down orientation before pumping, as symbolized by the black arrows. This gives rise to parallel or antiparallel alignments of the spin pair. The parallel and antiparallel alignment are nearly equally populated according to Boltzmann's law for standard X-band measurement conditions. The pump pulse can induce three possible events. First, it is possible to invert neither of the two  $\mathbf{B}$  spins, which leaves the dipolar field  $B_{dip,A}$  [eq. (2-63)] at spin  $\mathbf{A}$  unchanged (black arrows after pumping in scheme 2.1). This leads to the unmodulated part in the form factor  $F_3$ . The relative intensity of the unmodulated part amounts to  $(1-\lambda)^2$ , which can be obtained by summing the probabilities given in Scheme 2.1 for arrows of the same color after pumping. Secondly, it is possible to change the orientation of one of the  $\mathbf{B}$  spins (blue arrows in



scheme 2.1). If the EPR spectrum of the  $\mathbf{B}$  spins is identical, it is reasonable to assume identical inversion efficiencies for  $\mathbf{B}^1$  and  $\mathbf{B}^2$ . Then, the probability for a single spin flip of either one of the  $\mathbf{B}$  spins amounts to  $\lambda(1-\lambda)$ . The single spin flip events give rise to two two-spin correlation functions  $P_2(\mathbf{B}^1)$  and  $P_2(\mathbf{B}^2)$  as defined by eq. (2-58) which can be summed up to yield  $P_3$  (two-spin correlation within a three-spin system):

$$\begin{aligned}
2\lambda(1-\lambda)P_3 &= \iint W(r_{\mathbf{B}^1})\lambda(1-\lambda) \cdot \cos(v_{dip}(r_{\mathbf{B}^1}, \theta_{\mathbf{B}^1})\Delta t) \varepsilon(\theta_{\mathbf{B}^1}) d\theta_{\mathbf{B}^1} dr_{\mathbf{B}^1} \\
&+ \iint W(r_{\mathbf{B}^2})\lambda(1-\lambda) \cdot \cos(v_{dip}(r_{\mathbf{B}^2}, \theta_{\mathbf{B}^2})\Delta t) \varepsilon(\theta_{\mathbf{B}^2}) d\theta_{\mathbf{B}^2} dr_{\mathbf{B}^2} \\
&= \lambda(1-\lambda)P_2(\mathbf{B}^1) + \lambda(1-\lambda)P_2(\mathbf{B}^2)
\end{aligned} \tag{2-64}$$

Taken together, the relative contribution of the two-spin correlation functions to  $F_3$  amounts to  $2\lambda(1-\lambda)$ . Finally, if both  $\mathbf{B}$  spins are inverted by the pump pulse, the dipolar field can change in two different ways (red arrows in scheme 2.1). If both  $\mathbf{B}$  spin are flipped up (or down), the changes of their respective dipolar fields add up. Consequently, a sum frequency is observed in PELDOR experiments. On the other hand, if one spin is flipped up while the other one is flipped down the change of the dipolar field is partially or completely cancelled out, leading to the occurrence of difference frequencies in the PELDOR experiment. This behavior is described by a three-spin correlation function  $T_3$ :

$$\begin{aligned}
\lambda^2 T_3 &= \iint W(r_{\mathbf{B}^1})W(r_{\mathbf{B}^2})\lambda^2 \cdot \cos(v_{dip}(r_{\mathbf{B}^1}, \theta_{\mathbf{B}^1})\Delta t) \varepsilon(\theta_{\mathbf{B}^1}) \cdot \\
&\cos(v_{dip}(r_{\mathbf{B}^2}, \theta_{\mathbf{B}^2})\Delta t) \varepsilon(\theta_{\mathbf{B}^2}) d\theta_{\mathbf{B}^1} dr_{\mathbf{B}^1} dr_{\mathbf{B}^2}
\end{aligned} \tag{2-65}$$

In eq. (2-65) it has been assumed that the angles  $\theta_{\mathbf{B}^1}$  and  $\theta_{\mathbf{B}^2}$  are correlated:

$$\theta_{\mathbf{B}^2} = f(\theta_{\mathbf{B}^1}) \tag{2-66}$$

Then, it is sufficient to integrate over one of the angles  $\theta$  since it defines the other angle. Importantly, the three-spin correlation function is obtained by multiplying the two-spin correlation functions at a given orientation and then integrating over all required orientations. Summing up the unmodulated part  $(1-\lambda)^2$  and eqs. (2-64) and (2-65) yields the normalized form factor  $F_3$ :

$$F_3 = (1-\lambda)^2 + 2\lambda(1-\lambda)P_3 + \lambda^2 T_3 \tag{2-67}$$

If no correlation between the the angles  $\theta_{\mathbf{B}^1}$  and  $\theta_{\mathbf{B}^2}$  is assumed, the formfactor  $F_3$  can be obtained by taking the product of the two form factors  $F_2(\mathbf{B}^1)$  and  $F_2(\mathbf{B}^2)$ :

$$F_3 = F_2(\mathbf{B}^1) \cdot F_2(\mathbf{B}^2) = \left( (1 - \lambda) + \lambda P_2(\mathbf{B}^1) \right) \cdot \left( (1 - \lambda) + \lambda P_2(\mathbf{B}^2) \right) = (1 - \lambda)^2 + \lambda(1 - \lambda) \left( P_2(\mathbf{B}^1) + P_2(\mathbf{B}^2) \right) + \lambda^2 P_2(\mathbf{B}^1) P_2(\mathbf{B}^2) \quad (2-68)$$

In this product approach, identical terms for the two-spin correlation function as given in eq. (2-67) are obtained. However, the term in  $\lambda^2$  is different as no angular correlation has been taken into account in the product function. The form factors of multi-spin systems in which more than three spin centers contribute can be obtained by extending the outlined product approach to include the appropriate number of factors. Finally, eqs. (2-65), (2-67), and (2-68) provide an experimental approach to suppress contributions by the three-spin correlation functions, which have a contribution proportional to the square of the inversion efficiency  $\lambda^2$ . This value can be reduced by using pump pulses of reduced power in the so-called power-scaling approach.<sup>157</sup>

### 2.3.7. Relaxation Induced Dipolar Modulation Enhancement

The relaxation induced dipolar modulation enhancement (RIDME) experiment is a single MW frequency experiment, examples of RIDME sequences are given in Figures 2.5c and 2.5d. As with PELDOR, the principle is most easily explained for the shortest pulse sequence, the three-pulse RIDME experiment (Figure 2.5c).<sup>171,172</sup> The three-pulse RIDME experiment uses a stimulated echo for observation of the **A** spins while the intervals  $\tau$  are incremented. The interval  $T$  is chosen such that it equals or exceeds the spin lattice relaxation time of the **B** spins  $T_{1,\mathbf{B}}$ . This choice leads to statistical spin flips among the **B** spins during the interval  $T$ . If a single spin **B** runs through an uneven number of spin flips, the field under which the coherences of **A** evolve after the third pulse differs by the dipolar field exerted by spin **B** [eq. (2-53)] from the field which was felt between the first two pulses. The echo intensity is then modulated with  $\nu_{dip}$  yielding modulated time traces in complete analogy to the PELDOR experiment. The modulation depth in the RIDME experiment depends on the fraction of the **B** spins which undergoes a reorientation during the interval  $T$ . The reorientation proceeds by statistical processes on a time scale which is assumed to

be identical with the spin lattice relaxation time of the **B** spins  $T_{1,B}$ . Accordingly, the modulation depth  $V_{\lambda,RIDME}$  is approximately described by<sup>67</sup>

$$V_{\lambda,RIDME} = V_{\lambda,RIDME}^{max} (1 - e^{-\frac{T}{T_{1,B}}}) \quad (2-69)$$

The maximum modulation depth  $V_{\lambda,RIDME}^{max}$  for an  $s = \frac{1}{2}$  **B** spin amounts to 0.5, i.e. 50%.<sup>67,171</sup> This value can be derived by assuming that the spin up and spin down orientation for the **B** spin is approximately equal under standard X-band measurement conditions according to Boltzmann's law. During the interval  $T$ , each **B** spin can flip an either odd or even number of times. An odd number of flips alters the orientation of the corresponding **B** spin while an even number of flips leads to an unchanged orientation. Only those spins **B** which attain an orientation different from their orientation prior to the interval  $T$  contribute to the modulation of the RIDME time trace. As odd and even numbers of flips are equally likely a maximum of 50% of all **B** spins can contribute to the modulation in the RIDME experiment (assuming  $s = \frac{1}{2}$  for the **B** spin). The experimentally observed modulations depths are typically lower than the maximum of 50%.<sup>67</sup> Similar arguments show that the expected modulation depth is higher for higher spin quantum numbers at the **B** spin, as more orientations different from the orientation before the interval  $T$  are available for each **B** spin. The increased modulation depths for high spin **B** have also been confirmed experimentally.<sup>173</sup> However, if spin states differing by  $|\Delta m_s| = 2, 3$  and so on... are attained during the interval  $T$ , the resulting dipolar frequencies are higher harmonics of  $V_{dip}$ .<sup>173,174</sup> Inspection of eq. (2-69) reveals that 95% of the maximum modulation depth  $V_{\lambda,RIDME}^{max}$  is obtained for  $T = 3 \cdot T_{1,B}$ . During the interval  $T$ , the echo intensity of the observer spin **A**  $I_A$  drops exponentially with  $T_{1,A}$  according to eq. (2-70) (see also chapter 2.2).

$$I_A = I_{0,A} e^{-\frac{T}{T_{1A}}} \quad (2-70)$$

Eq. (2-70) predicts that 80% of the maximum echo intensity are conserved during the interval  $T$  if  $T_{1,A} = 5 \cdot T$  holds. The sensitivity  $S_{RIDME}$  of the RIDME experiment depends on the product of the echo intensity of the observer spin **A** and the modulation depth, yielding eq. (2-71):

$$S_{RIDME} = V_{\lambda,RIDME}^{max} (1 - e^{-\frac{T}{T_{1,B}}}) \cdot I_{0,A} e^{-\frac{T}{T_{1A}}} \quad (2-71)$$

Eq. (2-71) and the discussion above reveal that the best sensitivities are obtained for spin systems consisting of **A** and **B** spins for which  $T_{1,A} \gg T_{1,B}$  holds. This relation is normally valid when **A** is an organic radical and **B** a metal centered spin,<sup>123</sup> making mixed metal-nitroxide spin systems suited for RIDME measurements. In such mixed systems, RIDME offers further advantages. First, the **B** spins flip during the interval  $T$  owing to random local field fluctuations in their immediate environment regardless of the orientation of the **B** spins. Thus, the width of the spectrum of the **B** spins does not influence the modulation depth, as no selection owed to limited excitation bandwidth arises in RIDME. This does not only lead to an increased modulation depth as compared to PELDOR, but also reduces the extent of orientation selection to the selection imposed on the observed spin **A**.<sup>175,176</sup> Additionally, it has been shown that RIDME is more sensitive than PELDOR when measuring distances between metal and nitroxide spin centers.<sup>177,178</sup> Noteworthy, the roles as spins **A** and **B** for the organic radical and the metal center are usually reversed in PELDOR as compared to RIDME.<sup>175,177,178</sup> As discussed above, short values of  $T_{1,B}$  are favorable to obtain a good sensitivity. However, minimum values for  $T_{1,B}$  exist as flips of the spins **B** lead to modulation only if they occur during the interval  $T$ . Flips during the  $\tau_i$  intervals ( $i = 1$  and  $i = 1,2,3$  in the case of three- and five-pulse RIDME, respectively) affect the phase of the echo of the **A** spins in an incoherent manner and lead to reduced signal intensity. Thus,  $T_{1,B}$  should exceed the length of all  $\tau_i$  intervals which is usually achieved with values of  $T_{1,B}$  on the order of tens of microseconds. Finally, the sensitivity of the RIDME experiment is also affected by relaxation during the  $\tau_i$  intervals. During these intervals, the coherences of spins **A** decay with a time constant on the order of  $T_{2,A}$  or, more precisely,  $T_{M,A}$  (eq. (2-52) and chapter 2.2). Therefore, it is necessary to optimize three relaxation times ( $T_{1,B}$ ,  $T_{1,A}$ , and  $T_{M,A}$ ) at once in order to conduct a sensitive RIDME experiment. This can be challenging, especially in the case of compounds which contain identical radical centers, e.g. bisnitroxide compounds. Importantly, spectral diffusion occurs during the long interval  $T$  and leads to a decreased value of  $T_{M,A}$  as compared to the value which would occur in the PELDOR sequence. The decay of the RIDME time trace is therefore more rapid than the corresponding PELDOR time traces and is not described by a simple exponential decay curve.<sup>179</sup> Owing to the slower decay of the echo intensity, PELDOR can be superior for long distances. This was shown in a recent study using pairs of gadolinium(III) spin centers by Collauto *et al.*<sup>174</sup> There, correct distance

distributions have been obtained using PELDOR for a bis-gadolinium labeled protein with interspin separations of  $\sim 5.5$  nm. Distance distributions obtained from RIDME time traces contained the correct peak but showed more intense peaks at distances corresponding to higher harmonic oscillations stemming from  $|\Delta m_s| = 2$  and  $|\Delta m_s| = 3$  transitions of the **B** spins. The same study showed, however, that RIDME can be superior for measurements of shorter distances. These measurements have been performed in a model compound containing two like Gd(III) spin centers with small ZFS interactions ( $D < 1$  GHz) and an interspin separation of only  $\sim 2.3$  nm. In the case of the short interspin distance, the PELDOR time trace was heavily damped and it was impossible to obtain a correct distance distribution. This behavior was attributed to the occurrence of pseudo-secular contributions to the dipolar spin-spin interaction (chapter 2.1.3) in the PELDOR experiment using a frequency offset of only 100 MHz for pumping and observing. These interactions were observed to be less important in the RIDME experiment where spins from any region of the Gd(III) spectrum can act as **B** spins. Thus, the study of Collauto *et al.* also provides an example for the complementarity of PELDOR and RIDME.

Importantly, the three-pulse RIDME sequence is identical to the three-pulse ESEEM sequence (although different time intervals are incremented). Therefore, the resulting time traces can show strong modulations stemming from forbidden spin transitions. These can be suppressed by going to higher MW frequencies or using soft pulses.<sup>177</sup> Another commonly applied method is to measure two RIDME time traces, the first one having  $T < T_{1,B}$  and the second one with  $T > T_{1,B}$ . With these settings, only the second time trace is modulated by both the ESEEM transitions and the spin flip of the **B** spins. Division of the second time trace by the first time trace reduces or even removes the ESEEM modulations (chapters 6 and 7). Instead of changing the length of the interval  $T$  it is also possible to measure at different temperatures, thereby changing the value of  $T_{1,B}$ .<sup>177</sup> At the low temperature,  $T_{1,B} > T$  holds, yielding the unmodulated time trace, while the modulated time trace is obtained at higher temperatures where  $T_{1,B} < T$  is valid.

The three-pulse RIDME sequence suffers from the occurrence of an instrumental dead-time. To remove the dead-time from RIDME, the five-pulse RIDME sequence can be used (Figure 2.5d).<sup>175</sup> As in the four-pulse PELDOR experiment, the coherences formed by the first pulse are refocused prior to the spin flip events of the

**B** spins between the third and the fourth pulse. The third pulse can be applied at or even before the formation of the primary echo. The resulting echoes (see below) overlap with the fourth pulse at certain values of  $\tau_2$ , so that another refocusing pulse is necessary. This allows recording the evolution of the **A** spin coherences from the beginning on, i.e. at  $\tau_2 = 0$ . This method for generating an echo can also be applied to other sequences and has been termed remote echo detection.<sup>180</sup> As apparent from Figure 2.5d, the third and the fourth pulse give rise to two echoes which, after the fifth pulse, yield a refocused stimulated and a refocused virtual echo (RSE and RVE, respectively). Both of these echoes can be used to record RIDME time traces using different time incrementation schemes. As the interpulse separations are incremented in a different manner, recording the RSE echo leads to a non-constant time experiment in contrast to detection of the RVE. This introduces a steeper background decay function, as the echo intensity diminishes during incrementing  $\tau_2$  with a time constant of the order of  $T_M$ .<sup>175</sup> This leads to an additional damping of the modulations and broadens the resulting distance distribution. A detailed comparison between both detection schemes is presented in chapter 7.

### 2.3.8. The Choice of Spin Label

As already indicated in the previous two chapters, measurements of interspin distances are especially interesting in structural biology. Studies in this field require the attachment of spin labels to the biological macromolecule if it is diamagnetic, as is often the case. Figure 2.7 shows some examples of spin labels which have been used as spin labels in different studies.<sup>181</sup> The most frequently encountered spin labels are nitroxides, several of which have been designed to be linked selectively to certain sites in proteins or oligonucleotides.<sup>24,181</sup> Among the nitroxides, possibly the most frequently used one is the methanthiosulfonate spin label (MTSSL). MTSSL can be attached to cysteine residues in proteins by site directed spin labeling.<sup>38,53</sup> The sidechain of MTSSL, by which it is linked to the cysteine residue, is flexible, which can lead to broad distance distributions. One strategy to reduce the flexibility of the nitroxide spin labels is to bind it to two cysteine residues which are in close proximity within the protein (RX in Figure 2.7). For oligonucleotides, specific labeling strategies have been developed as well. One possibility is to attach the the spin label to one of the bases of the oligonucleotides. As an example, Figure 2.7 shows the 2,2,5,5-tetramethylpyrroline-1-yloxy-3-acetylene (TPA) spin label which was attached to a

iodosubstituted uracil base by a Sonogashira-Hagihara cross coupling reaction.<sup>182</sup> All nitroxide spin labels presented so far have four methyl groups adjacent to the spin center to sterically crowd the reaction nitroxide group and thus hinder the occurrence of disproportionation or reduction reactions.<sup>183</sup> While the reduced reactivity is a desired property for nitroxides used as spin label, the tetramethyl substitution pattern leads to a strong decrease of the  $T_M$  values at temperatures above 70 K. The fast loss of phase memory is caused by the alternating HFC fields of the protons on the rotating methyl groups.<sup>123</sup> This makes helium cooling necessary to achieve sensitive measurements using nitroxide spin labels. To overcome this limitation, it is possible to either replace the protons with deuterons<sup>176</sup> or to introduce spiro-cyclohexyl groups instead of the methyl groups (Spiro in Figure 2.7).<sup>184,185</sup> Nitroxides have an EPR spectrum which spans a width of approximately 200 MHz at X-band MW frequency. Thus, short MW pulses applied at the center of the nitroxide spectrum lead to the excitation of a large fraction of the spectrum in the sample. In EPR distance measurements this is of importance as each part of the spectrum represents certain orientations of the spin label. A non-uniform excitation would therefore select certain orientations of spins **A** or **B**. In many cases, the orientations of spins **A** and **B** with respect to each other and to the external magnetic field are correlated. Then, selective excitation would lead to a selection of a subset of angles  $\theta$  in eq (2-41). Instead of the complete Pake pattern one would then obtain a distorted spectrum with frequencies determined by the interspin separation  $r$  and the subset of selected angles  $\theta$ . Then, a safe extraction of the interspin distance from modulated time traces can only be obtained if the contributing orientations of the two spins in the external magnetic field are known. The low degree of orientation selection which can be obtained at X-band frequencies using nitroxide spin labels is lost at higher MW frequencies as the  $g$ -tensor anisotropy controls the width of the spectrum at high MW frequencies.<sup>67,186</sup> Thiosubstituted triarylmethyl radicals (TAM, an example is given in Figure 2.7) produce very narrow EPR spectra even at high MW frequencies owing to the low  $g$ -anisotropy of thiosubstituted TAMs and the absence of HFC to protons or other nuclei with  $I \neq 0$  nuclides in high natural abundance.<sup>187</sup> The narrow spectrum allows non-selective excitation and leads to large modulation depths when used for pumping in PELDOR experiments.<sup>188</sup> Narrow linewidths are also favorable for sensitive DQC experiments.<sup>188</sup> Additionally, the low spectral width leads to slow

relaxation behavior.<sup>189</sup> This allows measurements at temperatures above 80 K<sup>i</sup> and even at room temperature in liquid samples, which is a better approximation of the natural environment of the biomolecules than the usual frozen solvent matrices.<sup>189–191</sup> Conversely, metal centered spins usually have large spectral widths and relax rapidly, which complicates pulsed EPR distance measurements.<sup>54,123</sup> On the other hand, metal centered spins offer advantages in certain situations. As discussed in the introduction, many biological macromolecules contain paramagnetic metal centers which can be used as natural spin labels, strongly reducing the required labeling effort. The short spin lattice relaxation times allow fast shot repetition rates<sup>192</sup> and sensitive RIDME experiments (see chapter 2.3.7). The large spectral width can lead to strong orientation selection in EPR-based distance measurements. A high degree of orientation selectivity has often been observed in the case of copper centered spins. While the occurrence of strong orientation selection complicates distance measurements, it offers the possibility to elucidate the relative orientation of the spin labels.<sup>67,159–163</sup> Cunningham *et al.* proposed a facile, self-assembly strategy to introduce copper(II) spin labels into proteins.<sup>193</sup> The two required histidine residues may be introduced by site selective mutagenesis if not already present in the wildtype structure of the protein of interest (dHis-Cu in Figure 2.7). In Cunnighams study, orientation selection was found to play only a minor role. In the case of paramagnetic metal ions having a half-filled shell of valence electrons, like Gd(III) ( $4f^7$ ) and Mn(II) ( $3d^5$ ), a symmetric  $A_{1g}$  ground state is expected. This should reduce orientation selection for such ions. However, ZFS has to be accounted for as a complicating feature in these systems. For Gd(III), spin labels have been developed to introduce Gd(III) labels into proteins (Gd-DOTA in Figure 2.7),<sup>192,194</sup> while it has been shown that Mn(II) can be site-selectively introduced into RNA oligonucleotides by titration.<sup>47,195,196</sup> Iron is often contained in proteins ligated by a porphyrin group (an example is given in Figure 2.7, TPP), where different spin states for the iron can occur. For  $s = \frac{1}{2}$  states, PELDOR and RIDME studies have been conducted to measure distances between an organic radical center and the iron ion.<sup>170,177,197</sup> In the high spin state  $S = 5/2$ , a nitroxide-hemin distance has been obtained using saturation recovery studies.<sup>198</sup> Recently, excited triplet states of porphyrins and low-spin hemes with diamagnetic ground states have been used in EPR-based distance measurements.<sup>199,200</sup> Porphyrins and hemes can be excited to their triplet state by

---

<sup>i</sup> Such temperatures can also be achieved using nitroxides if they are spiro-cyclohexyl substituted.<sup>184</sup>



irradiation using laser irradiation of appropriate wave lengths. In the study by Di Valentin *et al.*, the excited triplet state porphyrin was used for observation. This allowed orientation selective PELDOR measurements with high sensitivity owed to a favorable polarization of the triplet state.<sup>67,199</sup> In the study by Hintze *et al.*, the laser pulse exciting the heme to its triplet state was used to replace the pump pulse in a three-pulse PELDOR experiment. This allowed non-orientation selective excitation of the heme and a dead-time free measurement despite using only two observer pulses, as the laser pump pulse does not interfere with the observer MW pulses. The modulation depth in this experiment is determined by the quantum yield of the triplet state generation and the polarization pattern of the excited triplet state.<sup>200</sup> Therefore, each type of spin label discussed so far has its own advantages and challenges and the choice critically depends on the type of sample and experiment. Finally, the different properties of the spin labels allow orthogonal spin labeling.<sup>201</sup> In orthogonal spin labeling, several types of spin labels are attached to one molecule. The different properties of each spin label allow addressing each of them selectively, thereby obtaining more than one distance from only one sample.

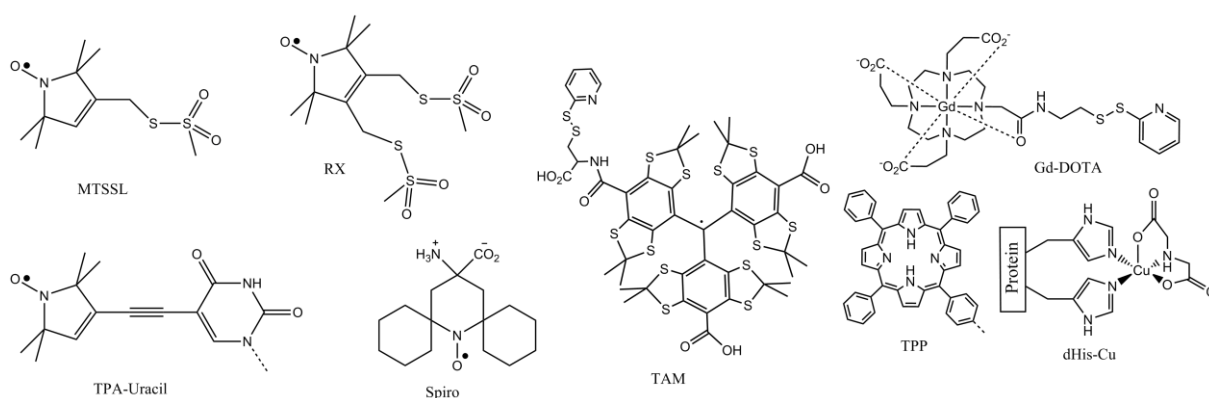


**Figure 2.7.** Spin labels discussed in the text. TPP is capable of taking up various, paramagnetic metal ions and can be excited to a paramagnetic triplet states.

## **Part II.**

# **EPR Distance Measurements Involving Metal Centers**

### 3. The Crystal Structure of 4''-{4-[(2,2,5,5-Tetramethyl-N-oxyl-3-pyrrolin-3-yl)ethynyl]-phenyl}-2,2':6',2''-terpyridine

Andreas Meyer,<sup>i</sup> Jennifer Wiecek,<sup>i</sup> Gregor Schnakenburg<sup>ii</sup> and Olav Schiemann<sup>i</sup>

Received 28th May 2015, published online 30th June 2015.

Reprinted with permission from

A. Meyer, J. Wiecek, G. Schnakenburg, and O. Schiemann, *Acta Crystallographica E* **2015**, *E71*, 870 - 874.

Copyright ©2015, International Union of Crystallography.

#### Own contributions to the manuscript

- Synthesis and crystallization of the title compound.
- Evaluation of the geometrical parameters of the crystal structure.
- Writing the manuscript.

The reprint of the publication can be found in appendix A.

---

<sup>i</sup> University of Bonn, Institute of Physical and Theoretical Chemistry, Wegelerstrasse 12, 53115 Bonn, Germany

<sup>ii</sup> University of Bonn, Institute of Inorganic Chemistry, Gerhard-Domagk-Strasse 1, 53121 Bonn, Germany.

## Introduction and Summary of Results

The second part of this thesis is concerned with conducting and optimizing distance measurements on small metal-nitroxide model complexes. To be suited as model systems for distance measurements these complexes need to have certain properties. Most importantly, the separation between the metal and the nitroxide centered spin needs to be known or to be predictable with high accuracy even if no X-ray crystallographic structure or any further experimental result is available. Therefore, the spacer between the metal and the nitroxide needs to be rigid and should not have a high degree of rotational freedom. 1,4-Phenylene and ethynylene building blocks provide such properties, as they are stiff moieties owed to their multiple bonds and symmetry with respect to rotations around their linking single bonds. Additionally, these fragments can be attached easily to an existing molecule by Sonogashira-Hagihara cross coupling reactions using commercially available reagents.<sup>202</sup> This allows devising a modular synthetic approach and opens up routes to a variety of ligands with different properties. Similarly, the immediate coordination sphere of the metal center should have a predictable structure, so that the number and the orientation of the ligands can be safely predicted prior to any measurement. Especially for high-spin metal centers, the coordination sphere should be highly symmetric to obtain low magnitude ZFS interactions.<sup>64</sup> Finally, the metal complexes need to be sufficiently stable in solution to yield EPR samples containing defined molecules. Such properties are provided by terpyridines (tpy) which are relatively rigid and exert a chelate effect. Furthermore, it is already known that tpy's are capable of taking up various metal ions in different oxidation states yielding octahedral bisterpyridine complexes with meridional ligation.<sup>203-205</sup> The flexible synthetic route to obtain ligands and the possibility to take up various metal ions have both been exploited. Two nitroxide bearing ligands have been synthesized and investigated. The first example, 4'-{4-[(2,2,5,5-tetramethyl-*N*-oxyl-3-pyrrolin-3-yl)ethynyl]-phenyl}-2,2':6',2''-terpyridine **3-1**, is described in detail in appendix A. **3-1** provides an interspin separation of approximately 16 Å. According to eq. (2-41), this gives rise to a dipolar coupling frequency of ~13 MHz at the singularities of the Pake pattern. An observation window as short as 400 ns would therefore suffice to record more than five full modulations, allowing highly sensitive measurements [cf. eq. (2-52)] at good spectral resolution. In order to aid the planned EPR spectroscopic investigations, the ligand was crystallized and subjected to X-ray crystallographic

investigations. The crystallographic investigation revealed, that the ligand **3-1** indeed has the expected geometry in which the distance between the nitroxide and the central pyridine ring of the terpyridine metal binding site amounts to 14.1 Å.<sup>i</sup> Only slight bending of the molecular backbone was observed. For example, the bond angles between the carbon atoms of the ethynylene group and its substituents deviate by less than 5° from 180°, which would be the expected angle for a linear alignment. Aside from the intramolecular geometrical parameters, the packing of the molecules within the crystal structure was investigated. It was observed that the terpyridine subunits are arranged in stacks and exhibit slipped face-to-face  $\pi$  interactions, while edge-on C-H $\cdots\pi$  interactions have been observed for the phenylene rings.<sup>206</sup> **3-1** was synthesized to obtain model complexes for distance measurements in which exchange coupling occurs as an additional parameter in the spin Hamiltonian. However, the corresponding studies have not been conducted so far and will be addressed in future work. Instead, the ligand 4'-{[4-(2,2':6',2''-terpyridyl-4'-yl)phenyl]ethynyl}-biphenyl-4-yl-(2,2,5,5-tetramethyl-*N*-oxyl-3-pyrrolin-3-yl)formate (to be introduced in chapter 4) was used for all distance measurements discussed in chapters 6 and 7.

---

<sup>i</sup> An approximate nitrogen-copper bond length of 2 Å has to be added to this value to arrive at the suggested interspin separation of ~16 Å.

## 4. Crystal Structure of 4'-{[4-(2,2':6',2''-Terpyridyl-4'-yl)phenyl]-ethynyl}biphenyl-4-yl-(2,2,5,5-tetramethyl-1-oxyl-3-pyrrolin-3-yl)formate Benzene 2.5-Solvate

Andreas Meyer,<sup>i</sup> Gregor Schnakenburg<sup>ii</sup> and Olav Schiemann<sup>i</sup>

Received 7th September 2015, published online 26th September 2015.

Reprinted with permission from

A. Meyer, G. Schnakenburg, and O. Schiemann, *Acta Crystallographica E* **2015**, *E71*, 1245 - 1249.

Copyright ©2015, International Union of Crystallography.

### Own contributions to the manuscript

- Synthesis and crystallization of the title compound.
- Evaluation of the geometrical parameters of the crystal structure.
- Writing the manuscript.

The reprint of the publication can be found in appendix B.

---

<sup>i</sup> University of Bonn, Institute of Physical and Theoretical Chemistry, Wegelerstr. 12, 53115 Bonn, Germany.

<sup>ii</sup> University of Bonn, Institute of Inorganic Chemistry, Gerhard-Domagk-Strasse 1, 53121 Bonn, Germany.

## Introduction and Summary of Results

The second ligand which was investigated in detail is 4'-{[4-(2,2':6',2''-terpyridyl-4'-yl)phenyl]-ethynyl}biphenyl-4-yl-(2,2,5,5-tetramethyl-*N*-oxyl-3-pyrrolin-3-yl)formate **4-1**. The ligand is similar to **3-1** with respect to its overall design concept, i.e. a terpyridine which is linked to a nitroxide by a rigid bridge of 1,4-phenylene and ethynylene units. However, **4-1** differs in two important aspects from **3-1**. First of all, the expected interspin separation in metal complexes of **4-1** amounts to ~26 Å. Therefore, an observation window of more than 1000 ns is necessary to observe three complete dipolar modulations which is 2.5 times larger than the expected observation window for **3-1**. Larger observation windows reduce the sensitivity of EPR distance measurements according to eq. (2-52). However, a required observation window exceeding 1000 ns makes complexes of **4-1** more relevant as a model system for biological macromolecules.<sup>24</sup> The greater interspin separation also reduces eventual exchange interactions as the magnitude of such interactions decreases exponentially with the interspin separation.<sup>207,208</sup> As a second difference, the nitroxide is linked to the aromatic spacer via a carboxylate group. This group is expected to disrupt exchange pathways, as the pyrrolin-*N*-oxyl and the terpyridine-phenylene-ethynylene system are then cross conjugated with the carboxylate group.<sup>209–212</sup> The introduction of the carboxylate group comes at the cost of an increased flexibility. Most importantly, the existence of rotational degree of freedom around the bond between the carbonyl carbon atom and the hydroxyl oxygen atom of the carboxylate group can be suspected, giving rise to a *cisoid* and a *transoid* conformation. The separation between the nitroxide and the terpyridine groups differs by ~0.5 nm in the depicted conformations. In the studies presented in appendices D and E however, narrow distance distributions with only one expected distance are preferred, as broad or complicated distance distributions give rise to strongly damped PELDOR and RIDME time traces. Furthermore, complicated distance distributions with more than one actual interspin distance hamper the identification of artifact peaks. Hence, the occurrence of the two conformers given in Figure 4.1 would render complexes of **4-1** unsuited as model systems for the performed studies (Figure 4.1). Theoretical and experimental results suggest, that such rotations around the carbon oxygen single bond of the carboxylate group are hindered and that the *transoid* conformation (Figure 4.1) is clearly preferred.<sup>213,214</sup> Previously, **4-1** has also been

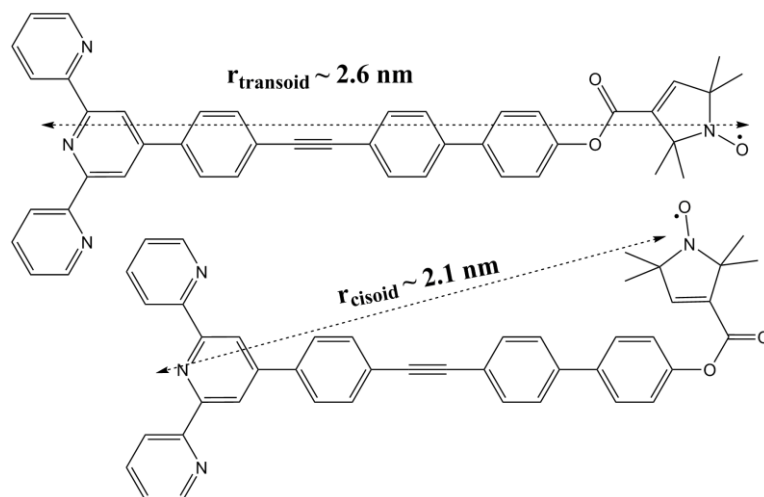


**Figure 4.1.** Two conformations of the carboxylate group giving rise to different distances between the nitroxide and the terpyridine groups.

used as ligand for zinc complexes and was also crystallized.<sup>215</sup> The solvents used for crystallization differed from those used herein, and different solvate crystals of **4-1** were obtained, namely the benzene solvate **4-2** (presented in appendix B) and the dichloromethane solvate **4-3**. Therefore, the crystallographic study also allowed elucidating if strong conformational differences of **4-1** are observed in different environments and if those differences would affect the interspin separation in metal complexes of **4-1**. In the study presented in appendix B, it was found that the carboxylate group assumes the *transoid* conformation in both **4-2** and **4-3**. Furthermore, the phenylene-ethynylene backbone was found to be only slightly bent in both crystal structures and that the separation between the nitroxyl group and the nitrogen atom of the central pyridine ring of the terpyridine ligand amounts to 2.5 nm. This is in good agreement with the expected value given for the *transoid* conformation in Figure 4.1. Concerning the intermolecular interactions, slipped face-to-face  $\pi$  stacking as well as edge-on C-H $\cdots\pi$  bonding was observed, similar to the features observed for **3-1**.



## 5. (Bis(terpyridine))copper(II) Tetraphenylborate: A Complex Example for the Jahn–Teller Effect

Andreas Meyer,<sup>i</sup> Gregor Schnakenburg,<sup>ii</sup> Robert Glaum,<sup>ii</sup> and Olav Schiemann<sup>i</sup>

Received 22th of May 2015, published online 14th August 2015.

Reprinted with permission from

A. Meyer, G. Schnakenburg, R. Glaum, and O. Schiemann, *Inorganic Chemistry* **2015**, *54*, 8456 - 8464.

Copyright ©2015, American Chemical Society.

### Own contributions to the manuscript

- Synthesis and crystallization of the title compound.
- Evaluation of the geometrical parameters of the crystal structure.
- Measurement and interpretation of the EPR spectra.
- Interpretation of the UV/vis spectra.
- Performing the AOM calculations.
- Writing the manuscript.

The reprint of the publication can be found in appendix C.

---

<sup>i</sup> University of Bonn, Institute of Physical and Theoretical Chemistry, Wegelerstr. 12, 53115 Bonn, Germany.

<sup>ii</sup> University of Bonn, Institute of Inorganic Chemistry, Gerhard-Domagk-Strasse 1, 53121 Bonn, Germany.

## Introduction and Summary of Results

Having obtained and analyzed ligand **4-1**, it was possible to prepare metal complexes suitable for EPR distance measurements. The resulting complexes showed EPR spectra typical of nitroxides and copper bisterpyridines,<sup>216–218</sup> indicating that any exchange interaction was suppressed sufficiently to be negligible. Moreover, initial EPR distance measurements could be conducted successfully. However, it turned out that the obtained time traces were not reproducible on a quantitative level in terms of modulation depth (PELDOR and RIDME) and the shape of the formfactor (PELDOR). It was also noted that the EPR spectrum and thus also the EPR parameters as e.g.  $\bar{g}$  change depending on the choice of the solvent system and the measurement temperature. Copper(II) ions are often highly plastic in their immediate coordination environment,<sup>219–221</sup> suggesting that a change of the solvent or of the temperature might lead to structural changes around the copper(II) ion. The occurrence of Jahn-Teller (JT) and pseudo Jahn-Teller (PJT) effects is one important reason for the observed plasticity in the coordination environment of the copper ions.<sup>220–224</sup> The JT and PJT effects lead to a coupling of the electronic and the geometrical structure via molecular vibrations. Crystal and ligand field treatments suggest that changes in the coordination geometry lead to changes in the electronic structure of the metal ion,<sup>225,226</sup> which relates to  $\bar{g}$  via eq. (2-7). It was necessary to study these effects in detail since changes in both the geometric and the electronic structure of the copper center affect EPR distance measurements. To do so, the unsubstituted copper bis(terpyridine) complex was synthesized as tetraphenylborate [Cu(tpy)<sub>2</sub>](BPh<sub>4</sub>)<sub>2</sub> **5-1**. In this complex, the EPR signal of the copper center is not superimposed with the signal of a nitroxide. Furthermore, it was possible to obtain single crystals of **5-1** suitable for X-ray crystallography and single crystal UV/Vis and EPR measurements. Additional experiments have been conducted on microcrystalline powders of **5-1**. The results have been analyzed using a crystal field approach and the angular overlap model. Finally, experiments on frozen solutions of **5-1** have been conducted and compared to the results obtained for the crystalline samples. Combining the above mentioned methods allowed obtaining a detailed picture of the geometric and electronic structure of copper bis(terpyridine) complexes. The X-ray crystallographic studies revealed that bis(terpyridine) copper(II) complex cations are elongated, distorted octahedra with  $D_{2d}$  symmetry and contain three pairs of Cu-N bonds. These pairs can be classified as long, intermediate, and short bond

pairs. Single crystal EPR showed that a rhombic  $g$ -tensor with principal values of  $g_x \approx 2.250$ ,  $g_y \approx 2.095$  and  $g_z \approx 2.045$  is expected at low temperatures. Additionally, the single crystal EPR measurements allowed relating the orientation of the principal axes of the  $g$ -tensor to the long, intermediate, and short bonds, respectively. It was possible to relate bond lengths and  $g$ -values by using the X-ray crystallographic information, the single crystal EPR data, and angular overlap calculations which were supported by UV/Vis spectroscopy on single crystals and microcrystalline powders. It was furthermore shown, that  $g$ -values similar to those observed using single crystals are obtained in a solvent system consisting of dimethylsulfoxide (DMSO) and methanol. Contrastingly, pure DMSO or DMSO mixed with chloroform produced  $g$ -tensors with higher  $g$ -anisotropy. This observation was attributed to a higher degree of PJT distortion of the coordination sphere or to the loss of one terpyridine ligand in the corresponding solvent systems. The possibility of ligand loss rendered these solvent systems unsuited for the EPR distance measurements discussed in chapter 6. Thus, the results obtained applying X-ray crystallography, UV/Vis and EPR spectroscopy using single crystals (X-ray, UV/Vis, and EPR), microcrystalline powders (UV/Vis and EPR) and frozen solutions (EPR) helped to achieve reproducible results in EPR distance measurements on the copper complexes of **4-1**. Furthermore, it was possible to obtain an understanding of the processes occurring in the coordination sphere of the copper center at different temperatures by conducting all experiments (EPR, X-ray diffraction, and UV/Vis) at different temperatures and observing the onset of the dynamical PJT effect at temperatures below 50 K. This understanding was relevant for the analysis of the distance measurements using copper complexes of **4-1**, as the dynamic structural changes in **5-1** strongly affected the  $g$ -values of the copper centered spin. Analogous dynamic processes were expected for the copper complexes of **4-1** regardless of the bulky substituent in the 4'-position of the terpyridine ligating subunit. The occurrence of such dynamic effects even at low temperatures emphasized the importance of conducting each distance measurement to be discussed in chapter 6 at an identical measurement temperature well below the onset point of the PJT effect.

## 6. Single and Double Nitroxide Labeled Bis(terpyridine)-copper(II): Influence of Orientation Selectivity and Multispin Effects on PELDOR and RIDME

Andreas Meyer,<sup>i</sup> Dinar Abdullin,<sup>i</sup> Gregor Schnakenburg,<sup>ii</sup> Olav Schiemann<sup>i</sup>

Received 10th December 2015, published online 24th February 2016.

Reprinted with permission from  
A. Meyer, D. Abdullin, G. Schnakenburg, and O. Schiemann, *Physical Chemistry Chemical Physics* **2016**, *18*, 9262 - 9271.  
Copyright ©2016, Royal Society of Chemistry.

### Own contributions to the manuscript

- Synthesis and crystallization of the measured compounds.
- Evaluation of the geometrical parameters of the crystal structure.
- Conducting the EPR Measurements.
- Interpretation of the EPR spectra and the RIDME time traces.
- Calculation of multispin effects.
- Writing the manuscript.

The reprint of the publication can be found in appendix D.

---

<sup>i</sup> University of Bonn, Institute of Physical and Theoretical Chemistry, Wegelerstr. 12, 53115 Bonn, Germany.

<sup>ii</sup> University of Bonn, Institute of Inorganic Chemistry, Gerhard-Domagk-Strasse 1, 53121 Bonn, Germany.

## Introduction and Summary of Results

The analysis of the relation of the geometric and the electronic structure of copper bisterpyridine complexes and how these affect the EPR parameters allowed proceeding to the copper(II) complexes of ligand **4-1**, specifically the heteroleptic complex  $[\text{Cu}(\mathbf{4-1})(\text{tpy})](\text{PF}_6)_2$  (**6-1a**) and the homoleptic complex  $[\text{Cu}(\mathbf{4-1})_2](\text{PF}_6)_2$  (**6-1b**). These copper compounds are low spin ( $s = \frac{1}{2}$ ) metal complexes bearing a nitroxide spin center separated by a distance of  $\sim 26$  Å determined by the ligand backbone (chapter 4), which makes these complexes suited as test systems for EPR distance measurements. Measurements on copper(II) systems have been reported in the literature and some of the main challenges of distance measurements in such systems have been discussed.<sup>160,227–230</sup> Therefore, the copper complexes could be used to set up measurement protocols for the subsequent experiments on the more challenging high-spin ( $S = 5/2$ ) manganese analogue of **6-1b**. Aside from this pragmatic aspect, the measurements would also shed light on some aspects not investigated previously. For example, **6-1b** represents a three-spin system where one spin center is a metal ion with spectroscopic properties strongly different from those of the nitroxides in the ligand **4-1**, thus forming an  $\text{AB}_2$ -spin-system. A similar system has been investigated before by Narr *et al.*<sup>231</sup> However, the primary aim of Narr's early study was to establish the feasibility of copper-nitroxide distance determinations using PELDOR. The RIDME experiment was not conducted in this study and orientation selectivity was observed but not analysed in detail. The occurrence of multi-spin effects (MSE) in distance measurements<sup>155–157,232</sup> was also not treated before. In the  $\text{AB}_2$ -spin-system at hand, distortion of the time traces in PELDOR experiments by the combined effects of orientation selection and MSE is expected if the nitroxide is used for pumping. On the other hand, the  $\text{AB}_2$  composition of **6-1b** allows selective excitation of one type of spin, opening up a possibility to suppress MSE by using the nitroxide for observation in either PELDOR or RIDME. MSE can also be used to assess how many spins are actually coupled to each other in a given spin system.<sup>155</sup> Counting the spins per molecule allows investigating the inertness of the copper complexes with respect to ligand-solvent (**6-1a** and **6-1b**) or ligand-ligand exchange (only **6-1a**) in solution.<sup>203,215</sup> For complexes **6-1a** and **6-1b**, the occurrence of orientation selectivity is expected in the distance measurements. This selectivity can be accounted for using PeldorFit.<sup>230</sup> The crystal structures of **4-1** and **6-1b** (see below) in combination with the detailed information concerning the orientation of the

molecular and the  $g$ -tensor framework of the copper center in bis(terpyridine) complexes (chapter 5) allowed analyzing the geometrical relation between the spin centers independent of any EPR measurement. Comparison of the PeldorFit parameters (i.e. the distance  $r$  and the angles  $\phi$  and  $\zeta$ , Figure 6.1) with the values expected from crystallography can then be used to decide whether the fitting parameters are only effective parameters or if they have an actual geometric significance.

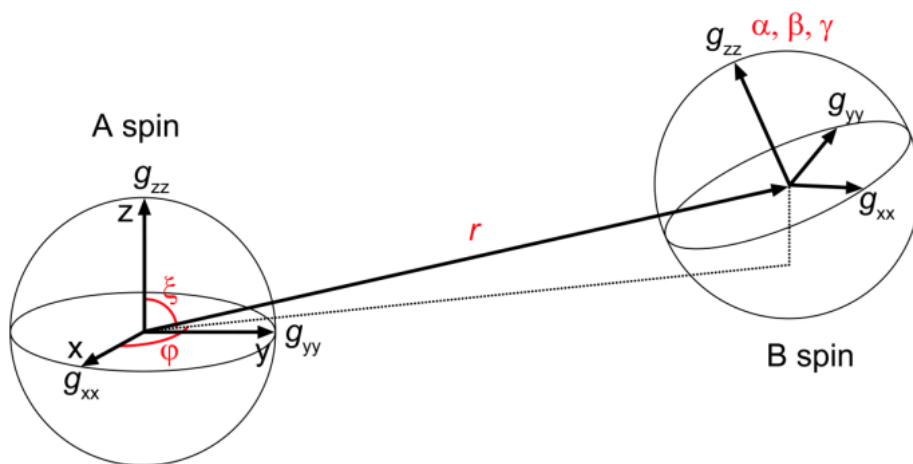


**Figure 6.1.** Geometric parameters used by PeldorFit. A spin = observer spin, B spin = pumped spin. Figure reproduced from the original publication concerned with PeldorFit by Abdullin *et al.*<sup>230</sup>

Finally, no detailed comparison of the RIDME and PELDOR experiment in terms of orientation selection, sensitivity, and the ability to selectively measure a single interspin distance has been performed before on such a complex spin system. Thus, the investigations on the copper model systems contributed to this work in a twofold manner. First, the investigation served as preparation for the more challenging, high-spin manganese(II) system discussed in chapter 7. Additionally, it also represents a study on a sophisticated metal-nitroxide spin system shedding light on some new aspects of EPR distance measurements involving metal centers. The first point addressed in the study presented in appendix D was the ligand exchange equilibrium for **6-1a**. Measuring PELDOR time traces using the nitroxide for both observation and pumping should result in unmodulated time traces for pure **6-1a**. However, the experimental time traces obtained show modulations corresponding to the internitroxide distance of  $\sim 52$  Å. Repeating the same experiment on **6-1b** and comparing the modulation depths of both experiments revealed that samples having

the same elemental composition as pure **6-1a** would have actually consist of three different copper complexes, namely  $[\text{Cu}(\text{tpy})_2](\text{PF}_6)_2$ , **6-1a**, and **6-1b** in equal amounts. These complexes are formed via ligand exchange reactions and the resulting mixtures are referred to as **6-1x**. PELDOR measurements aimed at obtaining the copper-nitroxide distance in **6-1x** and **6-1b** yielded time traces which were strongly distorted by orientation selection. It was possible to account for these effects by using PeldorFit to simulate the PELDOR time traces. The obtained geometrical fitting parameters agree with the expectations based on the crystal structures of **4-1**, **6-1b**, and the EPR parameters obtained for **5-1**. The observed modulation depths were much larger for **6-1b** than for **6-1x**, which is caused by the occurrence of MSE. However, the respective form factors differed only slightly, although three-spin correlations are expected to occur in three-spin systems showing MSE. These three-spin correlations supposedly lead to deformations of the form factor. To investigate these seemingly contradicting results a combined experimental and theoretical approach was chosen. Experimentally, the pump pulse power was reduced and a series of PELDOR measurements aimed at the copper-nitroxide distance in **6-1b** was conducted. Reducing the power of the pump pulse reduced its inversion efficiency and therefore suppresses three-spin correlations (see chapter 2.3.6). The obtained form factor showed fewer deviations from the form factor of **6-1x** compared to the form factor obtained with full pumping power, indicating that the slight deviations observed using the full power pump pulses were indeed caused by three-spin correlations. Additionally, MSE have been simulated using the equations given in chapter 2.3.6 and the geometrical factors  $\alpha(\theta)$  given by PeldorFit for **6-1x** to obtain theoretical form factors for **6-1x**, **6-1b**, and the hypothetical, pure **6-1a**. The simulated time traces showed modulation depths matching the experimental ones. Additionally, the three-spin correlation function was found to only slightly distort the form factors. The deviations in these theoretical form factors occurred at the same positions where deviations between the form factors have been observed experimentally. This showed that MSE did indeed occur in the orientation selective PELDOR measurements and also supported the analysis of the chemical composition of **6-1x**. The copper nitroxide distance was also measured using RIDME for both systems. RIDME was shown to suppress orientation selection and yielded distance distributions with only a single peak at the correct distance of 2.53 nm. It was found that RIDME is more sensitive and suppresses MSE. Finally, the

occurrence of axial  $g$ -tensors was investigated by acidifying samples of **6-1x** and **6-1b**. This was found to have the same effect on the EPR parameters observed previously on **5-1** using solvent systems consisting of either pure DMSO or mixtures of DMSO and  $\text{CDCl}_3$ . In such systems, it was no longer possible to measure an internitroxide distance using PELDOR, as only unmodulated time traces could be obtained. This suggested that one of the ligands is replaced by solvent molecules in acidified solvent systems. Analysis of the modulation depths of PELDOR and RIDME measurements aimed at the copper nitroxide distance further validated this interpretation. Additionally, the PELDOR time traces obtained in acidified samples have been simulated using PeldorFit. The obtained geometrical parameters allowed suggesting a square-pyramidal coordination geometry for the copper-terpyridine solvent complexes.



## 7. PELDOR and RIDME Measurements on a High-Spin Manganese(II) Bisnitroxide Model Complex

Andreas Meyer,<sup>i</sup> Olav Schiemann<sup>i</sup>

Received 22th January 2016, published online 9th May 2016.

Reprinted with permission from  
A. Meyer and O. Schiemann, *Journal of Physical Chemistry A* **2016**, *120*, 3463 - 3472.  
Copyright ©2016, American Chemical Society.

### Own contributions to the manuscript

- Synthesis measured compounds.
- Conducting the EPR Measurements.
- Interpretation of the EPR data.
- Writing the manuscript.

The reprint of the publication can be found in appendix E.

---

<sup>i</sup> Institute of Physical and Theoretical Chemistry, University of Bonn, Wegelerstr. 12, Bonn, Germany.

## Introduction and Summary of Results

The investigation of the manganese(II) complex  $[\text{Mn}(\mathbf{4-1})_2](\text{PF}_6)_2$  (= **7-1**, the manganese(II) analogue of  $[\text{Cu}(\mathbf{4-1})_2](\text{PF}_6)_2$  (**6-1b**) discussed in the previous chapter) represents the final chapter dealing with EPR distance measurements involving metal ions. A high-spin  ${}^6A_1$  ground state is expected for the manganese ion, which leads to the occurrence of ZFS interactions. It has been shown that ZFS occurs in bis(terpyridine) manganese(II) complexes despite the symmetric ground state. The reasons for the occurrence of ZFS are slight deviations from the ideal, high symmetry. These deviations reinstall the SOC contribution to the ZFS as well as a considerable contribution from spin-spin interaction to the ZFS.<sup>109–112,233</sup> The ZFS interactions broaden the spectrum, as electron spin transitions from the different  $M_s$  states occur at different resonance fields.<sup>56,65</sup> Additionally, transitions with  $|\Delta M_s| > 1$  can occur. The ZFS tensor  $\bar{D}$  reacts very sensitively even to slight geometric changes around the spin center.<sup>233</sup> Hence, varying degrees of deviation from the ideal coordination sphere around the manganese ion in **7-1b** (as observed for its copper(II) analogue **6-1b**) would lead to further broadening by the occurrence of  $\bar{D}$  strain effects. The occurrence of ZFS opens up further relaxation pathways and thus enhances the relaxation of the manganese centered spins.<sup>123,234–236</sup> Finally, the absorption lines in high-spin complexes are broadened by 2<sup>nd</sup> order mixing of different spin states if the high field condition is not met.<sup>67</sup> Then, the magnetic quantum numbers  $m_s$  are no longer good quantum numbers. It is therefore expected, that measurements at higher MW frequency should yield results which are more readily analyzed. In contrast, for the copper complexes discussed in chapter 6, the higher MW frequency led to increased spectral widths owed to the large  $g$ -anisotropy of the copper center in **6-1a** and **6-1b**. For **7-1b**, the  ${}^6A_1$  ground state is expected to result in nearly isotropic  $g$ - and  $A$ -values,<sup>233,237</sup> which should drastically reduce orientation selection effects. As the geometries of **6-1b** and **7-1** are very similar, multi-spin effects should behave completely analogous to those observed for **6-1b**. Furthermore, the close similarity between **6-1b** and **7-1** allows analyzing the spectroscopic data easily, as striking spectroscopic differences could be attributed to the ZFS. The main results of the investigation presented in appendix E are briefly summarized here. One of the striking differences between **6-1b** and **7-1** is the necessity to measure at Q-band MW frequency to obtain a manganese(II) signal.

This signal could be fitted using a  $D$  value of 1.5 GHz in addition to isotropic  $g$ - and  $A$ -values of 2.004 and 250 MHz, respectively. It was possible to measure the manganese-nitroxide distance both with PELDOR and with RIDME. The PELDOR time traces measured at two observer positions did not show signs of strong orientation selection and could be analyzed with DeerAnalysis to yield distance distributions dominated by one peak at 2.68 nm. This distance corresponds to the expected manganese-nitroxide distance. A strong influence of interstate mixing for the manganese spin on the PELDOR time traces could not be observed, as this would supposedly lead to broad distance distributions. The intense main peak was accompanied by low intensity artifact peaks, especially for the case of a frequency offset of  $\nu_{obs} - \nu_{pump} = 90$  MHz. Repeating the PELDOR measurement using reduced pump power led to fewer artifact peaks, suggesting that MSE are one source for the artifact peaks. Measuring the manganese-nitroxide separation with RIDME to further suppress MSE and orientation selection yielded time traces which could be converted to distance distributions without those weak artifact peaks observed in PELDOR. However, strong artifact peaks caused by higher harmonics of the dipolar coupling frequency could be observed. These higher harmonics were attributed to  $|\Delta M_s| = 2$  and  $|\Delta M_s| = 3$  transitions of the manganese spin during the interval  $T$  of the RIDME sequence. In addition to the metal-nitroxide distance, the nitroxide-nitroxide distance was measured using PELDOR. The resulting time traces were modulated by two dipolar frequencies corresponding to the nitroxide-nitroxide interaction and to the nitroxide-manganese interaction. This was caused by simultaneous pumping of the manganese spin when attempting to pump the nitroxide since the spectra of both spin centers are superimposed over the whole width of the nitroxide spectrum. Finally, the chemical behaviour of **7-1** was investigated. Comparison of the modulation depths of the different PELDOR time traces allowed estimating that ~30% of the ligands in **7-1** have been replaced by solvent molecules.

## **Part III.**

# **Characterization of [Si<sub>2</sub>]-Radicals and Titanocene Complexes Using Electron Paramagnetic Resonance**

## 8. One-Electron Oxidation of a Disilicon(0) Compound: An Experimental and Theoretical Study of NHC-trapped $[\text{Si}_2]^+$

Marius I. Arz,<sup>i</sup> Martin Straßmann,<sup>i</sup> Andreas Meyer,<sup>ii</sup> Gregor Schnakenburg,<sup>i</sup> Olav Schiemann,<sup>ii</sup> and Alexander C. Filippou<sup>i</sup>

Received 5th June 2015, published online 5th August 2015.

Reprinted with permission from  
M. I. Arz, M. Straßmann, A. Meyer, G. Schnakenburg, O. Schiemann, and A. C. Filippou, *Chemistry - A European Journal* **2015**, *21*, 12509 - 12516.  
Copyright ©2015, WILEY-VCH Verlag GmbH & Co. KGaA, Weinheim.

### Own contributions to the manuscript

- Conducting the EPR measurements.
- Interpretation of the EPR spectra.
- Writing parts of the manuscript.

The reprint of the publication can be found in appendix F.

---

<sup>i</sup> Institut für Anorganische Chemie, Universität Bonn, Gerhard-Domagk-Straße 1, 53121 Bonn, Germany.

<sup>ii</sup> Institut für Physikalische und Theoretische Chemie, Universität Bonn, Wegelerstr. 12, 53115 Bonn, Germany.

## Introduction and Summary of Results

The first chapter of the 3<sup>rd</sup> part of this thesis is the investigation of an *N*-heterocyclic carbene (NHC) substituted disilicon radical cation  $[\text{Si}_2(\text{Idipp})_2]^+$  **8-1<sup>+</sup>** (Idipp = 1,3-bis(2,6-diisopropylphenyl)imidazole-2-ylidene), which was synthesized by M. Arz in the group of Prof. Filippou and might be a model for the unsubstituted disilicon cation  $[\text{Si}_2]^+$ . **8-1<sup>+</sup>** is obtained by electrochemical or chemical one-electron oxidation of the neutral disilicon(0) precursor  $\text{Si}_2(\text{Idipp})_2$  **8-1**. In accordance with its symmetric substitution pattern, **8-1** is a symmetric molecule as evidenced by X-ray crystallography and NMR spectroscopy.<sup>238</sup> Its oxidation product **8-1<sup>+</sup>** on the other hand surprisingly shows only  $C_1$  symmetry instead of  $C_i$  or  $C_2$  symmetry in its crystal structure. This is reflected in the inequivalent pair of Si-C<sub>NHC</sub> bond lengths amounting to 1.899 and 1.910 Å, respectively, or even more clearly in the inequivalent pair of Si-Si-C<sub>NHC</sub> bond angles of 109.9 and 101.9°. In the crystal structure, deviations from the ideal symmetry may be explained by packing effects.<sup>239,240</sup> However, such packing effects cannot be easily quantified or even verified. Comparison with structure of related compounds provides further information on possible molecular structures for **8-1<sup>+</sup>**. An analogous reduction of symmetry upon oxidation was observed in the case of the digermene dianion  $[\text{Ge}_2\text{R}_2]^{2-}$  (R= aryl substituent) leading to  $[\text{Ge}_2\text{R}_2]^-$ , which are isolobal Ge analogues of **8-1** and **8-1<sup>+</sup>**, respectively.<sup>241,242</sup> The diphosphorus radical cation  $[\text{P}_2(\text{Idipp})_2]^+$  shows a molecular structure similar to that of **8-1<sup>+</sup>**. There, the two phosphorus atoms are clearly inequivalent with P-C<sub>NHC</sub> bond lengths of 1.795 and 1.810 Å and P-P-C<sub>NHC</sub> bond angles of 102.7 and 96.7°. Contrastingly, equivalent phosphorus atoms are observed in  $[\text{P}_2(\text{caac})_2]^+$  (caac = cyclic alkyl(amino)carbene, equivalent P-C<sub>NHC</sub> bond lengths of 1.799 Å with P-P-C<sub>NHC</sub> bond angles of 101.8° and equivalent P-C<sub>NHC</sub> bond lengths of 1.776 Å with P-P-C<sub>NHC</sub> bond angles of 102.2° for the two independent cations in the asymmetric unit) in their crystalline state reported by Back *et al.*<sup>243</sup> Very slight differences between the two silicon atoms have been observed in a silylsubstituted disilyne radical anion  $[\text{Si}_2\text{R}_2]^-$  (R = silyl substituent), which is isolobal to **8-1<sup>+</sup>**, by Kinjo *et al.* (differences in the Si<sub>Silyne</sub>-Si<sub>Silyl</sub> bond lengths and the Si<sub>Silyne</sub>-Si<sub>Silyne</sub>-Si<sub>Silyl</sub> bond angles of 0.01 Å and 1°, respectively).<sup>244</sup> The cited studies present four similar molecules with either symmetrical ( $[\text{P}_2(\text{caac})_2]^+$ ), slightly distorted ( $[\text{Si}_2\text{R}_2]^-$ ) or heavily distorted ( $[\text{Ge}_2\text{R}_2]^-$  and  $[\text{P}_2(\text{Idipp})_2]^+$ ) structures. Therefore, it is not clear why packing effects should lead to lower symmetries in some cases but in others not. Noteworthy, DFT calculations

on **8-1<sup>+</sup>** predicted a  $C_1$  symmetrical structure as global minimum, in accordance with the observations from the crystal structure. It is also known, albeit not always appreciated,<sup>i</sup> that every polyatomic system is subject to the PJT effects (see also chapter 5).<sup>245</sup> Therefore, it is actually not surprising to find low symmetry structures. The variety of structures observed experimentally in related compounds and the theoretical framework of the PJT effects justify a more detailed investigation of the structure, while assigning the observed low symmetry structure to packing effects only occurring in the crystal would have been superficial. EPR spectroscopy with its high sensitivity to structural changes in spin centers (see chapter 1 and 2) allowed investigating the structure of **8-1<sup>+</sup>** in liquid and frozen solution. The spectroscopic study presented in appendix F is summed up briefly. In liquid solution, EPR spectroscopy was used to observe the satellite signals caused by  $^{29}\text{Si}$  nuclei in their natural abundance. In these liquid samples, both silicon atoms were observed to be equivalent on the time scale of the measurement down to the freezing point of the solvent diethylether (-116 °C). The main signal caused primarily by the  $^{28}\text{Si}^{28}\text{Si}$  isotopomer<sup>ii</sup> was centered at an isotropic  $g$ -value of 1.9979 and was flanked by two satellite lines on both sides with a field separation of ~1.5 mT. The intensity of these satellite lines amounted to approximately 10% of the main signal. The occurrence of just one doublet with this relative intensity suggested that the satellites are caused by two equal isotopomers  $^{28}\text{Si}^{29}\text{Si}$  and  $^{29}\text{Si}^{28}\text{Si}$ . If those isotopomers were unequal one would expect to observe two distinct doublets each with only approximately 5% intensity. Additionally, the main signal was flanked at both sides by a further set of satellite lines caused by the  $^{29}\text{Si}^{29}\text{Si}$  isotopomer at separations of ~3 mT to the  $^{28}\text{Si}^{28}\text{Si}$  signal with an intensity of approximately 0.2%. This separation is supposed to amount to the sum of the coupling constants to each silicon nucleus in the disilicon radical. The observed separation is twice the value observed for the first set of satellite lines. This was taken further indication of the equality of both silicon atoms in liquid solution. A similar analysis of the satellites in frozen solutions at 50 K indicated that the silicon atoms are inequivalent and have hyperfine coupling constants which

---

<sup>i</sup> While many concepts to predict molecular structures are taught (like hybridization, the VSEPR model, steric hindrance, Walsh diagrams etc...), it is rarely mentioned that these are manifestations of the PJT effect.<sup>245</sup>

<sup>ii</sup> Approximately 10% of this peak's intensity is caused by isotopomers in which one or both  $^{28}\text{Si}$  nuclides are replaced by  $^{30}\text{Si}$  nuclides. These nuclides cannot be distinguished by EPR spectroscopy. For brevity, only  $^{28}\text{Si}$  is written in the introductory texts of chapters 8 and 9 when actually both nuclides  $^{28}\text{Si}$  and  $^{30}\text{Si}$  are meant.

differ by ~45 MHz. Thus, it was necessary to differentiate  $^{28}\text{Si}^{29}\text{Si}$  and  $^{29}\text{Si}^{28}\text{Si}$ , i.e. to label the Si nuclei with either **A** or **B** subscripts. Such a labelling is in agreement with the structure obtained using X-ray crystallography. Furthermore, DFT calculations also suggested inequivalent Si nuclei in the equilibrium structure of the disilicon radical. These results could be harmonized using DFT calculations and Eyring's transition state theory. Using DFT, a low energy pathway which allows interconversion of the isotopomers with an activation energy of ~6 kJ/mol could be found. The interconversion of isotopomers can be symbolized by the reaction  $^{29}\text{Si}_\text{A}^{28}\text{Si}_\text{B} \rightarrow ^{29}\text{Si}_\text{B}^{28}\text{Si}_\text{A}$ . Using Eyring's theory, it could be shown that the satellites owed to  $^{29}\text{Si}_\text{A}^{28}\text{Si}_\text{B}$  and  $^{29}\text{Si}_\text{B}^{28}\text{Si}_\text{A}$  would still coalesce even at the freezing point of the solvent. Thus, the experimental and theoretical data suggest the apparent equivalence of the two silicon nuclei in the liquid state is caused by dynamic interconversion of isomers involving, according to DFT calculations, a combined bending and torsion of the NHC substituents.



## 9. The Si<sub>2</sub>H Radical Supported by Two N-heterocyclic Carbenes

Marius I. Arz,<sup>i</sup> Gregor Schnakenburg,<sup>i</sup> Andreas Meyer,<sup>ii</sup> Olav Schiemann,<sup>ii</sup> and Alexander C. Filippou<sup>i</sup>

Received 9th April 2016, published online 9th May 2016.

Reprinted with permission from  
M. I. Arz, G. Schnakenburg, A. Meyer, O. Schiemann, and A. C. Filippou, *Chemical Science* **2016**, 7, 4973 - 4979.  
Copyright ©2016, Royal Society of Chemistry.

### Own contributions to the manuscript

- Conducting the EPR measurements.
- Interpretation of the EPR spectra.
- Writing parts of the manuscript.

The publication can be found in appendix G.

---

<sup>i</sup> Institut für Anorganische Chemie, Universität Bonn, Gerhard-Domagk-Straße 1, 53121 Bonn, Germany.

<sup>ii</sup> Institut für Physikalische und Theoretische Chemie, Universität Bonn, Wegelerstr. 12, 53115 Bonn, Germany.

## Introduction and Summary of Results

The reactions of  $\text{Si}_2(\text{Idipp})_2$  (**8-1**) with small electrophilic reagents were investigated after the synthesis and investigation of **8-1** and **8-1<sup>+</sup>**.<sup>246</sup> Using  $[\text{H}(\text{OEt}_2)_2][\text{B}(\text{Ar}^{\text{F}})_4]$  ( $\text{Ar}^{\text{F}} = \text{C}_6\text{H}_3\text{-3,5-(CF}_3)_2$ ), it was possible to obtain  $[\text{HSi}_2(\text{Idipp})_2]^+$  (**9-1H<sup>+</sup>**), which could be reduced by  $\text{KC}_8$  leading to the neutral radical  $[\text{HSi}_2(\text{Idipp})_2]^\cdot$  (**9-1H<sup>\cdot</sup>**). For **9-1H<sup>+</sup>**, rapid 1,2-H-migration was observed using NMR spectroscopy at ambient temperature whereas crystallography showed localization of the hydrogen atom on a single silicon atom. Further hydrogen rearrangement reactions are known from other fields of chemistry (see chapter 10 for another example). For **9-1H<sup>\cdot</sup>** on the other hand, the crystal structure showed a symmetrical structure with half occupancy of the hydrogen sites. Owing to the low temporal resolution of standard X-ray crystallography (see also chapter 5), this observation can either be explained by statistical disorder in the crystal or by a dynamic migration of the hydrogen atom. Solid state infrared spectroscopy revealed a Si-H vibrational wavenumber of  $2089\text{ cm}^{-1}$ , indicative of terminally coordinated H atoms in the solid state structure. To investigate whether or not the hydrogen nucleus migrates in solution, variable temperature cw EPR spectroscopy in liquid solution was used. In liquid solution, the NHC nitrogen and silicon hyperfine coupling constants give rise to distinct coupling patterns depending on the equivalence or inequivalence of the silicon atoms and the nitrogen nuclei of the NHC ligands. Accounting for 1,2-H-migration and an eventual rotation of the NHC ligands gives rise to the situations summarized in Figure 9.1. Using liquid solutions of **9-1H<sup>\cdot</sup>** in hexane, cw EPR spectroscopy experiments were conducted at various temperatures. At room temperature, a multi-line signal centered at an isotropic  $g$ -value of 2.0056 could be observed. Its HFC structure could be simulated by assuming coupling to two pairs of equivalent nitrogen nuclei in the NHC substituents with isotropic coupling constants of  $a_{\text{iso}}(^{14}\text{N}_\text{A}) = 6.9\text{ MHz}$  and  $a_{\text{iso}}(^{14}\text{N}_\text{B}) = 2.8\text{ MHz}$ , respectively, and one hydrogen nucleus with an isotropic coupling constant of  $a_{\text{iso}}(^1\text{H}) = 17.1\text{ MHz}$ . The presence of two pairs of equivalent nitrogen nuclei requires the occurrence of one of two dynamic processes, namely either rotation of the carbene substituents or migration of the H atom (Figure 9.1). By repeating the cw EPR measurements in a temperature range of 183 - 336 K, it was attempted to freeze out the active process at low temperatures or to activate the inactive process at high temperatures. Activation or deactivation of one of these processes was assumed to lead to a different HFC pattern. However, no change of the multi-line

pattern was observed in this temperature range and it was concluded that the active process has very low activation barriers while the inactive process is kinetically hindered. H atom migration is known to proceed even at low temperatures (see also chapter 10). Furthermore, H atom migration can even proceed in the presence of high activation barriers via atom tunneling.<sup>247</sup> Therefore, the H atom migration process seems to be more plausible using qualitative arguments. To address which process is active, the <sup>29</sup>Si hyperfine lines observed in EPR spectroscopy have been analyzed. The analysis of the EPR data was supported by DFT calculations. The calculations suggested stable structures if the H atom is bound terminally to one of the two silicon nuclei. Neither a stable minimum structure nor a transition state with a bridging H atom could be found in these calculations. In the stable structures, the spin density is four times higher on the two-coordinated silicon nucleus Si2 than on the hydrogen bearing silicon atom Si1. Using this information, the EPR spectrum was fitted using <sup>29</sup>Si HFC coupling constants of  $a_{iso}(Si2) = 48.6$  MHz and  $a_{iso}(Si1) = 12.2$  MHz, assuming eq. (2-17) to be valid. These values reproduced the observed satellite lines nicely. Therefore, the EPR spectroscopic observations agree with the structures obtained by the DFT calculations. If the H atom is indeed localized on a single silicon nucleus one must assume rotation of the carbene substituents as cause for the pairwise equivalence of the carbene-nitrogen nuclei.

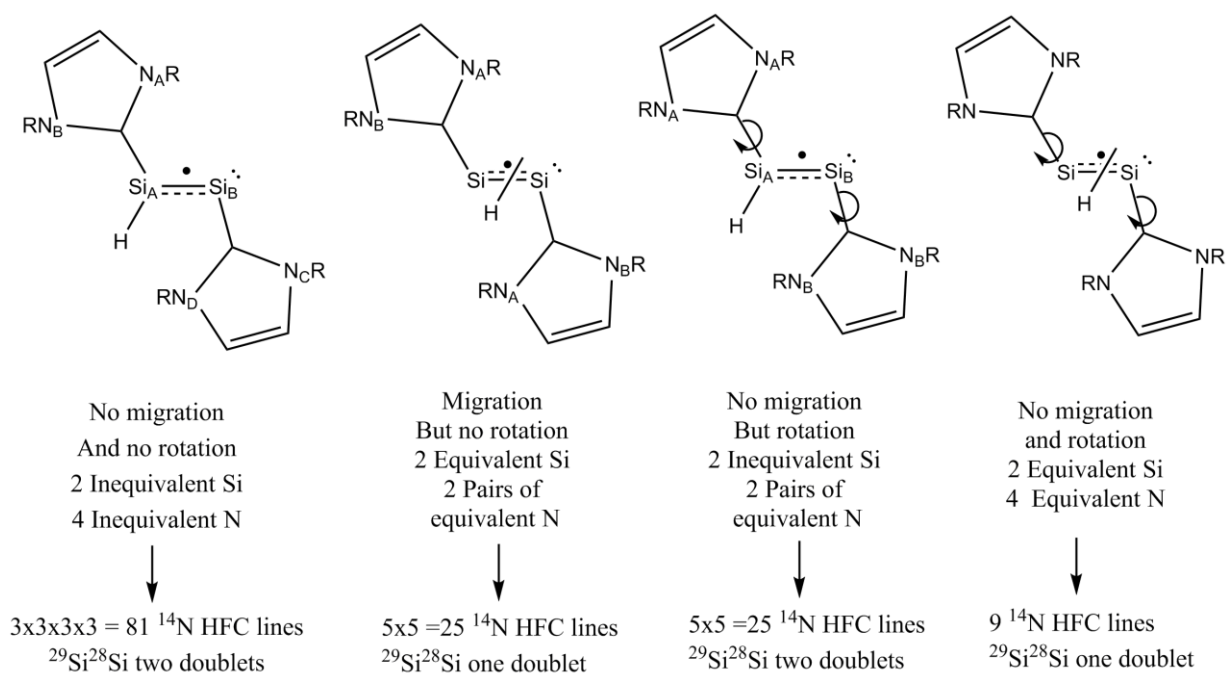


**Figure 9.1.** Different possible dynamics for **9-1H** (R = 2,6-<sup>i</sup>Pr-Ph) and the consequences on the hyperfine splitting pattern. The EPR spectrum is further split by hyperfine coupling to the hydrogen nucleus (see below).

## 10. Highly Active Titanocene-Catalysts for Epoxide Hydrosilylation – Synthesis, Theory, Kinetics, EPR

Dina Schwarz G. Henriques,<sup>i</sup> Katharina Zimmer,<sup>i</sup> Sven Klare,<sup>i</sup> Andreas Meyer,<sup>ii</sup> Elena Rojo-Wiechel,<sup>i</sup> Mirko Bauer,<sup>iii</sup> Rebecca Sure,<sup>iii</sup> Stefan Grimme,<sup>iii</sup> Olav Schiemann,<sup>ii</sup> Robert A. Flowers II<sup>iv</sup> and Andreas Gansäuer<sup>i</sup>

Received 3rd February 2016, published online 29th April 2016.

Reprinted with permission from

D. Schwarz G. Henriques, K. Zimmer, S. Klare, A. Meyer, E. Rojo-Wiechel, M. Bauer, R. Sure, S. Grimme, O. Schiemann, R. A. Flowers, and A. Gansäuer, *Angewandte Chemie International Edition* **2016**, *55*, 7671 –7675.

Copyright ©2016, WILEY-VCH Verlag GmbH & Co. KGaA, Weinheim.

### Own contributions to the manuscript

- Conducting the EPR and ENDOR Measurements.
- Interpretation of the EPR and ENDOR spectra.
- Writing parts of the manuscript.

The publication can be found in appendix H.

---

<sup>i</sup> Kekulé-Institut für Organische Chemie und Biochemie, Universität Bonn, Gerhard-Domagk-Straße 1, 53121 Bonn, Germany.

<sup>ii</sup> Institut für Physikalische und Theoretische Chemie, Universität Bonn, Wegelerstr. 12, 53115 Bonn, Germany.

<sup>iii</sup> Mulliken Center for Theoretical Chemistry, Universität Bonn, Beringstr. 4, 53115 Bonn, Germany.

<sup>iv</sup> Department of Chemistry, Lehigh University, Bethlehem, PA 18015 USA.

## Introduction and Summary of Results

The final chapter of this thesis is devoted to the investigation of epoxide hydrosilylation reactions catalyzed by reactive titanocene(III) species which are formed *in situ*. In the catalytic cycle, titanocene(III) hydrides are generated by reaction of different titanocene precursors with silanes.<sup>248</sup> Then, the catalytic reaction is believed to proceed in three essential steps. First, the titanocene hydride opens the epoxides by one electron reduction of one C-O bond resulting in a transient, carbon centered  $\beta$ -titanocene(IV)oxy-radical. Subsequently, an intramolecular hydrogen atom transfer (HAT) from the titanocene(IV) residue to the unsaturated carbon radical center takes place giving rise to a titanocene(III)alkoxide complex. The final step of the catalytic cycle is a  $\sigma$ -bond metathesis of the titanocene(III)alkoxide and the silane, yielding the initial titanocene(III)hydride complex and the silylated alcohol. Thus, in each of these essential catalytic steps the occurrence of a paramagnetic species is expected. It is obvious that these species need to be observed under conditions which resemble the conditions of the actual reaction to obtain relevant results. Moreover, the species proposed to occur in the essential steps should be easily discernible by EPR spectroscopy owed to their expected  $g$ -values [carbon centered radicals vs titanocene(III) complexes, see chapter 2.1.1 and eq. (2-7)] and hyperfine splittings (titanocenehydride vs titanocenealkoxide species). Aside from information about the immediate atomic environment of the unpaired electron it is also possible to obtain information about their more distant surroundings using hyperfine resolving spectroscopic techniques like ENDOR (chapter 2.3.4).<sup>249,250</sup> This is of great importance, as previous EPR spectroscopic studies on titanocenes indicated a complex chemical behavior of these complexes including dimerization,<sup>251-254</sup> occurrence of multiple species during catalysis, some of which are inactive resting states,<sup>255</sup> and agostic interactions with supposedly innocent ligands.<sup>256-258</sup> This rich chemistry requires a more detailed analysis than the sole determination of the type of atom which carries the spin density and of its immediate neighbors. Finally, titanocenesilyl complexes have been reported which are another possible transient species occurring during the catalytic cycle.<sup>259-261</sup> Although not reported in any of the cited work, these should be discernible by identifying the <sup>29</sup>Si satellites in cw EPR spectroscopy. Thus, EPR spectroscopy is well suited to investigate the catalytic hydrosilylation reaction, as it allows investigating the actual

reaction mixtures, meaning all reagents dissolved in the solvent which also used during synthesis. Furthermore, it is also possible to take snapshots at different stages of the catalytic cycle by rapid freezing of the reaction mixtures. In appendix H, the identification of two reactive titanocenehydrides as well as the observation of a titanocenealkoxide species representing a resting state of the catalytic cycle are described in detail while a brief summary follows here. To observe titanocene hydride species with the ability of transferring H atoms, the catalyst precursor titanocene-dichloride was mixed with allyl Grignard reagents and, in a second step, with phenylsilane. In the absence of substrates this yields solutions of titanocenehydride species which were transferred to EPR sample tubes and subjected to room temperature cw EPR spectroscopy at X-band MW frequency. The resulting spectra were dominated by two signals with clearly resolved pentet and triplet HFC patterns and isotropic coupling constants of 8.75 and 20.5 MHz, respectively. The two signals were observed to be centered at isotropic  $g$ -values of 1.9970 (pentet) and 1.9929 (triplet). The HFC structure and the  $g$ -values could be confirmed at Q-band MW frequency. Using deuterated silane during preparation of the catalysts led to signals centered at the same isotropic  $g$ -values without resolved HFC structure. This allowed attributing the observed hyperfine structures to coupling to hydrogen nuclei and identifying the silane as the source of the hydrogen nuclei. Comparison with the data of previously reported compounds allowed assigning the triplet signal to a titanocene(III)-( $\mu$ -H)<sub>2</sub>-magnesiumbromide complex. The pentet was assigned to the adduct of titanocene(III)hydride and phenylsilane which was predicted to be a stable compound by DFT calculations. After addition of the epoxide, titanocene(III)hydride species could no longer be observed EPR spectroscopically. Kinetic investigations suggested the formation of titanocene(III) ligated by one epoxide ligand and one alkoxide ligand as resting state of the reaction. The alkoxide ligand is formed after one electron reduction and ring opening of the epoxide followed by H atom transfer. To validate this analysis, ENDOR spectroscopy was used to study frozen samples of the reaction mixtures. These mixtures have been prepared using either non-deuterated reagents, deuterated silane with protonated epoxide, protonated silane with deuterated epoxide, or deuterated silane with deuterated epoxide simultaneously. For each deuteration process fewer proton resonances could be recorded using Davies ENDOR. Instead, deuteron resonances could be observed with Mims ENDOR in the samples prepared with deuterated reagents. These

deuteron resonances must stem from deuterated ligands. The detailed analysis of the observations indicated the presence of an alkoxide ligand in the observed titanocene species and agrees with the proposed resting state structure, albeit it was not possible to obtain evidence whether or not an additional epoxide ligand was bound. However, DFT calculations predict an exergonic formation of the proposed titanocene(III)alkoxide-epoxide compound starting from titanocene(III)alkoxide. This complex is predicted to be more stable than the corresponding titanocene(III)hydride-epoxide complex. Therefore, DFT calculations lend further support for the proposed resting state structure.

## 11. Final Summary, Conclusions, and Outlook

Part II of this thesis presented the synthesis and characterization of metal nitroxide model systems for EPR distance measurements. These model systems have been prepared by ligating metal centers with nitroxide substituted terpyridine ligands. The ligands have been synthesized using a modular approach which allows access to various related ligand systems having different nitroxide-terpyridine separations. Ligand **3-1** provides a distance of  $\sim 16$  Å but was not used to prepare model complexes in this work, as the presence exchange interactions between the metal and the nitroxide spin center is expected. Future studies might include exchange coupled spin pairs for EPR-based distance determinations.

Ligand **4-1** provides an interspin separation of  $\sim 26$  Å when bound to a metal ion. Using **4-1**, it was possible to synthesize nitroxide-substituted terpyridine metal complexes using either copper(II) or manganese(II) ions. Moreover, the unsubstituted copper complex was synthesized as tetraphenylborate  $[\text{Cu}(\text{tpy})_2](\text{BPh}_4)_2$  **5-1** to study the chemical behavior and the EPR parameters of copper bis(terpyridine) complexes. Single crystal studies using X-ray diffraction, EPR and UV/Vis spectroscopy on **5-1** demonstrated the high plasticity of the first coordination sphere in copper(II) bis(terpyridine) complexes. It was possible to relate the observed geometries to the occurrence of either static or dynamic PJT effects, depending on the temperature. Furthermore, using AOM calculations it was possible to relate the observed principal values of  $\bar{g}$  with the observed Cu-N bond lengths and to obtain the orientation of the principal axes of  $\bar{g}$  within the molecular coordinate system.

The results obtained on **5-1** were used to aid interpreting the distance measurements on the copper complexes of **4-1**, namely the homoleptic complex **6-1b** ( $=[\text{Cu}(\mathbf{4-1})_2](\text{PF}_6)_2$ ) and the mixed spin system **6-1x**, which has the average composition  $[\text{Cu}(\text{tpy})(\mathbf{4-1})](\text{PF}_6)_2$ . In **6-1x** and **6-1b**, distance measurements have been conducted using the PELDOR and the RIDME sequence. Strong orientation selection has been observed in the PELDOR time traces. It was possible to account for the orientation selectivity and to obtain geometrical parameters with PeldorFit. The geometrical fitting parameters are in accordance with available X-ray data on **6-1b** and the results obtained previously on **5-1**. It was also shown, that multi-spin effects (MSE) occur in the orientation selective PELDOR time traces for both **6-1x** and **6-1b**. The MSE have been analyzed in detail experimentally by employing a



power-scaling approach and theoretically by subsequent addition of MSE to the simulated PeldorFit time traces. Thus, the first quantitative account of MSE in a system in which orientation selection occurs was given, albeit the results are only valid for the special case of a linear three-spin system in which only the outer two spins are pumped. Nonetheless, the used model can be extended to be suited for non-linear spin systems as well and subsequently included into PeldorFit, which might be pursued in future work. It was also shown, that the RIDME sequence (observing the RSE) provides higher sensitivity and suppresses orientation selectivity as well as MSE. Such suppression effects are especially valuable in the case of broad distance distributions which can be encountered in biological macromolecules.

For the manganese bis-nitroxide compound **7-1**, the same set of experiments as for its copper analogue **6-1b** have been conducted. The manganese(II) ion was found to be in an  $S = 5/2$  high spin state giving rise to ZFS with a  $D$  value of 1.5 GHz. Using PELDOR, no strong orientation selection was apparent and the time traces could be analyzed with DeerAnalysis to yield a correct distance distribution with a narrow intense peak centered at 2.68 nm. The good agreement between experimental and expected distance indicated that the ZFS of the manganese center did not strongly affect the observed dipolar coupling frequency due to mixing of the manganese spin states. The RIDME experiment was once again found to be more sensitive than PELDOR. In the study on **7-1**, both the RVE and the RSE have been used for observation. Intense artifact peaks at 81% (RVE and RSE) and 71% (RSE) of the expected interspin distance could be observed. These artifact peaks are caused by higher harmonics of the dipolar coupling frequency owed to the occurrence of  $\Delta M_s = 2$  and  $\Delta M_s = 3$  spin transitions of the manganese spins. Comparing the RSE and the RVE, it was found that the RVE provides better sensitivity, fewer artifact peaks, and a lower degree of modulation damping. The studies on manganese spin centers will be helpful in future studies, where manganese ions are planned to be used as spin probes in ribozymes.

Taken together, the studies on **6-1x**, **6-1b**, and **7-1** demonstrate which challenges are encountered when using metal centered spins in EPR distance measurements. The most important insight concerns the occurrence of artifact peaks in distance distributions, their relative intensity compared to the non-artifact peaks, and how to avoid the artifacts. Especially in the case of broad distance distributions, i.e. heavily

damped time traces, this is valuable knowledge when trying to analyze PELDOR or RIDME data. Furthermore, two different pulse sequences (PELDOR and RIDME) have been employed in the investigation of each spin system. The two experiments were found to be applicable in each case and to complement each other. This allows to confirm (or falsify) the results derived from one EPR experiment by comparison with the other experiment.

The electronic and geometric structures of disilicon radicals and the identification of reactive titanocene(III) species were described in part III of this thesis. The samples were prepared by PhD students from working groups of the different departments of the chemistry facility of Bonn.

In chapter 8, the disilicon radical cation **8-1<sup>+</sup>** was investigated. The symmetrical substitution pattern of **8-1<sup>+</sup>** suggests the occurrence of a  $C_2$  rotation axis or of an inversion center. Surprisingly, X-ray crystallography and DFT calculations suggested the absence of these symmetry elements. Therefore, frozen solutions of **8-1<sup>+</sup>** have been subjected to cw EPR spectroscopy. In these experiments, the detailed analysis of the satellite lines caused by natural abundance  $^{29}\text{Si}$  confirmed the absence of a  $C_2$  axis or an inversion center in **8-1<sup>+</sup>**. Repeating the cw EPR experiment in the liquid state and analysis of the satellite lines indicated the equivalence of the silicon nuclei in **8-1<sup>+</sup>** at elevated temperature. The apparent contradiction between frozen and liquid solutions could be resolved by identifying a low energy transition state using DFT calculations which allows rapid interconversion between isomers.

A similar question of symmetry arose for the hydrogen atom substituted disilicon radical **9-1H<sup>•</sup>**. There, room temperature cw EPR spectrum indicated the presence of two pairs of equivalent nitrogen nuclei in the NHC substituents. This finding could be explained by rapid rotation of the NHC substituents around the Si-C<sub>NHC</sub> bonds in a radical where the hydrogen atom is located terminally on one of the two silicon atoms. An alternative explanation would be the occurrence of 1,2-H-migration. DFT results favor the former interpretation. Additionally, the analysis of  $^{29}\text{Si}$  satellite lines agrees with this interpretation.

In the last chapter, titanocene(III) complexes generated in the course of a catalytic epoxide hydrosilylation have been investigated. Using room temperature cw EPR spectroscopy at different MW frequencies combined with modified preparation routes

employing deuterated silanes allowed identification of two different titanocene(III)-hydride species. One of these species is a titanocene(III)-( $\mu$ -H)<sub>2</sub>-Mg bromide species, which has been described before. The other species is the formal adduct of titanocene(III)hydride and phenylsilane. This species could be proposed with the help of DFT calculations. Using Davies and Mims ENDOR to detect proton and deuteron resonances, respectively, it was possible to investigate the resting state of the catalytic cycle and allowed identifying one of the titanocene(III) ligands as an alkoxide ligand. Kinetic studies and DFT calculations suggest that an epoxide molecule binds as another ligand. However, EPR spectroscopy could not prove the presence of an additional epoxide ligand.

The three conducted studies showed the potential of EPR spectroscopy to elucidate the electronic and geometrical structures of paramagnetic species. Even though large bodies of the results have been achieved using the simplest EPR experiment, namely X-band cw EPR spectroscopy, it was almost always necessary to combine the spectroscopic results with results of DFT calculations to draw definite conclusions. In the case of the silicon radicals, EPR spectroscopy led to a deeper understanding of the structure of the compounds and also allowed investigating the dynamics of the radicals in solution. The studies on the epoxide hydrosilylation reaction allowed identification of different titanocene species occurring during catalysis. This would not have been possible by the kinetic study, which was the basis for the proposed mechanism, alone. The study also showed that pulsed ENDOR spectroscopy can provide information regarding atoms outside the first coordination sphere of transition metal complexes. Further DFT studies are being conducted to achieve a more detailed analysis of the ENDOR spectra. This will possibly allow deriving further evidence for the proposed identity of the resting state species.

## 12. References

- (1) Fenn, J. B. *Angew. Chem. Int. Ed.* **2003**, *42*, 3871–3894.
- (2) Tanaka, K. *Angew. Chem. Int. Ed.* **2003**, *42*, 3860–3870.
- (3) Wüthrich, K. *Angew. Chem. Int. Ed.* **2003**, *42*, 3340–3363.
- (4) MacKinnon, R. *Angew. Chem. Int. Ed.* **2004**, *43*, 4265–4277.
- (5) Agre, P. *Angew. Chem. Int. Ed.* **2004**, *43*, 4278–4290.
- (6) Ciechanover, A. *Angew. Chem. Int. Ed.* **2005**, *44*, 5944–5967.
- (7) Hershko, A. *Angew. Chem. Int. Ed.* **2005**, *44*, 5932–5943.
- (8) Kornberg, R. *Angew. Chem. Int. Ed.* **2007**, *46*, 6956–6965.
- (9) Shimomura, O. *Angew. Chem. Int. Ed.* **2009**, *48*, 5590–5602.
- (10) Chalfie, M. *Angew. Chem. Int. Ed.* **2009**, *48*, 5603–5611.
- (11) Tsien, R. Y. *Angew. Chem. Int. Ed.* **2009**, *48*, 5612–5626.
- (12) Steitz, T. A. *Angew. Chem. Int. Ed.* **2010**, *49*, 4381–4398.
- (13) Ramakrishnan, V. *Angew. Chem. Int. Ed.* **2010**, *49*, 4355–4380.
- (14) Yonath, A. *Angew. Chem. Int. Ed.* **2010**, *49*, 4340–4354.
- (15) Karplus, M. *Angew. Chem. Int. Ed.* **2014**, *53*, 9992–10005.
- (16) Betzig, E.; Hell, S. W.; Moerner, W. E. *Nobel Media AB* **2014**.
- (17) Lindahl, T.; Modrich, P.; Sancar, A., *J. Assoc. Genet. Technol.*, **2015**.
- (18) Zaidi, Z. H.; Smith, D. L. *Protein Structure--function Relationship*; Springer, **1996**.
- (19) Campbell, I. D. *Nat. Rev. Mol. Cell Biol.* **2002**, *3*, 377–381.
- (20) Sherwood, D.; Cooper, J. *Crystals, X-Rays and Proteins: comprehensive protein crystallography*; OUP Oxford, 2010.
- (21) Overhauser, A. W. *Phys. Rev.* **1953**, *92*, 411–415.
- (22) Williamson, M. P.; Havel, T. F.; Wüthrich, K. *J. Mol. Biol.* **1985**, *182*, 295–315.
- (23) Shulman, R. *Biological applications of magnetic resonance*; Elsevier, **2012**.
- (24) Jeschke, G. *Annu. Rev. Phys. Chem.* **2012**, *63*, 419–446.
- (25) Van Doorslaer, S.; Vinck, E. *Phys. Chem. Chem. Phys.* **2007**, *9*, 4620–4638.
- (26) Prisner, T.; Rohrer, M.; MacMillan, F. *Annu. Rev. Phys. Chem.* **2001**, *52*, 279–313.
- (27) Förster, T. *Discuss. Faraday Soc.* **1959**, *27*, 7–17.
- (28) Hussain, S. A. *ArXiv Prepr. ArXiv09081815* **2009**.
- (29) Dykstra, M. J.; Reuss, L. E. *Biological electron microscopy: theory, techniques, and troubleshooting*; Springer Science & Business Media, **2011**.
- (30) Lučić, V.; Förster, F.; Baumeister, W. *Annu. Rev. Biochem.* **2005**, *74*, 833–865.
- (31) Kaczanowski, S.; Zielenkiewicz, P. *Theor. Chem. Acc.* **2010**, *125*, 643–650.

- (32) Karplus, M.; McCammon, J. A. *Nat. Struct. Mol. Biol.* **2002**, *9*, 646–652.
- (33) Berman, H.; Henrick, K.; Nakamura, H.; Markley, J. L. *Nucleic Acids Res.* **2007**, *35*, D301–D303.
- (34) Hemminga, M. A. *ESR Spectroscopy in Membrane Biophysics*; Springer, **2007**.
- (35) Reckel, S.; Löhr, F.; Dötsch, V. *ChemBioChem* **2005**, *6*, 1601–1606.
- (36) Serber, Z.; Corsini, L.; Durst, F.; Dötsch, V. In *Methods in Enzymology*; Academic Press, **2005**, *394*, 17–41.
- (37) Kleckner, I. R.; Foster, M. P. *BBA-Proteins Proteom.* **2011**, *1814*, 942–968.
- (38) Klare, J. P. *Biol. Chem.* **2013**, *394*, 1281–1300.
- (39) Kaim, W.; Schwederski, B. *Bioanorganische Chemie: zur Funktion chemischer Elemente in Lebensprozessen*; Springer-Verlag, **2013**.
- (40) Hanson, G.; Berliner, L. J. *High resolution EPR: applications to metalloenzymes and metals in medicine*; Biological Magnetic Resonance; Springer, **2009**.
- (41) Yano, J.; Yachandra, V. *Chem. Rev.* **2014**, *114*, 4175–4205.
- (42) Cullis, A. F.; Muirhead, H.; Perutz, M.; Rossmann, M.; North, A. *Proc. Roy. Soc. A* **1961**; *265*, 15–38.
- (43) Markl, J.; Decker, H. *Blood and tissue oxygen carriers*; Springer, **1992**.
- (44) Toscano, P. J.; Marzilli, L. G. *Prog. Inorg. Chem.* **1984**, *31*, 105–204.
- (45) Fontecilla-Camps, J. C.; Volbeda, A.; Cavazza, C.; Nicolet, Y. *Chem. Rev.* **2007**, *107*, 4273–4303.
- (46) Rees, D. C.; Tezcan, F. A.; Haynes, C. A.; Walton, M. Y.; Andrade, S.; Einsle, O.; Howard, J. B. *Philos. Trans. R. Soc. Lond. Math. Phys. Eng. Sci.* **2005**, *363*, 971–984.
- (47) Kisseleva, N.; Kraut, S.; Jäschke, A.; Schiemann, O. *HFSP J.* **2007**, *1*, 127–136.
- (48) Hunsicker, L. M.; DeRose, V. J. *J. Inorg. Biochem.* **2000**, *80*, 271–281.
- (49) Babor, M.; Gerzon, S.; Raveh, B.; Sobolev, V.; Edelman, M. *Proteins Struct. Funct. Bioinforma.* **2008**, *70*, 208–217.
- (50) La Mar, G. N.; Horrocks, W. D.; Holm, R. H. *NMR of paramagnetic molecules: principles and applications*; Elsevier, **2013**.
- (51) Lyubenova, S.; Maly, T.; Zwicker, K.; Brandt, U.; Ludwig, B.; Prisner, T. *Acc. Chem. Res.* **2009**, *43*, 181–189.
- (52) Hubbell, W. L.; Altenbach, C. *Curr. Opin. Struct. Biol.* **1994**, *4*, 566–573.
- (53) Klare, J. P.; Steinhoff, H.-J. *Photosynth. Res.* **2009**, *102*, 377–390.
- (54) Ji, M.; Ruthstein, S.; Saxena, S. *Acc. Chem. Res.* **2014**, *47*, 688–695.
- (55) Abdullin, D.; Florin, N.; Hagelueken, G.; Schiemann, O. *Angew. Chem. Int. Ed.* **2015**, *54*, 1827–1831.
- (56) Rieger, P. *Electron Spin Resonance*; The Royal Society of Chemistry, **2007**.

- (57) Mabbs, F. E.; Collison, D. *Electron paramagnetic resonance of d transition metal compounds*; Elsevier, **2013**.
- (58) Büttner, T.; Geier, J.; Frison, G.; Harmer, J.; Calle, C.; Schweiger, A.; Schönberg, H.; Grützmacher, H. *Science* **2005**, *307*, 235–238.
- (59) De Bruin, B.; Bill, E.; Bothe, E.; Weyhermüller, T.; Wieghardt, K. *Inorg. Chem.* **2000**, *39*, 2936–2947.
- (60) Scarborough, C. C.; Lancaster, K. M.; DeBeer, S.; Weyhermüller, T.; Sproules, S.; Wieghardt, K. *Inorg. Chem.* **2012**, *51*, 3718–3732.
- (61) Maurelli, S.; Livraghi, S.; Chiesa, M.; Giamello, E.; Van Doorslaer, S.; Di Valentin, C.; Pacchioni, G. *Inorg. Chem.* **2011**, *50*, 2385–2394.
- (62) Chiesa, M.; Giamello, E.; Van Doorslaer, S. *J. Am. Chem. Soc.* **2009**, *131*, 12664–12670.
- (63) Chiesa, M.; Paganini, M. C.; Giamello, E.; Murphy, D. M.; Di Valentin, C.; Pacchioni, G. *Acc. Chem. Res.* **2006**, *39*, 861–867.
- (64) Abragam, A.; Bleaney, B. *Electron paramagnetic Resonance of Transition Ions.*; Dover Publications Inc., USA, **1986**.
- (65) Atherton, N. M. *Principles of Electron Spin Resonance*; Ellis Horwood Ltd, **1993**.
- (66) Schweiger, A.; Jeschke, G. *Principles of Pulse Paramagnetic Resonance*; Oxford University Press, **2001**.
- (67) Möbius, K.; Savitsky, A. *High-Field EPR Spectroscopy on Proteins and their Model Systems: Characterization of Transient Paramagnetic States*; RSC Publishing, **2009**.
- (68) Bender, C. J.; Berliner, L. J. *EPR: Instrumental Methods*; Springer, **2004**.
- (69) Poole, C. P. *Electron Spin Resonance: A Comprehensive Treatise on Experimental Techniques*; Dover Publications Inc., **1997**.
- (70) Kahn, O. *Molecular Magnetism*, VCH Publ. Inc., **1993**.
- (71) Carrington, A. *Mol. Phys.* **1960**, *3*, 271–275.
- (72) Slichter, C. P. *Principles of magnetic resonance*; Springer Science & Business Media, **2013**.
- (73) Gerlach, W.; Stern, O. *Z. Für Phys.* **1922**, *9*, 349–352.
- (74) Dirac, P. A. M. *Proc. R. Soc. Lond. Math. Phys. Eng. Sci.* **1928**, *117*, 610–624.
- (75) Dirac, P. A. M. *Proc. R. Soc. Lond. Math. Phys. Eng. Sci.* **1928**, *118*, 351–361.
- (76) Van Vleck, J. H. *The Theory of Electric and Magnetic Susceptibilities*; Oxford University Press, **1932**.
- (77) Bloch, F.; Nordsieck, A. *Phys. Rev.* **1937**, *52*, 54–59.
- (78) Feynman, R. P. *Phys. Rev.* **1950**, *80*, 440–457.
- (79) Foley, H. M.; Kusch, P. *Phys. Rev.* **1948**, *73*, 412–412.
- (80) Tomonaga, S. *Prog. Theor. Phys.* **1946**, *1*, 27–42.
- (81) Schwinger, J. *Phys. Rev.* **1948**, *73*, 416–417.

- (82) Zeeman, P. *Philos. Mag. Ser. 5* **1897**, *44*, 55–60.
- (83) McWeeny, R. *Spins in Chemistry*; Dover Publications Inc., **2004**.
- (84) Bencini, A.; Gatteschi, D. *EPR of Exchange Coupled Systems*; Dover Publications Inc., **2012**.
- (85) Mabbs, F. E.; Machin, D. J. *Magnetism and Transition Metal Complexes*; Dover Publications Inc., **2008**.
- (86) Haken, H.; Wolf, H. C. *Atom- und Quantenphysik: Einführung in die experimentellen und theoretischen Grundlagen*; Springer, **2012**.
- (87) Landé, A. *Z. Für Phys.* **1923**, *19*, 112–123.
- (88) Brodsky, S. J.; Franke, V. A.; Hiller, J. R.; McCartor, G.; Paston, S. A.; Prokhvatilov, E. V. *Nucl. Phys. B* **2004**, *703*, 333–362.
- (89) Slater, J. C. *Phys. Rev.* **1930**, *36*, 57–64.
- (90) McConnell, H. M. *J. Chem. Phys.* **1956**, *25*, 709–711.
- (91) Hudson, A.; Luckhurst, G. R. *Chem. Rev.* **1969**, *69*, 191–225.
- (92) Kivelson, D. *J. Chem. Phys.* **1964**, *41*, 1904–1909.
- (93) Liang, Z.; Freed, J. H. *J. Phys. Chem. B* **1999**, *103*, 6384–6396.
- (94) Doussièrè, J.; Gaillard, J.; Vignais, P. V. *Biochemistry (Mosc.)* **1996**, *35*, 13400–13410.
- (95) Solomon, E. I.; Baldwin, M. J.; Lowery, M. D. *Chem. Rev.* **1992**, *92*, 521–542.
- (96) Peisach, J.; Blumberg, W. *Arch. Biochem. Biophys.* **1974**, *165*, 691–708.
- (97) Wertz, J. *Electron spin resonance: elementary theory and practical applications*; Springer Science & Business Media, **2012**.
- (98) Gerson, F.; Huber, W. *Electron spin resonance spectroscopy of organic radicals*; John Wiley & Sons, **2006**.
- (99) Banham, J. E.; Baker, C. M.; Ceola, S.; Day, I. J.; Grant, G. H.; Groenen, E. J. J.; Rodgers, C. T.; Jeschke, G.; Timmel, C. R. *J. Magn. Reson.* **2008**, *191*, 202–218.
- (100) Bertrand, P.; Camensuli, P.; More, C.; Guigliarelli, B. *J. Am. Chem. Soc.* **1996**, *118*, 1426–1434.
- (101) Riplinger, C.; Kao, J. P.; Rosen, G. M.; Kathirvelu, V.; Eaton, G. R.; Eaton, S. S.; Kutateladze, A.; Neese, F. *J. Am. Chem. Soc.* **2009**, *131*, 10092–10106.
- (102) Jeschke, G.; Polyhach, Y. *Phys. Chem. Chem. Phys.* **2007**, *9*, 1895–1910.
- (103) Dalaloyan, A.; Qi, M.; Ruthstein, S.; Vega, S.; Godt, A.; Feintuch, A.; Goldfarb, D. *Phys. Chem. Chem. Phys.* **2015**, *17*, 18464–18476.
- (104) Cohen, M. R.; Frydman, V.; Milko, P.; Iron, M. A.; Abdelkader, E. H.; Lee, M. D.; Swarbrick, J. D.; Raitsimring, A.; Otting, G.; Graham, B.; Feintuch, A.; Goldfarb, D. *Phys. Chem. Chem. Phys.* **2016**, *18*, 12847–12859.
- (105) Sinnecker, S.; Neese, F. *J. Phys. Chem. A* **2006**, *110*, 12267–12275.
- (106) Neese, F. *J. Am. Chem. Soc.* **2006**, *128*, 10213–10222.

- (107) Liakos, D. G.; Ganyushin, D.; Neese, F. *Inorg. Chem.* **2009**, *48*, 10572–10580.
- (108) Sundararajan, M.; Ganyushin, D.; Ye, S.; Neese, F. *Dalton Trans.* **2009**, *30*, 6021–6036.
- (109) Duboc, C.; Phoeung, T.; Zein, S.; Pécaut, J.; Collomb, M.-N.; Neese, F. *Inorg. Chem.* **2007**, *46*, 4905–4916.
- (110) Rich, J.; Castillo, C. E.; Romero, I.; Rodríguez, M.; Duboc, C.; Collomb, M.-N. *Eur. J. Inorg. Chem.* **2010**, *2010*, 3658–3665.
- (111) Romain, S.; Duboc, C.; Neese, F.; Rivière, E.; Hanton, L. R.; Blackman, A. G.; Philouze, C.; Leprêtre, J.-C.; Deronzier, A.; Collomb, M.-N. *Chem. – Eur. J.* **2009**, *15*, 980–988.
- (112) Zein, S.; Duboc, C.; Lubitz, W.; Neese, F. *Inorg. Chem.* **2008**, *47*, 134–142.
- (113) Zlatař, M.; Gruden, M.; Vassilyeva, O. Y.; Buvaylo, E. A.; Ponomarev, A.; Zvyagin, S.; Wosnitza, J.; Krzystek, J.; Garcia-Fernandez, P.; Duboc, C. *Inorg. Chem.* **2016**, *55*, 1192–1201.
- (114) Neese, F.; Solomon, E. I. *Inorg. Chem.* **1998**, *37*, 6568–6582.
- (115) Tait, C. E.; Neuhaus, P.; Anderson, H. L.; Timmel, C. R. *J. Am. Chem. Soc.* **2015**, *137*, 6670–6679.
- (116) Boča, R. *Coord. Chem. Rev.* **2004**, *248*, 757–815.
- (117) Krzystek, J.; Ozarowski, A.; Telser, J. *Coord. Chem. Rev.* **2006**, *250*, 2308–2324.
- (118) Goodenough, J. B.; Loeb, A. L. *Phys. Rev.* **1955**, *98*, 391.
- (119) Goodenough, J. B. *J. Phys. Chem. Solids* **1958**, *6*, 287–297.
- (120) Kanamori, J. *J. Phys. Chem. Solids* **1959**, *10*, 87–98.
- (121) Savitsky, A.; Dubinskii, A.; Plato, M.; Grishin, Y. A.; Zimmermann, H.; Mobius, K. *J. Phys. Chem. B* **2008**, *112*, 9079–9090.
- (122) Wedler, G. *Lehrbuch der Physikalischen Chemie*; Wiley-VCH, **2004**.
- (123) Eaton, S. S.; Eaton, G. R. In *Distance measurements in biological systems by EPR*; Springer, **2002**.
- (124) Blum, K. *Density Matrix Theory and Applications*; Plenum, **1998**.
- (125) Hore, P. J.; Jones, J. A.; Wimperis, S. *NMR: The Toolkit*; Oxford University Press, **2015**.
- (126) Hahn, E. L. *Phys. Rev.* **1950**, *80*, 580.
- (127) Bloom, A. L. *Phys. Rev.* **1955**, *98*, 1105.
- (128) Maly, T.; MacMillan, F.; Zwicker, K.; Kashani-Poor, N.; Brandt, U.; Prisner, T. F. *Biochemistry (Mosc.)* **2004**, *43*, 3969–3978.
- (129) Van Wonderen, J. H.; Kostrz, D. N.; Dennison, C.; MacMillan, F. *Angew. Chem.* **2013**, *125*, 2044–2047.
- (130) Mims, W. *Phys. Rev. B* **1972**, *5*, 2409.
- (131) Rowan, L.; Hahn, E.; Mims, W. *Phys. Rev.* **1965**, *137*, A61.



- (132) Goldfarb, D.; Kofman, V.; Libman, J.; Shanzer, A.; Rahmatouline, R.; Van Doorslaer, S.; Schweiger, A. *J. Am. Chem. Soc.* **1998**, *120*, 7020–7029.
- (133) Höfer, P.; Grupp, A.; Nebenführ, H.; Mehring, M. *Chem. Phys. Lett.* **1986**, *132*, 279–282.
- (134) Kasumaj, B.; Stoll, S. *J. Magn. Reson.* **2008**, *190*, 233–247.
- (135) Deligiannakis, Y.; Louloudi, M.; Hadjiliadis, N. *Coord. Chem. Rev.* **2000**, *204*, 1–112.
- (136) Lakshmi, K.; Brudvig, G. W. *Curr. Opin. Struct. Biol.* **2001**, *11*, 523–531.
- (137) Davies, E. *Phys. Lett. A* **1974**, *47*, 1–2.
- (138) Mims, W. *Proc. R. Soc. Lond. Ser. Math. Phys. Sci.* **1965**, *283*, 452–457.
- (139) Ward, R.; Bowman, A.; Sozudogru, E.; El-Mkami, H.; Owen-Hughes, T.; Norman, D. G. *J. Magn. Reson.* **2010**, *207*, 164–167.
- (140) Altenbach, C.; Marti, T.; Khorana, H.; Hubbell, W. *Science* **1990**, *248*, 1088–1092.
- (141) Altenbach, C.; Flitsch, S. L.; Khorana, H. G.; Hubbell, W. L. *Biochemistry (Mosc.)* **1989**, *28*, 7806–7812.
- (142) Hustedt, E. J.; Smirnov, A. I.; Laub, C. F.; Cobb, C. E.; Beth, A. H. *Biophys. J.* **1997**, *72*, 1861.
- (143) Borbat, P. P.; Freed, J. H. *Structural information from spin-labels and intrinsic paramagnetic centres in the biosciences*; Springer, **2013**.
- (144) Borbat, P. P.; Davis, J. H.; Butcher, S. E.; Freed, J. H. *J. Am. Chem. Soc.* **2004**, *126*, 7746–7747.
- (145) Borbat, P. P.; Freed, J. H. *Chem. Phys. Lett.* **1999**, *313*, 145–154.
- (146) Jeschke, G.; Pannier, M.; Godt, A.; Spiess, H. W. *Chem. Phys. Lett.* **2000**, *331*, 243–252.
- (147) Kurshev, V. V.; Raitsimring, A. M.; Tsvetkov, Y. D. *J. Magn. Reson.* **1969** **1989**, *81*, 441–454.
- (148) Budker, V.; Du, J.-L.; Seiter, M.; Eaton, G. R.; Eaton, S. S. *Biophys. J.* **1995**, *68*, 2531.
- (149) Hirsh, D. J.; McCracken, J.; Biczko, R.; Gesuelli, K.-A. *J. Phys. Chem. B* **2013**, *117*, 11960–11977.
- (150) Jäger, H.; Koch, A.; Maus, V.; Spiess, H. W.; Jeschke, G. *J. Magn. Reson.* **2008**, *194*, 254–263.
- (151) Lueders, P.; Razzaghi, S.; Jäger, H.; Tschaggelar, R.; Hemminga, M. A.; Yulikov, M.; Jeschke, G. *Mol. Phys.* **2013**, *111*, 2824–2833.
- (152) Milov, A.; Ponomarev, A.; Tsvetkov, Y. D. *Chem. Phys. Lett.* **1984**, *110*, 67–72.
- (153) Martin, R. E.; Pannier, M.; Diederich, F.; Gramlich, V.; Hubrich, M.; Spiess, H. W. *Angew. Chem. Int. Ed.* **1998**, *37*, 2833–2837.
- (154) Pannier, M.; Veit, S.; Godt, A.; Jeschke, G.; Spiess, H. W. *J. Magn. Reson.* **2011**, *213*, 316–325.

- (155) Bode, B. E.; Margraf, D.; Plackmeyer, J.; Dürner, G.; Prisner, T. F.; Schiemann, O. *J. Am. Chem. Soc.* **2007**, *129*, 6736–6745.
- (156) Jeschke, G.; Sajid, M.; Schulte, M.; Godt, A. *Phys. Chem. Chem. Phys.* **2009**, *11*, 6580–6591.
- (157) Von Hagens, T.; Polyhach, Y.; Sajid, M.; Godt, A.; Jeschke, G. *Phys. Chem. Chem. Phys.* **2013**, *15*, 5854–5866.
- (158) Chiang, Y.-W.; Borbat, P. P.; Freed, J. H. *J. Magn. Reson.* **2005**, *172*, 279–295.
- (159) Denysenkov, V. P.; Biglino, D.; Lubitz, W.; Prisner, T. F.; Bennati, M. *Angew. Chem. Int. Ed.* **2008**, *47*, 1224–1227.
- (160) Lovett, J.; Bowen, A.; Timmel, C.; Jones, M.; Dilworth, J.; Caprotti, D.; Bell, S.; Wong, L.; Harmer, J. *Phys. Chem. Chem. Phys.* **2009**, *11*, 6840–6848.
- (161) Milikisyants, S.; Groenen, E. J.; Huber, M. *J. Magn. Reson.* **2008**, *192*, 275–279.
- (162) Schiemann, O.; Cekan, P.; Margraf, D.; Prisner, T. F.; Sigurdsson, S. T. *Angew. Chem. Int. Ed.* **2009**, *48*, 3292–3295.
- (163) Bowen, A. M.; Jones, M. W.; Lovett, J. E.; Gaule, T. G.; McPherson, M. J.; Dilworth, J. R.; Timmel, C. R.; Harmer, J. R. *Phys. Chem. Chem. Phys.* **2016**, *18*, 5981–5994.
- (164) Larsen, R. G.; Singel, D. J. *J. Chem. Phys.* **1993**, *98*, 5134–5146.
- (165) Lovett, J. E.; Lovett, B. W.; Harmer, J. *J. Magn. Reson.* **2012**, *223*, 98–106.
- (166) Fajer, P. G.; Brown, L.; Song, L. *ESR spectroscopy in membrane biophysics*; Springer, **2007**.
- (167) El Mkami, H.; Norman, D. G. *Methods in Enzymology*; Academic Press, **2015**.
- (168) Spindler, P. E.; Glaser, S. J.; Skinner, T. E.; Prisner, T. F. *Angew. Chem. Int. Ed.* **2013**, *52*, 3425–3429.
- (169) Spindler, P. E.; Waclawska, I.; Endeward, B.; Plackmeyer, J.; Ziegler, C.; Prisner, T. F. *J. Phys. Chem. Lett.* **2015**, *6*, 4331–4335.
- (170) Motion, C. L.; Lovett, J. E.; Bell, S.; Cassidy, S. L.; Cruickshank, P. A.; Bolton, D. R.; Hunter, R. I.; El Mkami, H.; Van Doorslaer, S.; Smith, G. M. *J. Phys. Chem. Lett.* **2016**, *7*, 1411–1415.
- (171) Kulik, L.; Dzuba, S.; Grigoryev, I.; Tsvetkov, Y. D. *Chem. Phys. Lett.* **2001**, *343*, 315–324.
- (172) Kulik, L.; Paschenko, S.; Dzuba, S. *J. Magn. Reson.* **2002**, *159*, 237–241.
- (173) Razzaghi, S.; Qi, M.; Nalepa, A. I.; Godt, A.; Jeschke, G.; Savitsky, A.; Yulikov, M. *J. Phys. Chem. Lett.* **2014**, *5*, 3970–3975.
- (174) Collauto, A.; Frydman, V.; Lee, M. D.; Abdelkader, E. H.; Feintuch, A.; Swarbrick, J. D.; Graham, B.; Otting, G.; Goldfarb, D. *Phys. Chem. Chem. Phys.* **2016**.
- (175) Milikisyants, S.; Scarpelli, F.; Finiguerra, M. G.; Ubbink, M.; Huber, M. *J. Magn. Reson.* **2009**, *201*, 48–56.
- (176) Savitsky, A.; Dubinskii, A. A.; Zimmermann, H.; Lubitz, W.; Möbius, K. *J. Phys. Chem. B* **2011**, *115*, 11950–11963.

- (177) Abdullin, D.; Duthie, F.; Meyer, A.; Müller, E. S.; Hagelueken, G.; Schiemann, O. *J. Phys. Chem. B* **2015**, *119*, 13534–13542.
- (178) Meyer, A.; Abdullin, D.; Schnakenburg, G.; Schiemann, O. *Phys. Chem. Chem. Phys.* **2016**, *18*, 9262–9271.
- (179) Astashkin, A. V. *Methods Enzymol.* **2015**, *563*, 251–284.
- (180) Cho, H.; Pfenninger, S.; Gemperle, C.; Schweiger, A.; Ernst, R. R. *Chem. Phys. Lett.* **1989**, *160*, 391–395.
- (181) Fielding, A. J.; Heaven, G.; Hollas, M. A. *Molecules* **2014**, *19*, 16998–17025.
- (182) Piton, N.; Mu, Y.; Stock, G.; Prisner, T. F.; Schiemann, O.; Engels, J. W. *Nucleic Acids Res.* **2007**, *35*, 3128–3143.
- (183) Amar, M.; Bar, S.; Iron, M. A.; Toledo, H.; Tumanskii, B.; Shimon, L. J.; Botoshansky, M.; Fridman, N.; Szpilman, A. M. *Nat. Commun.* **2015**, *6*, 1–9.
- (184) Kathirvelu, V.; Smith, C.; Parks, C.; Mannan, M. A.; Miura, Y.; Takeshita, K.; Eaton, S. S.; Eaton, G. R. *Chem. Commun.* **2009**, *4*, 454–456.
- (185) Rajca, A.; Kathirvelu, V.; Roy, S. K.; Pink, M.; Rajca, S.; Sarkar, S.; Eaton, S. S.; Eaton, G. R. *Chem. – Eur. J.* **2010**, *16*, 5778–5782.
- (186) Tkach, I.; Halbmaier, K.; Höbartner, C.; Bennati, M. *Appl. Magn. Reson.* **2014**, *45*, 969–979.
- (187) Dhimitruka, I.; Grigorieva, O.; Zweier, J. L.; Khramtsov, V. V. *Bioorg. Med. Chem. Lett.* **2010**, *20*, 3946–3949.
- (188) Reginsson, G. W.; Kunjir, N. C.; Sigurdsson, S. T.; Schiemann, O. *Chem. – Eur. J.* **2012**, *18*, 13580–13584.
- (189) Kuzhelev, A. A.; Trukhin, D. V.; Krumkacheva, O. A.; Strizhakov, R. K.; Rogozhnikova, O. Y.; Troitskaya, T. I.; Fedin, M. V.; Tormyshev, V. M.; Bagryanskaya, E. G. *J. Phys. Chem. B* **2015**, *119*, 13630–13640.
- (190) Yang, Z.; Liu, Y.; Borbat, P.; Zweier, J. L.; Freed, J. H.; Hubbell, W. L. *J. Am. Chem. Soc.* **2012**, *134*, 9950–9952.
- (191) Shevelev, G. Y.; Krumkacheva, O. A.; Lomzov, A. A.; Kuzhelev, A. A.; Rogozhnikova, O. Y.; Trukhin, D. V.; Troitskaya, T. I.; Tormyshev, V. M.; Fedin, M. V.; Pysnyi, D. V.; Bagryanskaya, E. G. *J. Am. Chem. Soc.* **2014**, *136*, 9874–9877.
- (192) Matalon, E.; Huber, T.; Hagelueken, G.; Graham, B.; Frydman, V.; Feintuch, A.; Otting, G.; Goldfarb, D. *Angew. Chem. Int. Ed.* **2013**, *52*, 11831–11834.
- (193) Cunningham, T. F.; Putterman, M. R.; Desai, A.; Horne, W. S.; Saxena, S. *Angew. Chem. Int. Ed.* **2015**, *54*, 6330–6334.
- (194) Edwards, D. T.; Huber, T.; Hussain, S.; Stone, K. M.; Kinnebrew, M.; Kaminker, I.; Matalon, E.; Sherwin, M. S.; Goldfarb, D.; Han, S. *Structure* **2014**, *22*, 1677–1686.
- (195) Schiemann, O.; Fritscher, J.; Kisseleva, N.; Sigurdsson, S. T.; Prisner, T. F. *ChemBioChem* **2003**, *4*, 1057–1065.
- (196) Kaminker, I.; Bye, M.; Mendelman, N.; Gislason, K.; Sigurdsson, S. T.; Goldfarb, D. *Phys. Chem. Chem. Phys.* **2015**, *17*, 15098–15102.

- (197) Astashkin, A. V.; Elmore, B. O.; Fan, W.; Guillemette, J. G.; Feng, C. *J. Am. Chem. Soc.* **2010**, *132*, 12059–12067.
- (198) Zhou, Y.; Bowler, B. E.; Lynch, K.; Eaton, S. S.; Eaton, G. R. *Biophys. J.* **2000**, *79*, 1039–1052.
- (199) Di Valentin, M.; Albertini, M.; Zurlo, E.; Gobbo, M.; Carbonera, D. *J. Am. Chem. Soc.* **2014**, *136*, 6582–6585.
- (200) Hintze, C.; Bücker, D.; Domingo Köhler, S.; Jeschke, G.; Drescher, M. *J. Phys. Chem. Lett.* **2016**, *7*, 2204–2209.
- (201) Garbuio, L.; Bordignon, E.; Brooks, E. K.; Hubbell, W. L.; Jeschke, G.; Yulikov, M. *J. Phys. Chem. B* **2013**, *117*, 3145–3153.
- (202) Sonogashira, K. *J. Organomet. Chem.* **2002**, *653*, 46–49.
- (203) Hogg, R.; Wilkins, R. G. *J. Chem. Soc. Resumed* **1962**, *0*, 341–350.
- (204) Zhang, N.; Yang, J.; Hu, R.-X.; Zhang, M.-B. *Z. Für Anorg. Allg. Chem.* **2013**, *639*, 197–202.
- (205) Hofmeier, H.; Schubert, U. S. *Chem. Soc. Rev.* **2004**, *33*, 373–399.
- (206) Janiak, C. *J. Chem. Soc. Dalton Trans.* **2000**, *21*, 3885–3896.
- (207) Jeschke, G. *Macromol. Rapid Commun.* **2002**, *23*, 227–246.
- (208) Shinomiya, M.; Higashiguchi, K.; Matsuda, K. *J. Org. Chem.* **2013**, *78*, 9282–9290.
- (209) Phelan, N. F.; Orchin, M. *J. Chem. Educ.* **1968**, *45*, 633.
- (210) Ricks, A. B.; Solomon, G. C.; Colvin, M. T.; Scott, A. M.; Chen, K.; Ratner, M. A.; Wasielewski, M. R. *J. Am. Chem. Soc.* **2010**, *132*, 15427–15434.
- (211) Solomon, G. C.; Andrews, D. Q.; Van Duyne, R. P.; Ratner, M. A. *J. Am. Chem. Soc.* **2008**, *130*, 7788–7789.
- (212) Wautelet, P.; Le Moigne, J.; Videva, V.; Turek, P. *J. Org. Chem.* **2003**, *68*, 8025–8036.
- (213) Grindley, T. B. *Tetrahedron Lett.* **1982**, *23*, 1757–1760.
- (214) Wiberg, K. B.; Laidig, K. E. *J. Am. Chem. Soc.* **1987**, *109*, 5935–5943.
- (215) Ackermann, K.; Giannoulis, A.; Cordes, D. B.; Slawin, A. M. Z.; Bode, B. E. *Chem. Commun.* **2015**, *51*, 5257–5260.
- (216) Folgado, J. V.; Henke, W.; Allmann, R.; Stratemeier, H.; Beltran-Porter, D.; Rojo, T.; Reinen, D. *Inorg. Chem.* **1990**, *29*, 2035–2042.
- (217) Allmann, R.; Henke, W.; Reinen, D. *Inorg. Chem.* **1978**, *17*, 378–382.
- (218) Narr, E.; Zimmermann, H.; Godt, A.; Goldfarb, D.; Jeschke, G. *Phys. Chem. Chem. Phys.* **2003**, *5*, 3959–3967.
- (219) Murphy, B.; Hathaway, B. *Coord. Chem. Rev.* **2003**, *243*, 237–262.
- (220) Holm, R. H.; Kennepohl, P.; Solomon, E. I. *Chem. Rev.* **1996**, *96*, 2239–2314.
- (221) Sendovski, M.; Kanteev, M.; Ben-Yosef, V. S.; Adir, N.; Fishman, A. *J. Mol. Biol.* **2011**, *405*, 227–237.

- (222) De Munno, G.; Julve, M.; Lloret, F.; Cano, J.; Caneschi, A. *Inorg. Chem.* **1995**, *34*, 2048–2053.
- (223) Murphy, B.; Aljabri, M.; Ahmed, A. M.; Murphy, G.; Hathaway, B. J.; Light, M. E.; Geilbrich, T.; Hursthouse, M. B. *Dalton Trans.* **2006**, *2*, 357–367.
- (224) Tregenna-Piggott, P. L. W. *Inorg. Chem.* **2008**, *47*, 448–453.
- (225) Bersuker, I. B. *Electronic structure and properties of transition metal compounds: introduction to the theory*; John Wiley & Sons, **2010**.
- (226) Gade, L. H. *Koordinationschemie*; John Wiley & Sons, **2012**.
- (227) Van Amsterdam, I. M. C.; Ubbink, M.; Canters, G. W.; Huber, M. *Angew. Chem.* **2003**, *115*, 64–67.
- (228) Yang, Z.; Becker, J.; Saxena, S. *J. Magn. Reson.* **2007**, *188*, 337–343.
- (229) Yang, Z.; Kise, D.; Saxena, S. *J. Phys. Chem. B* **2010**, *114*, 6165–6174.
- (230) Abdullin, D.; Hagelueken, G.; Hunter, R. I.; Smith, G. M.; Schiemann, O. *Mol. Phys.* **2014**, *113*, 544–560.
- (231) Narr, E.; Godt, A.; Jeschke, G. *Angew. Chem. Int. Ed.* **2002**, *41*, 3907–3910.
- (232) Giannoulis, A.; Ward, R.; Branigan, E.; Naismith, J. H.; Bode, B. E. *Mol. Phys.* **2013**, *111*, 2845–2854.
- (233) Duboc, C.; Collomb, M.; Pécaut, J.; Deronzier, A.; Neese, F. *Chem. Eur. J.* **2008**, *14*, 6498–6509.
- (234) Carrington, A.; Luckhurst, G. *Mol. Phys.* **1964**, *8*, 125–132.
- (235) Herrick, R.; Stapleton, H. *J. Chem. Phys.* **1976**, *65*, 4786–4790.
- (236) Rast, S.; Fries, P.; Belorizky, E. *J. Chem. Phys.* **2000**, *113*, 8724–8735.
- (237) Gätjens, J.; Sjödin, M.; Pecoraro, V. L.; Un, S. *J. Am. Chem. Soc.* **2007**, *129*, 13825–13827.
- (238) Wang, Y.; Xie, Y.; Wei, P.; King, R. B.; Schaefer, H. F.; von R. Schleyer, P.; Robinson, G. H. *Science* **2008**, *321*, 1069–1071.
- (239) Buntine, M. A.; Hall, V. J.; Kosovel, F. J.; Tiekink, E. R. *J. Phys. Chem. A* **1998**, *102*, 2472–2482.
- (240) Mohamed-Ibrahim, M. I.; Chee, S. S.; Buntine, M. A.; Cox, M. J.; Tiekink, E. R. T. *Organometallics* **2000**, *19*, 5410–5415.
- (241) Pu, L.; Phillips, A. D.; Richards, A. F.; Stender, M.; Simons, R. S.; Olmstead, M. M.; Power, P. P. *J. Am. Chem. Soc.* **2003**, *125*, 11626–11636.
- (242) Power, P. P. *Organometallics* **2007**, *26*, 4362–4372.
- (243) Back, O.; Donnadiou, B.; Parameswaran, P.; Frenking, G.; Bertrand, G. *Nat Chem* **2010**, *2*, 369–373.
- (244) Kinjo, R.; Ichinohe, M.; Sekiguchi, A. *J. Am. Chem. Soc.* **2007**, *129*, 26–27.
- (245) Bersuker, I. B. *Chem. Rev.* **2013**, *113*, 1351–1390.

- (246) Arz, M. I.; Straßmann, M.; Geiß, D.; Schnakenburg, G.; Filippou, A. C. *J. Am. Chem. Soc.* **2016**, *138*, 4589–4600.
- (247) Meisner, J.; Kästner, J. *Angew. Chem. Int. Ed.* **2016**, *55*, 5400–5413.
- (248) Gansäuer, A.; Klatte, M.; Brändle, G. M.; Friedrich, J. *Angew. Chem. Int. Ed.* **2012**, *51*, 8891–8894.
- (249) Gansäuer, A.; Behlendorf, M.; Cangönül, A.; Kube, C.; Cuerva, J. M.; Friedrich, J.; van Gastel, M. *Angew. Chem. Int. Ed.* **2012**, *51*, 3266–3270.
- (250) Cangönül, A.; Behlendorf, M.; Gansäuer, A.; van Gastel, M. *Inorg. Chem.* **2013**, *52*, 11859–11866.
- (251) Samuel, E.; Harrod, J. F.; Gourier, D.; Dromzee, Y.; Robert, F.; Jeannin, Y. *Inorg. Chem.* **1992**, *31*, 3252–3259.
- (252) Xin, S.; Harrod, J. F.; Samuel, E. *J. Am. Chem. Soc.* **1994**, *116*, 11562–11563.
- (253) Samuel, E.; Harrod, J. F. *J. Am. Chem. Soc.* **1984**, *106*, 1859–1860.
- (254) Bercaw, J. E.; Brintzinger, H. H. *J. Am. Chem. Soc.* **1969**, *91*, 7301–7306.
- (255) Streuff, J.; Feurer, M.; Frey, G.; Steffani, A.; Kacprzak, S.; Weweler, J.; Leijendekker, L. H.; Kratzert, D.; Plattner, D. A. *J. Am. Chem. Soc.* **2015**, *137*, 14396–14405.
- (256) Lukens, W. W.; Smith, M. R.; Andersen, R. A. *J. Am. Chem. Soc.* **1996**, *118*, 1719–1728.
- (257) Troyanov, S. I.; Varga, V.; Mach, K. *J. Organomet. Chem.* **1993**, *461*, 85–90.
- (258) Lukešová, L.; Horáček, M.; Štěpnička, P.; Gyepes, R.; Císařová, I.; Kubišta, J.; Mach, K. *J. Organomet. Chem.* **2004**, *689*, 1919–1929.
- (259) Harrod, J. F.; Shu, R.; Woo, H.-G.; Samuel, E. *Can. J. Chem.* **2001**, *79*, 1075–1085.
- (260) Samuel, E.; Mu, Y.; Harrod, J. F.; Dromzee, Y.; Jeannin, Y. *J. Am. Chem. Soc.* **1990**, *112*, 3435–3439.
- (261) Aitken, C. T.; Harrod, J. F.; Samuel, E. *J. Am. Chem. Soc.* **1986**, *108*, 4059–4066.

# Appendices

# Appendix A

## The Crystal Structure of 4''-{4-[(2,2,5,5-Tetramethyl-*N*-oxyl-3-pyrrolin-3-yl)ethynyl]-phenyl}-2,2':6',2''-terpyridine

Andreas Meyer,<sup>i</sup> Jennifer Wiecek,<sup>i</sup> Gregor Schnakenburg<sup>ii</sup> and Olav Schiemann<sup>i</sup>

Received 28th May 2015, published online 30th June 2015.

Reprinted with permission from  
A. Meyer, J. Wiecek, G. Schnakenburg, and O. Schiemann, *Acta Crystallographica E*  
**2015**, *E71*, 870 - 874.  
Copyright ©2015, International Union of Crystallography.

### Own contributions to the manuscript

- Synthesis and crystallization of the title compound.
- Evaluation of the geometrical parameters of the crystal structure.
- Writing the manuscript.

---

<sup>i</sup> University of Bonn, Institute of Physical and Theoretical Chemistry, Wegelerstrasse 12, 53115 Bonn, Germany

<sup>ii</sup> University of Bonn, Institute of Inorganic Chemistry, Gerhard-Domagk-Strasse 1, 53121 Bonn, Germany.





# The crystal structure of 4'-{4-[(2,2,5,5-tetramethyl-*N*-oxyl-3-pyrrolin-3-yl)ethynyl]phenyl}-2,2':6',2''-terpyridine

Andreas Meyer,<sup>a</sup> Jennifer Wiecek,<sup>a</sup> Gregor Schnakenburg<sup>b</sup> and Olav Schiemann<sup>a\*</sup>

Received 28 May 2015

Accepted 23 June 2015

<sup>a</sup>University of Bonn, Institute of Physical and Theoretical Chemistry, Wegelerstrasse 12, 53115 Bonn, Germany, and

<sup>b</sup>University of Bonn, Institute of Inorganic Chemistry, Gerhard-Domagk-Strasse 1, 53121 Bonn, Germany.

\*Correspondence e-mail: schiemann@pc.uni-bonn.de

Edited by A. J. Lough, University of Toronto, Canada

**Keywords:** crystal structure; terpyridine; nitroxide; nitroxyl; C—H··· $\pi$  interactions;  $\pi$ – $\pi$  interactions; C—H···O hydrogen bonding

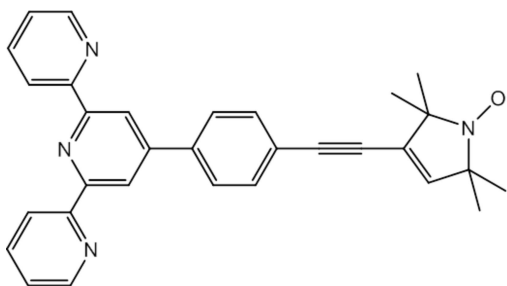
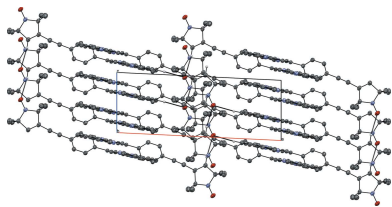
**CCDC reference:** 1408457

**Supporting information:** this article has supporting information at journals.iucr.org/e

The terpyridine group of the title compound, C<sub>31</sub>H<sub>27</sub>N<sub>4</sub>O, assumes an all-*transoid* conformation and is essentially planar with the dihedral angles between the mean planes of the central pyridine and the two outer rings amounting to 3.87 (5) and 1.98 (5)°. The pyrroline-*N*-oxyl group commonly seen in such nitroxyls is found in the title structure and the mean plane of the pyrroline ring subtends a dihedral angle of 88.44 (7)° to the mean plane of the central pyridine ring. The intramolecular separation between the nitrogen atom of the central pyridine unit of the terpyridine group and the nitroxyl group is 14.120 (2) Å. In the crystal, the molecules are arranged in layers stacked along [001]. Slipped face-to-face  $\pi$ – $\pi$  interactions between the pyridine rings are observed along this direction with the shortest centroid–centroid distances amounting to 3.700 (1) and 3.781 (1) Å. Furthermore, edge-on C—H··· $\pi$  interactions between the phenylene rings of neighbouring molecules are observed along this direction. A two-dimensional C—H···O hydrogen-bonded network is formed within the (010) plane. The shortest O···O separation between neighbouring molecules is 5.412 (3) Å.

## 1. Chemical context

The title compound, (**1**), was synthesized as a ligand for 3d metal ions as part of a pulsed EPR study on metal–nitroxyl model systems. The molecule contains a paramagnetic nitroxyl group and a terpyridine group. Nitroxyls have been the subject of magnetic studies in which exchange interactions have been detected (see, for example, Rajca *et al.*, 2006; Fritscher *et al.*, 2002). Furthermore, nitroxyls are used as spin labels for structural investigations of biological macromolecules (Reginsson & Schiemann, 2011). The structures of terpyridines have been investigated by Fallahpour *et al.* (1999), Eryazici *et al.* (2006), Bessel *et al.* (1992) and Grave *et al.* (2003) to name a few examples. The terpyridine moiety is known to form complexes with various metals. Numerous studies on metal complexes of terpyridine have been conducted, examples include those by Hogg & Wilkins (1962), Constable *et al.* (1999), Narr *et al.* (2002) and Folgado *et al.* (1990).



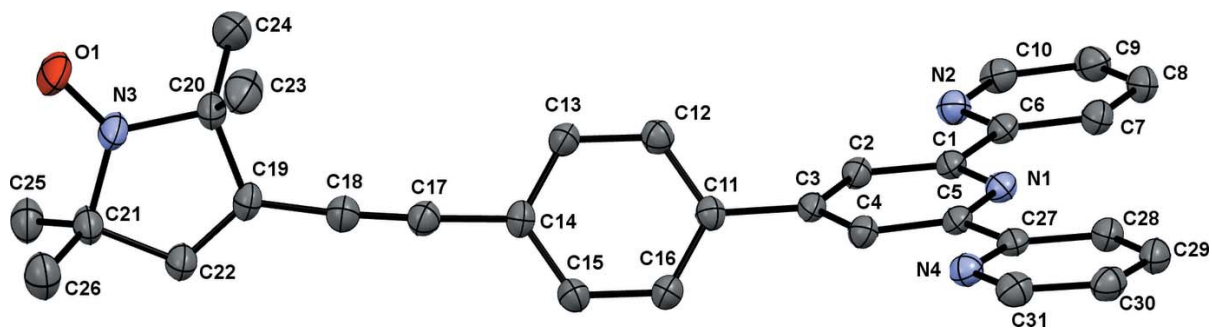


**Figure 1**  
The molecular structure of the title compound with displacement ellipsoids drawn at the 50% probability level. H atoms have been omitted for clarity.

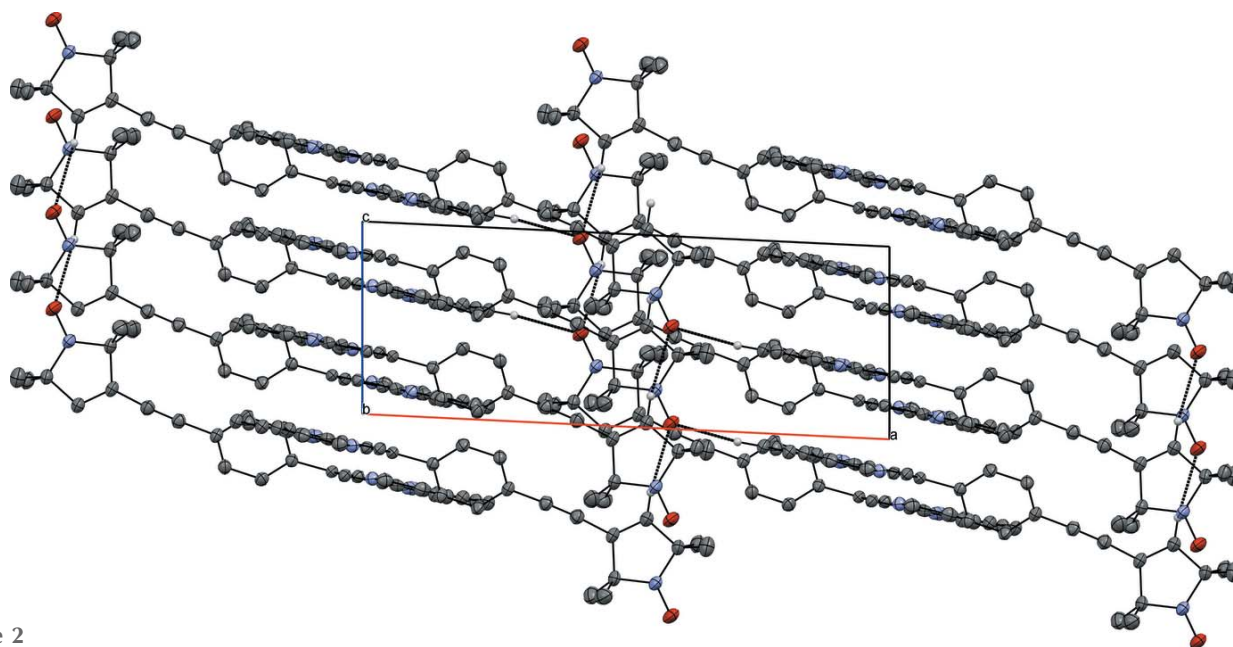


**Figure 2**  
Crystal packing of the title compound viewed along the *b* axis. Weak C—H...O hydrogen bonds are shown as dashed lines

## 2. Structural commentary

The structure of the title compound (**1**) is shown in Fig. 1. The terpyridine group of (**1**) assumes an all-*transoid* conformation and is essentially planar with angles between the mean planes of the central pyridine (N1, C1–C5, r.m.s deviation from the mean plane = 0.006 Å) and the two outer rings amounting to 3.87 (5)° (N4, C27–C31, r.m.s deviation from the mean plane = 0.003 Å) and 1.98 (5)° (N2, C6–C10, r.m.s deviation from the mean plane = 0.006 Å), respectively. The pyrroline-*N*-oxyl unit commonly found for such nitroxyls is seen in the structure and its mean plane (N3, C19–C22, r.m.s deviation from the mean plane = 0.006 Å) subtends a dihedral angle of 88.44 (7)° to the mean plane of the central pyridine ring (for similar structural motifs, see Margraf *et al.*, 2009 and Schuetz *et al.*, 2010). The subunits are linked by a 4-ethynylphenylene group. The mean plane of the phenylene group (C11–C16, r.m.s deviation from the mean plane < 0.001 Å) is tilted with respect to both the central pyridine ring [dihedral angle of 51.36 (5)°] and the pyrroline-*N*-oxyl [dihedral angle of 37.62 (7)°]. The angles C18–C17–C14 [177.35 (19)°] and

C17–C18–C19 [175.64 (18)°] are slightly lower than the 180° expected for a strictly linear shape of the molecular backbone. Two short intramolecular hydrogen–nitrogen distances are observed between the two *meta*-protons of the central pyridine subunit and the nitrogen atoms of the external pyridine rings (Table 1). Murguly *et al.* (1999) propose weak intramolecular hydrogen bonds for these atoms. The intramolecular separation between the terpyridine group and the nitroxyl amounts to 14.120 (2) Å (measured between O1 and N1).

**Table 1**  
Hydrogen-bond geometry (Å, °).

C<sub>g</sub> is the centroid of the C11–C16 ring.

<i>D</i> –H... <i>A</i>	<i>D</i> –H	H... <i>A</i>	<i>D</i> ... <i>A</i>	<i>D</i> –H... <i>A</i>
C2–H2...N2	0.95	2.50	2.815 (2)	99
C4–H4...N4	0.95	2.46	2.778 (2)	100
C8–H8...O1 <sup>i</sup>	0.95	2.59	3.529 (2)	170
C16–H16...C <sub>g</sub> <sup>ii</sup>	0.95	2.81	3.669 (2)	151
C22–H22...O1 <sup>iii</sup>	0.95	2.55	3.485 (2)	170

Symmetry codes: (i)  $x - 1, y, z + 1$ ; (ii)  $x, -y + \frac{1}{2}, z + \frac{1}{2}$ ; (iii)  $x, y, z + 1$ .

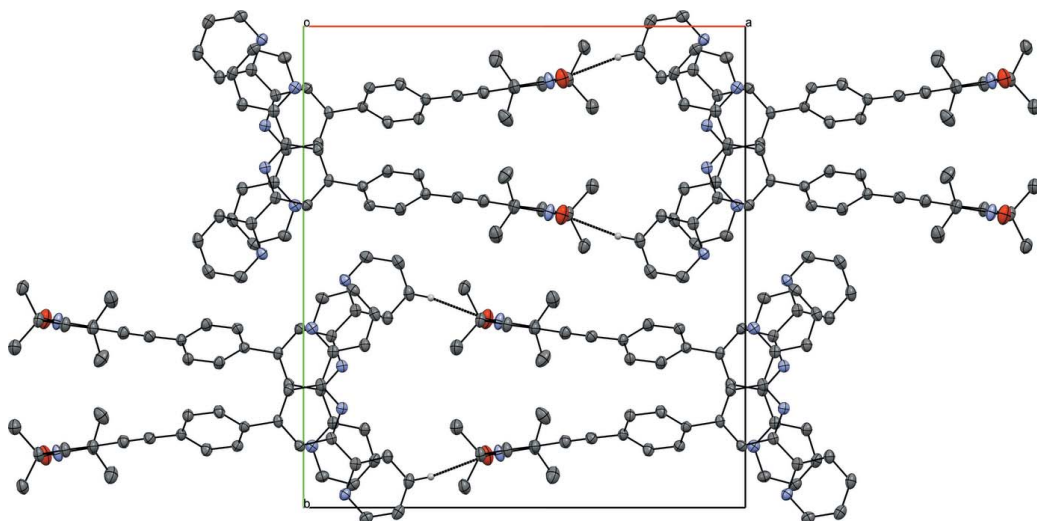


**Figure 3**  
Crystal packing of the title compound viewed along the *c* axis.

### 3. Supramolecular features

The packing within the crystal structure is shown in Figs. 2–4. The molecules are stacked in layers along [001] (Fig. 2.) The oxygen atom of the nitroxyl group forms weak hydrogen bonds to the protons of the *para*-C–H group and the pyrroline C–H group of neighbouring molecules (Table 1). These hydrogen bonds span a two-dimensional network within the (010) plane (Figs. 3 and 4).  $\pi$ - $\pi$  interactions are observed along [001] between the terpyridine subunits of neighbouring molecules (Figs. 3 and 5). These terpyridine subunits are arranged in a slipped face-to-face alignment (Janiak, 2000) with the shortest intermolecular distances between the pyridine rings amounting to 3.700 (1) Å (measured from the

centroid of N2, C6–C10 to the centroid of N4, C27–C31) and 3.781 (1) Å (centroid of N1, C1–C5 to the centroid of N4, C27–C31, see Fig. 5). Furthermore, the phenylene rings of neighbouring molecules show an edge-on C–H $\cdots\pi$  interaction along the same axis (Table 1 and Fig. 5). The nitroxyl groups are arranged in an alternating manner pointing in opposite directions. The shortest oxygen–oxygen separation between neighbouring molecules amounts to 5.412 (3) Å. The oxygen–oxygen distance is an important factor determining the strength of through space exchange interactions of nitroxyls (Rajca *et al.* 2006).

### 4. Database survey

The Cambridge Structural Database (CSD, Version 5.36; Groom & Allen, 2014) has been queried to find other terpyridine or 2,2,5,5-tetramethyl-*N*-oxyl-3-pyrroline derivatives. The terpyridine query revealed 3473 entries in the CSD

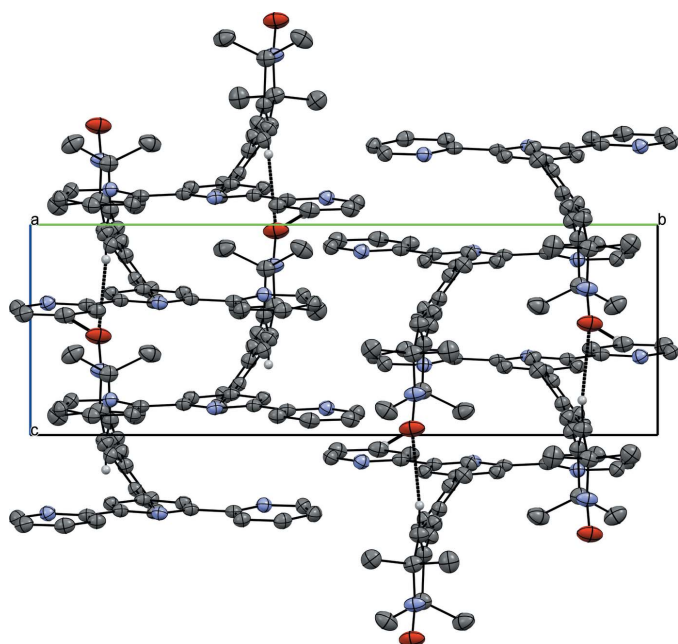


**Figure 4**  
Crystal packing of the title compound viewed along the *a* axis.

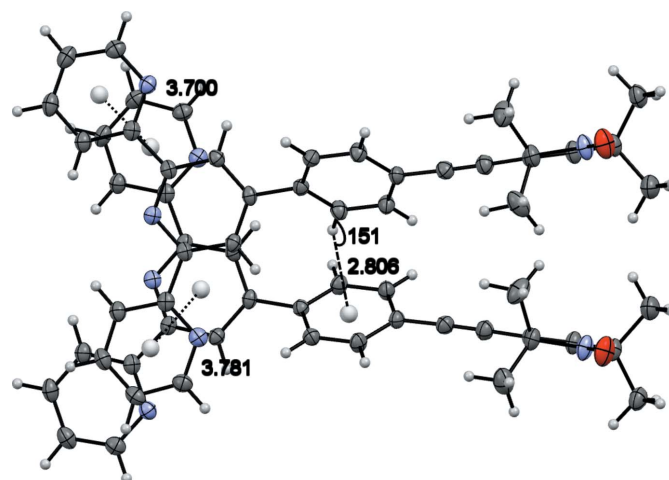


**Figure 5**  
Closest distances between pyridine rings and edge-on C–H $\cdots\pi$  contact.

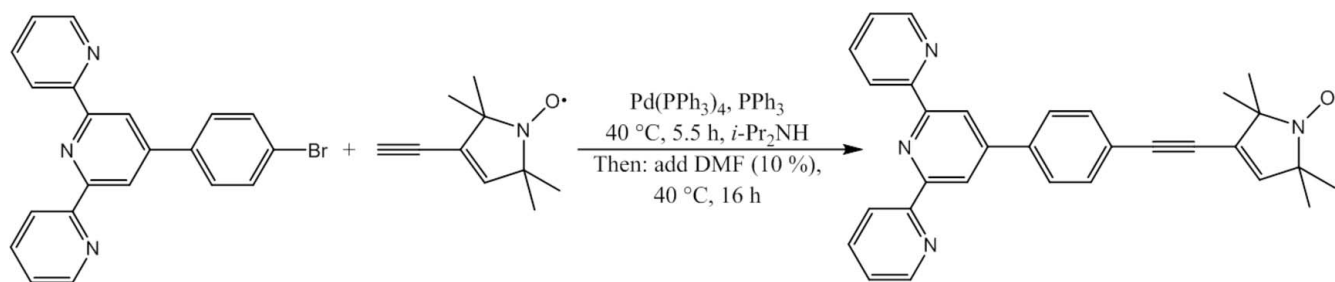


**Figure 6**  
Scheme illustrating the synthesis of **(1)**.

if metal complexes of terpyridine were included. For purely organic terpyridine compounds, the number of hits was reduced to 348. Only 33 results for 2,2,5,5-tetramethyl-*N*-oxyl-3-pyrroline derivatives were found in the CSD. A combined query for structures which include both terpyridine and 2,2,5,5-tetramethyl-*N*-oxyl-3-pyrroline derivatives did not result in any hit. However, the authors are aware of at least one published crystal structure of a compound which contains both structural motifs (Ackermann *et al.*, 2015).

## 5. Synthesis and crystallization

The title compound **(1)** is formed from 3-ethynyl-2,2,5,5-tetramethyl-3-pyrroline-*N*-oxyl and 4'-(4-bromophenyl)-2,2':6',2''-terpyridine using a Sonogashira–Hagihara cross-coupling reaction, as shown in Fig. 6. 222 mg (0.57 mmol) of 4'-(4-bromophenyl)-2,2':6',2''-terpyridine, 100 mg (0.61 mmol)

of 3-ethynyl-2,2,5,5-tetramethyl-3-pyrroline-*N*-oxyl, 20 mg (0.076 mmol) of PPh<sub>3</sub> and 40 mg (0.035 mmol) of Pd(PPh<sub>3</sub>)<sub>4</sub> were dissolved in 17 ml of *i*-Pr<sub>2</sub>NH and stirred at 313 K, yielding a yellow solution which turned orange over the course of 5 min. Additionally, an orange precipitate was formed simultaneously. After 5.5 h, 2 ml of dimethylformamide were added to the orange suspension. The stirring at 313 K was continued for 16 h, after which time the solvents were removed under reduced pressure. The orange residues were suspended in a mixture of dichloromethane and cyclohexane (1:2) and subsequently subjected to column chromatography using aluminum oxide as stationary phase. A mixture of dichloromethane and cyclohexane was used as eluent. The volumetric ratio of both solvents was changed stepwise during the purification (from 1:8 to 8:1). The desired product was obtained in a yellow fraction and could be isolated by removing the eluents under reduced pressure (yield 80%). The crystallization of **(1)** was achieved by slow evaporation of a solution of **(1)** in a 1:1 mixture of acetonitrile and dichloromethane. 4'-(4-Bromophenyl)-2,2':6',2''-terpyridine was purchased from TCI Europe. 3-Ethynyl-2,2,5,5-tetramethyl-3-pyrroline-*N*-oxyl was synthesized as described by Schiemann *et al.* (2007).

**Table 2**  
Experimental details.

Crystal data	
Chemical formula	C <sub>31</sub> H <sub>27</sub> N <sub>4</sub> O
<i>M<sub>r</sub></i>	471.56
Crystal system, space group	Monoclinic, <i>P</i> 2 <sub>1</sub> / <i>c</i>
Temperature (K)	123
<i>a</i> , <i>b</i> , <i>c</i> (Å)	18.5666 (8), 20.2009 (9), 6.7749 (2)
$\beta$ (°)	92.743 (3)
<i>V</i> (Å <sup>3</sup> )	2538.10 (17)
<i>Z</i>	4
Radiation type	Mo <i>K</i> $\alpha$
$\mu$ (mm <sup>-1</sup> )	0.08
Crystal size (mm)	0.34 × 0.12 × 0.08
Data collection	
Diffractometer	Nonius KappaCCD
Absorption correction	Multi-scan (Blessing, 1995)
<i>T<sub>min</sub></i> , <i>T<sub>max</sub></i>	0.883, 1.078
No. of measured, independent and observed [ <i>I</i> > 2 $\sigma$ ( <i>I</i> )] reflections	35758, 6691, 3221
<i>R<sub>int</sub></i>	0.118
( <i>sin</i> $\theta$ / $\lambda$ ) <sub>max</sub> (Å <sup>-1</sup> )	0.685
Refinement	
<i>R</i> [ <i>F</i> <sup>2</sup> > 2 $\sigma$ ( <i>F</i> <sup>2</sup> )], <i>wR</i> ( <i>F</i> <sup>2</sup> ), <i>S</i>	0.049, 0.122, 0.89
No. of reflections	6691
No. of parameters	329
H-atom treatment	H-atom parameters constrained
$\Delta\rho_{\max}$ , $\Delta\rho_{\min}$ (e Å <sup>-3</sup> )	0.19, -0.23

Computer programs: DENZO and SCALEPACK (Otwinowski & Minor, 1997), SHELXS97 (Sheldrick, 2008), SHELXL97 (Sheldrick, 2015) and OLEX2 (Dolomanov *et al.*, 2009).

## 6. Refinement

Crystal data, data collection and structure refinement details are summarized in Table 2. All H atoms were fixed geometrically and allowed to ride on their parent C atoms, with 0.98 Å with  $U_{\text{iso}}(\text{H}) = 1.5U_{\text{eq}}(\text{C})$  for methyl H atoms and C—H = 0.95 Å and  $U_{\text{iso}}(\text{H}) = 1.2U_{\text{eq}}(\text{C})$  for all other H atoms.

## Acknowledgements

The authors thank Professor Dr A. C. Filippou for providing X-ray infrastructure. OS thanks the DFG for funding via SFB 813.

## References

- Ackermann, K., Giannoulis, A., Cordes, D. B., Slawin, A. M. Z. & Bode, B. E. (2015). *Chem. Commun.* **51**, 5257–5260.  
 Bessel, C. A., See, R. F., Jameson, D. L., Churchill, M. R. & Takeuchi, K. J. (1992). *J. Chem. Soc. Dalton Trans.* pp. 3223–3228.  
 Blessing, R. H. (1995). *Acta Cryst.* **A51**, 33–38.

- Constable, E. C., Baum, G., Bill, E., Dyson, R., van Eldik, R., Fenske, D., Kaderli, D., Morris, D., Neubrand, A., Neuburger, M., Smith, D. R., Wieghardt, K., Zehnder, M. & Zuberbühler, A. D. (1999). *Chem. Eur. J.* **5**, 498–508.
- Dolomanov, O. V., Bourhis, L. J., Gildea, R. J., Howard, J. A. K. & Puschmann, H. (2009). *J. Appl. Cryst.* **42**, 339–341.
- Eryazici, I., Moorefield, C. N., Durmus, S. & Newkome, G. R. (2006). *J. Org. Chem.* **71**, 1009–1014.
- Fallahpour, R.-A., Neuburger, M. & Zehnder, M. (1999). *Polyhedron*, **18**, 2445–2454.
- Folgado, J. V., Henke, W., Allmann, R., Stratemeier, H., Beltrán-Porter, D., Rojo, T. & Reinen, D. (1990). *Inorg. Chem.* **29**, 2035–2042.
- Fritscher, J., Beyer, M. & Schiemann, O. (2002). *Chem. Phys. Lett.* **364**, 393–401.
- Grave, C., Lentz, D., Schäfer, A., Samorì, P., Rabe, P. J., Franke, P. & Schlüter, A. D. (2003). *J. Am. Chem. Soc.* **125**, 6907–6918.
- Groom, C. R. & Allen, F. H. (2014). *Angew. Chem. Int. Ed.* **53**, 662–671.
- Hogg, R. & Wilkins, R. G. (1962). *J. Chem. Soc.* pp. 341–350.
- Janiak, C. (2000). *J. Chem. Soc. Dalton Trans.* pp. 3885–3896.
- Margraf, D., Schuetz, D., Prisner, T. F. & Bats, J. W. (2009). *Acta Cryst.* **E65**, o1784.
- Murguly, E., Norsten, T. B. & Branda, N. (1999). *J. Chem. Soc. Perkin Trans. 2*, pp. 2789–2794.
- Narr, E., Godt, A. & Jeschke, G. (2002). *Angew. Chem. Int. Ed.* **41**, 3907–3910.
- Otwinowski, Z. & Minor, W. (1997). *Methods in Enzymology*, Vol. 276, Macromolecular Crystallography, Part A, edited by C. W. Carter Jr & R. M. Sweet, pp. 307–326. New York: Academic Press.
- Rajca, A., Mukherjee, S., Pink, M. & Rajca, S. (2006). *J. Am. Chem. Soc.* **128**, 13497–13507.
- Reginsson, G. W. & Schiemann, O. (2011). *Biochem. Soc. Trans.* **39**, 128–139.
- Schiemann, O., Piton, N., Plackmeyer, J., Bode, B. E., Prisner, T. F. & Engels, J. W. (2007). *Nat. Protoc.* **2**, 904–923.
- Schuetz, D., Margraf, D., Prisner, T. F. & Bats, J. W. (2010). *Acta Cryst.* **E66**, o729–o730.
- Sheldrick, G. M. (2008). *Acta Cryst.* **A64**, 112–122.
- Sheldrick, G. M. (2015). *Acta Cryst.* **C71**, 3–8.



## supporting information

*Acta Cryst.* (2015). E71, 870-874 [doi:10.1107/S2056989015012086]

## The crystal structure of 4'-{4-[(2,2,5,5-tetramethyl-*N*-oxyl-3-pyrrolin-3-yl)ethynyl]phenyl}-2,2':6',2''-terpyridine

Andreas Meyer, Jennifer Wiecek, Gregor Schnakenburg and Olav Schiemann

### Computing details

Data collection: *DENZO* and *SCALEPACK* (Otwinowski & Minor, 1997); cell refinement: *SCALEPACK* (Otwinowski & Minor, 1997); data reduction: *DENZO* and *SCALEPACK* (Otwinowski & Minor, 1997); program(s) used to solve structure: *SHELXS97* (Sheldrick, 2008); program(s) used to refine structure: *SHELXL97* (Sheldrick, 2015); molecular graphics: *OLEX2* (Dolomanov *et al.*, 2009); software used to prepare material for publication: *OLEX2* (Dolomanov *et al.*, 2009).

### 4'-{4-[(2,2,5,5-Tetramethyl-*N*-oxyl-3-pyrrolin-3-yl)ethynyl]phenyl}-2,2':6',2''-terpyridine

#### Crystal data

C<sub>31</sub>H<sub>27</sub>N<sub>4</sub>O

$M_r = 471.56$

Monoclinic, *P*2<sub>1</sub>/*c*

$a = 18.5666$  (8) Å

$b = 20.2009$  (9) Å

$c = 6.7749$  (2) Å

$\beta = 92.743$  (3)°

$V = 2538.10$  (17) Å<sup>3</sup>

$Z = 4$

$F(000) = 996$

$D_x = 1.234$  Mg m<sup>-3</sup>

Mo  $K\alpha$  radiation,  $\lambda = 0.71073$  Å

Cell parameters from 9616 reflections

$\theta = 1.0$ – $29.1$ °

$\mu = 0.08$  mm<sup>-1</sup>

$T = 123$  K

Needle, clear yellow

$0.34 \times 0.12 \times 0.08$  mm

#### Data collection

Nonius KappaCCD

diffractometer

Radiation source: sealed tube

Graphite monochromator

Detector resolution: 8 pixels mm<sup>-1</sup>

fine slicing  $\omega$  and  $\varphi$  scans

Absorption correction: multi-scan

(Blessing, 1995)

$T_{\min} = 0.883$ ,  $T_{\max} = 1.078$

35758 measured reflections

6691 independent reflections

3221 reflections with  $I > 2\sigma(I)$

$R_{\text{int}} = 0.118$

$\theta_{\max} = 29.2$ °,  $\theta_{\min} = 3.0$ °

$h = -25$ → $24$

$k = -24$ → $27$

$l = -9$ → $6$

#### Refinement

Refinement on  $F^2$

Least-squares matrix: full

$R[F^2 > 2\sigma(F^2)] = 0.049$

$wR(F^2) = 0.122$

$S = 0.89$

6691 reflections

329 parameters

0 restraints

Hydrogen site location: inferred from neighbouring sites

H-atom parameters constrained

$w = 1/[\sigma^2(F_o^2) + (0.052P)^2]$

where  $P = (F_o^2 + 2F_c^2)/3$

$(\Delta/\sigma)_{\max} < 0.001$

$\Delta\rho_{\max} = 0.19$  e Å<sup>-3</sup>

$\Delta\rho_{\min} = -0.23$  e Å<sup>-3</sup>

*Special details*

**Geometry.** All e.s.d.'s (except the e.s.d. in the dihedral angle between two l.s. planes) are estimated using the full covariance matrix. The cell e.s.d.'s are taken into account individually in the estimation of e.s.d.'s in distances, angles and torsion angles; correlations between e.s.d.'s in cell parameters are only used when they are defined by crystal symmetry. An approximate (isotropic) treatment of cell e.s.d.'s is used for estimating e.s.d.'s involving l.s. planes.

*Fractional atomic coordinates and isotropic or equivalent isotropic displacement parameters ( $\text{\AA}^2$ )*

	<i>x</i>	<i>y</i>	<i>z</i>	$U_{\text{iso}}^*/U_{\text{eq}}$
O1	0.58556 (7)	0.39166 (8)	0.02921 (17)	0.0449 (4)
N1	-0.08706 (7)	0.29387 (7)	0.87301 (18)	0.0235 (3)
N2	-0.09424 (7)	0.47223 (8)	0.87295 (19)	0.0264 (4)
N3	0.55647 (8)	0.38695 (8)	0.1947 (2)	0.0332 (4)
N4	-0.01906 (7)	0.12743 (7)	0.83306 (19)	0.0262 (3)
C1	-0.06315 (9)	0.35653 (9)	0.8599 (2)	0.0221 (4)
C2	0.00840 (9)	0.37160 (9)	0.8258 (2)	0.0228 (4)
H2	0.0234	0.4164	0.8158	0.027*
C3	0.05751 (9)	0.32063 (9)	0.8067 (2)	0.0224 (4)
C4	0.03323 (9)	0.25616 (9)	0.8239 (2)	0.0236 (4)
H4	0.0658	0.2202	0.8149	0.028*
C5	-0.03946 (9)	0.24445 (9)	0.8545 (2)	0.0223 (4)
C6	-0.11788 (9)	0.40962 (9)	0.8820 (2)	0.0244 (4)
C7	-0.19006 (9)	0.39411 (9)	0.9094 (2)	0.0280 (4)
H7	-0.2054	0.3493	0.9130	0.034*
C8	-0.23880 (10)	0.44516 (10)	0.9310 (2)	0.0316 (5)
H8	-0.2882	0.4359	0.9494	0.038*
C9	-0.21466 (10)	0.50989 (10)	0.9254 (2)	0.0319 (5)
H9	-0.2467	0.5459	0.9426	0.038*
C10	-0.14220 (10)	0.52080 (9)	0.8941 (2)	0.0292 (4)
H10	-0.1258	0.5653	0.8872	0.035*
C11	0.13389 (9)	0.33241 (9)	0.7586 (2)	0.0228 (4)
C12	0.14938 (9)	0.37194 (9)	0.5973 (2)	0.0260 (4)
H12	0.1113	0.3937	0.5245	0.031*
C13	0.21936 (9)	0.37982 (9)	0.5426 (2)	0.0273 (4)
H13	0.2290	0.4069	0.4323	0.033*
C14	0.27657 (9)	0.34827 (9)	0.6476 (2)	0.0244 (4)
C15	0.26114 (9)	0.30872 (9)	0.8088 (2)	0.0273 (4)
H15	0.2992	0.2870	0.8818	0.033*
C16	0.19076 (9)	0.30096 (9)	0.8632 (2)	0.0273 (4)
H16	0.1810	0.2738	0.9733	0.033*
C17	0.34837 (10)	0.35565 (9)	0.5825 (2)	0.0275 (4)
C18	0.40740 (9)	0.36297 (9)	0.5209 (2)	0.0294 (4)
C19	0.47510 (9)	0.37261 (9)	0.4332 (2)	0.0267 (4)
C20	0.47826 (9)	0.37532 (10)	0.2098 (2)	0.0294 (4)
C21	0.59915 (9)	0.38953 (10)	0.3860 (2)	0.0305 (4)
C22	0.53960 (9)	0.38011 (10)	0.5256 (3)	0.0308 (4)
H22	0.5471	0.3796	0.6653	0.037*
C23	0.45763 (11)	0.30952 (11)	0.1131 (3)	0.0445 (6)

H23A	0.4643	0.3122	-0.0293	0.067*
H23B	0.4070	0.2997	0.1357	0.067*
H23C	0.4883	0.2743	0.1706	0.067*
C24	0.43549 (11)	0.43246 (11)	0.1165 (3)	0.0444 (6)
H24A	0.4511	0.4741	0.1791	0.067*
H24B	0.3840	0.4257	0.1354	0.067*
H24C	0.4438	0.4344	-0.0252	0.067*
C25	0.63565 (10)	0.45658 (10)	0.4093 (3)	0.0374 (5)
H25A	0.6686	0.4631	0.3023	0.056*
H25B	0.6628	0.4584	0.5368	0.056*
H25C	0.5990	0.4915	0.4039	0.056*
C26	0.65362 (10)	0.33278 (11)	0.3968 (3)	0.0421 (5)
H26A	0.6280	0.2904	0.3849	0.063*
H26B	0.6812	0.3344	0.5236	0.063*
H26C	0.6866	0.3371	0.2887	0.063*
C27	-0.06712 (9)	0.17596 (9)	0.8639 (2)	0.0230 (4)
C28	-0.13860 (9)	0.16253 (9)	0.9022 (2)	0.0268 (4)
H28	-0.1714	0.1976	0.9238	0.032*
C29	-0.16099 (10)	0.09759 (9)	0.9083 (2)	0.0295 (4)
H29	-0.2095	0.0873	0.9348	0.035*
C30	-0.11244 (10)	0.04767 (9)	0.8756 (2)	0.0295 (4)
H30	-0.1268	0.0025	0.8789	0.035*
C31	-0.04244 (10)	0.06489 (9)	0.8381 (2)	0.0290 (4)
H31	-0.0091	0.0304	0.8145	0.035*

*Atomic displacement parameters (Å<sup>2</sup>)*

	$U^{11}$	$U^{22}$	$U^{33}$	$U^{12}$	$U^{13}$	$U^{23}$
O1	0.0353 (8)	0.0713 (12)	0.0294 (7)	-0.0087 (7)	0.0138 (6)	-0.0024 (7)
N1	0.0240 (8)	0.0271 (9)	0.0196 (7)	0.0008 (7)	0.0026 (6)	-0.0010 (6)
N2	0.0257 (9)	0.0283 (10)	0.0253 (7)	0.0025 (7)	0.0029 (6)	0.0004 (6)
N3	0.0245 (9)	0.0507 (12)	0.0250 (8)	-0.0073 (8)	0.0075 (6)	-0.0021 (7)
N4	0.0273 (8)	0.0282 (10)	0.0231 (7)	-0.0011 (7)	0.0018 (6)	-0.0003 (6)
C1	0.0209 (10)	0.0277 (11)	0.0179 (8)	-0.0020 (8)	0.0016 (6)	0.0002 (7)
C2	0.0224 (9)	0.0242 (10)	0.0219 (8)	-0.0020 (8)	0.0033 (6)	0.0002 (7)
C3	0.0188 (9)	0.0301 (11)	0.0183 (8)	-0.0022 (8)	0.0025 (6)	0.0000 (7)
C4	0.0218 (10)	0.0274 (11)	0.0221 (8)	0.0017 (8)	0.0043 (7)	0.0012 (7)
C5	0.0218 (9)	0.0284 (11)	0.0171 (7)	-0.0018 (8)	0.0032 (6)	0.0008 (7)
C6	0.0234 (10)	0.0314 (11)	0.0187 (8)	0.0007 (8)	0.0029 (7)	0.0003 (7)
C7	0.0239 (10)	0.0345 (12)	0.0259 (9)	-0.0004 (9)	0.0041 (7)	0.0001 (8)
C8	0.0225 (10)	0.0445 (14)	0.0282 (9)	0.0035 (9)	0.0055 (7)	0.0023 (8)
C9	0.0287 (11)	0.0387 (13)	0.0285 (9)	0.0104 (9)	0.0040 (7)	0.0033 (8)
C10	0.0329 (11)	0.0287 (11)	0.0261 (9)	0.0028 (9)	0.0018 (7)	0.0013 (8)
C11	0.0207 (9)	0.0234 (10)	0.0243 (8)	-0.0003 (8)	0.0026 (7)	-0.0023 (7)
C12	0.0234 (10)	0.0253 (11)	0.0293 (9)	0.0017 (8)	0.0020 (7)	0.0017 (7)
C13	0.0241 (10)	0.0316 (11)	0.0267 (9)	-0.0001 (8)	0.0053 (7)	0.0062 (8)
C14	0.0204 (9)	0.0255 (11)	0.0277 (9)	-0.0011 (8)	0.0060 (7)	-0.0007 (7)
C15	0.0213 (10)	0.0310 (11)	0.0297 (9)	0.0007 (8)	0.0011 (7)	0.0040 (8)



C16	0.0244 (10)	0.0314 (11)	0.0263 (9)	-0.0024 (8)	0.0035 (7)	0.0049 (8)
C17	0.0261 (11)	0.0279 (11)	0.0288 (9)	-0.0010 (8)	0.0035 (8)	0.0025 (7)
C18	0.0257 (11)	0.0320 (12)	0.0306 (9)	-0.0015 (9)	0.0031 (8)	0.0027 (8)
C19	0.0216 (10)	0.0292 (11)	0.0302 (9)	-0.0006 (8)	0.0085 (7)	0.0005 (8)
C20	0.0206 (10)	0.0379 (12)	0.0300 (9)	-0.0058 (9)	0.0042 (7)	0.0007 (8)
C21	0.0208 (10)	0.0406 (13)	0.0304 (9)	-0.0031 (9)	0.0039 (7)	-0.0028 (8)
C22	0.0236 (10)	0.0409 (13)	0.0281 (9)	-0.0031 (9)	0.0047 (7)	-0.0003 (8)
C23	0.0447 (13)	0.0543 (15)	0.0347 (11)	-0.0176 (11)	0.0054 (9)	-0.0079 (10)
C24	0.0350 (12)	0.0571 (16)	0.0414 (11)	0.0052 (11)	0.0050 (9)	0.0139 (10)
C25	0.0267 (11)	0.0446 (14)	0.0416 (11)	-0.0060 (9)	0.0078 (8)	-0.0031 (9)
C26	0.0297 (11)	0.0444 (14)	0.0526 (13)	0.0000 (10)	0.0070 (9)	0.0015 (10)
C27	0.0229 (10)	0.0299 (11)	0.0164 (8)	0.0001 (8)	0.0006 (6)	0.0003 (7)
C28	0.0234 (10)	0.0322 (12)	0.0248 (9)	-0.0010 (9)	0.0023 (7)	0.0017 (8)
C29	0.0245 (10)	0.0365 (12)	0.0276 (9)	-0.0069 (9)	0.0024 (7)	0.0021 (8)
C30	0.0336 (11)	0.0279 (11)	0.0270 (9)	-0.0070 (9)	0.0007 (7)	0.0022 (8)
C31	0.0327 (11)	0.0270 (11)	0.0273 (9)	-0.0020 (9)	0.0011 (7)	-0.0019 (8)

*Geometric parameters (Å, °)*

O1—N3	1.2712 (17)	C15—H15	0.9500
N1—C1	1.346 (2)	C15—C16	1.383 (2)
N1—C5	1.343 (2)	C16—H16	0.9500
N2—C6	1.341 (2)	C17—C18	1.200 (2)
N2—C10	1.337 (2)	C18—C19	1.429 (2)
N3—C20	1.479 (2)	C19—C20	1.519 (2)
N3—C21	1.487 (2)	C19—C22	1.333 (2)
N4—C27	1.349 (2)	C20—C23	1.523 (3)
N4—C31	1.337 (2)	C20—C24	1.521 (3)
C1—C2	1.393 (2)	C21—C22	1.501 (2)
C1—C6	1.490 (2)	C21—C25	1.519 (3)
C2—H2	0.9500	C21—C26	1.528 (3)
C2—C3	1.386 (2)	C22—H22	0.9500
C3—C4	1.385 (2)	C23—H23A	0.9800
C3—C11	1.489 (2)	C23—H23B	0.9800
C4—H4	0.9500	C23—H23C	0.9800
C4—C5	1.396 (2)	C24—H24A	0.9800
C5—C27	1.478 (2)	C24—H24B	0.9800
C6—C7	1.397 (2)	C24—H24C	0.9800
C7—H7	0.9500	C25—H25A	0.9800
C7—C8	1.384 (2)	C25—H25B	0.9800
C8—H8	0.9500	C25—H25C	0.9800
C8—C9	1.383 (3)	C26—H26A	0.9800
C9—H9	0.9500	C26—H26B	0.9800
C9—C10	1.389 (2)	C26—H26C	0.9800
C10—H10	0.9500	C27—C28	1.391 (2)
C11—C12	1.395 (2)	C28—H28	0.9500
C11—C16	1.396 (2)	C28—C29	1.377 (2)
C12—H12	0.9500	C29—H29	0.9500

C12—C13	1.377 (2)	C29—C30	1.377 (3)
C13—H13	0.9500	C30—H30	0.9500
C13—C14	1.403 (2)	C30—C31	1.381 (2)
C14—C15	1.394 (2)	C31—H31	0.9500
C14—C17	1.432 (2)		
C5—N1—C1	118.19 (14)	C22—C19—C18	127.46 (16)
C10—N2—C6	117.76 (15)	C22—C19—C20	112.80 (15)
O1—N3—C20	122.18 (13)	N3—C20—C19	99.16 (13)
O1—N3—C21	122.33 (13)	N3—C20—C23	109.66 (15)
C20—N3—C21	115.43 (12)	N3—C20—C24	110.21 (15)
C31—N4—C27	117.70 (15)	C19—C20—C23	112.11 (16)
N1—C1—C2	122.47 (16)	C19—C20—C24	113.40 (16)
N1—C1—C6	116.22 (15)	C24—C20—C23	111.60 (16)
C2—C1—C6	121.31 (16)	N3—C21—C22	99.62 (13)
C1—C2—H2	120.3	N3—C21—C25	109.78 (15)
C3—C2—C1	119.35 (16)	N3—C21—C26	109.83 (15)
C3—C2—H2	120.3	C22—C21—C25	112.68 (15)
C2—C3—C11	122.65 (16)	C22—C21—C26	112.36 (16)
C4—C3—C2	118.22 (15)	C25—C21—C26	111.89 (15)
C4—C3—C11	119.06 (15)	C19—C22—C21	112.98 (15)
C3—C4—H4	120.2	C19—C22—H22	123.5
C3—C4—C5	119.52 (17)	C21—C22—H22	123.5
C5—C4—H4	120.2	C20—C23—H23A	109.5
N1—C5—C4	122.23 (16)	C20—C23—H23B	109.5
N1—C5—C27	117.40 (15)	C20—C23—H23C	109.5
C4—C5—C27	120.36 (16)	H23A—C23—H23B	109.5
N2—C6—C1	116.62 (15)	H23A—C23—H23C	109.5
N2—C6—C7	122.39 (16)	H23B—C23—H23C	109.5
C7—C6—C1	120.99 (17)	C20—C24—H24A	109.5
C6—C7—H7	120.6	C20—C24—H24B	109.5
C8—C7—C6	118.88 (18)	C20—C24—H24C	109.5
C8—C7—H7	120.6	H24A—C24—H24B	109.5
C7—C8—H8	120.4	H24A—C24—H24C	109.5
C9—C8—C7	119.14 (17)	H24B—C24—H24C	109.5
C9—C8—H8	120.4	C21—C25—H25A	109.5
C8—C9—H9	120.9	C21—C25—H25B	109.5
C8—C9—C10	118.13 (17)	C21—C25—H25C	109.5
C10—C9—H9	120.9	H25A—C25—H25B	109.5
N2—C10—C9	123.68 (18)	H25A—C25—H25C	109.5
N2—C10—H10	118.2	H25B—C25—H25C	109.5
C9—C10—H10	118.2	C21—C26—H26A	109.5
C12—C11—C3	119.82 (15)	C21—C26—H26B	109.5
C12—C11—C16	118.62 (15)	C21—C26—H26C	109.5
C16—C11—C3	121.41 (15)	H26A—C26—H26B	109.5
C11—C12—H12	119.7	H26A—C26—H26C	109.5
C13—C12—C11	120.64 (16)	H26B—C26—H26C	109.5
C13—C12—H12	119.7	N4—C27—C5	116.10 (15)

C12—C13—H13	119.6	N4—C27—C28	122.10 (17)
C12—C13—C14	120.79 (16)	C28—C27—C5	121.80 (16)
C14—C13—H13	119.6	C27—C28—H28	120.5
C13—C14—C17	119.32 (15)	C29—C28—C27	118.90 (17)
C15—C14—C13	118.61 (15)	C29—C28—H28	120.5
C15—C14—C17	122.03 (16)	C28—C29—H29	120.3
C14—C15—H15	119.8	C28—C29—C30	119.45 (17)
C16—C15—C14	120.38 (16)	C30—C29—H29	120.3
C16—C15—H15	119.8	C29—C30—H30	120.9
C11—C16—H16	119.5	C29—C30—C31	118.29 (18)
C15—C16—C11	120.96 (16)	C31—C30—H30	120.9
C15—C16—H16	119.5	N4—C31—C30	123.55 (17)
C18—C17—C14	177.35 (19)	N4—C31—H31	118.2
C17—C18—C19	175.64 (18)	C30—C31—H31	118.2
C18—C19—C20	119.74 (15)		
O1—N3—C20—C19	178.70 (16)	C6—C7—C8—C9	-0.2 (2)
O1—N3—C20—C23	61.1 (2)	C7—C8—C9—C10	1.3 (2)
O1—N3—C20—C24	-62.1 (2)	C8—C9—C10—N2	-1.4 (2)
O1—N3—C21—C22	-178.63 (17)	C10—N2—C6—C1	-179.46 (13)
O1—N3—C21—C25	62.9 (2)	C10—N2—C6—C7	1.0 (2)
O1—N3—C21—C26	-60.5 (2)	C11—C3—C4—C5	-175.31 (13)
N1—C1—C2—C3	-0.7 (2)	C11—C12—C13—C14	0.0 (3)
N1—C1—C6—N2	178.75 (13)	C12—C11—C16—C15	0.1 (3)
N1—C1—C6—C7	-1.7 (2)	C12—C13—C14—C15	0.0 (3)
N1—C5—C27—N4	176.14 (13)	C12—C13—C14—C17	177.81 (16)
N1—C5—C27—C28	-3.8 (2)	C13—C14—C15—C16	0.0 (3)
N2—C6—C7—C8	-1.0 (2)	C14—C15—C16—C11	-0.1 (3)
N3—C21—C22—C19	0.7 (2)	C16—C11—C12—C13	-0.1 (3)
N4—C27—C28—C29	-0.1 (2)	C17—C14—C15—C16	-177.74 (17)
C1—N1—C5—C4	0.5 (2)	C18—C19—C20—N3	178.91 (16)
C1—N1—C5—C27	-178.37 (13)	C18—C19—C20—C23	-65.4 (2)
C1—C2—C3—C4	-0.5 (2)	C18—C19—C20—C24	62.1 (2)
C1—C2—C3—C11	176.34 (14)	C18—C19—C22—C21	-179.71 (19)
C1—C6—C7—C8	179.43 (14)	C20—N3—C21—C22	-1.4 (2)
C2—C1—C6—N2	-1.8 (2)	C20—N3—C21—C25	-119.89 (17)
C2—C1—C6—C7	177.78 (15)	C20—N3—C21—C26	116.68 (17)
C2—C3—C4—C5	1.6 (2)	C20—C19—C22—C21	0.1 (2)
C2—C3—C11—C12	-51.0 (2)	C21—N3—C20—C19	1.5 (2)
C2—C3—C11—C16	133.51 (18)	C21—N3—C20—C23	-116.05 (17)
C3—C4—C5—N1	-1.7 (2)	C21—N3—C20—C24	120.71 (17)
C3—C4—C5—C27	177.14 (13)	C22—C19—C20—N3	-1.0 (2)
C3—C11—C12—C13	-175.65 (16)	C22—C19—C20—C23	114.73 (18)
C3—C11—C16—C15	175.58 (16)	C22—C19—C20—C24	-117.78 (18)
C4—C3—C11—C12	125.74 (17)	C25—C21—C22—C19	117.02 (18)
C4—C3—C11—C16	-49.7 (2)	C26—C21—C22—C19	-115.47 (18)
C4—C5—C27—N4	-2.7 (2)	C27—N4—C31—C30	-0.9 (2)
C4—C5—C27—C28	177.36 (14)	C27—C28—C29—C30	-0.3 (2)

C5—N1—C1—C2	0.7 (2)	C28—C29—C30—C31	0.1 (2)
C5—N1—C1—C6	-179.79 (13)	C29—C30—C31—N4	0.5 (2)
C5—C27—C28—C29	179.78 (14)	C31—N4—C27—C5	-179.19 (13)
C6—N2—C10—C9	0.3 (2)	C31—N4—C27—C28	0.7 (2)
C6—C1—C2—C3	179.82 (13)		

*Hydrogen-bond geometry (Å, °)*

Cg is the centroid of the C11—C16 ring.

<i>D</i> —H... <i>A</i>	<i>D</i> —H	H... <i>A</i>	<i>D</i> ... <i>A</i>	<i>D</i> —H... <i>A</i>
C2—H2...N2	0.95	2.50	2.815 (2)	99
C4—H4...N4	0.95	2.46	2.778 (2)	100
C8—H8...O1 <sup>i</sup>	0.95	2.59	3.529 (2)	170
C16—H16...Cg <sup>ii</sup>	0.95	2.81	3.669 (2)	151
C22—H22...O1 <sup>iii</sup>	0.95	2.55	3.485 (2)	170

Symmetry codes: (i)  $x-1, y, z+1$ ; (ii)  $x, -y+1/2, z+1/2$ ; (iii)  $x, y, z+1$ .

# Appendix B

## **Crystal Structure of 4'-{[4-(2,2':6',2''-Terpyridyl-4'-yl)phenyl]-ethynyl}biphenyl-4-yl-(2,2,5,5-tetramethyl-1-oxyl-3-pyrrolin-3-yl)formate Benzene 2.5-Solvate**

Andreas Meyer,<sup>i</sup> Gregor Schnakenburg<sup>ii</sup> and Olav Schiemann<sup>i</sup>

Received 7th September 2015, published online 26th September 2015.

Reprinted with permission from  
A. Meyer, G. Schnakenburg, and O. Schiemann, *Acta Crystallographica E* **2015**, *E71*,  
1245 - 1249.  
Copyright ©2015, International Union of Crystallography.

### **Own contributions to the manuscript**

- Synthesis and crystallization of the title compound.
- Evaluation of the geometrical parameters of the crystal structure.
- Writing the manuscript.

---

<sup>i</sup> University of Bonn, Institute of Physical and Theoretical Chemistry, Wegelerstr. 12, 53115 Bonn, Germany.

<sup>ii</sup> University of Bonn, Institute of Inorganic Chemistry, Gerhard-Domagk-Strasse 1, 53121 Bonn, Germany.

Received 7 September 2015

Accepted 21 September 2015

Edited by H. Stoeckli-Evans, University of  
Neuchâtel, Switzerland

**Keywords:** crystal structure; terpyridine; nitroxyl; nitroxide; phenylethynylbiphenyl; ethynylphenyl; C—H $\cdots\pi$  interactions;  $\pi$ – $\pi$  interactions; hydrogen bonds

**CCDC reference:** 1426093

**Supporting information:** this article has supporting information at journals.iucr.org/e

# Crystal structure of 4'-{[4-(2,2':6',2''-terpyridyl-4'-yl)phenyl]ethynyl}biphenyl-4-yl (2,2,5,5-tetramethyl-1-oxyl-3-pyrrolin-3-yl)formate benzene 2.5-solvate

Andreas Meyer,<sup>a</sup> Gregor Schnakenburg<sup>b</sup> and Olav Schiemann<sup>a\*</sup>

<sup>a</sup>University of Bonn, Institute of Physical and Theoretical Chemistry, Wegelerstr. 12, 53115 Bonn, Germany, and

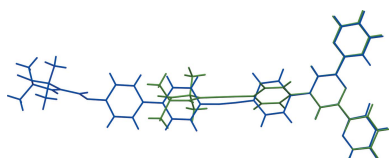
<sup>b</sup>University of Bonn, Institute of Inorganic Chemistry, Gerhard-Domagk-Strasse 1, 53121 Bonn, Germany.

\*Correspondence e-mail: schiemann@pc.uni-bonn.de

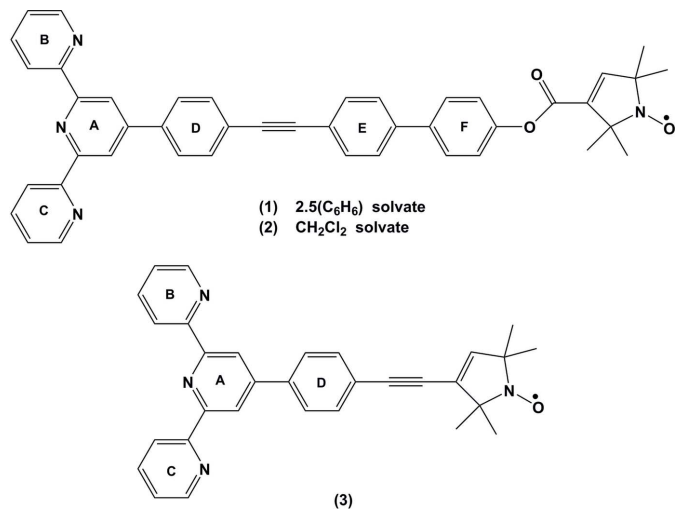
The title compound, C<sub>44</sub>H<sub>35</sub>N<sub>4</sub>O<sub>3</sub>·2.5C<sub>6</sub>H<sub>6</sub> (**1**), consists of a terpyridine and a *N*-oxylpyrroline-3-formate group separated by an aromatic spacer, *viz.* 4-(phenylethynyl)-1,1'-biphenyl. It crystallized in the triclinic space group  $P\bar{1}$  with two and a half benzene solvate molecules (one benzene molecule is located about an inversion center), while the dichloromethane solvate (**2**) of the same molecule [Ackermann *et al.* (2015). *Chem. Commun.* **51**, 5257–5260] crystallized in the tetragonal space group  $P4_2/n$ , with considerable disorder in the molecule. In (**1**), the terpyridine (terpy) group assumes an all-*trans* conformation typical for terpyridines. It is essentially planar with the two outer pyridine rings (*B* and *C*) inclined to the central pyridine ring (*A*) by 8.70 (15) and 14.55 (14)°, respectively. The planes of the aromatic spacer (*D*, *E* and *F*) are nearly coplanar with dihedral angles *D/E*, *D/F* and *E/F* being 3.42 (15), 5.80 (15) and 4.00 (16)°, respectively. It is twisted with respect to the terpy group with, for example, dihedral angle *A/D* being 24.48 (14)°. The mean plane of the *N*-oxylpyrroline is almost normal to the biphenyl ring *F*, making a dihedral angle of 86.57 (16)°, and it is inclined to pyridine ring *A* by 72.61 (15)°. The intramolecular separation between the O atom of the nitroxyl group and the N atom of the central pyridine ring of the terpyridine group is 25.044 (3) Å. In the crystal, molecules are linked by pairs of C—H $\cdots$ O hydrogen bonds, forming inversion dimers. The dimers stack along the *c* axis forming columns. Within and between the columns, the spaces are occupied by benzene molecules. The shortest oxygen–oxygen separation between nitroxyl groups is 4.004 (4) Å. The details of the title compound are compared with those of the dichloromethane solvate (**2**) and with the structure of a related molecule, 4'-{4-[(2,2,5,5-tetramethyl-*N*-oxyl-3-pyrrolin-3-yl)ethynyl]phenyl}-2,2':6',2''-terpyridine (**3**), which has an ethynylphenyl spacer [Meyer *et al.* (2015). *Acta Cryst.* **E71**, 870–874].

## 1. Chemical context

The title compound (**1**) was synthesized as a ligand for 3d metal ions in the framework of a pulsed EPR study on metal–nitroxyl model systems. It contains a nitroxyl group and a terpyridine (terpy) group which is capable of taking up metal ions. The title compound resembles compound (**3**) (4'-{4-[(2,2,5,5-tetramethyl-*N*-oxyl-3-pyrrolin-3-yl)ethynyl]phenyl}-2,2':6',2''-terpyridine), which has an ethynylphenyl spacer (Meyer *et al.*, 2015a), compared to the phenylethynylbiphenyl spacer in the title compound (**1**). Nitroxyls are of interest in various branches of chemistry including magnetochemistry (Rajca *et al.*, 2006; Fritscher *et al.*, 2002), synthetic chemistry (Hoover & Stahl, 2011; Fey *et al.*, 2001) and structural biology (Reginsson & Schiemann, 2011). Terpyridines show pH-dependent luminescence properties which have been analyzed in terms of a pH-dependent *cis*–*trans* isomerization (Naka-



moto, 1960; Fink & Ohnesorge, 1970). Structural investigations in the solid state reveal an exclusive preference for the *trans* conformation (Fallahpour *et al.*, 1999; Eryazici *et al.*, 2006; Bessel *et al.*, 1992; Grave *et al.*, 2003). Terpyridines have been shown to be versatile ligands for various metal ions (Hogg & Wilkins, 1962; Constable *et al.*, 1999; Narr *et al.*, 2002; Meyer *et al.*, 2015b; Folgado *et al.*, 1990).



## 2. Structural commentary

The molecular structure of the title compound, (1), is shown in Fig. 1. The crystal structure of the dichloromethane solvate (2) of the title compound has been reported (Ackermann *et al.*, 2015). However, these authors used a different protocol for the crystallization of (1) and the conformation of (2) differs markedly from the one presented herein, as shown in the structural overlay of the two compounds (Fig. 2). The structural overlay of compounds (1) and (3) also illustrate the differences in their conformations (Fig. 3).

In (1) the terpy group assumes the usual all-*trans* conformation (Meyer *et al.*, 2015a; Fallahpour *et al.*, 1999; Eryazici *et al.*,

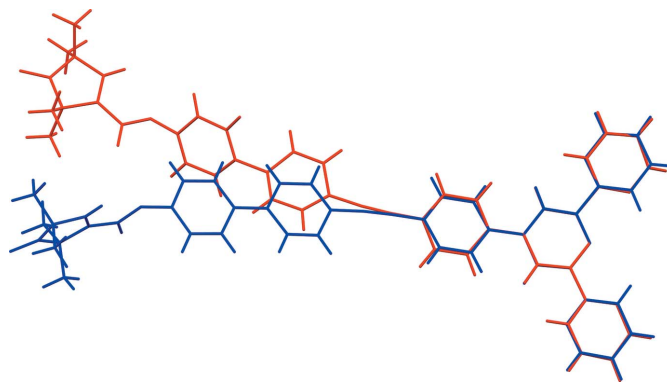


**Figure 2**  
 The structural overlay of compounds (1) and (2) [title compound (1) blue, compound (2) – the dichloromethane solvate (Ackermann *et al.*, 2015) – red].

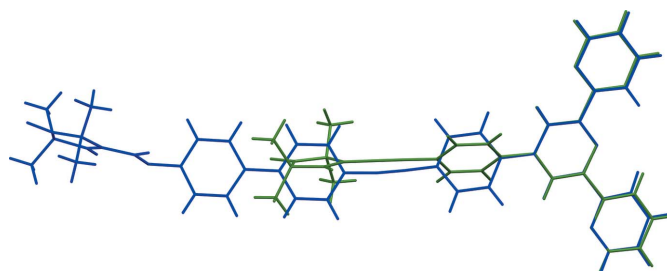


**Figure 3**  
 The structural overlay of compounds (1) and (3) [title compound (1) blue, compound (3) – (Meyer *et al.*, 2015a) – green].

*et al.*, 2006; Bessel *et al.*, 1992; Grave *et al.*, 2003). It is essentially planar with the two outer rings B (N3/C35–C39) and C (N4/C40–C44) being inclined to the central pyridine ring A (N2/C30–C34) by 8.70 (15) and 14.55 (14)°, respectively. The conformation of the nitroxyl group in (1) is similar to that found in (3), with a planar pyrroline (N1/C1–C4) ring assuming an angle of 72.61 (15)° to the central pyridine ring A [see also Margraf *et al.* (2009) and Schuetz *et al.* (2010)]. In (3) this dihedral angle is 88.44 (7)°, while in (2) the same dihedral angle is 21.6 (2)°.

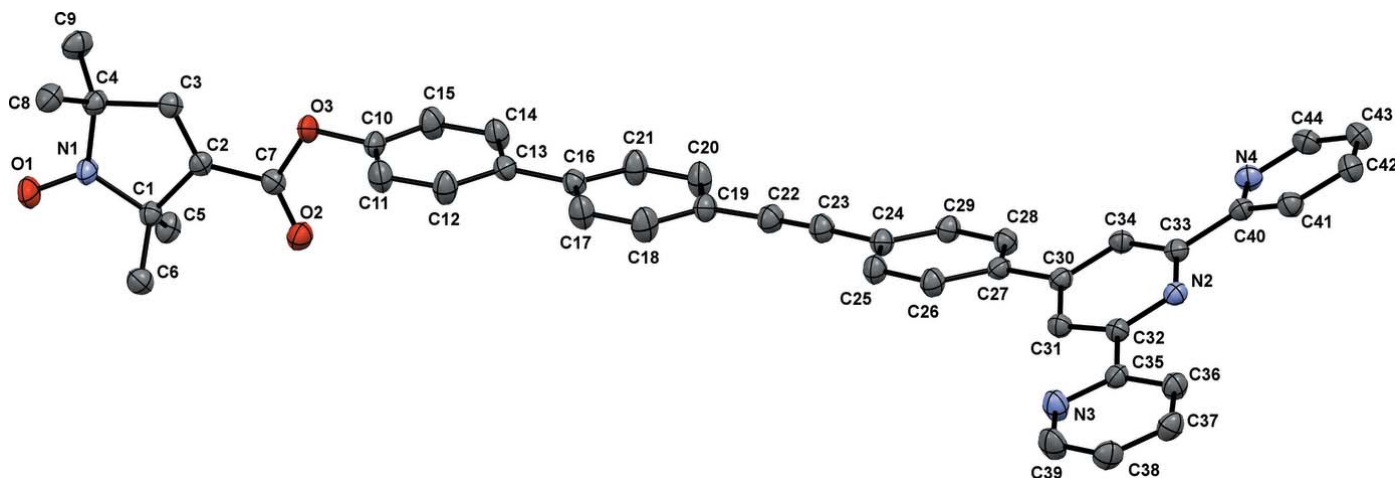


**Figure 1**  
 The molecular structure of the title compound (1), with atom labelling. Displacement ellipsoids are drawn at 50% probability level. The benzene molecules and the H atoms have been omitted for clarity.

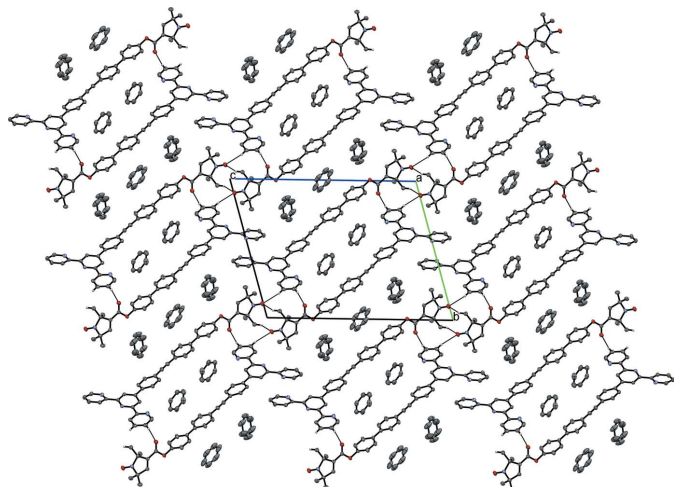


**Figure 4**  
Crystal packing of the title compound viewed along the *a* axis. Weak C—H···O hydrogen bonds are shown as dashed lines (see Table 1). H atoms not involved in C—H···O bonds have been omitted for clarity.

The *N*-oxylpyrroline-3-formate subunit is linked by a rigid spacer, consisting of a 4,4'-biphenylene, an ethynylene and a *p*-phenylene group, to the terpy subunit. The intramolecular separation of the nitroxyl and the terpy group is 25.044 (3) Å (measured between O1 and N2). The three phenyl groups within the spacer are nearly coplanar, with dihedral angles between the rings of 4.00 (16)°, for rings *D* (C10–C15) and *E* (C16–C21), and 3.42 (15)° for rings *E* and *F* (C24–C29). Compared to the structure of (3), the spacer is closer to coplanarity to the central pyridine ring: dihedral angle *A/D* is 24.48 (14)°, compared to 51.36 (7)° in (3). The ethynylene group is slightly bent as in (3), with angle C19–C22–C23 = 174.6 (3) and C22–C23–C24 = 177.8 (3)°. There are short C—H···N contacts in the molecule of 2.48 Å (H31···N3) and 2.49 Å (H34···N4). The same short contacts are also observed in (3). Such contacts have been classified as hydrogen bonds by Murguly *et al.* (1999).

**Table 1**  
Hydrogen-bond geometry (Å, °).

Cg4, Cg7 and Cg10 are the centroids of pyridine ring N4/C40–C44, spacer ring C24–C29 and benzene ring C54–C59, respectively.

<i>D</i> —H··· <i>A</i>	<i>D</i> —H	H··· <i>A</i>	<i>D</i> ··· <i>A</i>	<i>D</i> —H··· <i>A</i>
C37—H37···O1 <sup>i</sup>	0.95	2.65	3.228 (4)	120
C38—H38···O2 <sup>ii</sup>	0.95	2.55	3.485 (4)	169
C6—H6C···O1 <sup>iii</sup>	0.98	2.61	3.499 (4)	151
C9—H9B···Cg4 <sup>iv</sup>	0.96	2.79	3.602 (4)	140
C14—H14···Cg10 <sup>v</sup>	0.95	2.88	3.608 (4)	134
C14—H14···Cg10 <sup>vi</sup>	0.95	2.88	3.608 (4)	134
C55—H55···Cg7 <sup>vii</sup>	0.95	2.90	3.680 (3)	140

Symmetry codes: (i)  $x + 3, y + 1, z + 1$ ; (ii)  $-x + 4, -y + 1, -z + 1$ ; (iii)  $-x, -y, -z$ ; (iv)  $x - 2, y - 1, z - 1$ ; (v)  $x - 1, y, z$ ; (vi)  $-x + 2, -y, -z + 1$ ; (vii)  $-x + 3, -y + 1, -z + 1$ .

### 3. Supramolecular features

In the crystal of (1), Fig. 4, molecules form layers which are nearly coplanar with the (011) plane. Neighbouring layers differ in the orientation of the molecules and each layer is separated by layers of solvent molecules. This arrangement possibly leads to favorable dispersive interactions although only one short C—H··· $\pi$  contact is observed between the solvent molecules and molecules of (1) (Table 1). Short  $\pi$ – $\pi$  contacts are observed between the *C* rings of neighbouring molecules and between the *B* and *C* rings (Fig. 5). The centroid-to-centroid distances are 3.678 (2) and 3.8915 (18) Å, respectively, and can be classified as slipped face-to-face  $\pi$ -interactions (Janiak, 2000).

Within the planes, there are weak C—H···O hydrogen bonds between the nitroxyl-O atom and the *para*-hydrogen atom of pyridine ring *B* (Table 1). Furthermore, two weak hydrogen bonds per molecule are formed between pairs of layers (Table 1). One of these hydrogen bonds involves the nitroxyl O atom and a hydrogen atom of a methyl group of a molecule from a neighboring layer. The other hydrogen bond is formed between the carboxylic O atom of the carboxylate group and a *meta*-hydrogen atom of one of the outer pyridine rings of a molecule from a neighboring layer. As the layers are

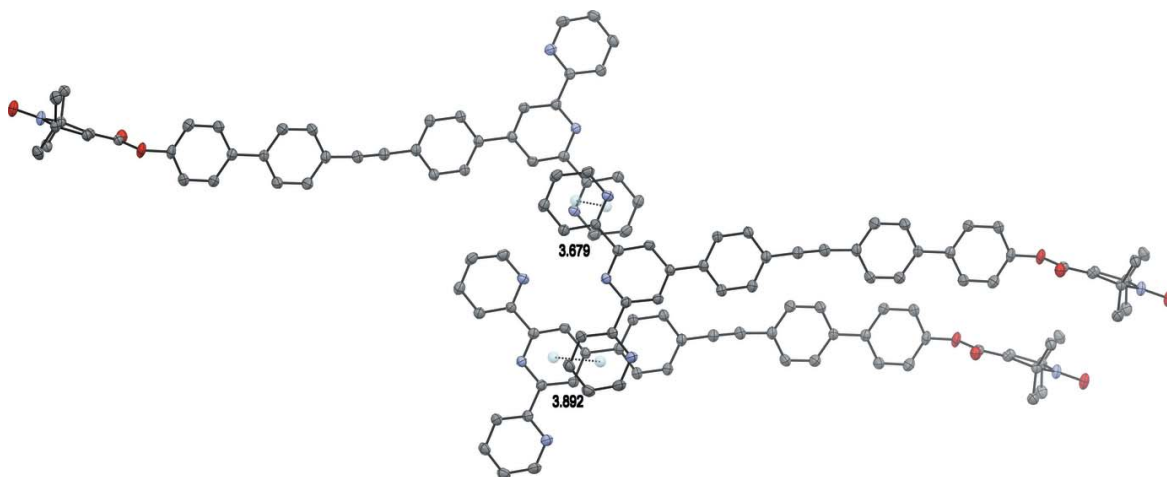


**Figure 5**  
 $\pi$ -stacking interactions between pyridine rings of neighboring molecules. H atoms have been omitted for clarity.



hydrogen bonded pair-wise, the structure can also be described as consisting of double-layers.

It is noteworthy that the arrangement of the molecules of the title compound strongly depends upon the solvents of crystallization. In compound (1), the molecules are arranged in layers and the benzene molecules fill out the channels between the layers formed by the aromatic spacers of the molecule. Close intermolecule contacts exist only between the functional groups. In the structure of (2) (Ackermann *et al.*, 2015), the solvent of crystallization is dichloromethane instead of benzene and molecules are arranged having fourfold rotational site symmetry. The solvent molecules fill out channels between the molecules of (2), as in (1). However, the CH<sub>2</sub>Cl<sub>2</sub> solvent molecules in (2) are in close proximity to the terpyridine groups instead of to the aromatic spacer. Weak hydrogen bonds are formed predominantly involving the O atoms as acceptors and the pyrroline and the pyridine rings as donors, as observed in (2) and (3). The shortest oxygen–oxygen separation between neighboring nitroxyl groups is 4.004 (4) Å. This O...O distance is an important factor determining the strength of through space exchange interactions of nitroxyls (Rajca *et al.* 2006).

#### 4. Database survey

The Cambridge Structural Database (CSD, Version 5.36; Groom & Allen, 2014) has not been updated since our presentation of the structure of (2). The CSD query revealed, that non-coordinated terpyridines are arranged in an all-*trans* conformation, unless they are either protonated, lithiated or cannot assume an all-*trans* conformation for reasons of steric hindrance.

#### 5. Synthesis and crystallization

The synthesis of the title compound (1), is illustrated in Fig. 6. 480 mg (1.45 mmol) of 4'-(4-ethynylphenyl)-2,2':6',2''-terpyridine (Grosshenny & Ziessel, 1993), 780 mg (1.69 mmol) of 4'-iodo-*p*-biphen-4-yl-*N*-oxyl-2,2,5,5-tetramethylpyrroline-3-formate (Bode *et al.*, 2008) and 85 mg (0.12 mmol) of tetrakis(triphenylphosphane)palladium(0) were dissolved in a mixture of 20 ml of triethylamine (TEA) and 9 ml of dimethylformamide (DMF) giving rise to an orange solution. The solution was heated to 323 K and stirred for 8 h after which the solvents were removed under reduced pressure. The resulting dark-orange powder was dissolved in dichloro-

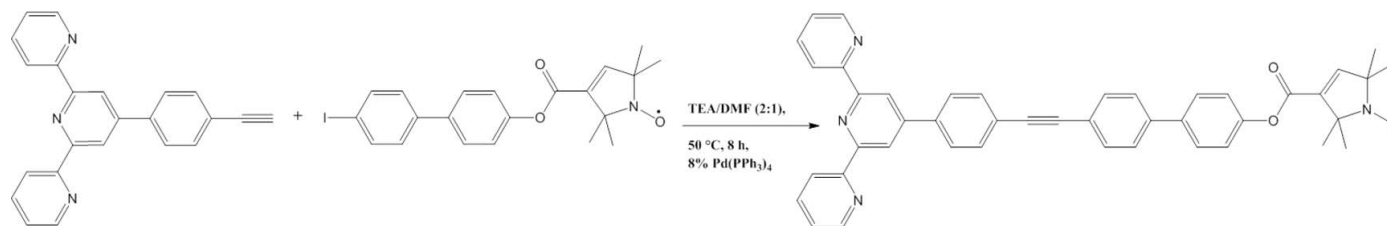


Figure 6  
The synthesis of the title compound (1).

Table 2  
Experimental details.

Crystal data	
Chemical formula	C <sub>44</sub> H <sub>35</sub> N <sub>4</sub> O <sub>3</sub> ·2.5C <sub>6</sub> H <sub>6</sub>
<i>M<sub>r</sub></i>	863.03
Crystal system, space group	Triclinic, <i>P</i> $\bar{1}$
Temperature (K)	123
<i>a</i> , <i>b</i> , <i>c</i> (Å)	5.7578 (1), 18.0559 (4), 23.3716 (6)
$\alpha$ , $\beta$ , $\gamma$ (°)	105.5870 (13), 93.7408 (13), 92.6002 (14)
<i>V</i> (Å <sup>3</sup> )	2330.41 (9)
<i>Z</i>	2
Radiation type	Mo <i>K</i> $\alpha$
$\mu$ (mm <sup>-1</sup> )	0.08
Crystal size (mm)	0.28 × 0.20 × 0.08
Data collection	
Diffractionmeter	Nonius KappaCCD
Absorption correction	Multi-scan ( <i>SORTAV</i> ; Blessing, 1995)
<i>T<sub>min</sub></i> , <i>T<sub>max</sub></i>	0.808, 1.000
No. of measured, independent and observed [ <i>I</i> > 2 $\sigma$ ( <i>I</i> )] reflections	74528, 11227, 6356
<i>R<sub>int</sub></i>	0.109
( <i>sin</i> $\theta$ / $\lambda$ ) <sub>max</sub> (Å <sup>-1</sup> )	0.661
Refinement	
<i>R</i> [ <i>F</i> <sup>2</sup> > 2 $\sigma$ ( <i>F</i> <sup>2</sup> )], <i>wR</i> ( <i>F</i> <sup>2</sup> ), <i>S</i>	0.071, 0.217, 1.07
No. of reflections	11227
No. of parameters	587
No. of restraints	1
H-atom treatment	H-atom parameters constrained
$\Delta\rho_{max}$ , $\Delta\rho_{min}$ (e Å <sup>-3</sup> )	0.33, -0.27

Computer programs: *HKL DENZO* and *SCALEPACK* (Otwinowski & Minor 1997), *SHELXS97* (Sheldrick, 2008), *SHELXL2013* (Sheldrick, 2015), *OLEX2* (Dolomanov *et al.*, 2009) and *Mercury* (Macrae *et al.*, 2008).

methane (DCM) and subjected to column chromatography using aluminum oxide (5% water, height 30 cm, diameter 2.3 cm). First, a mixture of DCM and hexane in a 1:2 ratio was used as eluent until all remaining educt, reagents and side products were eluted (approximately 200–300 ml). The column was then eluted using pure DCM to obtain a yellow solution. Removing the solvent yielded the product as a pale-yellow solid (yield: 90%). Crystals suitable for X-ray crystallography were obtained by layering a solution of (1) in benzene with *n*-hexane.

#### 6. Refinement

Crystal data, data collection and structure refinement details are summarized in Table 2. The H atoms were included in calculated positions and treated as riding atoms: C–H = 0.95–

0.98 Å with  $U_{\text{iso}}(\text{H}) = 1.5U_{\text{eq}}(\text{C})$  for methyl H atoms and  $1.2U_{\text{eq}}(\text{C})$  for other H atoms. 16 reflections with bad agreement were omitted from the final refinement cycles.

### Acknowledgements

The authors thank Professor Dr. A. C. Filippou for providing the X-ray infrastructure. OS thanks the DFG for funding via SFB 813.

### References

- Ackermann, K., Giannoulis, A., Cordes, D. B., Slawin, A. M. Z. & Bode, B. E. (2015). *Chem. Commun.* **51**, 5257–5260.
- Bessel, C. A., See, R. F., Jameson, D. L., Churchill, M. R. & Takeuchi, K. J. (1992). *J. Chem. Soc. Dalton Trans.* pp. 3223–3228.
- Blessing, R. H. (1995). *Acta Cryst.* **A51**, 33–38.
- Bode, E. B., Plackmeyer, J., Prisner, T. F. & Schiemann, O. (2008). *J. Phys. Chem. A*, **112**, 5064–5073.
- Constable, E. C., Baum, G., Bill, E., Dyson, R., van Eldik, R., Fenske, D., Kaderli, D., Morris, D., Neubrand, A., Neuburger, M., Smith, D. R., Wieghardt, K., Zehnder, M. & Zuberbühler, A. D. (1999). *Chem. Eur. J.* **5**, 498–508.
- Dolomanov, O. V., Bourhis, L. J., Gildea, R. J., Howard, J. A. K. & Puschmann, H. (2009). *J. Appl. Cryst.* **42**, 339–341.
- Eryazici, I., Moorefield, C. N., Durmus, S. & Newkome, G. R. (2006). *J. Org. Chem.* **71**, 1009–1014.
- Fallahpour, R.-A., Neuburger, M. & Zehnder, M. (1999). *Polyhedron*, **18**, 2445–2454.
- Fey, T., Fischer, H., Bachmann, S., Albert, K. & Bolm, C. (2001). *J. Org. Chem.* **66**, 8154–8159.
- Fink, D. W. & Ohnesorge, W. E. (1970). *J. Phys. Chem.* **74**, 72–77.
- Folgado, J. V., Henke, W., Allmann, R., Stratemeier, H., Beltrán-Porter, D., Rojo, T. & Reinen, D. (1990). *Inorg. Chem.* **29**, 2035–2042.
- Fritscher, J., Beyer, M. & Schiemann, O. (2002). *Chem. Phys. Lett.* **364**, 393–401.
- Grave, C., Lentz, D., Schäfer, A., Samorì, P., Rabe, P. J., Franke, P. & Schlüter, A. D. (2003). *J. Am. Chem. Soc.* **125**, 6907–6918.
- Groom, C. R. & Allen, F. H. (2014). *Angew. Chem. Int. Ed.* **53**, 662–671.
- Grosshenny, V. & Ziessel, R. (1993). *J. Organomet. Chem.* **453**, C19–C22.
- Hogg, R. & Wilkins, R. G. (1962). *J. Chem. Soc.* pp. 341–350.
- Hoover, J. M. & Stahl, S. S. (2011). *J. Am. Chem. Soc.* **133**, 16901–16910.
- Janiak, C. (2000). *J. Chem. Soc. Dalton Trans.* pp. 3885–3896.
- Macrae, C. F., Bruno, I. J., Chisholm, J. A., Edgington, P. R., McCabe, P., Pidcock, E., Rodriguez-Monge, L., Taylor, R., van de Streek, J. & Wood, P. A. (2008). *J. Appl. Cryst.* **41**, 466–470.
- Margraf, D., Schuetz, D., Prisner, T. F. & Bats, J. W. (2009). *Acta Cryst.* **E65**, o1784.
- Meyer, A., Schnakenburg, G., Glaum, R. & Schiemann, O. (2015b). *Inorg. Chem.* **54**, 8456–8464.
- Meyer, A., Wiecek, J., Schnakenburg, G. & Schiemann, O. (2015a). *Acta Cryst.* **E71**, 870–874.
- Murguly, E., Norsten, T. B. & Branda, N. (1999). *J. Chem. Soc. Perkin Trans. 2*, pp. 2789–2794.
- Nakamoto, K. (1960). *J. Phys. Chem.* **64**, 1420–1425.
- Narr, E., Godt, A. & Jeschke, G. (2002). *Angew. Chem. Int. Ed.* **41**, 3907–3910.
- Otwinowski, Z. & Minor, W. (1997). *Methods in Enzymology*, Vol. 276, *Macromolecular Crystallography*, Part A, edited by C. W. Carter Jr & R. M. Sweet, pp. 307–326. New York: Academic Press.
- Rajca, A., Mukherjee, S., Pink, M. & Rajca, S. (2006). *J. Am. Chem. Soc.* **128**, 13497–13507.
- Reginsson, G. W. & Schiemann, O. (2011). *Biochem. Soc. Trans.* **39**, 128–139.
- Schuetz, D., Margraf, D., Prisner, T. F. & Bats, J. W. (2010). *Acta Cryst.* **E66**, o729–o730.
- Sheldrick, G. M. (2008). *Acta Cryst.* **A64**, 112–122.
- Sheldrick, G. M. (2015). *Acta Cryst.* **C71**, 3–8.

## supporting information

*Acta Cryst.* (2015). E71, 1245-1249 [doi:10.1107/S2056989015017697]

## Crystal structure of 4'-{[4-(2,2':6',2''-terpyridyl-4'-yl)phenyl]ethynyl}biphenyl-4-yl (2,2,5,5-tetramethyl-1-oxyl-3-pyrrolin-3-yl)formate benzene 2.5-solvate

Andreas Meyer, Gregor Schnakenburg and Olav Schiemann

### Computing details

Data collection: *HKL DENZO* and *SCALEPACK* (Otwinowski & Minor 1997); cell refinement: *HKL SCALEPACK* (Otwinowski & Minor 1997); data reduction: *HKL DENZO* and *SCALEPACK* (Otwinowski & Minor 1997); program(s) used to solve structure: *SHELXS97* (Sheldrick, 2008); program(s) used to refine structure: *SHELXL2013* (Sheldrick, 2015); molecular graphics: *Olex2* (Dolomanov *et al.*, 2009) and *Mercury* (Macrae *et al.*, 2008); software used to prepare material for publication: *Olex2* (Dolomanov *et al.*, 2009).

### 4'-{[4-(2,2':6',2''-Terpyridyl-4'-yl)phenyl]ethynyl}biphenyl-4-yl (2,2,5,5-tetramethyl-1-oxyl-3-pyrrolin-3-yl)formate benzene 2.5-solvate

#### Crystal data

$C_{44}H_{35}N_4O_3 \cdot 2.5C_6H_6$

$M_r = 863.03$

Triclinic,  $P\bar{1}$

$a = 5.7578$  (1) Å

$b = 18.0559$  (4) Å

$c = 23.3716$  (6) Å

$\alpha = 105.5870$  (13)°

$\beta = 93.7408$  (13)°

$\gamma = 92.6002$  (14)°

$V = 2330.41$  (9) Å<sup>3</sup>

$Z = 2$

$F(000) = 912$

$D_x = 1.230$  Mg m<sup>-3</sup>

Mo  $K\alpha$  radiation,  $\lambda = 0.71073$  Å

Cell parameters from 12020 reflections

$\theta = 1.0$ – $29.1$ °

$\mu = 0.08$  mm<sup>-1</sup>

$T = 123$  K

Plate, yellow

$0.28 \times 0.20 \times 0.08$  mm

#### Data collection

Nonius KappaCCD  
diffractometer

fine slicing  $\varphi$  and  $\omega$  scans

Absorption correction: multi-scan  
(*SORTAV*; Blessing, 1995)

$T_{\min} = 0.808$ ,  $T_{\max} = 1.000$

74528 measured reflections

11227 independent reflections

6356 reflections with  $I > 2\sigma(I)$

$R_{\text{int}} = 0.109$

$\theta_{\max} = 28.0$ °,  $\theta_{\min} = 1.8$ °

$h = -7 \rightarrow 7$

$k = -23 \rightarrow 23$

$l = -30 \rightarrow 30$

#### Refinement

Refinement on  $F^2$

Least-squares matrix: full

$R[F^2 > 2\sigma(F^2)] = 0.071$

$wR(F^2) = 0.217$

$S = 1.07$

11227 reflections

587 parameters

1 restraint

Primary atom site location: structure-invariant  
direct methods

Secondary atom site location: difference Fourier  
map

Hydrogen site location: inferred from  
neighbouring sites

H-atom parameters constrained  
 $w = 1/[\sigma^2(F_o^2) + (0.0715P)^2 + 2.806P]$   
 where  $P = (F_o^2 + 2F_c^2)/3$

$(\Delta/\sigma)_{\max} < 0.001$   
 $\Delta\rho_{\max} = 0.33 \text{ e } \text{\AA}^{-3}$   
 $\Delta\rho_{\min} = -0.27 \text{ e } \text{\AA}^{-3}$

### Special details

**Geometry.** All e.s.d.'s (except the e.s.d. in the dihedral angle between two l.s. planes) are estimated using the full covariance matrix. The cell e.s.d.'s are taken into account individually in the estimation of e.s.d.'s in distances, angles and torsion angles; correlations between e.s.d.'s in cell parameters are only used when they are defined by crystal symmetry. An approximate (isotropic) treatment of cell e.s.d.'s is used for estimating e.s.d.'s involving l.s. planes.

### Fractional atomic coordinates and isotropic or equivalent isotropic displacement parameters ( $\text{\AA}^2$ )

	x	y	z	$U_{\text{iso}}^*/U_{\text{eq}}$
C1	0.2370 (5)	-0.01295 (16)	0.10190 (12)	0.0227 (6)
C2	0.3869 (5)	-0.03265 (16)	0.15104 (12)	0.0228 (6)
C3	0.4509 (5)	-0.10465 (16)	0.13551 (13)	0.0243 (6)
H3	0.5452	-0.1260	0.1611	0.029*
C4	0.3597 (5)	-0.14879 (16)	0.07364 (13)	0.0258 (6)
C5	-0.0104 (5)	0.00458 (18)	0.11846 (14)	0.0299 (7)
H5A	-0.1095	0.0036	0.0825	0.045*
H5B	-0.0082	0.0557	0.1468	0.045*
H5C	-0.0727	-0.0343	0.1367	0.045*
C6	0.3447 (5)	0.04980 (17)	0.07767 (14)	0.0294 (7)
H6A	0.5016	0.0368	0.0661	0.044*
H6B	0.3544	0.0991	0.1085	0.044*
H6C	0.2475	0.0539	0.0428	0.044*
C7	0.4547 (5)	0.02506 (17)	0.20817 (13)	0.0242 (6)
C8	0.5527 (5)	-0.17353 (18)	0.03214 (14)	0.0319 (7)
H8A	0.4832	-0.1971	-0.0085	0.048*
H8B	0.6441	-0.2110	0.0456	0.048*
H8C	0.6548	-0.1284	0.0326	0.048*
C9	0.1932 (5)	-0.21795 (18)	0.07291 (15)	0.0343 (7)
H9A	0.0694	-0.2006	0.0993	0.051*
H9B	0.2799	-0.2562	0.0867	0.051*
H9C	0.1238	-0.2412	0.0322	0.051*
C10	0.6996 (5)	0.04666 (16)	0.29676 (13)	0.0280 (7)
C11	0.9052 (6)	0.08515 (19)	0.29138 (14)	0.0358 (7)
H11	0.9637	0.0790	0.2534	0.043*
C12	1.0255 (6)	0.13289 (19)	0.34188 (14)	0.0342 (7)
H12	1.1682	0.1591	0.3381	0.041*
C13	0.9437 (5)	0.14379 (16)	0.39818 (13)	0.0256 (6)
C14	0.7358 (5)	0.10257 (19)	0.40168 (14)	0.0330 (7)
H14	0.6767	0.1076	0.4395	0.040*
C15	0.6137 (6)	0.05439 (19)	0.35106 (14)	0.0342 (7)
H15	0.4721	0.0271	0.3542	0.041*
C16	1.0710 (5)	0.19732 (17)	0.45189 (13)	0.0253 (6)
C17	1.2858 (6)	0.23439 (19)	0.44816 (14)	0.0360 (8)
H17	1.3476	0.2258	0.4104	0.043*
C18	1.4098 (6)	0.2824 (2)	0.49680 (14)	0.0361 (8)

---

H18	1.5546	0.3067	0.4922	0.043*
C19	1.3264 (5)	0.29639 (17)	0.55323 (13)	0.0285 (7)
C20	1.1098 (6)	0.2615 (2)	0.55805 (14)	0.0366 (8)
H20	1.0467	0.2711	0.5957	0.044*
C21	0.9861 (5)	0.21278 (19)	0.50809 (14)	0.0345 (7)
H21	0.8395	0.1893	0.5123	0.041*
C22	1.4677 (5)	0.34418 (17)	0.60378 (14)	0.0299 (7)
C23	1.6001 (5)	0.38338 (17)	0.64283 (13)	0.0288 (7)
C24	1.7619 (5)	0.43207 (17)	0.68813 (13)	0.0273 (6)
C25	1.9752 (5)	0.45919 (17)	0.67281 (13)	0.0296 (7)
H25	2.0113	0.4455	0.6324	0.036*
C26	2.1331 (5)	0.50571 (17)	0.71624 (13)	0.0285 (7)
H26	2.2755	0.5242	0.7051	0.034*
C27	2.0868 (5)	0.52596 (15)	0.77632 (13)	0.0235 (6)
C28	1.8728 (5)	0.49925 (16)	0.79124 (13)	0.0256 (6)
H28	1.8368	0.5129	0.8317	0.031*
C29	1.7132 (5)	0.45334 (16)	0.74799 (13)	0.0265 (6)
H29	1.5689	0.4361	0.7591	0.032*
C30	2.2616 (5)	0.57301 (15)	0.82326 (12)	0.0230 (6)
C31	2.4348 (5)	0.62120 (16)	0.80997 (13)	0.0247 (6)
H31	2.4364	0.6278	0.7710	0.030*
C32	2.6059 (5)	0.65965 (16)	0.85480 (12)	0.0241 (6)
C33	2.4383 (5)	0.60956 (16)	0.92376 (13)	0.0240 (6)
C34	2.2643 (5)	0.56824 (16)	0.88191 (12)	0.0244 (6)
H34	2.1482	0.5370	0.8931	0.029*
C35	2.7986 (5)	0.70819 (16)	0.84142 (13)	0.0249 (6)
C36	2.9585 (5)	0.75177 (17)	0.88581 (14)	0.0292 (7)
H36	2.9416	0.7538	0.9264	0.035*
C37	3.1439 (5)	0.79252 (17)	0.87052 (14)	0.0310 (7)
H37	3.2553	0.8228	0.9004	0.037*
C38	3.1634 (6)	0.78823 (18)	0.81163 (14)	0.0337 (7)
H38	3.2898	0.8146	0.7996	0.040*
C39	2.9941 (6)	0.7444 (2)	0.77017 (15)	0.0388 (8)
H39	3.0071	0.7421	0.7294	0.047*
C40	2.4478 (5)	0.60351 (15)	0.98644 (12)	0.0236 (6)
C41	2.6483 (5)	0.62869 (17)	1.02509 (13)	0.0279 (6)
H41	2.7844	0.6482	1.0117	0.033*
C42	2.6446 (6)	0.62468 (18)	1.08338 (13)	0.0320 (7)
H42	2.7765	0.6429	1.1111	0.038*
C43	2.4456 (6)	0.59362 (18)	1.10055 (14)	0.0333 (7)
H43	2.4384	0.5898	1.1402	0.040*
C44	2.2573 (6)	0.56820 (18)	1.05891 (14)	0.0324 (7)
H44	2.1224	0.5461	1.0709	0.039*
C45	0.4296 (6)	0.3900 (2)	0.35899 (16)	0.0421 (8)
H45	0.2895	0.3889	0.3349	0.050*
C46	0.4922 (7)	0.4522 (2)	0.40689 (16)	0.0465 (9)
H46	0.3934	0.4938	0.4163	0.056*
C47	0.6977 (7)	0.4549 (2)	0.44152 (17)	0.0527 (10)

H47	0.7416	0.4984	0.4743	0.063*
C48	0.8395 (7)	0.3934 (3)	0.42804 (18)	0.0557 (11)
H48	0.9812	0.3948	0.4516	0.067*
C49	0.7751 (7)	0.3310 (2)	0.38076 (17)	0.0507 (10)
H49	0.8713	0.2887	0.3717	0.061*
C50	0.5700 (7)	0.3294 (2)	0.34612 (16)	0.0446 (9)
H50	0.5262	0.2861	0.3132	0.053*
C51	0.7877 (6)	0.84135 (17)	0.29690 (18)	0.101 (2)
H51	0.6861	0.8779	0.3170	0.121*
C52	0.9878 (6)	0.86602 (14)	0.27527 (19)	0.0911 (18)
H52	1.0230	0.9195	0.2805	0.109*
C53	1.1364 (5)	0.8125 (2)	0.24592 (18)	0.097 (2)
H53	1.2732	0.8293	0.2311	0.117*
C54	1.0849 (6)	0.73429 (18)	0.23820 (15)	0.0828 (16)
H54	1.1864	0.6977	0.2181	0.099*
C55	0.8848 (6)	0.70963 (13)	0.25983 (16)	0.0666 (13)
H55	0.8495	0.6562	0.2546	0.080*
C56	0.7362 (5)	0.76315 (19)	0.28918 (17)	0.0800 (16)
H56	0.5994	0.7463	0.3040	0.096*
C57	1.2877 (8)	0.0159 (4)	0.4782 (3)	0.0794 (17)
H57	1.1403	0.0270	0.4629	0.095*
C58	1.3994 (10)	0.0665 (3)	0.5279 (3)	0.0766 (15)
H58	1.3291	0.1122	0.5471	0.092*
C59	1.6137 (11)	0.0509 (4)	0.5499 (3)	0.0865 (17)
H59	1.6928	0.0860	0.5841	0.104*
N1	0.2293 (4)	-0.08860 (14)	0.05611 (11)	0.0272 (5)
N2	2.6094 (4)	0.65448 (13)	0.91102 (10)	0.0233 (5)
N3	2.8130 (5)	0.70501 (16)	0.78374 (11)	0.0348 (6)
N4	2.2537 (4)	0.57284 (14)	1.00265 (11)	0.0286 (6)
O1	0.1208 (4)	-0.10055 (12)	0.00485 (9)	0.0358 (5)
O2	0.4049 (4)	0.09116 (12)	0.22097 (9)	0.0312 (5)
O3	0.5864 (4)	-0.00577 (12)	0.24535 (9)	0.0334 (5)

Atomic displacement parameters ( $\text{\AA}^2$ )

	$U^{11}$	$U^{22}$	$U^{33}$	$U^{12}$	$U^{13}$	$U^{23}$
C1	0.0219 (14)	0.0236 (14)	0.0216 (14)	0.0012 (11)	0.0000 (11)	0.0047 (11)
C2	0.0209 (13)	0.0238 (14)	0.0228 (14)	-0.0039 (11)	0.0002 (11)	0.0064 (11)
C3	0.0219 (14)	0.0243 (15)	0.0258 (15)	-0.0022 (11)	-0.0030 (11)	0.0070 (12)
C4	0.0251 (14)	0.0224 (14)	0.0275 (15)	-0.0001 (12)	-0.0033 (12)	0.0041 (12)
C5	0.0238 (15)	0.0324 (17)	0.0300 (17)	-0.0001 (13)	-0.0004 (12)	0.0036 (13)
C6	0.0287 (15)	0.0310 (16)	0.0288 (16)	-0.0024 (13)	-0.0009 (12)	0.0104 (13)
C7	0.0213 (14)	0.0265 (16)	0.0251 (15)	-0.0022 (12)	-0.0008 (11)	0.0087 (12)
C8	0.0319 (16)	0.0278 (16)	0.0333 (17)	0.0026 (13)	0.0014 (13)	0.0040 (13)
C9	0.0303 (16)	0.0278 (16)	0.0416 (19)	-0.0068 (13)	-0.0038 (14)	0.0071 (14)
C10	0.0353 (16)	0.0225 (15)	0.0220 (15)	-0.0013 (13)	-0.0093 (12)	0.0020 (12)
C11	0.0404 (18)	0.0417 (19)	0.0226 (16)	-0.0030 (15)	0.0012 (13)	0.0052 (14)
C12	0.0327 (17)	0.0395 (18)	0.0258 (16)	-0.0100 (14)	0.0016 (13)	0.0032 (14)

---

C13	0.0272 (15)	0.0255 (15)	0.0236 (15)	0.0014 (12)	-0.0021 (12)	0.0069 (12)
C14	0.0333 (17)	0.0409 (18)	0.0224 (16)	-0.0086 (14)	-0.0001 (13)	0.0070 (13)
C15	0.0324 (17)	0.0391 (18)	0.0276 (17)	-0.0108 (14)	-0.0033 (13)	0.0068 (14)
C16	0.0239 (14)	0.0285 (15)	0.0225 (15)	-0.0017 (12)	-0.0031 (11)	0.0067 (12)
C17	0.0350 (17)	0.045 (2)	0.0253 (16)	-0.0097 (15)	0.0019 (13)	0.0069 (14)
C18	0.0294 (16)	0.0439 (19)	0.0306 (17)	-0.0140 (14)	-0.0002 (13)	0.0059 (14)
C19	0.0288 (15)	0.0285 (16)	0.0254 (15)	-0.0020 (13)	-0.0055 (12)	0.0048 (12)
C20	0.0355 (17)	0.045 (2)	0.0228 (16)	-0.0098 (15)	0.0028 (13)	0.0007 (14)
C21	0.0299 (16)	0.0423 (19)	0.0264 (16)	-0.0095 (14)	0.0020 (13)	0.0027 (14)
C22	0.0293 (16)	0.0295 (16)	0.0286 (16)	-0.0029 (13)	-0.0015 (13)	0.0056 (13)
C23	0.0276 (15)	0.0311 (16)	0.0258 (16)	-0.0013 (13)	-0.0005 (12)	0.0057 (13)
C24	0.0282 (15)	0.0269 (15)	0.0247 (15)	-0.0016 (12)	-0.0040 (12)	0.0054 (12)
C25	0.0316 (16)	0.0307 (16)	0.0231 (15)	-0.0040 (13)	-0.0009 (12)	0.0032 (13)
C26	0.0265 (15)	0.0310 (16)	0.0258 (16)	-0.0039 (12)	-0.0012 (12)	0.0052 (13)
C27	0.0261 (14)	0.0180 (13)	0.0249 (15)	-0.0002 (11)	-0.0022 (11)	0.0047 (11)
C28	0.0247 (14)	0.0276 (15)	0.0236 (15)	-0.0021 (12)	-0.0014 (11)	0.0068 (12)
C29	0.0247 (14)	0.0260 (15)	0.0267 (16)	-0.0027 (12)	-0.0020 (12)	0.0051 (12)
C30	0.0242 (14)	0.0191 (14)	0.0244 (15)	-0.0009 (11)	-0.0001 (11)	0.0046 (11)
C31	0.0284 (15)	0.0235 (14)	0.0223 (15)	-0.0021 (12)	0.0013 (12)	0.0072 (12)
C32	0.0274 (15)	0.0222 (14)	0.0221 (15)	-0.0009 (12)	0.0000 (11)	0.0061 (11)
C33	0.0267 (14)	0.0207 (14)	0.0250 (15)	0.0011 (12)	0.0004 (12)	0.0073 (12)
C34	0.0270 (15)	0.0223 (14)	0.0243 (15)	-0.0023 (12)	0.0030 (12)	0.0075 (12)
C35	0.0292 (15)	0.0200 (14)	0.0238 (15)	-0.0009 (12)	0.0025 (12)	0.0031 (11)
C36	0.0308 (16)	0.0279 (16)	0.0271 (16)	-0.0054 (13)	-0.0001 (12)	0.0061 (13)
C37	0.0298 (16)	0.0253 (15)	0.0340 (17)	-0.0067 (13)	0.0000 (13)	0.0033 (13)
C38	0.0341 (17)	0.0300 (16)	0.0363 (18)	-0.0069 (13)	0.0060 (14)	0.0088 (14)
C39	0.046 (2)	0.044 (2)	0.0284 (17)	-0.0093 (16)	0.0064 (14)	0.0140 (15)
C40	0.0274 (15)	0.0191 (14)	0.0237 (15)	-0.0020 (11)	0.0011 (12)	0.0055 (11)
C41	0.0294 (15)	0.0266 (15)	0.0276 (16)	-0.0025 (12)	-0.0009 (12)	0.0089 (12)
C42	0.0380 (17)	0.0319 (17)	0.0252 (16)	0.0019 (14)	-0.0027 (13)	0.0075 (13)
C43	0.0464 (19)	0.0323 (17)	0.0230 (16)	0.0016 (14)	0.0025 (14)	0.0108 (13)
C44	0.0402 (18)	0.0302 (16)	0.0298 (17)	-0.0001 (14)	0.0037 (14)	0.0135 (13)
C45	0.0380 (19)	0.057 (2)	0.036 (2)	0.0008 (17)	0.0055 (15)	0.0213 (17)
C46	0.061 (2)	0.045 (2)	0.041 (2)	0.0118 (18)	0.0159 (18)	0.0194 (17)
C47	0.063 (3)	0.053 (2)	0.037 (2)	-0.012 (2)	0.0112 (18)	0.0051 (18)
C48	0.037 (2)	0.090 (3)	0.041 (2)	0.004 (2)	0.0034 (17)	0.021 (2)
C49	0.061 (2)	0.060 (3)	0.042 (2)	0.027 (2)	0.0204 (19)	0.026 (2)
C50	0.061 (2)	0.040 (2)	0.0322 (19)	-0.0056 (18)	0.0072 (17)	0.0103 (15)
C51	0.116 (5)	0.067 (3)	0.141 (6)	0.038 (3)	0.062 (4)	0.046 (4)
C52	0.081 (4)	0.060 (3)	0.152 (6)	0.009 (3)	0.020 (4)	0.059 (4)
C53	0.073 (3)	0.113 (5)	0.149 (6)	0.026 (3)	0.046 (4)	0.097 (4)
C54	0.099 (4)	0.069 (3)	0.088 (4)	0.040 (3)	0.028 (3)	0.025 (3)
C55	0.071 (3)	0.046 (2)	0.084 (3)	0.002 (2)	-0.015 (3)	0.025 (2)
C56	0.061 (3)	0.084 (4)	0.121 (5)	0.013 (3)	0.024 (3)	0.068 (3)
C57	0.048 (3)	0.109 (4)	0.119 (5)	0.026 (3)	0.031 (3)	0.088 (4)
C58	0.082 (4)	0.077 (4)	0.095 (4)	0.024 (3)	0.035 (3)	0.057 (3)
C59	0.093 (4)	0.102 (4)	0.088 (4)	-0.014 (4)	0.015 (3)	0.068 (4)
N1	0.0300 (13)	0.0256 (13)	0.0215 (13)	0.0024 (10)	-0.0069 (10)	0.0008 (10)

---

N2	0.0258 (12)	0.0205 (12)	0.0223 (12)	-0.0009 (10)	0.0013 (10)	0.0043 (10)
N3	0.0401 (15)	0.0379 (15)	0.0256 (14)	-0.0101 (12)	0.0026 (11)	0.0092 (12)
N4	0.0301 (13)	0.0276 (13)	0.0286 (14)	-0.0056 (11)	0.0028 (10)	0.0093 (11)
O1	0.0413 (13)	0.0371 (12)	0.0238 (11)	0.0037 (10)	-0.0113 (9)	0.0023 (9)
O2	0.0334 (11)	0.0276 (12)	0.0290 (12)	0.0003 (9)	-0.0022 (9)	0.0028 (9)
O3	0.0464 (13)	0.0265 (11)	0.0220 (11)	-0.0053 (10)	-0.0143 (9)	0.0030 (9)

*Geometric parameters (Å, °)*

C1—C2	1.519 (4)	C30—C34	1.395 (4)
C1—C5	1.526 (4)	C31—H31	0.9500
C1—C6	1.522 (4)	C31—C32	1.401 (4)
C1—N1	1.489 (4)	C32—C35	1.483 (4)
C2—C3	1.329 (4)	C32—N2	1.341 (4)
C2—C7	1.473 (4)	C33—C34	1.389 (4)
C3—H3	0.9500	C33—C40	1.496 (4)
C3—C4	1.498 (4)	C33—N2	1.346 (4)
C4—C8	1.526 (4)	C34—H34	0.9500
C4—C9	1.535 (4)	C35—C36	1.384 (4)
C4—N1	1.479 (4)	C35—N3	1.342 (4)
C5—H5A	0.9800	C36—H36	0.9500
C5—H5B	0.9800	C36—C37	1.389 (4)
C5—H5C	0.9800	C37—H37	0.9500
C6—H6A	0.9800	C37—C38	1.370 (4)
C6—H6B	0.9800	C38—H38	0.9500
C6—H6C	0.9800	C38—C39	1.382 (5)
C7—O2	1.203 (3)	C39—H39	0.9500
C7—O3	1.361 (3)	C39—N3	1.338 (4)
C8—H8A	0.9800	C40—C41	1.397 (4)
C8—H8B	0.9800	C40—N4	1.346 (4)
C8—H8C	0.9800	C41—H41	0.9500
C9—H9A	0.9800	C41—C42	1.385 (4)
C9—H9B	0.9800	C42—H42	0.9500
C9—H9C	0.9800	C42—C43	1.383 (4)
C10—C11	1.375 (4)	C43—H43	0.9500
C10—C15	1.367 (4)	C43—C44	1.382 (4)
C10—O3	1.413 (3)	C44—H44	0.9500
C11—H11	0.9500	C44—N4	1.339 (4)
C11—C12	1.381 (4)	C45—H45	0.9500
C12—H12	0.9500	C45—C46	1.371 (5)
C12—C13	1.394 (4)	C45—C50	1.370 (5)
C13—C14	1.399 (4)	C46—H46	0.9500
C13—C16	1.487 (4)	C46—C47	1.381 (6)
C14—H14	0.9500	C47—H47	0.9500
C14—C15	1.391 (4)	C47—C48	1.387 (6)
C15—H15	0.9500	C48—H48	0.9500
C16—C17	1.398 (4)	C48—C49	1.367 (6)
C16—C21	1.393 (4)	C49—H49	0.9500



C17—H17	0.9500	C49—C50	1.382 (5)
C17—C18	1.365 (4)	C50—H50	0.9500
C18—H18	0.9500	C51—H51	0.9500
C18—C19	1.396 (4)	C51—C52	1.3900
C19—C20	1.397 (4)	C51—C56	1.3900
C19—C22	1.437 (4)	C52—H52	0.9500
C20—H20	0.9500	C52—C53	1.3900
C20—C21	1.388 (4)	C53—H53	0.9500
C21—H21	0.9500	C53—C54	1.3900
C22—C23	1.195 (4)	C54—H54	0.9500
C23—C24	1.435 (4)	C54—C55	1.3900
C24—C25	1.405 (4)	C55—H55	0.9500
C24—C29	1.398 (4)	C55—C56	1.3900
C25—H25	0.9500	C56—H56	0.9500
C25—C26	1.384 (4)	C57—H57	0.9500
C26—H26	0.9500	C57—C58	1.370 (8)
C26—C27	1.399 (4)	C57—C59 <sup>i</sup>	1.376 (8)
C27—C28	1.402 (4)	C58—H58	0.9500
C27—C30	1.489 (4)	C58—C59	1.376 (7)
C28—H28	0.9500	C59—C57 <sup>i</sup>	1.376 (8)
C28—C29	1.383 (4)	C59—H59	0.9500
C29—H29	0.9500	N1—O1	1.274 (3)
C30—C31	1.398 (4)	O1—O1 <sup>ii</sup>	4.004 (4)
C2—C1—C5	113.1 (2)	C28—C29—C24	120.7 (3)
C2—C1—C6	114.8 (2)	C28—C29—H29	119.6
C6—C1—C5	110.6 (2)	C31—C30—C27	121.5 (3)
N1—C1—C2	98.8 (2)	C34—C30—C27	121.0 (2)
N1—C1—C5	108.9 (2)	C34—C30—C31	117.4 (2)
N1—C1—C6	109.8 (2)	C30—C31—H31	120.4
C3—C2—C1	112.7 (2)	C30—C31—C32	119.2 (3)
C3—C2—C7	125.8 (3)	C32—C31—H31	120.4
C7—C2—C1	121.4 (2)	C31—C32—C35	120.5 (3)
C2—C3—H3	123.3	N2—C32—C31	123.3 (3)
C2—C3—C4	113.4 (3)	N2—C32—C35	116.2 (2)
C4—C3—H3	123.3	C34—C33—C40	120.2 (2)
C3—C4—C8	113.1 (2)	N2—C33—C34	123.6 (3)
C3—C4—C9	112.5 (2)	N2—C33—C40	116.2 (2)
C8—C4—C9	110.9 (2)	C30—C34—H34	120.3
N1—C4—C3	99.6 (2)	C33—C34—C30	119.4 (3)
N1—C4—C8	110.1 (2)	C33—C34—H34	120.3
N1—C4—C9	110.2 (2)	C36—C35—C32	121.6 (3)
C1—C5—H5A	109.5	N3—C35—C32	116.1 (2)
C1—C5—H5B	109.5	N3—C35—C36	122.3 (3)
C1—C5—H5C	109.5	C35—C36—H36	120.3
H5A—C5—H5B	109.5	C35—C36—C37	119.4 (3)
H5A—C5—H5C	109.5	C37—C36—H36	120.3
H5B—C5—H5C	109.5	C36—C37—H37	120.6

C1—C6—H6A	109.5	C38—C37—C36	118.9 (3)
C1—C6—H6B	109.5	C38—C37—H37	120.6
C1—C6—H6C	109.5	C37—C38—H38	120.9
H6A—C6—H6B	109.5	C37—C38—C39	118.1 (3)
H6A—C6—H6C	109.5	C39—C38—H38	120.9
H6B—C6—H6C	109.5	C38—C39—H39	117.9
O2—C7—C2	125.5 (3)	N3—C39—C38	124.2 (3)
O2—C7—O3	123.5 (3)	N3—C39—H39	117.9
O3—C7—C2	111.0 (2)	C41—C40—C33	121.0 (3)
C4—C8—H8A	109.5	N4—C40—C33	116.1 (2)
C4—C8—H8B	109.5	N4—C40—C41	122.9 (3)
C4—C8—H8C	109.5	C40—C41—H41	120.7
H8A—C8—H8B	109.5	C42—C41—C40	118.6 (3)
H8A—C8—H8C	109.5	C42—C41—H41	120.7
H8B—C8—H8C	109.5	C41—C42—H42	120.6
C4—C9—H9A	109.5	C43—C42—C41	118.8 (3)
C4—C9—H9B	109.5	C43—C42—H42	120.6
C4—C9—H9C	109.5	C42—C43—H43	120.7
H9A—C9—H9B	109.5	C44—C43—C42	118.7 (3)
H9A—C9—H9C	109.5	C44—C43—H43	120.7
H9B—C9—H9C	109.5	C43—C44—H44	118.0
C11—C10—O3	118.5 (3)	N4—C44—C43	123.9 (3)
C15—C10—C11	121.2 (3)	N4—C44—H44	118.0
C15—C10—O3	120.1 (3)	C46—C45—H45	120.2
C10—C11—H11	120.4	C50—C45—H45	120.2
C10—C11—C12	119.2 (3)	C50—C45—C46	119.7 (4)
C12—C11—H11	120.4	C45—C46—H46	119.7
C11—C12—H12	119.0	C45—C46—C47	120.5 (4)
C11—C12—C13	121.9 (3)	C47—C46—H46	119.7
C13—C12—H12	119.0	C46—C47—H47	120.3
C12—C13—C14	117.0 (3)	C46—C47—C48	119.5 (4)
C12—C13—C16	121.4 (3)	C48—C47—H47	120.3
C14—C13—C16	121.7 (3)	C47—C48—H48	120.1
C13—C14—H14	119.3	C49—C48—C47	119.9 (4)
C15—C14—C13	121.4 (3)	C49—C48—H48	120.1
C15—C14—H14	119.3	C48—C49—H49	120.0
C10—C15—C14	119.3 (3)	C48—C49—C50	120.0 (4)
C10—C15—H15	120.4	C50—C49—H49	120.0
C14—C15—H15	120.4	C45—C50—C49	120.4 (4)
C17—C16—C13	120.9 (3)	C45—C50—H50	119.8
C21—C16—C13	122.5 (3)	C49—C50—H50	119.8
C21—C16—C17	116.6 (3)	C52—C51—H51	120.0
C16—C17—H17	118.8	C52—C51—C56	120.0
C18—C17—C16	122.4 (3)	C56—C51—H51	120.0
C18—C17—H17	118.8	C51—C52—H52	120.0
C17—C18—H18	119.6	C51—C52—C53	120.0
C17—C18—C19	120.8 (3)	C53—C52—H52	120.0
C19—C18—H18	119.6	C52—C53—H53	120.0

C18—C19—C20	118.0 (3)	C54—C53—C52	120.0
C18—C19—C22	119.1 (3)	C54—C53—H53	120.0
C20—C19—C22	122.9 (3)	C53—C54—H54	120.0
C19—C20—H20	119.8	C55—C54—C53	120.0
C21—C20—C19	120.4 (3)	C55—C54—H54	120.0
C21—C20—H20	119.8	C54—C55—H55	120.0
C16—C21—H21	119.1	C54—C55—C56	120.0
C20—C21—C16	121.8 (3)	C56—C55—H55	120.0
C20—C21—H21	119.1	C51—C56—H56	120.0
C23—C22—C19	174.6 (3)	C55—C56—C51	120.0
C22—C23—C24	177.8 (3)	C55—C56—H56	120.0
C25—C24—C23	120.0 (3)	C58—C57—H57	119.6
C29—C24—C23	121.5 (3)	C58—C57—C59 <sup>i</sup>	120.8 (5)
C29—C24—C25	118.5 (3)	C59 <sup>i</sup> —C57—H57	119.6
C24—C25—H25	119.8	C57—C58—H58	120.1
C26—C25—C24	120.4 (3)	C57—C58—C59	119.8 (5)
C26—C25—H25	119.8	C59—C58—H58	120.1
C25—C26—H26	119.4	C57 <sup>i</sup> —C59—H59	120.3
C25—C26—C27	121.2 (3)	C58—C59—C57 <sup>i</sup>	119.4 (6)
C27—C26—H26	119.4	C58—C59—H59	120.3
C26—C27—C28	118.1 (3)	C4—N1—C1	115.5 (2)
C26—C27—C30	121.1 (3)	O1—N1—C1	122.4 (2)
C28—C27—C30	120.8 (3)	O1—N1—C4	122.1 (2)
C27—C28—H28	119.5	C32—N2—C33	117.1 (2)
C29—C28—C27	121.0 (3)	C39—N3—C35	117.2 (3)
C29—C28—H28	119.5	C44—N4—C40	117.0 (3)
C24—C29—H29	119.6	C7—O3—C10	116.5 (2)
C1—C2—C3—C4	-0.1 (3)	C27—C30—C31—C32	-175.1 (3)
C1—C2—C7—O2	-1.5 (4)	C27—C30—C34—C33	176.3 (3)
C1—C2—C7—O3	179.4 (2)	C28—C27—C30—C31	-158.0 (3)
C2—C1—N1—C4	-0.5 (3)	C28—C27—C30—C34	24.6 (4)
C2—C1—N1—O1	-179.4 (2)	C29—C24—C25—C26	0.2 (5)
C2—C3—C4—C8	116.6 (3)	C30—C27—C28—C29	-177.8 (3)
C2—C3—C4—C9	-116.8 (3)	C30—C31—C32—C35	177.0 (3)
C2—C3—C4—N1	-0.2 (3)	C30—C31—C32—N2	-2.0 (4)
C2—C7—O3—C10	168.2 (2)	C31—C30—C34—C33	-1.2 (4)
C3—C2—C7—O2	176.4 (3)	C31—C32—C35—C36	174.6 (3)
C3—C2—C7—O3	-2.6 (4)	C31—C32—C35—N3	-7.8 (4)
C3—C4—N1—C1	0.4 (3)	C31—C32—N2—C33	0.2 (4)
C3—C4—N1—O1	179.4 (2)	C32—C35—C36—C37	176.1 (3)
C5—C1—C2—C3	115.3 (3)	C32—C35—N3—C39	-175.8 (3)
C5—C1—C2—C7	-66.5 (3)	C33—C40—C41—C42	177.4 (3)
C5—C1—N1—C4	-118.7 (3)	C33—C40—N4—C44	-178.8 (3)
C5—C1—N1—O1	62.4 (3)	C34—C30—C31—C32	2.4 (4)
C6—C1—C2—C3	-116.4 (3)	C34—C33—C40—C41	164.3 (3)
C6—C1—C2—C7	61.8 (3)	C34—C33—C40—N4	-15.8 (4)
C6—C1—N1—C4	120.0 (3)	C34—C33—N2—C32	1.1 (4)

C6—C1—N1—O1	-58.9 (3)	C35—C32—N2—C33	-178.8 (2)
C7—C2—C3—C4	-178.2 (3)	C35—C36—C37—C38	-0.1 (5)
C8—C4—N1—C1	-118.6 (3)	C36—C35—N3—C39	1.8 (5)
C8—C4—N1—O1	60.4 (3)	C36—C37—C38—C39	1.2 (5)
C9—C4—N1—C1	118.8 (3)	C37—C38—C39—N3	-0.8 (5)
C9—C4—N1—O1	-62.3 (4)	C38—C39—N3—C35	-0.7 (5)
C10—C11—C12—C13	-0.6 (5)	C40—C33—C34—C30	-178.3 (3)
C11—C10—C15—C14	0.5 (5)	C40—C33—N2—C32	179.0 (2)
C11—C10—O3—C7	-80.9 (4)	C40—C41—C42—C43	2.1 (4)
C11—C12—C13—C14	1.5 (5)	C41—C40—N4—C44	1.1 (4)
C11—C12—C13—C16	-178.0 (3)	C41—C42—C43—C44	-0.4 (5)
C12—C13—C14—C15	-1.5 (5)	C42—C43—C44—N4	-1.1 (5)
C12—C13—C16—C17	-4.5 (5)	C43—C44—N4—C40	0.8 (5)
C12—C13—C16—C21	176.1 (3)	C45—C46—C47—C48	-0.9 (6)
C13—C14—C15—C10	0.5 (5)	C46—C45—C50—C49	-0.6 (5)
C13—C16—C17—C18	-178.4 (3)	C46—C47—C48—C49	0.0 (6)
C13—C16—C21—C20	178.4 (3)	C47—C48—C49—C50	0.6 (6)
C14—C13—C16—C17	176.0 (3)	C48—C49—C50—C45	-0.3 (5)
C14—C13—C16—C21	-3.4 (5)	C50—C45—C46—C47	1.2 (5)
C15—C10—C11—C12	-0.5 (5)	C51—C52—C53—C54	0.0
C15—C10—O3—C7	103.6 (3)	C52—C51—C56—C55	0.0
C16—C13—C14—C15	178.0 (3)	C52—C53—C54—C55	0.0
C16—C17—C18—C19	0.4 (5)	C53—C54—C55—C56	0.0
C17—C16—C21—C20	-1.0 (5)	C54—C55—C56—C51	0.0
C17—C18—C19—C20	-1.8 (5)	C56—C51—C52—C53	0.0
C17—C18—C19—C22	176.8 (3)	C57—C58—C59—C57 <sup>i</sup>	-0.5 (8)
C18—C19—C20—C21	1.8 (5)	C59 <sup>i</sup> —C57—C58—C59	0.5 (8)
C19—C20—C21—C16	-0.4 (5)	N1—C1—C2—C3	0.4 (3)
C21—C16—C17—C18	1.0 (5)	N1—C1—C2—C7	178.5 (2)
C22—C19—C20—C21	-176.7 (3)	N2—C32—C35—C36	-6.4 (4)
C23—C24—C25—C26	-179.5 (3)	N2—C32—C35—N3	171.3 (3)
C23—C24—C29—C28	178.9 (3)	N2—C33—C34—C30	-0.5 (4)
C24—C25—C26—C27	1.0 (5)	N2—C33—C40—C41	-13.7 (4)
C25—C24—C29—C28	-0.8 (4)	N2—C33—C40—N4	166.2 (2)
C25—C26—C27—C28	-1.5 (4)	N3—C35—C36—C37	-1.5 (5)
C25—C26—C27—C30	177.1 (3)	N4—C40—C41—C42	-2.5 (4)
C26—C27—C28—C29	0.9 (4)	O2—C7—O3—C10	-10.8 (4)
C26—C27—C30—C31	23.4 (4)	O3—C10—C11—C12	-175.9 (3)
C26—C27—C30—C34	-154.0 (3)	O3—C10—C15—C14	175.9 (3)
C27—C28—C29—C24	0.3 (4)		

Symmetry codes: (i)  $-x+3, -y, -z+1$ ; (ii)  $-x, -y, -z$ .

#### Hydrogen-bond geometry ( $\text{\AA}, ^\circ$ )

Cg4, Cg7 and Cg10 are the centroids of pyridine ring N4/C40–C44, spacer ring C24–C29 and benzene ring C54–C59, respectively.

$D-H\cdots A$	$D-H$	$H\cdots A$	$D\cdots A$	$D-H\cdots A$
C37—H37 <sup>iii</sup> —O1 <sup>iii</sup>	0.95	2.65	3.228 (4)	120

---

C38—H38...O2 <sup>iv</sup>	0.95	2.55	3.485 (4)	169
C6—H6C...O1 <sup>ii</sup>	0.98	2.61	3.499 (4)	151
C9—H9B...Cg4 <sup>v</sup>	0.96	2.79	3.602 (4)	140
C14—H14...Cg10 <sup>vi</sup>	0.95	2.88	3.608 (4)	134
C14—H14...Cg10 <sup>vii</sup>	0.95	2.88	3.608 (4)	134
C55—H55...Cg7 <sup>viii</sup>	0.95	2.90	3.680 (3)	140

---

Symmetry codes: (ii)  $-x, -y, -z$ ; (iii)  $x+3, y+1, z+1$ ; (iv)  $-x+4, -y+1, -z+1$ ; (v)  $x-2, y-1, z-1$ ; (vi)  $x-1, y, z$ ; (vii)  $-x+2, -y, -z+1$ ; (viii)  $-x+3, -y+1, -z+1$ .

# Appendix C

## **(Bis(terpyridine))copper(II) Tetrphenylborate: A Complex Example for the Jahn–Teller Effect**

Andreas Meyer,<sup>i</sup> Gregor Schnakenburg,<sup>ii</sup> Robert Glaum,<sup>ii</sup> and Olav Schiemann<sup>i</sup>

Received 22th of May 2015, published online 14th August 2015.

Reprinted with permission from  
A. Meyer, G. Schnakenburg, R. Glaum, and O. Schiemann, *Inorganic Chemistry* **2015**, *54*, 8456 - 8464.  
Copyright ©2015, American Chemical Society.

### **Own contributions to the manuscript**

- Synthesis and crystallization of the title compound.
- Evaluation of the geometrical parameters of the crystal structure.
- Measurement and interpretation of the EPR spectra.
- Interpretation of the UV/vis spectra.
- Performing the AOM calculations.
- Writing the manuscript.

---

<sup>i</sup> University of Bonn, Institute of Physical and Theoretical Chemistry, Wegelerstr. 12, 53115 Bonn, Germany.

<sup>ii</sup> University of Bonn, Institute of Inorganic Chemistry, Gerhard-Domagk-Strasse 1, 53121 Bonn, Germany.

# (Bis(terpyridine))copper(II) Tetraphenylborate: A Complex Example for the Jahn–Teller Effect

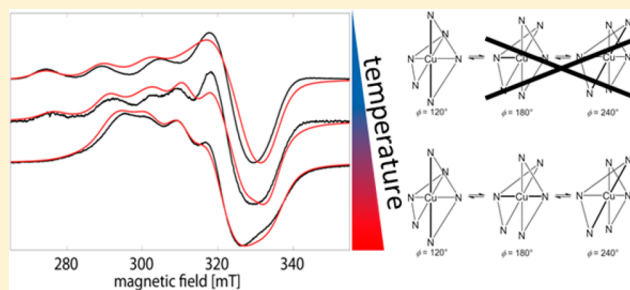
Andreas Meyer,<sup>†</sup> Gregor Schnakenburg,<sup>‡</sup> Robert Glaum,<sup>\*,‡</sup> and Olav Schiemann<sup>\*,†</sup>

<sup>†</sup>Institute of Physical and Theoretical Chemistry, University of Bonn, Wegelerstr. 12, Bonn, Germany

<sup>‡</sup>Institute of Inorganic Chemistry, University of Bonn, Gerhard-Domagk-Str. 1, Bonn, Germany

## Supporting Information

**ABSTRACT:** The surprisingly complicated crystal structure of (bis(terpyridine))copper(II) tetraphenylborate  $[\text{Cu}(\text{tpy})_2](\text{BPh}_4)_2$  ( $\text{tpy} = 2,2':6',2''\text{-terpyridine}$ ) consists of six crystallographically independent  $[\text{Cu}(\text{tpy})_2]^{2+}$  complexes. At ambient temperature, five out of six  $[\text{Cu}^{\text{II}}\text{N}_6]$  chromophores appear to be compressed octahedra, while at 100 K, four exhibit elongated and only two compressed octahedral geometry. Temperature dependent single crystal UV/vis (100, 298 K) and EPR measurements (20, 100, 298 K) as well as AOM calculations suggest that the octahedra which show apparently compressed octahedral geometry (XRD) result from dynamic Jahn–Teller behavior of elongated octahedra  $[\text{Cu}^{\text{II}}\text{N}_6]$ . The detailed correlation of structural and spectroscopic data allows an understanding of the strongly solvent-dependent structures of the  $[\text{Cu}(\text{tpy})_2]^{2+}$  complex in solution.



## INTRODUCTION

Almost 80 years ago, Jahn and Teller showed that nonlinear, polyatomic systems in orbitally degenerate states are unstable with respect to nuclear displacements which lower the symmetry of the system.<sup>1</sup> The reason for this Jahn–Teller effect (JTE) is that the electron distribution is less symmetric than the nuclear distribution in such a situation and that the adiabatic approximation becomes invalid.<sup>2,3</sup> Extending the theory of the JTE to account for interactions of the ground state with excited states gives rise to the pseudo Jahn–Teller effect (PJTE).<sup>4</sup> The PJTE removes the restriction to nonlinear molecules and degenerate ground states imposed by Jahn and Teller. Recently, it was shown that the JTE and the PJTE are the only source of structural instability of polyatomic systems in their high symmetry configuration.<sup>2,5</sup> Therefore, the JTE and the PJTE have implications for virtually every chemical system that contains more than two atoms.<sup>5</sup> The reviews<sup>2,3,5</sup> by Bersuker give an up-to-date overview over both the JTE and the PJTE. While the occurrence of JTE or PJTE is not always appreciated in studies dealing with main group elements, its occurrence is more frequently discussed for transition metal complexes, e.g. in complexes of iron,<sup>6–11</sup> cobalt,<sup>12,13</sup> manganese,<sup>14–16</sup> and other metal ions.<sup>17–20</sup> Copper complexes are certainly the most widely studied JT active systems.<sup>21–30</sup> Experimentally, a major pitfall when studying JTE and PJTE system is the occurrence of dynamic effects.<sup>31</sup> As the JTE and the PJTE are brought about by vibrations, molecules in the regime of dynamic JTE or PJTE interconvert between different structures with the frequency of vibrations (i.e., interconversion frequencies in the terahertz range).<sup>2,3,5</sup> Such behavior leads to the observation of structures having an apparently higher

symmetry than expected for JT-active systems using methods with time scales which are longer than the period of the molecular vibrations such as X-ray diffraction (usually several minutes) and EPR measurement (GHz regime).<sup>31</sup> The observation of electronic transitions on the other hand is expected to proceed much faster than molecular vibrations, and therefore electronic absorption spectroscopy should be able to reveal the true geometries of JT active complexes. While the experimental techniques to distinguish between dynamic and static JTE for crystalline samples have been developed by several researchers,<sup>31–33</sup> the investigation of solutions is more demanding.<sup>34–36</sup>

Here, we present the synthesis and temperature dependent X-ray crystallographic, EPR and UV/vis/NIR spectroscopic characterization of  $[\text{Cu}(\text{tpy})_2](\text{BPh}_4)_2$ , **1**. The obtained detailed understanding of the correlation between structure and EPR properties will be applied to interpret the strongly solvent-dependent EPR behavior of the  $[\text{Cu}(\text{tpy})_2]^{2+}$  cation in solution.

## EXPERIMENTAL SECTION

**Synthesis.** Methanol and DMSO (Sigma-Aldrich; chromatographical grade purity) have been used without further purification. Deuterated solvents for EPR (Deutero) and 2,2':6',2''-terpyridine (TCI Europe) were also used as bought. Metal salts have been purchased from Sigma-Aldrich.

**Bis(2,2':6',2''-terpyridine)copper(II)bis(tetraphenylborate), 1.** A total of 80 mg (0.34 mmol) of 2,2':6',2''-terpyridine was dissolved in 6 mL of methanol, yielding a pale yellow solution. A total of 20 mg (0.15 mmol) of anhydrous copper dichloride dissolved in 3 mL of

Received: May 22, 2015

Published: August 14, 2015

Table 1. Lattice Parameters of  $[\text{Cu}(\text{tpy})_2](\text{BPh}_4)_2$  at 100, 123, and 293 K

measurement	crystal	T/K	a/Å	b/Å	c/Å	$\beta$ /deg
1	A	293(2)	40.278(3)	24.8878(17)	41.972(3)	116.277(2)
2	A	123(2)	40.001(2)	24.5857(2)	41.630(2)	116.319(2)
3	B	100(2)	39.9543(15)	24.5916(9)	41.6151(14)	116.252(2)

methanol were added to that solution, giving rise to an intensely colored green solution which was stirred at 50 °C for 5 min. A roughly 3-fold excess of sodium tetraphenylborate dissolved in methanol was then added, leading to the immediate precipitation of a green solid. The solvent was filtered off at 0 °C, and the remaining solid was washed three times with 4 mL of methanol at 0 °C. Drying under reduced pressure yielded **1** as a green powder. Crystals suitable for X-ray crystal structure determination were obtained from a saturated solution of **1** in DMSO, which was left overnight in an open vial (Yield: 90%). NMR: All  $^1\text{H}$  resonances of the ligand have been broadened beyond recognition. The only remaining resonances at 7.16, 6.91, and 6.77 ppm are assigned to the tetraphenylborate anion. Anal. Calcd for **1**: C, 80.17, H 5.35, N 7.19. Found: C, 80.15; H, 5.25; N, 7.16. ESI-MS: 264.6 ( $[\text{Cu}(\text{tpy})_2]^{2+}$ , 90%), 296.1( $[\text{Cu}(\text{tpy})]^+$ , 100%), 365.2 ( $[\text{Na}_2\text{BPh}_4]^+$ , 55%).

**X-ray diffraction.** X-ray diffraction experiments with **1** have been conducted on two different crystals, A and B, at three different temperatures (Table 1). The monoclinic structure (space group  $P2_1/c$ ) obtained using crystal B is in complete agreement with crystal A. In the temperature range from 100 to 293 K, no phase transition is observed in the XRD experiments, and the cell parameters vary only slightly with temperature (Table 1).

Intensity data were collected on a BRUKER X8-KappaApexII diffractometer using graphite monochromated Mo  $K\alpha$  radiation ( $\lambda = 0.71073$  Å). The diffractometer was equipped with a low-temperature device (Kryoflex, Bruker AXS GmbH, 100(2) K). Intensities were measured within 892 frames by fine-slicing  $\omega$  and  $\varphi$  scans (rotational increment 0.5°; 60 s exposure time per frame) and corrected for background, polarization, and Lorentz effects. An empirical absorption correction was applied to the data set.<sup>37</sup> The structure was solved by direct methods and refined by the least-squares procedure implemented in the ShelX program system,<sup>38</sup> allowing for anisotropic displacement parameters. Hydrogen atoms were included isotropically using the riding model on the bound carbon atoms. CCDC 1061926–1061928 contain the supplementary crystallographic data for this paper, which can be obtained free of charge from The Cambridge Crystallographic Data Centre via [www.ccdc.cam.ac.uk/data\\_request/cif](http://www.ccdc.cam.ac.uk/data_request/cif). For further details, see the Supporting Information.

**Single Crystal UV/vis/NIR Spectroscopy.** A transparent dichroic crystal (blue/green; main crystal faces (001)/(00 $\bar{1}$ ); approximate thickness  $d = 0.1$  mm) was selected using an optical microscope and placed on the sample holder (aperture) using a small amount of grease. Polarized single crystal UV/vis/NIR spectra covering the spectral range from 5800 to 36 000  $\text{cm}^{-1}$  have been recorded using a modified CARY 17 microcrystal spectrophotometer (spectral service, ANU Canberra, Australia). A halogen lamp was used as a light source. A photomultiplier (PMT) and a liquid nitrogen cooled Ge photodiode were used as detector systems for the UV and the visible region (11 111–36 000  $\text{cm}^{-1}$ ) and the NIR region (5800–16 666  $\text{cm}^{-1}$ ), respectively. For measurement in both spectral regions, the slit width was set to 0.08 mm. The reference intensities  $I_0$  were measured with the same aperture, however, without the crystal. The spectra (Figure 3) show absorbance  $A = -\log I/I_0$  vs wavenumber.

**EPR Spectroscopy.** EPR samples were prepared by filling 0.3 mL of 200  $\mu\text{M}$  solutions of  $[\text{Cu}(\text{tpy})_2](\text{BPh}_4)_2$  in  $d_6$ -DMSO or mixtures of  $d_6$ -DMSO with either  $d_4$ -methanol or  $d_1$ -chloroform into quartz glass EPR tubes having an outer diameter of about 3.8 mm. The samples were then shock frozen using liquid nitrogen. For single crystal measurements, paper strips having a width of 1–2 mm were cut from a sheet of paper. A small amount of vacuum grease was put on one end of such a paper strip, which was used to mount the single crystals. Alignment of the crystals was achieved by visual inspection and

controlled on EPR spectra obtained in preliminary experiments. For the powder measurements, single crystals have been carefully ground until a homogeneous powder was obtained. The homogeneity of these powders was evaluated by verifying the independence of the EPR spectrum from the sample orientation in the EPR spectrometer.

All EPR experiments were performed on a Bruker ELEXSYS E580 EPR spectrometer. A Super High-Q resonator and an Oxford ESR900 helium gas-flow cryostat were employed for cw measurements at X-band frequencies. For single crystal measurements, a programmable Bruker E 218-1001 goniometer was mounted on the SHQ resonator, allowing for free rotation around one axis. EPR measurements at Q-band frequencies were performed using an EN 5107D2 resonator and an Oxford CF935 helium gas-flow cryostat. Measurement parameters of the EPR experiments presented below are detailed in Tables S8–S10, S12, and S13 in the Supporting Information. Spectra were simulated using the “pepper” routine of the EasySpin program package.<sup>39</sup>

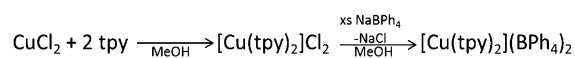
**AOM Calculations.** AOM calculations have been performed using the CAMMAG program.<sup>40</sup> The X-ray structures have been used as input geometries for the copper complexes. Only the first ligand sphere, i.e. the nitrogen donor atoms, has been considered. The  $e_\sigma$  parameter was set to 6800  $\text{cm}^{-1}$  at a copper nitrogen distance  $d_0 = 2.00$  Å. A radial dependence of  $e_\sigma = 6800 \text{ cm}^{-1} \times (d_0/d)^{-5}$  has been assumed.<sup>41</sup> The ligand  $\pi$  interactions perpendicular to the plane of the ligands have been accounted for by using  $e_\pi = 1/8e_\sigma$  while the in-plane  $\pi$ -interaction was assumed to be negligible. Configuration interaction between the metal 4s and 3d orbitals was included by introducing the parameter  $e_{ds} = 0.15e_\sigma$  as discussed by Smith.<sup>42</sup> The orbital reduction factor  $k$  and the spin orbit coupling constant  $\zeta$  were set to 0.8 and 664  $\text{cm}^{-1}$ , respectively. The whole parametrization is in accordance with parameters used for describing similar systems.<sup>41–45</sup> Yet, the AOM parameters should not be overinterpreted in a physical sense, especially since a positive  $e_\pi$  parameter implies  $\pi$ -donating character, which is unusual for pyridine type ligands.

**Choice of the Molecular Coordinate System.** The molecular coordinate system has been chosen in accordance with the requirements imposed by group theory. Accordingly, the axis of highest symmetry is defined as the  $z$  axis.<sup>46</sup> Choosing the  $z$  axis in this way leads to an unusual denomination of the orbitals in some geometries described in the Results section as the axis of elongation and is not coinciding with the molecular  $z$  axis but is instead assigned to the molecular  $x$  axis. An elongated octahedron in such a coordinate system has a  $y^2 - z^2$  SOMO and an  $x^2$  HOMO in the one electron picture.<sup>24</sup> These orbitals have the same properties as the more conventional  $x^2 - y^2$  and  $z^2$  orbitals. A detailed discussion of the choice of the axis system is given in the Supporting Information.

## RESULTS AND DISCUSSION

The synthesis of the tetraphenylborate of  $\text{Cu}(\text{tpy})_2^{2+}$  proceeds in a straightforward manner (Scheme 1). Mixing  $\text{CuCl}_2$  and 2.2 equiv of tpy in methanol gives rise to intensely green colored solutions. Subsequent addition of an excess of sodium tetraphenylborate dissolved in methanol leads to immediate precipitation of  $[\text{Cu}(\text{tpy})_2](\text{BPh}_4)_2$  (**1**) as a green powder

### Scheme 1. Synthesis of **1**





which does not require any further purification after filtration and washing with methanol.

Interestingly, there have been publications on related copper(II) compounds which state that the obtained products or solutions are brown.<sup>47–49</sup> Our observations during the synthesis of **1** indicate that the brown color is a result of contamination with  $\text{Cu}^+$  ions which stem either from impurities in the copper(II) salt used as a starting material or from partial reduction of copper(II) (for details, see the [Supporting Information](#)). Saturated DMSO solutions of **1** lead to crystallization of **1** as plate-like crystals with predominant faces (001) and (00 $\bar{1}$ ). These crystals exhibit dichroic behavior (green/blue).

The crystal structure of **1** is typical<sup>23,50–52</sup> in the sense that the two tpy ligands are arranged for each Cu complex in a meridional fashion, thus giving rise to distorted octahedral coordination spheres (Figures 1 and 2). The angular strain

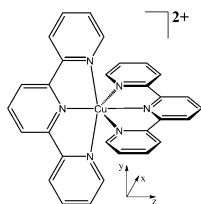


**Figure 1.** Schematic representation of the coordination structure of **1** with  $D_{2d}$  symmetry.

within the ligand backbone pulls the outer N donors out of the equatorial plane leading to a  $D_{2d}$  symmetric structure. Complexes of this symmetry are subject to PJT distortions.<sup>25</sup>

However, compared to other homoleptic copper complexes of 2,2':6',2''-terpyridine, the crystal structure of **1** is surprisingly

complex with six independent  $[\text{Cu}(\text{tpy})_2]^{2+}$  cations in the asymmetric unit (Figure 2).<sup>23,50–52</sup> In all chromophores at all temperatures (100, 123, 293 K), the shortest distances  $d(\text{Cu}-\text{N})$  (1.95–2.04 Å) are observed between copper and the central nitrogen atom of the two ligand molecules. It will be of importance for the explanation of the observed dichroic behavior that all these short interatomic vectors are aligned along the crystallographic  $a$  axis (Figure 2) with only small angular deviations. At ambient temperatures, five (A–E) out of the six chromophores  $[\text{Cu}^{\text{II}}\text{N}_6]$  (Figure 2) appear to have compressed octahedral geometry very similar to the schematic  $D_{2d}$  symmetric coordination polyhedron in Figure 1 with four long distances  $d(\text{Cu}-\text{N}) \approx 2.17$  Å. Chromophore F (Figure 2) shows already at ambient temperature a slightly different distortion resembling an elongation, with two of the equatorial ligands at somewhat longer ( $d(\text{Cu}-\text{N}) = 2.19$  and 2.25 Å) and the others at slightly shorter distances ( $d(\text{Cu}-\text{N}) = 2.09$  and 2.09 Å). On cooling to 100 K, a very similar distortion pattern is assumed by chromophores A, C, and E, while B and D remain practically unchanged and the distortion of F approaches that of a typical 4 + 2 elongated octahedron.

Overall, the various  $[\text{Cu}^{\text{II}}\text{N}_6]$  chromophores appear to change from  $D_{2d}$  symmetry with a 2 + 4 distance distribution at higher temperatures to  $C_{2v}$  symmetry and 4 + 2 distance distribution at lower temperatures. This change can be related to a temperature dependent competition between the strain trying to establish the optimum (undistorted) conformation of the ligand molecules and the forces trying to optimize the electronic energy of the coordinated cations. While at low temperatures, the electronic requirements of the  $\text{Cu}^{2+}$  ions ( $d^9$  electron configuration) with their static Jahn–Teller effect are dominant. The occurrence of only a single elongated structure instead of two statistically disordered elongated octahedra is indicative of a cooperation between lattice forces and the JTE

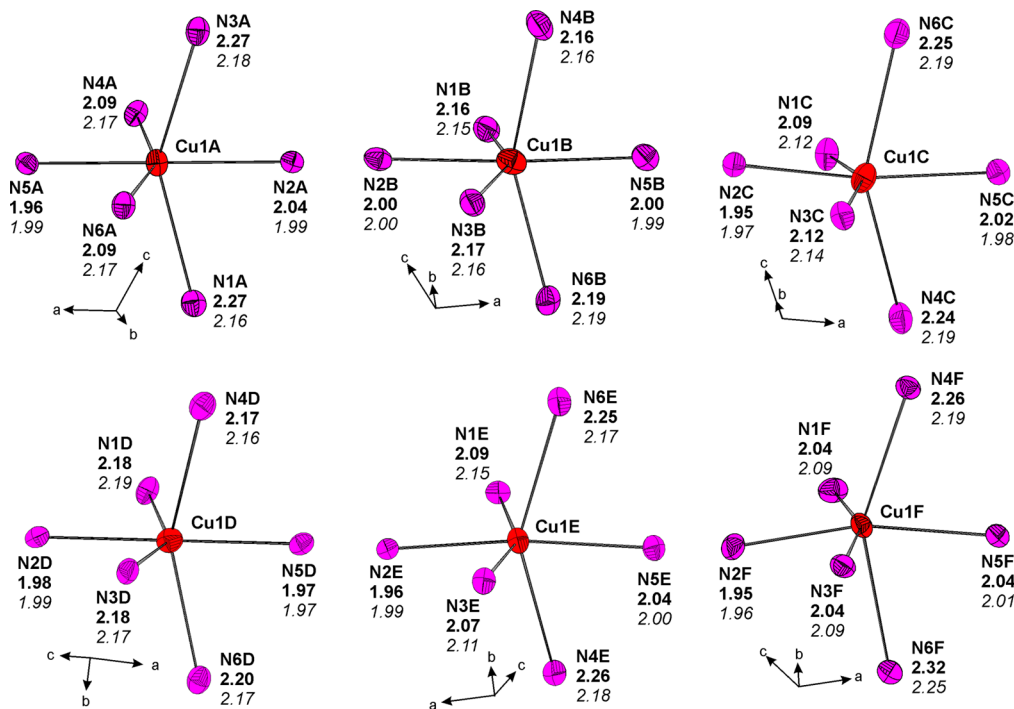


**Figure 2.** ORTEP style representation of the six crystallographically independent cations labeled A–F of  $[\text{Cu}(\text{tpy})_2](\text{BPh}_4)_2$  at  $T = 100$  K. Ellipsoids at the 30% probability level, distances  $d(\text{Cu}-\text{N})$  in Å at 100 K (bold); distances at 298 K (in *italics*). ESDs for distances are better than  $\pm 0.01$  Å. Red ellipsoids represent Cu, and pink represent N atoms.

leading to one global minimum structure.<sup>33</sup> At ambient temperature, a dynamic JT behavior takes over. The apparently compressed structures observed using XRD experiments result from the averaging of the interconversion between two minimum structures. It appears to be noteworthy that the dynamic behavior of the various chromophores in the crystal structure of **1** is so different. Inspection of the crystal structure reveals that the cation anion separation as well as the cavity size of the cations appear to be no determinants of the different dynamic behavior. However, the static octahedra do show more C–H $\cdots\pi$  contacts between the complex cations and the anions than the compressed ones (16 contacts for the static octahedra compared to five contacts for the dynamic octahedra with a separation of less than 2.7 Å, see the Supporting Information for details). Similar observations have been made on iron complexes.<sup>10,11</sup>

Although conversion from elongated at low temperatures to apparently compressed octahedra at room temperature is typical for a transition from a static to a two-dimensional dynamic JT effect,<sup>33</sup> the XRD data alone are not fully conclusive. We have therefore applied temperature dependent UV/vis/NIR and EPR spectroscopy to corroborate the conclusions from the structural investigation.

The single crystal UV/vis/NIR spectra (Figure 3) recorded at room temperature and 100 K show two broad absorption

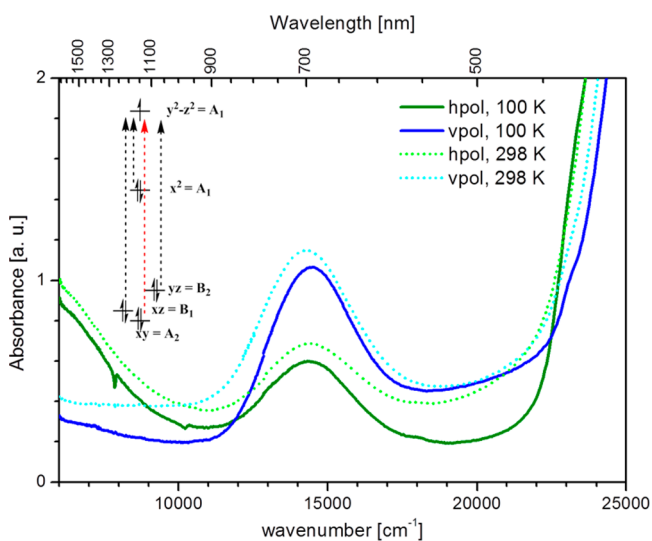


**Figure 3.** UV/vis/NIR spectra of a single crystal of **1** using polarized light. hpol = horizontally polarized light, vpol = vertically polarized light. Inset: d electron energy levels and allowed (black dotted arrows) and forbidden (red dotted arrows) transitions.

bands at  $\tilde{\nu}_1 \approx 6000 \text{ cm}^{-1}$  and  $\tilde{\nu}_2 \approx 14\,400 \text{ cm}^{-1}$  with pronounced polarization. The low energy transition allows estimation of a JT stabilization of  $\tilde{\nu}_{\text{JT}} \approx (\tilde{\nu}_1/4) = 1500 \text{ cm}^{-1}$ .<sup>23</sup> The maximum of the band at  $6000 \text{ cm}^{-1}$  was confirmed by an additionally recorded powder reflectance spectrum (see Supporting Information, Figure S1). The high-energy absorptions at wavenumbers higher than  $23\,000 \text{ cm}^{-1}$  are assigned to charge transfer transitions.<sup>24</sup> There is no significant difference in band intensities in the spectra recorded at ambient temperature and 100 K. This points to a static dipole mechanism for the d–d electronic transitions. Very clearly, the apparent changes in coordination geometry as deduced from the XRD study are not reflected by the UV/vis/NIR

spectral behavior of the chromophores. In addition, it is quite unusual that a crystal structure containing six chemically similar, however crystallographically independent, chromophores exhibits dichroic behavior with strongly polarized bands. Typically, one would expect for such a situation averaging of orientation dependency in absorption properties. However, despite the complexity of the crystal structure of **1**, the two short Cu–N bonds of the central pyridine rings of each chromophore [ $\text{Cu}^{\text{II}}\text{N}_6$ ] (the molecular  $z$  axis according to group theory; see Figure 1) are pointing almost parallel to the crystallographic  $a$  axis (Figure 2). The horizontal polarization (hpol) direction in our spectra is parallel to this axis. The vertical polarization (vpol) is aligned parallel to the crystallographic  $b$  axis. Assuming the selection rules for electronic excitation via a static dipole mechanism for an elongated octahedron [ $\text{Cu}^{\text{II}}\text{N}_6$ ] of  $C_{2v}$  symmetry ( $C_2$  parallel to the bond between  $\text{Cu}^{2+}$  and the nitrogen of the central pyridine rings) explains the observed polarizations: Excitation of an electron from  $x^2$  to  $y^2-z^2$  ( $\tilde{\nu}_1 \approx 6000 \text{ cm}^{-1}$ ; for orbital denomination see Figure 3) will occur only with light polarized along the short bonds Cu–N to the central pyridine rings (hpol). The electronic transitions  $xz, yz \rightarrow y^2-z^2$  ( $\tilde{\nu}_2 \approx 14\,400 \text{ cm}^{-1}$ ) can be excited by light polarized along the vpol direction (parallel to the crystallographic  $b$  axis). Since the octahedra are not perfectly aligned, the corresponding excitation will also occur (to a smaller extent) with light polarized along the crystallographic  $a$  axis (hpol).<sup>46,53,54</sup> Owing to the high time resolution of UV/vis/NIR spectroscopy, the electronic transitions of the elongated octahedra are observed for those cations, which are distorted by the dynamic JT effect and appear to be compressed in XRD experiments. Note also that the low energy transition would be forbidden along any polarization direction in a hypothetical, static,  $D_{2d}$  symmetrical compressed octahedral chromophore. Furthermore, since only two octahedra appear to be compressed at 100 K compared to five at 293 K, one would expect a marked decrease of the intensity of the low energy transition at higher temperatures if the compressed octahedra were indeed static. Yet, such an intensity change is also not observed. Conclusively, the polarized absorption spectra confirm the presence of elongated chromophores [ $\text{Cu}^{\text{II}}\text{N}_6$ ] in **1** at 100 and 293 K but do not show signs of statically compressed octahedra, in agreement with the interpretation of the XRD data.

EPR spectra have been recorded at the temperatures of the UV/vis/NIR and XRD experiments. Furthermore, the experimental setup allowed extending the temperature range below 100 K. The spectra of the powder of **1** recorded at various temperatures at the X-band are shown in Figure 4.

Figure 4 shows how the relatively narrow four-line spectrum at room temperature is gradually converted into a broad four-line spectrum with the highest spectral density on the high field side at 20 K. In the intermediate temperature range a five line spectrum is observed, indicative of the simultaneous occurrence of apparently compressed and elongated octahedral complexes. Noteworthy, changes in the multiline pattern occur until the lowest temperature of 20 K.

Taking into account the results from the XRD experiments, this means that one octahedron is still static at room temperature while others appear to be dynamic down to temperatures as low as 40 K. Using 300 and 40 K as approximate transition temperatures and  $400 \text{ cm}^{-1}$  for the JT active vibration,<sup>21</sup> barrier heights of  $250 \text{ cm}^{-1}$  to more than  $1800 \text{ cm}^{-1}$  can be estimated for the interconversion between

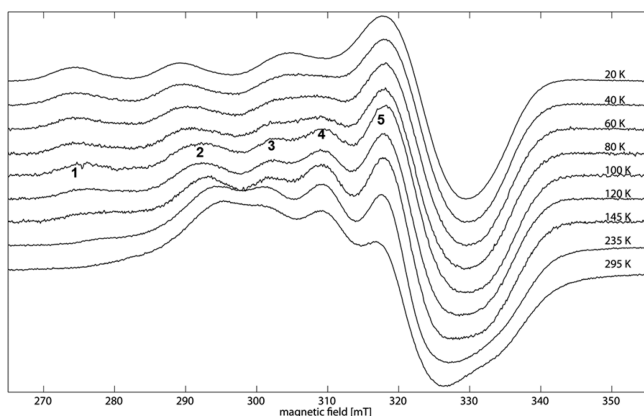


**Figure 4.** X-band EPR spectra of neat powdered **1** at various temperatures. The numbers 1–5 mark the five-line spectrum indicative of simultaneous occurrence of dynamic and static octahedra.

the two possible axes of elongation of the different cations observed crystallographically.<sup>20</sup> The lowest value for the cation which interacts the least with the surrounding lattice is in good agreement with values calculated for an isolated bis-(terpyridine)copper cation.<sup>55</sup> The highest barrier on the other hand is similar to the value obtained on a similar  $[\text{Cu}^{\text{II}}\text{N}_6]$  compound in which JT distortions have been reported.<sup>24</sup> It is noteworthy that the highest barrier is slightly higher than the estimated JT stabilization. This emphasizes the importance of the cooperative nature of lattice and JT forces.

In order to obtain more insight, the powder spectra obtained at room temperature, 100 K, and 20 K have also been recorded at Q-band frequencies and investigated more thoroughly. The spectra taken at room temperature show high spectral densities at their low field sides (295–330 and 1080–1130 mT, respectively). The shape of the EPR spectra corresponds to an inverse axial  $g$  tensor<sup>31</sup> for which  $g_x = g_y > g_z$ . Inverse axial  $g$  tensors are expected for compressed octahedra.<sup>31</sup> The shoulders at the low field sides of the spectra (285 and 1060 mT, respectively) are attributed to the elongated cation F. The spectra can be simulated best with the corresponding 5:1 ratio of compressed to elongated octahedra (Figure 5). At 100 K, the spectra can be simulated assuming four elongated and two effectively compressed octahedra (Figure 5). At 20 K, the X- and Q-band EPR spectra can be simulated assuming only static elongated octahedra (Figure 5).

In addition to the EPR experiments on the polycrystalline powder, single crystal EPR spectra have been recorded. The single crystal spectra could be simulated using the same set of parameters as for the powder spectra. As an example, the single crystal spectra taken at 100 K are shown in Figure 6 (the others are shown in the Supporting Information). Taking the complexity of the spectra into account, a satisfying agreement between experimental and simulated spectra is achieved at all orientations. Even for the crystal orientations shown in Figure 6c) where the EPR lines are heavily overlapping, the agreement of simulation and experiment is still acceptable. The parameters used to simulate the EPR spectra agree with the results of the AOM calculations (see Supporting Information). A noteworthy exception is the value of  $g_z$  for the apparently compressed octahedra, which was calculated to be nearly equal to the free electron  $g$  value,  $g_e = 2.0023$ . Experimentally, no  $g_z$  values lower than 2.04–2.05 have been observed which would be expected for elongated octahedra. This can be understood as an indication of the dynamic nature of the apparently compressed octahedra,<sup>31</sup> as the calculations were only performed with the average, seemingly compressed XRD structure (see Supporting Information).

It was possible to consistently simulate all EPR spectra and to theoretically validate the EPR parameters used in the simulations. Furthermore, the high quality of the XRD data obtained at 100 K provides a large body of structural information. Therefore, it should be possible to correlate the XRD structures with EPR parameters. Such a correlation requires knowledge of the distortion pathways of the  $[\text{Cu}^{\text{II}}\text{N}_6]$  cations and how these distortions affect the expected EPR parameters. To investigate the distortion pathways, the structural parameters obtained from the XRD experiment at 100 K are inspected. It is noted that the average bond lengths of the bonds along the  $z$  axis from the  $\text{Cu}^{2+}$  ion to the central pyridine rings of the tpy ligands  $\langle d_z \rangle$  as well as the bond lengths to the outer pyridine rings in the  $xy$  plane  $\langle d_{xy} \rangle$  are the same for all six cations A–F. They amount to  $\langle d_z \rangle = 1.993 \pm 0.009 \text{ \AA}$  and  $\langle d_{xy} \rangle = 2.175 \pm 0.007 \text{ \AA}$ . This finding suggests that removal of one ligand from the  $\text{Cu}^{2+}$  ion by a given distance leads to an equal approach of the other ligand.<sup>56,57</sup> For the ligand displacements  $\Delta d_{z+}$  and  $\Delta d_{z-}$  along the molecular  $z$  axis, it is found:

$$\Delta d_{z+} = -\Delta d_{z-} \quad (1)$$

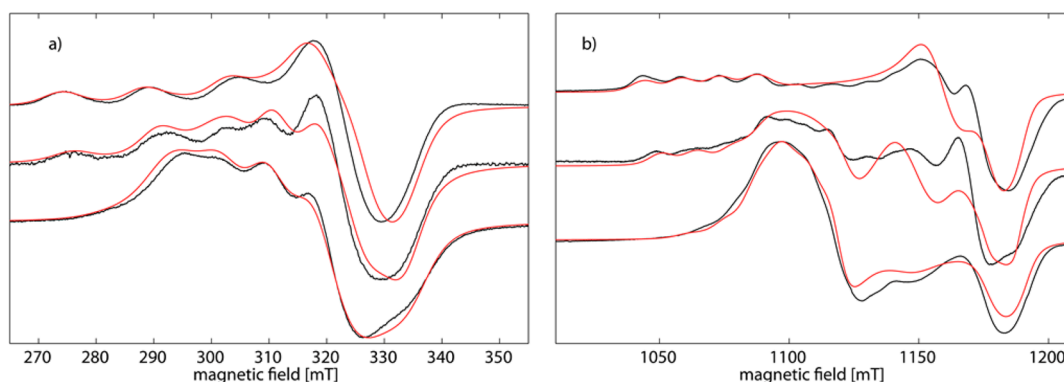


**Figure 5.** EPR spectra of neat powdered samples of **1** at different temperatures (from top to bottom  $T = 20, 100,$  and  $293 \text{ K}$ ) and mw frequencies, (a) X-band and (b) Q-band. The black lines are the experimental data; the red lines are the corresponding simulations. The parameters used to simulate these spectra are given in Tables S5–S7.



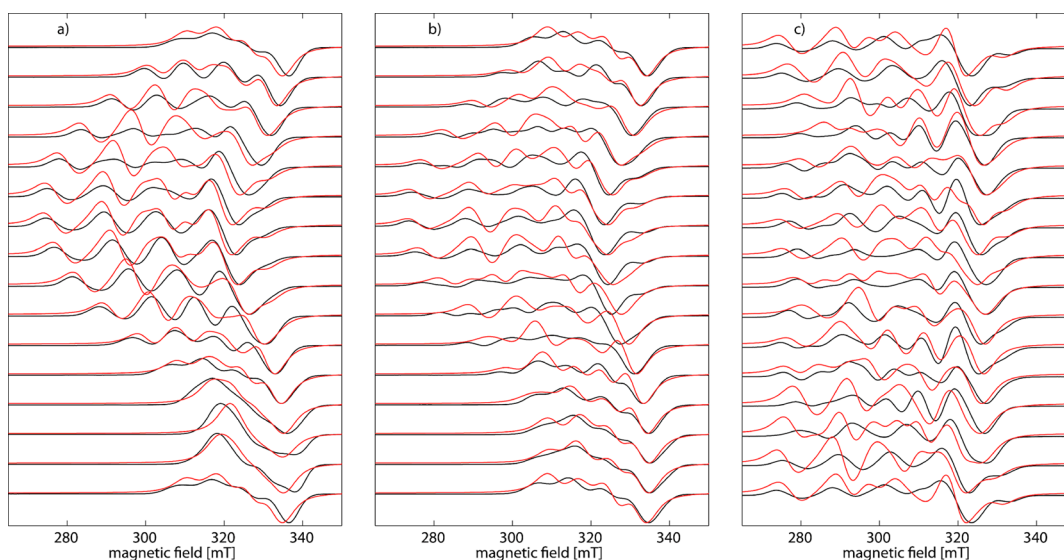
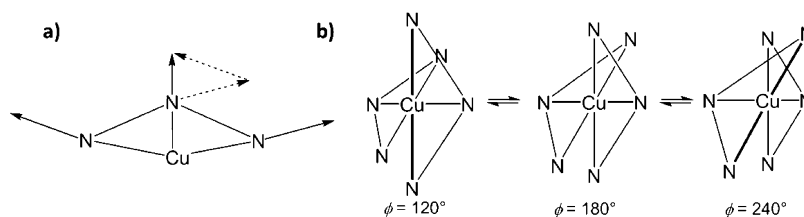


**Figure 6.** Single crystal EPR measurements at 100 K (black lines) and corresponding simulations thereof (red lines). (a) Rotation around crystallographic *b* axis. (b) Axis of rotation perpendicular to crystallographic *a* and *b* axes. (c) Rotation around the crystallographic *a* axis. See [Supporting Information](#) for single crystal spectrum taken at 20 K and room temperature.

**Scheme 2.** (a) Vector Model of the Displacement of the Nitrogen Donor Atoms<sup>a</sup> and (b) Interconversion of the Different Complex Conformers<sup>b</sup>



<sup>a</sup>The outer pyridine donor groups are displaced along their bond vectors. The displacement vector of the central pyridine ring is the sum of the displacement vectors of the outer pyridine rings. <sup>b</sup>The bold bonds indicate the unique axes.

In addition, if the central pyridine of one tpy ligand approaches the  $\text{Cu}^{2+}$  ion, the outer pyridine rings of that ligand do so as well and the other way round. However, the extent of the displacement of the outer rings is larger than for the central rings. If the *x* axis is chosen as the axis of elongation, inspection of the bond lengths observed in the crystal structure leads to the formulation of eq 2, which correlates the displacements<sup>25,58–60</sup> of the outer pyridine rings in the *xy* plane with  $\Delta d_{z+}$ :

$$\Delta d_x = -\Delta d_y = 2.38\Delta d_{z+} \quad (2)$$

The ligand displacements  $\Delta d_x$  and  $\Delta d_y$  are the changes of the bond lengths Cu–N along the *x* and *y* axes, respectively, and are equal in magnitude but opposite in sign. The vibration described by the displacements  $\Delta d_x$  and  $\Delta d_y$  is the  $\epsilon$  vibration in the JT E  $\otimes$  e framework. However, the  $\epsilon$  vibration does not contain a displacement of the ligands along the molecular *z* axis. Therefore, the displacement along the *z* axis must result from the rigid ligand structure, which forces the central pyridine ring to follow the movement of the outer pyridine rings. The correlation coefficient of 2.38 with a standard deviation of 0.29 is in agreement with a geometrical model of the ligand displacement if the outer pyridine rings are assumed to be displaced along their Cu–N bonds (Scheme 2a and [Supporting Information](#) for details). In the case of a  $D_{2d}$  symmetric compound, application of the PJT ( $A \oplus B$ )  $\otimes$  b framework

might be considered more appropriate.<sup>2,25</sup> In this framework, the ligand displacement described above as  $\epsilon$  vibration has  $b_1$  symmetry, which is the expected symmetry within the PJT ( $A \oplus B$ )  $\otimes$  b framework.<sup>2,25</sup> The same conclusions are drawn in both frameworks and only the labeling of the vibration would change in the PJT framework. Here, the JT E  $\otimes$  e framework is used to describe the ligand displacements as the JT radius  $\rho$  and angle  $\phi$  introduced in this framework are used as descriptors of the geometry.

The displacements described by eqs 1 and 2 also suffice to illustrate the interconversion of an octahedron elongated along the *x* axis (JT angle of  $\phi = 120^\circ$ ) passing through a compressed state ( $\phi = 180^\circ$ ) over to a structure elongated along the *y* axis ( $\phi = 240^\circ$ ; Scheme 2b).

As all ligand displacements are correlated, a single displacement parameter suffices to describe all bond length parameters of the first ligand sphere. These bond length parameters can be correlated with the experimental EPR parameters using the equations given in the paper of Ammeter et al.<sup>21</sup> The  $g_x$  and  $g_y$  values react very sensitively to structural changes and can be reliably obtained from experimental data. The difference of these two values is expected to increase upon going from  $\phi = 180^\circ$  to  $\phi = 120^\circ$ . A correlation of  $\Delta d_{z+}$  with  $g_x - g_y$  for the six  $[\text{Cu}^{\text{II}}\text{N}_6]$  ions at 100 K is shown in Figure 7.

These correlations between structure and EPR parameters gained on the solid state samples of 1 can now be applied to

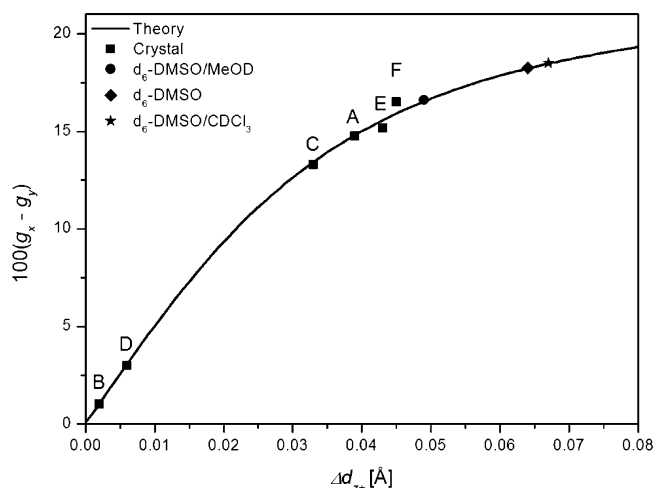


**Figure 7.** Correlation of  $\Delta d_{z^+}$  with  $g_x - g_y$  obtained from the EPR. The black line is the fit to the data points according to theoretical expectations.<sup>21</sup> A, B, C, D, E, and F are the six different  $[\text{Cu}^{11}\text{N}_6]$  ions in the crystal structure at 100 K. For frozen solutions,  $g_x - g_y$  was obtained from simulation of the EPR spectra and subsequently used to infer the ligand displacement  $\Delta d_{z^+}$  (see below).

gain insight about the structure of **1** in frozen solution. To that end, EPR samples of **1** dissolved in various solvent systems have been prepared and their EPR spectra at the X- and Q-bands have been recorded in order to evaluate the cation geometry depending upon the solvent. The results of these experiments are summed up in Figure 8.

The EPR spectra of solutions of **1** depend markedly on the choice of the solvent system. In polar solvents like  $d_6$ -DMSO or mixtures of  $d_6$ -DMSO/MeOD, a rhombic  $g$  tensor is observed ( $g_x > g_y > g_z$ ). If a less polar solvent mixture like  $d_6$ -DMSO/ $\text{CDCl}_3$  is used, an axial  $g$  tensor is observed ( $g_x > g_y = g_z$ ). The nitrogen hyperfine coupling (HFC) structure displayed in the X-band EPR spectra of **1** dissolved in the solvent mixtures indicates that the Cu(II) ions are indeed ligated by six nitrogen donor atoms. Only in the case of pure  $d_6$ -DMSO could the nitrogen HFC structure not be resolved, as pure  $d_6$ -DMSO does not yield glassy samples. The obtained  $g$  and copper HFC values are given in Table S11 and lie within the bounds of those used to simulate the spectra of powdered or crystalline **1**. Assuming that the relation between geometric and EPR parameters is the same in solution and the solid state, one can calculate the geometric parameters for the complexes in

solution with eqs 1 and 2, and the  $\Delta d_{z^+}$  value can be read off from the graph in Figure 7. The obtained results are listed in Table 2.

According to Table 2, all cations found in frozen solution at 20 K correspond to elongated octahedra. However, the degree of distortion indicated by the JT radius  $\rho$  and the JT angle  $\phi$  depends on the solvent. In the mixture of deuterated methanol and DMSO, the cation structure resembles those of the cations found in the crystal structure at 100 K, which still have a marked orthorhombic distortion as indicated by their JT angle  $\phi \gtrsim 130^\circ$ . The other solutions contain cations that are closer to an ideal elongated structure along the  $x$  axis with JT angles  $\phi$  close to  $120^\circ$  and JT radii  $> 0.38 \text{ \AA}$ . These values lie outside those observed crystallographically, which might indicate that the structural change is more complicated in  $d_6$ -DMSO and  $d_6$ -DMSO/ $\text{CDCl}_3$  mixtures than just a more pronounced elongation. Therefore, the assignment of the structure in the case of the  $d_6$ -DMSO/MeOD solution has a higher degree of confidence than for the other solution. Further experiments on frozen solutions using for example MD simulations; EPR hyperfine spectroscopy; or EXAFS, XANES, and LAXS might be used to gain deeper insight into the structures in different solutions.

Note that the theoretical treatment also yields expressions for the SOMO and the HOMO.<sup>21</sup> Both these orbitals have antibonding character. For all observed elongated structures, the HOMO in this framework has nearly pure  $x^2$  character. This means that only very weak bonding forces and therefore very elastic bonds between the  $\text{Cu}^{2+}$  ion and the outer pyridine rings of the remote tpy ligand are expected.<sup>61</sup> Thus, the remote ligand is activated for ligand displacement.<sup>35</sup>

## CONCLUSION

The tetraphenylborate of the (bis(terpyridine))copper(II) complex **1** crystallizes in a remarkably complicated structure. The crystal structure revealed the existence of six crystallographically independent complex cations with highly variable bond lengths of  $d_x \approx 2.175\text{--}2.300 \text{ \AA}$ ,  $d_y \approx 2.045\text{--}2.175 \text{ \AA}$ , and  $d_z \approx 1.955\text{--}2.045 \text{ \AA}$ , and each of these cations shows different dynamic behavior. In addition to the X-ray experiments, UV/vis/NIR and EPR spectroscopy have been applied to investigate the behavior of the different complex cations. The intensity of the electronic transitions at  $6000$  and  $14\,400 \text{ cm}^{-1}$  was used to confirm the dynamic nature of the apparently compressed octahedra. The low-energy transition can be used to estimate a JT stabilization of  $1500 \text{ cm}^{-1}$ . In EPR spectroscopically, the  $g$

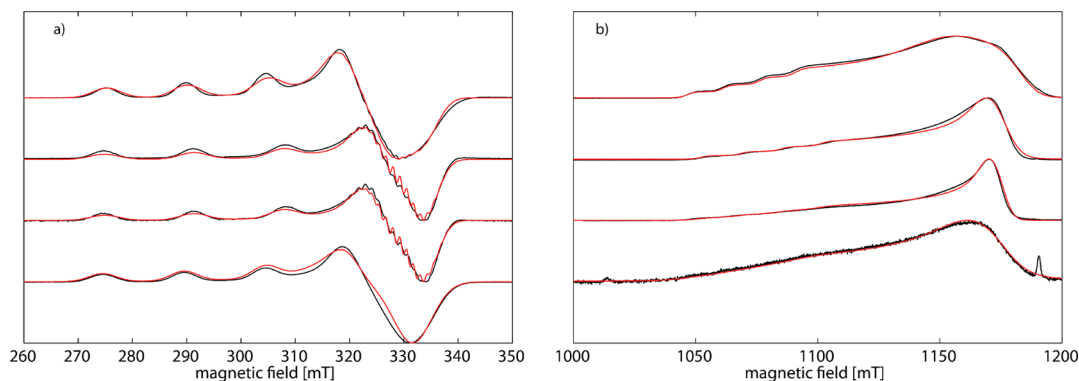


**Figure 8.** Spectra of frozen solutions of **1** at (a) X- (b) and Q-band frequencies in  $d_6$ -DMSO,  $d_6$ -DMSO/ $\text{CDCl}_3$  (1:3), DMSO/ $\text{CDCl}_3$  (1:5), and  $d_6$ -DMSO/MeOD (1:1.5) (from bottom to top).  $T = 20 \text{ K}$ . Black: experimental spectra. Red: simulated spectra.

Table 2. Geometrical Parameters of  $[\text{Cu}(\text{tpy})_2]^{2+}$  Inferred from EPR Spectra of Frozen Solutions of **1**<sup>a</sup>

solvent	$100 \cdot \Delta g_{xy}$	$\Delta d_{z+}/\text{Å}$	$d_{z+}/\text{Å}$	$d_{z-}/\text{Å}$	$d_x/\text{Å}$	$d_y/\text{Å}$	$\rho/\text{Å}$	$\phi/\text{deg}$
<i>d</i> <sub>6</sub> -DMSO	18.25	0.064	2.057	1.929	2.327	2.023	0.381	123.9
<i>d</i> <sub>6</sub> -DMSO/MeOD	16.6	0.049	2.042	1.944	2.292	2.058	0.322	130.8
<i>d</i> <sub>6</sub> -DMSO/ $\text{CDCl}_3$ <sup>b</sup>	18.5	0.067	2.060	1.926	2.334	2.016	0.402	122.3

<sup>a</sup>The bond lengths have been calculated using  $d_{z+} = \langle d_z \rangle + \Delta d_{z+}$ ,  $d_{z-} = \langle d_z \rangle + \Delta d_{z-}$ ,  $d_x = \langle d_{xy} \rangle + \Delta d_x$  and  $d_y = \langle d_{xy} \rangle + \Delta d_y$ . <sup>b</sup>The EPR parameters are the same for both mixtures of *d*<sub>6</sub>-DMSO and  $\text{CDCl}_3$  (1:3 and 1:5).

values have been correlated with the structures of the cations. The *g* values amount to  $g_x \approx 2.260$ ,  $g_y \approx 2.110$ , and  $g_z \approx 2.045$  for static elongated octahedra and to  $g_x \approx 2.185 \approx g_y$ , and  $g_z \approx 2.045$  of the apparently compressed octahedra, where the  $g_z$  value of the latter is another indication of the dynamic nature of the cations. The experimental results have been analyzed using the angular overlap model. To account for the dynamic behavior of the cations, their potential energy surface has to be assumed to contain two minima corresponding to elongation along the molecular *x* and *y* axes, respectively. The hypothetical compressed structure lies on the saddle point in between the two minima, which is also the energetic barrier for interconversion of the two elongated isomers. For those cations that reach the dynamic JT at lower temperatures, the energy barrier between the two minima has to be smaller than for those that reach the dynamic JT at higher temperature. The energy barrier can be estimated to lie between 250 and 1800  $\text{cm}^{-1}$ . The different barrier heights may be explained by secondary cation contacts.

In addition, experiments on frozen solutions revealed that the structure of the cations is also affected by the solvent matrix. Since the EPR parameters of the  $\text{Cu}^{2+}$  ion react very sensitively on even slight changes of the bonding parameters of the ligating atoms, it was possible to infer details concerning the structure of the first coordination sphere, assuming that the description of the complex as a  $[\text{Cu}^{\text{II}}\text{N}_6]$  octahedron is still valid. In order to obtain a deeper understanding of the origin of the different dynamic behaviors of the  $[\text{Cu}^{\text{II}}\text{N}_6]$  octahedra, quantum chemical and further experiments on solutions are ongoing.

## ■ ASSOCIATED CONTENT

### Supporting Information

The Supporting Information is available free of charge on the ACS Publications website at DOI: 10.1021/acs.inorgchem.5b01157.

Simulation parameters and simulations of single crystal EPR spectra, UV/vis/NIR spectra of the neat powdered **1**, UV/vis/NIR spectra of solutions of **1**, and a discussion of the color of **1** (PDF)

## ■ AUTHOR INFORMATION

### Corresponding Authors

\*E-mail: rglaum@uni-bonn.de.

\*E-mail: schiemann@pc.uni-bonn.de.

### Notes

The authors declare no competing financial interest.

## ■ ACKNOWLEDGMENTS

We thank V. Dittrich for performing the UV/vis/NIR measurements and Prof. Dr. A. Filippou for access to his X-ray diffractometers. O.S. and R.G. thank the DFG for funding via SFB 813.

## ■ REFERENCES

- Jahn, H. A.; Teller, E. *Proc. R. Soc. London, Ser. A* **1937**, *161*, 220–235.
- Bersuker, I. B. *The Jahn-Teller Effect*; Cambridge University Press: New York, 2006.
- Bersuker, I. B. *Chem. Rev.* **2001**, *101*, 1067–1114.
- Fulton, R. L.; Gouterman, M. J. *Chem. Phys.* **1961**, *35*, 1059–1071.
- Bersuker, I. B. *Chem. Rev.* **2013**, *113*, 1351–1390.
- Constable, E. C.; Baum, G.; Bill, E.; Dyson, R.; van Eldik, R.; Fenske, D.; Kaderli, S.; Morris, D.; Neubrand, A.; Neuburger, M.; Smith, D. R.; Wieghardt, K.; Zehnder, M.; Zuberbühler, A. D. *Chem. - Eur. J.* **1999**, *5*, 498–508.
- Zhang, X.; Lawson Daku, M. L.; Zhang, J.; Suarez-Alcantara, K.; Jennings, G.; Kurtz, C. A.; Canton, S. E. *J. Phys. Chem. C* **2015**, *119*, 3312–3321.
- Kershaw Cook, L. J.; Thorp-Greenwood, F. L.; Comyn, T. P.; Cespedes, O.; Chastanet, G.; Halcrow, M. A. *Inorg. Chem.* **2015**, *54*, 6319–6330.
- Nihei, M.; Shiga, T.; Maeda, Y.; Oshio, H. *Coord. Chem. Rev.* **2007**, *251*, 2606–2621.
- Hasegawa, Y.; Sakamoto, R.; Takahashi, K.; Nishihara, H. *Inorg. Chem.* **2013**, *52*, 1658–1665.
- Vela, S.; Novoa, J. J.; Ribas-Arino, J. *Phys. Chem. Chem. Phys.* **2014**, *16*, 27012–27024.
- Ramakrishna, B.; Salzer, A.; Ruppli, U.; Ammeter, J.; Kölle, U. *Inorg. Chem.* **1986**, *25*, 1364–1368.
- Waizump, K.; Takuno, M.; Fukushima, N.; Masuda, H. *J. Coord. Chem.* **1998**, *44*, 269–279.
- Barra, A.; Gatteschi, D.; Sessoli, R.; Abbati, G. L.; Cornia, A.; Fabretti, A. C.; Uytterhoeven, M. G. *Angew. Chem., Int. Ed. Engl.* **1997**, *36*, 2329–2331.
- Hargittai, M.; Réffy, B.; Kolonits, M.; Marsden, C. J.; Heully, J.-L. *J. Am. Chem. Soc.* **1997**, *119*, 9042–9048.
- Romain, S.; Duboc, C.; Neese, F.; Rivière, E.; Hanton, L. R.; Blackman, A. G.; Philouze, C.; Leprêtre, J.; Deronzier, A.; Collomb, M. *Chem. - Eur. J.* **2009**, *15*, 980–988.
- Bruyndonckx, R.; Daul, C.; Manoharan, P.; Deiss, E. *Inorg. Chem.* **1997**, *36*, 4251–4256.
- Khomenko, V.; Langer, K.; Rager, H.; Fett, A. *Phys. Chem. Miner.* **1998**, *25*, 338–346.
- Thauern, H.; Glaum, R. *Inorg. Chem.* **2007**, *46*, 2057–2066.
- Barriuso, M. T.; Ortiz-Sevilla, B.; Aramburu, J. A.; García-Fernández, P.; García-Lastra, J. M.; Moreno, M. *Inorg. Chem.* **2013**, *52*, 9338–9348.
- Ammeter, J.; Bürgi, H.; Gamp, E.; Meyer-Sandrin, V.; Jensen, W. *Inorg. Chem.* **1979**, *18*, 733–750.
- Comba, P.; Kerscher, M. *Cryst. Eng.* **2003**, *6*, 197–211.
- Folgado, J. V.; Henke, W.; Allmann, R.; Stratemeier, H.; Beltran-Porter, D.; Rojo, T.; Reinen, D. *Inorg. Chem.* **1990**, *29*, 2035–2042.
- Mack, K.; Wünsche von Leupoldt, A.; Förster, C.; Ezhevskaya, M.; Hinderberger, D.; Klinkhammer, K. W.; Heinze, K. *Inorg. Chem.* **2012**, *51*, 7851–7858.
- Murphy, B.; Hathaway, B. *Coord. Chem. Rev.* **2003**, *243*, 237–262.
- Bacci, M. *Chem. Phys.* **1986**, *104*, 191–199.
- Simmons, C. J.; Hathaway, B. J.; Amornjarusiri, K.; Santarsiero, B. D.; Clearfield, A. *J. Am. Chem. Soc.* **1987**, *109*, 1947–1958.

- (28) Simmons, C. J.; Hitchman, M. A.; Stratemeier, H.; Schultz, A. J. *J. Am. Chem. Soc.* **1993**, *115*, 11304–11311.
- (29) Docherty, R.; Tuna, F.; Kilner, C. A.; McInnes, E. J.; Halcrow, M. A. *Chem. Commun.* **2012**, *48*, 4055–4057.
- (30) Hitchman, M. A.; Maaskant, W.; van der Plas, J.; Simmons, C. J.; Stratemeier, H. *J. Am. Chem. Soc.* **1999**, *121*, 1488–1501.
- (31) Halcrow, M. A. *Dalton Trans.* **2003**, 4375–4384.
- (32) Murphy, B.; Hathaway, B. *Coord. Chem. Rev.* **2003**, *243*, 237–262.
- (33) Falvello, L. *J. Chem. Soc., Dalton Trans.* **1997**, 4463–4476.
- (34) Persson, I.; Persson, P.; Sandström, M.; Ullström, A.-S. *J. Chem. Soc., Dalton Trans.* **2002**, 1256–1265.
- (35) Schwenk, C. F.; Rode, B. M. *ChemPhysChem* **2003**, *4*, 931–943.
- (36) Chaboy, J.; Muñoz-Páez, A.; Merkling, P. J.; Marcos, E. S. *J. Chem. Phys.* **2006**, *124*, 064509.
- (37) SADABS; Bruker AXS Inc.: Billerica, MA, 2001.
- (38) Sheldrick, G. *Acta Crystallogr., Sect. A: Found. Crystallogr.* **2008**, *64*, 112–122.
- (39) Stoll, S.; Schweiger, A. *J. Magn. Reson.* **2006**, *178*, 42–55.
- (40) Cruse, D. A.; Davies, J. E.; Gerloch, M.; Harding, J. H.; Mackey, D. J.; McMeeking, R. F. *CAMMAG, A FORTRAN Computing Package*; University Chemical Laboratory, Cambridge, England, 1979.
- (41) McDonald, R. G.; Hitchman, M. A. *Inorg. Chem.* **1990**, *29*, 3074–3080.
- (42) Smith, D. W. *Inorg. Chim. Acta* **1977**, *22*, 107–110.
- (43) Astley, T.; Canty, A. J.; Hitchman, M. A.; Rowbottom, G. L.; Skelton, B. W.; White, A. H. *J. Chem. Soc., Dalton Trans.* **1991**, 1981–1990.
- (44) Astley, T.; Gulbis, J. M.; Hitchman, M. A.; Tiekink, E. R. T. *J. Chem. Soc., Dalton Trans.* **1993**, 509–515.
- (45) Astley, T.; Ellis, P. J.; Freeman, H. C.; Hitchman, M. A.; Keene, F. R.; Tiekink, E. R. *J. Chem. Soc., Dalton Trans.* **1995**, 595–601.
- (46) Harris, D. C.; Bertolucci, M. D. *Symmetry and Spectroscopy*; Dover Publications Inc.: Mineola, NY, 1989.
- (47) Narr, E.; Zimmermann, H.; Godt, A.; Goldfarb, D.; Jeschke, G. *Phys. Chem. Chem. Phys.* **2003**, *5*, 3959–3967.
- (48) Hoover, J. M.; Ryland, B. L.; Stahl, S. S. *J. Am. Chem. Soc.* **2013**, *135* (6), 2357–2367.
- (49) De Bruin, B.; Bill, E.; Bothe, E.; Weyhermüller, T.; Wieghardt, K. *Inorg. Chem.* **2000**, *39*, 2936–2947.
- (50) Allmann, R.; Henke, W.; Reinen, D. *Inorg. Chem.* **1978**, *17*, 378–382.
- (51) Valdes-Martinez, J.; Toscano, R. A.; Salazar-Mendoza, D. *Acta Crystallogr., Sect. E: Struct. Rep. Online* **2001**, *57*, m331–m332.
- (52) Hitchman, M. A.; Yablokov, Y. V.; Petrashen, V. E.; Augustyniak-Jablokov, M. A.; Stratemeier, H.; Riley, M. J.; Łukaszewicz, K.; Tomaszewski, P. E.; Pietraszko, A. *Inorg. Chem.* **2002**, *41*, 229–238.
- (53) Cotton, F. A. *Chemical Applications of Group Theory*; Wiley-Interscience, 1989.
- (54) Hitchman, M. A.; Riley, M. J.; Solomon, E. I.; Lever, A. B. P. *Inorganic Electronic Structure and Spectroscopy*; Wiley-Interscience: New York.
- (55) Deeth, R. J.; Hearnshaw, L. J. A. *Dalton Trans.* **2006**, 1092–1100.
- (56) Comba, P.; Okon, N.; Remenyi, R. *J. Comput. Chem.* **1999**, *20*, 781–785.
- (57) Bürgi, H. B.; Dunitz, J. D. In *Structure Correlation*; Wiley-VCH Verlag GmbH: Weinheim, Germany, 1994; pp 163–204.
- (58) Comba, P. *Coord. Chem. Rev.* **1999**, *185–186*, 81–98.
- (59) Der Heyde, T. A. *Angew. Chem., Int. Ed. Engl.* **1994**, *33*, 823–839.
- (60) Murphy, G.; Nagle, P.; Murphy, B.; Hathaway, B. *J. Chem. Soc., Dalton Trans.* **1997**, 2645–2652.
- (61) Comba, P.; Schiek, W. *Coord. Chem. Rev.* **2003**, *238–239*, 21–29.

# (Bis(terpyridine))copper(II) Tetraphenylborate: A Complex Example for the Jahn-Teller Effect

*Andreas Meyer<sup>§</sup>, Gregor Schnakenburg<sup>+</sup>, Robert Glaum<sup>+\*</sup>, Olav Schieman<sup>§\*</sup>*

<sup>§</sup>Institute of Physical and Theoretical Chemistry, University of Bonn, Wegelerstr. 12, Bonn,  
Germany

<sup>+</sup>Institute of Inorganic Chemistry, University of Bonn, Gerhard-Domagk-Str. 1, Bonn,  
Germany

## **Supporting Information**



## Content

<b>1. Crystal structure determination of 1</b> .....	3
<b>2. UV/Vis/NIR measurements on crystalline and powdered 1</b> .....	4
2.1 Diffuse Powder Reflectance measurement on <b>1</b> : Experimental .....	4
2.2 UV/Vis/NIR measurements on neat powdered <b>1</b> : Results: .....	5
2.3 UV/Vis/NIR transitions predicted by the AOM.....	5
2.4 Selection rules in UV/Vis/NIR spectroscopy.....	6
<b>3. Experimental and angular overlap EPR parameters of single crystal and powder EPR spectra</b> .....	8
<b>4. EPR measurements on frozen solutions of 1</b> .....	13
<b>5. Constrained displacement of the donor groups</b> .....	15
<b>6. Theoretical considerations</b> .....	16
6.1 <i>g</i> values in dynamically distorted octahedra.....	16
6.2 The choice of the coordinate system .....	17
<b>7. The color change from green to brown</b> .....	18
<b>8. On the origin of the different static structures and dynamic behavior</b> .....	19
<b>9. References</b> .....	21

## 1. Crystal structure determination of 1

**Table S1.** Crystal data and structure refinement for the different X-ray experiments on compound 1.

Empirical formula	C <sub>78</sub> H <sub>62</sub> B <sub>2</sub> CuN <sub>6</sub>	C <sub>78</sub> H <sub>62</sub> B <sub>2</sub> CuN <sub>6</sub>	C <sub>78</sub> H <sub>62</sub> B <sub>2</sub> CuN <sub>6</sub>
Moiety formula	C <sub>30</sub> H <sub>22</sub> CuN <sub>6</sub> , 2(C <sub>24</sub> H <sub>20</sub> B)	C <sub>30</sub> H <sub>22</sub> CuN <sub>6</sub> , 2(C <sub>24</sub> H <sub>20</sub> B)	C <sub>30</sub> H <sub>22</sub> CuN <sub>6</sub> , 2(C <sub>24</sub> H <sub>20</sub> B)
Formula weight	1168.50 g/mol	1168.50 g/mol	1168.50 g/mol
Temperature	100(2) K	293(2) K	123(2) K
Wavelength	0.71073 Å	0.71073 Å	0.71073 Å
Crystal system, space group	monoclinic, P2 <sub>1</sub> /c	monoclinic, P2 <sub>1</sub> /c	monoclinic, P2 <sub>1</sub> /c
Unit cell dimensions	a = 39.9543(15) Å α = 90 ° b = 24.5916(9) Å β = 116.252(2) ° c = 41.6151(14) Å γ = 90 °	a = 40.278(3) Å α = 90 ° b = 24.8878(17) Å β = 116.277(2) ° c = 41.972(3) Å γ = 90 °	a = 40.001(2) Å α = 90 ° b = 24.5857(12) Å β = 116.319(2) ° c = 41.630(2) Å γ = 90 °
Volume	36671(2) Å <sup>3</sup>	37727(5) Å <sup>3</sup>	36697(5) Å <sup>3</sup>
Z, Calculated density	24, 1.270 g/cm <sup>3</sup>	24, 1.234 g/cm <sup>3</sup>	24, 1.269 g/cm <sup>3</sup>
Absorption coefficient	0.409 mm <sup>-1</sup>	0.397 mm <sup>-1</sup>	0.409 mm <sup>-1</sup>
F(000)	14664	14664	14664
Crystal size	0.38 x 0.34 x 0.22 mm <sup>3</sup>	0.34 x 0.22 x 0.18 mm <sup>3</sup>	0.34 x 0.22 x 0.18 mm <sup>3</sup>
θ-range for data collection	1.00 – 28.0°	1.00 – 28.0°	1.02 – 25.3°
Limiting indices	-52 ≤ h ≤ 52, -15 ≤ k ≤ 32, -36 ≤ l ≤ 54	-42 ≤ h ≤ 53, -32 ≤ k ≤ 31, -55 ≤ l ≤ 54	-40 ≤ h ≤ 48, -29 ≤ k ≤ 29, -49 ≤ l ≤ 48
Reflections collected / unique	250343 / 88380 [R <sub>int</sub> = 0.051]	300663 / 90953 [R <sub>int</sub> = 0.2638]	245562 / 66430 [R <sub>int</sub> = 0.1614]
Completeness to θ = 25.25°	99.8 %	99.8 %	92.1%
Absorption correction	Empirical	Empirical	Empirical
Max. and min. transmission	0.9154 and 0.8601	0.7459 and 0.5847	0.7459 and 0.5847
Refinement method	Full-matrix least squares on F <sup>2</sup>	Full-matrix least squares on F <sup>2</sup>	Full-matrix least squares on F <sup>2</sup>
Data / restraints / parameters	88380 / 12 / 4699	90953 / 272 / 4699	66430 / 102 / 4699
Goodness-of-fit on F <sup>2</sup>	1.009	0.876	0.978
Final R indices [I > σ(I)]	R <sub>1</sub> = 0.0509, wR <sub>2</sub> = 0.1140	R <sub>1</sub> = 0.0826, wR <sub>2</sub> = 0.1482	R <sub>1</sub> = 0.0696, wR <sub>2</sub> = 0.1532
R indices (all data)	R <sub>1</sub> = 0.1143, wR <sub>2</sub> = 0.1392	R <sub>1</sub> = 0.3905, wR <sub>2</sub> = 0.2427	R <sub>1</sub> = 0.1903, wR <sub>2</sub> = 0.2042
Largest diff. peak / hole	0.901 and -0.805 eÅ <sup>-3</sup>	0.480 and -0.510 eÅ <sup>-3</sup>	1.850 and -0.820 eÅ <sup>-3</sup>

## **2. UV/Vis/NIR measurements on crystalline and powdered 1**

### 2.1 Diffuse Powder Reflectance measurement on 1: Experimental

The diffuse powder reflectance spectra were recorded at ambient temperature using a CARY 14 spectrophotometer for the UV range (200-600 nm) and a CARY 17 for the visible and NIR range (300-2600 nm) both manufactured by OLIS Inc. USA. The spectrometers were equipped with an integrating sphere, a halogen lamp (200 - 2000 nm) used as light source and a combination of a prism and a grating used as monochromator. The spectral range was divided into three regions which were individually measured using three different experimental set ups (Table S2).

**Table S2.** Experimental set up for diffuse reflectance measurements.

<b>Spectral region</b>	<b>Ranges [nm]</b>	<b>Data points</b>	<b>Step width [nm]</b>	<b>Slit width [mm]</b>	<b>Band width [nm]</b>	<b>Integration time [s]</b>	<b>Detector</b>
UV	200 - 600	800	0.5	0.1	0.11 - 0.37	0.5	PMT <sup>a</sup> (Cary 14)
Vis	300 - 900	600	1	0.06	0.14 - 0.22	1	PMT <sup>a</sup> (Cary 17)
NIR	600 - 2600	500	4	1.4 - 2.2	5	1	PbS <sup>b</sup> (Cary 17)

<sup>a</sup> PMT = Photomultiplier. <sup>b</sup> PbS = Lead sulfide

In the UV and visible regions the spectroscopic data was collected using a fixed slit width and a variable band width. In the NIR region, the slit width was varied while the band width was kept constant. For the measurement, 100 mg of **1** have been diluted with 400 mg of BaSO<sub>4</sub>. This powder was placed on a white teflon sample holder and then polished to obtain a smooth surface. A spectrum of neat BaSO<sub>4</sub> was recorded to obtain a reference spectrum. (K/S) was calculated using the Kubelka-Munk function with diffuse reflectance  $R_{diff} = I_{sample} / I_{BaSO_4}$

## 2.2 UV/Vis/NIR measurements on neat powdered **1**: Results:

The UV/Vis/NIR results obtained on powdered **1** agree with the results obtained in the single crystal measurements (Figure S1). d-d transitions are observed at wavenumbers lower than  $7500\text{ cm}^{-1}$  and in between  $13000$  and  $16500\text{ cm}^{-1}$ . Absorptions at higher wavenumbers correspond to CT transitions.

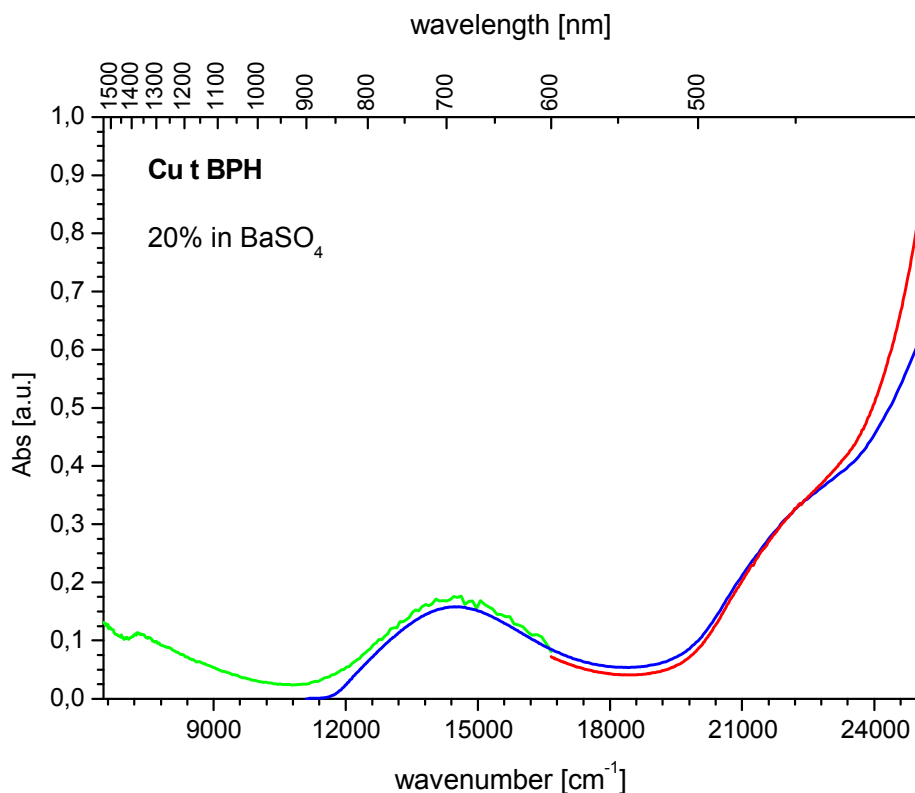


**Figure S1.** UV/Vis/NIR measurements on neat, powdered **1** diluted by grinding with BaSO<sub>4</sub> (1:4). The different colors indicate the different experimental set ups (table S2) used in the corresponding region of the spectrum.

## 2.3 UV/Vis/NIR transitions predicted by the AOM

The full UV/Vis/NIR data as predicted by AOM is listed in tables S3 and S4 for room temperature and 100 K respectively. The four d-d transitions are ordered from low to high energy. For an assignment of the transitions to certain d-orbitals, see the discussion “Selection rules in UV/Vis/NIR spectroscopy” (chapter 2.4).

**Table S3.** Wavenumbers of the four d-d transitions predicted by AOM using cation structures **A - F** obtained from the room temperature XRD data.

<b>Cation</b>	<b>Transition 1</b>	<b>Transition 2</b>	<b>Transition 3</b>	<b>Transition 4</b>
<b>A</b>	4420	13428	14248	15664
<b>B</b>	4457	13298	14073	16810
<b>C</b>	4862	14286	15246	15468
<b>D</b>	5116	14277	15097	16403
<b>E</b>	4015	13541	14516	14790
<b>F</b>	5457	14612	15581	15897

**Table S4.** Wavenumbers of the four d-d transitions predicted by the AOM using the cation structures **A - F** obtained from the XRD data recorded at  $T = 100$  K.

<b>Cation</b>	<b>Transition 1</b>	<b>Transition 2</b>	<b>Transition 3</b>	<b>Transition 4</b>
<b>A</b>	5805	14132	15055	15790
<b>B</b>	4283	13554	14522	14822
<b>C</b>	5292	14223	15202	15386
<b>D</b>	5325	14065	15024	16304
<b>E</b>	5724	14229	15216	15741
<b>F</b>	6742	15221	16213	16611

#### 2.4 Selection rules in UV/Vis/NIR spectroscopy

Discussion of selection rules in UV/Vis/NIR spectroscopy can be found in any textbook concerned with group theory for chemists. The book by Harris and Bertolucci<sup>1</sup> has been used here.

The starting point of the discussion is Figure S2 in which the energy levels of the d orbitals depending on the symmetry of the coordination shell are presented.

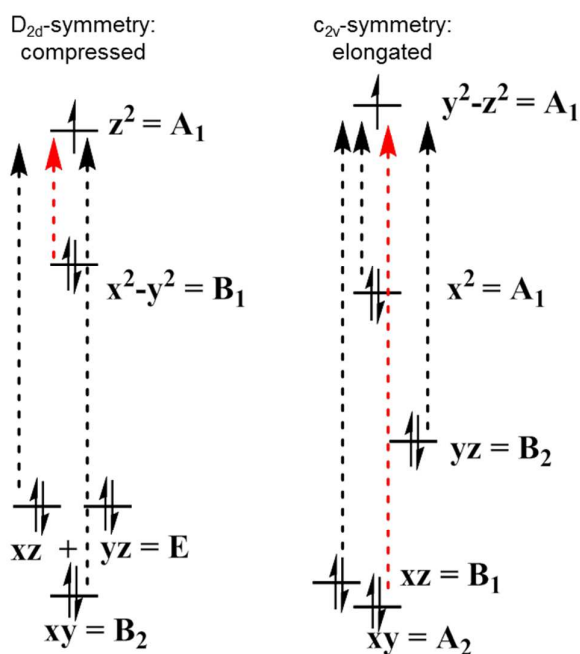


**Figure S2.** Energy levels of the d orbitals depending on the geometry of the coordination shell. The dashed arrows show the possible UV/Vis transitions, red color indicates forbidden transitions.

According to Figure 1 and the discussion in the main text, the hypothetic compressed octahedron has  $D_{2d}$  symmetry. The orbital denominations and the symmetry labels in Figure S2 have been chosen in accordance with this point group. The electromagnetic radiation has either  $E$  symmetry (polarization along  $x$  and  $y$ ) or  $B_2$  symmetry (polarization along  $z$ , parallel to the axis of symmetry). Thus the matrix elements of the transitions 1-4 indicated in Figure S2 are given by:

$$\text{Tr. 1: } \langle A_1 \left| \begin{matrix} E \\ B_2 \end{matrix} \right| B_1 \rangle = \langle \begin{matrix} E \\ B_2 \end{matrix} \rangle \rightarrow \textit{forbidden}$$

$$\text{Tr. 2 and 3: } \langle A_1 \left| \begin{matrix} E \\ B_2 \end{matrix} \right| E \rangle = \langle \begin{matrix} A_1 + A_2 + B_1 + B_2 \\ E \end{matrix} \rangle \rightarrow \textit{allowed along } x/y$$

$$\text{Tr. 4: } \langle A_1 \left| \begin{matrix} E \\ B_2 \end{matrix} \right| B_2 \rangle = \langle \begin{matrix} E \\ A_1 \end{matrix} \rangle \rightarrow \textit{allowed along } z$$

The elongated structures on the other hand are best described as  $C_{2v}$  symmetrical. The polarized radiation has  $B_1$ ,  $B_2$  and  $A_1$  symmetry ( $x$ -,  $y$ - and  $z$ -polarization respectively). The matrix elements of the UV/Vis/NIR transitions are therefore:

$$\text{Tr. 1: } \langle A_1 \left| \begin{matrix} B_1 \\ B_2 \\ A_1 \end{matrix} \right| A_1 \rangle = \langle \begin{matrix} B_1 \\ B_2 \\ A_1 \end{matrix} \rangle \rightarrow \textit{allowed along } z$$

$$\text{Tr. 2: } \left\langle A_1 \begin{vmatrix} B_1 \\ B_2 \\ A_1 \end{vmatrix} B_1 \right\rangle = \left\langle \begin{matrix} A_1 \\ A_2 \\ B_1 \end{matrix} \right\rangle \rightarrow \text{allowed along } x$$

$$\text{Tr. 3: } \left\langle A_1 \begin{vmatrix} B_1 \\ B_2 \\ A_1 \end{vmatrix} B_2 \right\rangle = \left\langle \begin{matrix} A_2 \\ A_1 \\ B_2 \end{matrix} \right\rangle \rightarrow \text{allowed along } y$$

$$\text{Tr. 4: } \left\langle A_1 \begin{vmatrix} B_1 \\ B_2 \\ A_1 \end{vmatrix} A_2 \right\rangle = \left\langle \begin{matrix} B_2 \\ B_1 \\ A_2 \end{matrix} \right\rangle \rightarrow \text{forbidden}$$

### **3. Experimental and angular overlap EPR parameters of single crystal and powder EPR spectra**

Simulations of the EPR spectra of the single crystals at the temperatures of 293 K and 20 K are shown in Figures S3 and S4. At room temperature, when most cations behave essentially dynamical, good agreement is achieved as the EPR parameters along the  $x$  and  $y$  axes become essentially identical. Note that all spectra (single crystal and powders at X- and Q-band) measured at a given temperature have been simulated with the same set of parameters (see Tables S5, S6 and S7).

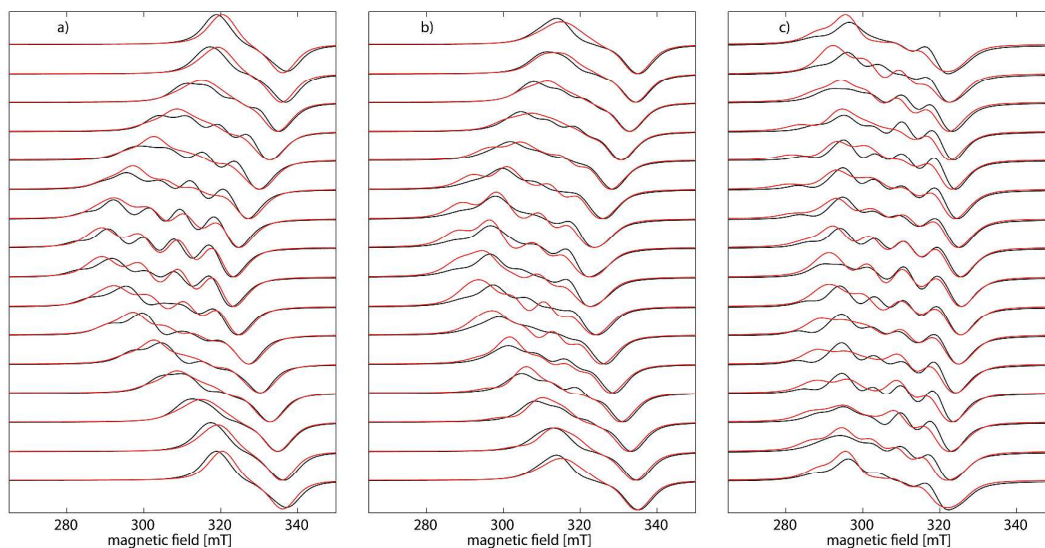


**Figure S3.** Single crystal EPR measurements at 293 K (black lines) and corresponding simulations thereof (red lines). **a)** Rotation around crystallographic  $b$  axis. **b)** Axis of rotation perpendicular to

crystallographic *a* and *b* axes. **c)** Rotation around the crystallographic *a* axis.

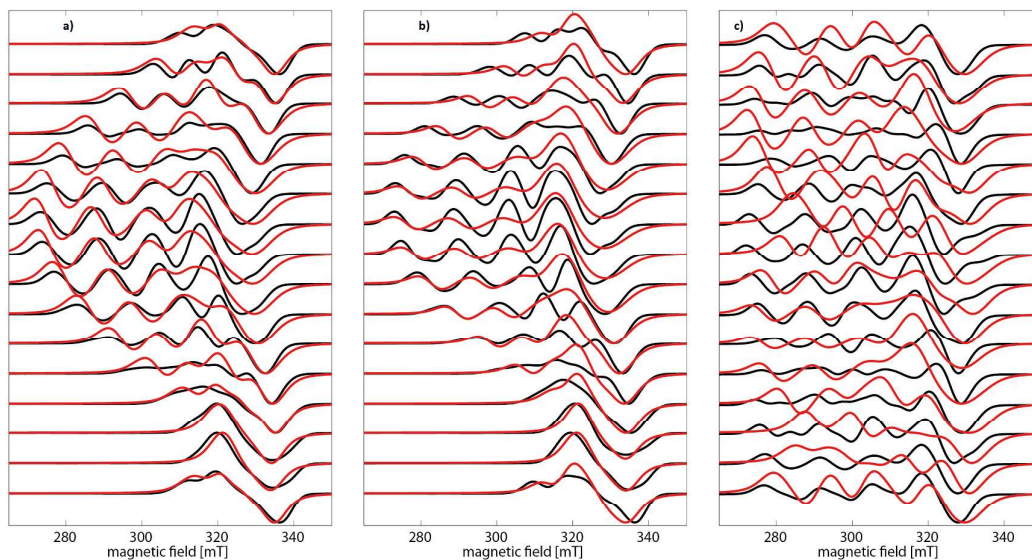


**Figure S4.** Single crystal EPR measurements at 20 K (black lines) and corresponding simulations thereof (red lines). **a)** Rotation around crystallographic *b* axis. **b)** Axis of rotation perpendicular to crystallographic *a* and *b* axes. **c)** Rotation around the crystallographic *a* axis.



**Table S5.** EPR parameters used to simulate single crystal and powder spectra at room temperature and  $g$  values obtained using the structures of the cations in the crystal structure at the same temperature.

<b>Cation</b>	<b>Parameter</b>	<b>x</b>	<b>y</b>	<b>z</b>	<b>Iso</b>
<b>A</b>	$g_{exp}$	2.196	2.178	2.041	2.138
	$g_{AOM}$	2.225	2.215	1.994	2.148
	A [MHz]	270	210	-105	125.0
<b>B</b>	$g_{exp}$	2.189	2.182	2.041	2.137
	$g_{AOM}$	2.231	2.214	1.994	2.149
	A [MHz]	263	195	-105	117.7
<b>C</b>	$g_{exp}$	2.209	2.165	2.041	2.138
	$g_{AOM}$	2.232	2.176	1.999	2.138
	A [MHz]	315	165	-105	125.0
<b>D</b>	$g_{exp}$	2.189	2.182	2.041	2.137
	$g_{AOM}$	2.216	2.200	1.996	2.139
	A [MHz]	263	195	-105	117.7
<b>E</b>	$g_{exp}$	2.196	2.178	2.041	2.138
	$g_{AOM}$	2.249	2.173	2.002	2.144
	A [MHz]	308	183	-105	128.7
<b>F</b>	$g_{exp}$	2.24	2.121	2.048	2.136
	$g_{AOM}$	2.257	2.105	2.033	2.133
	A [MHz]	365	115	-105	125

**Table S6.** EPR parameters used to simulate single crystal and powder spectra at  $T = 100$  K and  $g$  values obtained using the structures of the cations in the crystal structure at the same temperature.

<b>Cation</b>	<b>Parameter</b>	<b>x</b>	<b>y</b>	<b>z</b>	<b>Iso</b>
<b>A</b>	$g_{exp}$	2.273	2.125	2.044	2.141
	$g_{AOM}$	2.275	2.109	2.028	2.140
	A [MHz]	440	110	-90	150.3
<b>B</b>	$g_{exp}$	2.185	2.175	2.038	2.133
	$g_{AOM}$	2.222	2.209	1.995	2.144
	A [MHz]	290	190	-85	131.7
<b>C</b>	$g_{exp}$	2.266	2.133	2.044	2.141
	$g_{AOM}$	2.258	2.133	2.017	2.138
	A [MHz]	440	110	-90	150.3
<b>D</b>	$g_{exp}$	2.195	2.165	2.038	2.133
	$g_{AOM}$	2.219	2.200	1.995	2.140
	A [MHz]	265	215	-85	131.7
<b>E</b>	$g_{exp}$	2.275	2.123	2.044	2.141
	$g_{AOM}$	2.268	2.107	2.031	2.138
	A [MHz]	440	110	-90	150.3
<b>F</b>	$g_{exp}$	2.230	2.068	2.058	2.141
	$g_{AOM}$	2.251	2.071	2.057	2.128
	A [MHz]	475	-55	-65	118.3

As no crystal structure has been obtained at 20 K, no AOM calculations have been conducted. For the simulation of the spectra only elongated octahedra have been considered. However, five of these were simulated with parameters similar to the parameters used for cations **A** - **E** while one was simulated like cation **F** which was found to be more strongly distorted by XRD. The EPR parameters used for each group are summarized in table S7.

**Table S7.** EPR parameters used to simulate single crystal and powder spectra at  $T = 20$  K.

Fraction	Parameter	x	y	z	Iso
<b>5/6</b> "elongated"	$g_{exp}$	2.267	2.087	2.045	2.133
	$A(Cu)$ [MHz]	458	68	-85	147.0
<b>1/6</b> "cation F"	$g_{exp}$	2.23	2.060	2.053	2.114
	$A(Cu)$ [MHz]	485	-45	-40	133.3

The different HFC constants used for copper are also related to the structure of the copper cations as they strongly depend on the electronic ground state. Detailed accounts are given in several textbooks.<sup>2-4</sup> In short, the HFC constants are made up of an isotropic contribution  $a_{iso}$  and a dipolar contribution  $\bar{T}$ . The dipolar contribution for the two different, pure ground states are

$$\bar{T}_{y^2-z^2} = \frac{\mu_0}{4\pi} g_e \mu_B \gamma^2 \begin{pmatrix} -2 & 0 & 0 \\ 0 & 1 & 0 \\ 0 & 0 & 1 \end{pmatrix}$$

and

$$\bar{T}_{z^2} = \frac{\mu_0}{4\pi} g_e \mu_B \gamma^2 \begin{pmatrix} -1 & 0 & 0 \\ 0 & -1 & 0 \\ 0 & 0 & 2 \end{pmatrix}$$

Without making any assumptions about the isotropic contribution it becomes apparent, that the unique hyperfine coupling constant is aligned along x for the  $y^2-z^2$  ground state and along z for  $z^2$  ground state of the hypothetical, static octahedron with its axis of compression aligned along z. In our simulations, the largest coupling constant is placed along x for all elongated octahedra as required by theory. The intermediate coupling constant is often similar in magnitude to the smallest coupling constant but of opposite sign. We have no experimental means to decide about the sign of the coupling constant and the choice of a positive sign is arbitrary. For a pure  $y^2-z^2$  ground state, the negative sign is indicated. For the dynamically distorted, apparently compressed octahedra, the expected dipolar coupling tensor is the average of two dipolar tensors  $\bar{T}_{y^2-z^2}$  and  $\bar{T}_{x^2-z^2}$  (axis of elongation interchanging between x and y). The obtained average is therefore placing the unique HFC constant along z, in agreement with our simulations.

The measurement parameters of the single crystal EPR measurements are listed in table S8, those of the EPR measurements on powder samples in tables S9 and S10. A resolution of 1.0 - 1.2 measurement points per 0.1 mT of magnetic field was used for all measurements and found to be sufficient to obtain reliable spectra.

**Table S8.** Measurement parameters for the cw EPR measurements on single crystals of **1** at X-band frequencies. *MA* = modulation amplitude, *CT* = conversion time, *TC* = time constant, *P* = microwave power, *T* = temperature.

<b>MA [mT]</b>	<b>CT [ms]</b>	<b>TC [ms]</b>	<b>P [mW]</b>	<b>T [K]</b>
0.4	31.0	20.48	20.0	293
0.4	31.0	20.48	20.0	100
0.4	31.0	20.48	20.0	20

**Table S9.** Measurement parameters for the cw EPR measurements on powders of **1** at X-band frequencies. *MA* = modulation amplitude, *CT* = conversion time, *TC* = time constant, *P* = microwave power, *T* = temperature.

<b>MA [mT]</b>	<b>CT [ms]</b>	<b>TC [ms]</b>	<b>P [mW]</b>	<b>T [K]</b>
0.4	25	20.48	0.63	293
0.4	25	20.48	0.10	100
0.4	25	20.48	0.10	20

**Table S10.** Measurement parameters for the cw EPR measurements on powders of **1** at Q-band frequencies. *MA* = modulation amplitude, *CT* = conversion time, *TC* = time constant, *P* = microwave power, *T* = temperature.

<b>MA [mT]</b>	<b>CT [ms]</b>	<b>TC [ms]</b>	<b>P [mW]</b>	<b>T [K]</b>
0.45	21	20.48	0.13	293
0.45	21	20.48	$4.1 \cdot 10^{-4}$	100
0.45	21	20.48	$4.1 \cdot 10^{-4}$	20

#### **4. EPR measurements on frozen solutions of 1**

The full set of EPR parameters used to simulate the EPR spectra of frozen solutions of **1** is listed in Table S11. The same set of parameters has been used for both X- and Q-band spectra.

**Table S11.** Simulation parameters used to fit the EPR spectra of frozen solutions of **1** dissolved in MeOD/d<sub>6</sub>-DMSO (1.5:1) and CDCl<sub>3</sub>/d<sub>6</sub>-DMSO (5:1 and 3:1) and neat d<sub>6</sub>-DMSO. The HFC constants are given in MHz and their sign cannot be obtained from EPR spectra and has been chosen arbitrarily.

Solvent	$g_x$	$g_y$	$g_z$	$100 \cdot \Delta g_{xy}$	$A_x(\text{Cu})$	$A_y(\text{Cu})$	$A_z(\text{Cu})$
d <sub>6</sub> -DMSO/MeOD	2.2540	2.0960	2.0440	16.6	458	30	-89
d <sub>6</sub> -DMSO/CDCl <sub>3</sub>	2.2390	2.0540	2.0540	18.5	505	-40	-40
DMSO	2.2575	2.0750	2.0560	18.3	465	65	-95

Additionally, the HFC constants of the nitrogen donor atoms have been considered in all spectra in which nitrogen HFC structure was resolved. These were reproduced by accounting for six nitrogen atoms having axial HFC coupling tensors with  $A_{\parallel} = 41.5$  MHz and  $A_{\perp} = 33$  MHz.<sup>2</sup>

The measurement parameters for the frozen solution EPR at X-band frequencies measurements are listed in table S12.

**Table S12.** Measurement parameters for the cw EPR measurements on frozen solutions of **1** at X-band frequencies.  $MA$  = modulation amplitude,  $CT$  = conversion time,  $TC$  = time constant,  $P$  = microwave power,  $T$  = temperature.

Solvent	$MA$ [mT]	$CT$ [ms]	$TC$ [ms]	$P$ [mW]	$T$ [K]
d <sub>6</sub> -DMSO/MeOD	0.5	25	20.48	0.01	20
d <sub>6</sub> -DMSO/CDCl <sub>3</sub>	0.5	25	20.48	0.01	20
d <sub>6</sub> -DMSO	0.5	25	20.48	0.10	20

At Q-band frequencies pulsed EPR measurements have been conducted as the resonator is better suited for pulsed measurements than for cw measurements and the frozen solution samples gave rise to intense echo signals. The standard two pulse echo experiment consisting of a  $\pi/2$  and a  $\pi$  pulse (twice as long as the  $\pi/2$  pulse) separated by a time interval  $\tau$  was used to obtain the echo signal. The parameters are given in table S13.

**Table S13.** Measurement parameters for the pulsed EPR measurements on frozen solutions of **1** at Q-band frequencies.  $\pi/2$  = length of  $\pi/2$  pulse,  $\tau$  = separation between  $\pi/2$  and a  $\pi$  pulse,  $SRT$  = shot repetition time,  $P$  = microwave power,  $T$  = temperature.

Solvent	$\pi/2$ [ns]	$\tau$ [ms]	SRT [ $\mu$ s]	P [mW]	T [K]
d <sub>6</sub> -DMSO/MeOD	14	140	500	13.0	20
d <sub>6</sub> -DMSO/CDCl <sub>3</sub>	14	140	500	13.0	20
d <sub>6</sub> -DMSO	14	140	500	13.0	20

## 5. Constrained displacement of the donor groups

The distortions of the [Cu(tpy)<sub>2</sub>]<sup>2+</sup> ions have been treated along the lines of the pseudo Jahn-Teller (PJT) (A ⊕ B) ⊗ b framework.<sup>3-5</sup> Therefore, the distortions must result from JT active vibration modes. The displacement along the molecular x and y axes described by equation (2) in the main text is in agreement with the *b*<sub>1</sub> vibration in the PJT (A ⊕ B) ⊗ b framework:

$$b_1 = \frac{1}{2}(0 + 0 + x - x - y + y) \quad (S1)$$

Equation (S1) symbolically represents the displacements of the atoms N<sub>1</sub>, N<sub>2</sub>, N<sub>3</sub>, N<sub>4</sub>, N<sub>5</sub> and N<sub>6</sub> as labeled in Figure S5. Equation (1) in the main text describes the displacement of the atoms along the molecular z axis. This vibration has *b*<sub>2</sub> symmetry in the *D*<sub>2d</sub> point group and is not a JT active mode. The pyridine moieties cannot move independently because they are part of the rigid terpyridine ligand backbone. If the  $\varepsilon$  vibration displaces the external pyridine rings by a distance *d* along their Cu-N bond vectors as indicated in Figure S5 one obtains the following displacement vectors  $\overrightarrow{\Delta d}_i$  for atoms *i*:

$$\overrightarrow{\Delta d}_{N_3} = d \cdot \begin{pmatrix} \cos\alpha & 0 & -\sin\alpha \\ 0 & 1 & 0 \\ \sin\alpha & 0 & \cos\alpha \end{pmatrix} \begin{pmatrix} 1 \\ 0 \\ 0 \end{pmatrix} = d \cdot \begin{pmatrix} 0.974 \\ 0 \\ 0.225 \end{pmatrix}$$

$$\overrightarrow{\Delta d}_{N_4} = d \cdot \begin{pmatrix} \cos\alpha & 0 & \sin\alpha \\ 0 & 1 & 0 \\ -\sin\alpha & 0 & \cos\alpha \end{pmatrix} \begin{pmatrix} -1 \\ 0 \\ 0 \end{pmatrix} = d \cdot \begin{pmatrix} -0.974 \\ 0 \\ 0.225 \end{pmatrix}$$

The angle  $\alpha$  amounts to 13° and has been calculated according to Figure S5 and taking  $\beta = 154^\circ$  as observed in the crystal structure. For the central pyridine ring, which would not move if the ligands could be displaced in an unrestrained manner, vector addition yields

$$\overline{\Delta d}_{N_1} = \overline{\Delta d}_{N_3} + \overline{\Delta d}_{N_4} = d \cdot \begin{pmatrix} 0 \\ 0 \\ 0.45 \end{pmatrix}$$

and

$$\frac{|\overline{\Delta d}_{N_1}|}{|\overline{\Delta d}_{N_4}|} = 2.22$$

in agreement with the correlation coefficient obtained using the XRD data and given in equation (2).

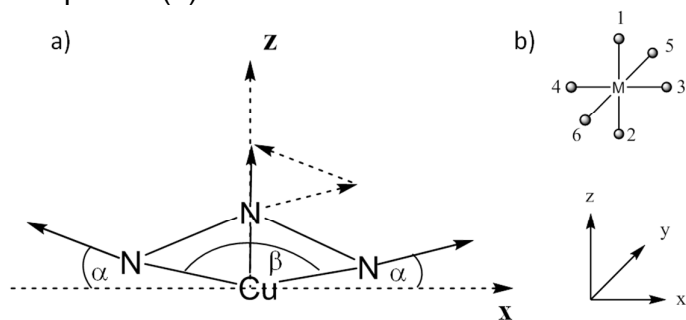


**Figure S5.** a) Vector picture of the ligand displacement. b) Numbering scheme for the  $b_{1g}$  vibration.

## 6. Theoretical considerations

### 6.1 $g$ values in dynamically distorted octahedra

Equations and discussions about the  $g$  tensors for static complex geometries are discussed by Ammeter<sup>4</sup> and in the book by Abragam and Bleaney.<sup>6</sup> The theory outlined therein does only provide results for static geometries, the same is true of the AOM calculations performed herein. If the axis of elongation is interchanging between the  $x$  and  $y$  direction this leads to apparently compressed structure in X-ray crystal structure determinations. Furthermore, average  $g$  values will be obtained.<sup>7</sup> Figure S6 illustrates the  $g$  values in dependence of the JT angle  $\phi$ .

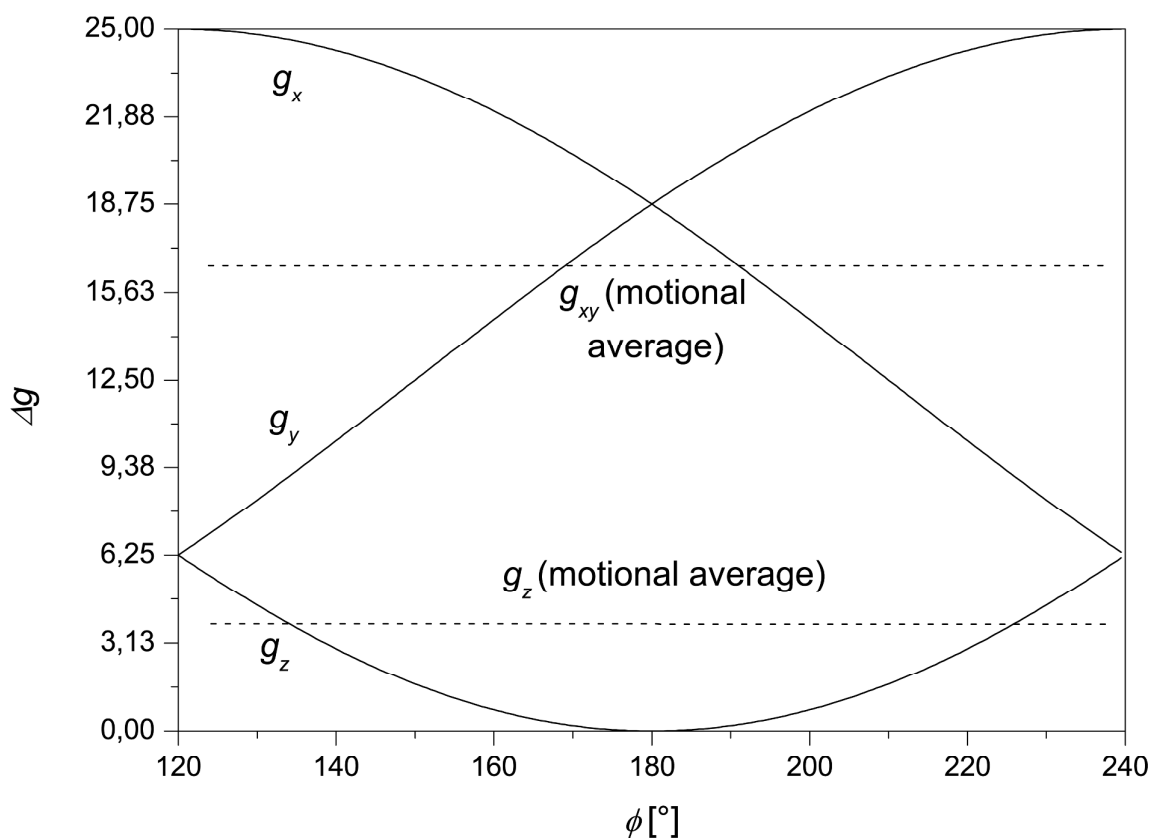


**Figure S6.** Dependence of the  $g$  shifts  $\Delta g$  and the JT angle  $\phi$ .<sup>4</sup> The dashed lines present estimated motional averages. An exact calculation is only possible if the vibrational trajectories were completely known.

Noteworthy, the  $g_x$  and  $g_y$  values are interchanged as  $\phi$  changes from  $120^\circ$  to  $240^\circ$ . Therefore, the average value of  $g_x$  and  $g_y$  is almost equal to the value expected for static compressed octahedra. The  $g_z$  value on the other hand is expected to be equal to  $g_e$  for an ideal compressed octahedron while it is larger than  $g_e$  in all other structures. Thus, the interconversion of the  $x$  and  $y$  axes leads to a  $g_z$  value which is considerably higher than  $g_e$  even for apparently compressed octahedral structures, in agreement with the observed high values for  $g_z$ .

## 6.2 The choice of the coordinate system

In order to obtain a molecular coordinate system which is independent of the observed distortions around the  $\text{Cu}^{2+}$  ion a group theoretical approach has been chosen. In this approach, a hypothetical undistorted  $[\text{Cu}^{\text{II}}\text{N}_6]$  octahedron of  $O_h$  symmetry is sequentially distorted using group/subgroup relations.<sup>1,8</sup> The first



symmetry reduction is a shortening along the Cu-N bonds to the central pyridine rings leading to  $D_{4h}$  symmetry. The  $z$  axis is then placed along the axis of highest symmetry which is identical to the Cu-N bonds involving the central pyridine rings. This axis remains the  $z$  axis in all subsequent distortions. Therefore, the axis of elongation is not assigned to the molecular  $z$  axis as it is done conventionally. The two different approaches are summarized in Figure S7.

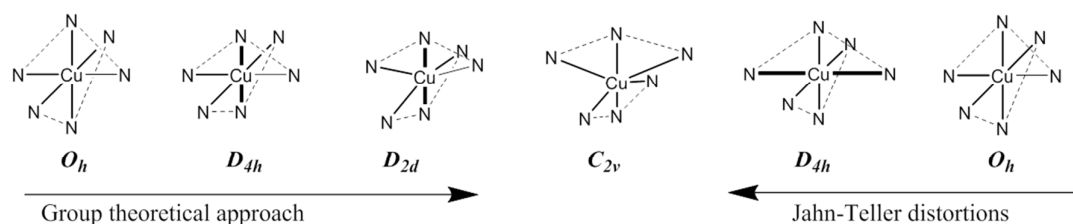


**Figure S7.** Conceptual, subsequent symmetry reductions of the hypothetical  $O_h$  symmetric  $[Cu^{II}N_6]$  complex cation using either group theoretical or JT conventions for the assignment of the molecular coordinate system. The arrows point towards coordination geometries of lower symmetry and the bold bonds indicate the corresponding molecular  $z$ -axis.

## 7. The color change from green to brown

During the work on **1** and other  $Cu^{2+}$ -bisterpyridine-complexes color changes from brown to green or the other way round were observed. With respect to the catalytic activity of many  $CuN_x$  complexes this matter was investigated in some detail.<sup>9</sup> The results obtained during the work here indicate, that  $Cu$ -tpy complexes are highly reactive with respect to redox reactions and that traces of  $Cu(I)$  are responsible for the occurrence of a brown color. Compound **1** itself is stable under most conditions. Application of heat and presence of protic solvents were found to promote the change of color from green to brown in **1**. Brown compounds turned immediately green when they were contacted with non-degassed solvents. A reduction of **1** was achieved by applying heat to a concentrated DMSO solution for a few minutes and was indicated by the change of color of the solution from green to dark brown. The color changed back to green within a few seconds when contacted to air. Extraction of that DMSO solution using hexane yielded a colorless hexane solution which contained biphenyl as evidenced by mass spectrometry ( $m/z = 154.1$ ) and NMR.

This finding leads to conclude that the reductant is the tetraphenylborate anion, as supposed in the literature.<sup>10</sup> This is also in accordance with the increased propensity

of **1** to turn brown if contacted with protic solvents.<sup>10</sup> Additionally, CV studies on related copper compounds suggest that the reduction of the copper center takes place in a similar potential range.<sup>11</sup>

This conclusion is further corroborated by the notably higher color stability of the hexafluorophosphate analogues of the various copper bisterpyridine compounds synthesized in our labs.

### **8. On the origin of the different static structures and dynamic behavior**

Two interactions have been considered in order to elucidate the origin of the different static structures and dynamic behaviors of cations **A - F**. The first of these interaction is the coulomb interaction between cations and anions. The coulomb interaction is distance dependent and therefore the arrangement of the anions with respect to the cations has to be rationalized. It turns out, that each cation is surrounded by four anions in a flattened tetrahedral geometry. Figure S8 show this arrangement and a similarity to the crystal structure of  $\alpha$ -SiO<sub>2</sub> is revealed. Table z lists the Cu - B separations  $d_1 - d_4$  for each tetrahedron along with some geometrical parameters which have been calculated from these distances.

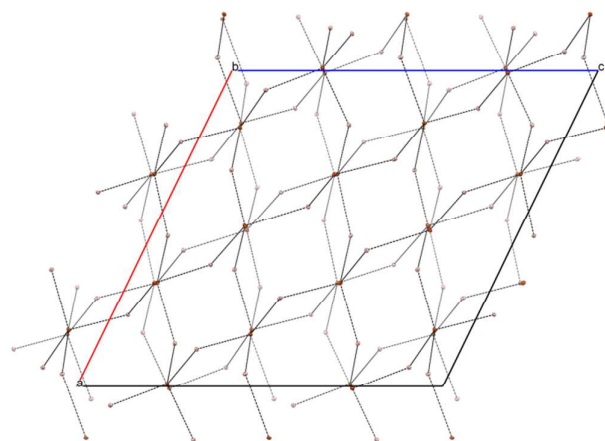


**Figure S8.** Crystal structure of **1** viewed along the *b* axis. Only Cu and B atoms are shown.

**Table S14.** Anion-cation distances using the B and Cu atoms as centers of the ionic charges.

	<b>A</b>	<b>B</b>	<b>C</b>	<b>D</b>	<b>E</b>	<b>F</b>
$d_1$ [Å]	6.713	6.904	6.616	6.881	6.942	6.369
$d_2$ [Å]	7.044	7.131	6.927	7.194	6.973	7.184
$d_3$ [Å]	7.222	7.231	7.635	7.217	7.048	7.668
$d_4$ [Å]	7.247	7.295	7.671	7.418	7.251	8.037
$d_1/d_2$	0.953	0.968	0.955	0.956	0.996	0.887
$d_1/d_4$	0.926	0.946	0.862	0.892	0.957	0.792
$\langle d \rangle^a$ [Å]	7.057	7.140	7.212	7.178	7.054	7.315
$V^b$ [Å <sup>3</sup> ]	89.101	92.311	95.132	93.764	88.987	99.236

<sup>a</sup>: Average of distances  $d_1 - d_4$ . <sup>b</sup>: Volume calculated using the  $\langle d \rangle$  values given in the table and an undistorted tetrahedral geometry with the B atoms at the vertices of the tetrahedron.

Inspection of table S14 reveals that the Cu - B separation is not suited to investigate the origin of the different static structures and dynamic behavior of cations **A - F**. This is most easily appreciated by comparison of the two most distorted and structurally similar cations **E** and **F**. For cation **F** the shortest Cu - B separation  $d_1$  is shorter by more than 11% as compared to the second shortest distance  $d_2$ . The difference to the longest distance  $d_4$  amounts to more than 20%. For cation **E** on the other hand the second shortest distance is almost as short as the shortest distance and even the longest Cu - B separation is only 4.3% longer than the shortest distance. Inspection of the average Cu - B separation reveals strong differences between **E** and **F** as well: the average Cu - B separation is more than 0.25 Å larger for cation **F** as compared to **E**. A similar argument can be given if cations **A** and **C** are compared to **B** and **D**. While **A** and **C** show distorted structures at 100 K, **B** and **D** are still dynamic. The geometric parameters listed in table S14 on the other hand are fairly similar for these cations. The analysis given above reduces the ions to point charges centered at the

Cu and B atoms, respectively. This is a strong simplification as both types of ions are voluminous complex ions. For both ions the charge is expected to be to some extent delocalized over the ligand or substituents, respectively. For that reason, specific cation anion interactions have been investigated. To that end, all C-H $\cdots$ C contacts shorter than 2.7 Å have been elucidated. 22 of such close contacts have been found, 21 of which having a proton of a terpyridine ring as the H-Bond donor. This large imbalance is expected as the terpyridine ligands are expected to be electron deficient while the phenyl substituents of the anions are expected to be electron rich. Closer inspection of the C-H $\cdots$ C contacts reveals that the distorted cations **A**, **C**, **E** and **F** appear to participate in more such H-Bonds than **B** and **D** (an average of 4 and 2.5 H-Bonds respectively, table S15). If H-bonds shorter than 2.6 Å are considered, the observed trend is confirmed, as six of the existing seven H-bonds are formed from the distorted cations **A**, **C**, **E** and **F**. (table S15).

**Table S15.** Number of H<sub>tpy</sub> $\cdots$ C-bonds shorter than 2.7 Å. Values in parentheses are the number of H<sub>tpy</sub> $\cdots$ C-bonds shorter than 2.6 Å.

	<b>A</b>	<b>B</b>	<b>C</b>	<b>D</b>	<b>E</b>	<b>F</b>
<b>H<math>\cdots</math>C-bonds</b>	5 (2)	1 (0)	3 (2)	4 (1)	3 (1)	5 (1)

## **9. References**

- (1) Harris, D. C.; Bertolucci, M. D. *Symmetry and Spectroscopy*, Dover Publications Inc.: Mineola, N. Y., USA, 1989.
- (2) Narr, E.; Zimmermann, H.; Godt, A.; Goldfarb, D.; Jeschke, G. *Phys. Chem. Chem. Phys.* **2003**, *5*, 3959–3967.
- (3) Allmann, R.; Henke, W.; Reinen, D. *Inorg. Chem.* **1978**, *17*, 378–382.
- (4) Ammeter, J.; Bürgi, H.; Gamp, E.; Meyer-Sandrin, V.; Jensen, W. *Inorg. Chem.* **1979**, *18*, 733–750.
- (5) Folgado, J. V.; Henke, W.; Allmann, R.; Stratemeier, H.; Beltran-Porter, D.; Rojo, T.; Reinen, D. *Inorg. Chem.* **1990**, *29*, 2035–2042.
- (6) Abragam, A.; Bleaney, B. *Electron paramagnetic Resonance of Transition Ions.*; Dover Publications Inc.: Mineola, N. Y., USA, 1986.
- (7) Halcrow, M. A. *Dalton Trans.* **2003**, 4375–4384.
- (8) Cotton, F. A. *Chemical Applications of Group Theory*, Wiley-Interscience, 1989.

- (9) Hoover, J. M.; Ryland, B. L.; Stahl, S. S. *J. Am. Chem. Soc.* **2013**, *135*, 2357–2367.
- (10) Pal, P. K.; Chowdhury, S.; Drew, M. G. B.; Datta, D. *New J. Chem.* **2002**, *26*, 367–371.
- (11) De Bruin, B.; Bill, E.; Bothe, E.; Weyhermüller, T.; Wieghardt, K. *Inorg. Chem.* **2000**, *39*, 2936–2947.

# Appendix D

## Single and Double Nitroxide Labeled Bis(terpyridine)-copper(II): Influence of Orientation Selectivity and Multispin Effects on PELDOR and RIDME

Andreas Meyer,<sup>i</sup> Dinar Abdullin,<sup>i</sup> Gregor Schnakenburg,<sup>ii</sup> Olav Schiemann<sup>i</sup>

Received 10th December 2015, published online 24th February 2016.

Reprinted with permission from

A. Meyer, D. Abdullin, G. Schnakenburg, and O. Schiemann, *Physical Chemistry Chemical Physics* **2016**, *18*, 9262 - 9271.

Copyright ©2016, Royal Society of Chemistry.

### Own contributions to the manuscript

- Synthesis and crystallization of the measured compounds.
- Evaluation of the geometrical parameters of the crystal structure.
- Conducting the EPR Measurements.
- Interpretation of the EPR spectra and the RIDME time traces.
- Calculation of multispin effects.
- Writing the manuscript.

---

<sup>i</sup> University of Bonn, Institute of Physical and Theoretical Chemistry, Wegelerstr. 12, 53115 Bonn, Germany.

<sup>ii</sup> University of Bonn, Institute of Inorganic Chemistry, Gerhard-Domagk-Strasse 1, 53121 Bonn, Germany.



Cite this: *Phys. Chem. Chem. Phys.*,  
2016, **18**, 9262

# Single and double nitroxide labeled bis(terpyridine)-copper(II): influence of orientation selectivity and multispin effects on PELDOR and RIDME†

Andreas Meyer,<sup>a</sup> Dinar Abdullin,<sup>a</sup> Gregor Schnakenburg<sup>b</sup> and Olav Schiemann<sup>\*a</sup>

A rigid, nitroxide substituted terpyridine ligand has been used to synthesize hetero- and homoleptic bis-terpyridine complexes of copper(II). The homoleptic complex represents a three-spin system, while the metal ion in the heteroleptic complex is in average bound to one nitroxide bearing ligand. Both complexes are used as model systems for EPR distance measurements using pulsed electron–electron double resonance (PELDOR or DEER) and relaxation induced dipolar modulation enhancement (RIDME) sequences. The results of both methods are analyzed using detailed geometric data obtained from the crystal structure of the homoleptic complex as well as information concerning ligand scrambling and the electronic structure of the copper center. In addition, both methods are compared with respect to their sensitivity, the extent of orientation selectivity and the influence of multispin effects.

Received 10th December 2015,  
Accepted 24th February 2016

DOI: 10.1039/c5cp07621h

www.rsc.org/pccp

## Introduction

Electron paramagnetic resonance (EPR) is a spectroscopic method which can be used to elucidate the structure of biological macromolecules.<sup>1,2</sup> In particular, pulsed EPR techniques that measure the dipolar coupling between unpaired electrons are used to obtain coarse grained structures of large protein complexes or oligonucleotides,<sup>3–6</sup> to follow their structural changes during function<sup>7–10</sup> or to localize paramagnetic centers within them.<sup>11,12</sup> Out of these so-called pulsed dipolar spectroscopy (PDS) methods, pulsed electron–electron double resonance (PELDOR or DEER)<sup>13–15</sup> is the most prominent one. However, it has been shown that double quantum coherence (DQC)<sup>16–18</sup> and relaxation induced dipolar modulation enhancement (RIDME)<sup>19–22</sup> may offer advantages in certain situations. Since PDS complements other analytical methods like X-ray crystallography and nuclear magnetic resonance, its application together with these methods has evolved as an important tool in structural biology.<sup>23,24</sup> In the standard experiment, two nitroxide spin labels are site-specifically attached to the desired positions in the biomolecule and the distance between the two nitroxide spin labels is determined using PELDOR. Repetition of the experiment using different labeling positions leads to geometrical

constraints, which can then be used to model the structure of or follow changes in the macromolecular structure.

In recent years, several studies have also been conducted with more than two labels in a biomolecular complex.<sup>25–30</sup> In these cases the so-called multispin effects have to be taken into account when analyzing the data.<sup>31–33</sup> Multispin effects arise when the echo intensity is modulated by the dipole–dipole interaction of a detected spin with two or more spins. In such a situation, one observes not only the dipolar coupling frequencies  $\nu_{\text{dip}}^i$  of each spin  $i$  but also combinations thereof, *i.e.* the sums and differences  $\nu_{ij} = \nu_i \pm \nu_j$ . Instead of using two artificially introduced spin labels one can also use paramagnetic centers which are intrinsic to the biomolecules of interest. These intrinsic spin centers can be organic radicals such as semiquinone or tyrosyl radicals<sup>34–40</sup> but also paramagnetic metal ions.<sup>41</sup> The EPR spectroscopic properties of metal centered spins can be more challenging than those of organic radicals due to fast relaxation times, orientation selectivity and spin density distribution.<sup>42–55</sup> In this work, the influence of multispin effects on both PELDOR and RIDME sequences in model complexes of types AB and AB<sub>2</sub> is investigated, where A and B represent copper and nitroxide spin centers, respectively. Furthermore, the performance of these two experiments is critically compared and the influence of the Jahn–Teller effect and ligand scrambling is investigated.

## Experimental

### Syntheses

**2,5-Dihydro-2,2,5,5-tetramethylpyrrole-N-oxyl-3-(4'-(4-(2,2':6',2''-terpyridyl)-phenylethynyl)-p-biphen-4-ylcarboxylate))-2,2':6',2''-terpyridinecopper(II) bis(hexafluorophosphate) (2a/2x).** 14.5 mg

<sup>a</sup> Institute of Physical and Theoretical Chemistry, Rheinische Friedrich-Wilhelms-University Bonn, Wegelerstr. 12, 53115 Bonn, Germany.

E-mail: schiemann@pc.uni-bonn.de

<sup>b</sup> Institute of Inorganic Chemistry, Rheinische Friedrich-Wilhelms-University Bonn, Gerhard-Domagk-Str. 1, 53121 Bonn, Germany

† Electronic supplementary information (ESI) available. CCDC 1441273. For ESI and crystallographic data in CIF or other electronic format see DOI: 10.1039/c5cp07621h

(0.085 mmol) of  $\text{CuCl}_2 \cdot 2\text{H}_2\text{O}$  was dissolved in 1.5 mL of a 3 : 1 mixture of acetonitrile and isopropanol. 43.5 mg (0.172 mmol) of silver hexafluorophosphate dissolved in 1.3 mL of acetonitrile was added to the resulting green solution leading to immediate precipitation of silver chloride. The solution was filtered off and subsequently mixed with 55.4 mg (0.083 mmol) of the ligand 4'-((4-(2,2':6',2''-terpyridyl)phenyl)ethynyl)biphen-4-yl-(2,2,5,5-tetramethyl-*N*-oxyl-pyrroline)-3-formate **1** and 19.3 mg (0.083 mmol) of 2,2':6',2''-terpyridine (tpy) dissolved in 5 mL of dichloromethane leading to the formation of a green solution and precipitate. 12 mL of isopropanol was added and the volume of the solution was reduced by about 30% under reduced pressure. The remaining colorless solution was filtered off at 0 °C yielding a green solid, which was washed two times with 2.5 mL of isopropanol and then dried *in vacuo* (yield 75%, 79.9 mg, 0.064 mmol). Owing to ligand scrambling, it was not possible to isolate **2a** as a pure substance. Samples, which have the same elemental composition as pure **2a**, are called **2x** in the following (see discussion). Anal. calcd for **2a**: C, 56.49, H, 3.70, N, 7.82. Found: C, 56.59; H, 3.85; N, 7.42. ESI-MS:  $m/z$  481.7 ( $[\mathbf{2a}-2\text{PF}_6]^{2+}$ ) (50%).

**Bis-(2,5-dihydro-2,2,5,5-tetramethylpyrrole-*N*-oxyle-3-(4'-(4-(2,2':6',2''-terpyridyl)-phenylethynyl-*p*-biphen-4-ylcarboxylate))-copper(II) bis(hexafluorophosphate) (**2b**)**. 15 mg (0.088 mmol) of  $\text{CuCl}_2 \cdot 2\text{H}_2\text{O}$  was dissolved in 1.5 mL of acetonitrile. 5.4 mL of a 0.033 M solution of silver hexafluorophosphate in acetonitrile was added to the resulting green solution leading to immediate precipitation of silver chloride. The solution was filtered off and subsequently mixed with 148 mg (0.222 mmol) of **1** dissolved in 8 mL of dichloromethane leading to the formation of a green precipitate. The remaining solution was filtered off at 0 °C yielding a green solid. The green solid was washed two times with 2.5 mL of a mixture of acetonitrile and isopropanol (1 : 3) and then dried *in vacuo* (yield 70%, 104.0 mg, 0.062 mmol). Crystals suitable for X-ray crystallography were obtained by layering the solution in acetone with cyclohexane. Anal. calcd for **2b**: C, 62.58, H, 4.18, N, 6.63. Found: C, 62.15; H, 4.35; N, 6.72. ESI-MS:  $m/z$  698.8 ( $[\mathbf{2b}-2\text{PF}_6]^{2+}$ ) (70%).

### EPR measurements and data analysis

All EPR experiments were performed on a Bruker ELEXSYS 580 EPR spectrometer. For the pulsed EPR measurements at X-band frequencies an MD5 dielectric ring resonator and an Oxford CF935 cryostat were employed. Using a 1 kW travelling wave tube (TWT) amplifier (Applied Systems Engineering) minimal  $\pi/2$  pulse lengths of 10 ns were obtained. Measurements at Q-band frequencies were performed using an ER 5106QT-2 resonator and an Oxford CF935 helium gas-flow cryostat. The MW pulses were amplified using a 150 W TWT amplifier manufactured by Applied Systems Engineering. Typical  $\pi/2$  pulse lengths of 14 ns were obtained using this set up. All EPR measurements were conducted at  $T = 20$  K. For the distance determination between the copper center and the nitroxides using the PELDOR sequence, the observer frequency was placed approximately 150 MHz to the high frequency side of the resonator dip. RIDME time traces were recorded at two different interpulse separations between the third and the fourth pulse.

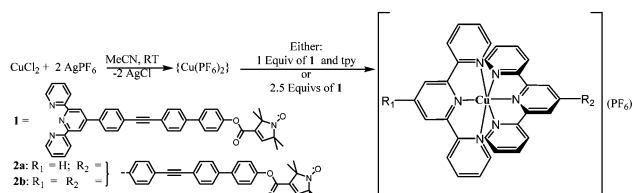
The refocused stimulated echo was used for data acquisition. Division of the time trace with large interpulse separation by the time trace with low interpulse separation leads to suppression of ESEEM artifact peaks.<sup>19–21</sup> The measurement parameters are detailed in the ESI† To compare the signal to noise ratios in PELDOR and RIDME for **2b**, both time traces are fixed to the same length, here 1200 ns, and are averaged over all field positions measured. The RIDME time trace is then divided by the RIDME reference time trace and the result is normalized to 1 at  $t = 0$ . Then the PELDOR and RIDME time traces are corrected for the background decay and are renormalized. This yields for both time traces  $S = 1$ . Then the signal intensity  $S$  is multiplied by the modulation depths  $V_i$  of the two time traces.  $V_i$  is then divided by the average noise  $\langle N \rangle$  of the time traces, yielding  $V_i/\langle N \rangle$ . In order to account for different measurement times this value is then divided by the square root of the measurement time yielding  $S/N = V_i/(\langle N \rangle \sqrt{t})$ .

EPR spectra were simulated using the EasySpin<sup>56</sup> program package. The program PeldorFit<sup>57</sup> was used to analyze the PELDOR time traces. DeerAnalysis<sup>58</sup> (DA) was employed for the analysis of RIDME time traces. The used pulse sequences are depicted in the ESI† along with the measurement parameters and the EPR parameters obtained from simulation of the obtained data.

## Results and discussion

### Synthesis, chemistry and structures of **1**, **2a** and **2b**

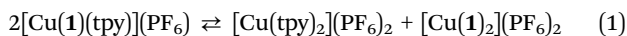
In order to study multispin effects in a model system containing different types of spin centers, a complex that contains a paramagnetic metal center and either one or two nitroxides was necessary. Inspired by a publication from the Jeschke lab,<sup>42</sup> this was realized by attaching the chelating terpyridine ligand **1** either one or two times to a copper ion forming the hetero- $[\text{Cu}(\mathbf{1}(\text{tpy}))^{2+}]$  **2a** (tpy = 2,2':6',2''-terpyridine) or homoleptic  $[\text{Cu}(\mathbf{1})_2]^{2+}$  **2b** complexes, respectively (Scheme 1). The nitroxide unit in **1** is connected to the terpyridine ring *via* a rigid phenylene-acetylene framework to ensure a relatively narrow distance distribution.<sup>42,43</sup> The carboxylate group was introduced to prevent exchange interaction between the copper and the nitroxide spin centers.<sup>43,47</sup> The synthesis of **1** has been described elsewhere<sup>59</sup> and is a slight modification of the procedure reported by Ackermann *et al.*<sup>60</sup> Terpyridine complexes of copper are known to be labile with respect to ligand exchange according to eqn (1).<sup>61</sup> As the ligand exchange proceeds very fast the equilibrium concentrations of the constituting species are reached within a



Scheme 1 Synthesis of **2a** and **2b**.



few seconds.<sup>61</sup> Therefore, a stepwise synthesis involving the isolation of a precursor compound (e.g.  $[\text{Cu}(\text{tpy})\text{Cl}_2]$ ) appears not to be sensible and both ligands have been added simultaneously during the synthesis of **2a**. In addition, the enthalpy of the fast ligand exchange reaction is expected to be negligible; thus the maximization of the mixing entropy is the only factor determining the equilibrium concentrations of the species in eqn (1).



The mixing entropy is maximized if all species in eqn (1) occur in equal amounts. Thus, no samples of pure **2a** could be obtained. Instead, samples of the average composition of **2a** are expected to contain **2a**, **2b** and  $[\text{Cu}(\text{tpy})_2](\text{PF}_6)_2$  in equal concentrations and are therefore called **2x** from here on. Initially, **2x** and **2b** have been synthesized as tetraphenylborates. However, the tetraphenylborate complexes tend to turn brown in the solid state and in solution at room temperature in the absence of air, which was attributed to the reduction of the copper complex cation by the tetraphenylborate anion.<sup>62</sup> Therefore, copper(II) hexafluorophosphate was generated *in situ* by reacting the dihydrate of copper(II) chloride with silver hexafluorophosphate in acetonitrile. Under these conditions, silver chloride precipitates and the remaining solution can be separated and used as a source for both copper(II) cations and hexafluorophosphate anions.

Using the hexafluorophosphate anion also enabled the crystallization of **2b** (Fig. 1a). The crystal structure reveals two crystallographically independent cations. At 123 K, one of these cations is subjected to dynamic Jahn–Teller distortions, while the other one experiences static distortions (see ESI<sup>†</sup>), similar to observations made on the unsubstituted copper bisterpyridine complex.<sup>63,64</sup> An average nitroxide copper distance of 26.49 Å is found for the two independent cations (see ESI<sup>†</sup>). The average nitroxide–nitroxide separation is slightly less than twice the average nitroxide–copper distance and amounts to 52.00 Å, due to the slightly bent geometry with average bending angles of  $157.9^\circ$  between the two nitroxides and the orientation of the other components of the  $g$  tensors since the nitroxides can assume various torsional angles with respect to each other and also with respect to the copper center (see ESI<sup>†</sup>). Finally, another noteworthy feature of the crystal structure is the relative orientation of the spin centers with respect to each other. The  $g$  tensor frameworks of the spin centers are illustrated in Fig. 1a. The alignment of the  $x$  axes of the  $g$  tensors of both nitroxides and the  $g_z$  axis of the copper center deviates from collinearity by an angle of  $35.0 \pm 6.4^\circ$ . Note that the geometry of the copper center can be described as an elongated octahedron with approximate  $D_{2d}$  symmetry.<sup>64</sup> The  $z$  axis of the copper center was chosen in accordance with the theoretical requirements for the  $D_{2d}$  group and is not identical to the axis of elongation (Fig. 1b). A similar angle of  $33.2 \pm 2.3^\circ$  is found for the  $g_x$  axes of the nitroxides and the interspin vector between the copper and the nitroxides (Fig. 1). Assuming that the rotation of the nitroxides around the ester linkage is the dominant motion of the molecules, the orientations of the  $x$  axes of the nitroxides, the  $z$  axis of the copper center and the parallel component of the dipolar

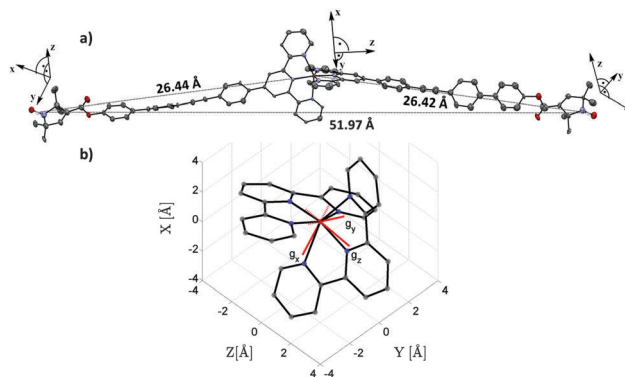


Fig. 1 (a) Molecular structure of the complex cation of **2b** as revealed by X-ray crystallography. The local  $g$  tensor coordinate systems of the spin centers are indicated.<sup>64</sup> The coordinate systems of the hyperfine coupling tensors are assumed to be collinear with the  $g$  tensor coordinate systems. Color code: orange = copper, blue = nitrogen, grey = carbon, red = oxygen. Hydrogen atoms have been omitted for clarity. (b) Orientation of the  $g$  tensor coordinate system as predicted by DFT (see ESI<sup>†</sup> for details). The coordination polyhedron can be described as an elongated octahedron with approximate  $D_{2d}$  symmetry. This group requires the  $z$  axis to be along Cu–N bonds of the central pyridine rings of each tpy ligand. The elongation occurs along the  $g_x$  direction.

coupling tensor are strongly correlated. This is not true for the copper center. All distances and angles have been measured from the middle of the N–O bonds of the nitroxides. The structural information obtained from the crystal structure of **2b** provides a comparison for the PELDOR derived geometric parameters of **2x** and **2b**. The crystallographically found interspin distance between the nitroxide and the copper centered spins is mostly determined by the structure of the rigid ligand and is neither expected to deviate heavily in solution nor between **2a** and **2b**. The immediate coordination sphere of bis(terpyridine) complexes was shown to be similar in frozen solution and the crystal phase in the sense that an elongated octahedral coordination with approximate  $D_{2d}$  symmetry is observed in both cases, frozen solution and crystal phase (Fig. 1b).<sup>64,65</sup>

### Solvent dependence of the EPR parameters

**2x** and **2b** consist of (bis(terpyridine))copper complexes. The EPR spectrum of the unsubstituted (bis(terpyridine))copper complex  $[\text{Cu}(\text{tpy})_2]^{2+}$  was found to depend on the choice of solvent.<sup>64</sup> For  $[\text{Cu}(\text{tpy})_2]^{2+}$  it was observed that using a mixture of methanol and DMSO leads to orthorhombic EPR signals of the copper centered spin ( $g_x > g_y > g_z$ ), while a mixture of chloroform and DMSO leads to axial EPR signals ( $g_x > g_y = g_z$ ). These changes have been interpreted in terms of a differing extent of Jahn–Teller (JT) elongation along the molecular  $x$  axis of the copper center brought about by the molecular  $b_1$  vibration.<sup>59</sup> Within this framework, the JT elongation is accompanied by one ligand approaching the metal center and a simultaneous departing motion of the other ligand. Since the axial EPR signal of  $[\text{Cu}(\text{tpy})_2]^{2+}$  in a mixture of chloroform and DMSO corresponds to a degree of elongation which was not observed in the crystal structure, it was suggested that the distal ligand might be replaced by solvent molecules if the molecular

$b_1$  vibration proceeds too far.<sup>66</sup> For **2x** and **2b**, a mixture of DMSO and methanol also led to rhombic EPR signals of the copper centered spin, while mixtures of deuterated chloroform and DMSO produced axial EPR signals. Importantly, we noticed that the observed changes occur less reliably when protonated chloroform was used instead of deuterated chloroform. As deuterated chloroform is not stabilized and may contain acid, we repeated the experiments in methanolic solutions to which sulfuric acid was added (methanol/DMSO ratio 1.5 : 1 and 0.1 M sulfuric acid). It was indeed found that addition of acid to samples of  $[\text{Cu}(\text{tpy})_2]^{2+}$ , **2x** and **2b** also yields axial EPR signals. The EPR spectra of **2x** and **2b** in neutral and acidic mixtures of DMSO and methanol (1 : 1.5) at two MW frequencies are shown in Fig. 2. The spectra obtained in neutral solutions are typical for nitroxides and copper terpyridine complexes with the copper signal appearing to be orthorhombic ( $g_y \approx 2.093$  and  $g_z \approx 2.042$ ).<sup>64</sup> In acidic solution (or  $\text{CDCl}_3/\text{DMSO}$  mixtures), the copper signal becomes axial with  $g_y \approx g_z \approx 2.062$ . Furthermore, the  $g_x$  value of the copper centered spin increases noticeably in addition to the copper hyperfine coupling constant along that direction. The observed EPR parameters agree with those found for the unsubstituted complex  $[\text{Cu}(\text{tpy})_2]^{2+}$ .<sup>64</sup>

Importantly, the spectral width of the copper signal exceeds the spectral width of the nitroxide by a factor of more than 10 in both orthorhombic and axial situations. Furthermore, the relaxation processes are much faster for the copper spins than for the nitroxide spins. As an example, the approximate spin lattice relaxation time of the nitroxide at X-band frequencies amounts to 3000  $\mu\text{s}$  in **2x** and **2b** at 20 K and thus exceeds the spin lattice relaxation time of copper in the rhombic situation by two orders of magnitude (ESI<sup>†</sup>). In the following discussion, the focus will be first on the orthorhombic situation.

### PELDOR for the orthorhombic copper EPR signals

**Inter-nitroxide distance and ligand exchange.** The inter-nitroxide separation was measured for **2x** and **2b** (Fig. 3). Interestingly, modulations are observed for both **2x** and **2b**.

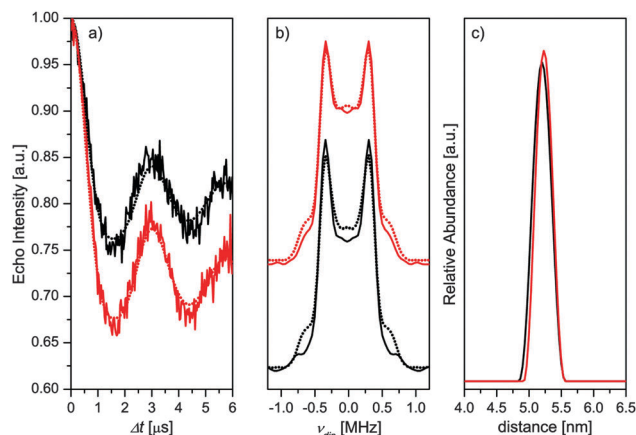


Fig. 3 Results of the Q-band inter-nitroxide distance measurements of **2x** (black lines) and **2b** (red lines). (a) Time traces (dotted lines: fit using DeerAnalysis), (b) Fourier transforms of the time traces and (c) the resulting distance distributions.

This suggests that **2x** is indeed subject to ligand scrambling as described by eqn (1) and is not identical to complex **2a**, which has only one nitroxide and thus no nitroxide–nitroxide distance. The frequencies and the corresponding distance distributions with the most probable distance of  $52.3 \pm 1.2 \text{ \AA}$  are within error the same for both samples and correspond to the nitroxide–nitroxide distance of 52  $\text{\AA}$  found in the X-ray structure. The modulation depth  $V_{d,2b} = 30\%$  found for **2b** corresponds, for the used pump pulse length of 18 ns, to two coupled nitroxides and thus indicates the absence of ligand replacement by solvent. The reason for the occurrence of the nitroxide–nitroxide distance in samples of **2x** is due to the aforementioned ligand scrambling leading to the formation of **2b** and of  $[\text{Cu}(\text{tpy})_2]^{2+}$  in solutions of **2x**. The observed modulation depths allow validating the expected equilibrium concentrations of the species given in eqn (1) in **2x**. The modulation depth  $V_{d,2x}$  of the nitroxide–nitroxide PELDOR experiment of **2x** can be calculated using

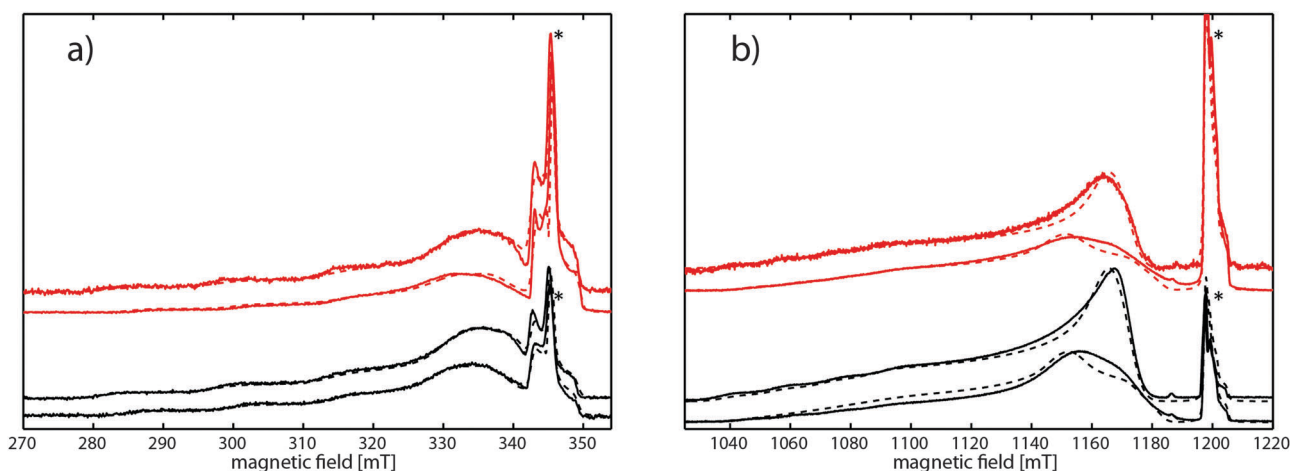


Fig. 2 Echo detected field swept EPR spectra (full lines) and their simulations (dashed lines) of **2x** (black lines) and **2b** (red lines) at (a) X-band frequencies and (b) Q-band frequencies. For both **2x** and **2b** two spectra are given. The lower one of the two spectra corresponds to a neutral solution of DMSO and methanol (1 : 1.5), while the upper one corresponds to an acidic solution in the same solvent system (see text for discussion). The nitroxide parts of the EPR signals are marked with asterisks.

Table 1 Parameters for the calculation of modulation depths

Species	$V_{\lambda,s}$ (%)	$I_{rel}$	$c_{eq,s}$ (%)	$V_{\lambda,s}I_{rel,s}c_{eq,s}$ (%)
[Cu(tpy) <sub>2</sub> ](PF <sub>6</sub> ) <sub>2</sub>	0	0	33.3	0
<b>2a</b>	0	1	33.3	0
<b>2b</b>	30	2	33.3	20

the contributions of each species from eqn (1). With the modulation depths  $V_{\lambda,s}$ , the relative echo intensities  $I_{rel,s}$  of the nitroxide signal and the equilibrium concentrations  $c_{eq,s}$  of the individual species  $s$ , this leads to eqn (2):

$$V_{\lambda,2x} = \sum_s (V_{\lambda,s} I_{rel,s} c_{eq,s}) \quad (2)$$

The modulation depth of  $V_{\lambda,2x} = 21\%$  observed in **2x** amounts to roughly 2/3 of  $\lambda_{2b}$ . Thus, the observed value agrees with expectations based on entropy driven ligand scrambling (Table 1).<sup>60</sup>

**Nitroxide-copper distance.** PELDOR measurements with selective pulses on copper centered spins are subject to strong orientation selectivity effects.<sup>42–46</sup> Orientation selectivity occurs if the orientations of pumped and observed spin centers are correlated. The extent of orientation selection observed in the PELDOR experiment is determined by several factors including the width of the EPR signals of both types of spins, the bandwidth of the used pulses and the choice of the position for pumping and probing in the corresponding EPR signals (ESI†). Fig. 4 shows the results of the X-band PELDOR measurements on **2x** and **2b**. The detection pulses were applied on the copper signal and positioned +150 MHz to +600 MHz from the pumping pulse centered on the maximum of the nitroxide spectrum. This yields different PELDOR time traces depending on the position of the detection pulses.

PELDOR measurements at Q-band frequencies were not feasible because the frequency separation between the copper and nitroxide part of the spectrum is larger than the bandwidth of the resonator. Fig. 4 reveals high selectivity for the parallel component of the dipolar coupling tensor for a frequency offset of 150 MHz, which decreases as the frequency offset is increased for both **2x** and **2b**. This finding is in complete agreement with

expectations based on the orientation of the  $g$  tensor frames as shown in Fig. 1. The strong orientation selectivity prevented an analysis of the PELDOR time traces using DeerAnalysis, even after summing up the time traces of all frequency offsets. Due to the limited bandwidth of the resonator, further increasing the range of frequency offsets was not possible either. Therefore, the time traces of **2x** and **2b** have been analyzed using the program PeldorFit which takes into account orientation selectivity explicitly (Fig. 4).<sup>57</sup> The EPR parameters obtained from fitting the field sweep EPR spectra as well as the measurement parameters used for the PELDOR experiments have been used as input for the PeldorFit simulations. The resulting fits show good agreement between simulated and experimental time traces. Moreover, the geometric parameters obtained from the fits are in accordance with those obtained from studies on the unsubstituted bisterpyridine complex [Cu(tpy)<sub>2</sub>]<sup>2+</sup> and from the crystal structure of **2b** (ESI†). Most noteworthy, PeldorFit yields an angle between the copper-nitroxide joining vector and the  $g_x$  axis of the copper centered spin of  $\zeta = 81.4 \pm 2.8^\circ$  and  $82.1 \pm 1.0^\circ$  for **2x** and **2b**, respectively, in agreement with the geometry shown in Fig. 1. The copper-nitroxide distances obtained from the simulation of the PELDOR time traces of **2x** and **2b** amount to 25.8 Å and 26.0 Å, respectively, both with a standard deviation of 1 Å. The observed values are in good agreement with the distances obtained from the crystal structure (average distance of 26.49 Å). A slight deviation to shorter distances is reasonable, since the copper center spin is partially delocalized on the ligating nitrogen nuclei.<sup>43,67</sup> The width of the distance distribution on the other hand does not reflect the spatial extent of the spin delocalization and has a large error.

The influence of multispin effects can be discussed based on the theory given by von Hagens *et al.*, which describes the expected modulation depth  $V_{\lambda}$  in terms of the inversion efficiency  $\lambda$  of the pumped spins.<sup>31</sup> The theory also accounts for the contribution of pair and three-spin correlation functions ( $P$  and  $T$ , respectively) to the PELDOR form factor. The resulting equations for the form factors  $F$  of two- and three-spin systems are given as

$$F_2 = 1 - \lambda + \lambda P_2 \quad (3)$$

$$F_3 = 1 - 2\lambda + \lambda^2 + \lambda(1 - \lambda)P_3 + \lambda^2 T_3 \quad (4)$$

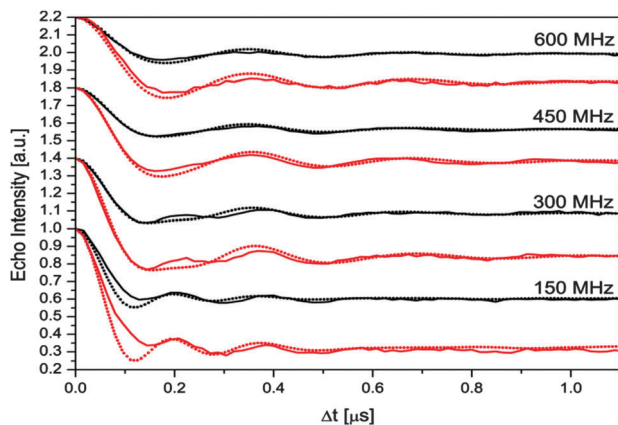


Fig. 4 PELDOR time traces of **2x** (black, full lines) and **2b** (red, full lines) and their simulations (dotted lines).

The expected modulation depths  $V_{\lambda}$  correspond to the sum of the coefficients of the pair and the three-spin correlations. Note that a weighted average of eqn (3) and (4) needs to be used for **2x** to account for the occurrence of different copper(II) complexes in these samples. Experimentally, the observed modulation depth  $V_{\lambda,exp}$  for **2b** is higher by about a constant factor of 77% compared to **2x** at all frequency offsets. While this finding seems to be surprising, the modulation depths observed for **2x** and **2b** could be simulated. In these simulations, the same orientation selectivity as derived by PeldorFit was used. Multispin effects have been introduced retroactively taking into account eqn (3) and (4) and the chemical equilibrium described by eqn (1) (Table 2; see ESI† for more details). The good agreement between simulated and observed modulation depths

**Table 2** Experimental and calculated modulation depths  $V_i$  (%)

$\Delta\nu$ (MHz)	$V_{i,\text{exp}}$ ( <b>2a</b> )	$V_{i,\text{cal}}$ ( <b>2a</b> )	$V_{i,\text{exp}}$ ( <b>2b</b> )	$V_{i,\text{cal}}$ ( <b>2b</b> )
150	40	42	70	70
300	31	30	56	56
450	24	23	42	43
600	21	20	37	38

implies that the theory outlined by von Hagens *et al.* is applicable to the model spin systems investigated in this work. Since the observed modulation depths are relatively high the occurrence of combination frequencies might be expected. These could manifest themselves in marked changes of the form factor; for example extrema of the time traces could occur at other positions or further extrema could occur.<sup>28,31</sup> Experimentally, only at the two lowest frequency offsets with the highest modulation depths slight differences between the time traces of **2x** and **2b** are observed, aside from the increased modulation depths. To check whether or not these deviations are caused by multispin effects, the time traces of **2b** have been recorded using an attenuation of 20 dB for the ELDOR channel while leaving all other measurement parameters unchanged. This led to a decrease in the modulation depth of almost 80% and to form factors of **2x** and **2b** that are superimposable (Fig. 5), supporting the idea that these differences are due to multispin effects. Also, no marked changes in the form factor are observed if multispin effects are introduced subsequently in the PeldorFit time traces as explained above (Fig. S20 and S21 in the ESI†). Importantly, the slight deviations are negligible when the PELDOR time traces are analyzed using PeldorFit and the obtained geometrical parameters for **2x** and **2b** are consequently nearly identical.

**RIDME for the orthorhombic copper EPR signals.** Owing to the faster relaxation of the copper centered spin as compared to the nitroxide spins the RIDME experiment is a valuable alternative to the PELDOR experiment.<sup>21</sup> In the RIDME experiment, the nitroxide spins are observed and the copper centered spin

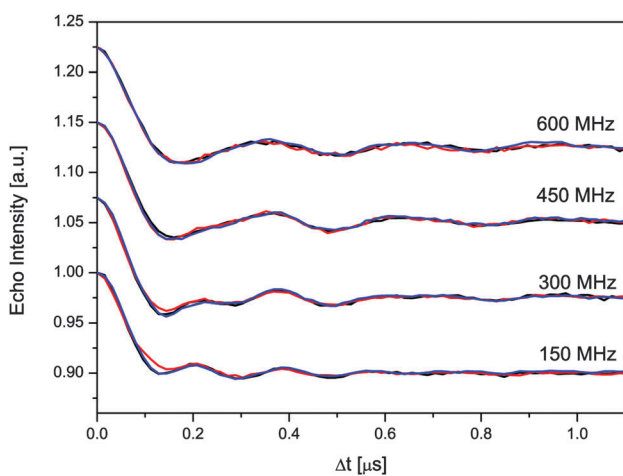


**Fig. 5** PELDOR time traces scaled to a modulation depth of 10% of **2x** (black lines), **2b** (red lines) and **2b** using an ELDOR attenuation of 20 dB (blue lines).

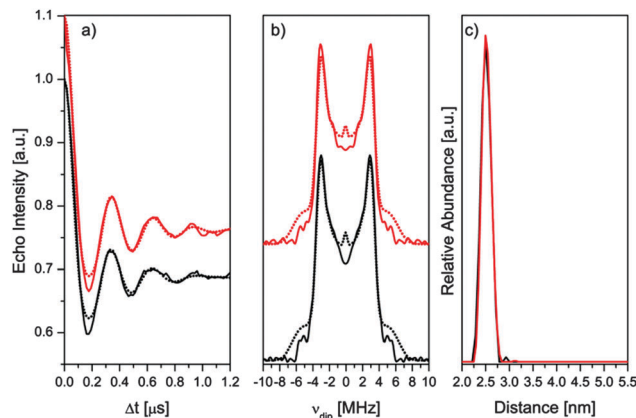


**Fig. 6** RIDME time traces of **2x** (black lines) and **2b** (red lines) averaged over five field positions recorded at X-band frequencies, their Fourier transforms and the resulting distance distributions and simulations thereof obtained using DeerAnalysis (dotted lines). The time traces at the individual field positions are shown in the ESI.†

flips during the large time interval  $T$ . Consequently, orientation selectivity should be less pronounced in the RIDME experiment, as the smaller width of the nitroxide EPR signals leads to a less selective excitation. This assumption was confirmed by conducting the dead time free five-pulse RIDME experiment depending on the field position (ESI†).<sup>20</sup> However, the obtained time traces still have been summed up in order to further reduce the extent of orientation selection, with the results being shown in Fig. 6.

The field averaged RIDME time traces were analyzed using DeerAnalysis. The obtained distance distribution yields a distance of 25.1 Å for both **2x** and **2b** ( $\sigma = 1.0$  Å), which is in reasonable agreement with the results obtained after analyzing the PELDOR time traces using PeldorFit. No multispin effects have been observed in the RIDME experiments at X-band frequencies when going from **2x** to **2b**, as indicated by the identical modulation depths and coinciding form factors. The absence of multispin effects is expected, as only the copper spin changes its orientation during the large interpulse separation  $T$ . Of course, measurements on **2b** are more sensitive than those on **2x** owing to the twofold higher effective concentration of nitroxide in **2b**.

Normalizing both data sets to identical measurement times (*i.e.* dividing by the square root of the total measurement time) yields at X-band frequencies S/N values of 4 and 11.5 for RIDME and PELDOR, respectively. Thus, the signal to noise ratio for the field averaged RIDME experiment is about a factor of three worse than the field averaged PELDOR experiment. The lower sensitivity of RIDME compared to PELDOR seems to be in contrast with the previous results obtained on an Fe(III) sample.<sup>21</sup> However, the modulation depth in the PELDOR experiment at 150 MHz on **2x** is four times as high as for the Fe(III) sample. Furthermore, the spectral density of **2x** and **2b** has higher values at the positions used for observation than in the case of the Fe(III) sample. Therefore, the PELDOR experiment is more sensitive for **2x** and **2b** than for the Fe(III) sample. The opposite is true for the



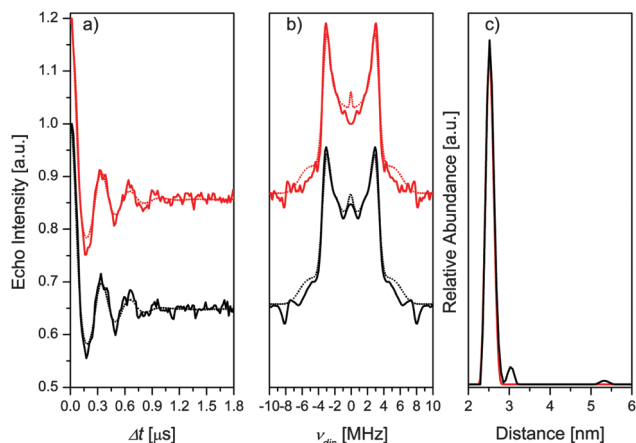


Fig. 7 RIDME time traces and their Fourier transforms at different effective  $g$  values of the nitroxide signal position recorded at Q-band frequencies of **2a** (black lines) and **2b** (red lines). The summed time traces have been simulated (dotted lines) and transformed into distance distributions using DeerAnalysis. The time traces at the individual field positions are shown in the ESI.†

RIDME experiment, as the nitroxide in **2x** and **2b** has a short phase memory time  $T_M$  of only  $\sim 550$  ns. This  $T_M$  is much shorter than the corresponding value in the Fe(III) sample and strongly decreases the sensitivity of the RIDME experiment for **2x** and **2b**. Therefore, RIDME is less sensitive in the case at hand.

Additionally, RIDME experiments have been conducted at Q-band frequencies as well (Fig. 7). Inspection of Fig. 7 reveals no differences in the time traces of **2x** and **2b** in agreement with the results obtained at X-band frequencies. In contrast to the measurements at X-band frequencies, orientation selectivity appears to be important for the RIDME experiment at Q-band frequencies, as apparent from the strong field dependence of the form factors and their Fourier transforms (ESI†). Summation of all time traces yields a time trace in which orientation selection is strongly reduced. Conversion of the summed time trace into a distance distribution using DeerAnalysis yields  $25.3 \pm 1.0$  Å as the most probable distance in excellent agreement with the result obtained at X-band frequencies. The RIDME modulation depth at Q-band frequencies is very similar to that at X-band frequencies. This is in accordance with expectations, as the modulation depth in RIDME experiments is a consequence of spontaneous spin flip events at the faster relaxing copper centered spin. These spontaneous spin flips occur to an extent of up to 50% independent of the MW frequency, because the time window  $T$  is chosen accordingly. Owing to the higher polarization and the better filling factor at Q-band frequencies, the sensitivity of the RIDME experiment is almost eight times higher than that at X-band frequencies. Correspondingly, Q-band RIDME is also 2.3 times more sensitive than the X-band PELDOR experiment. A Cu(II)-nitroxide PELDOR experiment at Q-band frequencies is not possible, because the pump pulse on the nitroxide and the probe pulses on the Cu(II) signal cannot be accommodated within the same cavity.

**The effect of very strong Jahn–Teller elongation and the influence of the solvent.** As shown in Fig. 2, the EPR parameters

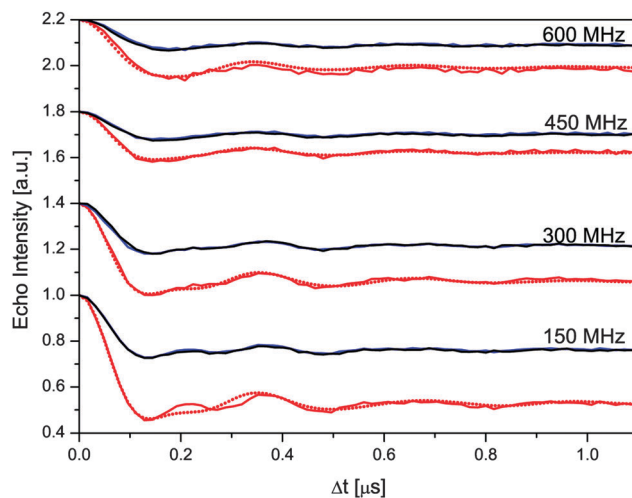


Fig. 8 PELDOR time traces of **2a** (black lines) and **2b** (red lines) in acidic solution. The blue time trace is the time trace of **2b** scaled to the same modulation depth as **2a**. The time traces of **2b** have been simulated using PeldorFit (red, dotted lines).

of the copper EPR signal change heavily in acidic solution. The changes in the EPR parameters should be reflected in the EPR distance measurements as well. This is indeed the case, as can be seen by comparing Fig. 4 (neutral) and Fig. 8 (acidic).

Three major changes are observed: first, the orientation selectivity for the parallel component of the dipolar coupling tensor is reduced in acidic solution (Fig. 8) as compared to the time traces in neutral solution (Fig. 4). The reason for this is that the selectivity for the  $g_z$  value of the copper center corresponds to the selection of the parallel coupling component. In neutral solution, rhombic spectra are observed and  $g_z$  is considerably lower than  $g_y$ . In acidic solution on the other hand, the EPR spectra of **2x** and **2b** are axial with  $g_y \approx g_z$ . Therefore, the selectivity for  $g_z$  and thereby also for the parallel component of the dipolar coupling tensor is decreased in acidic solution. The second observation concerns the reduced modulation depths for all time traces of **2x** and **2b**. This is an indication of the complete removal of one ligand. Furthermore, in acidic solution the modulation depth for **2x** is 50% of the modulation depth of **2b** for all time traces. Finally, the time traces of **2x** and **2b** are now superimposable while deviations are found in neutral solution. While the first observation could be explained in terms of a different degree of JT elongation, this is not true for the other two observations. Instead, all of these observations can be explained by assuming the following reaction to occur in acidic solution:



Only the removal of the tpy ligands is considered in eqn (5), but it is suggested that one or more solvent molecules replace these ligands. Furthermore, it is also known that terpyridines can be protonated, which would also help to detach one of the ligands from the central copper(II) ion.<sup>68</sup> For **2b**,  $\text{L} = \text{L}' = 1$  and both product complexes are identical, while for **2a**  $\text{L} = \text{tpy}$  and  $\text{L}' = 1$  leading to different product complexes, only one of which gives

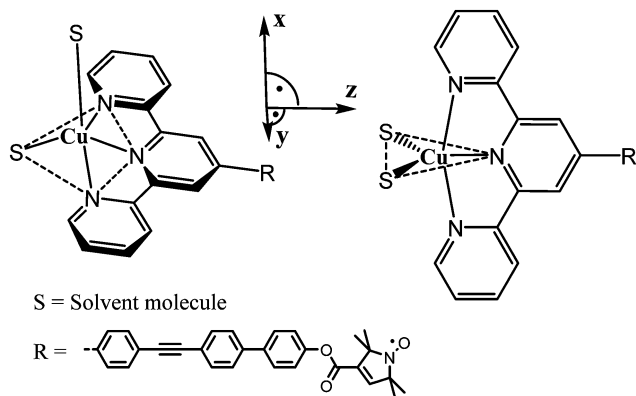


Fig. 9 Proposed complex geometries for fivefold coordinated copper centers originating from loss of one terpyridine ligand from **2a** and **2b** and the corresponding, approximate  $g$  tensor coordinate system. The equatorial planes are indicated by dashed lines.

rise to modulations in PELDOR time traces, thereby reducing the observed modulation depth by 50% in acidic samples of **2x**. As all product complexes in eqn (2) have maximally one nitroxide bearing ligand **1**, no multispin effects are expected to occur and to distort the time traces as indeed observed. The interpretation given above is strongly supported by the absence of modulations if attempts are made to measure the inter-nitroxide distance using PELDOR (ESI<sup>†</sup>).

The time traces of **2b** in acidic solution have been simulated using PeldorFit. The obtained mean distance is slightly shorter than those obtained for the time traces measured in neutral solution and amounts to  $25.7 \pm 0.9$  Å. The angle  $\zeta = 76.4 \pm 2.5^\circ$  is also slightly reduced. The deviations from the results obtained in neutral solution are too small to allow a conclusive analysis of the immediate coordination sphere of the copper center, *i.e.* whether or not the other ligand is now indeed bound more closely as suggested previously.<sup>64</sup> If a coordination number of five is assumed (one terpyridine ligand and two solvent molecules), the obtained parameters are in accordance with a square pyramidal coordination in which the nitroxide substituent is turned away from the  $z$  axis of the  $g$  tensor. A trigonal bipyramidal coordination seems less plausible, as an increased value for  $\zeta$  would then be expected (Fig. 9).

## Conclusions

Two copper nitroxide model systems for pulsed dipolar EPR spectroscopy analysis have been investigated in this work. The availability of a crystal structure provided detailed structural information of the complexes. The structures obtained using X-ray crystallography are assumed to be identical to those in solution if rhombic spectra are obtained. The crystallographic data allowed for an in-depth analysis of the PELDOR and RIDME experiments in the rhombic situations. The PELDOR data were analyzed using the PeldorFit program to account for orientation selectivity effects. Multispin effects are observed in mixture **2x** and the pure homoleptic three-spin system **2b** using

the PELDOR sequence. However, the observed multispin effects are not very marked and PeldorFit yielded results which agree with the molecular structures observed using crystallography despite neglecting multispin effects. In addition to the PELDOR measurements, RIDME measurements have been conducted. The orientation selectivity in RIDME was shown to be not very marked at X-band frequencies, in full agreement with the previous results on iron centered spins.<sup>21</sup> However, at Q-band frequencies, strong orientation selectivity can be observed using the RIDME sequence. Multispin effects have not been observed in the RIDME experiments. Thus, in spin systems with one fast relaxing spin and two slowly relaxing spins as those investigated in this work, multispin effects occur in the standard PELDOR experiment (observation of one fast relaxing spin) but not in the RIDME experiment (observation of two slowly relaxing spins). In order to extend the investigation of multispin effects to EPR distance measurements, an inverted spin system with two fast relaxing and one slowly relaxing spin is proposed. In addition, the solvent dependence of the EPR parameters observed for the related compound  $[\text{Cu}(\text{tpy})_2]^{2+}$  was also observed for **2x** and **2b**. Using PELDOR and RIDME it was possible to evaluate the interpretation, which was given earlier. The new data suggest that axial spectra are obtained after complete removal of one terpyridine based ligand. Whether or not the other terpyridine based ligand is now bound more closely cannot be answered conclusively. However, the obtained data are in accordance with a complex structure, in which the terpyridine moiety is in the equatorial plane of the coordination sphere.

## Acknowledgements

Financial support of the SFB813 "Chemistry at Spin Centers" is gratefully acknowledged. Prof. Dr A. Filippou is thanked for access to his X-ray facilities.

## Notes and references

- 1 G. Jeschke, *Annu. Rev. Phys. Chem.*, 2012, **63**, 419–446.
- 2 O. Schiemann and T. F. Prisner, *Q. Rev. Biophys.*, 2007, **40**, 1–53.
- 3 G. Jeschke, *Annu. Rev. Phys. Chem.*, 2012, **63**, 419–446.
- 4 O. Schiemann, N. Piton, J. Plackmeyer, B. E. Bode, T. F. Prisner and J. W. Engels, *Nat. Protoc.*, 2007, **2**, 904–923.
- 5 O. Duss, E. Michel, M. Yulikov, M. Schubert, G. Jeschke and F. H.-T. Allain, *Nature*, 2014, **509**, 588–592.
- 6 D. B. Gophane, B. Endeward, T. F. Prisner and S. T. Sigurdsson, *Chem. – Eur. J.*, 2014, **20**, 15913–15919.
- 7 I. Smirnova, V. Kasho, J.-Y. Choe, C. Altenbach, W. L. Hubbell and H. R. Kaback, *Proc. Natl. Acad. Sci. U. S. A.*, 2007, **104**, 16504–16509.
- 8 A. Marko, V. Denysenkov, D. Margraf, P. Cekan, O. Schiemann, S. T. Sigurdsson and T. F. Prisner, *J. Am. Chem. Soc.*, 2011, **133**, 13375–13379.

- 9 H. S. Mchaourab, P. R. Steed and K. Kazmier, *Structure*, 2011, **19**, 1549–1561.
- 10 T. Prisner, A. Marko and S. T. Sigurdsson, *J. Magn. Reson.*, 2015, **252**, 187–198.
- 11 B. J. Gaffney, M. D. Bradshaw, S. D. Frausto, F. Wu, J. H. Freed and P. Borbat, *Biophys. J.*, 2012, **103**, 2134–2144.
- 12 D. Abdullin, N. Florin, G. Hagelueken and O. Schiemann, *Angew. Chem.*, 2015, **127**, 1847–1851.
- 13 A. D. Milov, A. B. Ponomarev and Y. D. Tsvetkov, *Chem. Phys. Lett.*, 1984, **110**, 67–72.
- 14 R. E. Martin, M. Pannier, F. Diederich, V. Gramlich, M. Hubrich and H. W. Spiess, *Angew. Chem.*, 1998, **110**, 2993–2998.
- 15 M. Pannier, S. Veit, A. Godt, G. Jeschke and H. Spiess, *J. Magn. Reson.*, 2000, **142**, 331–340.
- 16 P. P. Borbat, J. H. Davis, S. E. Butcher and J. H. Freed, *J. Am. Chem. Soc.*, 2004, **126**, 7746–7747.
- 17 P. P. Borbat and J. H. Freed, *Chem. Phys. Lett.*, 1999, **313**, 145–154.
- 18 P. P. Borbat, H. S. Mchaourab and J. H. Freed, *J. Am. Chem. Soc.*, 2002, **124**, 5304–5314.
- 19 L. V. Kulik, S. A. Dzuba, I. A. Grigoryev and Y. D. Tsvetkov, *Chem. Phys. Lett.*, 2001, **343**, 315–324.
- 20 S. Milikisyants, F. Scarpelli, M. G. Finiguerra, M. Ubbink and M. Huber, *J. Magn. Reson.*, 2009, **201**, 48–56.
- 21 D. Abdullin, F. Duthie, A. Meyer, E. S. Müller, G. Hagelueken and O. Schiemann, *J. Phys. Chem. B*, 2015, **119**, 13534–13542.
- 22 A. V. Astashkin, in *Methods Enzymol.*, ed. P. Z. Qin and K. Warncke, Academic Press, 2015, vol. 563, pp. 251–284.
- 23 A. V. Astashkin, H. Hara and A. Kawamori, *J. Chem. Phys.*, 1998, **108**, 3805–3812.
- 24 G. Jeschke, *Annu. Rev. Phys. Chem.*, 2012, **63**, 419–446.
- 25 G. Jeschke, A. Bender, T. Schweikardt, G. Panek, H. Decker and H. Paulsen, *J. Biol. Chem.*, 2005, **280**, 18623–18630.
- 26 J. Bhatnagar, P. P. Borbat, A. M. Pollard, A. M. Bilwes, J. H. Freed and B. R. Crane, *Biochemistry*, 2010, **49**, 3824–3841.
- 27 D. T. Edwards, T. Huber, S. Hussain, K. M. Stone, M. Kinnebrew, I. Kaminker, E. Matalon, M. S. Sherwin, D. Goldfarb and S. Han, *Structure*, 2014, **22**, 1677–1686.
- 28 A. Giannoulis, R. Ward, E. Branigan, J. H. Naismith and B. E. Bode, *Mol. Phys.*, 2013, **111**, 2845–2854.
- 29 M. J. N. Junk, H. W. Spiess and D. Hinderberger, *J. Magn. Reson.*, 2011, **210**, 210–217.
- 30 C. Pliotas, R. Ward, E. Branigan, A. Rasmussen, G. Hagelueken, H. Huang, S. S. Black, I. R. Booth, O. Schiemann and J. H. Naismith, *Proc. Natl. Acad. Sci. U. S. A.*, 2012, **109**(40), E2675–E2682.
- 31 T. Von Hagens, Y. Polyhach, M. Sajid, A. Godt and G. Jeschke, *Phys. Chem. Chem. Phys.*, 2013, **15**, 5854–5866.
- 32 G. Jeschke, M. Sajid, M. Schulte and A. Godt, *Phys. Chem. Chem. Phys.*, 2009, **11**(31), 6580–6591.
- 33 A. Giannoulis, R. Ward, E. Branigan, J. H. Naismith and B. E. Bode, *Mol. Phys.*, 2013, **111**, 2845–2854.
- 34 F. MacMillan, A. Kannt, J. Behr, T. Prisner and H. Michel, *Biochemistry*, 1999, **38**, 9179–9184.
- 35 P. Dorlet, A. W. Rutherford and S. Un, *Biochemistry*, 2000, **39**, 7826–7834.
- 36 S. Un, C. Gerez, E. Elleingand and M. Fontecave, *J. Am. Chem. Soc.*, 2001, **123**, 3048–3054.
- 37 J. Stubbe and W. A. van der Donk, *Chem. Rev.*, 1998, **98**, 705–762.
- 38 H. Levanon and K. Möbius, *Annu. Rev. Biophys. Biomol. Struct.*, 1997, **26**, 495–540.
- 39 S. Rigby, J. Basran, J. Combe, A. Mohsen, H. Toogood, A. van Thiel, M. Sutcliffe, D. Leys, A. Munro and N. Scrutton, *Biochem. Soc. Trans.*, 2005, **33**, 754–757.
- 40 C. M. Gomes, J. B. Vicente, A. Wasserfallen and M. Teixeira, *Biochemistry*, 2000, **39**, 16230–16237.
- 41 K. J. Waldron, J. C. Rutherford, D. Ford and N. J. Robinson, *Nature*, 2009, **460**, 823–830.
- 42 E. Narr, A. Godt and G. Jeschke, *Angew. Chem., Int. Ed.*, 2002, **41**, 3907–3910.
- 43 B. E. Bode, J. Plackmeyer, T. F. Prisner and O. Schiemann, *J. Phys. Chem. A*, 2008, **112**, 5064–5073.
- 44 Z. Yang, J. Becker and S. Saxena, *J. Magn. Reson.*, 2007, **188**, 337–343.
- 45 Z. Yang, D. Kise and S. Saxena, *J. Phys. Chem. B*, 2010, **114**, 6165–6174.
- 46 M. Ji, S. Ruthstein and S. Saxena, *Acc. Chem. Res.*, 2013, **47**, 688–695.
- 47 B. E. Bode, J. Plackmeyer, M. Bolte, T. F. Prisner and O. Schiemann, *J. Organomet. Chem.*, 2009, **694**, 1172–1179.
- 48 J. Coremans, O. Poluektov, E. Groenen, G. Canters, H. Nar and A. Messerschmidt, *J. Am. Chem. Soc.*, 1997, **119**, 4726–4731.
- 49 T. E. Edwards, T. M. Okonogi and S. T. Sigurdsson, *Chem. Biol.*, 2002, **9**, 699–706.
- 50 L. V. Kulik, B. Epel, W. Lubitz and J. Messinger, *J. Am. Chem. Soc.*, 2007, **129**, 13421–13435.
- 51 Y. Zhou, B. E. Bowler, K. Lynch, S. S. Eaton and G. R. Eaton, *Biophys. J.*, 2000, **79**, 1039–1052.
- 52 L. Garbuio, E. Bordignon, E. K. Brooks, W. L. Hubbell, G. Jeschke and M. Yulikov, *J. Phys. Chem. B*, 2013, **117**, 3145–3153.
- 53 E. Matalon, T. Huber, G. Hagelueken, B. Graham, V. Frydman, A. Feintuch, G. Otting and D. Goldfarb, *Angew. Chem., Int. Ed.*, 2013, **52**, 11831–11834.
- 54 J. H. Van Wonderen, D. N. Kostrz, C. Dennison and F. MacMillan, *Angew. Chem.*, 2013, **125**, 2044–2047.
- 55 S. Razzaghi, M. Qi, A. I. Nalepa, A. Godt, G. Jeschke, A. Savitsky and M. Yulikov, *J. Phys. Chem. Lett.*, 2014, **5**, 3970–3975.
- 56 S. Stoll and A. Schweiger, *J. Magn. Reson.*, 2006, **178**(1), 42–55.
- 57 D. Abdullin, G. Hagelueken, R. I. Hunter, G. M. Smith and O. Schiemann, *Mol. Phys.*, 2014, **113**, 544–560.
- 58 G. Jeschke, V. Chechik, P. Ionita, A. Godt, H. Zimmermann, J. Banham, C. R. Timmel, D. Hilger and H. Jung, *Appl. Magn. Reson.*, 2006, **30**, 473–498.
- 59 A. Meyer, G. Schnakenburg and O. Schiemann, *Acta Crystallogr., Sect. E: Crystallogr. Commun.*, 2015, **71**, 1245–1249.

- 60 K. Ackermann, A. Giannoulis, D. Cordes, A. Slawin and B. Bode, *Chem. Commun.*, 2015, 5257–5260.
- 61 R. Hogg and R. G. Wilkins, *J. Chem. Soc.*, 1962, 341–350.
- 62 P. K. Pal, S. Chowdhury, M. G. B. Drew and D. Datta, *New J. Chem.*, 2002, 26(3), 367–371.
- 63 R. Allmann, W. Henke and D. Reinen, *Inorg. Chem.*, 1978, 17, 378–382.
- 64 A. Meyer, G. Schnakenburg, R. Glaum and O. Schiemann, *Inorg. Chem.*, 2015, 54, 8456–8464.
- 65 E. Narr, H. Zimmermann, A. Godt, D. Goldfarb and G. Jeschke, *Phys. Chem. Chem. Phys.*, 2003, 5, 3959–3967.
- 66 L. J. Kershaw Cook, J. Fisher, L. P. Harding and M. A. Halcrow, *Dalton Trans.*, 2015, 44, 9417–9425.
- 67 C. Riplinger, J. P. Y. Kao, G. M. Rosen, V. Kathirvelu, G. R. Eaton, S. S. Eaton, A. Kutateladze and F. Neese, *J. Am. Chem. Soc.*, 2009, 131, 10092–10106.
- 68 D. W. Fink and W. E. Ohnesorge, *J. Phys. Chem.*, 1970, 74, 72–77.



# **Single and Double Nitroxide Labeled Bis(terpyridine)copper(II): The Influence of Multispin and Jahn-Teller Effects on PELDOR and RIDME†**

Andreas Meyer<sup>a</sup>, Dinar Abdullin<sup>a</sup>, Gregor Schnakenburg<sup>b</sup>, Olav Schiemann<sup>a,\*</sup>

<sup>a</sup>Rheinische Friedrich-Wilhelms-University Bonn, Institute of Physical and Theoretical  
Chemistry, Wegelerstr. 12, 53115 Bonn, Germany. E-mail: schiemann@pc.uni-  
bonn.de; Tel: +49 0228 732989

<sup>b</sup>Institute of Inorganic Chemistry, Rheinische Friedrich-Wilhelms-University Bonn,  
Gerhard-Domagk-Str. 1, 53121 Bonn, Germany.

Supporting Information

1 Crystal structure of 2b and comparison with geometric parameters obtained from PeldorFit .....	3
2 Pulse sequences used in this work .....	10
3 EPR parameters and further EPR measurements on 2x and 2b. ....	10
3.1 EPR spectra and EPR Parameters of 2x and 2b.....	10
3.2 PELDOR and RIDME measurements on 2x and 2b.....	12
3.3 Inversion recovery of the copper signal of 2x and 2b .....	15
3.4 Phase memory times of the nitroxide and the copper signal in 2x and 2b .....	17
4 Multispin effects in PELDOR of 2x and 2b .....	19
References .....	24

## 1 Crystal structure of **2b** and comparison with geometric parameters obtained from PeldorFit

Clear green blocks of **2b**·4acetone·cyclohexane were obtained from a layered acetone/cyclohexane mixture. The data collection was performed on a STOE-IPDS-2T diffractometer (area detector) using graphite monochromated Mo- $K_{\alpha}$  radiation ( $\lambda = 0.71073 \text{ \AA}$ ). The diffractometer was equipped with a low-temperature device (Cryostream 700er series, Oxford Cryosystems, 123 K). Intensities were measured by fine-slicing  $\varphi$  and  $\omega$ -scans and corrected for background, polarization and Lorentz effects. A numerical absorption correction was applied for the data set. The structure was solved by direct methods and refined anisotropically by the least-squares procedure implemented in the ShelX program system.<sup>1</sup> Hydrogen atoms were included isotropically using the riding model on the bound carbon atoms.

CCDC-1441273 contains the supplementary crystallographic data for this paper, which can be obtained free of charge from The Cambridge Crystallographic Data Centre via [www.ccdc.cam.ac.uk/data\\_request/cif](http://www.ccdc.cam.ac.uk/data_request/cif).

Details of the X-ray diffraction experiment on **2b** are given in Table S1.

**Table S1.** Crystal data and structure refinement for the different X-ray experiments on compound **2b**.

Empirical formula	$C_{215}H_{218}Cu_2F_{24}N_{16}O_{21}P_4$
Moiety formula	$2(C_{88}H_{70}CuN_8O_6)$ , $4(F_6P)$ , $9(C_3H_6O)$ , $2(C_6H_{12})$
Formula weight	4069.00 g/mol
Temperature	123(2) K
Wavelength	0.71073 $\text{\AA}$
Crystal system, space group	triclinic, P -1
Unit cell dimensions	$a = 20.1608(8) \text{ \AA}$ $\alpha = 71.678(3)^\circ$ $b = 22.3481(8) \text{ \AA}$ $\beta = 67.478(3)^\circ$ $c = 25.7380(6) \text{ \AA}$ $\gamma = 86.691(3)^\circ$
Volume	$10142.9(7) \text{ \AA}^3$
Z, Calculated density	2, 1.332 g/cm <sup>3</sup>
Absorption coefficient	0.332 mm <sup>-1</sup>
F(000)	4244.0
Crystal size	0.31 x 0.15 x 0.12 mm <sup>3</sup>
$\theta$ -range for data collection	2.6 – 25.25°

<sup>1</sup> G. M. Sheldrick, *Acta Cryst.*, **2008**, A64, 112-122.

Limiting indices	$-20 \leq h \leq 24, -26 \leq k \leq 26, -24 \leq l \leq 30$
Reflections collected / unique	62874 / 36067 [ $R_{\text{int}} = 0.0839$ ]
Completeness to $\theta = 25.25^\circ$	98.3 %
Absorption correction	Numerical
Max. and min. transmission	0.9395 and 0.6176
Refinement method	Full-matrix least squares on $F^2$
Data / restraints / parameters	36067 / 96 / 2573
Goodness-of-fit on $F^2$	0.717
Final R indices [ $I > 2\sigma(I)$ ]	$R_1 = 0.0614, wR_2 = 0.1036$
R indices (all data)	$R_1 = 0.1895, wR_2 = 0.1242$
Largest diff. peak / hole	0.570 and $-0.340 \text{ e}\text{\AA}^{-3}$

**2b** crystallizes in the triclinic space group  $P\bar{1}$ . The asymmetric unit (Figure S1) contains two independent cations **A** and **B** which differ slightly in their geometric parameters. Relevant geometrical parameters for the two different cations of **2b** as obtained from the crystal structure are defined in Figure S2 and listed in Table S2. In addition to the parameters defined in Figure S2, the angles  $\psi$  and  $\chi$  between the mean planes of the pyrrolidine-*N*-oxides and the  $g_x, g_z$  plane of the copper center are given in Table S2 (see also Figure S3).

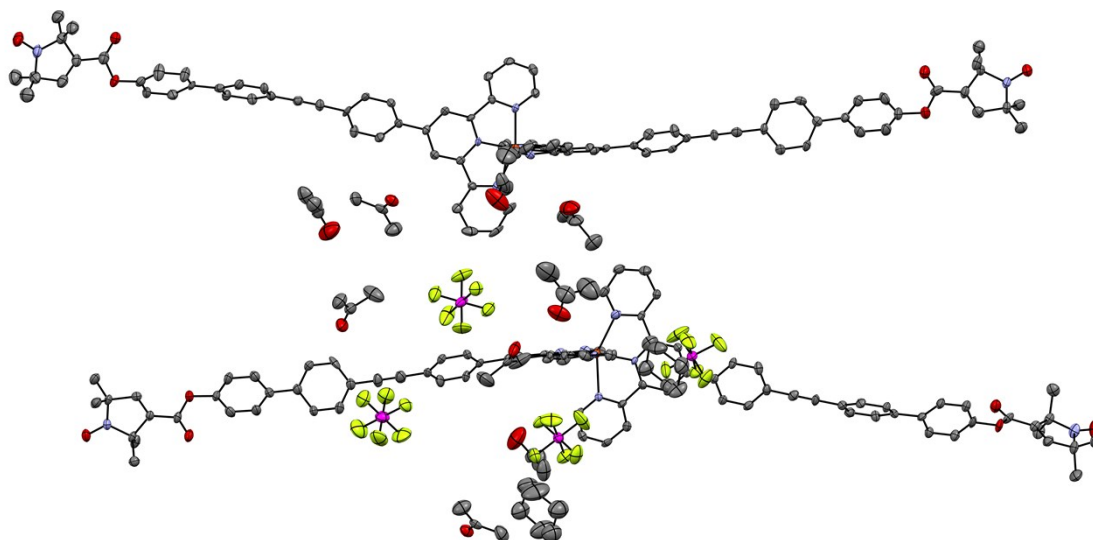


**Figure S1.** The asymmetric unit of the unit cell of **2b**. Red atoms = O, blue atoms = N, grey atoms = C, dark orange atom = Cu, yellow atoms = F, purple atoms = P. Hydrogen atoms have been omitted for clarity.

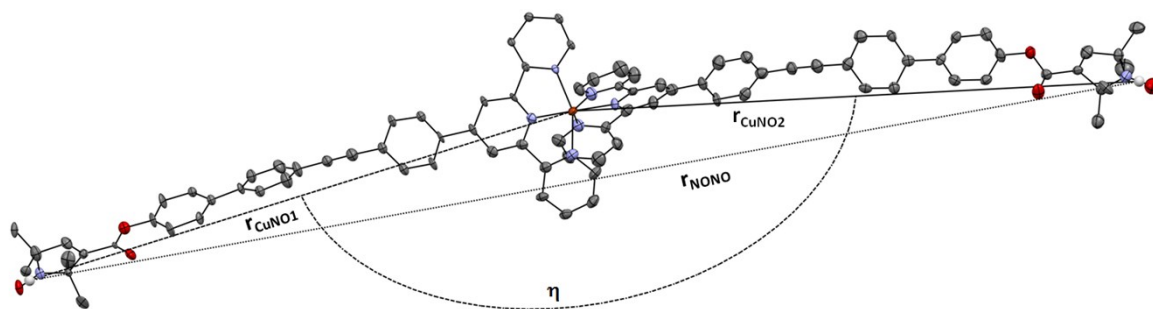


**Figure S2.** One exemplary complex cation from the crystal structure of **2b** to illustrate the meaning of the distance parameters and the angle  $\eta$  as discussed in the text. Red atoms = O, blue atoms = N, grey atoms = C, dark orange atom = Cu. Hydrogen atoms have been omitted for clarity.

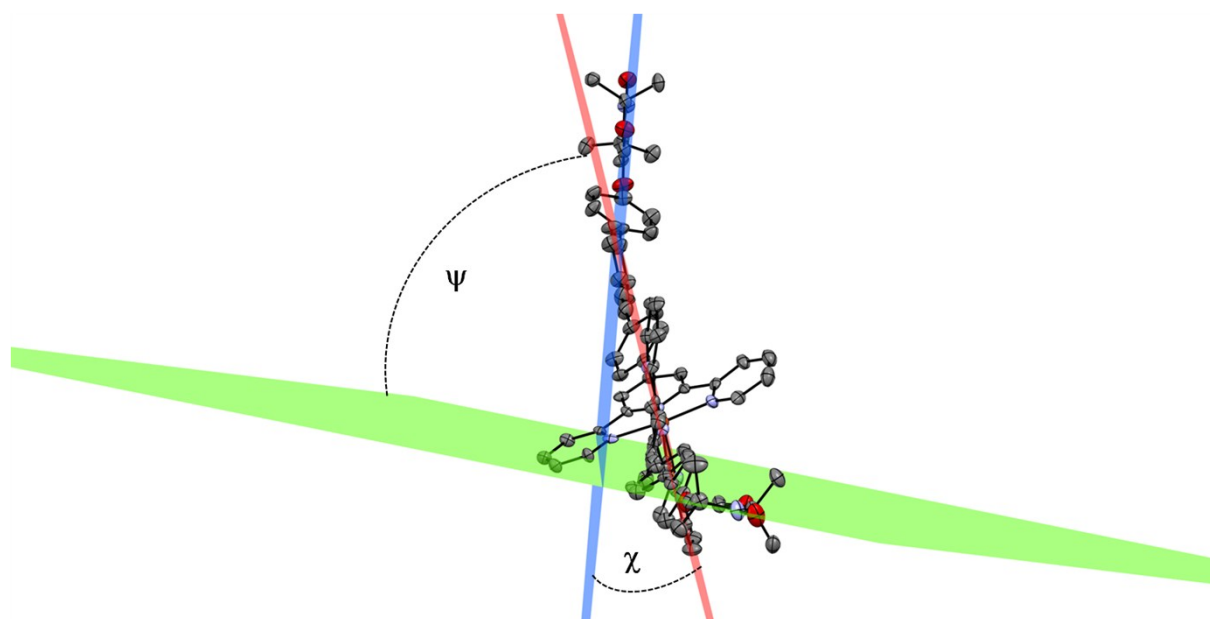


**Figure S3.** One exemplary complex cation from the crystal structure of **2b** to illustrate the meaning of the angles  $\psi$  and  $\chi$  as discussed in the text. Red atoms = O, blue atoms = N, grey atoms = C, dark orange atom = Cu. Hydrogen atoms have been omitted for clarity.

**Table S2.** Geometrical parameters for the independent complex cations in the crystal structure of **2b**.

	$r_{\text{CuNO1}}$ [Å]	$r_{\text{CuNO2}}$ [Å]	$\langle r_{\text{CuNO}} \rangle$ [Å]	$r_{\text{NONO}}$ [Å]	$\eta$ [deg]	$\psi$ [deg]	$\chi$ [deg]
<b>A</b>	26.42	26.44	26.43	51.98	156.8	19.2	66.8
<b>B</b>	26.46	26.62	26.54	52.00	159.0	70.1	78.5

All geometrical parameters given in Table S2 are taken from the crystal structure and are related to the geometric parameters optimized by PeldorFit. The original geometric parameters from PeldorFit (the mean values of the inter-spin distance and the five angles describing the positions and relative orientations of the spin centers and the corresponding distribution widths) were varied in the ranges specified in our previous publication.<sup>1</sup> The distances are the main parameter of interest in the PELDOR experiments and detailed analysis of the independent cations in the crystal structure allows giving estimates about the range of distances to expect. The angle  $\alpha$  is the angle between the two vectors interconnecting one nitroxide with the copper

spin center. Note, that these vectors are similarly aligned as the N-O bond (and thereby the  $g_x$  component) of the nitroxides and the bonds of the copper atom to the nitrogen donors of the central pyridine rings of the tpy ligands (and thereby the  $g_z$  component of the copper spin center). The relation between the geometric structure and the orientation of the  $g$  tensor of the copper terpyridine center is also discussed in the main text and in a previous study in greater detail.<sup>2</sup> The  $g$  tensor coordinate system for a copper terpyridine complex elongated along the molecular  $x$  axis is shown in detail in Figure S4. The orientation of the  $g$  tensor in Figure S4 was obtained using DFT calculations (B3LYP functional with TZVPP basis sets as implemented in ORCA<sup>3</sup>). The structure of cation **F** from the crystal structure<sup>1</sup> of the unsubstituted (bis(terpyridine))copper(II) bis(tetraphenylborate) was used as input geometry. The obtained orientation of the  $g$  tensor with respect to the molecular geometry agrees completely with those given in the aforementioned study.

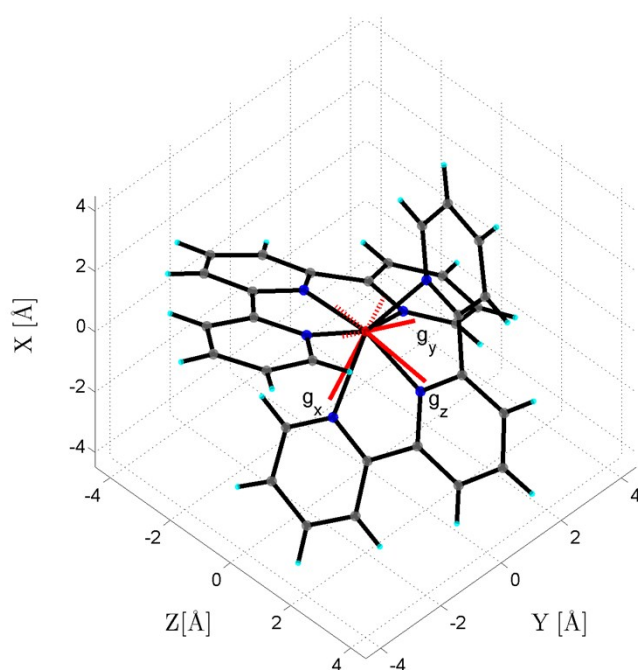


**Figure S4.**  $g$  tensor frame-work of the terpyridine ligated copper center. Red atom = Cu; Blue atoms = N; Grey atoms = C, Teal atoms = H.

Importantly, the vectors, which interconnect the nitroxides and the copper center are parallel to the parallel component of the dipolar coupling tensor. This is of importance for the EPR based distance measurements, as it implies that selectivity for the  $g_z$  value of the copper center is also selective for the parallel component of the dipolar coupling tensor, although the bent structure of the complex **2b** leads to deviations from perfect colinearity. The effects of the bending of the molecule can be estimated by inspecting the structure of the two independent cations in the crystal structure of

**2b.** A noteworthy feature about the molecular bending is that it appears to occur around the  $g_y$  axis of the copper center and is brought about by non-symmetric displacements of the remote pyridine rings as illustrated in Figure S5. The complexes in the crystal structure of **2b** have that in common with the most strongly distorted cation **F** of the unsubstituted (bis(terpyridine))copper(II) bis(tetraphenylborate) which is shown in Figure S4.

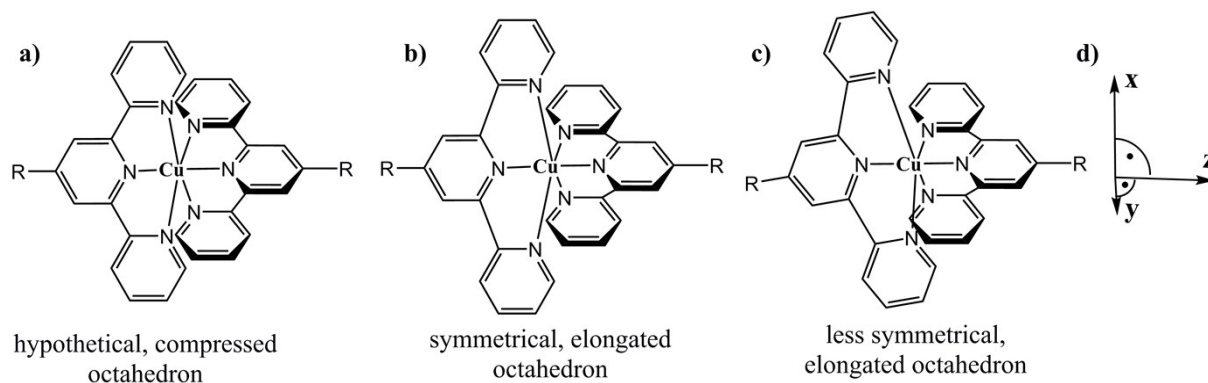


**Figure S5.** Schematic coordination geometries of the cations of **2b** (a – c) and approximate  $g$  tensor coordinate system (d).

Taking together the features discussed above and illustrated in Figures S2 - S5 reveals that  $\eta$  is related to the angle  $\zeta$  in the program PeldorFit, which defines the angle between the interspin vectors and the highest  $g$  value of the observer spin (i.e. the copper centered spin).<sup>1</sup> Therefore,  $\zeta$  should be approximately equal to  $\eta/2$ , which is indeed found by PeldorFit. Similarly, the angle  $\phi$  defined as the angle between the interspin vector and the smallest  $g$  value of the copper center can be estimated to be close to  $90 - \alpha/2$ . This is indeed found using PeldorFit as shown in Table S3.

**Table S3.** Geometric parameters obtained from PeldorFit and from the crystal structure of **2b**.

	$r$ [nm]	$\zeta$ [°]	$\phi$ [°]
<b>2x</b>	2.58	81.4	5.5
<b>2b</b>	2.60	82.1	0.7
<b>2b (acidic)</b>	2.57	76.4	37.2
<b>2b (crystal)<sup>a</sup></b>	2.64 – 2.66	78.4 – 79.5	10.5 – 11.6

<sup>a</sup> All parameter values are taken from Table S1. Instead of giving average values and standard deviations, the highest and lowest values for each parameter have been given in order to specify a range of expected values. The values for  $\zeta$  and  $\phi$  are calculated for the crystal structure as described in the text.

The values listed in table S3 are those which are in our experience more reliable than the Euler angles, as defined in PeldorFit.<sup>1</sup> The Euler angles  $\alpha$ ,  $\beta$  and  $\gamma$  on the other hand usually do not show clearly defined minima. The reason for that is the low resolution of the  $g$  tensor of the nitroxide and the two lower  $g$  values of the copper  $g$  tensor at X-band frequency. Therefore, the PeldorFit data do not allow analyzing the angles  $\psi$  and  $\chi$  in frozen solution EPR samples. To further quantify the analysis of the PeldorFit parameters, error profiles of each PeldorFit parameter were calculated. In these calculations, one parameter and its width were varied while all other parameters were kept at their optimum values. The results of these calculations are shown in Figures S6 - S8.

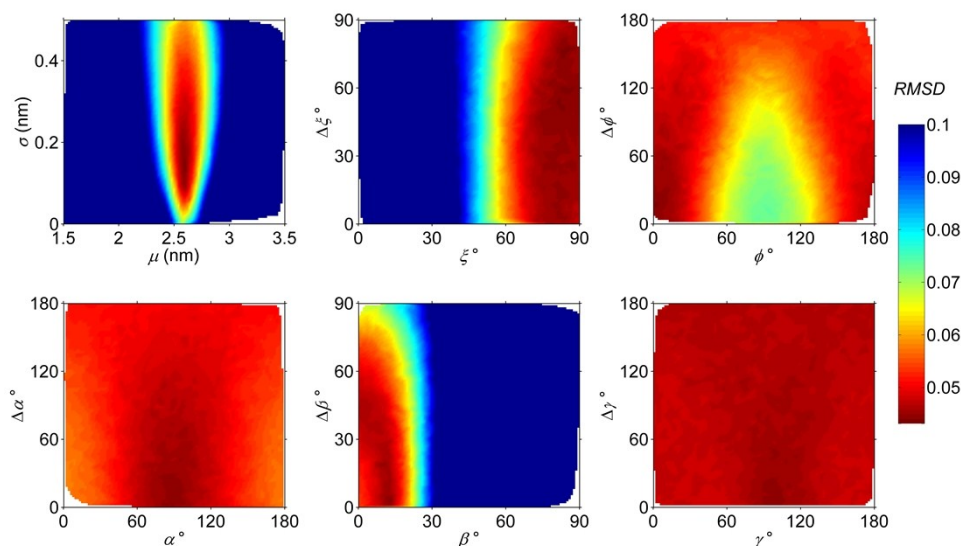


**Figure S6.** Error profiles for each PeldorFit parameter for measurements of **2x** in neutral solution (DMSO/MeOH, 1:1.5)

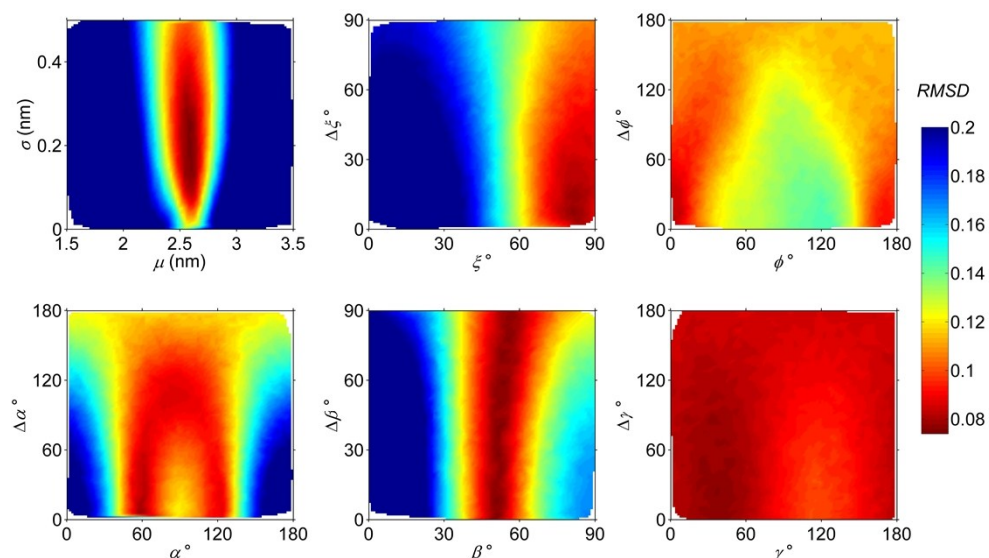


**Figure S7.** Error profiles for each PeldorFit parameter for measurements of **2b** in neutral solution (DMSO/MeOH, 1:1.5)



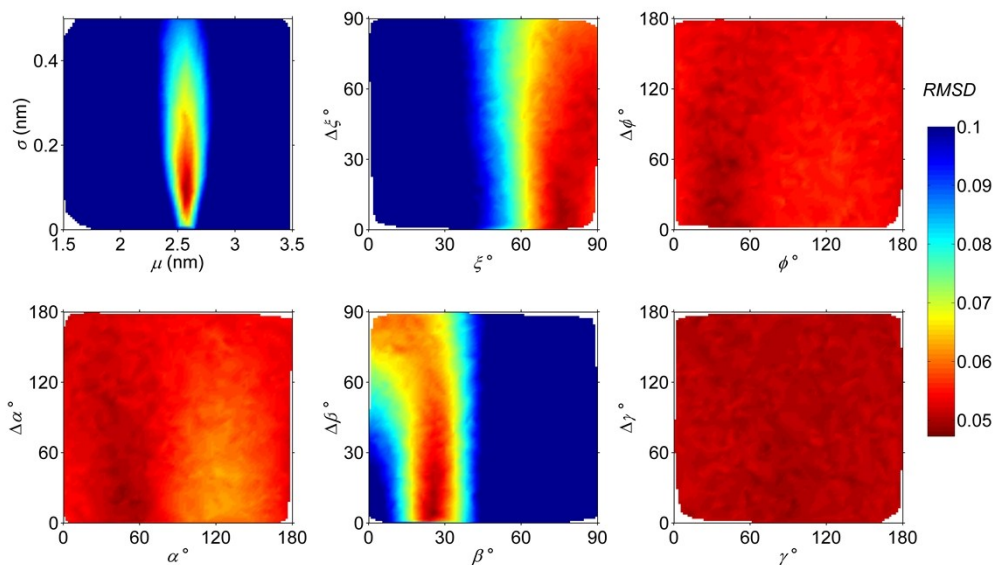
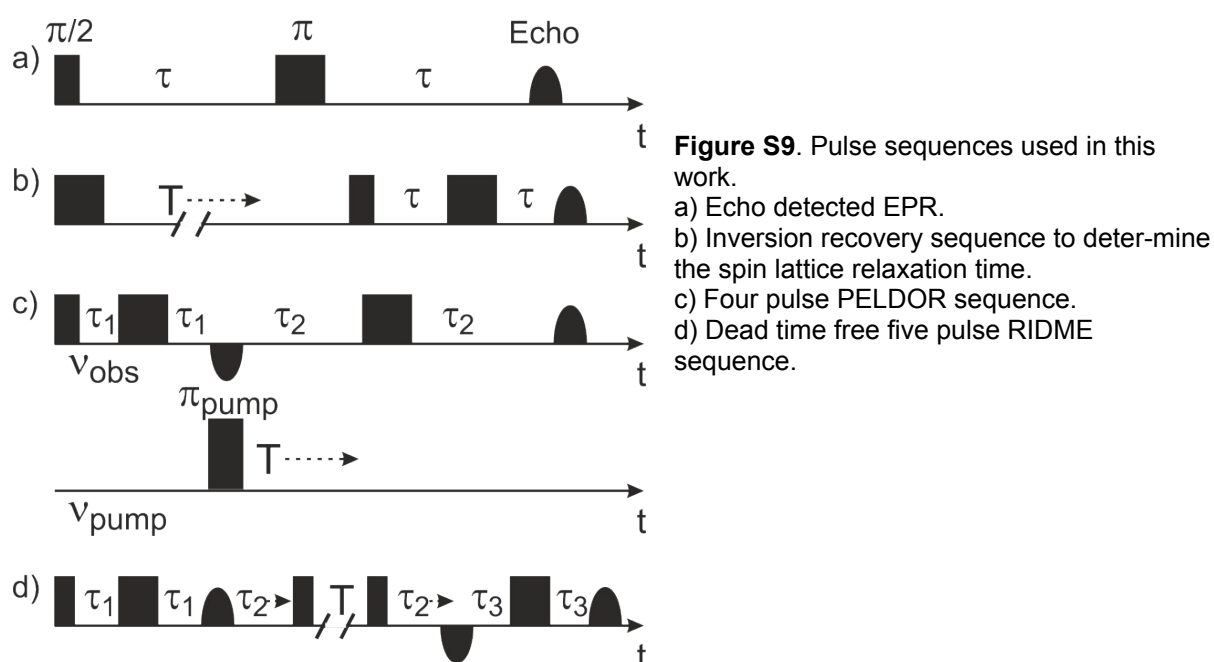


**Figure S8.** Error profiles for each PeldorFit parameter for measurements of **2b** in acidic solution (DMSO/MeOH, 1:1.5)

For all samples (**2x**, **2b**, and **2b** under acidic conditions) an optimum distance is found to be located in a narrow minimum along the distance axis. The width of the distance distribution  $\sigma$  on the other hand is not very strongly defined for **2a** and **2b** in neutral solutions. In acidic solution, this value is has a narrower minimum in the error profile. The error profiles for  $\zeta$  look similar for all samples. This is expected, as the geometries observed crystallographically and those discussed in the main text for the acidic sample of **2b** each have similar orientations of the  $g$  tensor of the copper centered spin and the copper-nitroxide vector. The angle  $\phi$ , which relates the lowest  $g$  tensor value of the observer spin and the interspin vector, is less well defined for all samples. Especially, under acidic conditions it is nearly undefined. Since the lowest and the intermediate  $g$  tensor value of the copper  $g$  tensor are similar under neutral and nearly equal under acidic conditions this seems reasonable. At least one of the Euler angles in each sample is completely undefined. As these angles are strongly interrelated, none of the Euler angles should be considered as clearly defined, even if a clear minimum occurs in the error profiles. As shown in the original publication, several symmetry related, equivalent solutions are obtained with respect to the angular parameters used by PeldorFit.

## 2 Pulse sequences used in this work

Figure S9 summarizes the pulse sequences used in this work



## 3 EPR parameters and further EPR measurements on 2x and 2b.

In the following subsections, the measurement parameters and parameters used to simulate the obtained data are detailed. Furthermore, data which was not shown in the main text is presented. Most experiments have been conducted in neutral and acidic solution. While the parameters used for the simulation of the data differs for the two types of solution, the measurement parameters are identical for both types of solution, unless otherwise specified.

### 3.1 EPR spectra and EPR Parameters of 2x and 2b

EPR spectra of **2x** and **2b** have been obtained using a two pulse echo sequences and are shown in the main text. The  $g$  values and hyperfine coupling constants  $A$  of **2x** and **2b** have been obtained by simulating these spectra. The simulation parameters are listed in Table S4 for neutral solutions and in Table S5 for acidic solutions. The measurement parameters used to obtain the echo detected EPR spectra for both kinds of solution are listed in Table S6.

**Table S4.** Parameters used to simulate the EPR spectra of **2x** and **2b** in neutral solution at X- and Q-band.

Compound	2x	2b	2x	2b
<b>MW-Band</b>	X	X	Q	Q
$g_x$ (Cu)	2.256	2.256	2.257	2.256
$g_y$ (Cu)	2.093	2.093	2.092	2.093
$g_z$ (Cu)	2.042	2.042	2.043	2.042
$A_x$ (Cu) [MHz]	455	455	455	455
$A_y$ (Cu) [MHz]	70	70	70	70
$A_z$ (Cu) [MHz]	-90	-90	-90	-90
$g_x$ (NO)	2.0085	2.0085	2.0091	2.0091
$g_y$ (NO)	2.0063	2.0063	2.0075	2.0075
$g_z$ (NO)	2.0025	2.0025	2.0024	2.0024
$A_x$ (NO) [MHz]	11	11	15	15
$A_y$ (NO) [MHz]	16	16	15	15
$A_z$ (NO) [MHz]	95	95	95	95

**Table S5.** Parameters used to simulate the EPR spectra of **2x** and **2b** in acidic solution at X- and Q-band.

Compound	2x	2b	2x	2b
<b>MW-Band</b>	X	X	Q	Q
$g_x$ (Cu)	2.268	2.268	2.265	2.265
$g_y$ (Cu)	2.063	2.064	2.062	2.062
$g_z$ (Cu)	2.060	2.064	2.058	2.060
$A_x$ (Cu) [MHz]	505	502	510	507
$A_y$ (Cu) [MHz]	-55	-55	-50	-50
$A_z$ (Cu) [MHz]	-65	-65	-65	-65
$g_x$ (NO)	2.0088	2.0088	2.0091	2.0091
$g_y$ (NO)	2.0065	2.0065	2.0075	2.0075
$g_z$ (NO)	2.0025	2.0025	2.0024	2.0024
$A_x$ (NO) [MHz]	11	11	15	15
$A_y$ (NO) [MHz]	16	16	15	15
$A_z$ (NO) [MHz]	95	95	95	95

**Table S6.** Measurement parameters used to obtain echo detected EPR spectra of **2x** and **2b** at X- and Q-band.

Compound	2x	2b	2x	2b
<b>MW-Band</b>	X	X	Q	Q
$p_1$ [ns]	12	10	20	22
$p_2$ [ns]	24	20	20	22
$\tau$ [ns]	140	140	440	440
<b>SRT</b> [ $\mu$ s]	997	997	997	997

$p_1$  = length of first pulse,  $p_2$  = length of second pulse,  $t$  = separation between first and second pulse, SRT = shot repetition time.

The acquisition gate was set to cover the whole optimized echo and about 20 ns of at each side of the optimized echo. The shot repetition times are adjusted to allow for

fast acquisition of the copper signal. If the nitroxide signal is to be observed (as in RIDME), longer short repetition times are necessary.

### 3.2 PELDOR and RIDME measurements on 2x and 2b

The parameters of the PELDOR measurements on **2x** and **2b** at X-band frequencies are given in Table S7. Identical parameters have been used for **2x** and **2b**. The copper signal was used for observation and the detection frequency was set to about 150 MHz to the high frequency side of the resonator dip.

**Table S7.** Parameters of the PELDOR measurements on **2x** and **2b** at X-band frequencies.

$\Delta\nu$ [MHz]	<b>150</b>	<b>300</b>	<b>450</b>	<b>600</b>
$p_1$ [ns]	12	12	12	12
$p_2$ [ns]	24	24	24	24
$P_{pump}$ [ns]	18	26	26	56
$\tau$ [ns]	140	140	440	440
<b>SRT</b> [ $\mu$ s]	9900	9900	9900	9900
$B_0$ [mT]	345.2	340.2	334.8	329.5

The nitroxide-nitroxide distance determination was performed at Q-band frequencies as at X-band frequencies the nitroxide and copper signal overlap. The parameters are listed in Table S8. The parameters obtained using PeldorFit are discussed in the main text and listed in the section concerned with the crystal structure of **2b**.

**Table S8.** Parameters of the internitroxide PELDOR measurements on **2x** and **2b** at Q-band frequencies.

<b>Species</b>	<b>2x</b>	<b>2b</b>
$\nu_{obs}$ [GHz]	33.777	33.941
$\Delta\nu$ [MHz]	70	70
$p_1$ [ns]	14	12
$p_2$ [ns]	28	24
$P_{pump}$ [ns]	24	26
$\tau$ [ns]	460	460
<b>SRT</b> [ $\mu$ s]	9900	9900
$B_0$ [mT]	1203.9	1209.4

The RIDME experiment in neutral solution was conducted at X- and Q-Band frequencies. Identical parameters have been used for **2x** and **2b**. The parameters are listed in Table S9. The individual RIDME time traces at X- and Q-band frequencies are shown in Figures S10 and S11.

**Table S9.** Parameters of the RIDME measurements on **2x** and **2b** at both MW bands.

MW-band	X	Q
$P_{\pi/2}$ [ns]	10	14
$P_{\pi}$ [ns]	20	28
$\tau_1$ [ns]	140	440
$\tau_2$ [ns]	180	420
$T$ [ $\mu$ s]	100	80
$SRT$ [ $\mu$ s]	9900	9900

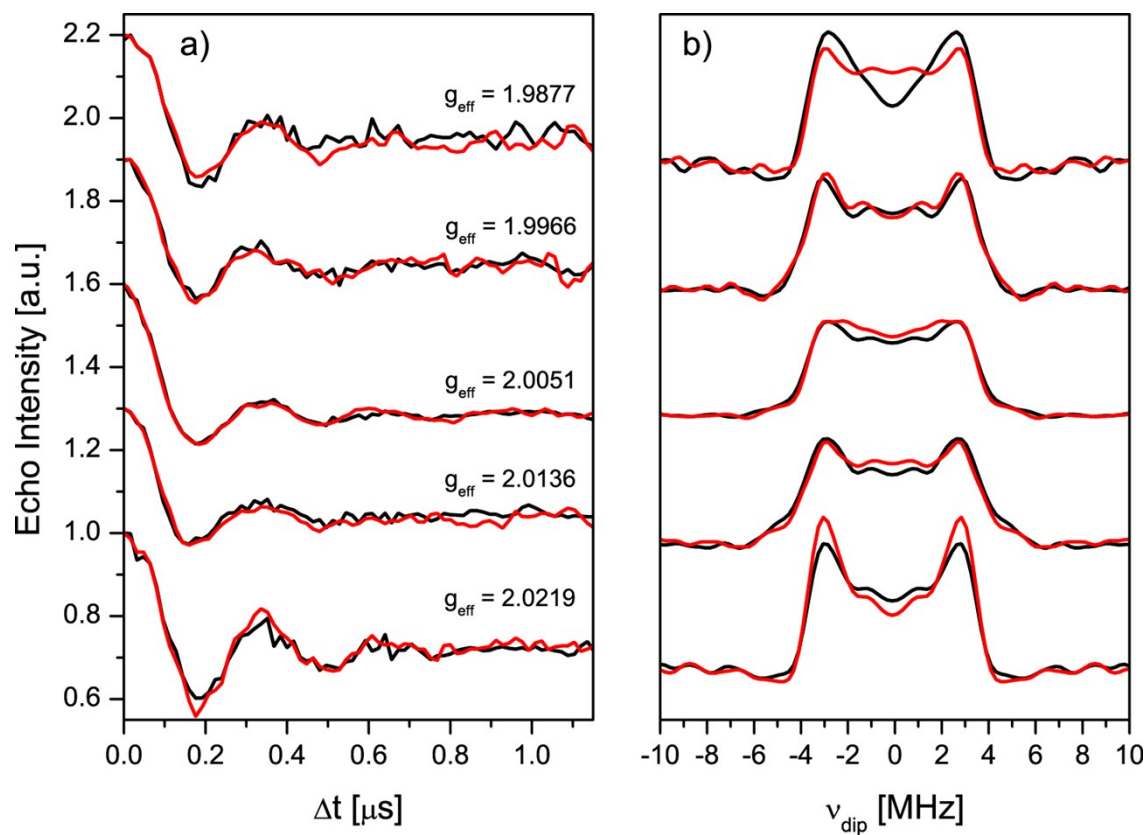


**Figure S10.** RIDME time traces and their Fourier transforms (a) and b), respectively) at different effective  $g$  values of the nitroxide signal position recorded at X-band frequencies of **2x** (black lines) and **2b** (red lines).

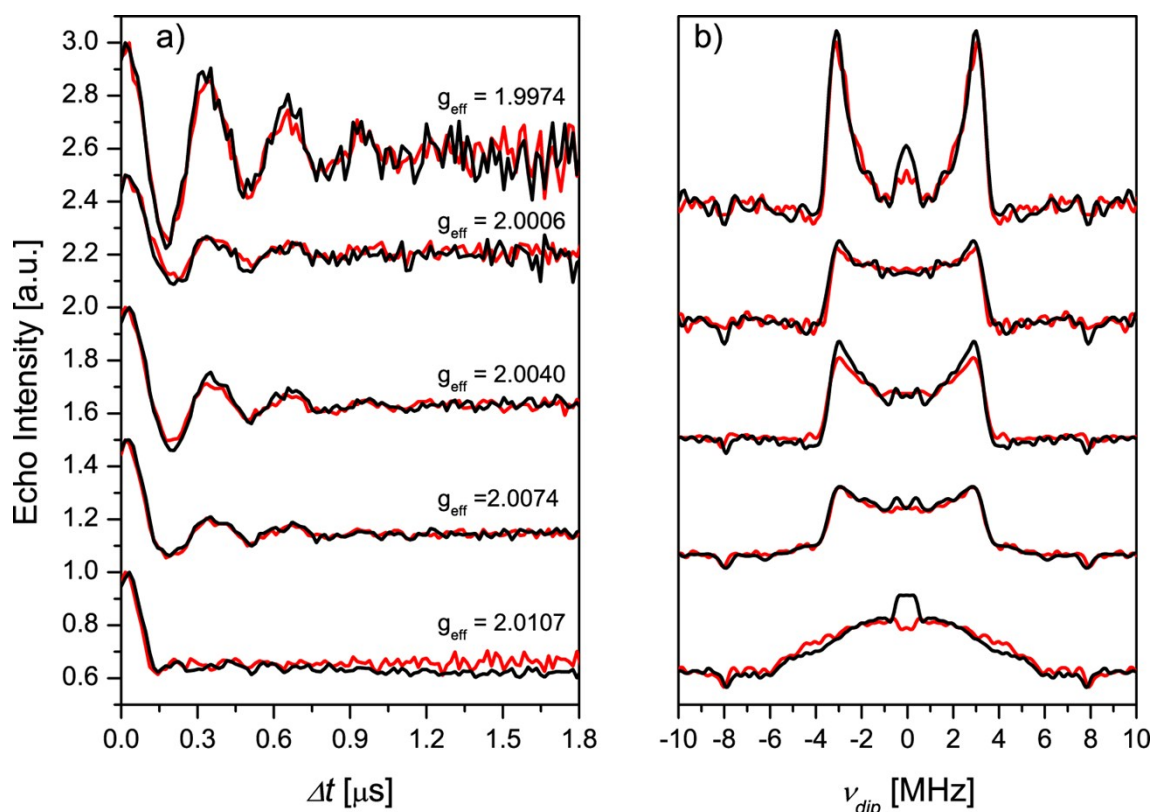


**Figure S11.** RIDME time traces and their Fourier transforms at different effective  $g$  values of the nitroxide signal position recorded at Q-band frequencies of **2x** (black lines) and **2b** (red lines).

The RIDME experiment was also conducted in acidic solution for **2b** at Q-band frequencies (Figure S12).

For the measurements in acidic solution, the interpulse separation has been increased by a factor of 4.5 with respect to the measurement in neutral solution, in accordance with the results obtained using the inversion recovery experiment. The obtained modulation depths are now approximately 50% lower than in neutral methanolic solutions. This is expected, if one of the nitroxide ligands is completely removed from complex **2b** as discussed in the main text. With respect to orientation selection, similar results as in neutral solution are obtained, as the orientations election is entirely determined by the selection of the nitroxide part of the EPR signal and the nitroxide signal is not affected by addition of acid to the solvent system. Besides having a lower modulation depth, the overall quality of the obtained data is worse than for neutral solution. For example, a larger residual contribution of the deuteron modulation is visible in the RIDME time traces. This observation is attributed to the fact, that the echo signal used to record the RIDME time trace is comprised of two contributions in equal weight, namely the nitroxides still bound to the copper center and the nitroxides which are removed from the copper center and

therefore do not show modulations owed to electron electron coupling. As the obtained time trace is a sum of two contributions, removal of the ESEEM modulations as described for the time traces in neutral solution might be less efficient. Despite the reduced data quality, a mean copper-nitroxide distance of  $2.48 \pm 0.06$  nm could be obtained, which is slightly lower than the value observed in neutral solution.

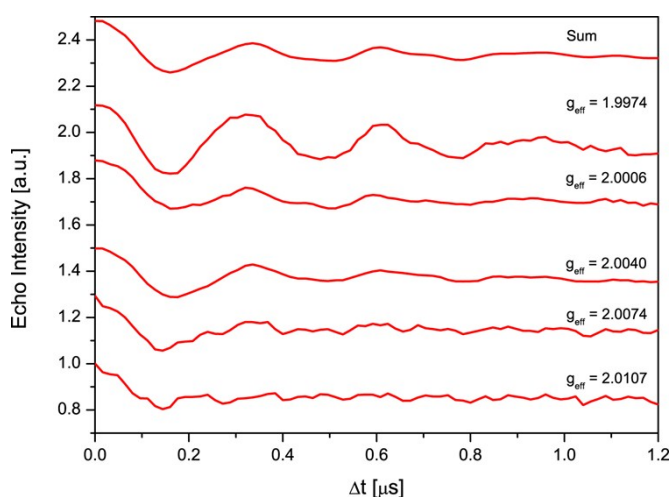


**Figure S12.** RIDME time traces of **2b** in acidic solution and their Fourier transforms at different effective  $g$  values of the nitroxide signal position recorded at Q-band frequencies.

As mentioned in the main text, the nitroxide nitroxide distance could no longer be measured in **2b** in the acidified solvent system. The corresponding time trace is shown in Figure S13.

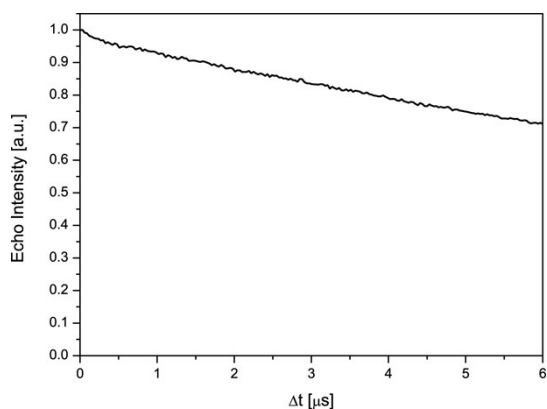


**Figure S13.** PELDOR measurement of the nitroxide nitroxide distance in **2b** in the acidified solvent system (deuterated DMSO/MeOD, 1:1.5, acidified using  $\text{H}_2\text{SO}_4$ ) at Q-band frequency.

### [3.3 Inversion recovery of the copper signal of 2x and 2b](#)

The spin lattice relaxation times of the copper signal of **2x** and **2b** have been measured using the inversion recovery sequence. The inversion recovery time traces

have been fitted empirically using equation (S1) for the echo intensity  $I$  as a function of the interpulse separation  $T$ .

$$I = I_0 \left( 1 - ae^{-T/T_1^a} - be^{-T/T_1^b} \right) \text{ with } a + b = 1 \quad (\text{S1})$$

The results of the inversion recovery experiments for neutral solutions are summarized in Figure S14 and Table S11.

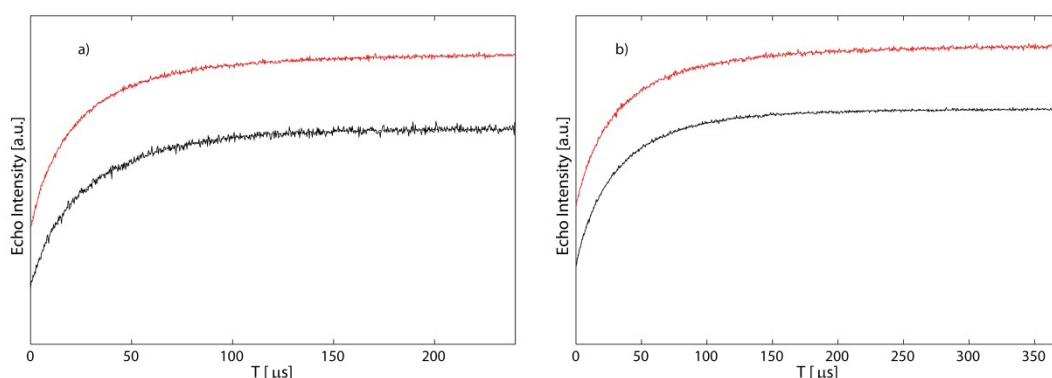


**Figure S14.** Inversion recovery time traces of **2x** (black lines) and **2b** (red lines) and corresponding biexponential fitting functions (dashed lines) at a) X-band frequencies in DMSO/MeOH (1:1.5) and b) Q-band frequencies in  $d_6$ -DMSO/MeOD (1:1.5). The inversion recovery time traces have been recorded at the maximum intensity of the copper signal. Fitting and measurement parameters are given in Tables S10 and S11.

**Table S10.** Fitting Parameters of the inversion recovery time traces

Compound and MW frequency	$a$	$T_1^a$ [ $\mu\text{s}$ ]	$b$	$T_1^b$ [ $\mu\text{s}$ ]	$T_1^{av}$ [ $\mu\text{s}$ ]
<b>2x</b> , X	$0.74 \pm 0.03$	$38.8 \pm 0.9$	$0.26 \pm 0.03$	$9.8 \pm 0.9$	31.3
<b>2b</b> , X	$0.53 \pm 0.01$	$44.6 \pm 0.9$	$0.47 \pm 0.01$	$12.8 \pm 0.9$	29.7
<b>2x</b> , Q	$0.59 \pm 0.02$	$51.9 \pm 0.8$	$0.41 \pm 0.02$	$17.0 \pm 0.5$	37.6
<b>2b</b> , Q	$0.47 \pm 0.02$	$72.0 \pm 2.0$	$0.53 \pm 0.02$	$19.8 \pm 0.6$	44.3

**Table S11.** Measurement parameters used to obtain echo detected EPR spectra of **2x** and **2b** at X- and Q-band.

Compound	<b>2x</b>	<b>2b</b>	<b>2x</b>	<b>2b</b>
<b>MW-Band</b>	X	X	Q	Q
$p_1$ [ns]	24	20	28	28
$p_2$ [ns]	12	10	14	14
$p_3$ [ns]	24	20	28	28
$T$ [ns]	1000	1000	1000	1000
$\tau$ [ns]	200	200	440	440
<b>SRT</b> [ $\mu\text{s}$ ]	1910	1910	997	997

$p_1$  = length of first pulse,  $p_2$  = length of second pulse,  $p_3$  = length of third pulse,  $T$  = separation between first and second pulse,  $\tau$  = separation between second and third pulse,  $SRT$  = shot repetition time.



The inversion recovery was repeated for **2x** and **2b** in acidic solution at X-band frequency and for **2b** also at Q-band frequency. The results are summarized in Figure S15 and Table S12. Noteworthy, the spin lattice relaxation time of the copper spin center differed very strongly from the spin lattice relaxation time in neutral solution (Figure S15 and Table S12).

The strong increase of the spin lattice relaxation by one order of magnitude is another hint for the presence of different species (i.e. copper complexes in which one terpyridine based ligand has been replaced by solvent molecules), as identical species with just slight differences in the details of the first coordination sphere would probably have very similar relaxation behavior.

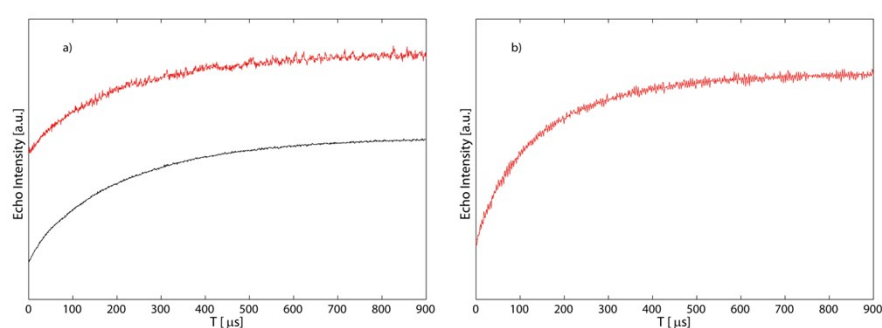


**Figure S15.** Inversion recovery time traces of spectra of **2x** (black lines) and **2b** (red lines) and their simulations (dashed lines) in 0.1 M sulfuric acid solutions at a) X-band frequencies (MeOH and DMSO, 1.5:1) and b) Q-band frequencies (MeOD and  $d_6$ -DMSO, 1.5:1). The inversion recovery time traces have been recorded at the maximum intensity of the copper signal. Fitting parameters are given in Tables S12.

**Table S12.** Fitting parameters of the inversion recovery time traces in acidic solutions.

Compound and MW frequency	$a$	$T_1^a$ [ $\mu$ s]	$b$	$T_1^b$ [ $\mu$ s]	$T_1^{av}$ [ $\mu$ s]
<b>2x</b> , X	$0.88 \pm 0.01$	$231.0 \pm 1.0$	$0.12 \pm 0.01$	$38.0 \pm 2.0$	207.8
<b>2b</b> , X	$0.70 \pm 0.04$	$280.0 \pm 10.0$	$0.30 \pm 0.04$	$90.0 \pm 10.0$	223.0
<b>2b</b> , Q	$0.72 \pm 0.03$	$196.0 \pm 5.0$	$0.28 \pm 0.02$	$57.0 \pm 5.0$	157.1

### 3.4 Phase memory times of the nitroxide and the copper signal in **2x** and **2b**

The phase memory times of the observed spin coherences strongly affect the sensitivity of both the PELDOR and the RIDME experiments. The copper signal was not used for observation at Q-band frequencies and was therefore not measured. The phase memory times  $T_M$  of **2x** and **2b** have been measured using the two pulse ESEEM sequence. The results of these measurements are shown in Figures S16 - S18.

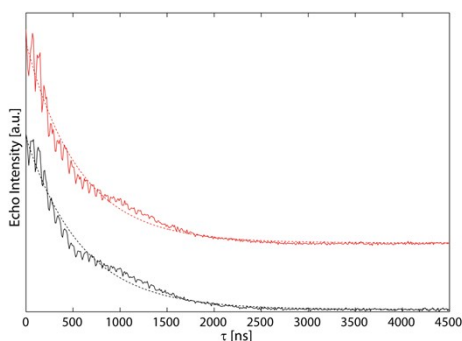


**Figure S16.** Two pulse ESEEM time traces (full lines) and simulations of the background function (dashed lines) of the copper signal of **2x** (black lines) and **2b** (red lines) in DMSO/MeOH (1:1.5) at X-band MW frequencies and a temperature of 20 K. The ESEEM time traces have been recorded at the maximum intensity of the copper signal.

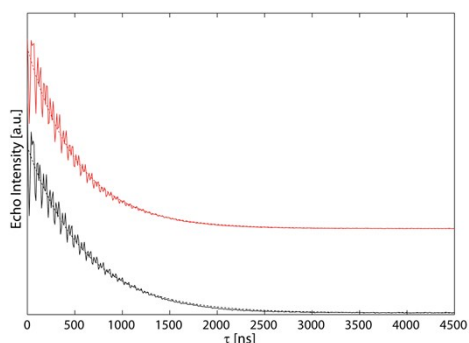


**Figure S17.** Two pulse ESEEM time traces (full lines) and the simulations of the background function (dashed lines) of the nitroxide signal of **2x** (black lines) and **2b** (red lines) in DMSO/MeOH (1:1.5) at X-band MW frequencies and a temperature of 20 K. The ESEEM time traces have been recorded at the maximum intensity of the nitroxide signal.

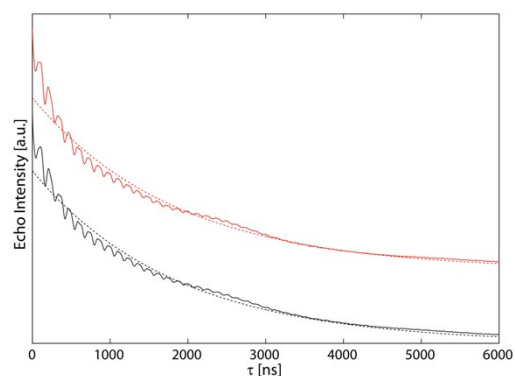


**Figure S18.** Two pulse ESEEM time traces (full lines) and simulations of the background function (dashed lines) of the nitroxide signal of **2x** (black lines) and **2b** (red lines) in d6-DMSO/MeOD (1:1.5) at Q-band MW frequencies and a temperature of 20 K. The ESEEM time traces have been recorded at the maximum intensity of the copper signal.

The ESEEM time traces have been fitted empirically using equation (S2) for the echo intensity  $I$  as a function of the interpulse separation  $\tau$ .

$$I = I_0 e^{-\tau/T_M} \quad (\text{S2})$$

The obtained Fitting parameters are given in Table S13.

**Table S13.** Fitting parameters of the two pulse ESEEM time traces of **2x** and **2b** at X- and Q-band (T = 20 K).

Compound and MW frequency	$T_M^{Cu}(X)$ [ns]	$T_M^{NO}(X)$ [ns]	$T_M^{NO}(Q)$ [ns]
<b>2x</b>	590 ± 5	605 ± 5	1835 ± 5
<b>2b</b>	560 ± 5	530 ± 5	1934 ± 5

At X-band, a mixture of DMSO and MeOH was used as solvent system (1:1.5). The occurrence of very strong deuteron modulations prevented the use of deuterated solvents at X-band frequency, as a complete removal of the deuteron modulations in the RIDME experiment could not be achieved. At Q-band frequency, the deuteron modulations are not as strong as at X-band frequency and could be removed from the RIDME time traces. The strongly increased phase memory times at Q-band frequencies are probably primarily owed to the use of deuterated solvents (changes in that order of magnitude have been reported before).<sup>4</sup> The measurement parameters are given in Table S14 and have been chosen identical for the copper and nitroxide signal, except for the *SRT*.

**Table S14.** Measurement parameters of the two pulse ESEEM time traces of **2x** and **2b** at X- and Q-band.

MW-band	X	Q
$P_{\pi/2}$ [ns]	10	14
$P_{\pi}$ [ns]	20	28
<i>SRT</i> <sup>a</sup> [μs]	300/9900	9900

<sup>a</sup> *SRT*s for the copper and nitroxide signal, respectively.

#### 4 Multispin effects in PELDOR of **2x** and **2b**

As mentioned in the main text, the occurrence of combination frequencies owed multispin effects can change the PELDOR form factor markedly. The occurrence of combination frequencies could manifest itself in the appearance of further extrema in the time traces, a shift of the existing extrema or a more pronounced damping to

name ea few possibilities. However, none of the aforementioned effects is observed. Aside from the increased modulation depth only subtle differences occur in the formfactor of the PELDOR time traces of **2x** and **2b**. As samples of **2x** always contain **2b** in relatively large fractions (~33%) the identification of multispin effects is further hampered. Three methods to investigate the origin of these slight deviations have been chosen: First, the PELDOR experiments on **2b** have been repeated using an ELDOR attenuation of 20 dB. The results of these measurements are shown and discussed in the main text and also in Figure S19. Secondly, the PELDOR measurements on **2b** have been repeated using the nitroxide for observation. As the copper is used for pumping and only one copper per molecule is available for pumping, no multispin effects are expected to occur using this set-up. The corresponding time traces are shown in Figure S19.

In accordance with the results obtained using the high ELDOR attenuation, no large changes of the formfactor are observed if the nitroxide is used for observation at any of the used frequency offsets. Surprisingly, the time trace at an offset of 150 MHz shows a large contribution owed to a low frequency modulation. The deviations caused by this low frequency modulation exceed those observed using any of the other measurement set-ups. As it was not possible to use the same pulse lengths using the “inverted” set-up as for the normal set-up (i.e. using copper for observation), an in depth analysis of the origin of this low frequency modulation is very difficult. An attempted analysis would be further complicated by the fact, that the nitroxide and copper signals overlap and therefore both contribute to the observed echo. Besides the pronounced low frequency modulation observed at 150 MHz frequency offset, no marked changes are observed using the inverted set-up. The absence of marked changes in both the attenuated and the inverted PELDOR experiment seem to corroborate the hypothesis, that multispin effects do not cause a marked change in the PELDOR formfactor. Finally, in addition to these experimental approaches, PELDOR time traces in which multispin effects are accounted for have been calculated. To do so the equations given by von Hagens *et al.*<sup>5</sup> have been combined with the orientation selection calculated by PeldorFit. In addition to this, one needs to consider orientation correlation of all three spin centers. Although the crystal structure implies a slight bending between the two copper nitroxide vectors (angle  $\alpha < 180^\circ$ ) a fully stretched complex geometry with  $\alpha = 180^\circ$  has been

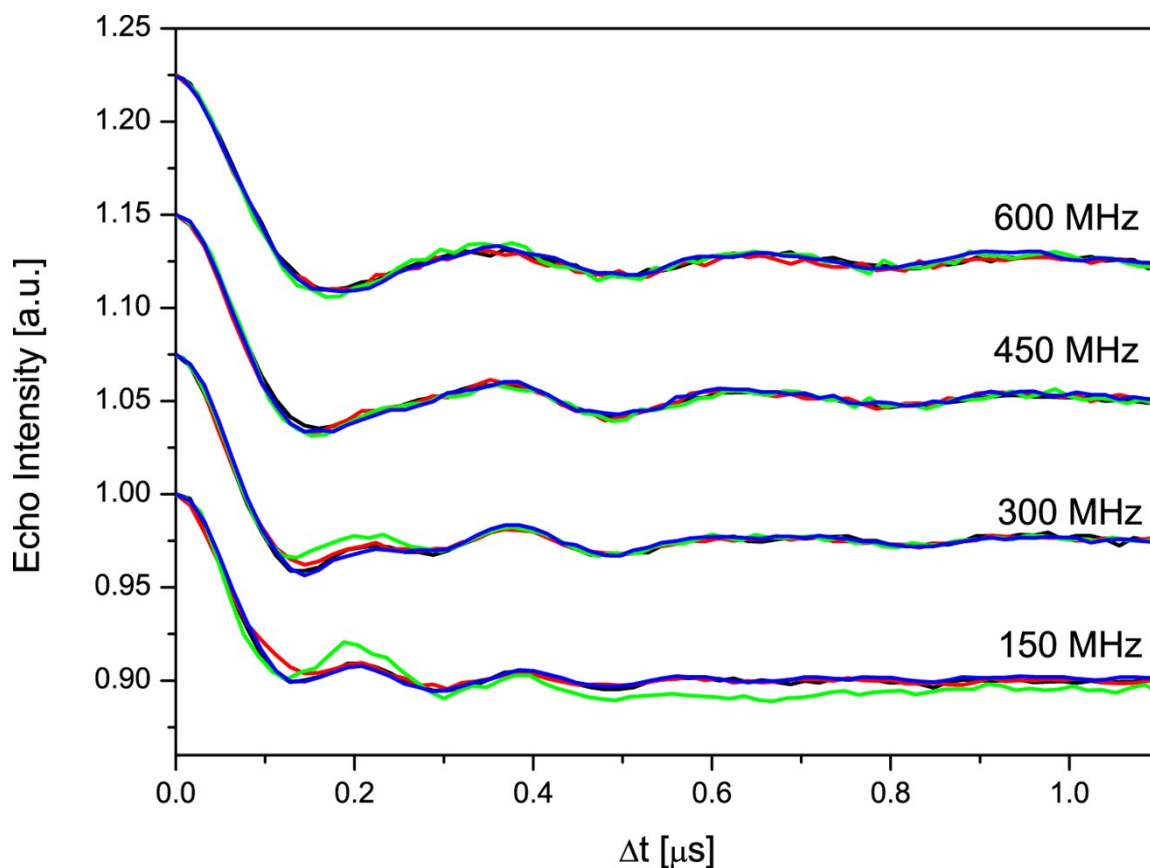


**Figure S19.** Background subtracted PELDOR time traces (scaled for ease of comparison to the same modulation depth of 10%) of **2x** observed on the copper center (black time trace), **2b** observed on the copper (red time trace), **2b** observed on the copper using an ELDOR attenuation of 20 dB (blue time trace) and **2b** observed on the nitroxide spin center (green time trace).

assumed. This implies that the angle between the field vector and both nitroxide copper vectors is identical. Furthermore, a distribution of distances as predicted by PeldorFit and the chemical equilibrium as described by equation (S2) was taken into account. The results of these theoretical considerations are shown in Figure S20 and Table S16.

**Table S16.** Observed and calculated modulation depths.

$\Delta\nu$ [MHz]	150	300	450	600
$V\lambda_{obs}$ ( <b>2x</b> ) [%]	40	31	24	21
$V\lambda_{calc}$ ( <b>2x</b> ) [%]	42	30	23	20
$V\lambda_{obs}$ ( <b>2b</b> ) [%]	70	56	42	37
$V\lambda_{calc}$ ( <b>2x</b> ) [%]	70	56	43	38

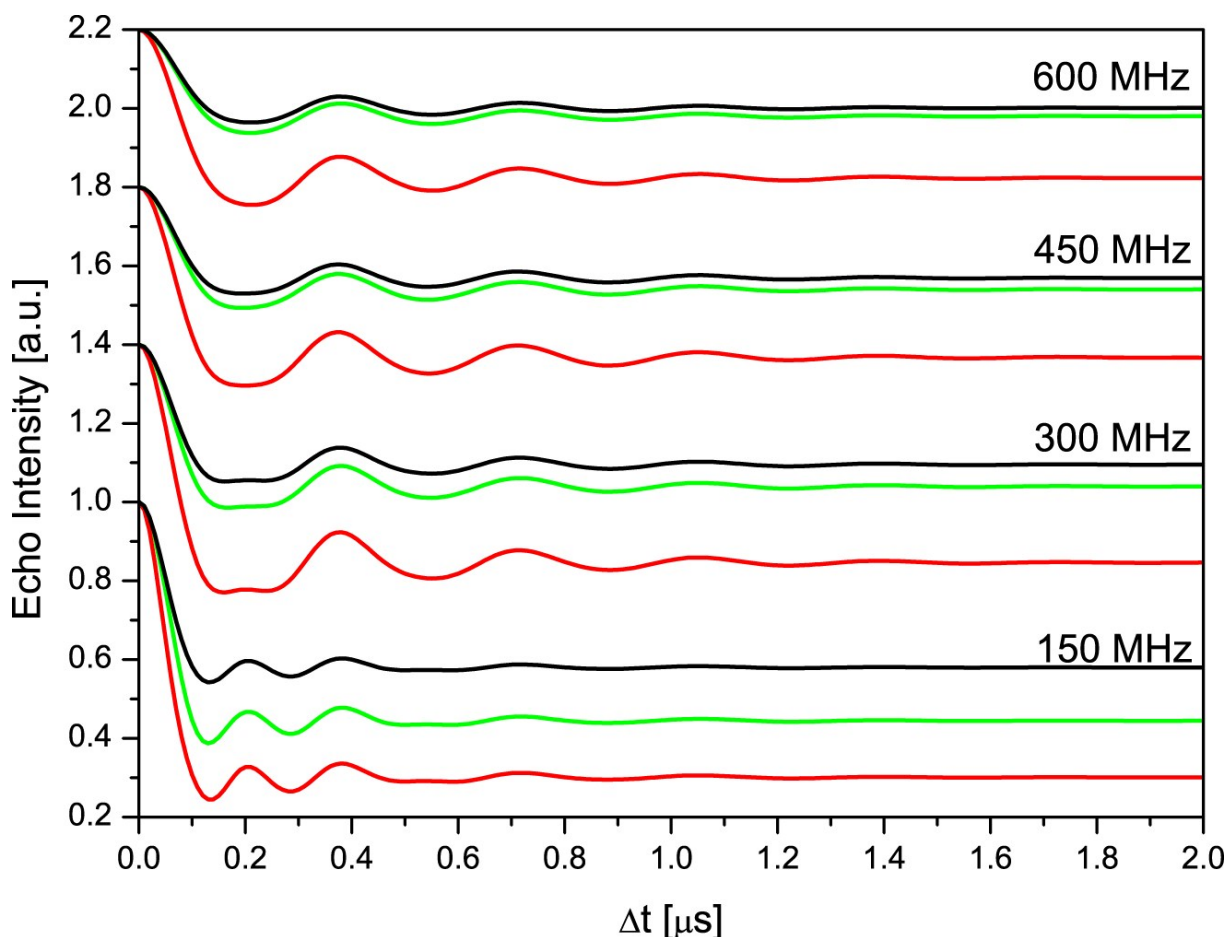


**Figure S20.** Calculated time traces using the orientational selectivity deduced by PeldorFit for **2x** (black lines), **2b** (red lines) and hypothetical pure two spin contribution (green lines).

Despite the simplified geometric model ( $\alpha = 180^\circ$ ), the simulation demonstrates the absence of marked multispin effects, aside from the increase in modulation depth. If the simulated time traces shown in Figure S21 are scaled to an identical modulation depth one can observe, that the very weak deviations in the different simulated time traces occur at the same position as found experimentally, namely mostly during the first modulation period (Figure S21). Furthermore, the simulations also allow understanding the reason for the absence of marked multispin effects. The exact antiparallel orientation which was assumed in the simulations for the two nitroxide spin, leads to equal dipolar coupling frequencies for the two nitroxide-copper spin pairs in the three spin system. The combination frequencies are therefore zero and twice the expected dipolar coupling frequency for the difference and sum frequencies, respectively. Thus, the difference frequencies lead to an apparent reduction of the modulation depth, as those frequencies are subtracted with the background during data processing. The sum frequencies on the other hand could lead to deviations in the formfactor. However, the relatively low

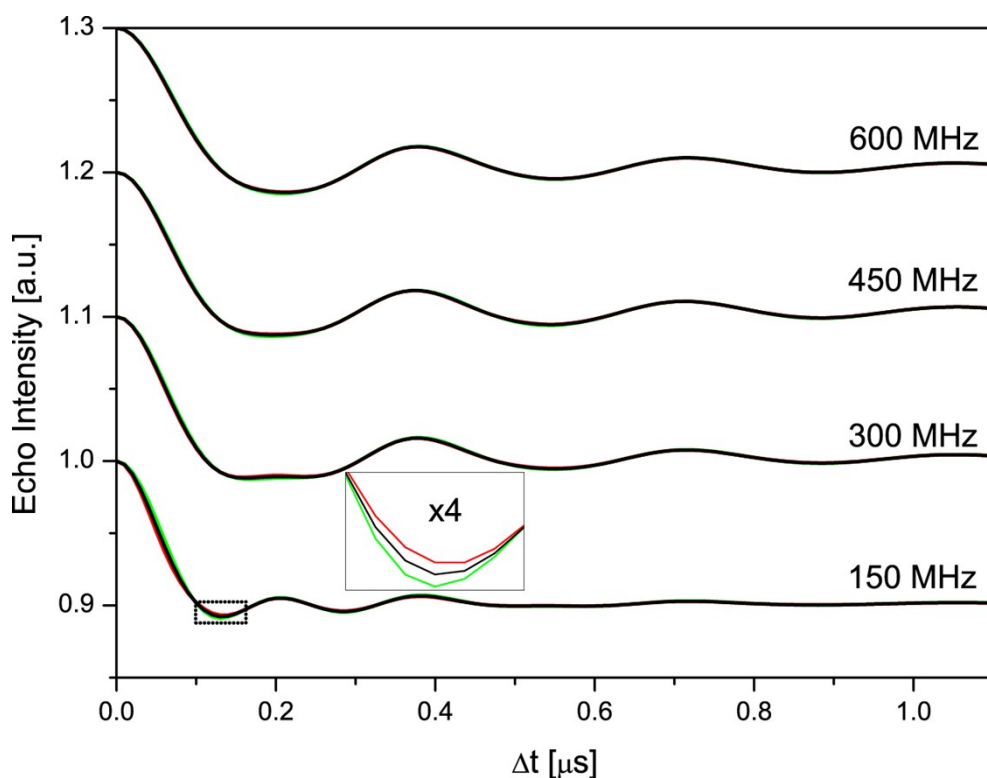


**Figure S21.** Calculated time traces using the orientational selectivity deduced by PeldorFit for **2x** (black lines), **2b** (red lines) and hypothetical pure two spin contribution (green lines) scaled to an identical modulation depth of 10%. The deviations are very weak and occur mostly during the first modulation period, as observed experimentally. The inset shows the marked part of the time trace in fourfold magnification.

probability for sum-frequencies which lie outside the range of frequencies which are already observed in the two-spin contribution leads to three-spin contributions which are not clearly visible in the time traces.

To conclude the discussion concerning multispin effects, the argument is summarized briefly. For different kinds of PELDOR experiments have been conducted. These experiments are measurements using the standard PELDOR set-up on **2x** (occurrence of multispin effects expected as roughly one third of the molecules are actually the threespin system **2b**), measurements using the standard PELDOR set-up on **2b** (occurrence of more pronounced multispin effects in comparison to **2x**), measurements using the standard PELDOR set-up with an ELDOR attenuation of 20 dB on **2b** (suppression of multispin effects owed to low inversion efficiency) and measurements using an inverted PELDOR set-up on **2b** (no multispin effects expected as only a single, copper centered spin is flipped by the pump pulse). None of these experiments showed marked deviations in their form factors as compared to any of the other experiments. Noteworthy, results which have

been obtained previously on a three-nitroxide spin system, in which orientation selectivity does not play a prominent role, do not show occurrence of further extrema or any shift of the position of the existing extrema in the form factor either, thereby favoring the latter explanation for the absence of marked multispin effects.<sup>5,6</sup> Additionally, multispin effects have been taken into account retroactively into the PELDOR simulations, using a simple geometric model ( $\alpha = 180^\circ$ ). The obtained theoretical time traces have modulations depths which agree with those observed experimentally. This agreement rules out a reduced probability for simultaneous spin flips, as the observed modulations depths are determined by the probability of single and simultaneous spin flips. Furthermore, the obtained theoretical time traces lack marked changes in their form factors as well. The very slight deviations occur mostly in the same regions, as those observed experimentally. Taking the results of the experiments and the theoretical considerations together strongly favors the occurrence of multispin effects which do not cause marked changes in the form factors.

## References

- (1) Abdullin, D.; Hagelueken, G.; Hunter, R. I.; Smith, G. M.; Schiemann, O. *Mol. Phys.* **2014**, *113* (6), 544–560.
- (2) Meyer, A.; Schnakenburg, G.; Glaum, R.; Schiemann, O. *Inorg. Chem.* **2015**, *54* (17), 8456–8464.
- (3) Neese, F. *Wiley Interdiscip. Rev. Comput. Mol. Sci.* **2012**, *2* (1), 73–78.
- (4) Jeschke, G.; Polyhach, Y. *Phys. Chem. Chem. Phys.* **2007**, *9* (16), 1895–1910.
- (5) Von Hagens, T.; Polyhach, Y.; Sajid, M.; Godt, A.; Jeschke, G. *Phys. Chem. Chem. Phys.* **2013**, *15* (16), 5854–5866.
- (6) Giannoulis, A.; Ward, R.; Branigan, E.; Naismith, J. H.; Bode, B. E. *Mol. Phys.* **2013**, *111* (18-19), 2845–2854.



# Appendix E

## PELDOR and RIDME Measurements on a High-Spin Manganese(II) Bisnitroxide Model Complex

Andreas Meyer,<sup>i</sup> Olav Schiemann<sup>i</sup>

Received 22th January 2016, published online 9th May 2016.

Reprinted with permission from

A. Meyer and O. Schiemann, *Journal of Physical Chemistry A* **2016**, *120*, 3463 - 3472.

Copyright ©2016, American Chemical Society.

### Own contributions to the manuscript

- Synthesis measured compounds.
- Conducting the EPR Measurements.
- Interpretation of the EPR data.
- Writing the manuscript.

---

<sup>i</sup> Institute of Physical and Theoretical Chemistry, University of Bonn, Wegelerstr. 12, Bonn, Germany.

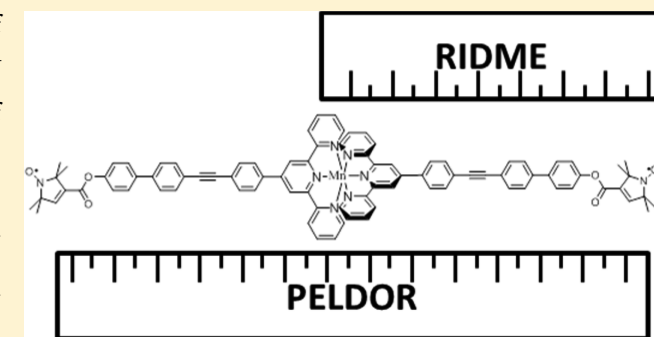
# PELDOR and RIDME Measurements on a High-Spin Manganese(II) Bisnitroxide Model Complex

Andreas Meyer and Olav Schiemann\*

Institute of Physical and Theoretical Chemistry, University of Bonn, Wegelerstr. 12, Bonn, Germany

## Supporting Information

**ABSTRACT:** A homoleptic bisnitroxide complex of manganese(II) was synthesized as a model system for EPR spectroscopic distance determinations involving high-spin metal ions and more than one distance. The performance of the RIDME experiment is compared with that of the more frequently used PELDOR experiment. It is shown that the PELDOR experiment yields both distances, Mn(II)–nitroxide and nitroxide–nitroxide, and that they can be separated to a certain extent, whereas the RIDME experiment yields only the Mn(II)–nitroxide distance. Both pulse sequences yield artifacts, either due to multispin effects or higher electron-spin transitions. Orientation selection is mostly introduced by the nitroxide signal and can be averaged out by variation of the observer field in the RIDME experiment. Thus, both methods



might be used complementarily to obtain a reliable picture of an unknown system.

## INTRODUCTION

The measurement of interspin distances in spin-labeled macromolecules using electron paramagnetic resonance (EPR) spectroscopy is a powerful tool to elucidate the structure and conformational distribution of these macromolecules.<sup>1</sup> Since its introduction, the dead-time free pulsed electron–electron double resonance (PELDOR or DEER) experiment<sup>2–4</sup> is probably the most prominent of the EPR experiments to determine distances between nitroxide spin labels in the range from 1.5 to 15 nm.<sup>5</sup> In contrast to binding two nitroxide spin labels to a protein or oligonucleotide, one can also make use of intrinsic paramagnetic centers like semiquinone<sup>6</sup> or tyrosyl<sup>7</sup> radicals, metal clusters,<sup>8</sup> or metal ions.<sup>9,10</sup> Recently, it has been shown that PELDOR can also be used for the localization of spin-labeled ligands<sup>11</sup> or paramagnetic metal centers<sup>12</sup> in proteins using trilateration. However, PELDOR measurements involving metal centers are usually more demanding than measurements involving only nitroxides, owing to orientation selection, broad spectral width, largely different *g*-tensors, and faster relaxation behavior.<sup>8,13,14</sup> While many examples involving copper-centered spins have been reported,<sup>15–21</sup> examples of other metal centers are still rather scarce.<sup>22–25</sup> Especially, high-spin metal ions are further complicated by the occurrence of zero-field splitting and various electron spin transitions.<sup>26–31</sup> Nevertheless, a series of experiments from the Goldfarb lab established Gd(III) labels as an alternative for nitroxide labels.<sup>32–34</sup> These labels yield in high-field/high-frequency PELDOR experiments a better sensitivity than nitroxides<sup>35</sup> and largely reduce multispin effects.<sup>36</sup>

Instead of changing the type of label,<sup>37–40</sup> it has been demonstrated that the relaxation-induced dipolar modulation enhancement (RIDME)<sup>41,42</sup> experiment can be a more sensitive method than PELDOR when measuring interspin distances between nitroxides and paramagnetic, low-spin metal centers like, for example, Cu(II)<sup>43</sup> or Fe(III).<sup>23,44,45</sup> However, it was also demonstrated that multiples of the dipolar frequency occur when using RIDME on high-spin metal ions like Gd(III).<sup>29</sup> Recently, Akhmetzyanov et al. reported successful PELDOR measurements on a heteroleptic manganese(II)–nitroxide model system,<sup>46</sup> and Sun Un<sup>47,48</sup> and Goldfarb<sup>49</sup> reported PELDOR measurements on high-spin Mn(II) in proteins. An early example of PELDOR involving Mn(II), albeit in a low-spin state, was reported by Astashkin et al.<sup>50</sup>

Here, the synthesis as well as PELDOR and RIDME measurements are reported on the model system (1) with one Mn(II) and two nitroxide spin centers (Scheme 1). The performance of the two pulsed EPR experiments is compared.

## EXPERIMENTAL SECTION

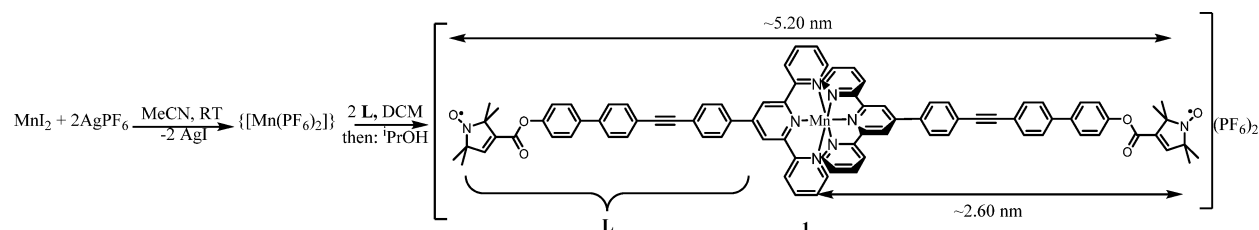
**Syntheses.** All syntheses and sample handling were conducted under exclusion of oxygen using Schlenk conditions. The synthesis of the ligand 2,5-dihydro-2,2,5,5-tetramethylpyrrole-*N*-oxyl-3-(4'-(4-(2,2':6',2''-terpyridyl)-phenylethynyl)-*p*-biphen-4-yl)carboxylate **L** has been described elsewhere.<sup>51</sup> Manganese diiodide and silver hexafluorophosphate were

Received: January 22, 2016

Revised: May 7, 2016

Published: May 9, 2016

## Scheme 1. Synthesis of Model Compound 1



purchased from Sigma-Aldrich and were used without further purification. Acetonitrile and dichloromethane were purchased in sealed bottles from Sigma-Aldrich and were used after bubbling argon gas through them for 15 min. Isopropanol was purchased from Sigma-Aldrich and was used after bubbling argon gas through it for 15 min. Deuterated solvents for EPR samples were purchased from Deutero Europe.

*Bis(2,5-dihydro-2,2,5,5-tetramethylpyrrole-N-oxyle-3-(4-(4-(2,2':6',2''-terpyridyl)-phenylethynyl-p-biphen-4-yl)-carboxylate)manganese(II) bis(tetraphenylborate) 1.* Manganese diiodide (13 mg, 0.042 mmol) was dissolved in 1 mL of dry acetonitrile at room temperature and mixed with 24 mg (0.095 mmol) of silver hexafluorophosphate dissolved in 0.5 mL of acetonitrile leading to immediate precipitation of silver iodide. The remaining solution was filtered off, and the precipitate was washed two times with 1 mL of acetonitrile. The filtrate was then mixed with 58 mg (0.086 mmol) of **L** dissolved in 2 mL of dichloromethane. The solution was stirred for 10 min before the volume of the solution was reduced by 30% under reduced pressure. Isopropanol (15 mL) was added to the remaining solution leading to the formation of an orange precipitate. The remaining solution was filtered off, and the precipitate was washed two times with 5 mL of isopropanol. Then, the precipitate was dried under reduced pressure yielding the product as light orange powder (80% yield). Anal. Calcd for **1**: C, 62.90; H, 4.20; N, 6.67. Found: C, 62.53; H, 4.33; N, 6.62%. ESI-MS:  $m/z = 694.73$  ( $[\text{Mn}(\text{L})_2]^{2+}$ ).

**Electron Paramagnetic Resonance Spectroscopy.** EPR samples were prepared by filling a 150  $\mu\text{M}$  solution of **1** (deuterated acetonitrile and deuterated dichloromethane, 1:3 v/v) in quartz glass EPR tubes having an outer diameter of  $\sim 3$  mm. The samples were then shock frozen in liquid nitrogen before transferring them to the precooled cavity. All results presented herein, except for the EPR spectrum shown in Figure 2a, were obtained on the same sample.

All EPR experiments (Figure 1) were performed on a Bruker ELEXSYS E580 EPR spectrometer at  $T = 5$  K and at Q-band frequencies using an ER 5106QT-2 resonator and an Oxford CF935 helium gas-flow cryostat. The microwave (MW) pulses were amplified using a 150 W TWT amplifier manufactured by Applied Systems Engineering.

The Hahn echo detected field sweep EPR spectrum was recorded with a  $\pi/2$  and  $\pi$  pulse length of 8 and 16 ns (pulses optimized on the nitroxide signal), respectively, using the full MW power (i.e., 0 dB attenuation). The interpulse delay was 500 ns, and the shot repetition time was 2 ms. The magnetic field was swept from 1003 to 1403 mT with a resolution of 0.1 mT per point (one scan). The experiment was repeated using an attenuation of 7 dB (pulse optimization on the manganese) leading to a more intense manganese signal.

The EPR spectra were simulated using the “pepper” routine of the EasySpin program package and the parameters given in

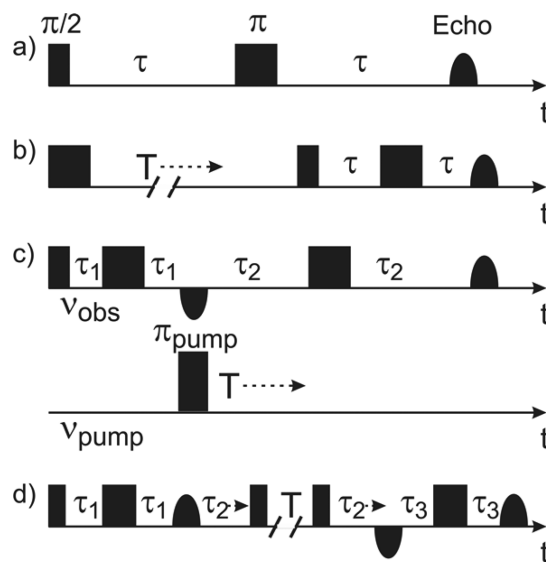


**Figure 1.** Pulse sequences used in this work. (a) Two-pulse Hahn echo detected field swept EPR. (b) Inversion recovery pulse sequence. (c) The dead-time free four-pulse PELDOR sequence. (d) The dead-time free five-pulse RIDME sequence.

**Table 1.**<sup>52</sup> The peak-to-peak line width was set to 1 mT for both the Gaussian and the Lorentzian contribution. The  $A$  and  $g$ -tensors were assumed to be collinear.

**Table 1. Parameters Used to Simulate the Electron Paramagnetic Resonance Spectra of 1**

	$g_x$	$g_y$	$g_z$	$A_x$ [MHz]	$A_y$ [MHz]	$A_z$ [MHz]
Mn	2.0040	2.0040	2.0040	250	250	250
NO	2.0100	2.0072	2.0027	16	16	95

The parameters for the inversion recovery (IR) experiments are collected in Table 2, and the IR curves were fitted biexponentially using 1.

$$I = I_0(1 - 2(w_1 e^{-t/T_1^1} + w_2 e^{-t/T_1^2})); \quad w_1 + w_2 = 1 \quad (1)$$

For the PELDOR measurements, the pump pulse was applied in the center of the cavity, and the observer pulses at the side of the resonator dip. The observer pulse lengths were used at 0 dB attenuation and were adjusted to yield the most intense echo signal at the observer frequency. A two-step phase cycle was used to eliminate baseline offsets. The magnetic field settings and the frequency offsets for the PELDOR measurement P1–P8 are specified in Figure 2 and Table 3 along with the other parameters.

The RIDME experiment was conducted at seven positions throughout the nitroxide signal and subsequently summed to obtain time traces with reduced distortions owed to orientation

**Table 2. Parameters Used for the Inversion Recovery Experiments on **1** ( $\nu_{\text{obs}} = 33.517$  GHz)**

parameters	Mn(II)	nitroxide
$\pi/2$ [ns]	8	8
$\pi$ [ns]	16	16
$T$ [ns]	1000	1000
$\tau$ [ns]	500	500
SRT <sup>a</sup> [ $\mu$ s]	970	19990
$B_0$ [mT]	1206.0	1210.0
SPP <sup>b</sup>	10	10
Att [dB] <sup>c</sup>	7	0

<sup>a</sup>SRT = shot repetition time. <sup>b</sup>SPP = shots per point. <sup>c</sup>Att = MW attenuation.

selection. The RIDME experiment was conducted by using either the refocused stimulated echo (RSE) or the refocused virtual echo (RVE). An eight-step phase cycle was used to eliminate unwanted echoes. The RIDME time traces were recorded at two different interpulse separations between the third and the fourth pulse. Division of the time trace with large interpulse separation by the time trace with low interpulse separation leads to suppression of ESEEM artifact peaks.<sup>2,3,41,42</sup> The measurement parameters are detailed in Table 4. In the plot of the time traces,  $\Delta t$  signifies the evolution time of the dipolar modulation.

To compare the signal-to-noise ratios in PELDOR and RIDME for **1**, both time traces are fixed to the same dipolar evolution time, here 1800 ns, and are averaged over all field positions measured in case of the RIDME experiment. The RIDME time trace is then divided by the RIDME reference time trace, and the result is normalized to 1 at  $t = 0$ . Then the PELDOR and the RIDME time traces are corrected for the background decay and are renormalized. This yields for both time traces  $S = 1$ . Then the signal intensity  $S$  is multiplied by the modulation depths  $V_\lambda$  of the two time traces.  $V_\lambda$  is then divided by the average noise  $\langle N \rangle$  of the time traces, yielding  $V_\lambda/\langle N \rangle$ . Division by the square root of the measurement time yields the normalized signal-to-noise (S/N) ratio per  $\text{min}^{1/2}$ , which will be stated in the text. The PELDOR and RIDME time traces were simulated using DeerAnalysis.<sup>54</sup>

## RESULTS AND DISCUSSION

For the synthesis of **1**,  $\{[\text{Mn}(\text{PF}_6)_2]\}$  is generated in situ as the source of the manganese(II) cations. Addition of a slight excess of the ligand **L** at room temperature to the solution allows precipitating **1** using isopropanol (Scheme 1). The homoleptic

**Table 4. Measurement Parameters Used for RIDME ( $\nu_{\text{obs}} = 33.517$  GHz)**

parameters	RSE	RVE
$\pi/2$ [ns]	8	8
$\pi$ [ns]	16	16
$T^a$ [ $\mu$ s]	3/25	3/25
$\tau_1$ [ns]	520	520
$\tau_2^b$ [ns]	-40	-40
$\tau_3$ [ns]	500	500
SRT <sup>c</sup> [ $\mu$ s]	2000	2000
Att <sup>d</sup> [dB]	0	0
averages <sup>e</sup>	130	36
SPP <sup>f</sup>	3	3
duration <sup>g</sup> [mins]	270	155

<sup>a</sup>The two values correspond to the measurement of the background decay function with no dipolar modulations and the measurement with dipolar modulations. <sup>b</sup>Initial value for  $\tau_2$ . <sup>c</sup>SRT = Shot repetition time. <sup>d</sup>Att = microwave attenuation. <sup>e</sup>The same amount of averages was used for both values of the interpulse separation  $T$ . <sup>f</sup>SPP = shots per point. <sup>g</sup>Duration = total measurement time, accounting for the need to record a nonmodulated RIDME time trace and the measurements at different field positions.

complex **1** was chosen over the heteroleptic complex<sup>34</sup>  $[\text{Mn}(\text{L})(\text{tpy})]^{2+}$  in this study, as the heteroleptic complex is expected to give rise to a mixture of  $[\text{Mn}(\text{tpy})_2]^{2+}$ ,  $[\text{Mn}(\text{L})_2]^{2+}$ , and  $[\text{Mn}(\text{L})(\text{tpy})]^{2+}$  in solution maybe also accompanied by ligand/solvent replacement.<sup>55</sup>

Dissolving **1** in a 1:3 mixture of deuterated dimethyl sulfoxide (DMSO- $d_6$ ) and  $\text{CDCl}_3$  leads to the EPR spectrum in Figure 2a with the typical Mn(II) hyperfine coupling sextet observable at X-band MW frequency. However, in this case it was impossible to conduct successful PELDOR or RIDME measurements. We attribute this to the lability of Mn(II) bis-terpyridine complexes in this solvent, which leads to the replacement of the terpyridine ligands by solvent molecules.<sup>46,55</sup> Therefore, a mixture of deuterated acetonitrile and dichloromethane (1:3) was used instead, which led to the spectrum shown in Figure 2b and allowed conducting successful PELDOR and RIDME measurements. The intense central signal is due to the nitroxide-centered spin and could be simulated with spin-Hamiltonian parameters typical for nitroxides (Table 1). In the presence of the nearby manganese center the spin–lattice relaxation time of the nitroxide center is strongly reduced, and it is possible to obtain the unsaturated nitroxide signal without the need for low repetition rates. At 5 K, shot repetition times (SRT) of 2  $\mu$ s were found to be

**Table 3. Parameters Used for the PELDOR Measurements ( $\nu_{\text{pump}} = 33.517$  GHz)**

	$\pi/2$ [ns]	$\pi$ [ns]	$\pi_{\text{pump}}$ [ns]	$\tau_1^a$ [ns]	$\tau_2$ [ns]	SRT [ $\mu$ s]	$B_0$ [mT]	O/P <sup>b</sup>	$\Delta\nu^c$ [MHz]	SPP <sup>d</sup>	dur <sup>e</sup> [mins]
P1	14	28	16	540	1800	200	1192.5	B/C	90	50	19
P2 <sup>f</sup>	14	28	16	540	1800	200	1192.5	B/C	90	50	15
P3	22	44	16	540	1800	200	1192.5	A/C	150	50	19
P4	20	40	16	540	6500	2000	1192.5	D/C	-90	10	32
P5	20	40	16	540	6500	2000	1195.7	C/D	90	10	17
P6	20	40	10	540	6500	2000	1195.7	C/D	90	10	5
P7 <sup>g</sup>	20	40	16	540	6500	2000	1195.7	C/D	90	10	8
P8	20	40	10	540	5300	2000	1189.2	C/B	90	10	9

<sup>a</sup> $\tau_1$  was incremented in 10 steps of 12 ns to average deuteron ESEEM modulations. <sup>b</sup>O/P = Observer and pump positions in Figure 2. <sup>c</sup> $\Delta\nu = \nu_{\text{obs}} - \nu_{\text{pump}}$ . <sup>d</sup>SPP = shots per point. <sup>e</sup>Duration = total measurement time in minutes. <sup>f</sup>ELDOR channel attenuated by 20 dB. <sup>g</sup>Inversion recovery filter used with an inversion pulse of 16 ns and an interpulse separation of 8  $\mu$ s between the inversion pulse and the following PELDOR sequence.<sup>53</sup>

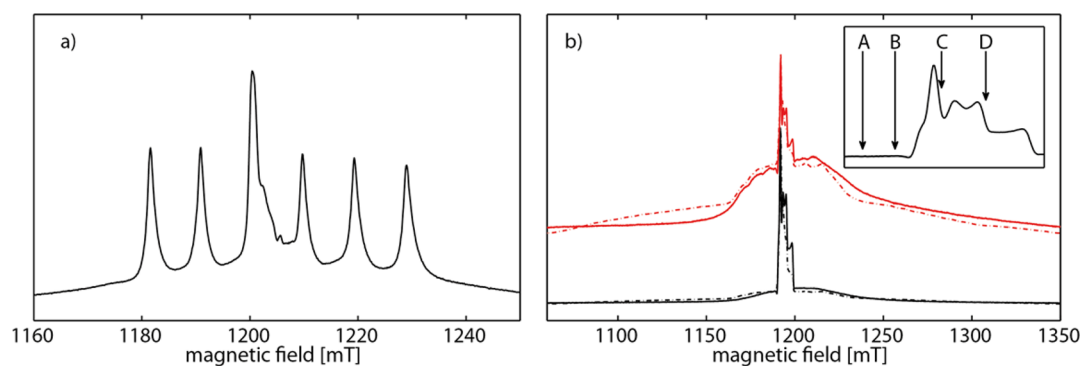


**Figure 2.** Two-pulse Hahn echo detected field-swept EPR spectra of **1** (solid line) at Q-band overlaid with the simulation (dashed line) in (a) DMSO- $d_6$  and CDCl $_3$  (1:3) and (b) deuterated acetonitrile and dichloromethane (1:3). (inset) The positions of the pump and observer pulses in the PELDOR experiments as specified in Table 3.

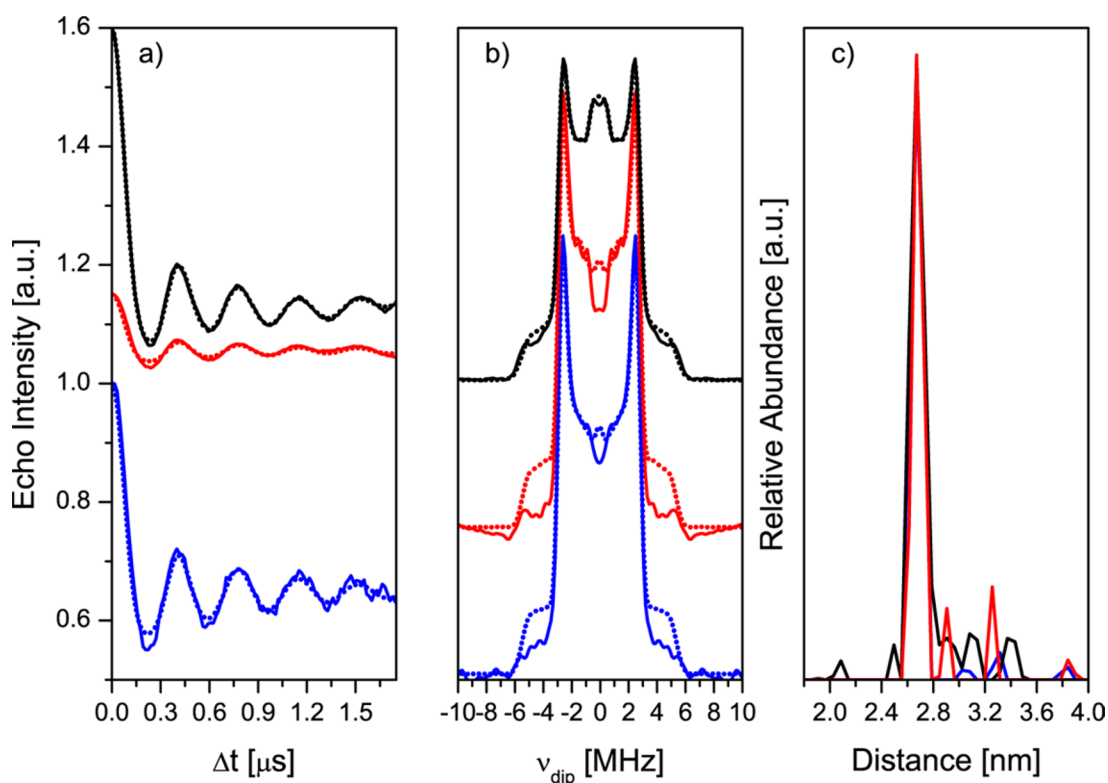


**Figure 3.** Q-band PELDOR measurement aimed at the manganese–nitroxide distance in **1** using the experimental set ups P1, P2, and P3 (black, red, and blue lines, respectively) as specified in Table 3. (a) Background-corrected time traces and simulations using DeerAnalysis (full and dotted lines, respectively), (b) experimental and simulated Fourier transform of the time traces (full and dotted lines, respectively), and (c) the corresponding, normalized distance distributions (regularization parameter  $\alpha = 0.01$ ).

sufficient to obtain an optimized nitroxide echo. In comparison, an SRT of 10  $\mu\text{s}$  had to be used for the nitroxide in the copper analogue of **1** at a temperature of 20 K.<sup>43</sup> In the absence of metal centers, temperatures of 35–40 K must be used to obtain SRT values as low as 2  $\mu\text{s}$ .<sup>56,57</sup> The broad absorption underneath this signal is due to the Mn(II) spin center. This signal can be enhanced by attenuating the MW power by 7 dB (red graph in Figure 2b) because the nutation frequency  $\omega_{\text{nut}}$  does depend on the spin quantum numbers  $S$  and  $m_s$  (2).<sup>58</sup> For example, the nutation frequency  $\omega_{\text{nut}}$  for the  $m_s = -1/2$  to  $m_s = +1/2$  transition of a spin with  $S = 5/2$  is three times higher than the nutation frequency  $\omega_{1/2}$  of an  $S = 1/2$  spin.

$$\omega_{\text{nut}} = \sqrt{S(S+1) - m_s(m_s - 1)} \omega_{1/2} \quad (2)$$

Using an MW attenuation of 7 dB to reduce the flipping angle of the Mn(II)-centered spins yields not only a more intense Mn(II) signal but also better resolves the splitting of the manganese lines. A similar spectrum, however, with unresolved Mn(II) splitting, has been observed for the analogous heteroleptic complex.<sup>46</sup> The Mn(II) spectrum could be simulated with zero-field splitting parameters  $|D|$  and  $|E|$  of 1500 and 300 MHz, respectively, and the hyperfine coupling and  $g$ -tensor parameters given in Table 1. These zero-field splitting values are in agreement with values from previous studies.<sup>46,59</sup> The value of  $D$  is higher than for unstrained, symmetric, six-coordinate complexes but still lies in the typical range of  $D$  values found for six-coordinate Mn(II) complexes.<sup>49,60–64</sup> Noteworthy, it was not possible to obtain an



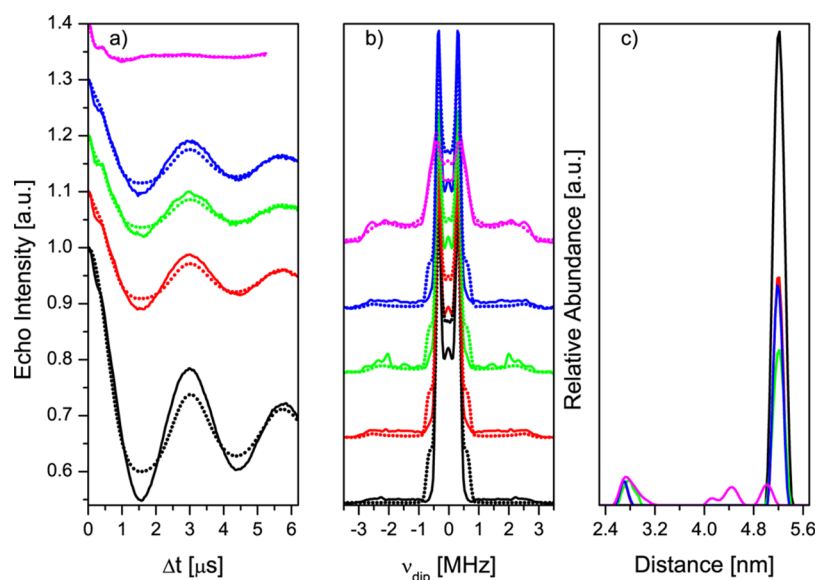


**Figure 4.** Results of the Q-band PELDOR measurements aimed at selecting the nitroxide–nitroxide distance of **1** using the experimental setups P4 (black), P5 (red), P6 (green), P7 (blue), and P8 (purple). (a) Background corrected time traces and simulations using DeerAnalysis (full and dotted lines, respectively), (b) experimental and simulated Fourier transforms of the time traces (full and dotted lines, respectively), and (c) the corresponding distance distributions (regularization parameter  $\alpha = 1$ ).

echo-detected EPR spectrum of the Mn(II)-centered spin of **1** in this solvent mixture at X-band frequencies.

Performing distance measurements on complex **1** should yield two different distances, the two equal Mn(II)–nitroxide distances, and one nitroxide–nitroxide distance. Three PELDOR experiments using the manganese-centered spins for observation and the nitroxide for pumping were conducted to obtain the manganese–nitroxide distance. The results of the PELDOR measurements are shown in Figure 3.

In all experiments shown in Figure 3, the pump pulse is applied on the nitroxide spectrum close to its maximum intensity and the detection pulses at 90 or 150 MHz higher frequency on Mn(II). All time traces show only weak orientation selection. On the one hand, this is due to the position of the pump pulse on the nitroxide spectrum, at which all orientations are excited. On the other hand, only little orientation selection on the manganese-centered spin is expected, since the manganese spin center has a highly symmetric  ${}^6A_1$  electronic ground state even though the ligand reduces the overall symmetry of the complex to  $D_{2d}$ .<sup>65</sup> In addition, it is suspected that zero-field splitting effects are probably diminished due to a distribution of magnitudes and orientations in the zero-field splitting tensor similar to the situation observed for Gd(III).<sup>66</sup> In the first experiment P1 (black lines in Figure 3), a frequency offset of 90 MHz was used. This setup yields a modulation depth of 45% and an S/N of  $18.6 \text{ min}^{-1/2}$ . The modulation depth is 250% higher than the value observed by Akhmetzyanov et al. for the heteroleptic complex.<sup>46</sup> For identical pumping pulse lengths, one would expect an increase in modulation depth of 95% for the homoleptic over the heteroleptic complex.<sup>43,67–69</sup> The much larger observed increase of the modulation depth suggests a lower degree of ligand dissociation in the solvent system used in the study here. The corresponding distance distribution shows one dominating peak at  $2.68 \pm 0.06 \text{ nm}$  in agreement with the value of 2.65 nm for the analogous, heteroleptic Mn(II) complex as reported by Akhmetzyanov et al.<sup>46</sup> Furthermore, this distance fits nicely to the known geometry

of the ligand<sup>51</sup> and is also similar to the metal nitroxide distance of 2.64 nm found using EPR spectroscopy and X-ray crystallography for the copper analogue of complex **1**.<sup>43</sup> Furthermore, the width of the distance distribution is even slightly lower than for the copper analogue of **1**, indicating that no additional zero-field splitting induced damping of the modulations occurs, in agreement with results obtained by Yulikov et al.<sup>70</sup> Thus, the settings of the pulse sequence enabled a separation of the Mn(II)–nitroxide distance from the nitroxide–nitroxide distance. However, the dominating distance peak is accompanied by a series of small peaks (less than 10% intensity relative to the dominating peak). These peaks do not correspond to expected distances but may stem from multispin effects,<sup>67–69</sup> partial overlap of pump and observer pulses and residual orientation selection. Experiment P2 (red lines in Figure 3) uses the same parameters as P1, except for an attenuation of 20 dB of the pump pulse. Attenuating the ELDOR channel decreases the inversion efficiency of the pumped spins and should therefore reduce at least some of the artifact peaks if they are due to multispin effects.<sup>69,71</sup> And indeed, the amount of artifact peaks in the distance distribution is reduced, and while the dominating peak appears at the same position it is slightly narrower than in P1 ( $2.68 \pm 0.04 \text{ nm}$ ). This behavior indicates that multispin effects are one of the reasons for the artifact peaks. That multispin effects contribute in PELDOR experiments of AB<sub>2</sub> systems was also observed for the Cu analogue of **1**.<sup>43</sup> In experiment P3 (blue lines in Figure 3), the frequency offset was increased to 150 MHz. This leads to a reduced S/N of  $5.6 \text{ min}^{-1/2}$ , but at the same time the amount of artifact peaks in the distance distribution is largely reduced as well. Therefore, experiment P3 suggests that in addition to orientation selection and multispin effects, the overlap of pump and observer pulse may also lead to slight distortions of the time trace.<sup>1,72</sup> Another possible source for the low-intensity distance peaks are distortions of the Pake pattern owed to a large zero-field splitting interaction and breakdown of the high-field approximation as observed before for a nitroxide-labeled Gd(III)–terpyridine complex.<sup>73</sup> For the

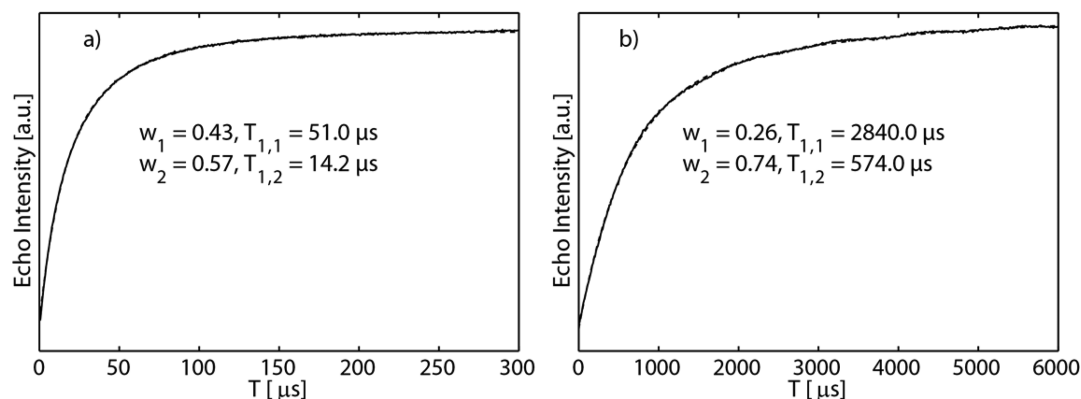


**Figure 5.** Q-band IR time traces (full lines) and their biexponential fits (dotted lines) on (a) the manganese and (b) the nitroxide signal.

Mn(II)/nitroxide case here, the  $D$  value of 1.5 GHz corresponds to 4.5% of the Q-band MW frequency, which is comparable to the 6.3% found for pairs of gadolinium(III) ions at W-band ( $D$  value of 6 GHz). However, the notable deviations of the Pake patterns observed in that case were only seen for  $\Delta m_s = 1$  electron spin transitions involving the higher  $m_s$  spin quantum numbers  $\pm 7/2$  and  $\pm 5/2$ .<sup>26</sup> Thus, this effect is probably less pronounced here in the Mn(II) case. Yulikov et al. reported numerical examples for Gd(III) nitroxide pairs,<sup>70</sup> which indicate that a  $D$  value of 600 MHz at X-band would not lead to a significant broadening of the distance distribution, but small artifact peaks were observed in their work. It can therefore be expected that a  $D$  value of 1500 MHz at Q-band frequencies would affect the distance distribution in a similar minor way.

For measurements of the nitroxide–nitroxide distance, the pump pulse and the observer pulses were placed on the nitroxide spectrum (Figure 2, entries P4–P7 in Table 3). The results of these experiments are shown in Figure 4.

All time traces in Figure 4 show contributions of two different modulations with modulation periods of  $\sim 2900$  and  $360$  ns, corresponding to frequencies of 0.34 and 2.78 MHz, respectively. Such frequencies translate into distances of 5.25 and 2.65 nm, which are the nitroxide–nitroxide and the manganese–nitroxide distances. This is reasonable, as the nitroxide and the manganese EPR spectra are superimposed. Therefore, if the nitroxide is used for observation, contributions of the manganese-centered spin are expected. In experiment P4 (black lines in Figure 4), the nitroxide is pumped at the same position as in experiments P1–P3 with a frequency offset of  $-90$  MHz. The resulting time trace shows a slightly increased orientation selection (suppression of the parallel component of the dipolar coupling), and a large modulation depth of 33% is observed. The higher-frequency modulation is visible in the beginning of the time trace. However, the small contribution of the higher-frequency modulation is treated as noise by DeerAnalysis, so that only one peak at  $5.21 \pm 0.08$  nm appears in the distance distribution. Experiment P5 (red lines in Figure 4) uses the same parameters as P4 but with interchanged pump and observer pulses. Therefore, the same orientation selection is observed. The modulation depth is, however, considerably lower and amounts to only 16%. Noteworthy, the contribution of the higher-frequency modulation appears to be unaffected by interchanging pump and observer pulses. Since this leads to a higher relative contribution of the high-frequency modulation, DeerAnalysis no longer treats this modulation as noise, and a second peak appears in the distance distribution centered at

2.69 nm. The relative heights of the peaks in the distance distribution (1:10 favoring the larger distance) allows to estimate a modulation depth of  $\sim 2\%$  for the high-frequency modulation. In experiment P6 (green lines in Figure 4), the length of the pump pulse is reduced to 10 ns. This should increase the contribution of the manganese spin on cost of the nitroxide spin because the turning angle of the pulse is now matched to the manganese spin and underturns the nitroxide spin (eq 2). And indeed, the integrated intensity of the manganese–nitroxide distance peak increases on expense of that of the nitroxide–nitroxide distance. In experiment P7 (blue lines in Figure 4), an inversion recovery filter is applied prior to the usual PELDOR sequence.<sup>53</sup> The inversion recovery filter is supposed to suppress contributions of the manganese spin if it acts as observed spin. However, the form factor of experiment P7 is virtually identical to the form factor of experiment P5 as are their resulting distance distributions. This suggests that the manganese-centered spin is not contributing as observer spin but rather as pumped spin. This is also in agreement with expectations based on the phase memory time of the manganese-centered spin of  $\sim 1.3 \mu\text{s}$  (see Supporting Information). The large observation windows used in experiments P4–P7 lead to pulse sequences that exceed  $10 \mu\text{s}$  total length, that is, almost 8 times more than the phase memory time of the manganese-centered spin. Finally, in experiment P8 (purple lines in Figure 4), the pump pulse is placed outside the nitroxide spectrum, using a setup similar to that in P1 but with pump and observer pulses interchanged. The corresponding time trace has a modulation depth of only 5%. The distance distribution shows a peak at 2.62 nm, which is identical to the peak observed in experiment P6, where a pump pulse of equal duration was used. Aside from that peak, broad peaks at 4.3 and 5.1 nm are observed. These distances correspond to the Pake pattern of the nitroxide–nitroxide distance due to off-resonance excitation of the low field edge of the nitroxide spectrum by the pump pulse. As shown on the copper analogue, predominant excitation along the  $x$  direction of the nitroxide leads to a pronounced parallel component of the dipolar coupling tensor<sup>43</sup> and thus to distance peaks at the actual nitroxide–nitroxide distance and at 81% of the actual distance. Thus, a completely selective measurement of the nitroxide–nitroxide distance was not possible using PELDOR. Similar measurements were performed before on nitroxide-labeled copper(II) and gadolinium(III) terpyridine complexes. Large  $g$  shifts of the copper-centered spin reduce or even remove spectral overlap in the case of copper–nitroxide systems, therefore allowing a more selective PELDOR experiment.<sup>21,43</sup> In the gadolinium

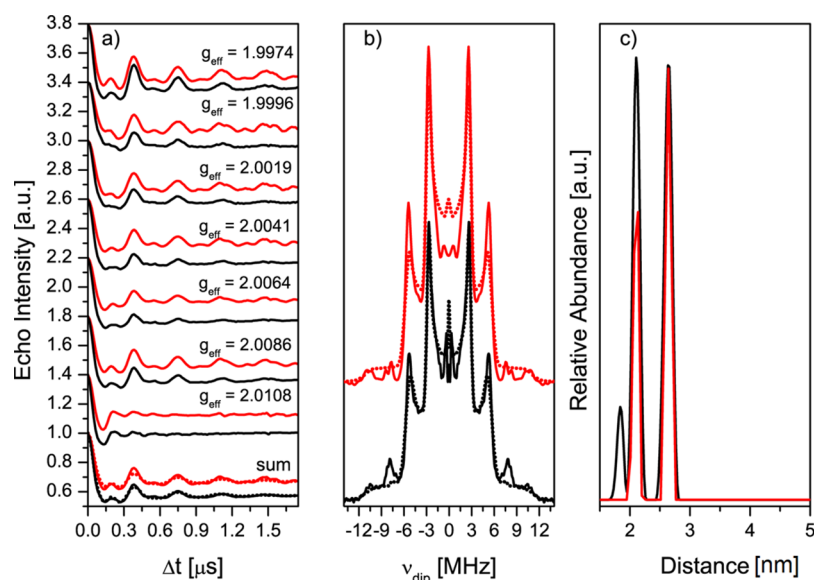
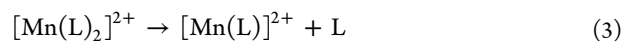


**Figure 6.** Q-band dead-time free RIDME measurements on **1** using the RSE (black lines) and RVE (red lines) of the nitroxide for observation. (a) RIDME time traces at the field positions used and their sum. The summed time traces were simulated with DeerAnalysis (dotted line), (b) Fourier transform of the summed time trace, and (c) the corresponding distance distribution (regularization parameter = 0.1).

case, the nitroxide and the gadolinium spectrum overlap. The obtained distance distribution is in this case very broad and might contain a contribution stemming from the Gd–nitroxide distance.<sup>73</sup> Nonetheless, the experimental setup P4–P7 clearly favors the nitroxide–nitroxide distance, especially the setup P4.

The modulation depths in experiments P1 and P4 allow estimating to which degree the ligand molecules L were replaced by solvent molecules S. Taking into account the contribution of the higher-frequency modulation, an inversion efficiency  $I$  of roughly 31% is obtained for the pumped nitroxides. This is  $\sim 30\%$  lower than observed in a bisnitroxide model compound using a similar setup. This means that the dissociation degree  $\alpha$  of the complex **1** amounts to roughly 30% according to 3.



Using the theory given by Bode et al.,<sup>68</sup> the expected modulation depth in experiment P1 can be calculated using the dissociation degree  $\alpha$  and inversion efficiency  $I$  estimated above.

$$V_{\lambda, \text{calc}} = \alpha \cdot I + (1 - \alpha) \cdot (2I - I^2) = 46\% \quad (4)$$

This value is very close to the experimentally observed value of 45%.

In addition, the dead-time free RIDME experiment was performed to check how it performs in comparison with the PELDOR experiment. To find the right value for the inter pulse delay  $T$ , IR experiments were performed on the nitroxide and the Mn(II) signal yielding the curves in Figure 5. Biexponential IR curves were obtained for both the nitroxide and the manganese spin center. Such biexponential behavior is expected for a slowly relaxing spin, which shows dipolar interaction with a fast-relaxing spin (i.e., for the nitroxide-centered spin).<sup>74</sup> The occurrence of a biexponential decay for the fast-relaxing Mn(II) may reflect the presence of more than one Mn(II) species caused by ligand/solvent exchange. On the basis of the determined  $T_1$  time constants and the observations made on

other systems,<sup>23,43</sup> a delay time of 25  $\mu\text{s}$  was chosen for a sensitive RIDME measurement.

Placing the dead-time free RIDME pulse sequence on several positions of the nitroxide signal of **1** yields the time traces in Figure 6.

The RIDME experiment was conducted in two different ways using either the refocused stimulated echo (RSE, black lines in Figure 6) or the refocused virtual echo (RVE, red lines in Figure 6). For both echoes, only at  $g_{\text{eff}} = 2.0108$  strong orientation selection is observed. Nevertheless, all time traces were summed for the sake of reducing orientation selectivity and analyzed with DeerAnalysis. The summed time trace shows a modulation depth of 43% (RSE) and 33% (RVE). Despite the lower modulation depth, the RVE RIDME is more sensitive than the RSE RIDME, with S/N values of 34 and 23  $\text{min}^{-1/2}$ , respectively. Both experiments are thus slightly more sensitive than PELDOR, by a factor of 1.8 and 1.2, respectively. In principle, the RIDME experiment is even more sensitive if the division by the reference time trace for ESEEM suppression can be avoided. This could be achieved, for example, by working at higher microwave frequencies or by performing the Q-band RIDME experiment in protonated solvents.<sup>22</sup>

As also observed for a Gd(III)–Gd(III) model system, the Fourier transforms of both summed time traces show Pake patterns for the  $|\Delta m_s| = 1, 2,$  and  $3$  transitions of the high-spin Mn(II) center.<sup>29</sup> Note that the parallel component of the  $|\Delta m_s| = 3$  transition is not resolved. Transforming the time traces into the distance domain yields a distance distribution with peaks at 1.81 (only RSE), 2.08, and 2.63 nm with widths of 0.06 and 0.04 nm for the RSE and RVE, respectively. The latter peak, already observed using PELDOR, corresponds to the Mn(II)–nitroxide distance. The former two are 21% and 31% shorter than the actual interspin distance and correspond to the  $|\Delta m_s| = 2$  and  $|\Delta m_s| = 3$  electron-spin transitions. While the peak corresponding to the actual distance is easily discerned from the artifact peaks in the model study at hand, this might not be the case for more complicated systems. Interestingly, the RVE RIDME is not only superior in terms of S/N but also contains lower contributions from the  $|\Delta m_s| = 2$  and  $|\Delta m_s| = 3$



transitions. Additionally, the modulations are less damped than in the RSE RIDME, which leads to narrower distance peaks. Beyond the higher electron spin transitions the distance distributions show no additional peaks as in the PELDOR experiments. This indicates that the summed RIDME time traces do not suffer from orientation selectivity, zero-field splitting induced distortions, or multispin effects.

## CONCLUSION

With respect to Mn(II)–nitroxide distance measurements with PELDOR, the homoleptic bis-terpyridine manganese(II) complex **1** led to similar results as those obtained by Akhmetzyanov et al. on the related heteroleptic complex.<sup>46</sup> In addition and as for three-spin nitroxide systems, the homoleptic AB<sub>2</sub> system used here gives rise to multispin effects in the PELDOR experiment. The residual orientation selectivity appears to be dominated by the orientation selection of the pumped nitroxide and cannot be fully removed owing to bandwidth limitations. The zero-field splitting of the manganese spin induces if at all only minor artifact peaks in the distance distribution. In contrast, the RIDME derived distance distribution contains intense artifact peaks, owing to the occurrence of integer multiples of the actual dipolar coupling frequency due to higher electron-spin transitions. Field averaging allows full removal of orientation selection from RIDME. Regarding the separation of the Mn(II)–nitroxide and the nitroxide–nitroxide distances in PELDOR, the Mn(II)–nitroxide distance could be easily separated by detecting on the Mn(II) and pumping on the nitroxide signal, while the nitroxide–nitroxide distance could not be measured without a contribution of the Mn(II)–nitroxide distance, as the manganese and nitroxide spectra overlap and the Mn(II)-centered spin always contributes as pumped spin. In addition, an investigation of the modulation depths allowed estimating the dissociation degree of complex **1** to 30%. In RIDME only the Mn(II)–nitroxide distance could be measured, which is an advantage with respect to assigning the distances but a disadvantage with respect to getting as much information as possible. Because of the <sup>6</sup>A<sub>1</sub> ground state of Mn(II), orientation selectivity did not play a prominent role in either experiment, PELDOR or RIDME. In terms of sensitivity, both RIDME experiments are slightly more sensitive than the PELDOR experiment. Thus, both methods, PELDOR and RIDME, have their advantages and disadvantages in the case at hand and might be used indeed together to yield a reliable picture of an unknown system.

## ASSOCIATED CONTENT

### Supporting Information

The Supporting Information is available free of charge on the ACS Publications website at DOI: 10.1021/acs.jpca.6b00716.

Two-pulse ESEEM time traces and their Fourier transforms. PELDOR and RIDME time traces. (PDF)

## AUTHOR INFORMATION

### Corresponding Author

\*E-mail: schiemann@pc.uni-bonn.de.

### Notes

The authors declare no competing financial interest.

## ACKNOWLEDGMENTS

We gratefully acknowledge the Deutsche Forschungsgemeinschaft for funding through the SFB813.

## REFERENCES

- (1) Jeschke, G. DEER Distance Measurements on Proteins. *Annu. Rev. Phys. Chem.* **2012**, *63*, 419–446.
- (2) Milov, A. D.; Ponomarev, A. B.; Tsvetkov, Y. D. Electron-Electron Double Resonance in Electron Spin Echo: Model Biradical Systems and the Sensitized Photolysis of Decalin. *Chem. Phys. Lett.* **1984**, *110*, 67–72.
- (3) Pannier, M.; Veit, S.; Godt, A.; Jeschke, G.; Spiess, H. W. Dead-Time Free Measurement of Dipole–Dipole Interactions Between Electron Spins. *J. Magn. Reson.* **2011**, *213*, 316–325.
- (4) Martin, R. E.; Pannier, M.; Diederich, F.; Gramlich, V.; Hubrich, M.; Spiess, H. W. Determination of End-to-End Distances in a Series of TEMPO Diradicals of up to 2.8 nm Length with a New Four-Pulse Double Electron Resonance Experiment. *Angew. Chem., Int. Ed.* **1998**, *37*, 2833–2837.
- (5) El Mkami, H.; Norman, D. G. EPR Distance Measurements in Deuterated Proteins. *Methods Enzymol.* **2015**, *564*, 125–152.
- (6) Stuehr, D. J.; Ikeda-Saito, M. Spectral Characterization of Brain and Macrophage Nitric Oxide Synthases. Cytochrome P-450-Like Heme Proteins that Contain a Flavin Semiquinone Radical. *J. Biol. Chem.* **1992**, *267*, 20547–20550.
- (7) Un, S.; Gerez, C.; Elleingand, E.; Fontecave, M. Sensitivity of Tyrosyl Radical g-Values to Changes in Protein Structure: A High-Field EPR Study of Mutants of Ribonucleotide Reductase. *J. Am. Chem. Soc.* **2001**, *123*, 3048–3054.
- (8) Bowen, A.; Tait, C.; Timmel, C.; Harmer, J. Orientation-Selective DEER Using Rigid Spin Labels, Cofactors, Metals, and Clusters. In *Structural Information from Spin-Labels and Intrinsic Paramagnetic Centres in the Biosciences*; Timmel, C. R., Harmer, J. R., Eds.; Structure and Bonding; Springer: Berlin, Germany, 2013; Vol. 152, pp 283–327.
- (9) Yang, Z.; Kise, D.; Saxena, S. An Approach towards the Measurement of Nanometer Range Distances Based on Cu<sup>2+</sup> Ions and ESR. *J. Phys. Chem. B* **2010**, *114*, 6165–6174.
- (10) Asada, M.; Mino, H. Location of the High-Affinity Mn<sup>2+</sup> Site in Photosystem II Detected by PELDOR. *J. Phys. Chem. B* **2015**, *119*, 10139–10144.
- (11) Gaffney, B. J.; Bradshaw, M. D.; Frausto, S. D.; Wu, F.; Freed, J. H.; Borbat, P. Locating a Lipid at the Portal to the Lipoxygenase Active Site. *Biophys. J.* **2012**, *103*, 2134–2144.
- (12) Abdullin, D.; Florin, N.; Hagelueken, G.; Schiemann, O. EPR-Based Approach for the Localization of Paramagnetic Metal Ions in Biomolecules. *Angew. Chem.* **2015**, *127*, 1847–1851.
- (13) Ji, M.; Ruthstein, S.; Saxena, S. Paramagnetic Metal Ions in Pulsed ESR Distance Distribution Measurements. *Acc. Chem. Res.* **2014**, *47*, 688–695.
- (14) Lovett, J.; Bowen, A.; Timmel, C.; Jones, M.; Dilworth, J.; Caprotti, D.; Bell, S.; Wong, L.; Harmer, J. Structural Information from Orientationally Selective DEER spectroscopy. *Phys. Chem. Chem. Phys.* **2009**, *11*, 6840–6848.
- (15) Abdullin, D.; Hagelueken, G.; Hunter, R. I.; Smith, G. M.; Schiemann, O. Geometric Model-Based Fitting Algorithm for Orientation-Selective PELDOR Data. *Mol. Phys.* **2015**, *113*, 544–560.
- (16) Bode, B. E.; Plackmeyer, J.; Prisner, T. F.; Schiemann, O. PELDOR Measurements on a Nitroxide-Labeled Cu(II) Porphyrin: Orientation Selection, Spin-Density Distribution, and Conformational Flexibility. *J. Phys. Chem. A* **2008**, *112*, 5064–5073.
- (17) Bode, B. E.; Plackmeyer, J.; Bolte, M.; Prisner, T. F.; Schiemann, O. PELDOR on an Exchange Coupled Nitroxide Copper(II) Spin Pair. *J. Organomet. Chem.* **2009**, *694*, 1172–1179.
- (18) Merz, G. E.; Borbat, P. P.; Pratt, A. J.; Getzoff, E. D.; Freed, J. H.; Crane, B. R. Copper-Based Pulsed Dipolar ESR Spectroscopy as a Probe of Protein Conformation Linked to Disease States. *Biophys. J.* **2014**, *107*, 1669–1674.

- (19) Ruthstein, S.; Ji, M.; Mehta, P.; Jen-Jacobson, L.; Saxena, S. Sensitive  $\text{Cu}^{2+}$ – $\text{Cu}^{2+}$  Distance Measurements in a Protein–DNA Complex by Double-Quantum Coherence ESR. *J. Phys. Chem. B* **2013**, *117*, 6227–6230.
- (20) Yang, Z.; Becker, J.; Saxena, S. On  $\text{Cu(II)}$ – $\text{Cu(II)}$  Distance Measurements Using Pulsed Electron Electron Double Resonance. *J. Magn. Reson.* **2007**, *188*, 337–343.
- (21) Narr, E.; Godt, A.; Jeschke, G. Selective Measurements of a Nitroxide–Nitroxide Separation of 5 nm and a Nitroxide–Copper Separation of 2.5 nm in a Terpyridine-Based Copper(II) Complex by Pulse EPR Spectroscopy. *Angew. Chem., Int. Ed.* **2002**, *41*, 3907–3910.
- (22) Spindler, P. E.; Glaser, S. J.; Skinner, T. E.; Prisner, T. F. Broadband Inversion PELDOR Spectroscopy with Partially Adiabatic Shaped Pulses. *Angew. Chem., Int. Ed.* **2013**, *52*, 3425–3429.
- (23) Abdullin, D.; Duthie, F.; Meyer, A.; Müller, E. S.; Hagelueken, G.; Schiemann, O. Comparison of PELDOR and RIDME for Distance Measurements between Nitroxides and Low-Spin Fe(III) Ions. *J. Phys. Chem. B* **2015**, *119*, 13534–13542.
- (24) Ezhevskaya, M.; Bordignon, E.; Polyhach, Y.; Moens, L.; Dewilde, S.; Jeschke, G.; Van Doorslaer, S. Distance Determination between Low-Spin ferric Haem and Nitroxide Spin Label using DEER: the Neuroglobin Case. *Mol. Phys.* **2013**, *111*, 2855–2864.
- (25) Motion, C. L.; Lovett, J. E.; Bell, S.; Cassidy, S. L.; Cruickshank, P. A. S.; Bolton, D. R.; Hunter, R. I.; El Mkami, H.; Van Doorslaer, S.; Smith, G. M. DEER Sensitivity between Iron Centers and Nitroxides in Heme-Containing Proteins Improves Dramatically Using Broadband, High-Field EPR. *J. Phys. Chem. Lett.* **2016**, *7*, 1411–1415.
- (26) Goldfarb, D.  $\text{Gd}^{3+}$  Spin Labeling for Distance Measurements by Pulse EPR Spectroscopy. *Phys. Chem. Chem. Phys.* **2014**, *16*, 9685–9699.
- (27) Rakowsky, M. H.; Zecevic, A.; Eaton, G. R.; Eaton, S. S. Determination of High-Spin Iron(III)–nitroxyl Distances in Spin-Labeled Porphyrins by Time-Domain EPR. *J. Magn. Reson.* **1998**, *131*, 97–110.
- (28) Kaminker, I.; Bye, M.; Mendelman, N.; Gislason, K.; Sigurdsson, S. T.; Goldfarb, D. Distance Measurements between Manganese(II) and Nitroxide Spin-Labels by DEER Determine a Binding Site of  $\text{Mn}^{2+}$  in the HP92 Loop of Ribosomal RNA. *Phys. Chem. Chem. Phys.* **2015**, *17*, 15098–15102.
- (29) Razzaghi, S.; Qi, M.; Nalepa, A. I.; Godt, A.; Jeschke, G.; Savitsky, A.; Yulikov, M. RIDME Spectroscopy with  $\text{Gd(III)}$  Centers. *J. Phys. Chem. Lett.* **2014**, *5*, 3970–3975.
- (30) Hirsh, D. J.; McCracken, J.; Bicz, R.; Gesuelli, K.-A. Saturation-Recovery EPR with Nitroxyl Radical–Dy(III) Spin Pairs: Distances and Orientations. *J. Phys. Chem. B* **2013**, *117*, 11960–11977.
- (31) Hirsh, D. J.; Beck, W. F.; Innes, J. B.; Brudvig, G. W. Using Saturation-Recovery EPR to Measure Distances in Proteins: Applications to Photosystem II. *Biochemistry* **1992**, *31*, 532–541.
- (32) Yagi, H.; Banerjee, D.; Graham, B.; Huber, T.; Goldfarb, D.; Otting, G. Gadolinium Tagging for High-Precision Measurements of 6 nm Distances in Protein Assemblies by EPR. *J. Am. Chem. Soc.* **2011**, *133*, 10418–10421.
- (33) Abdelkader, E. H.; Lee, M. D.; Feintuch, A.; Ramirez Cohen, M.; Swarbrick, J. D.; Otting, G.; Graham, B.; Goldfarb, D. A New  $\text{Gd}^{3+}$  Spin Label for  $\text{Gd}^{3+}$ – $\text{Gd}^{3+}$  Distance Measurements in Proteins Produces Narrow Distance Distributions. *J. Phys. Chem. Lett.* **2015**, *6*, 5016–5021.
- (34) Dalaloyan, A.; Qi, M.; Ruthstein, S.; Vega, S.; Godt, A.; Feintuch, A.; Goldfarb, D.  $\text{Gd(III)}$ – $\text{Gd(III)}$  EPR Distance Measurements - the Range of Accessible Distances and the Impact of Zero Field Splitting. *Phys. Chem. Chem. Phys.* **2015**, *17*, 18464–18476.
- (35) Matalon, E.; Huber, T.; Hagelueken, G.; Graham, B.; Frydman, V.; Feintuch, A.; Otting, G.; Goldfarb, D. Gadolinium(III) Spin Labels for High-Sensitivity Distance Measurements in Transmembrane Helices. *Angew. Chem.* **2013**, *125*, 12047–12050.
- (36) Edwards, D. T.; Huber, T.; Hussain, S.; Stone, K. M.; Kinnebrew, M.; Kaminker, I.; Matalon, E.; Sherwin, M. S.; Goldfarb, D.; Han, S. Determining the Oligomeric Structure of Proteorhodopsin by  $\text{Gd}^{3+}$ -Based Pulsed Dipolar Spectroscopy of Multiple Distances. *Structure* **2014**, *22*, 1677–1686.
- (37) Yang, Z.; Liu, Y.; Borbat, P.; Zweier, J. L.; Freed, J. H.; Hubbell, W. L. Pulsed ESR Dipolar Spectroscopy for Distance Measurements in Immobilized Spin Labeled Proteins in Liquid Solution. *J. Am. Chem. Soc.* **2012**, *134*, 9950–9952.
- (38) Kuzhelev, A. A.; Trukhin, D. V.; Krumkacheva, O. A.; Strizhakov, R. K.; Rogozhnikova, O. Y.; Troitskaya, T. I.; Fedin, M. V.; Tormyshev, V. M.; Bagryanskaya, E. G. Room-Temperature Electron Spin Relaxation of Triarylmethyl Radicals at the X- and Q-Bands. *J. Phys. Chem. B* **2015**, *119*, 13630–13640.
- (39) Reginsson, G. W.; Kunjir, N. C.; Sigurdsson, S. T.; Schiemann, O. Trityl Radicals: Spin Labels for Nanometer-Distance Measurements. *Chem. - Eur. J.* **2012**, *18*, 13580–13584.
- (40) Kunjir, N. C.; Reginsson, G. W.; Schiemann, O.; Sigurdsson, S. T. Measurements of Short Distances between Trityl Spin Labels with CW EPR, DQC and PELDOR. *Phys. Chem. Chem. Phys.* **2013**, *15*, 19673–19685.
- (41) Kulik, L. V.; Dzuba, S. A.; Grigoryev, I. A.; Tsvetkov, Y. D. Electron Dipole–Dipole Interaction in ESEEM of Nitroxide Biradicals. *Chem. Phys. Lett.* **2001**, *343*, 315–324.
- (42) Milikisyants, S.; Scarpelli, F.; Finiguerra, M. G.; Ubbink, M.; Huber, M. A Pulsed EPR Method to Determine Distances between Paramagnetic Centers with Strong Spectral Anisotropy and Radicals: The Dead-Time Free RIDME Sequence. *J. Magn. Reson.* **2009**, *201*, 48–56.
- (43) Meyer, A.; Abdullin, D.; Schnakenburg, G.; Schiemann, O. Single and Double Nitroxide Labeled Bis(terpyridine)-copper(II): Influence of Orientation Selectivity and Multispin Effects on PELDOR and RIDME. *Phys. Chem. Chem. Phys.* **2016**, *18*, 9262–9271.
- (44) Astashkin, A. V.; Chen, L.; Zhou, X.; Li, H.; Poulos, T. L.; Liu, K. J.; Guillemette, J. G.; Feng, C. Pulsed Electron Paramagnetic Resonance Study of Domain Docking in Neuronal Nitric Oxide Synthase: The Calmodulin and Output State Perspective. *J. Phys. Chem. A* **2014**, *118*, 6864–6872.
- (45) Astashkin, A. V.; Elmore, B. O.; Fan, W.; Guillemette, J. G.; Feng, C. Pulsed EPR Determination of the Distance between Heme Iron and FMN Centers in a Human Inducible Nitric Oxide Synthase. *J. Am. Chem. Soc.* **2010**, *132*, 12059–12067.
- (46) Akhmetzyanov, D.; Plackmeyer, J.; Endeward, B.; Denysenkov, V.; Prisner, T. Pulsed Electron–Electron Double Resonance Spectroscopy between a High-Spin  $\text{Mn}^{2+}$  Ion and a Nitroxide Spin Label. *Phys. Chem. Chem. Phys.* **2015**, *17*, 6760–6766.
- (47) Ching, H. V.; Demay-Drouhard, P.; Bertrand, H. C.; Policar, C.; Tabares, L. C.; Un, S. Nanometric Distance Measurements Between  $\text{Mn(II)}$  DOTA Centers. *Phys. Chem. Chem. Phys.* **2015**, *17*, 23368–23377.
- (48) Ching, H. Y. V.; Mascali, F. C.; Bertrand, H. C.; Bruch, E. M.; Demay-Drouhard, P.; Rasia, R. M.; Policar, C.; Tabares, L. C.; Un, S. The Use of  $\text{Mn(II)}$  Bound to His-Tags as Genetically Encodable Spin-Label for Nanometric Distance Determination in Proteins. *J. Phys. Chem. Lett.* **2016**, *7*, 1072–1076.
- (49) Banerjee, D.; Yagi, H.; Huber, T.; Otting, G.; Goldfarb, D. Nanometer-Range Distance Measurement in a Protein Using  $\text{Mn}^{2+}$  Tags. *J. Phys. Chem. Lett.* **2012**, *3*, 157–160.
- (50) Astashkin, A. V.; Hara, H.; Kawamori, A. The Pulsed Electron–Electron Double Resonance and “2 + 1” Electron Spin Echo Study of the Oriented Oxygen-Evolving and Mn-Depleted Preparations of Photosystem II. *J. Chem. Phys.* **1998**, *108*, 3805–3812.
- (51) Meyer, A.; Schnakenburg, G.; Schiemann, O. Crystal Structure of 4'-{[4-(2,2':6',2''-Terpyridyl-4'-yl)phenyl]ethynyl}biphenyl-4-yl-(2,2,5,5-tetramethyl-1-oxyl-3-pyrrolin-3-yl)- formate Benzene 2.5-Solvate. *Acta Crystallogr. Sect. E* **2015**, *71*, 1245–1249.
- (52) Stoll, S.; Schweiger, A. EasySpin, a Comprehensive Software Package for Spectral Simulation and Analysis in EPR. *J. Magn. Reson.* **2006**, *178*, 42–55.
- (53) van Wonderen, J. H.; Kostrz, D. N.; Dennison, C.; MacMillan, F. Refined Distances Between Paramagnetic Centers of a Multi-

Copper Nitrite Reductase Determined by Pulsed EPR (iDEER) Spectroscopy. *Angew. Chem., Int. Ed.* **2013**, *52*, 1990–1993.

(54) Jeschke, G.; Chechik, V.; Ionita, P.; Godt, A.; Zimmermann, H.; Banham, J.; Timmel, C. R.; Hilger, D.; Jung, H. DeerAnalysis2006—a Comprehensive Software Package for Analyzing Pulsed ELDOR Data. *Appl. Magn. Reson.* **2006**, *30*, 473–498.

(55) Hogg, R.; Wilkins, R. G. 57. Exchange Studies of Certain Chelate Compounds of the Transitional Metals. Part VIII. 2,2',2''-Terpyridine Complexes. *J. Chem. Soc.* **1962**, *0* (0), 341–350.

(56) Schiemann, O.; Cekan, P.; Margraf, D.; Prisner, T. F.; Sigurdsson, S. T. Relative Orientation of Rigid Nitroxides by PELDOR: Beyond Distance Measurements in Nucleic Acids. *Angew. Chem., Int. Ed.* **2009**, *48*, 3292–3295.

(57) Schiemann, O.; Piton, N.; Mu, Y.; Stock, G.; Engels, J. W.; Prisner, T. F. A PELDOR-Based Nanometer Distance Ruler for Oligonucleotides. *J. Am. Chem. Soc.* **2004**, *126*, 5722–5729.

(58) Astashkin, A. V.; Schweiger, A. Electron-Spin Transient Nutation: a New Approach to Simplify the Interpretation of ESR Spectra. *Chem. Phys. Lett.* **1990**, *174*, 595–602.

(59) Gätjens, J.; Sjödin, M.; Pecoraro, V. L.; Un, S. The Relationship between the Manganese(II) Zero-Field Interaction and Mn(II)/Mn(III) Redox Potential of Mn(4'-X-terpy)<sub>2</sub> Complexes. *J. Am. Chem. Soc.* **2007**, *129*, 13825–13827.

(60) Stich, T. A.; Lahiri, S.; Yeagle, G.; Dicus, M.; Brynda, M.; Gunn, A.; Aznar, C.; DeRose, V. J.; Britt, R. D. Multifrequency Pulsed EPR Studies of Biologically Relevant Manganese(II) Complexes. *Appl. Magn. Reson.* **2007**, *31*, 321–341.

(61) Duboc, C.; Collomb, M.-N.; Neese, F. Understanding the Zero-Field Splitting of Mononuclear Manganese(II) Complexes from Combined EPR Spectroscopy and Quantum Chemistry. *Appl. Magn. Reson.* **2010**, *37*, 229–245.

(62) Garcia-Rubio, I.; Angerhofer, A.; Schweiger, A. EPR and HYSCORE Investigation of the Electronic Structure of the Model Complex Mn(imidazole)<sub>6</sub>: Exploring Mn(II)–Imidazole Binding Using Single Crystals. *J. Magn. Reson.* **2007**, *184*, 130–142.

(63) Duboc, C.; Collomb, M.; Pécaut, J.; Deronzier, A.; Neese, F. Definition of Magneto-Structural Correlations for the Mn(II) Ion. *Chem. - Eur. J.* **2008**, *14*, 6498–6509.

(64) de Bruin, B.; Bill, E.; Bothe, E.; Weyhermüller, T.; Wieghardt, K. Molecular and Electronic Structures of Bis(pyridine-2,6-Diimine)metal Complexes [ML<sub>2</sub>](PF<sub>6</sub>)<sub>n</sub> (n = 0, 1, 2, 3; M = Mn, Fe, Co, Ni, Cu, Zn). *Inorg. Chem.* **2000**, *39*, 2936–2947.

(65) Meyer, A.; Schnakenburg, G.; Glaum, R.; Schiemann, O. (Bis(terpyridine))copper(II) Tetraphenylborate: A Complex Example for the Jahn–Teller Effect. *Inorg. Chem.* **2015**, *54*, 8456–8464.

(66) Raitsimring, A. M.; Astashkin, A. V.; Poluektov, O. G.; Caravan, P. High-Field Pulsed EPR and ENDOR of Gd<sup>3+</sup> Complexes in Glassy Solutions. *Appl. Magn. Reson.* **2005**, *28* (3), 281–295.

(67) Jeschke, G.; Sajid, M.; Schulte, M.; Godt, A. Three-Spin Correlations in Double Electron–Electron Resonance. *Phys. Chem. Chem. Phys.* **2009**, *11*, 6580–6591.

(68) Bode, B. E.; Margraf, D.; Plackmeyer, J.; Dürner, G.; Prisner, T. F.; Schiemann, O. Counting the Monomers in Nanometer-Sized Oligomers by Pulsed Electron–Electron Double Resonance. *J. Am. Chem. Soc.* **2007**, *129*, 6736–6745.

(69) von Hagens, T.; Polyhach, Y.; Sajid, M.; Godt, A.; Jeschke, G. Suppression of Ghost Distances in Multiple-Spin Double Electron–Electron Resonance. *Phys. Chem. Chem. Phys.* **2013**, *15*, 5854–5866.

(70) Yulikov, M.; Lueders, P.; Farooq Warsi, M.; Chechik, V.; Jeschke, G. Distance Measurements in Au Nanoparticles Functionalized with Nitroxide Radicals and Gd<sup>3+</sup>-DTPA Chelate Complexes. *Phys. Chem. Chem. Phys.* **2012**, *14*, 10732–10746.

(71) Valera, S.; Ackermann, K.; Plotas, C.; Huang, H.; Naismith, J. H.; Bode, B. E. Accurate Extraction of Nanometer Distances in Multimers by Pulse EPR. *Chem. - Eur. J.* **2016**, *22*, 4700–4703.

(72) Salikhov, K. M.; Khairuzhdinov, I. T.; Zaripov, R. B. Three-Pulse ELDOR Theory Revisited. *Appl. Magn. Reson.* **2014**, *45*, 573–619.

(73) Lueders, P.; Jeschke, G.; Yulikov, M. Double Electron–Electron Resonance Measured Between Gd<sup>3+</sup> Ions and Nitroxide Radicals. *J. Phys. Chem. Lett.* **2011**, *2*, 604–609.

(74) Hung, S.-C.; Grant, C. V.; Peloquin, J. M.; Waldeck, A. R.; Britt, R. D.; Chan, S. I. Electron Spin–Lattice Relaxation Measurement of the 3Fe-4S (S-3) Cluster in Succinate: Ubiquinone Reductase from *Paracoccus Denitrificans*. A Detailed Analysis Based on a Dipole–Dipole Interaction Model. *J. Phys. Chem. A* **2000**, *104*, 4402–4412.

**PELDOR and RIDME Measurements on a High-Spin Manganese(II) Bisnitroxide  
Model Complex**

**Andreas Meyer, Olav Schiemann\***

*Institute of Physical and Theoretical Chemistry, University of Bonn, Wegelerstr. 12,  
Bonn, Germany*

\*Author to whom correspondence should be addressed. [schiemann@pc.uni-bonn.de](mailto:schiemann@pc.uni-bonn.de);

# Supporting Information

## Content

2-pulse ESEEM experiment on <b>1</b> .....	3
PELDOR time traces before background correction.....	5
RIDME time traces before background correction.....	7

## 2-pulse ESEEM experiment on 1

The 2-pulse ESEEM experiment was conducted on the nitroxide and manganese spin center to obtain an estimate of their phase memory time. The measurement parameters are given in Table S1.

**Table S1.** Measurement parameters used for the 2-pulse ESEEM experiment on 1 ( $\nu_{obs} = 33.517$  GHz).

Spin center	Manganese (7 dB)	Nitroxide (0 dB)
$\rho_1$ [ns]	8	8
$\rho_2$ [ns]	16	16
SRT [ $\mu$ s]	300	2000
$B_0$ [mT]	1186.0	1192.4

The decay function of the obtained time traces have been fitted biexponentially according to equation S1.

$$I = I_0 \left( 1 - 2(w_1 e^{-t/T_1^1} + w_2 e^{-t/T_1^2}) \right); w_1 + w_2 = 1 \quad (S1)$$

The obtained results are shown in Figure S1 and summarized in Table S2.

**Table S2.** Fitting parameters used for the 2-pulse ESEEM time traces of 1.

Time trace	$w_1$	$T_1^1$ [ns]	$w_2$	$T_1^2$ [ns]
a) Manganese	0.68	1312	0.32	96
b) Nitroxide	0.75	2670	0.25	2700

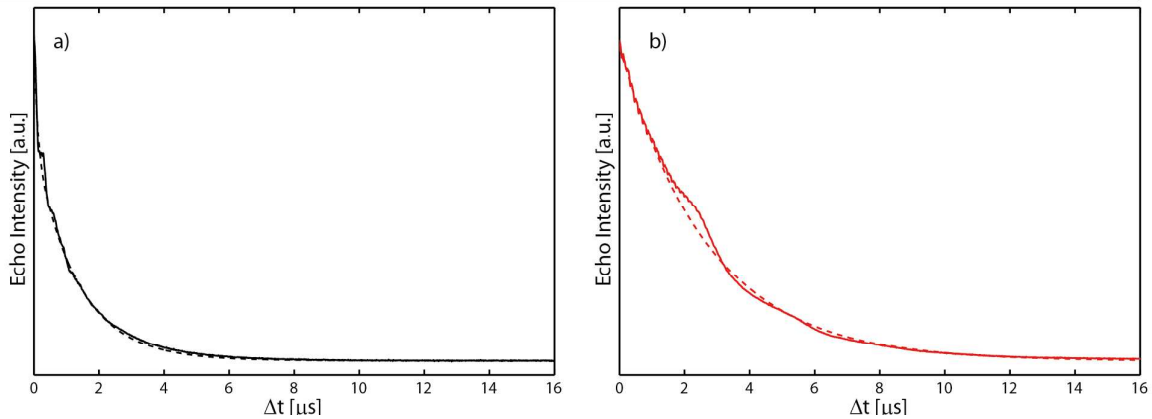


**Figure S1.** 2-pulse ESEEM time traces (full lines) and their biexponential fits (dotted lines) of a) the manganese signal (black) and b) the nitroxide signal (red).



Noteworthy about the 2-pulse ESEEM time trace of the manganese center is the absence of strong deuteron modulations, indicating the low extent of ligand replacement by solvent molecules. On the other hand, a peak at twice the deuteron frequency is present for both the nitroxide and the manganese spectrum. Thus, both signals are modulated by hyperfine coupling to deuterons of the solvent.

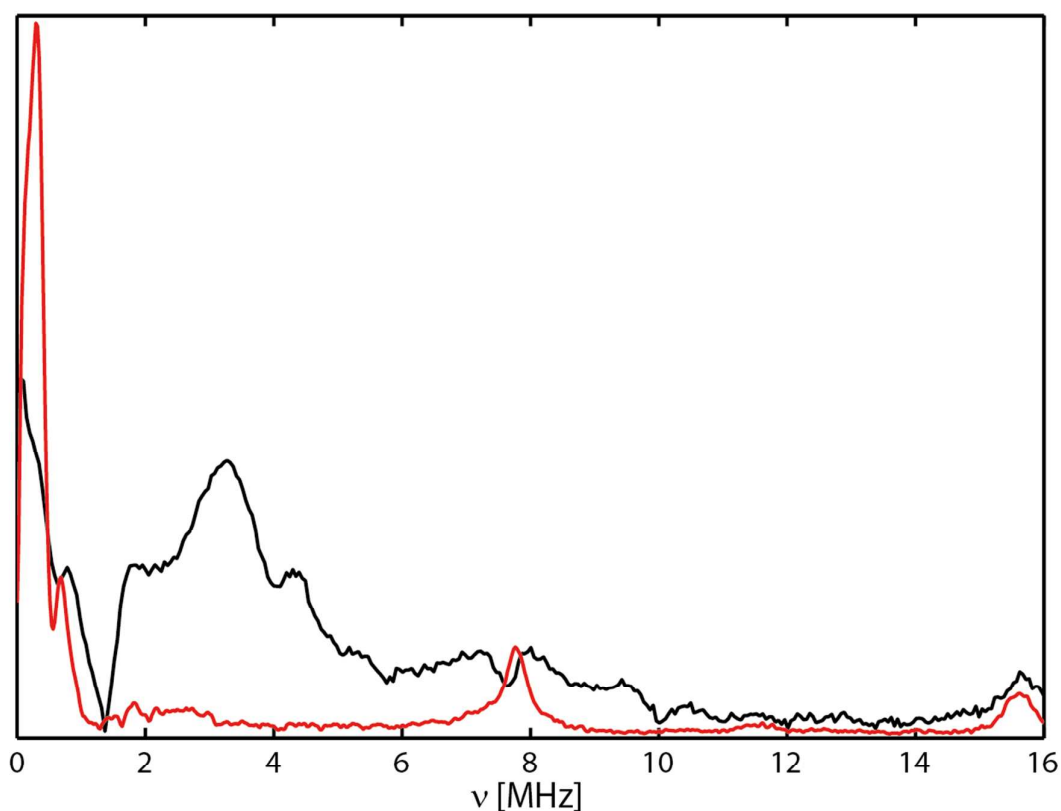


**Figure S2.** Fourier transform of the 2-pulse ESEEM time traces shown in Figure S1. Black line: Fourier transform of the manganese time trace. Red line: Fourier transform of the nitroxide time trace.

### PELDOR time traces before background correction

Figures S3 and S4 show the time traces of the PELDOR experiments with the observer pulses on the manganese and on the nitroxide, respectively. The measurement parameters are detailed in Table 3 in the main text. Figure S5 shows the RIDME time traces at both values of  $T$  as detailed in Table 4 in the main text.

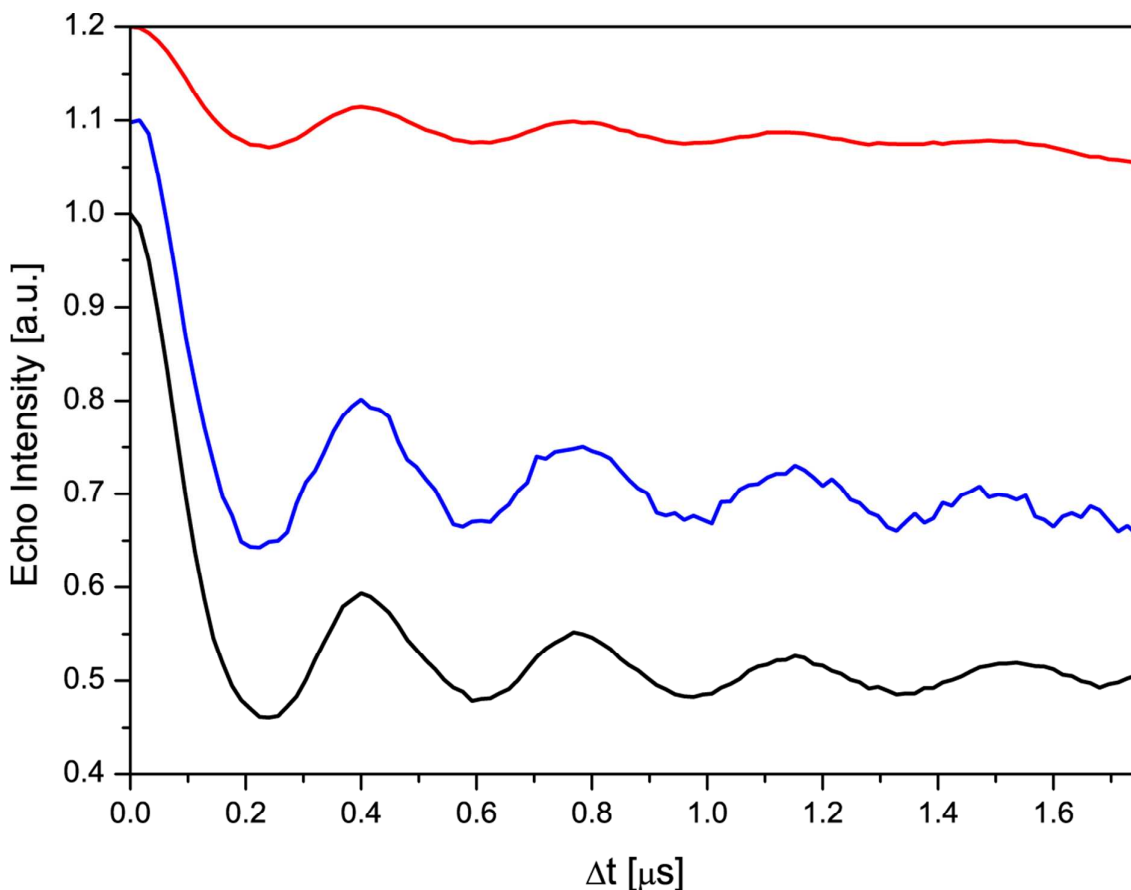


**Figure S3.** Q-band PELDOR time traces of the manganese-nitroxide distance in **1** before background correction using the experimental set ups **P1**, **P2** and **P3** (black, red and blue lines, respectively) as specified in Table 3 in the main text.



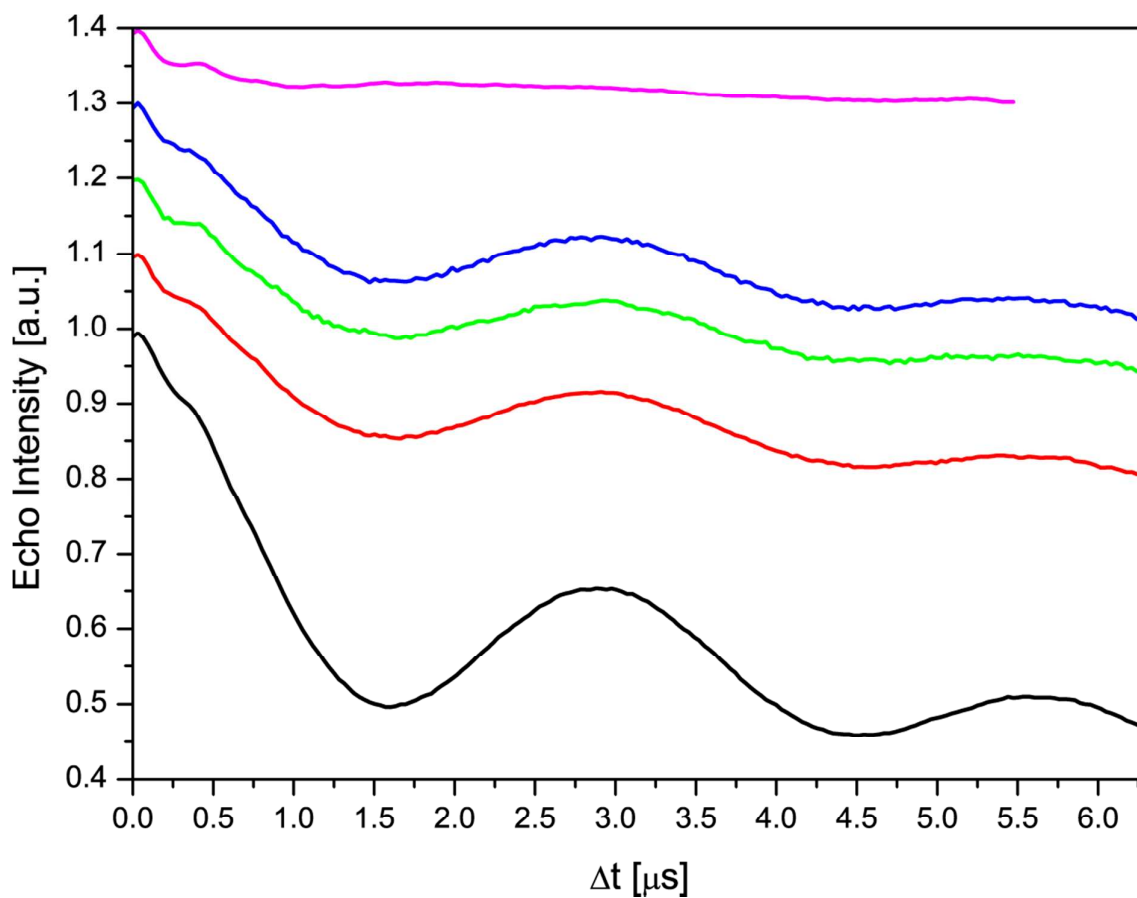


**Figure S4.** Q-band PELDOR time traces of the nitroxide-nitroxide distance in **1** before background correction using the experimental set ups **P4** (black), **P5** (red), **P6** (green), **P7** (blue) and **P8** (purple) as specified in Table 3 in the main text.

### RIDME time traces before background correction

Figure S5 and S6 show the RIDME time traces using the refocused stimulated echo for observation (Figure S5) or the refocused virtual echo (Figure S6) at both values of  $T$  as detailed in Table 4 in the main text.

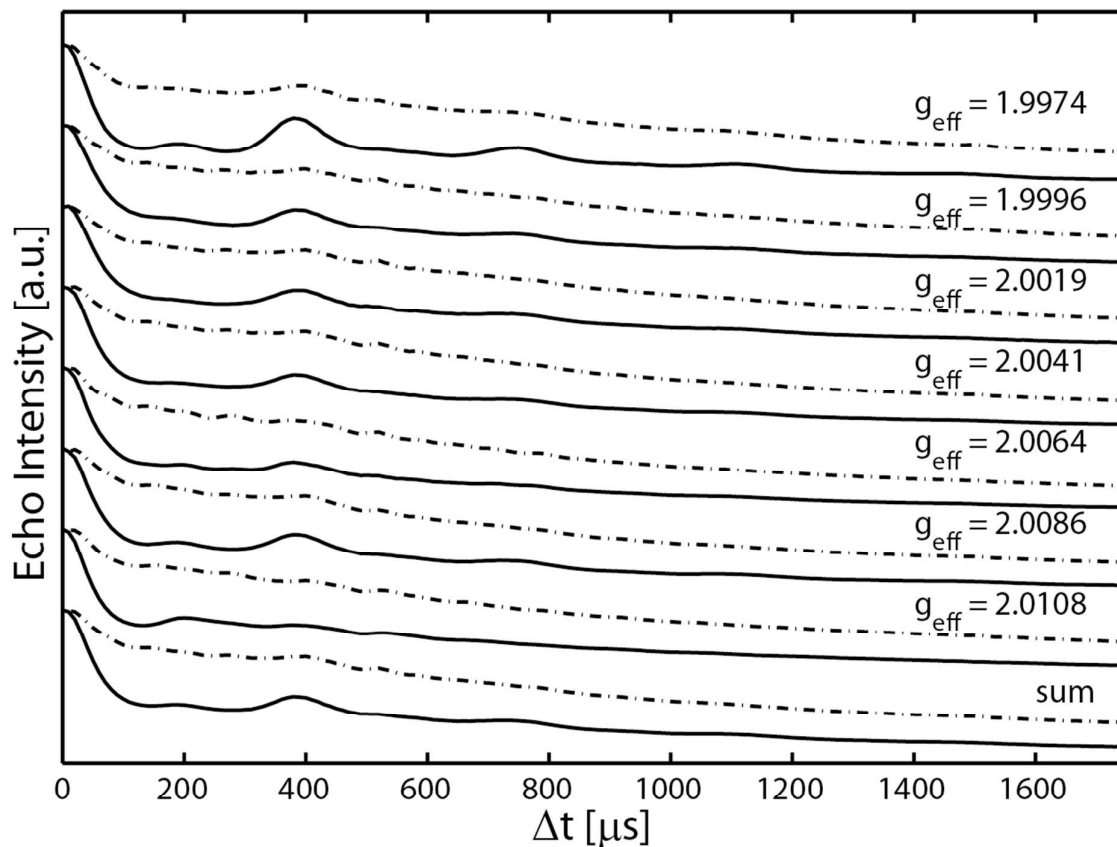


**Figure S5.** Q-band RSE RIDME time traces at  $T = 3 \mu\text{s}$  (dashed lines) and  $T = 25 \mu\text{s}$  (full lines).

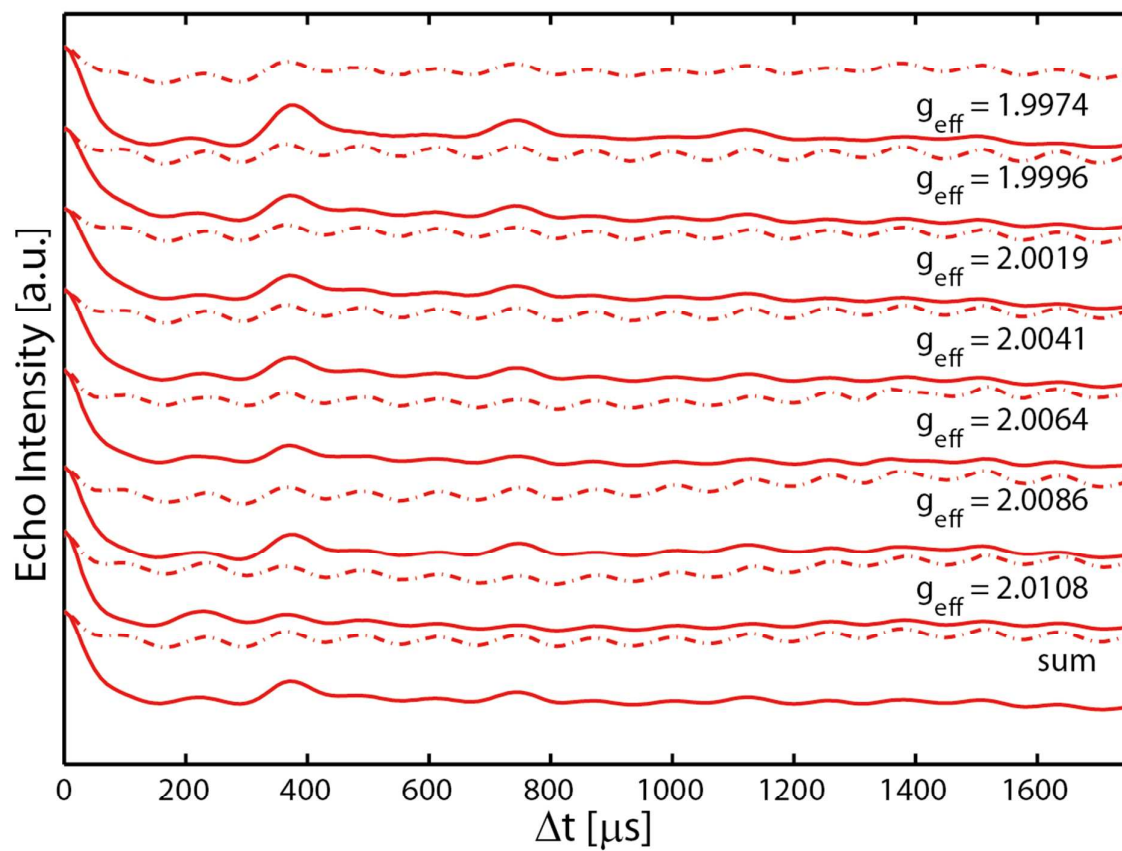


**Figure S6.** Q-band RVE RIDME time traces at  $T = 3 \mu\text{s}$  (dashed lines) and  $T = 25 \mu\text{s}$  (full lines).

# Appendix F

## One-Electron Oxidation of a Disilicon(0) Compound: An Experimental and Theoretical Study of NHC-trapped $[\text{Si}_2]^+$

Marius I. Arz,<sup>i</sup> Martin Straßmann,<sup>i</sup> Gregor Schnakenburg,<sup>i</sup> Andreas Meyer,<sup>ii</sup> Olav Schiemann,<sup>ii</sup> and Alexander C. Filippou<sup>i</sup>

Received 5th June 2015, published online 5th August 2015.

Reprinted with permission from

M. I. Arz, M. Straßmann, G. Schnakenburg, A. Meyer, O. Schiemann, and A. C. Filippou, *Chemistry - A European Journal* **2015**, 21, 12509 - 12516.

Copyright ©2015, WILEY-VCH Verlag GmbH & Co. KGaA, Weinheim.

### Own contributions to the manuscript

- Conducting the EPR measurements.
- Interpretation of the EPR spectra.
- Writing parts of the manuscript.

---

<sup>i</sup> Institut für Anorganische Chemie, Universität Bonn, Gerhard-Domagk-Straße 1, 53121 Bonn, Germany.

<sup>ii</sup> Institut für Physikalische und Theoretische Chemie, Universität Bonn, Wegelerstr. 12, 53115 Bonn, Germany.

## Disilicon Compounds

One-Electron Oxidation of a Disilicon(0) Compound: An Experimental and Theoretical Study of  $[\text{Si}_2]^+$  Trapped by N-Heterocyclic CarbenesMarius I. Arz,<sup>[a]</sup> Martin Straßmann,<sup>[a]</sup> Andreas Meyer,<sup>[b]</sup> Gregor Schnakenburg,<sup>[a]</sup> Olav Schiemann,<sup>\*[b]</sup> and Alexander C. Filippou<sup>\*[a]</sup>

**Abstract:** One-electron oxidation of the disilicon(0) compound  $\text{Si}_2(\text{Idipp})_2$  (**1**,  $\text{Idipp} = 1,3\text{-bis}(2,6\text{-diisopropylphenyl})\text{-imidazolin-2-ylidene}$ ) with  $[\text{Fe}(\text{C}_5\text{Me}_5)_2][\text{B}(\text{Ar}^F)_4]$  ( $\text{Ar}^F = \text{C}_6\text{H}_3\text{-}3,5\text{-(CF}_3)_2$ ) affords selectively the green radical salt  $[\text{Si}_2(\text{Idipp})_2][\text{B}(\text{Ar}^F)_4]$  (**1**- $[\text{B}(\text{Ar}^F)_4]$ ). Oxidation of the centrosymmetric **1** occurs reversibly at a low redox potential ( $E_{1/2} = -1.250$  V vs.  $\text{Fc}^+/\text{Fc}$ ), and is accompanied by considerable structural changes as shown by single-crystal X-ray structural analysis of **1**- $[\text{B}(\text{Ar}^F)_4]$ . These include a shortening of the Si–Si bond, a widening of the Si–Si– $\text{C}_{\text{NHC}}$  angles, and a lowering of the symmetry, leading to a quite different conformation of the NHC substituents at the two inequivalent Si sites in  $1^+$ .

Comparative quantum chemical calculations of **1** and  $1^+$  indicate that electron ejection occurs from the symmetric ( $n_+$ ) combination of the Si lone pairs (HOMO). EPR studies of **1**- $[\text{B}(\text{Ar}^F)_4]$  in frozen solution verified the inequivalency of the two Si sites observed in the solid-state, and point in agreement with the theoretical results to an almost equal distribution of the spin density over the two Si atoms, leading to quite similar  $^{29}\text{Si}$  hyperfine coupling tensors in  $1^+$ . EPR studies of **1**- $[\text{B}(\text{Ar}^F)_4]$  in liquid solution unraveled a topomerization with a low activation barrier that interconverts the two Si sites in  $1^+$ .

## Introduction

The structures and properties of small silicon clusters are of fundamental importance for the understanding of the transition from molecular behavior to that of bulk silicon and have significant implications for the chemical vapor deposition (CVD) of amorphous and crystalline silicon in the semiconductor industry.<sup>[1]</sup> In this context the electronic structure of the silicon dimer ( $\text{Si}_2$ ) was investigated experimentally and by quantum theory, and the relevance of  $\text{Si}_2$  in cluster formation was pointed out in few studies.<sup>[2]</sup> In comparison, studies on the  $[\text{Si}_2]^+$  cation are far less common and include mainly quantum chemical calculations.<sup>[3]</sup> The quartet ground state structure of  $[\text{Si}_2]^+$  was established by electron spin-resonance (ESR) studies in noble-gas matrices at 4 K.<sup>[4]</sup>

Main-group element chemistry has witnessed a renaissance in recent years following the discovery that N-heterocyclic car-

benes (NHCs) can be used to trap highly reactive, unsaturated main-group species.<sup>[5]</sup> This provided access to a series of unusual zerovalent compounds, such as  $\text{E}_2(\text{NHC})_2$  ( $\text{E} = \text{Si}–\text{Sn}$ ,<sup>[6]</sup>  $\text{B}$ ,<sup>[7]</sup>  $\text{P}$ ,<sup>[8a]</sup>  $\text{As}$ <sup>[8b]</sup>) or  $\text{E}(\text{bNHC})$  ( $\text{E} = \text{Si}$ ,  $\text{Ge}$ ; ( $\text{bNHC}$ ) = chelating bis-N-heterocyclic carbene).<sup>[9]</sup> Appealing examples in low-valent silicon chemistry for the complexation proclivity of N-heterocyclic carbenes include the isolation of NHC adducts of  $\text{SiX}_2$  ( $\text{X} = \text{Cl}$ ,  $\text{Br}$ ,  $\text{I}$ ),<sup>[10]</sup>  $\text{Si}(\text{Cl})\text{R}$  ( $\text{R} = \text{aryl}$ ,  $\text{amino}$ ),<sup>[11]</sup>  $[\text{SiR}]^+$  ( $\text{R} = \text{I}$ ,  $\text{aryl}$ ),<sup>[10d,12]</sup>  $\text{Si}^{2+}$ ,<sup>[10d]</sup>  $\text{SiR}(\text{Si}(\text{R})=\text{SiR}_2)$  ( $\text{R} = \text{aryl}$ ),<sup>[13]</sup>  $\text{R}_2\text{Si}=\text{Ge}$ ,<sup>[14]</sup> or the  $\text{Si}^0$  compound  $\text{Si}_2(\text{Idipp})_2$  (**1**,  $\text{Idipp} = 1,3\text{-bis}(2,6\text{-diisopropylphenyl})\text{-imidazolin-2-ylidene}$ ),<sup>[6a]</sup> which has been described as a base-stabilized allotrope of silicon.<sup>[15]</sup> This description was fortified by quantum chemical calculations suggesting that **1** can be viewed as a  $\text{Si}_2$  molecule trapped in its excited ( $^1\Delta_g$ ) electronic state by two NHCs.<sup>[16]</sup> However, such a description can be questioned given the quite different lowest-energy configuration of  $\text{Si}_2$  (triplet,  $\text{X}^3\Sigma_g^-$ )<sup>[3]</sup> from that of **1** and the rather large Si– $\text{C}_{\text{NHC}}$  bond dissociation energies, which have to date prevented the use of **1** as a source of  $\text{Si}_2$  in reactions.<sup>[17]</sup> Notably, a recent experimental and theoretical study uncovered the isobal analogy of **1** with the diphosphene  $\text{P}_2\text{Mes}^*_2$  ( $\text{Mes}^* = 2,4,6\text{-tBu}_3\text{-C}_6\text{H}_2$ ) and the NHC-stabilized phosphasilenyliidene ( $\text{Idipp})\text{Si}=\text{PMes}^*$ .<sup>[18]</sup> In all three of these double-bond compounds, the lowest-unoccupied molecular orbital (LUMO) is the antibonding E–E  $\pi^*$  orbital, the highest-occupied molecular orbital (HOMO) the symmetric ( $n_+$ ) combination of the lone-pair orbitals<sup>[19]</sup> and the HOMO–1 the E–E  $\pi$ -bonding orbital, with the disilicon compound **1** revealing the smallest

[a] M. I. Arz, M. Straßmann, Dr. G. Schnakenburg, Prof. Dr. A. C. Filippou  
Institut für Anorganische Chemie  
Rheinische Friedrich-Wilhelms-Universität Bonn  
Gerhard-Domagk-Strasse 1, 53121 Bonn (Germany)  
E-mail: filippou@uni-bonn.de

[b] A. Meyer, Prof. Dr. O. Schiemann  
Institut für Physikalische und Theoretische Chemie  
Rheinische Friedrich-Wilhelms-Universität Bonn  
Wegelerstrasse 12, 53115 Bonn (Germany)  
E-mail: schiemann@pc.uni-bonn.de

Supporting information for this article is available on the WWW under <http://dx.doi.org/10.1002/chem.201502199>.

energy gap of only 0.03 eV between the HOMO and HOMO–1 orbital. This electronic situation raised the question as to whether ejection of one electron from **1** would occur from the  $n_+$  level to give a  $\sigma$  radical or from the  $\pi$  level to give a  $\pi$  radical. The outcome of the one-electron oxidation of **1** was expected to have a major influence on the structure and reactivity of the resulting radical cation  $[\text{Si}_2(\text{Idipp})_2]^{+\bullet}$  (**1**<sup>+</sup>) given the known differences between organic  $\sigma$ - and  $\pi$ -type radicals.<sup>[20,21]</sup> Studies addressing this issue in the case of the isolobal diphosphene radical cations  $[\text{P}_2\text{R}_2]^{+\bullet}$  were hampered by the high reactivity of these ions, which precluded so far their isolation.<sup>[22]</sup> EPR spectroscopy of  $[\text{P}_2\text{Mes}^*_2]^{+\bullet}$  generated by  $\gamma$ -irradiation of  $\text{P}_2\text{Mes}^*_2$  in dilute Freon solution at 77 K suggested the presence of a  $\sigma$ -type radical,<sup>[23]</sup> and the lowest energy ionization band in the photoelectron spectra of  $\text{P}_2\text{R}_2$  was assigned using quantum chemical methods,<sup>[24]</sup> which have shown that the order of the closely spaced  $n_+$  and  $\pi$ -orbital depends on the R substituent,<sup>[24]</sup> and in the case of aryl diphosphenes also on the aryl twist angle.<sup>[25]</sup> Remarkably the same subtle change of the  $n_+$  and  $\pi$ -orbital sequence was found recently for the isolobal  $\text{Si}_2(\text{NHC})_2$  compounds by quantum chemical calculations.<sup>[6a,18,26]</sup> This prompted us to probe the one-electron oxidation of **1** and carry out a comprehensive experimental and theoretical study of the structure, properties and dynamics of the **1**<sup>+</sup> radical ion, which can be strikingly viewed as NHC-trapped  $[\text{Si}_2]^{+\bullet}$ .

## Results and Discussion

### Experimental studies

At first, the stability of the radical cation **1**<sup>+</sup> was addressed under electrochemical conditions. For this purpose, cyclic voltammetric studies of **1** were carried out in fluorobenzene, tetrahydrofuran, and 1,2-difluorobenzene at room temperature. The cyclic voltammograms (CVs) in all solvents used showed a reversible one-electron oxidation of **1** at a low half-wave potential ( $E_{1/2}$ ), which is slightly solvent-dependent, ranging from –0.794 V (THF and 1,2- $\text{C}_6\text{H}_4\text{F}_2$ ) to –0.730 V ( $\text{C}_6\text{H}_5\text{F}$ ) vs. the  $[\text{Fe}(\text{C}_5\text{Me}_5)_2]^{+/0}$  redox couple (Figure 1).<sup>[18,27,28]</sup> No redox wave was found at more negative potentials (until –2.0 V), suggest-

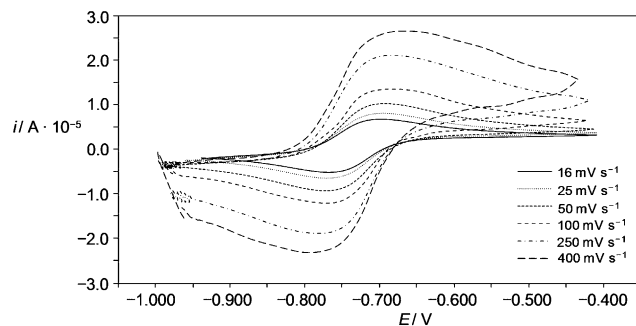
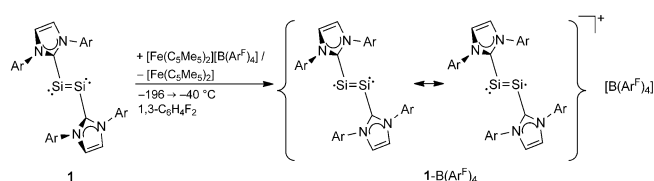


**Figure 1.** Single-wave cyclic voltammograms of **1** at different scan rates in fluorobenzene at room temperature in the potential range –1.050 to –0.350 V; reference electrode: dmfc<sup>+</sup>/dmfc/0.1 M N(*n*Bu)<sub>4</sub>PF<sub>6</sub>/C<sub>6</sub>H<sub>5</sub>F (dmfc = decamethylferrocene).

ing that **1** cannot be easily reduced. Furthermore two irreversible oxidation processes were observed in  $\text{C}_6\text{H}_5\text{F}$  at  $E_{1/2} = 0.658$  and 1.001 V (scan rate: 50  $\text{mV s}^{-1}$ ) suggesting that a rapid follow-up reaction occurs upon further oxidation of the radical cation **1**<sup>+</sup> to a putative dicationic analogue of a disilyne (**1**<sup>2+</sup>).<sup>[27]</sup> Remarkably, the electrochemical properties of **1** differ considerably from those of  $\text{Si}_2(\text{CAAC})_2$ , the disilicon analogue of **1** containing cyclic alkyl(amino)carbene (CAAC) substituents, which displays in THF a quasi-reversible one-electron reduction at  $E_{1/2} = -1.40$  V.<sup>[29]</sup> This difference can be rationalized with the much stronger  $\pi$ -acceptor properties of CAACs.<sup>[30]</sup> The CVs of **1** also differ markedly from those of the diphosphenes  $\text{P}_2\text{R}_2$  ( $\text{R} = \text{C}(\text{SiMe}_3)_3$ ,  $\text{Mes}^*$ , *m*-terphenyl), which show a reversible one-electron reduction at  $E_{1/2} = -2.23$  to  $-1.82$  V and an irreversible oxidation at large potentials ( $E_{1/2} = 0.90$ – $1.44$  V).<sup>[18,22,31,32]</sup> This marked difference reflects the large increase of both the LUMO and HOMO energies occurring upon replacement of the two PR fragments in  $\text{P}_2\text{R}_2$  by the much less electronegative, isolobal  $\text{Si}(\text{Idipp})$  fragments in **1**.<sup>[18]</sup> This energy shift reduces considerably the electron affinity of **1** and decreases its ionization potential,<sup>[33]</sup> rendering **1** a strong one-electron reducing agent that is comparable with cobaltocene ( $E_{1/2} = -0.85$  V)<sup>[34]</sup> or  $\text{P}_2(\text{Idipp})_2$  ( $E_{1/2} = -0.97$  V).<sup>[35]</sup>

Following the results of cyclic voltammetry, we attempted the chemical one-electron oxidation of **1** using  $[\text{Fe}(\text{C}_5\text{Me}_5)_2][\text{B}(\text{Ar}^F)_4]$  **[Ar<sup>F</sup>]<sub>4</sub>**<sup>[36]</sup> as oxidant (Scheme 1). In fact, vacuum transfer of 1,3- $\text{C}_6\text{H}_4\text{F}_2$  to an equimolar mixture of red-colored **1** and green-colored  $[\text{Fe}(\text{C}_5\text{Me}_5)_2][\text{B}(\text{Ar}^F)_4]$  at –196 °C followed by



**Scheme 1.** One-electron oxidation of **1** leading to **1-B(Ar<sup>F</sup>)<sub>4</sub>**. Compound **1** and the two resonance forms of **1**<sup>+</sup> are depicted without formal charges; the electron lone pairs at the silicon atoms are indicated by two dots and the unpaired electron by one dot.

warming of the mixture to –40 °C was accompanied by a color change to intense green. Addition of *n*-hexane to the dark-green solution followed by crystallization at –60 °C afforded the radical salt **1-B(Ar<sup>F</sup>)<sub>4</sub>** in 71% yield as a green extremely sensitive solid, which turns instantaneous to a white solid upon exposure to air. **1-B(Ar<sup>F</sup>)<sub>4</sub>** is reduced selectively back to **1** upon treatment with one equiv of  $\text{C}_8\text{K}$  in THF.<sup>[27]</sup> Thus, **1**<sup>+</sup>/**1** is a rare example of a chemically reversible Si-based redox system.<sup>[37]</sup>

**1-B(Ar<sup>F</sup>)<sub>4</sub>** can be stored at –30 °C for several months without apparent sign of decomposition on visual inspection or using EPR spectroscopy. However, storage of the solid at room temperature for approximately one day afforded a red solid of unknown composition. Similarly, greenish solutions of intact **1-B(Ar<sup>F</sup>)<sub>4</sub>** in fluorobenzene or diethyl ether at –30 °C turned rapidly brown–red after warming to room temperature, indicating an increased thermolability of **1-B(Ar<sup>F</sup>)<sub>4</sub>** in solution. Monitoring

of the decomposition of  $1\text{-B}(\text{Ar}^{\text{F}})_4$  in diethyl ether at ambient temperature by cw X-band EPR spectroscopy revealed a mono-exponential decay with a half-life  $t_{1/2}$  of 14218 s, leading to EPR-silent products in a brown-red solution. Several paramagnetic intermediates of low concentration were detected during the decay and one of these could be identified as the radical cation  $[\text{SiH}_2(\text{Idipp})]^+$  on the basis of the hyperfine splitting pattern of its EPR signal (triplet of quintets of triplets) and the magnitude of the hyperfine coupling constants ( $A(^1\text{H}^{\alpha}) = 1.2$  mT,  $A(^{14}\text{N}^{\gamma}) = 0.2$  mT,  $A(^1\text{H}^{\delta}) = 0.05$  mT).<sup>[27]</sup> Analysis of the EPR silent products by  $^1\text{H}$  NMR spectroscopy indicated an unselective decomposition of  $1\text{-B}(\text{Ar}^{\text{F}})_4$  to a mixture of Idipp-containing products including **1** and  $(\text{HIdipp})[\text{B}(\text{Ar}^{\text{F}})_4]$ .

The crystal structure of  $1\text{-B}(\text{Ar}^{\text{F}})_4 \cdot 2(1,3\text{-C}_6\text{H}_4\text{F}_2)$  is composed of well-separated radical cations  $1^+$  and borate anions with the closest  $\text{Si}\cdots\text{F}$  contact (5.92(1) Å) being significantly longer than the sum of the crystallographic van der Waals radii of silicon and fluorine (3.6 Å).<sup>[38]</sup> The radical cation  $1^+$  features as **1** a *trans*-bent planar  $\text{C}_{\text{NHC}}\text{-Si-Si-C}_{\text{NHC}}$  core with a torsion angle of  $174.3(4)^\circ$  (Figure 2, left). The Si–Si bond length of  $1^+$  (2.178(3) Å) is 2.3% shorter than that of **1** (2.229(1) Å)<sup>[6a]</sup> and

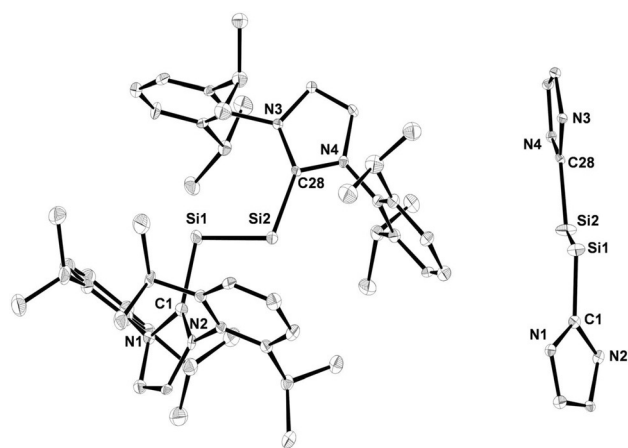


**Figure 2.** Left: DIAMOND plot of the molecular structure of the radical cation  $1^+$  in the single crystal of  $1\text{-B}(\text{Ar}^{\text{F}})_4 \cdot 2(1,3\text{-C}_6\text{H}_4\text{F}_2)$ .<sup>[51]</sup> Thermal ellipsoids are set at 30% probability at 100(2) K. Hydrogen atoms are omitted for clarity. Selected bond lengths [Å], bond angles [ $^\circ$ ], and torsion angles [ $^\circ$ ]: Si1–Si2 2.178(3), Si1–C1 1.910(8), Si2–C28 1.899(7); C1–Si1–Si2 101.9(2), C28–Si2–Si1 109.9(2); C1–Si–Si2–C28 174.3(4), N2–C1–Si1–Si2 53.1(8), N3–C28–Si2–Si1 2.6(8). Right: View of the radical cation along the  $\text{C}_{\text{NHC}}\text{-Si-Si-C}_{\text{NHC}}$  core showing the different conformation of the NHC rings; the dipp substituents were not drawn for better visibility.

compares very well with the internal Si–Si bond of the disilyne radical anion in  $[\text{K}(\text{dme})_4][\text{Si}_2(\text{Si}^i\text{PrDsi}_2)_2]$  (2.173(1) Å,  $\text{Dsi} = \text{CH}(\text{SiMe}_3)_2$ ) substantiating the isolobal relationship between the two ions.<sup>[39]</sup> Contraction of the Si–Si bond of  $1^+$  suggests an increase in the Si–Si bond order as shown by the increased Wiberg bond index (WBI;  $\text{WBI}(\text{Si}-\text{Si})$  of  $1^+ = 2.046$ ;  $\text{WBI}(\text{Si}-\text{Si})$  of **1** = 1.703).<sup>[27]</sup> It originates according to natural bond orbital (NBO) analysis from a decreased lone-pair repulsion, and an increase in bonding Si–Si electron density occurring upon depopulation of the  $n_+$  orbital.<sup>[27]</sup> In contrast, removal of one electron from the  $\text{Si}=\text{Si}$   $\pi$ -bonding orbital of **1** would be ex-

pected to lead to an elongation of the Si–Si bond as observed in the one-electron oxidation of disilenes.<sup>[40]</sup> Another distinct structural change provoked by the one-electron oxidation is a reduction of the symmetry from centrosymmetric in **1** ( $C_2$ ) to  $C_1$  in  $1^+$ , rendering the two Si sites (Si1 and Si2) inequivalent. In fact, the Si2–C28 bond (1.899(7) Å) in  $1^+$  is shorter than the Si1–C1 bond (1.910(8) Å), and both Si– $\text{C}_{\text{NHC}}$  bonds of  $1^+$  are slightly shorter than those of **1** (Si– $\text{C}_{\text{NHC}} = 1.927(2)$  Å).<sup>[6a]</sup> Furthermore, the angle at Si2 ( $\angle \text{C28-Si2-Si1} = 109.9(2)^\circ$ ) is larger than that at Si1 ( $\angle \text{C1-Si1-Si2} = 101.9(2)^\circ$ ), and both angles are more obtuse than those of **1** ( $\angle \text{C}_{\text{NHC}}\text{-Si-Si} = 93.37(5)^\circ$ ).<sup>[6a]</sup> These structural trends can be rationalized according to NBO analyses with the increased *s*-character of the Si natural hybrid orbitals employed in the Si– $\text{C}_{\text{NHC}}$  and the Si–Si  $\sigma$ -bonding of  $1^+$ , and are consistent with the slightly larger spin density at Si2 obtained by the DFT calculations.<sup>[27]</sup> Finally, a change in the conformation of the NHC substituents is observed upon one-electron oxidation of **1**. Thus, whereas in **1** the NHC groups adopt an orthogonal conformation ( $\angle \text{N}_{\text{NHC}}\text{-C}_{\text{NHC}}\text{-Si-Si} = 90.8^\circ$ ),<sup>[6a]</sup> in  $1^+$  the Si2-bonded NHC group is almost coplanar with the  $\text{C}_{\text{NHC}}\text{-Si-Si-C}_{\text{NHC}}$  plane ( $\angle \text{N3-C28-Si2-Si1} = 2.6(8)^\circ$ ), while the Si1-bonded NHC group is twisted out of the  $\text{C}_{\text{NHC}}\text{-Si-Si-C}_{\text{NHC}}$  plane, as shown by the torsion angle  $\text{N2-C1-Si1-Si2}$  of  $53.1(8)^\circ$  (Figure 2, right). Remarkably, the same structural differences as described above between  $1^+$  and **1** have been previously observed between the one- and two-electron reduction product of the digermene  $\text{Ge}_2\text{R}_2$  ( $\text{R} = \text{C}_6\text{H}_2\text{-2,6-(C}_6\text{H}_3\text{-2,4,6-}i\text{Pr}_3)_2$ ),<sup>[41]</sup> indicating the isolobal analogy of  $1^+$  with  $[\text{Ge}_2\text{R}_2]^-$  and of **1** with  $[\text{Ge}_2\text{R}_2]^{2-}$ .

The electronic structure of  $1\text{-B}(\text{Ar}^{\text{F}})_4$  was investigated by continuous-wave (cw) EPR spectroscopy.<sup>[27]</sup> The EPR spectrum at X-band frequencies (9.4 GHz) of  $1\text{-B}(\text{Ar}^{\text{F}})_4$  recorded in liquid diethyl ether solution at 220 K showed an intense signal at a  $g_{\text{iso}}$  value of 1.9979 (Figure 3a). This signal originates from the  $1^+$  isotopomers (90.9% relative abundance) containing the magnetically inactive nuclei  $^{28}\text{Si}$  (natural abundance: 92.23%) and  $^{30}\text{Si}$  (natural abundance: 3.1%). Remarkably, the  $g_{\text{iso}}$  value of  $1^+$  compares well to that of the isolobal disilyne radical anion in  $[\text{K}(\text{dme})_4][\text{Si}_2(\text{Si}^i\text{PrDsi}_2)_2]$  ( $g_{\text{iso}} = 1.99962$ ).<sup>[39]</sup> It is however smaller than that of the free electron ( $g_e = 2.0023$ ), in contrast to the commonly larger *g*-values of Si-centered radicals ranging from 2.0027–2.0077.<sup>[42,43]</sup> The central EPR signal of  $1\text{-B}(\text{Ar}^{\text{F}})_4$  in the liquid phase is flanked by a pair of inner and outer satellite signals, which originate from the  $1^+$  isotopomers bearing one or two magnetically active  $^{29}\text{Si}$  nuclei ( $I = 1/2$ , natural abundance: 4.67%), respectively (Figure 3a). The observed multiplicity pattern of the  $^{29}\text{Si}$  satellite signals and their relative intensities suggests unequivocally the presence of two equivalent Si sites, with the  $^{28/30}\text{Si}^{29}\text{Si}$  isotopomers (relative abundance: 8.9%) giving rise to a doublet signal (inner pair of satellites) and the  $^{29}\text{Si}^{29}\text{Si}$  isotopomer (relative abundance 0.2%) giving rise to a triplet signal (the central line of the triplet coincides with the intense signal of the  $^{28/30}\text{Si}^{28/30}\text{Si}$  isotopomers and so only the outer lines are visible).<sup>[44]</sup> The signals are separated by half the value of the isotropic hyperfine coupling constant ( $A_{\text{iso}}(^{29}\text{Si}) = 5.99$  mT). Notably, the hyperfine coupling in  $1^+$  is considerably larger than in other Si radicals, in which the unpaired electron



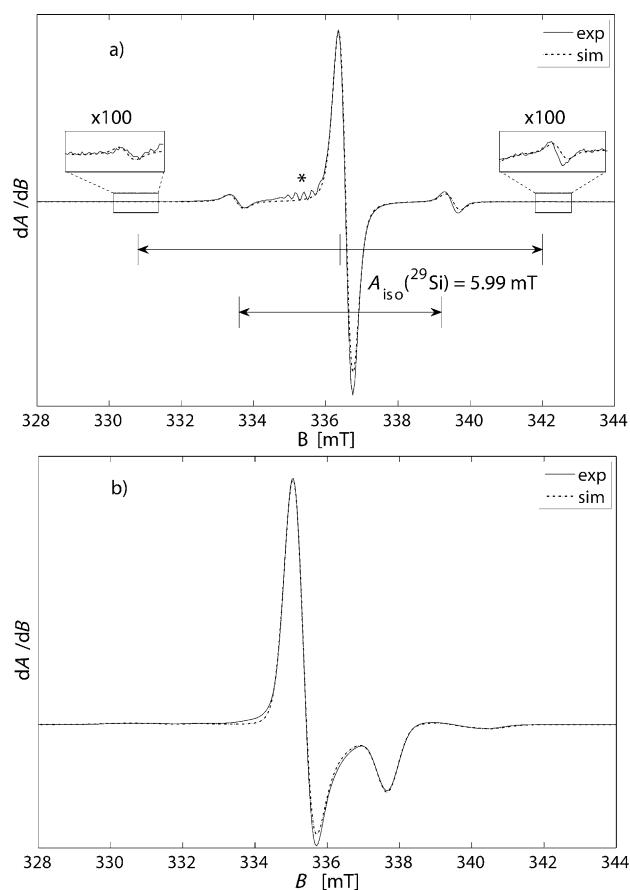


**Figure 3.** Experimental (—) and simulated (.....) cw X-band EPR spectra of 1-B(Ar<sup>F</sup>)<sub>4</sub> in diethyl ether at a) *T* = 220 K (liquid state) and b) *T* = 50 K (frozen state). The marked signal (\*) in a) originates from a decay product of 1-B(Ar<sup>F</sup>)<sub>4</sub>.

is delocalized over two Si atoms, such as the disilene radical cation [Si<sub>2</sub>(SiMe<sub>2</sub>But<sub>2</sub>)<sub>4</sub>]<sup>+</sup> (*A*<sub>iso</sub>(<sup>29</sup>Si<sup>•+</sup>) = 2.30 mT),<sup>[40]</sup> or the disilyne radical anion [Si<sub>2</sub>(SiPrDsi<sub>2</sub>)<sub>2</sub>]<sup>-</sup> (*A*<sub>iso</sub>(<sup>29</sup>Si<sup>•-</sup>) = 3.92 mT)<sup>[39]</sup> and is 3.5 times larger than that in the [Si<sub>2</sub>]<sup>+</sup> cation in its X<sup>4</sup>Σ<sub>g</sub><sup>-</sup> ground state (*A*<sub>iso</sub>(<sup>29</sup>Si)<sub>calc.</sub> = 1.51–1.71 mT).<sup>[4]</sup> This comparison suggests an increased *s*-character of the SOMO of 1-B(Ar<sup>F</sup>)<sub>4</sub> supporting the σ-radical character of 1<sup>+</sup>, and reflects the quite different electronic ground state of 1<sup>+</sup> (*S* = 1/2) from that of [Si<sub>2</sub>]<sup>+</sup> (*S* = 3/2).<sup>[3,45]</sup>

The equivalency of the two Si atoms of 1<sup>+</sup> in solution raised the question as to whether the C<sub>1</sub>-symmetric structure of 1<sup>+</sup> is a result of anisotropic interactions in the solid state or an intrinsic property of 1<sup>+</sup>, and which is the process in case of a C<sub>1</sub>-symmetric minimum structure equilibrating the two Si sites in solution. These issues were addressed by analyzing the EPR spectra of 1-B(Ar<sup>F</sup>)<sub>4</sub> in frozen solution and in the solid state in combination with quantum chemical calculations. The X-band EPR-spectrum of 1-B(Ar<sup>F</sup>)<sub>4</sub> in frozen diethyl ether solution at 50 K showed an intense signal between 334 mT and 338 mT, which could be simulated best with a *g*-tensor of weak orthorhombicity (*g*<sub>11</sub> = 2.0031, *g*<sub>22</sub> = 2.0026, *g*<sub>33</sub> = 1.9880) (Figure 3 b). The *g*-tensor could also be used for the simulation of the corresponding X-band spectrum in the liquid phase as well as for

a Q-band spectrum (34.1 GHz) of a solid state sample of 1-B(Ar<sup>F</sup>)<sub>4</sub>, and compares moreover favorably with the calculated *g*-tensor at the TPSSh/aug-cc-pVTZ/SVP level of theory (Table 1). The X-band spectrum of 1-B(Ar<sup>F</sup>)<sub>4</sub> in frozen solution further displayed two broad satellites of weak intensity at both sides of the intense major signal. Several cases were consid-

**Table 1.** Comparison of the calculated (TPSSh/aug-cc-pVTZ/SVP) *g* and *A*(<sup>29</sup>Si) tensor components of the optimized C<sub>1</sub>-symmetric minimum structure of 1<sup>+</sup> (B3LYP/6-311 + G\*\*/6-31G\*) with the experimental values obtained from the EPR spectrum of 1-B(Ar<sup>F</sup>)<sub>4</sub> in frozen solution; hyperfine couplings are given in mT.<sup>[a,b]</sup>

	<i>g</i> <sub>11</sub>	<i>g</i> <sub>22</sub>	<i>g</i> <sub>33</sub>	<i>g</i> <sub>iso</sub>
calculated	2.0036	2.0022	1.9888	1.9982
experimental	2.0031	2.0026	1.9880	1.9979
	<i>A</i> <sub>11</sub> <sup>Si1</sup>	<i>A</i> <sub>22</sub> <sup>Si1</sup>	<i>A</i> <sub>33</sub> <sup>Si1</sup>	<i>A</i> <sub>iso</sub> <sup>Si1</sup>
calculated	-2.14	-8.29	-2.46	-4.30
experimental	3.11	8.64	3.82	5.19
	<i>A</i> <sub>11</sub> <sup>Si2</sup>	<i>A</i> <sub>22</sub> <sup>Si2</sup>	<i>A</i> <sub>33</sub> <sup>Si2</sup>	<i>A</i> <sub>iso</sub> <sup>Si2</sup>
calculated	-2.70	-9.03	-3.09	-4.94
experimental	4.71	10.25	5.42	6.79

[a] The isotropic values were calculated as the average of the *g* and *A*(<sup>29</sup>Si) tensor components: *g*<sub>iso</sub> = (*g*<sub>11</sub> + *g*<sub>22</sub> + *g*<sub>33</sub>)/3 and *A*<sub>iso</sub> = (*A*<sub>11</sub> + *A*<sub>22</sub> + *A*<sub>33</sub>)/3. [b] The sign of the *A*(<sup>29</sup>Si) values cannot be determined in cw experiments. However, the relative sign of the principal values *A*<sub>11</sub>, *A*<sub>22</sub>, and *A*<sub>33</sub> of the hyperfine coupling tensor could be determined and only equal signs led to a good fit of the experimental spectra. This was supported by the DFT calculations, which gave negative values for the Si hyperfine coupling constants due to the negative value of the magnetic moment of the <sup>29</sup>Si nucleus and the positive value of the spin density at both Si atoms.

ered to assign all components of the *A*(<sup>29</sup>Si) hyperfine coupling tensors, which proved to be quite challenging owing to the superposition of the satellite signals with the intense central signal and the large line width of the signals.<sup>[27]</sup> These cases were validated by quantification of the deviation between the simulated and the experimental spectrum. The smallest deviation was obtained assuming the presence of two magnetically inequivalent Si atoms Si1 and Si2 differing in the isotropic but not in the dipolar part of the hyperfine coupling.<sup>[27]</sup> The derived EPR parameters were backed up by quantum chemical calculations, which revealed a very good agreement of the calculated with the experimental *g* values and consistent trends in the principal values of the hyperfine coupling tensors (Table 1).<sup>[27]</sup>

The observation of a C<sub>1</sub>-symmetric structure of 1-B(Ar<sup>F</sup>)<sub>4</sub> with two magnetically inequivalent Si atoms in the solid-state and in frozen solution, but of a higher symmetric structure with two magnetically equivalent Si atoms in solution, suggested that a topomerization<sup>[46]</sup> takes place in solution, leading to a positional exchange of the two Si sites. Attempts to detect this dynamic process by EPR spectroscopy in solution were not successful, since even at 157 K, the melting point *T*<sub>m</sub> of diethyl ether, the EPR spectrum showed only equivalent Si sites. Taking into account the difference of the hyperfine coupling



constants of the two inequivalent  $^{29}\text{Si}$  nuclei in frozen solution ( $\Delta\nu=45$  MHz), an upper limit for the Gibbs energy of activation  $\Delta G^\ddagger$  ( $<13.5$  kJ mol $^{-1}$ ) and a low limit for the exchange rate  $k_{\text{ex}}$  ( $>100$  MHz) was calculated for the dynamic process.<sup>[27]</sup>

### Quantum-chemical calculations

To elucidate whether a topomerization process is operative in solution, the potential energy hypersurface of  $1^+$  was analyzed at the B3LYP/6-311+G\*\*/6-31G\* level of theory. This analysis ensued an overall  $C_1$  symmetric minimum structure of  $1^+$  as found by X-ray crystallography and furthermore fully reproduced the experimentally observed structural differences between  $1^+$  and **1** (Table 2).<sup>[27]</sup> A comparison of the calculated (gas-phase) with the experimental bonding parameters of  $1^+$  derived from the X-ray diffraction analysis of **1**-B(Ar<sup>F</sup>)<sub>4</sub> revealed

Table 2. Comparison of selected calculated (B3LYP/6-311+G**/6-31G*) and experimental bond lengths [Å], bond angles [°], and torsion angles [°] of $1^+$ and <b>1</b> .								
		Si1–Si2	Si1–C1	Si2–C28	C1–Si1–Si2	C28–Si2–Si1	N2–C1–Si1–Si2	N3–C28–Si2–Si1
$1^+$	calcd	2.223	1.944	1.942	106.6	108.5	39.4	23.4
	exptl	2.178(3)	1.910(8)	1.899(7)	101.9(2)	109.9(2)	53.1(8)	2.6(8)
<b>1</b>	calcd	2.247	1.954	1.954	98.8	98.8	87.8	–87.8
	exptl <sup>[a]</sup>	2.229(1)	1.927(2)	1.927(2)	93.37(5)	93.37(5)	90.8(1)	–90.8(1)

[a] The experimental bonding parameters of **1** were taken from Ref. [6a].

an overall good agreement, with the calculated Si–Si and Si–C<sub>NHC</sub> bond lengths being roughly 2% larger than the experimental values (Table 2). The calculated and experimental structure of  $1^+$  differ mostly in the conformation of the two N-heterocyclic carbenes as evidenced by the torsion angles N2–C1–Si1–Si2 and N3–C28–Si2–Si1 (Table 2). This difference is not surprising given the minor energy of only few kJ mol $^{-1}$  required to change these torsion angles (Figure 4). In general, the structural differences between the Si1 and Si2 site in the  $C_1$  symmetric minimum structure of  $1^+$  were calculated to be smaller in the gas-phase than found in the solid-state by X-ray crystallography (Table 2).

Along with the global  $C_1$ -symmetric minimum structure also a local minimum structure of  $C_i$  symmetry was found on the energy hypersurface, lying only 3 kJ mol $^{-1}$  higher in energy (Figure 4). A quadratic synchronous transit (QST2) calculation<sup>[47]</sup> established that the two minimum structures are connected via a transition state, which lies only 6 kJ mol $^{-1}$  higher in energy than the  $C_1$  symmetric ground-state structure. The transition state shows an imaginary frequency at  $-4$  cm $^{-1}$  and interconverts the two minimum structures along a mode involving a combined bending and torsion of the NHC substituents (Figure 4). The calculated energy barrier is much lower than the low limit for spectroscopic detection by EPR spectroscopy ( $\Delta G^\ddagger < 13.5$  kJ mol $^{-1}$ ) and is fully consistent with the observed topomerization of  $1^+$  in diethyl ether solution occurring rapidly even at the melting point of the solvent.<sup>[48]</sup>

A complete active-space self-consistent field (CASSCF)<sup>[49]</sup> (5,4)/TZVP calculation of  $1^+$  was carried out with an active

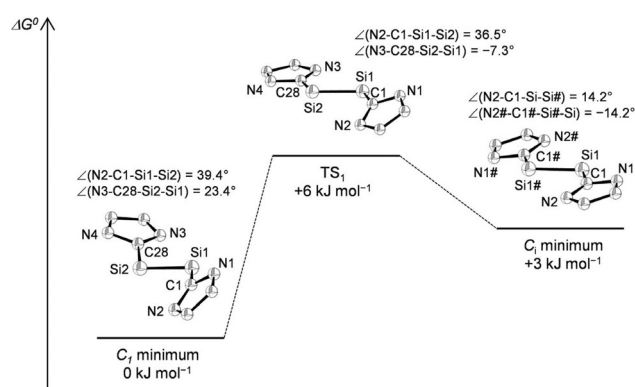


Figure 4. Schematic Gibbs energy profile ( $T=298$  K) for the topomerization of  $1^+$  showing the B3LYP/6-311+G\*\*/6-31G\* optimized  $C_1$  and  $C_i$  symmetric minimum structures and the interconnecting transition state  $TS_1$ . The 2,6-diisopropylphenyl groups and the hydrogen atoms are omitted for clarity.

space built from the DFT-derived symmetric ( $n_+$ ) and antisymmetric ( $n_-$ ) combination of the lone pair orbitals and the Si=Si  $\pi$  and  $\pi^*$  orbitals in order to elucidate, whether a multiconfigurational wave function is necessary for the description of  $1^+$ . The obtained CAS orbitals with their energy values and occupancies

are depicted in Figure 5. Two determinants are necessary to describe the electronic structure of  $1^+$ . The major determinant with a contribution of 94% to the overall wave function has

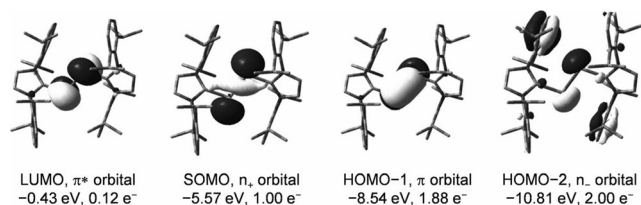


Figure 5. Calculated CASSCF (5,4)/TZVP orbitals of  $1^+$  with their corresponding energy eigenvalues and occupancies; iso surface value: 0.04 e bohr $^{-1}$ .

the configuration [2-2-1-0], in which the  $n_-$  Si lone pair orbital (HOMO–2) and Si=Si  $\pi$ -orbital (HOMO–1) are fully occupied, the  $n_+$  orbital (SOMO) is singly occupied and the Si=Si  $\pi^*$ -orbital (LUMO) is empty. This corroborates the description of  $1^+$  as a  $\sigma$ -type radical. The minor determinant with the configuration [2-0-1-2] has only a small contribution (6%) to the overall wave function. The energy gap between the  $n_+$  and Si=Si  $\pi$ -orbital ( $\Delta E_{\text{SOMO-HOMO-1}}=2.97$  eV) is considerably larger than that in **1** ( $\Delta E_{\text{HOMO-HOMO-1}}=0.03$  eV), indicating that a significant energetic separation of the  $n_+$  orbital and the Si=Si  $\pi$ -orbital occurs upon one-electron oxidation of **1**.

A comparison of the frontier orbitals of the radical cation  $1^+$  with those of the disilyne radical anions  $[\text{Si}_2\text{R}_2]^-$  ( $\text{R}=\text{singly}$

bonded silyl substituent)<sup>[39]</sup> reveals the similar electronic structure (isolobal analogy) of the two opposite charged ions, which can also be illustrated by the canonical formulae given in Figure 6.

The CASSCF(5,4) results indicate, that the radical cation  $1^+$  can be approximately described by a one-determinant

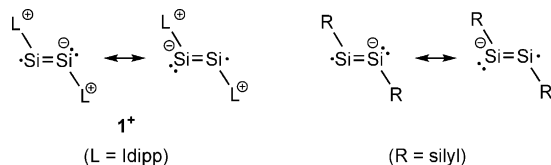


**Figure 6.** Canonical formulae of  $1^+$  (left) and  $[\text{Si}_2\text{R}_2]^-$  (right). Formal charges are encircled; two dots indicate the lone pairs of electrons and one dot the unpaired electrons.

method. This suggests that the EPR parameters of  $1^+$  can be reasonably well calculated using DFT methods.<sup>[27]</sup> Calculations at three different levels of theory gave an excellent agreement between the experimental and the calculated  $g$  tensors, and consistent trends in the principal values of the experimental and calculated hyperfine coupling tensors (Table 1).<sup>[27]</sup> Notably, the absolute value of  $A_{\text{iso}}(^{29}\text{Si})$  is slightly larger at the Si2 site. This can be rationalized with the increased spin density at this atom. In fact, a Mulliken spin density analysis revealed that the overall spin density of  $1^+$  is mainly distributed over the Si1 and Si2 atoms and is slightly larger on the Si2 atom (Si1: 46%, Si2: 48%). Furthermore, a slightly larger contribution of the Si2 atom orbitals to the SOMO was found (Si1: 34.3%, Si2: 34.8%).

The charge distribution in  $1^+$  was studied by natural population analysis and compared with that in  $1$ . One-electron oxidation to give the radical cation  $1^+$  leads to an increase of the Si partial charge from  $-0.10$  in  $1$  to  $+0.24$  (Si1) and  $+0.22$  (Si2) in  $1^+$ . This shows that oxidation mainly occurs at the Si atoms leading to an overall removal of  $0.66 e^-$  from these atoms.

Finally, the enthalpies of the stepwise dissociation of the Idipp groups from  $1^+$  were calculated at the B3LYP/6-311+G\*\*/6-31G\* level of theory and compared with those of  $1$  to analyze the Si–C<sub>NHC</sub> bond strengths (Table 3).<sup>[27]</sup> Dissociation of the first Idipp group from  $1^+$  needs a considerably lower energy ( $D^0(0)_1=243.1 \text{ kJ mol}^{-1}$ ) than that of the second Idipp from  $[\text{Si}_2(\text{Idipp})]^+$  ( $D^0(0)_2=431.3 \text{ kJ mol}^{-1}$ ; Table 3). The same trend is observed for the successive dissociation of Idipp from  $1$ . The overall energy required to dissociate  $1^+$  into  $[\text{Si}_2]^+$  ( $X^4\Sigma_g^-$ ) and two Idipp ( $D^0(0)_1+D^0(0)_2=674.4 \text{ kJ mol}^{-1}$ ) is more than twice the dissociation energy consumed to transform  $1$  into  $[\text{Si}_2]$  ( $X^3\Sigma_g^-$ ) and two Idipp ( $D^0(0)_3+D^0(0)_4=311.5 \text{ kJ mol}^{-1}$ ; Table 3). This can be explained with the increased charge separation (Coulomb energy) in  $1^+$ . Remarkably, the successive dissociation of both Idipp groups from  $1^+$  require a considerably higher energy (243.1 and  $431.3 \text{ kJ mol}^{-1}$ ) than those of typical C<sub>NHC</sub>→Si donor–acceptor bonds (for example,  $D^0(0)$  of  $\text{SiX}_2(\text{Idipp})$  (X = Cl, Br, I) =  $121\text{--}124 \text{ kJ mol}^{-1}$ )<sup>[10b,d]</sup> suggesting the presence of more covalent Si–C<sub>NHC</sub> bonds in  $1^+$ .<sup>[50]</sup> Notably, the fragment ion  $[\text{Si}_2(\text{Idipp})]^+$  resulting after dis-

**Table 3.** Calculated ZPVE (zero point vibrational energy) corrected bond dissociation enthalpies at 0 K ( $D^0(0)$ ) for the stepwise dissociation of Idipp from  $1^+$  and  $1$ .<sup>[a]</sup>

			$D^0(0)$ [kJ mol <sup>-1</sup> ]	
$[\text{Si}_2(\text{Idipp})_2]^+$ (S = 1/2)	→	$[\text{Si}_2(\text{Idipp})]^+$ (S = 1/2)	+ Idipp (S = 0)	243.1 (1)
$[\text{Si}_2(\text{Idipp})]^+$ (S = 1/2)	→	$[\text{Si}_2]^+$ ( $X^4\Sigma_g^-$ ) <sup>[b]</sup> (S = 3/2)	+ Idipp (S = 0)	431.3 (2)
$\text{Si}_2(\text{Idipp})_2$ (S = 0)	→	$\text{Si}_2(\text{Idipp})$ (S = 0)	+ Idipp (S = 0)	126.5 (3)
$\text{Si}_2(\text{Idipp})$ (S = 0)	→	$\text{Si}_2$ ( $X^3\Sigma_g^-$ ) <sup>[c]</sup> (S = 1)	+ Idipp (S = 0)	185.0 (4)

[a] The total spin angular momentum  $S$  of each species is written in parenthesis below the species and the term symbol of selected fragments is given in parenthesis after the fragment. [b] The valence electronic configuration of  $[\text{Si}_2]^+$  in the  $X^4\Sigma_g^-$  ground state is  $4\sigma_g^2 4\sigma_u^2 5\sigma_g^1 2\pi_u^2$ . [c] The valence electronic configuration of  $\text{Si}_2$  in the  $X^3\Sigma_g^-$  ground state is  $4\sigma_g^2 4\sigma_u^2 5\sigma_g^2 2\pi_u^2$ .

sociation of the first Idipp has a doublet ground state as  $1^+$ , but in contrast to  $1^+$  is a  $\pi$ -type radical, in which the Si=Si  $\pi$ -orbital is the SOMO followed by the  $n_+$  orbital (HOMO–1). Similarly, in  $[\text{Si}_2(\text{Idipp})]$  the order of two highest occupied molecular orbitals is reversed compared to  $1$  with the Si=Si  $\pi$ -orbital being the HOMO followed by the  $n_+$  orbital (HOMO–1). This explains why upon one-electron oxidation of  $[\text{Si}_2(\text{Idipp})]$  to give  $[\text{Si}_2(\text{Idipp})]^+$ , which involves a removal of one electron from the Si=Si  $\pi$ -bonding orbital, the Si–Si bond length is considerably increased from 2.206 to 2.346 Å, whereas the opposite is observed in the 1e-oxidation of  $1$  ( $d(\text{Si}–\text{Si})_{\text{calc.}}=2.247 \text{ \AA}$ ) to give  $1^+$  ( $d(\text{Si}–\text{Si})_{\text{calc.}}=2.223 \text{ \AA}$ ) (Table 2).<sup>[27]</sup>

## Conclusion

The present comprehensive structural, spectroscopic, and theoretical study of  $1\text{-B}(\text{Ar}^{\text{F}})_4$  suggests that the radical cation  $[\text{Si}_2(\text{Idipp})_2]^+$  should be rather regarded as the unprecedented cationic counterpart of the disilyne radical anions  $[\text{Si}_2\text{R}_2]^-$  (R = singly bonded silyl group) than a bis-NHC adduct of  $[\text{Si}_2]^+$ . Implications of this electronic analogy, which can be traced back to the isolobal relationship between a Si(Idipp) and a  $[\text{SiR}]^-$  fragment in low-valent silicon chemistry are currently under study.

## Acknowledgements

We thank the Deutsche Forschungsgemeinschaft (SFB813, “Chemistry at Spin Centers”) for the financial support of this work. We also thank Dr. B. Lewall for the cyclovoltammetric studies and A. Martens for the elemental analyses.

**Keywords:** multiple bonds • N-heterocyclic carbenes • radical ions • silicon

- [1] a) M. L. Mandich, W. D. Reents, Jr., K. D. Kolenbrander, *Pure Appl. Chem.* **1990**, *62*, 1653; b) K. Raghavachari, *Phase Transitions* **1990**, *24–26*, 61; c) F. Baletto, R. Ferrando, *Rev. Mod. Phys.* **2005**, *77*, 371.
- [2] Selected references on Si<sub>2</sub>: a) A. E. Douglas, *Can. J. Phys.* **1955**, *33*, 801; b) D. E. Milligan, M. E. Jacox, *J. Chem. Phys.* **1970**, *52*, 2594; c) K. P. Huber, G. Herzberg, *Molecular Spectra and Molecular Structure: Constants of Diatomic Molecules*, Van Nostrand Reinhold Co. Inc., New York, **1979**; d) P. J. Bruna, S. D. Peyerimhoff, R. J. Buenker, *J. Chem. Phys.* **1980**, *72*, 5437; e) S. D. Peyerimhoff, R. J. Buenker, *Chem. Phys.* **1982**, *72*, 111; f) P. Ho, W. G. Breiland, *Appl. Phys. Lett.* **1984**, *44*, 51; g) K. Raghavachari, *J. Chem. Phys.* **1986**, *84*, 5672; h) C. B. Winstead, S. J. Paukstis, J. L. Gole, *Chem. Phys. Lett.* **1995**, *237*, 81; i) D. A. Dixon, D. Feller, K. A. Peterson, J. L. Gole, *J. Phys. Chem. A* **2000**, *104*, 2326; j) O. Kostko, S. R. Leone, M. A. Duncan, M. Ahmed, *J. Phys. Chem. A* **2010**, *114*, 3176.
- [3] a) P. J. Bruna, C. Petrongolo, R. J. Buenker, S. D. Peyerimhoff, *J. Chem. Phys.* **1981**, *74*, 4611; b) A. D. McLean, B. Liu, G. S. Chandler, *J. Chem. Phys.* **1984**, *80*, 5130; c) H. Jörg, N. Rösch, J. R. Sabin, B. I. Dunlap, *Chem. Phys. Lett.* **1985**, *114*, 529; d) B. K. Rao, E. Blaisten-Barojas, *Chem. Phys. Lett.* **1988**, *150*, 259; e) S. Nigam, C. Majumder, S. K. Kulshreshtha, *J. Chem. Phys.* **2004**, *121*, 7756; f) Y. Liu, H. Zhai, X. Zhang, Y. Liu, *Chem. Phys.* **2013**, *425*, 156.
- [4] L. B. Knight, Jr., J. O. Herlong, R. Babb, E. Earl, D. W. Hill, C. A. Arrington, *J. Phys. Chem.* **1991**, *95*, 2732.
- [5] For selected reviews (highlights) on the NHC chemistry of main-group elements, see: a) Y. Wang, G. H. Robinson, *Chem. Commun.* **2009**, 5201; b) R. Wolf, W. Uhl, *Angew. Chem. Int. Ed.* **2009**, *48*, 6774; *Angew. Chem.* **2009**, *121*, 6905; c) D. Martin, M. Soleilhavoup, G. Bertrand, *Chem. Sci.* **2011**, *2*, 389; d) Y. Xiong, S. Yao, M. Driess, *Angew. Chem. Int. Ed.* **2013**, *52*, 4302; *Angew. Chem.* **2013**, *125*, 4398; e) R. S. Ghadwal, R. Azhakar, H. W. Roesky, *Acc. Chem. Res.* **2013**, *46*, 444; f) D. J. D. Wilson, J. L. Dutton, *Chem. Eur. J.* **2013**, *19*, 13626; g) C. D. Martin, M. Soleilhavoup, G. Bertrand, *Chem. Sci.* **2013**, *4*, 3020; h) Y. Wang, G. H. Robinson, *Inorg. Chem.* **2014**, *53*, 11815.
- [6] a) Y. Wang, Y. Xie, P. Wei, R. B. King, H. F. Schaefer III, P. von R. Schleyer, G. H. Robinson, *Science* **2008**, *321*, 1069; b) A. Sidiropoulos, C. Jones, A. Stasch, S. Klein, G. Frenking, *Angew. Chem. Int. Ed.* **2009**, *48*, 9701; *Angew. Chem.* **2009**, *121*, 9881; c) C. Jones, A. Sidiropoulos, N. Holzmann, G. Frenking, A. Stasch, *Chem. Commun.* **2012**, *48*, 9855.
- [7] H. Braunschweig, R. D. Dewhurst, K. Hammond, J. Mies, K. Radacki, A. Vargas, *Science* **2012**, *336*, 1420.
- [8] a) Y. Wang, Y. Xie, P. Wei, R. B. King, H. F. Schaefer III, P. von R. Schleyer, G. H. Robinson, *J. Am. Chem. Soc.* **2008**, *130*, 14970; b) M. Y. Abraham, Y. Wang, Y. Xie, P. Wei, H. F. Schaefer III, P. von R. Schleyer, G. H. Robinson, *Chem. Eur. J.* **2010**, *16*, 432.
- [9] a) Y. Xiong, S. Yao, G. Tan, S. Inoue, M. Driess, *J. Am. Chem. Soc.* **2013**, *135*, 5004; b) Y. Xiong, S. Yao, S. Inoue, J. D. Epping, M. Driess, *Angew. Chem. Int. Ed.* **2013**, *52*, 7147; *Angew. Chem.* **2013**, *125*, 7287.
- [10] a) R. S. Ghadwal, H. W. Roesky, S. Merkel, J. Henn, D. Stalke, *Angew. Chem. Int. Ed.* **2009**, *48*, 5683; *Angew. Chem.* **2009**, *121*, 5793; b) A. C. Filippou, O. Chernov, G. Schnakenburg, *Angew. Chem. Int. Ed.* **2009**, *48*, 5687; *Angew. Chem.* **2009**, *121*, 5797; c) A. C. Filippou, O. Chernov, G. Schnakenburg, *Chem. Eur. J.* **2011**, *17*, 13574; d) A. C. Filippou, Y. N. Lebedev, O. Chernov, M. Straßmann, G. Schnakenburg, *Angew. Chem. Int. Ed.* **2013**, *52*, 6974; *Angew. Chem.* **2013**, *125*, 7112.
- [11] a) A. C. Filippou, O. Chernov, B. Blom, K. W. Stumpf, G. Schnakenburg, *Chem. Eur. J.* **2010**, *16*, 2866; b) H. Cui, C. Cui, *Dalton Trans.* **2011**, *40*, 11937.
- [12] a) T. Agou, N. Hayakawa, T. Sasamori, T. Matsuo, D. Hashizume, N. Tokito, *Chem. Eur. J.* **2014**, *20*, 9246; b) S. U. Ahmad, T. Szilvási, S. Inoue, *Chem. Commun.* **2014**, *50*, 12619.
- [13] M. J. Cowley, V. Huch, H. S. Rzepa, D. Scheschkeewitz, *Nat. Chem.* **2013**, *5*, 876.
- [14] a) A. Jana, V. Huch, D. Scheschkeewitz, *Angew. Chem. Int. Ed.* **2013**, *52*, 12179; *Angew. Chem.* **2013**, *125*, 12401; b) A. Jana, M. Majumdar, V. Huch, M. Zimmer, D. Scheschkeewitz, *Dalton Trans.* **2014**, *43*, 5175.
- [15] C. A. Dyker, G. Bertrand, *Science* **2008**, *321*, 1050.
- [16] G. Frenking, R. Tonner, in *The Chemical Bond—Chemical Bonding Across the Periodic Table, chapt. 4* (Eds.: G. Frenking, S. Shaik), Wiley-VCH, Weinheim, **2014**, pp. 71–112.
- [17] The B3LYP/6–311+G\*\*/6–31G\* computed ZVPE corrected (ZVPE=zero point vibrational energy) bond dissociation energies for the stepwise dissociation of the carbene groups from Si<sub>2</sub>(Idipp)<sub>2</sub> at 0 K mount 126.5 kJ mol<sup>-1</sup> (Si<sub>2</sub>(Idipp)<sub>2</sub>→Si<sub>2</sub>(Idipp) (S=0)+Idipp (S=0)) and 185.0 kJ mol<sup>-1</sup> (Si<sub>2</sub>(Idipp)<sub>2</sub>→Si<sub>2</sub> (S=1, X<sup>3</sup>Σ<sub>g</sub><sup>-</sup>)+Idipp (S=0)), respectively (S is the total spin angular momentum of the electronically and geometrically relaxed fragments; see Table 3 and Supporting Information). The sum of the two values (311.5 kJ mol<sup>-1</sup>) compares well with that calculated for the model compound Si<sub>2</sub>L<sub>2</sub> (L=:C[N(Me)CH]<sub>2</sub>) (338.7 kJ mol<sup>-1</sup>) at the B3LYP/6–311+G\*\* level of theory (Ref. [6a]).
- [18] D. Geiß, M. I. Arz, M. Straßmann, G. Schnakenburg, A. C. Filippou, *Angew. Chem. Int. Ed.* **2015**, *54*, 2739; *Angew. Chem.* **2015**, *127*, 2777.
- [19] For the notation of the symmetry-adapted lone-pair combinations, see: a) E. Haselbach, E. Heilbronner, *Helv. Chim. Acta* **1970**, *53*, 684; b) R. Hoffmann, *Acc. Chem. Res.* **1971**, *4*, 1.
- [20] For pioneering work on organic σ and π radicals, see: a) P. S. Skell, J. C. Day, *J. Am. Chem. Soc.* **1978**, *100*, 1951; b) J. Lessard, D. Griller, K. U. Ingold, *J. Am. Chem. Soc.* **1980**, *102*, 3262; c) P. S. Skell, D. D. May, *J. Am. Chem. Soc.* **1981**, *103*, 967; d) M. J. S. Dewar, A. H. Pakiari, A. B. Pierini, *J. Am. Chem. Soc.* **1982**, *104*, 3242.
- [21] F. Gerson, W. Huber, *Electron Spin Resonance Spectroscopy of Organic Radicals*, Wiley-VCH, Weinheim, Germany, **2003**.
- [22] a) M. Culcasi, G. Gronchi, J. Escudié, C. Couret, L. Pujol, P. Tordo, *J. Am. Chem. Soc.* **1986**, *108*, 3130; b) A. J. Bard, A. H. Cowley, J. E. Kilduff, J. K. Leland, N. C. Norman, M. Pakulski, G. A. Heath, *J. Chem. Soc. Dalton Trans.* **1987**, 249.
- [23] C. J. Rhodes, *J. Chem. Soc. Chem. Commun.* **1989**, 949.
- [24] a) B. Çetinkaya, M. F. Lappert, J. G. Stamper, R. J. Suffolk, *J. Electron Spectrosc. Relat. Phenom.* **1983**, *32*, 133; b) D. Gonbeau, G. Pfister-Guillouzo, *J. Electron Spectrosc. Relat. Phenom.* **1984**, *33*, 279; c) V. Galasso, *Chem. Phys.* **1984**, *83*, 407; d) R. Gleiter, G. Friedrich, M. Yoshifuji, K. Shibayama, N. Inamoto, *Chem. Lett.* **1984**, *13*, 313; e) A. H. Cowley, *Polyhedron* **1984**, *3*, 389; f) T. L. Allen, A. C. Scheiner, Y. Yamaguchi, H. F. Schaefer III, *J. Am. Chem. Soc.* **1986**, *108*, 7579; g) T. L. Allen, A. C. Scheiner, H. F. Schaefer III, *J. Phys. Chem.* **1990**, *94*, 7780; h) C. Glidewell, *J. Organomet. Chem.* **1991**, *409*, 171; i) L. Weber, *Chem. Rev.* **1992**, *92*, 1839; j) K. Miqueu, J.-M. Sotiropoulos, G. Pfister-Guillouzo, H. Ranaivonjatovo, J. Escudié, *J. Mol. Struct.* **2001**, *545*, 139.
- [25] H.-L. Peng, J. L. Payton, J. D. Protasiewicz, M. C. Simpson, *J. Phys. Chem. A* **2009**, *113*, 7054.
- [26] D. J. D. Wilson, S. A. Couchman, J. L. Dutton, *Inorg. Chem.* **2012**, *51*, 7657.
- [27] Details of the cyclic voltammetric studies are given in the Supporting Information, which also contains the synthesis, the reduction, the EPR spectroscopic and decay studies of 1-B(Ar<sup>F</sup>)<sub>2</sub>, as well as the comparative quantum chemical studies and bonding analyses of **1** and **1**<sup>+</sup>.
- [28] All potentials in the text are given vs. the [Fe(C<sub>5</sub>Me<sub>5</sub>)<sub>2</sub>]<sup>+0</sup> redox couple, which was chosen as the reference standard for the CV experiments of **1** owing to its favorable properties versus the [Fe(C<sub>5</sub>H<sub>5</sub>)<sub>2</sub>]<sup>+0</sup> redox couple: a) I. Noviadri, K. N. Brown, D. S. Fleming, P. T. Gulyas, P. A. Lay, A. F. Masters, L. Phillips, *J. Phys. Chem. B* **1999**, *103*, 6713; b) J. R. Aranzas, M.-C. Daniel, D. Astruc, *Can. J. Chem.* **2006**, *84*, 288. For comparison reasons, the half-wave potential of the [Fe(C<sub>5</sub>H<sub>5</sub>)<sub>2</sub>]<sup>+0</sup> redox couple was also determined under the same conditions and found to be 0.440 V (in THF), 0.520 V (in C<sub>6</sub>H<sub>5</sub>F) and 0.562 V (in 1,2-C<sub>6</sub>H<sub>4</sub>F<sub>2</sub>) versus the [Fe(C<sub>5</sub>Me<sub>5</sub>)<sub>2</sub>]<sup>+0</sup> redox couple.
- [29] K. C. Mondal, P. P. Samuel, H. W. Roesky, R. R. Aysin, L. A. Leites, S. Neudeck, J. Lübben, B. Dittrich, N. Holzmann, M. Hermann, G. Frenking, *J. Am. Chem. Soc.* **2014**, *136*, 8919.
- [30] M. Melaimi, M. Soleilhavoup, G. Bertrand, *Angew. Chem. Int. Ed.* **2010**, *49*, 8810; *Angew. Chem.* **2010**, *122*, 8992.
- [31] S. Shah, S. C. Burdette, S. Swavey, F. L. Urbach, J. D. Protasiewicz, *Organometallics* **1997**, *16*, 3395 and references therein.
- [32] The redox potentials of the diphosphenes are given in Ref. [31] vs. the saturated calomel electrode and were converted to the [Fe(C<sub>5</sub>Me<sub>5</sub>)<sub>2</sub>]<sup>+0</sup> redox scale using the half-wave potential of SCE (E<sub>1/2</sub> = -0.08 V) versus the [Fe(C<sub>5</sub>Me<sub>5</sub>)<sub>2</sub>]<sup>+0</sup> redox couple determined in THF in our laboratory. For (SiMe<sub>3</sub>)<sub>3</sub>CP=PC(SiMe<sub>3</sub>)<sub>3</sub>, an irreversible one-electron oxidation was reported in CH<sub>2</sub>Cl<sub>2</sub> at room temperature, which however turns reversible at -75 °C (E<sub>1/2</sub> = 1.6 V (vs. SCE)) (Ref. [22b]).
- [33] The electron affinities and ionization potentials of related compounds can be correlated with their LUMO and HOMO energies, respectively:

- a) C.-G. Zhan, J. A. Nichols, D. A. Dixon, *J. Phys. Chem. A* **2003**, *107*, 4184; b) I. Dance, *Inorg. Chem.* **2006**, *45*, 5084.
- [34] N. G. Connelly, W. E. Geiger, *Chem. Rev.* **1996**, *96*, 877.
- [35] O. Back, B. Donnadieu, P. Parameswaran, G. Frenking, G. Bertrand, *Nat. Chem.* **2010**, *2*, 369; the redox potential of  $P_2(\text{ldipp})_2$  is given in this publication versus the  $[\text{Fe}(\text{C}_5\text{H}_5)_2]^{+/0}$  redox couple ( $E_{1/2}$  in THF = -1.41 V). Its value was converted to the  $[\text{Fe}(\text{C}_5\text{Me}_5)_2]^{+/0}$  redox scale using the half-wave potential of the  $[\text{Fe}(\text{C}_5\text{H}_5)_2]^{+/0}$  redox couple ( $E_{1/2}$  = 0.44 V) in THF versus the  $[\text{Fe}(\text{C}_5\text{Me}_5)_2]^{+/0}$  redox couple determined in our laboratory.  $P_2(\text{ldipp})_2$  contains two electrons more than  $\text{Si}_2(\text{ldipp})_2$  in an antibonding P–P  $\pi^*$  orbital, and is therefore also a strong reducing agent.
- [36] I. Chávez, A. Alvarez-Carena, E. Molins, A. Roig, W. Maniukiewicz, A. Arancibia, V. Arancibia, H. Brand, J. M. Manriquez, *J. Organomet. Chem.* **2000**, *601*, 126.
- [37] a) T. Matsuno, M. Ichinohe, A. Sekiguchi, *Angew. Chem. Int. Ed.* **2002**, *41*, 1575; *Angew. Chem.* **2002**, *114*, 1645; b) H. Maruyama, H. Nakano, M. Nakamoto, A. Sekiguchi, *Angew. Chem. Int. Ed.* **2014**, *53*, 1324; *Angew. Chem.* **2014**, *126*, 1348.
- [38] S. S. Batsanov, *Inorg. Mater.* **2001**, *37*, 871.
- [39] a) R. Kinjo, M. Ichinohe, A. Sekiguchi, *J. Am. Chem. Soc.* **2007**, *129*, 26; b) A. Sekiguchi, R. Kinjo, M. Ichinohe, *Synth. Met.* **2009**, *159*, 773.
- [40] S. Inoue, M. Ichinohe, A. Sekiguchi, *J. Am. Chem. Soc.* **2008**, *130*, 6078.
- [41] a) L. Pu, A. D. Phillips, A. F. Richards, M. Stender, R. S. Simons, M. M. Olmstead, P. P. Power, *J. Am. Chem. Soc.* **2003**, *125*, 11626; b) P. P. Power, *Organometallics* **2007**, *26*, 4362.
- [42] a) C. Chatgililoglu, *Chem. Rev.* **1995**, *95*, 1229; b) P. P. Power, *Chem. Rev.* **2003**, *103*, 789; c) V. Y. Lee, A. Sekiguchi, *Organometallic Compounds of Low-Coordinate Si, Ge, Sn and Pb; From Phantom Species to Stable Compounds*, Wiley, Chichester, UK, **2010**.
- [43] The low  $g$ -value of  $1^+$  results from the small  $g_{33}$  tensor component, which according to quantum-chemical calculations lies in the C1-Si1-Si2-C28 plane (perpendicular to the Si=Si  $\pi$ -bond) in an almost parallel orientation to the Si2–C28 bond ( $\angle g_{33}\text{-Si2-C28} = 8.7^\circ$ ), and a slightly tilted orientation to the Si1–C1 bond ( $\angle g_{33}\text{-Si1-C1} = 18.3^\circ$ ) (see Figure S15 in the Supporting Information).
- [44] In the case of two non-equivalent Si atoms, two doublets (4.45% each) with different hyperfine coupling would be expected for the two different  $^{28/30}\text{Si}^{29}\text{Si}$  isotopomers and a doublet of doublets (0.2%) for the  $^{29}\text{Si}^{29}\text{Si}$  isotopomer.
- [45] Notably, the  $A(^{29}\text{Si})$  value of  $1^+$  compares well with those of planar, spin-localized silyl radicals: a) A. Sekiguchi, T. Fukawa, M. Nakamoto, V. Y. Lee, M. Ichinohe, *J. Am. Chem. Soc.* **2002**, *124*, 9865; b) A. Sekiguchi, S. Inoue, M. Ichinohe, Y. Arai, *J. Am. Chem. Soc.* **2004**, *126*, 9626; c) G. Molev, B. Tumanski, D. Sheberla, M. Botoshansky, D. Bravo-Zhivotovskii, Y. Apeloig, *J. Am. Chem. Soc.* **2009**, *131*, 11698.
- [46] G. Binsch, E. L. Eliel, H. Kessler, *Angew. Chem. Int. Ed. Engl.* **1971**, *10*, 570; *Angew. Chem.* **1971**, *83*, 618.
- [47] a) C. Peng, H. B. Schlegel, *Isr. J. Chem.* **1993**, *33*, 449; b) C. Peng, P. Y. Ayala, H. B. Schlegel, M. J. Frisch, *J. Comput. Chem.* **1996**, *17*, 49.
- [48] An equilibrium in solution between a  $C_1$  and  $C_i$  symmetric structure, which lies on the side of the  $C_1$  symmetric structure, cannot be excluded given the experimental and theoretical results.
- [49] P.-A. Malmqvist, A. Rendell, B. O. Roos, *J. Phys. Chem.* **1990**, *94*, 5477 and references therein.
- [50] R. Walsh, *Acc. Chem. Res.* **1981**, *14*, 246.
- [51] CCDC 1056561 (1-B(Ar<sup>F</sup>)<sub>4</sub>-2(1,3-C<sub>6</sub>H<sub>4</sub>F<sub>2</sub>)) contains the supplementary crystallographic data for this paper. These data are provided free of charge by The Cambridge Crystallographic Data Centre.

Received: June 5, 2015

# CHEMISTRY

## A **European** Journal

### Supporting Information

#### **One-Electron Oxidation of a Disilicon(0) Compound: An Experimental and Theoretical Study of $[\text{Si}_2]^+$ Trapped by N-Heterocyclic Carbenes**

Marius I. Arz,<sup>[a]</sup> Martin Straßmann,<sup>[a]</sup> Andreas Meyer,<sup>[b]</sup> Gregor Schnakenburg,<sup>[a]</sup> Olav Schiemann,<sup>\*[b]</sup> and Alexander C. Filippou<sup>\*[a]</sup>

chem\_201502199\_sm\_miscellaneous\_information.pdf

**Supporting Information****Table of contents**

1. Experimental Section – General Part	S2
2. Synthesis of $[\text{Si}_2(\text{Idipp})_2][\text{B}(\text{Ar}^{\text{F}})_4]$ ( $\mathbf{1-B}(\text{Ar}^{\text{F}})_4$ )	S2
3. Reduction of $\mathbf{1-B}(\text{Ar}^{\text{F}})_4$ with $\text{C}_8\text{K}$	S3
4. Crystal structure determination of $\mathbf{1-B}(\text{Ar}^{\text{F}})_4 \cdot 2(1,3\text{-C}_6\text{H}_4\text{F}_2)$	S3
5. Cyclic voltammetric studies of $\text{Si}_2(\text{Idipp})_2$ ( $\mathbf{1}$ )	S5
6. EPR spectroscopic analysis of $\mathbf{1-B}(\text{Ar}^{\text{F}})_4$	S9
7. Decay studies of $\mathbf{1-B}(\text{Ar}^{\text{F}})_4$	S15
8. Comparative electronic structure calculations of $\mathbf{1}^+$ and $\mathbf{1}$	S18



## 1. Experimental Section – General Part

All experiments were carried out under an atmosphere of argon using Schlenk or glove box techniques. The commercially available argon had a purity of  $\geq 99.996\%$  and was further passed through a gas purification system to remove traces of  $O_2$  and  $H_2O$ . The glassware was dried in an oven at approximately  $110\text{ }^\circ\text{C}$  and baked under vacuum prior to use. *n*-hexane was refluxed several days over sodium wire/benzophenone/tetraglyme (0.5 vol%), purged several times with argon during reflux and distilled off and degassed prior to use. 1,3-difluorobenzene and fluorobenzene were stirred several days over  $CaH_2$  and then trap-to-trap condensed and degassed. The diethyl ether ( $Et_2O$ ) used for the EPR samples was stirred several days over  $LiAlH_4$ , and then trap-to-trap condensed and degassed prior to use. The tetrahydrofuran (THF) used for the cyclic voltammetric studies was refluxed several days over sodium wire, and then trap-to-trap condensed and degassed prior to use. All solvents were stored in the glove box.  $Si_2(\text{Idipp})_2$  (**1**) (Idipp = 1,3-bis(2,6-diisopropylphenyl)-imidazolin-2-ylidene)<sup>[1]</sup> and  $[Fe(C_5Me_5)_2][B(Ar^F)_4]$  ( $Ar^F = 3,5\text{-}C_6H_3(CF_3)_2$ )<sup>[2]</sup> were synthesized following the published procedures with slight modifications. The C, H, N analyses of  $1\text{-}B(Ar^F)_4$  were carried out three times on an Elementar Vario Micro elemental analyzer. The individual C, H, N values did not differ by more than  $\pm 0.3\%$ . The mean C, H, N values are given below for compound  $1\text{-}B(Ar^F)_4$ .

## 2. Synthesis of $[Si_2(\text{Idipp})_2][B(Ar^F)_4]$ ( $1\text{-}B(Ar^F)_4$ )

A Schlenk tube was charged with **1** (100 mg, 0.12 mmol) and  $[Fe(C_5Me_5)_2][B(Ar^F)_4]$  (143 mg, 0.12 mmol). 1,3-difluorobenzene (6 mL) was vacuum transferred into the Schlenk tube at  $-196\text{ }^\circ\text{C}$ . The mixture was warmed to  $-40\text{ }^\circ\text{C}$  and stirred for 30 minutes at  $-40\text{ }^\circ\text{C}$ , whereupon a green solution was obtained. Precooled *n*-hexane ( $-50\text{ }^\circ\text{C}$ , 6 mL) was added with a transfer cannula ( $\varnothing = 1\text{ mm}$ ) to the solution. The solution was filtered from a tiny amount of a red-green solid into a precooled ( $-50\text{ }^\circ\text{C}$ ) receiver Schlenk tube using a filter cannula ( $\varnothing = 1\text{ mm}$ ). Storage of the clear, green filtrate for 4 days at  $-60\text{ }^\circ\text{C}$  afforded green crystals of  $1\text{-}B(Ar^F)_4$ . The mother liquor was decanted off with a transfer cannula ( $\varnothing = 1\text{ mm}$ ), and the crystals were dried under vacuum ( $1\cdot 10^{-2}\text{ mbar}$ ) for 2 h at  $0\text{ }^\circ\text{C}$ . Yield: 145 mg (0.09 mmol, 71%). The crystals were stored in a glove box at  $-30\text{ }^\circ\text{C}$  and did not show any decomposition over a period of several months. Upon grinding the crystals a green powder was obtained, that turned brown due to decomposition after storage for approximately 6 h at ambient temperature. Elemental analysis calcd. (%) for  $C_{86}H_{84}BF_{24}N_4Si_2$  (1696.56): C 60.88, H 4.99, N 3.30; found: C 60.50, H 4.84, N 3.19%.

[1] Y. Wang, Y. Xie, P. Wei, R. B. King, H. F. Schaefer III, P. v. R. Schleyer, G. H. Robinson, *Science* **2008**, 321, 1069.

[2] I. Chávez, A. Alvarez-Carena, E. Molins, A. Roig, W. Maniukiewicz, A. Arancibia, V. Arancibia, H. Brand, J. M. Manríquez, *J. Organomet. Chem.* **2000**, 601, 126.

### 3. Reduction of $1\text{-B}(\text{Ar}^{\text{F}})_4$ with $\text{C}_8\text{K}$

A Schlenk tube was charged with  $1\text{-B}(\text{Ar}^{\text{F}})_4$  (25 mg, 15  $\mu\text{mol}$ ) and  $\text{C}_8\text{K}$  (2 mg, 15  $\mu\text{mol}$ ). THF (1.5 mL) was vacuum transferred into the Schlenk tube at  $-196\text{ }^\circ\text{C}$ . The mixture was warmed to  $-60\text{ }^\circ\text{C}$  and a dark-red suspension with a small amount of a black precipitate was rapidly obtained as soon as all solvent had melted. The suspension was stirred for 1 h at  $-60\text{ }^\circ\text{C}$  and subsequently warmed to ambient temperature. After removal of the volatiles under vacuum, a dark-red solid containing small particles of a black solid was obtained. The solid was digested in  $\text{C}_6\text{D}_6$  and filtered into an NMR tube. The recorded  $^1\text{H}$  NMR spectrum showed the signals of  $\mathbf{1}^{[1]}$  indicating the selective formation of  $\mathbf{1}$  upon one-electron reduction of  $1\text{-B}(\text{Ar}^{\text{F}})_4$ .

### 4. Crystal structure determination of $1\text{-B}(\text{Ar}^{\text{F}})_4\cdot 2(1,3\text{-C}_6\text{H}_4\text{F}_2)$

Green plates of  $1\text{-B}(\text{Ar}^{\text{F}})_4\cdot 2(1,3\text{-C}_6\text{H}_4\text{F}_2)$  suitable for single-crystal x-ray diffraction were obtained upon crystallization from a 1,3-difluorobenzene/*n*-hexane mixture (1:1) at  $-60\text{ }^\circ\text{C}$  as described in the synthetic part. The solvent was decanted from the crystals with a transfer cannula at  $-60\text{ }^\circ\text{C}$  and Fomblin® was added directly at low temperature under a stream of argon. The crystals were mounted on the goniometer under a slight stream of liquid nitrogen at low temperature.

The data collection was performed on a Bruker X8-KappaApex II diffractometer (area detector) using graphite monochromated  $\text{Mo-K}_\alpha$  radiation ( $\lambda = 0.7107\text{ \AA}$ ). The diffractometer was equipped with a low-temperature device (Kryoflex I, Bruker AXS, Karlsruhe, 100 K). Intensities were measured by fine-slicing  $\omega$  and  $\varphi$ -scans and corrected for background, polarization and Lorentz effects. An empirical absorption correction was applied for all data sets.<sup>[3]</sup> The structures were solved by direct methods and refined anisotropically by the least-squares procedure implemented in the SHELX program system.<sup>[4]</sup> Hydrogen atoms were included using the riding model on the bound carbon atoms. Selected crystallographic refinement data are listed in Table S1.

CCDC-1056561 contains the supplementary crystallographic data for this paper, which can be obtained free of charge from the Cambridge Crystallographic Data Centre via [www.ccdc.cam.ac.uk/data\\_request/cif](http://www.ccdc.cam.ac.uk/data_request/cif).

The molecular structure of  $1\text{-B}(\text{Ar}^{\text{F}})_4\cdot 2(1,3\text{-C}_6\text{H}_4\text{F}_2)$  presented in this manuscript shows a limited completeness to  $\theta = 25.25^\circ$  of 64.5% arising from numerous strong overlapping reflections of a non-merohedrally twinned specimen of the compound. Several attempts to obtain a crystal structure of higher quality failed so far even from different freshly prepared batches of single crystals due to a pathological twinning phenomenon. This might arise from the unbalanced unit cell lengths in  $1\text{-B}(\text{Ar}^{\text{F}})_4\cdot 2(1,3\text{-C}_6\text{H}_4\text{F}_2)$  leading to very thin plate-like crystals, where several of the extreme thin plates grow together with a small rotational displacement with respect to each other. The data collection was

[3] SADABS, 2009/2, AXS, 2009.

[4] G. M. Sheldrick, SHELXS97 and SHELXL97, University of Göttingen, Germany, 1997.



performed after indexing two domains using the CELL\_NOW program.<sup>[3]</sup> The refined twin law (0.99983 0.00069 -0.00018 0.00031 -1.00000 0.00008 -1.83353 -0.00125 -0.99983) representing a 180° rotation around the reciprocal axis of 1.000 0.002 -0.925 underlines the slight rotational displacement leading to strong overlapping reflections. However, the other crystallographic parameters (goodness-of-fit, data/parameter ratio) show an overall acceptable structure quality, which could not be further improved.

**Table S1.** Crystal data and refinement for 1-B(Ar<sup>F</sup>)<sub>4</sub>·2(1,3-C<sub>6</sub>H<sub>4</sub>F<sub>2</sub>).

Empirical formula	C <sub>98</sub> H <sub>92</sub> BF <sub>28</sub> N <sub>4</sub> Si <sub>2</sub>
Moiety formula	C <sub>54</sub> H <sub>72</sub> N <sub>4</sub> Si <sub>2</sub> , C <sub>32</sub> H <sub>12</sub> BF <sub>24</sub> , 2(1,3-C <sub>6</sub> H <sub>4</sub> F <sub>2</sub> )
Formula weight	1924.75 g mol <sup>-1</sup>
Temperature	100(2) K
Wavelength	0.71073 Å
Crystal system, space group	monoclinic, <i>P</i> 2 <sub>1</sub> / <i>c</i>
Unit cell dimensions	<i>a</i> = 22.001(3) Å, $\alpha$ = 90° <i>b</i> = 12.574(1) Å, $\beta$ = 120.405(4)° <i>c</i> = 39.847(5) Å, $\gamma$ = 90°
Volume	9507(2) Å <sup>3</sup>
Z, Calculated density	4, 1.345 mg m <sup>-3</sup>
Absorption coefficient	0.140 mm <sup>-1</sup>
<i>F</i> (000)	3972
Crystal size	0.60 × 0.32 × 0.02 mm
$\theta$ -range for data collection	1.72 – 25.25°
Limiting indices	-25 ≤ <i>h</i> ≤ 19, 0 ≤ <i>k</i> ≤ 15, 0 ≤ <i>l</i> ≤ 47
Reflections collected / unique	32299 / 11102 [ <i>R</i> <sub>int</sub> = 0.0687]
Completeness to $\theta$ = 25.25°	64.5 %
Absorption correction	Empirical
Max. and min. transmission	0.9972 and 0.9206
Refinement method	Full-matrix least squares on <i>F</i> <sup>2</sup>
Data / restraints / parameters	11102 / 1054 / 1437
Goodness-of-fit on <i>F</i> <sup>2</sup>	1.076
Final <i>R</i> indices [ <i>I</i> > $\sigma$ ( <i>I</i> )]	<i>R</i> <sub>1</sub> = 0.0723, <i>wR</i> <sub>2</sub> = 0.1606
<i>R</i> indices (all data)	<i>R</i> <sub>1</sub> = 0.1045, <i>wR</i> <sub>2</sub> = 0.1766
Largest diff. peak / hole	0.472 / -0.423 e Å <sup>-3</sup>

## 5. Cyclic voltammetric studies of Si<sub>2</sub>(Idipp)<sub>2</sub> (**1**)

The cyclic voltammetric studies of **1** were performed with an Autolab Eco electrochemical workstation composed of an Autolab PGSTAT 20 potentiostat/galvanostat. The results were analyzed with the Autolab software version 4.9. All experiments were carried out in a glove box under argon in a gas-tight specially designed full-glass three-electrode cell at room temperature. A glass-carbon disk electrode ( $\varnothing = 2$  mm) was used as working electrode, a Pt wire of 1 mm diameter as counter electrode and a 4 mM [Fe(C<sub>5</sub>Me<sub>5</sub>)<sub>2</sub>]<sup>+</sup>/[Fe(C<sub>5</sub>Me<sub>5</sub>)<sub>2</sub>] / 0.1 M N(*n*Bu)<sub>4</sub>(PF<sub>6</sub>) / C<sub>6</sub>H<sub>5</sub>F or THF solution as reference electrode, which was separated from the substrate/electrolyte solution with a Vycor frit (4 mm).<sup>[5]</sup>

All experiments were carried out in fluorobenzene or THF solution containing tetra-*n*-butylammonium hexafluorophosphate, N(*n*Bu)<sub>4</sub>(PF<sub>6</sub>), as supporting electrolyte in a concentration of 0.1 M. The electrolyte was recrystallized twice from ethanol and dried for 24 h at 80 °C using a drying pistol. *iR*-drop compensation was applied for all experiments.

All potentials are given relative to the reference electrode. For comparison reasons, the half-wave potential of the redox couple [Fe(C<sub>5</sub>H<sub>5</sub>)<sub>2</sub>]<sup>+</sup>/[Fe(C<sub>5</sub>H<sub>5</sub>)<sub>2</sub>] (Fc<sup>+</sup>/Fc) was determined by separate cyclic voltammetric experiments versus the [Fe(C<sub>5</sub>Me<sub>5</sub>)<sub>2</sub>]<sup>+</sup>/[Fe(C<sub>5</sub>Me<sub>5</sub>)<sub>2</sub>] (dmfc<sup>+</sup>/dmfc) reference electrode under the same conditions in fluorobenzene and THF and found to be  $E_{1/2} = +520$  mV and  $E_{1/2} = +440$  mV, respectively.

The cyclic voltammograms of Si<sub>2</sub>(Idipp)<sub>2</sub> (**1**) in fluorobenzene are depicted in Figures S1 and S2.

The Si(0) compound undergoes a reversible one-electron transfer process at a half-wave potential  $E_{1/2}(1)$  of  $-730$  mV (Figure S2). The following parameters were used to verify the reversibility of the one-electron transfer process: a) the half-wave potential was found to be constant and the peak current ratio  $i_{pc} / i_{pa} = 1$  for all scan rates ( $\nu$ ) ranging from 16 – 400 mV s<sup>-1</sup> (Table S2); b) the peak potential separation  $\Delta E_p$  did not change with increasing scan rate, and ranged from 68 mV – 78 mV being slightly higher than the value expected for an ideal one-electron Nernstian process (58 mV), but similar with that found for decamethylferrocene under the same conditions (Table S2) (the slightly larger values of  $\Delta E_p$  can be attributed to incomplete *iR* compensation); and c) a plot of the cathodic peak current  $i_{pc}$  against the square root of the scan rate confirmed an almost linear relationship (Figure S3).

Two irreversible electron transfer processes were also observed in the cyclic voltammogram of **1** in fluorobenzene at  $E_{1/2}(2) = +658$  mV and  $E_{1/2}(3) = +1001$  mV at a scan rate of 50 mV s<sup>-1</sup> (Figure S1). For both electron-transfer processes the ratio of the cathodic and anodic peak currents ( $\nu = 50$  mV s<sup>-1</sup>) was found to be considerably smaller than one, and the peak potential separation much larger than the expected 58 mV value (Table S2). These observations suggest a rapid follow-up chemical reaction occurring upon oxidation of the radical cation **1**<sup>+</sup> to a putative disilyne dication (**1**<sup>2+</sup>).

[5] The [Fe(C<sub>5</sub>Me<sub>5</sub>)<sub>2</sub>]<sup>+/0</sup> (dmfc<sup>+</sup>/dmfc) redox couple has been shown to be a superior reference standard for potentials to the [Fe(C<sub>5</sub>H<sub>5</sub>)<sub>2</sub>]<sup>+/0</sup> (Fc<sup>+</sup>/Fc) redox couple, see: I. Noviadri, K. N. Brown, D. S. Fleming, P. T. Gulyas, P. A. Lay, A. F. Masters, L. Phillips, *J. Phys. Chem. B* **1999**, *103*, 6713.

The redox behavior of **1** was also studied in THF by cyclic voltammetry and compound **1** found to undergo as in fluorobenzene a reversible one-electron oxidation at  $E_{1/2} = -794$  mV (Figures S4 and S5, Table S3). A small solvent dependence of the redox potential of the one-electron oxidation of **1** was observed (Table S4).

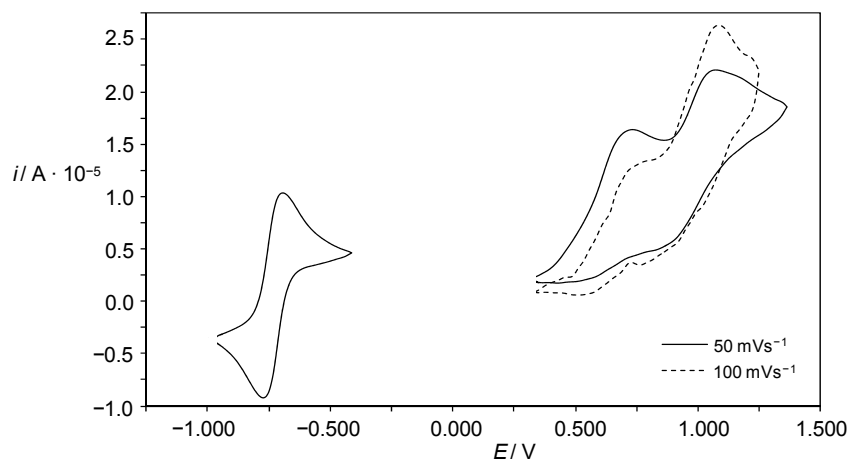


**Figure S1.** Single scan cyclic voltammograms of **1** in fluorobenzene at room temperature in the potential range of (-1.250) – (+1.500) V at scan rates of 50 and 100 mV s<sup>-1</sup>; reference electrode: dmfc<sup>+</sup>/dmfc / 0.1 M N(nBu)<sub>4</sub>(PF<sub>6</sub>) / C<sub>6</sub>H<sub>5</sub>F solution.

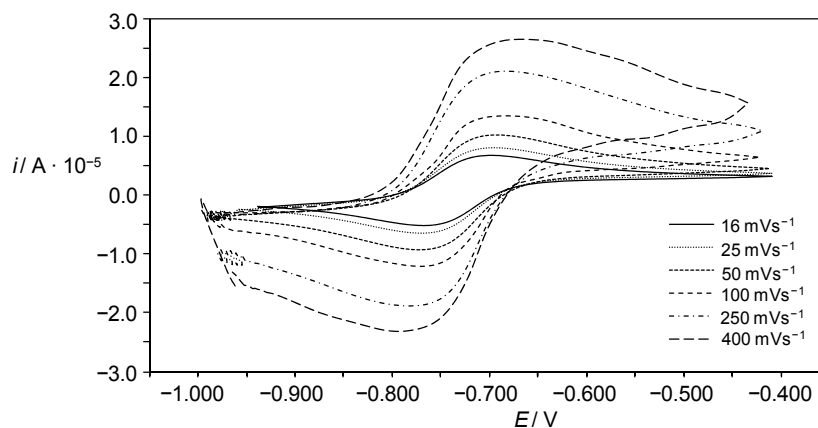


**Figure S2.** Single-scan cyclic voltammograms of **1** in fluorobenzene at room temperature in the potential range of (-1.100) – (-0.300) V at different scan rates; reference electrode: dmfc<sup>+</sup>/dmfc / 0.1 M N(nBu)<sub>4</sub>(PF<sub>6</sub>) / C<sub>6</sub>H<sub>5</sub>F solution.

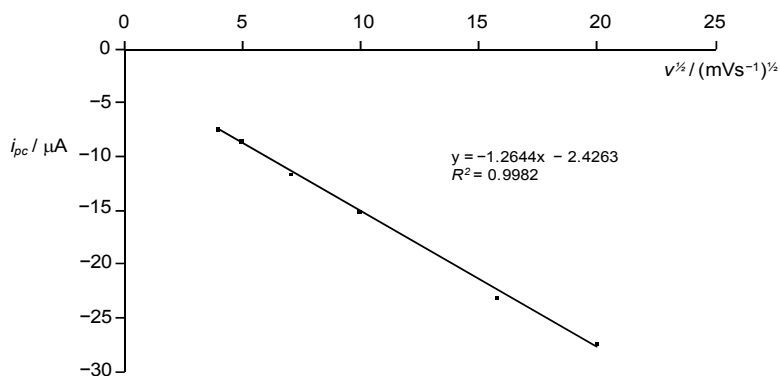


**Figure S3.** Plot of the cathodic peak current  $i_{pc}$  against the square root of the scan rate  $v^{1/2}$  for the reversible oxidation of **1** in fluorobenzene at  $E_{1/2} = -730$  mV.

**Table S2.** Cyclic voltammetric results of **1** in fluorobenzene.<sup>§</sup>

$v$ [mV s <sup>-1</sup> ]	$\Delta E_p$ [mV]	$i_{pc} / i_{pa}$	$E_{1/2} = (E_{pa} + E_{pc}) / 2$ [mV]
16	68	1.00	-731
25	70	1.01	-731
50	70	1.00	-732
100	78	1.00	-730
250	78	1.04	-730
400	72	1.03	-728
50	116	0.16	+658
	110	0.88	+1001

<sup>§</sup>  $v$ : scan rate;  $\Delta E_p$ : peak potential separation;  $\Delta E_p = E_{pa} - E_{pc}$ , where  $E_{pa}$  is the anodic peak potential and  $E_{pc}$  the cathodic peak potential;  $i_{pc} / i_{pa}$ : ratio of cathodic and anodic peak current;  $E_{1/2}$ : half wave potential. Potentials are given versus the dmfc<sup>+</sup>/dmfc / 0.1 M N(nBu)<sub>4</sub>(PF<sub>6</sub>) / C<sub>6</sub>H<sub>5</sub>F reference electrode.

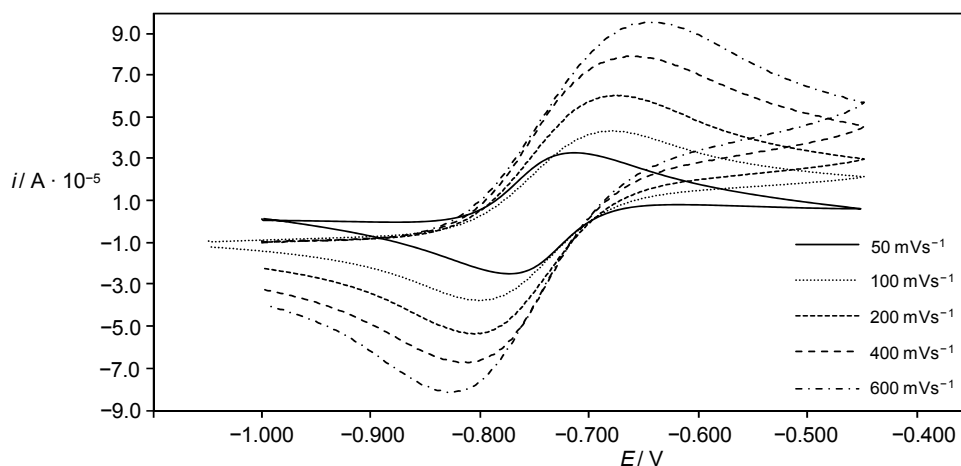


**Figure S4.** Single-scan cyclic voltammograms of **1** in THF at room temperature in the potential range of (-1.150) – (-0.400) V at different scan rates; reference electrode: dmfc<sup>+</sup>/dmfc / 0.1 M N(nBu)<sub>4</sub>(PF<sub>6</sub>) / THF solution.

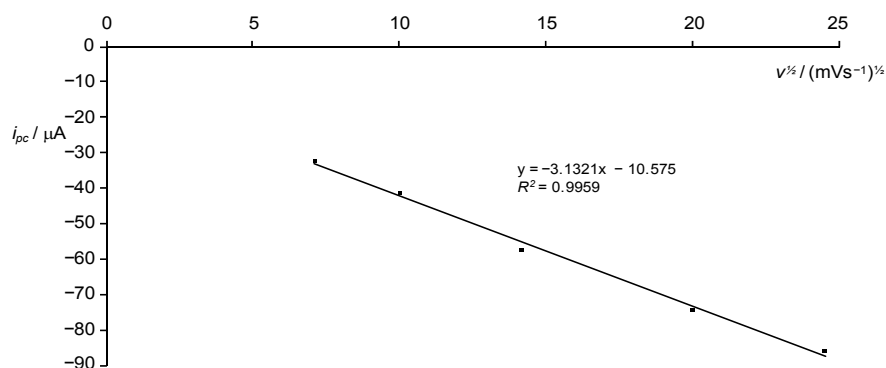


**Figure S5.** Plot of the cathodic peak current  $i_{pc}$  against the square root of the scan rate  $v^{1/2}$  for the reversible oxidation of **1** in THF at  $E_{1/2} = -794$  mV.

**Table S3.** Cyclic voltammetric results of **1** in THF.<sup>§</sup>

$\nu$ [mV s <sup>-1</sup> ]	$\Delta E_p$ [mV]	$i_{pc} / i_{pa}$	$E_{1/2} = (E_{pa} + E_{pc}) / 2$ [mV]
50	64	1.00	-794
100	62	1.05	-794
200	56	1.07	-794
400	68	1.06	-793
600	66	1.06	-793

<sup>§</sup>  $\nu$ : scan rate;  $\Delta E_p$ : peak potential separation;  $\Delta E_p = E_{pa} - E_{pc}$ , where  $E_{pa}$  is the anodic peak potential and  $E_{pc}$  the cathodic peak potential;  $i_{pc} / i_{pa}$ : ratio of cathodic and anodic peak current;  $E_{1/2}$ : half wave potential. Potentials are given versus the dmfc<sup>+</sup>/dmfc / 0.1 M N(nBu)<sub>4</sub>(PF<sub>6</sub>) / THF reference electrode.

**Table S4.** Half-wave potentials of the reversible one-electron oxidation of **1** in fluorobenzene and THF.

Solvent	$E_{1/2}$ vs. dmfc <sup>+</sup> /dmfc [mV]	$E_{1/2}$ vs. Fc <sup>+</sup> /Fc [mV]
C <sub>6</sub> H <sub>5</sub> F	-730 mV	-1250 <sup>§</sup>
THF	-794 mV	-1234 <sup>#</sup>

<sup>§</sup> The half-wave potential vs. Fc/Fc<sup>+</sup> in fluorobenzene was calculated using the following equation  $E_{1/2}(\text{vs. Fc}^+/\text{Fc}) [\text{mV}] = E_{1/2}(\text{vs. dmfc}^+/\text{dmfc}) [\text{mV}] - 520 \text{ mV}$ .

<sup>#</sup> The half-wave potential vs. Fc/Fc<sup>+</sup> in THF was calculated using the following equation  $E_{1/2}(\text{vs. Fc}^+/\text{Fc}) [\text{mV}] = E_{1/2}(\text{vs. dmfc}^+/\text{dmfc}) [\text{mV}] - 440 \text{ mV}$ .

## 6. EPR spectroscopic analysis of 1-B(Ar<sup>F</sup>)<sub>4</sub>

The samples used for the EPR experiments were prepared in the following way: a small amount of solid 1-B(Ar<sup>F</sup>)<sub>4</sub> (approximately 2 – 4 mg) was transferred into a quartz glass EPR tube in a glove box. The solvent was trap-to-trap condensed into the tube under vacuum and the tube was sealed off under vacuum with an oxygen/hydrogen burner. The compound was dissolved by shaking the sealed tube in a cooling bath of diethyl ether at –110 °C and after the solution turned green, the tube was frozen in a liquid nitrogen cooling bath.

All EPR experiments were performed on a Bruker ELEXSYS E580 EPR spectrometer. A Super High-Q resonator and an Oxford ESR900 helium gas-flow cryostat were employed for the continuous-wave (cw) measurements at X-band frequencies. Cw measurements at Q-band frequencies were performed using an EN 5107D2 resonator and an Oxford CF935 helium gas-flow cryostat. Details of the measurement parameters are given in Table S5. Spectra were simulated using the garlic and the pepper routine of the EasySpin program package<sup>[6]</sup> for the spectra of the liquid and the frozen solutions, respectively. The simulation parameters for all spectra are depicted in Table S6.

**Table S5.** Parameters used for EPR measurements shown in Figure S6.<sup>§</sup>

Fig.	<i>T</i> [K]	$\nu$ [GHz]	<i>MA</i> [G]	<i>P</i> [mW]	<i>RG</i> [dB]	<i>CT</i> [ms]	<i>TC</i> [ms]	<i>CF</i> [mT]	<i>SW</i> [mT]	<i>NP</i>
S6 a)	50	9.3956	1	0.0063	36	25	20.48	335.5	36	900
S6 b)	220	9.4129	2	0.0020	40	21	20.48	337.5	25	500
S6 c)	120	34.1455	0.5	0.4111	5	41	20.48	1220.1	50	800

<sup>§</sup> Abbreviations: *T* = temperature,  $\nu$  = microwave frequency, *MA* = modulation amplitude, *P* = microwave power, *RG* = receiver gain, *CT* = conversion time, *TC* = time constant, *CF* = center field, *SW* = sweep width, *NP* = number of points on the field axis. For all measurements lower scan rates and modulation amplitudes were checked to see if the resolution could be improved, which was not the case.

**Table S6.** *g* and hyperfine coupling constants (hfcc) *A*(<sup>29</sup>Si) values used to simulate the spectra.<sup>§</sup>

	11	22	33	iso <sup>#</sup>
<i>g</i>	2.0031	2.0026	1.9880	1.9979
<i>A</i> ( <sup>29</sup> Si) [mT]*	3.91	9.45	4.62	5.99
<i>A</i> <sup>A</sup> ( <sup>29</sup> Si) [mT]	4.71	10.25	5.42	6.79
<i>A</i> <sup>B</sup> ( <sup>29</sup> Si) [mT]	3.11	8.64	3.82	5.19

<sup>§</sup> A Voigtian lineshape was used with linewidths of 0.621 and 0.108 mT for the Gaussian and the Lorentzian contribution, respectively. The sign of the hyperfine coupling constants cannot be obtained in cw experiments. However, the relative sign of the principal values could be determined: only equal signs led to a good fit for the spectrum of the liquid sample. This was supported by the DFT calculations, which yielded negative signs for all Si hyperfine coupling constants.

<sup>#</sup> The isotropic values were calculated as the average of the anisotropic *g*-values and hyperfine coupling constants:  $g_{\text{iso}} = (g_{11} + g_{22} + g_{33}) / 3$  and  $A^{(\text{29Si})}_{\text{iso}} = [A^{(\text{29Si})}_{11} + A^{(\text{29Si})}_{22} + A^{(\text{29Si})}_{33}] / 3$ .

\* This set of hfcc was used to simulate the spectrum of the liquid solution, and is the average of the hfcc values used for the different Si atoms to simulate the spectrum of the frozen solution.

[6] S. Stoll, A. Schweiger, *J. Magn. Reson.* **2006**, *178*, 42.

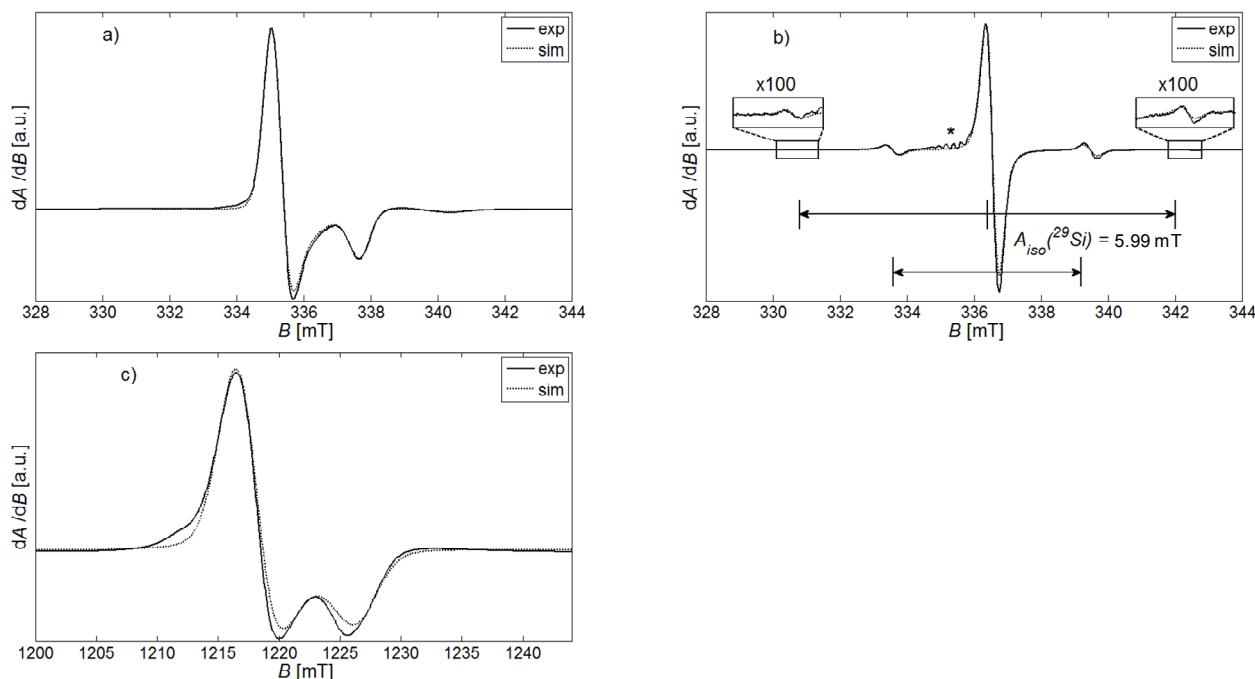


**Figure S6.** Experimental and simulated cw X-band EPR spectra of  $1\text{-B}(\text{Ar}^{\text{F}})_4$  in diethyl ether at a)  $T = 50$  K and b)  $T = 220$  K. The marked feature (\*) originates from an impurity due to partial decay of  $1\text{-B}(\text{Ar}^{\text{F}})_4$ . c) Experimental and simulated Q-band cw EPR spectra of  $1\text{-B}(\text{Ar}^{\text{F}})_4$  as a non-dilute powdered solid at  $T = 120$  K.

The intensity pattern in the X-band spectrum in the liquid state [Figure S6, b)] can be explained by considering the natural abundance of the magnetically active  $^{29}\text{Si}$  ( $I = 1/2$ ) nuclei, which is 4.67 %. Thus 90.9 % of  $\text{Si}_2(\text{ldipp})_2^+$  ( $1^+$ ) consists only of magnetically inactive nuclei ( $^{28}\text{Si}$ :  $I = 0$ , natural abundance: 92.23 %;  $^{30}\text{Si}$ :  $I = 0$ , natural abundance: 3.1 %) causing the intense central resonance. On the other hand 8.9 % of  $1^+$  contain one, and 0.2 % of  $1^+$  two  $^{29}\text{Si}$  nuclei. The isotopomers  $^{28/30}\text{Si}^{28/30}\text{Si}$ ,  $^{28/30}\text{Si}^{29}\text{Si}/^{29}\text{Si}^{28/30}\text{Si}$  and  $^{29}\text{Si}^{29}\text{Si}$  of  $1^+$  give rise to different hyperfine splitting patterns, depending on whether the nuclei are equivalent or not.<sup>[7]</sup>

In case of two equivalent Si nuclei one would expect a singlet signal for the  $^{28/30}\text{Si}^{28/30}\text{Si}$  isotopomers, a doublet signal for the two identical  $^{28/30}\text{Si}^{29}\text{Si}$  and  $^{29}\text{Si}^{28/30}\text{Si}$  isotopomers and a triplet signal for the  $^{29}\text{Si}^{29}\text{Si}$  isotopomer. Each line would be in this case separated by half the isotropic value of the hyperfine coupling constant. Since the central line of the triplet signal coincides with the intense signal of the  $^{28/30}\text{Si}^{28/30}\text{Si}$  isotopomers, only four satellites are expected to be observed.

In case of two non-equivalent Si nuclei one would have to differentiate between two cases of  $^{28/30}\text{Si}^{29}\text{Si}$  isotopomers, since the unpaired electron could be localized either on the magnetically active  $^{29}\text{Si}$  or the magnetically inactive  $^{28/30}\text{Si}$  nuclei. This situation would result in a singlet signal for the  $^{28/30}\text{Si}^{28/30}\text{Si}$  isotopomers, two doublets with different hyperfine splitting for the two different isotopomers  $^{28/30}\text{Si}^{29}\text{Si}$  and  $^{29}\text{Si}^{28/30}\text{Si}$  and a doublet of a doublet for the  $^{29}\text{Si}^{29}\text{Si}$  isotopomer. In this case, the lines would be

[7] The magnetically inactive  $^{28}\text{Si}$  and  $^{30}\text{Si}$  nuclei were merged to  $^{28/30}\text{Si}$  for the sake of simplicity.

unequally spaced and up to 8 satellite lines would be expected. The intensity pattern for both cases is given in Table S7.

Four satellites were observed in the cw EPR spectrum of  $1\text{-B}(\text{Ar}^{\text{F}})_4$  in liquid  $\text{Et}_2\text{O}$  solution. These were placed in equal distance to each other and displayed an intensity pattern corresponding to two magnetically equivalent Si nuclei. Thus, EPR spectroscopy indicates two equivalent Si nuclei for  $1\text{-B}(\text{Ar}^{\text{F}})_4$  in liquid solution. However, in frozen solution, two different isotropic hfcc, which differ by  $\Delta\nu = 45$  MHz, were assumed for the Si nuclei to explain the EPR spectrum (vide infra).<sup>[8]</sup> Therefore, the equivalence of the Si nuclei in the liquid state suggests a rapid positional exchange (topomerization) of the two Si sites. The following equation can be used to evaluate the energetics of this topomerization at the temperature of coalescence  $T_c$ :<sup>[9]</sup>

$$\Delta G^\ddagger = 0.0191 \cdot T_c \cdot \left[ 9.97 + \lg\left(\frac{T_c}{\Delta\nu}\right) \right] \text{ [kJmol}^{-1}\text{]}$$

Experimentally the point of coalescence was not observed. Instead a rapid topomerization was observed as soon as the solvent melted. Thus, only an upper bound for the Gibbs activation energy of topomerization can be given, if the melting point  $T_M = 157$  K of the solvent (diethyl ether) is used instead of the temperature of coalescence. With the frequency difference of  $\Delta\nu = 45$  MHz one obtains  $\Delta G^\ddagger \leq 13.5$  kJ mol<sup>-1</sup>. This energy barrier corresponds to a low limit of  $k_{\text{ex}} \geq 100$  MHz for the exchange rate constant  $k_{\text{ex}}$ . The low limit is valid at the point of coalescence where the rate constant can be calculated as  $k_{\text{ex}} \approx 2.22 \cdot \Delta\nu$ .

**Table S7.** Expected hyperfine splitting pattern and the corresponding relative intensity in the case of either equivalent or non-equivalent Si nuclei.

	<sup>28/30</sup> Si <sup>28/30</sup> Si	<sup>28/30</sup> Si <sup>29</sup> Si / <sup>29</sup> Si <sup>28/30</sup> Si	<sup>29</sup> Si <sup>29</sup> Si
<b>equivalent Si</b>	singlet (90.9%)	doublet (8.9%)	triplet (0.2%)
<b>non-equivalent Si</b>	singlet (90.9%)	two doublets (each 4.45%)	doublet of doublet (0.2%)

The equivalence of the Si nuclei in liquid solution was clearly indicated by the hyperfine structure of the isotropic spectrum (vide supra). In comparison, validation whether the equivalence of the Si nuclei is maintained in the solid state, proved not to be an easy task using cw EPR spectroscopy on the sample in frozen solution. Some insight could be gained by quantification of the deviation between the simulated and experimental spectrum. The solid state spectrum can be treated as a sum of solid state spectra corresponding to the various isotopomers in complete analogy to the situation in the liquid state detailed above. Since the <sup>28</sup>Si<sup>28</sup>Si isotopomer is the dominating species the deviation between the

[8] The equation 1 mT  $\approx$  28 MHz can be used in good approximation for the conversion of units.

[9] M. Hesse, H. Meier, B. Zeeh, *Spektroskopische Methoden in der organischen Chemie*, 7., überarbeitete Auflage, Georg Thieme Verlag, Stuttgart, **2005**.



simulated and experimental spectrum is dominated by its spectral contribution as well. For that reason it was sensible to consider the deviation in certain regions of the spectrum, which can be safely assigned to the other isotopomers (Figure S7).

To quantify the absolute deviation  $\Delta$  between simulated and experimental spectrum the following equation was used:

$$\Delta = \sum_{B_{min}}^{B_{max}} |I_{exp}(B) - I_{sim}(B)|$$

$\Delta$  is thereby defined as the sum of the deviations between the experimental and simulated spectral intensity  $I$  for all field values  $B$ . The deviations  $\Delta_1$  for the first satellites originating from the  $^{28/30}\text{Si}^{29}\text{Si}$  and the  $^{29}\text{Si}^{28/30}\text{Si}$  isotopomers are defined analogously, the sum being restricted to the field values indicated by the boxes in Figure S7. The left box in Figure S7 contains the satellites assigned to the  $^{29}\text{Si}^{29}\text{Si}$  isotopomer and was used for calculating the deviation  $\Delta_2$  in the same way. The high field satellite of that isotopomer was not used in the calculation of  $\Delta_2$  due to severe baseline deviations in this region of the spectrum.

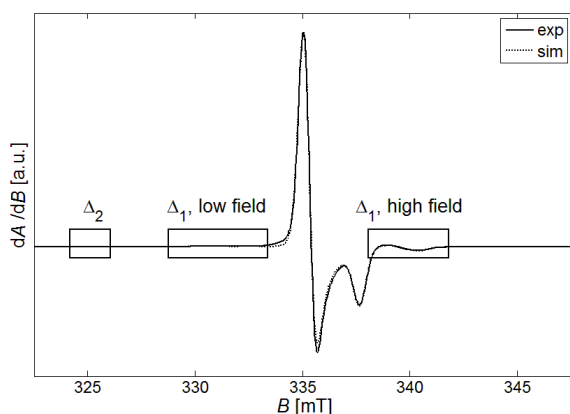


**Figure S7.** Frozen solution spectrum and simulation of  $1\text{-B}(\text{Ar}^{\text{F}})_4$ . The boxes mark the field regions of the spectrum, which were used to calculate the deviations  $\Delta_1$  and  $\Delta_2$  corresponding to the satellite signals of the  $^{28/30}\text{Si}^{29}\text{Si}/^{29}\text{Si}^{28/30}\text{Si}$  and  $^{29}\text{Si}^{29}\text{Si}$  isotopomers, respectively. The corresponding spectral regions are magnified in Figure S8.

Five different cases have been considered. In case **A** both Si nuclei were assumed to be equivalent and have the same hyperfine coupling tensor, which was used to simulate the spectrum of the liquid solution (see Table S6). Inequivalent nuclei were assumed in cases **B** and **C**, the difference between these two cases lying in the realization of that inequivalence. In case **B**, the hyperfine coupling tensor of one Si nucleus was multiplied by 1.1, while the hyperfine tensor of the other Si nucleus was multiplied by 0.9. In case **C**, the principal values of the hyperfine coupling tensors were increased by 0.80 mT for one Si nucleus and decreased by 0.80 mT for the other one. Cases **B** and **C** both correspond to an increase in spin density on one nucleus at the expense of spin density at the other nucleus. This leaves the average isotropic value of the hyperfine coupling constant expected for a rapid topomerization of the two different isotopomers  $^{28/30}\text{Si}^{29}\text{Si}$  and  $^{29}\text{Si}^{28/30}\text{Si}$  in the liquid state unchanged. The physical models for cases **B** and **C** are different however. In case **B** both the isotropic as well as the dipolar part of the hyperfine coupling were changed. In case **C** only the isotropic part of the

hyperfine interaction was changed. Case **C** thus corresponds to an increased s-orbital character at the strongly coupled Si nucleus and a decreased s-character at the weakly coupled nucleus, respectively. Case **D** simulated a situation in which two different conformers of  $1^+$  exist in frozen solution. The Si nuclei within each isomer were assumed to be equivalent, however the nuclei of the one isomer were assumed to be stronger coupled than the nuclei of the other isomer. The hyperfine coupling tensors assumed for both isomers were the same as for the different Si nuclei in case **C**. Finally in case **E** several conformers with identical Si nuclei were considered similarly to case **D**. However, in case **E** a more general approach was chosen by introducing a large hyperfine coupling distribution into the simulation spectrum of the frozen solution, thereby assuming a statistical ensemble of conformers, which are structurally similar corresponding to a distribution of hyperfine coupling tensors. The five different cases are summarized in Table S8.

**Table S8.** The five different cases considered for the interpretation of the solid state spectrum of  $1\text{-B}(\text{Ar}^{\text{F}})_4$ .<sup>§</sup>

Case	No. of isomers	Si nuclei	hfcc tensors
<b>A</b>	1	equivalent	$A$
<b>B</b>	1	non equivalent	$1.1 \cdot A, 0.9 \cdot A$
<b>C</b>	1	non equivalent	$A + 0.80 \text{ mT}, A - 0.80 \text{ mT}$
<b>D</b>	2	equivalent	$A + 0.80 \text{ mT}, A - 0.80 \text{ mT}$
<b>E</b>	distribution	equivalent	distribution of $A$

<sup>§</sup> Abbreviations: hfcc = hyperfine coupling constant,  $A$  = hyperfine coupling tensor from Table S6.

Investigation of the five cases described above showed that the absolute deviation  $\Delta$  of the whole spectrum changed at most by about 9 %. However, case **A** where just one isomer having equivalent Si nuclei was considered yielded the largest deviation between experimental and simulated spectrum. Closer inspection of the sources of these deviations showed, that the deviations in the satellite regions were more than proportionally affected by changing the simulation parameters. The deviations  $\Delta_1$  for all other cases were about 56 – 65 % lower than in case **A**, the largest decrease being obtained in case **C** (65 %). Furthermore, the change of  $\Delta_1$  in these cases was almost as large as the change of the total deviation  $\Delta$ . Owing to the low intensity of the second satellites, the values for  $\Delta_2$  were rather small for all cases considered. Thus, the decrease in  $\Delta_2$  for cases **B** and **C** relative to case **A** was not that significant. This result was to be expected, since the hyperfine coupling to one of the inequivalent Si nuclei was increased by the same amount as it was decreased for the other nucleus. The strong increase of  $\Delta_2$  for case **D** and **E**, however rules out the existence of two conformers or a distribution of conformers with equivalent nuclei. Thus, while a set of different conformers could explain the broad satellites of the isotopomers  $^{28/30}\text{Si}^{29}\text{Si}$  and  $^{29}\text{Si}^{28/30}\text{Si}$ , it could not explain the sharp features belonging to the  $^{29}\text{Si}^{29}\text{Si}$  isotopomer.

The best numerical results were obtained for case **C**. Based on the results of the error validation, which are summed up in Figure S8 and Table S9, it is more reasonable to assume the presence of two inequivalent Si nuclei in the structure of **1-B(Ar<sup>F</sup>)<sub>4</sub>** even in frozen solution.

**Table S9.** Results of the error validation described above.<sup>§</sup>

Case	$\Delta_{norm}$	$\Delta_1 \cdot 10$	$\Delta_{1A} - \Delta_{1i} / \Delta_A - \Delta_i$	$\Delta_2 \cdot 10^6$
<b>A</b>	1	1.07	-	5.80
<b>B</b>	0.92	0.38	0.97	10.5
<b>C</b>	0.91	0.46	0.78	10.5
<b>D</b>	0.92	0.47	0.82	137.5
<b>E</b>	0.92	0.42	0.99	42.1

<sup>§</sup> The total deviation  $\Delta$  as well as the deviations  $\Delta_1$  and  $\Delta_2$  were normalized to the maximum deviation obtained in case **A**.  $\Delta_{1A} - \Delta_{1i} / \Delta_A - \Delta_i$  is the ratio of change in  $\Delta_1$  to the change in total deviation  $\Delta$  for the cases **B**, **C** and **D** compared to case **A**, i.e.  $\Delta_{1A} - \Delta_{1i} / \Delta_A - \Delta_i = [\Delta_1(\text{case A}) - \Delta_1(\text{case B, C, D or E})] / [\Delta(\text{case A}) - \Delta(\text{case B, C, D or E})]$ . The deviation  $\Delta_2$  for the second satellites was calculated taking into account a correction for the shifted baseline (see Figure S8). The baseline was chosen such as to minimize the error of the second satellite in case **A**. All other cases were treated with the same baseline as in case **A**.

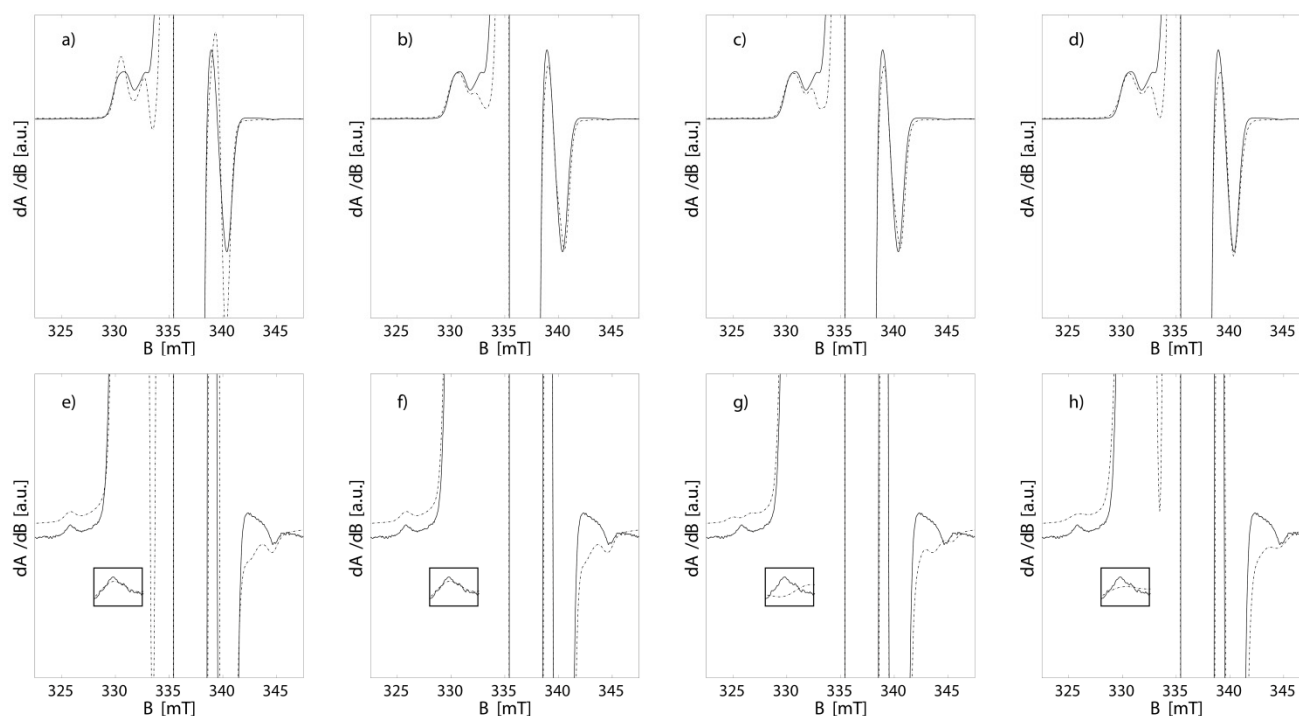


**Figure S8.** Satellite regions of the spectra magnified for the  $^{28/30}\text{Si}^{29}\text{Si}$  and  $^{29}\text{Si}^{28/30}\text{Si}$  isotopomers [a] - d)] and the  $^{29}\text{Si}^{29}\text{Si}$  isotopomer [e] - h)]. Case **A** is represented in a) and e), case **C** in b) and f), case **D** in c) and g) and case **E** in d) and h). Case **B** is very similar to case **C** and was thus omitted. The inset shows the region used to calculate the error of the  $^{29}\text{Si}^{29}\text{Si}$  satellite with the applied baseline correction magnified by a factor of 2.5. A distinction between case **B** and **C** is not possible based solely on the presented EPR spectra and the corresponding simulations. Case **A** does not reproduce the satellites belonging to the  $^{28/30}\text{Si}^{29}\text{Si}$  and  $^{29}\text{Si}^{28/30}\text{Si}$  isotopomers. Cases **D** and **E** reproduce these satellites. However they fail to reproduce the satellite signals of the  $^{29}\text{Si}^{29}\text{Si}$  isotopomer yielding either a doublet of peaks or a very broad peak in contrast to the very sharp peak observed experimentally.

## 7. Decay studies of 1-[B(Ar<sup>F</sup>)<sub>4</sub>]

The decay of 1-B(Ar<sup>F</sup>)<sub>4</sub> in diethyl ether solution at room temperature was analyzed by cw X-band EPR spectroscopy. Spectra were recorded over 14 h out of which three representative spectra are depicted in Figure S9. The spectra revealed a decrease of the signal of 1<sup>+</sup>, suggesting that the decay of 1-B(Ar<sup>F</sup>)<sub>4</sub> leads in the end to EPR silent products, which yield a brown-red solution.

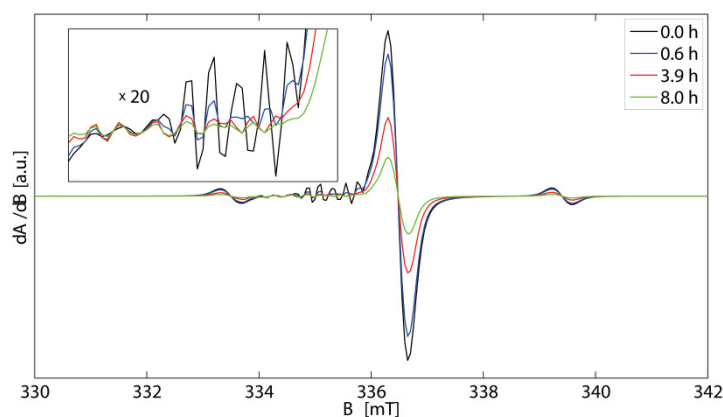


**Figure S9.** CW X-band EPR-spectra of 1-B(Ar<sup>F</sup>)<sub>4</sub> in diethyl ether solution at ambient temperature recorded at  $t = 0$  s (black curve), 0.6 h (blue curve), 3.9 h (red curve) and 8.0 h (green curve).

The time dependence of the EPR signal intensity of 1<sup>+</sup> (Figure S10) could be well fitted by assuming a monoexponential decay law (equation (1)) with a time constant (mean life time)  $\tau$  of 20512 s.

$$y(t) = 127.75e^{-t/\tau} \quad (\text{Eq. 1})$$

The half-life  $t_{1/2}$  of the persistent radical 1<sup>+</sup> was calculated to be 14218 s using equation (2).

$$t_{1/2} = \ln(2) \cdot \tau \quad (\text{Eq. 2})$$

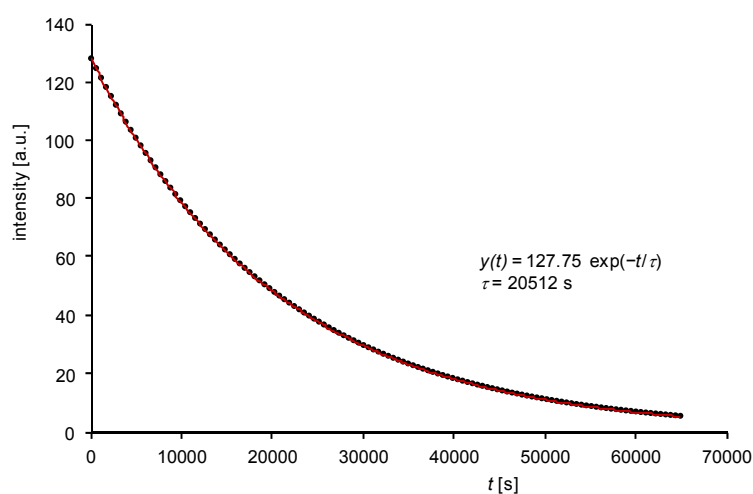


**Figure S10.** Plot of the intensity of the central signal of 1<sup>+</sup> in the cw X-band EPR spectrum versus time (dotted black line). The fit of the experimental data (red line) follows the decay law given by equation (2).

Furthermore, the EPR spectra in Figure S9 revealed the occurrence of additional paramagnetic species during the decay of  $1^+$ . A detailed analysis of all of these species was not possible due to their signals decaying rapidly, having low intensities and displaying non-resolved and overlapping spectra.

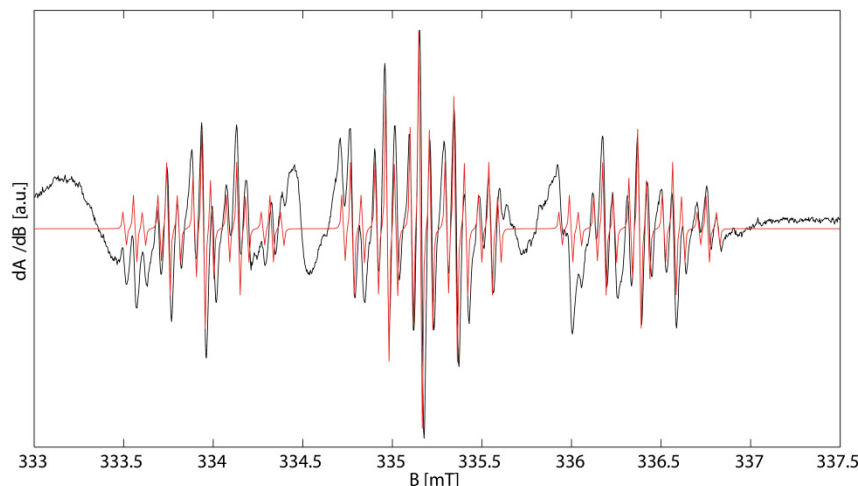


**Figure S11.** Experimental (black curve) and simulated (red curve) cw EPR spectra of  $1$ -[B(Ar<sup>F</sup>)<sub>4</sub>] after 14 h of decay in diethyl ether at ambient temperature. The central signal of residual  $1^+$  was subtracted. The broad signal at 333.3 mT corresponds to the  $^{28/30}\text{Si}^{29}\text{Si}$  satellite signal of residual  $1^+$ . The very well resolved multiline signal at 335.2 mT (red curve) could be simulated and tentatively assigned to the radical cation  $[\text{SiH}_2(\text{Idipp})]^+$ , whereas the origin of the two broad signals at 334.5 and 335.9 mT remains unknown.

However, after  $t = 49600$  s (ca. 14 h), a high resolution cw EPR spectrum of one of the species could be obtained. At this time, the signal of  $1^+$  was still observable ( $I = 6.7\% \cdot I_0$ ) as the most intense signal, but subtracting this signal yielded the spectrum in Figure S11. This spectrum contained several signals: a broad signal at 333.3 mT, which is the low-field  $^{28/30}\text{Si}^{29}\text{Si}$  satellite signal of residual  $1^+$ , two broad signals at 334.5 mT and 335.9 mT, which may constitute a doublet signal of one species, and a very well resolved multiline signal spanning a field range from 333.4 to 336.8 mT.

Whereas the two broad signals could not be accounted for, the highly resolved multiline signal could be analyzed and simulated. It displays a triplet of a quintet of a triplet structure. Such a hyperfine pattern could result from coupling to two pairs of equivalent hydrogen nuclei and one pair of equivalent nitrogen nuclei with the hyperfine coupling constants  $A(^1\text{H}) = 1.2$  mT,  $A(^{14}\text{N}) = 0.2$  mT and  $A(^1\text{H}) = 0.05$  mT, respectively. The splitting pattern and the magnitude of the hyperfine coupling constants may be related to the radical cation  $[\text{SiH}_2(\text{Idipp})]^+$ . Due to the low intensity of this signal, no  $^{29}\text{Si}$  satellite signals could be detected. The hyperfine coupling constants of the presumed radical cation  $[\text{SiH}_2(\text{Idipp})]^+$  compare very well with those of structurally related radicals, e.g. the  $A(^1\text{H}^\alpha)$  hyperfine coupling constant of 1.2 mT is similar to that of the silyl radical  $\text{MeSiH}_2$  (1.182 mT)<sup>[10]</sup> and the  $A(^{14}\text{N}^\gamma)$  hyperfine coupling constant of 0.2 mT compares well with that of the NHC-stabilized silylene radical

[10] C. Chatgililoglu, *Chem. Rev.* **1995**, *95*, 1229.

cation in  $[\text{Si}(\text{Si}t\text{Bu}_3)_2(\text{IMe}_4)][\text{BAR}_4]$  (0.26 mT;  $\text{IMe}_4 = \text{C}[\text{N}(\text{Me})\text{CMe}]_2$ ,  $\text{Ar} = \text{C}_6\text{F}_4\text{-4-SiMe}_2t\text{Bu}$ ).<sup>[11]</sup> It should be noted that the  $A(^1\text{H}^\alpha)$  hyperfine coupling constant of the presumed radical cation  $[\text{SiH}_2(\text{Idipp})]^+$  differs significantly from that of  $[\text{SiH}_2]^+$  ( $A(^1\text{H}) = 4.18$  mT,  $A(^{29}\text{Si}) = 30.1$  mT,  $g = 2.0010$ ), which was detected by EPR spectroscopy in a neon matrix at 4 K.<sup>[12]</sup>

The rapid decay of all EPR active species and the low intensity of their EPR signals did not allow any further structural characterization.

The decay of **1**- $[\text{B}(\text{Ar}^{\text{F}})_4]$  was also carried out on a laboratory scale. Therefore, 30 mg (18  $\mu\text{mol}$ ) of **1**- $[\text{B}(\text{Ar}^{\text{F}})_4]$  were placed in a Schlenk tube, and diethyl ether (2 mL) was vacuum-transferred into the Schlenk tube at  $-196$  °C. The mixture was warmed to  $-60$  °C, whereupon a green solution was obtained. The solution was warmed to room temperature over 10 minutes to afford a brown solution, which turned red after ca. 1 h. Precipitation of a colorless solid was also observed. After 20 h, the solvent was removed under vacuum to yield a red solid, which is sparingly soluble in benzene and good soluble in THF. The  $^1\text{H}$  NMR spectrum of the soluble part of the red solid in  $\text{C}_6\text{D}_6$  (red solution) revealed the presence of **1** and some Idipp. The  $^1\text{H}$  NMR spectrum of the red solid in  $\text{THF-}d_8$  (dark-red solution) suggested an unselective decomposition and showed besides the signals of  $[\text{IdippH}][\text{B}(\text{Ar}^{\text{F}})_4]$  several other signals of unknown components. The  $^{29}\text{Si}\{^1\text{H}\}$  NMR spectrum in  $\text{THF-}d_8$  showed a signal of low intensity at  $\delta = -46.4$  ppm, which could be assigned by a  $^1\text{H-}^{29}\text{Si}$  correlation spectrum to a Si-H containing species displaying a low-intensity  $^1\text{H}$ -NMR signal at  $\delta = 3.96$  ppm. From the coupling pattern in the  $^1\text{H-}^{29}\text{Si}$  correlation spectrum a  $^1J(\text{Si,H})$  coupling of 214 Hz and a  $^2J(\text{Si,H})$  coupling of 11 Hz to the  $^{29}\text{Si}$  signal could be deduced, which suggests a H-Si-Si-H connectivity with chemically equivalent Si and H atoms, respectively. Furthermore, two  $^{29}\text{Si}$  NMR signals were observed at  $-11.6$  ppm and  $-84.2$  ppm featuring a  $^2J(\text{Si,H})$  coupling constant of 9 Hz for the former signal and a  $^1J(\text{Si,H})$  coupling constant of 228 Hz for the latter signal. Both signals show a correlation to the same  $^1\text{H}$  signal, which appears as a doublet at 3.87 ppm with a  $J(\text{H,H})$  value of 3.1 Hz. This suggests the presence of a compound with a Si-Si-H connectivity. Due to the low content of these species no  $\nu(\text{Si-H})$  stretching vibrational bands were detected in the IR spectrum of the red solid.

[11] H. Tanaka, M. Ichinohe, A. Sekiguchi, *J. Am. Chem. Soc.* **2012**, *134*, 5540.

[12] L. B. Knight, M. Winiski, P. Kudelko, C. A. Arrington, *J. Chem. Phys.* **1989**, *91*, 3368.

## 8. Comparative electronic structure calculations of 1<sup>+</sup> and 1

The DFT calculations were carried out using the hybrid three-parameter functional of Becke and the correlation functional of Lee, Yang and Parr (B3LYP)<sup>[13]</sup> in combination with the 6-311+G\*\* basis set for the silicon, nitrogen and carbene carbon atoms and the 6-31G\* basis set for the peripheral carbon and hydrogen atoms.<sup>[14]</sup> The optimizations were carried out starting from the solid state structures, using the Gaussian03 program package and its internal standard convergence criteria.<sup>[15]</sup> Higher symmetric structures were optimized with symmetry restraints. The optimized geometries were verified as minima on the potential energy surface by numerical evaluation of their vibrational frequencies, which were also used to calculate the zero point vibrational energies. All thermodynamic energies were calculated using standard procedures.<sup>[16]</sup>  $D^0(0)$  is the zeropoint vibrational energy (ZPVE) corrected enthalpy for the dissociation to the electronically and geometrically relaxed fragments at 0 K. The bond cleavage energy (*BCE*) is the energy required to cleave the Si-C bond without electronic and geometric relaxation of the corresponding fragments (compare Table S15 for further information). NBO analyses were performed using NBO5.0.<sup>[17]</sup>

Analysis of the potential energy surface revealed the presence of at least two minimum structures of which the overall minimum structure is  $C_{1v}$ -symmetric, as found in the solid state by single-crystal X-ray crystallography. An almost isoenergetic  $C_s$ -symmetric minimum structure was also found 3 kJ mol<sup>-1</sup> higher in energy. A QST2 calculation<sup>[18]</sup> revealed that the  $C_{1v}$ - and  $C_s$ -symmetric minimum structures are connected via a low energy transition state, which lies 6 kJ mol<sup>-1</sup> higher in energy than the  $C_{1v}$ -symmetric structure and shows exactly one imaginary frequency at -4 cm<sup>-1</sup> (Figure S12). The Gibbs free energy profile at 298 K (Figure S12) suggests a rapid positional exchange of the two Si sites even at low temperatures as evidenced by EPR spectroscopy.

[13] a) A. D. Becke, *J. Chem. Phys.* **1993**, *98*, 5648; b) C. Lee, W. Yang, R. G. Parr, *Phys. Rev. B* **1988**, *37*, 785.

[14] P. C. Hariharan, J. A. Pople, *Theor. Chim. Acta* **1973**, *28*, 213.

[15] M. J. Frisch, G. W. Trucks, H. B. Schlegel, G. E. Scuseria, M. A. Robb, J. R. Cheeseman, J. A. Montgomery, Jr., T. Vreven, K. N. Kudin, J. C. Burant, J. M. Millam, S. S. Iyengar, J. Tomasi, V. Barone, B. Mennucci, M. Cossi, G. Scalmani, N. Rega, G. A. Petersson, H. Nakatsuji, M. Hada, M. Ehara, K. Toyota, R. Fukuda, J. Hasegawa, M. Ishida, T. Nakajima, Y. Honda, O. Kitao, H. Nakai, M. Klene, X. Li, J. E. Knox, H. P. Hratchian, J. B. Cross, C. Adamo, J. Jaramillo, R. Gomperts, R. E. Stratmann, O. Yazyev, A. J. Austin, R. Cammi, C. Pomelli, J. W. Ochterski, P. Y. Ayala, K. Morokuma, G. A. Voth, P. Salvador, J. J. Dannenberg, V. G. Zakrzewski, S. Dapprich, A. D. Daniels, M. C. Strain, O. Farkas, D. K. Malick, A. D. Rabuck, K. Raghavachari, J. B. Foresman, J. V. Ortiz, Q. Cui, A. G. Baboul, S. Clifford, J. Cioslowski, B. B. Stefanov, G. Liu, A. Liashenko, P. Piskorz, I. Komaromi, R. L. Martin, D. J. Fox, T. Keith, M. A. Al-Laham, C. Y. Peng, A. Nanayakkara, M. Challacombe, P. M. W. Gill, B. Johnson, W. Chen, M. W. Wong, C. Gonzalez, and J. A. Pople, *GAUSSIAN 03, Revision B.05*, Gaussian, Inc., Pittsburgh PA, **2003**.

[16] For details see: J. Foresman, A. E. Frisch, *Exploring Chemistry with Electronic Structure Methods*, 2<sup>nd</sup> ed., Gaussian, Inc. Pittsburgh, PA, **1996**.

[17] NBO 5.0 Program. E. D. Glendening, J. K. Badenhoop, A. E. Reed, J. E. Carpenter, J. A. Bohmann, C. M. Morales, F. Weinhold, Theoretical Chemistry Institute, University of Wisconsin, Madison, **2001**.

[18] a) C. Peng, H. B. Schlegel, *Israel J. of Chem.* **1993**, *33*, 449; b) C. Peng, P. Y. Ayala, H. B. Schlegel, M. J. Frisch, *J. Comput. Chem.* **1996**, *17*, 49.

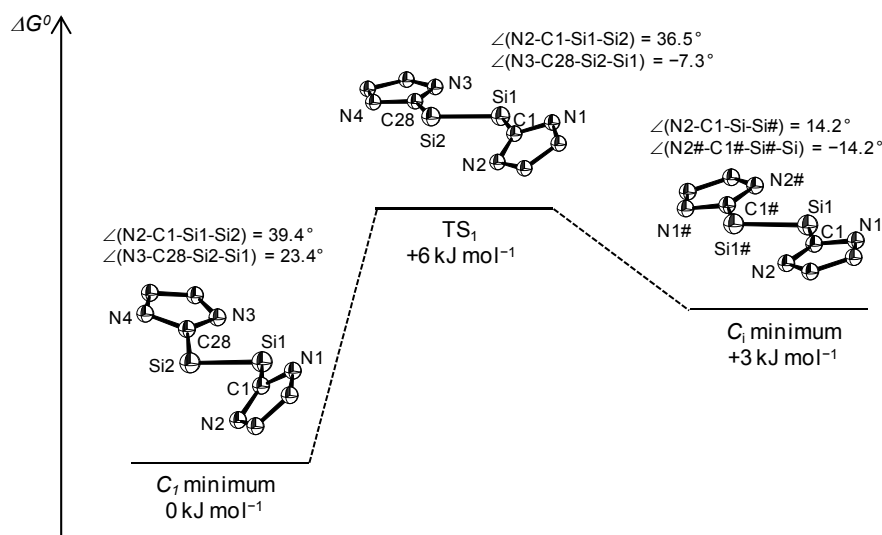


**Figure S12.** Schematic Gibbs free enthalpy profile ( $T = 298$  K) for the conformational isomerization of  $1^+$  rendering the two silicon sites equivalent with the B3LYP/6-311+G\*\*/6-31G\* optimized  $C_1$  and  $C_i$  symmetric minimum structures and the transition state  $TS_1$ . The 2,6-diisopropylphenyl groups and the hydrogen atoms are omitted for clarity.

**Table S10.** Selected calculated and experimental bonding parameters of  $1^+$ .

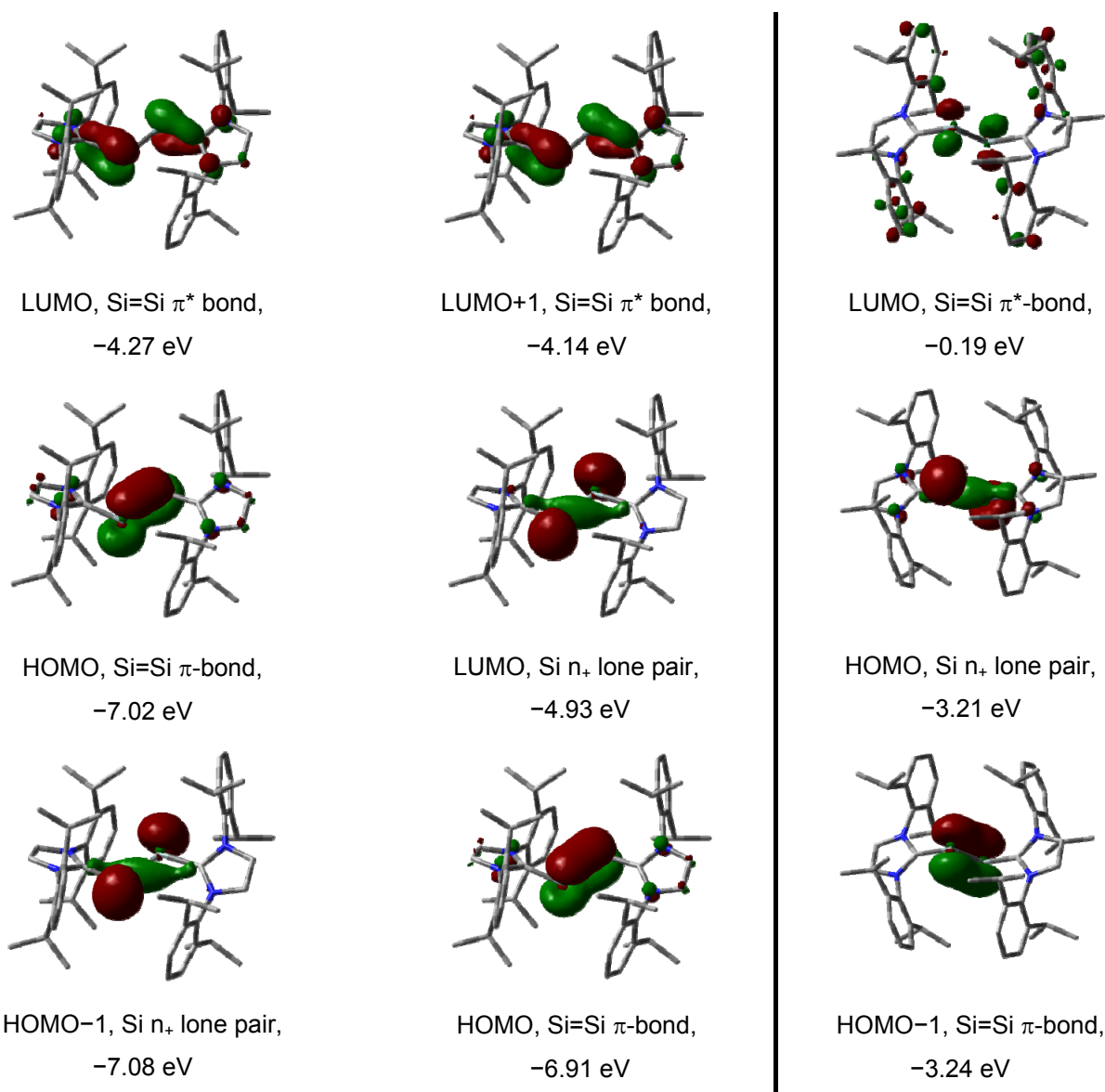
$d(a-b)$ [Å]	Si1–Si2	Si1–C1	Si2–C28	C1–N1	N1–C2	C2–C3	C3–N2
$C_1$	2.223	1.944	1.942	1.368	1.383	1.357	1.386
$TS_1$	2.217	1.947	1.940	1.369	1.382	1.358	1.385
$C_i$	2.229	1.950	1.950	1.371	1.382	1.357	1.384
X-Ray	2.178(3)	1.910(8)	1.899(7)	1.376(9)	1.398(9)	1.340(10)	1.385(8)
$d(a-b)$ [Å]	N2–C1	C28–N3	N3–C29	C29–C30	C30–N4	N4–C28	
$C_1$	1.368	1.368	1.385	1.358	1.382	1.369	
$TS_1$	1.368	1.368	1.385	1.358	1.381	1.369	
$C_i$	1.369	1.369	1.384	1.357	1.382	1.371	
X-Ray	1.369(9)	1.369(8)	1.377(8)	1.349(9)	1.386(8)	1.377(8)	
$\angle(a-b-c)$ [°]	C1–Si1–Si2	Si1–Si2–C28	$\angle(a-b-c-d)$ [°]		C1–Si1–Si2–C28	N2–C1–Si1–Si2	N3–C28–Si2–Si1
$C_1$	106.6	108.5	$C_1$	169.3	39.4	23.4	
$TS_1$	106.7	108.9	$TS_1$	-178.0	36.5	-7.3	
$C_i$	108.8	108.8	$C_i$	180.0	14.2	-14.2	
X-Ray	101.9(2)	109.9(2)	X-Ray	174.3(4)	53.1(8)	2.6(8)	

Table S10 contains selected bond lengths, bond angles and dihedral angles of the calculated structures of  $1^+$  and of the experimentally determined structure of  $1-B(Ar^F)_4 \cdot 2(1,3-C_6H_4F_2)$ . A comparison of the calculated  $C_1$ -symmetric ground-state structure of  $1^+$  with the molecular structure derived from the X-ray diffraction analysis reveals a very good agreement of the calculated and experimental intraannular bond lengths of the N-heterocyclic carbenes (NHCs), whereas the calculated Si-Si and Si-C<sub>NHC</sub> bond lengths are roughly 2% larger than the experimental values. The conformation of the two N-heterocyclic carbenes differs in both the calculated and the experimental structure as evidenced by the dihedral angles N2-C1-Si1-Si2 and N3-C28-Si2-Si1. The Si2-bonded NHC adopts a periplanar conformation with respect to the C-Si-Si plane [torsion angle: exp.: 2.6(8)° calcd: 23.4°], whereas the Si1-bonded NHC has a gauche (clinal) conformation [exp.: 53.1(8)°; calcd: 39.4°]. The



difference between the experimental and calculated torsion angles is not high if one takes into consideration, that the energy required to change the dihedral angle amounts only a few  $\text{kJ mol}^{-1}$ .

The  $\alpha$ - and  $\beta$ -spin Kohn-Sham (KS) orbitals of the  $C_7$ -symmetric minimum structure of  $1^+$  and their energy eigenvalues as well as the KS orbitals of  $1$  and their energy eigenvalues are depicted in Figure S13. An analysis of the orbitals reveals that the oxidation leads to a removal of one electron from the former HOMO ( $n_+$  lone pair orbital) of  $1$ . The  $n_+$  lone pair is the symmetric combination of the lone-pair orbitals at the Si atoms.



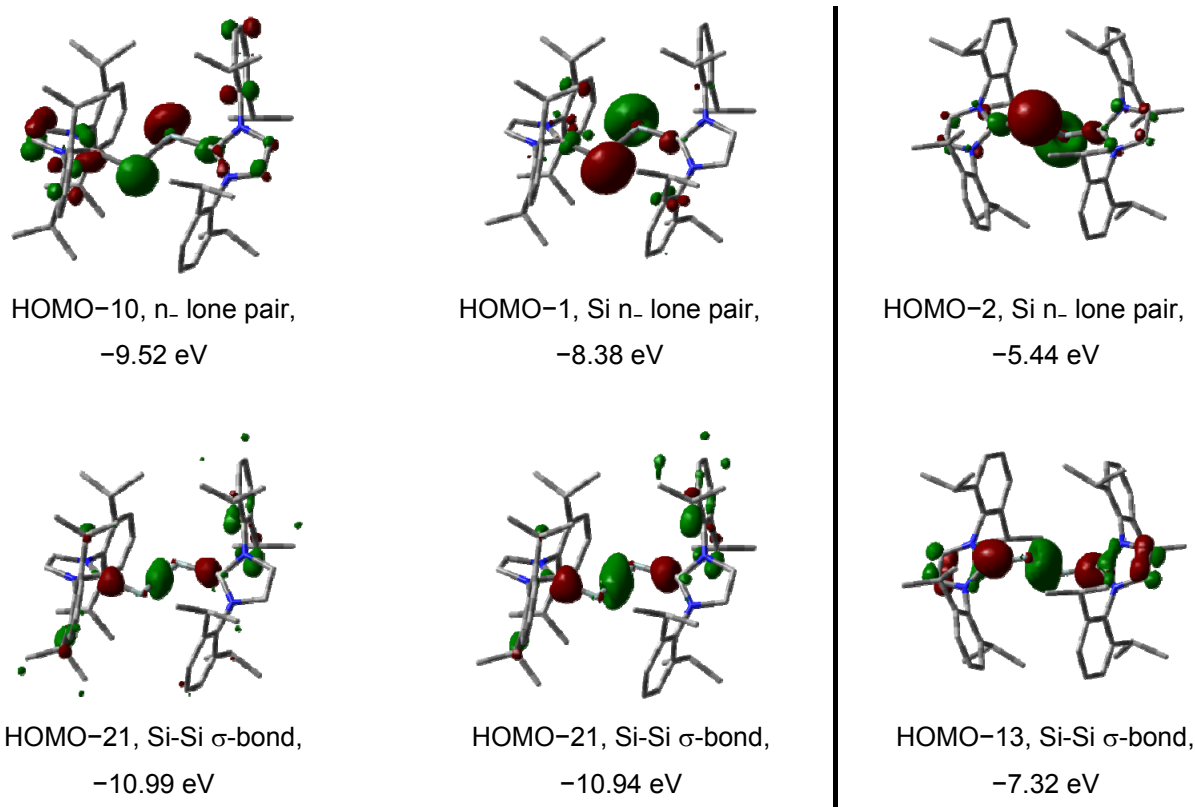


**Figure S13.** Selected  $\alpha$ -spin (left) and  $\beta$ -spin (middle) KS orbitals of the  $C_1$ -symmetric minimum structure of  $\mathbf{1}^+$  and KS orbitals of the  $C_1$ -symmetric minimum structure of  $\mathbf{1}$  (right) with their energy eigenvalues; iso surface value =  $0.05 \text{ e bohr}^{-3}$ .

A CASSCF<sup>[19]</sup> (5,4)/TZVP calculation was performed with the DFT-derived LUMO (Si=Si  $\pi^*$ -bond), SOMO (Si  $n_+$  lone pair orbital), HOMO (Si=Si  $\pi$ -bond) and HOMO-1 (Si  $n_-$  lone pair) to find out, whether a multiconfigurational wavefunction is necessary to describe the electronic structure of  $\mathbf{1}^+$ . The obtained CAS-orbitals and their energy eigenvalues are depicted in Figure S14. The calculation gave an occupancy of the  $n_-$  lone pair orbital (HOMO-2) with  $2.0 e^-$  and of the Si=Si  $\pi$ -orbital (HOMO-1) with  $1.87 e^-$ , whereas  $1.00 e^-$  are located in the  $n_+$  orbital (SOMO), which also contains 99.8 % of the overall spin density. The Si=Si  $\pi^*$ -bond (LUMO) is also slightly occupied with  $0.12 e^-$ . The CAS-calculation reveals that two determinants are necessary to describe the electronic structure of  $\mathbf{1}^+$ . The contribution of the dominant determinant with the configuration [2-2-1-0] to the overall wave function is 94 %, and of the minor determinant with the configuration [2-0-1-2] only 6 %. This indicates that a one-determinant method is sufficient to describe the electronic structure of  $\mathbf{1}^+$ . Therefore, calculations of the EPR parameters were performed using DFT methods (see below).

[19] B. O. Roos, P. R. Taylor, *Chem. Phys.* **1980**, *48*, 157.

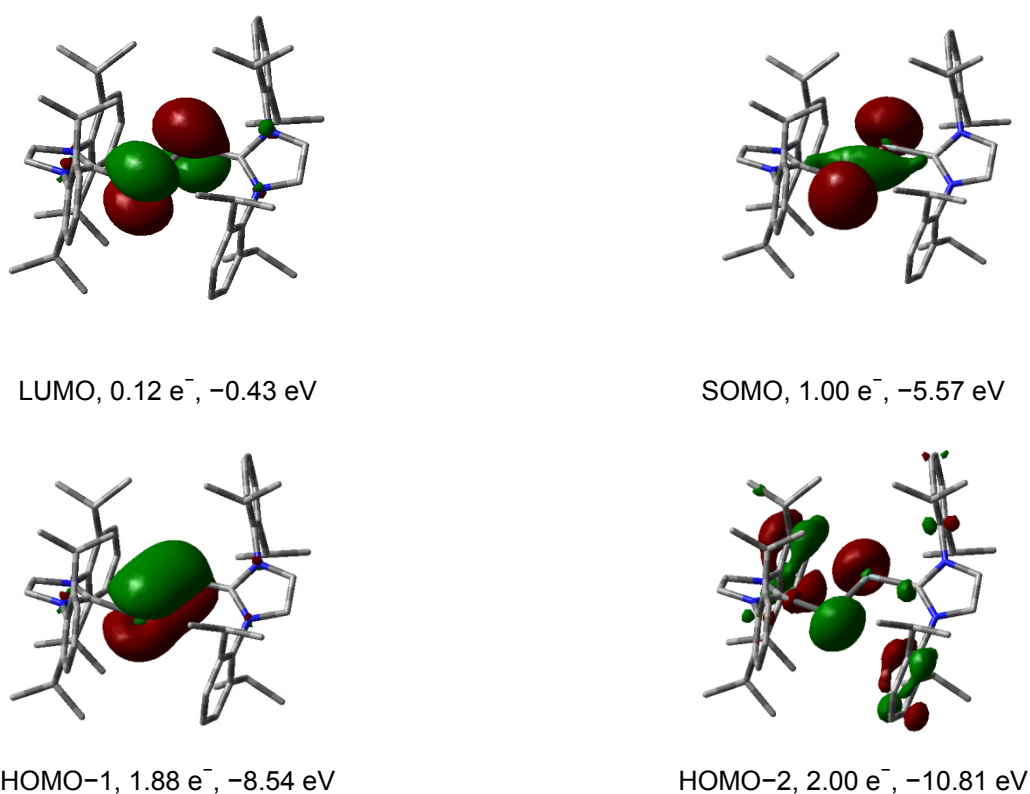


**Figure S14.** CASSCF (5,4) orbitals with their occupancies and energy eigenvalues. Iso surface value = 0.04 e bohr<sup>-3</sup>.

The  $g$ -tensor values and  $A(^{29}\text{Si})$  hyperfine coupling constants (hfcc's) of the  $C_1$ - and  $C_1$ -symmetric minimum structures of  $\mathbf{1}^+$  and the transition state connecting the two minimum structures were calculated and compared to the experimental values derived from the EPR spectrum of  $\mathbf{1}\text{-B}(\text{Ar}^{\text{F}})_4$  in frozen diethyl ether solution at 50 K (Tables S11 and S12). The orientation of the  $g$ -tensor components is given in Figure S15.

The calculations of the EPR parameters were carried out at three different levels of theory using the B3LYP functional in combination with the TZVPP<sup>[20]</sup> basis sets for all atoms, or using the TPSSh<sup>[21]</sup> hybrid density functional either in combination with the SVP basis sets for all atoms, or in combination with the correlation consistent TPSSh/aug-cc-pVTZ<sup>[22]</sup> basis sets for the Si, N and carbene ring C atoms and the SVP basis sets for the peripheral atoms.

A comparison of the calculated and experimental  $g$  values reveals a very good agreement at all chosen levels of theory. The absolute values of the calculated hyperfine coupling constants of the  $C_1$ -symmetric minimum structure of  $\mathbf{1}^+$  are slightly smaller than the experimental values at all levels of theory. No effect of the basis set (aug-cc-pVTZ versus SVP) was found on the calculated hyperfine coupling constants using the TPSSh functional, and only small differences (ca. 10%) were found

[20] A. Schaefer, H. Horn and R. Ahlrichs, *J. Chem. Phys.* **1992**, 97, 2571.

[21] J. Tao, J. P. Perdew, V. N. Staroverov, G. E. Scuseria, *Phys. Rev. Lett.* **2003**, 91, 146401.

[22] T. H. Dunning, Jr., *J. Chem. Phys.* **1989**, 90, 1007

between the calculated hyperfine coupling constants values at the B3LYP/TZVPP and the TPSSh/aug-cc-pVTZ levels of theory. The calculated  $A_{iso}({}^{29}\text{Si})$  at both silicon atoms have a negative value because of the negative value of the magnetic moment of the  ${}^{29}\text{Si}$  nucleus and the positive value of the spin density at both silicon atoms. As pointed out in the legend of Table S6 the sign of the experimental hyperfine coupling constants cannot be determined in cw experiments, however, the relative sign of the principal values could be determined and was shown to be equal. The slightly larger absolute value of  $A_{iso}$  at the silicon atom Si2 than that at Si1 is fully consistent with the results of the DFT spin-density calculations, showing a slightly larger contribution of the Si2 atom orbitals (34.8 %) than that of the Si1 atom orbitals (34.3 %) to the SOMO. Furthermore, a Mulliken spin density analysis reveals that the overall spin density of  $\mathbf{1}^+$  is mainly localized on the Si1 and Si2 atoms and slightly larger on the Si2 atom (Si1: 46 %; Si2: 48 %).<sup>[23]</sup>

**Table S11.** Calculated EPR parameters of the  $C_{1-}$  and  $C_{1-}$ -symmetric minimum structures of  $\mathbf{1}^+$  and the transition state (TS<sub>1</sub>) and comparison with the experimental values derived from the EPR spectrum of  $\mathbf{1-B}(\text{Ar}^{\text{F}})_4$  in frozen Et<sub>2</sub>O solution at 50 K.

$C_{1-}$ -minimum	$g_{11}$	$g_{22}$	$g_{33}$	$g_{iso}$	$A_{iso}^{\text{Si1}}$ [mT]	$A_{iso}^{\text{Si2}}$ [mT]
B3LYP/TZVPP	2.0033	2.0023	1.9864	1.9974	-3.89	-4.49
TPSSh/SVP	2.0037	2.0023	1.9887	1.9982	-4.27	-4.95
TPSSh/aug-cc-pVTZ/SVP	2.0036	2.0022	1.9888	1.9982	-4.30	-4.94
TS <sub>1</sub>	$g_{11}$	$g_{22}$	$g_{33}$	$g_{iso}$	$A_{iso}^{\text{Si1}}$ [mT]	$A_{iso}^{\text{Si2}}$ [mT]
B3LYP/TZVPP	2.0030	2.0022	1.9855	1.9969	-3.69	-4.96
TPSSh/SVP	2.0029	2.0021	1.9890	1.9980	-4.19	-5.34
TPSSh/aug-cc-pVTZ/SVP	2.0033	2.0021	1.9882	1.9979	-4.19	-5.41
$C_{1-}$ -minimum	$g_{11}$	$g_{22}$	$g_{33}$	$g_{iso}$	$A_{iso}^{\text{Si1}}$ [mT]	$A_{iso}^{\text{Si2}}$ [mT]
B3LYP/TZVPP	2.0030	2.0021	1.9846	1.9966	-4.32	-4.32
TPSSh/SVP	2.0035	2.0021	1.9874	1.9977	-4.75	-4.75
TPSSh/aug-cc-pVTZ/SVP	2.0033	2.0021	1.9875	1.9977	-4.76	-4.76
Experiment	2.0031	2.0026	1.9880	1.9979	5.19	6.79

**Table S12.** Calculated  $A({}^{29}\text{Si})$  hfc tensors of the  $C_{1-}$ -symmetric minimum structure of  $\mathbf{1}^+$  and comparison with the experimental values derived from the EPR spectrum of  $\mathbf{1}$  in frozen diethyl ether solution at 50 K. All values are given in mT.<sup>§</sup>

	$A_{11}^{\text{Si1}}$	$A_{22}^{\text{Si1}}$	$A_{33}^{\text{Si1}}$	$A_{11}^{\text{Si2}}$	$A_{22}^{\text{Si2}}$	$A_{33}^{\text{Si2}}$
B3LYP/TZVPP	-1.72	-7.92	-2.02	-2.26	-8.64	-2.58
TPSSh/SVP	-2.12	-8.27	-2.43	-2.71	-9.04	-3.10
TPSSh/aug-cc-pVTZ/SVP	-2.14	-8.29	-2.46	-2.70	-9.03	-3.09
Experiment (50 K)	3.11	8.64	3.82	4.71	10.25	5.42

<sup>§</sup> The calculated  $A({}^{29}\text{Si})$  hfc are usually slightly lower compared to the experimentally observed values, see: L. Hermosilla, P. Calle, J. M. García de la Vega, C. Sieiro, *J. Phys. Chem. A* **2005**, *109*, 7626.

[23] R. S. Mulliken, *J. Chem. Phys.* **1955**, *23*, 1833.

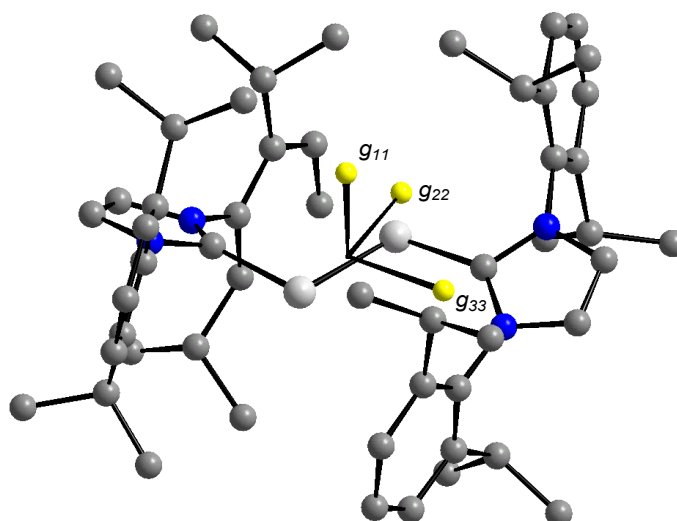


**Figure S15.** Orientation of the  $g$ -tensor components.

The results of the natural population analysis (NPA) are summarized in Table S13. Oxidation of **1** to the radical cation  $\mathbf{1}^+$  is accompanied by an increase of the partial charge from  $-0.10$  at both silicon atoms in **1** to  $+0.24$  at the atom Si1 and  $+0.22$  at the Si atom Si2 in  $\mathbf{1}^+$ . This indicates that oxidation mainly occurs at the Si atoms leading to an overall charge reduction of  $0.66 e^-$  at these atoms. The almost equal partial positive charge at the two silicon atoms in  $\mathbf{1}^+$  reflects the almost equal spin density distribution over the two Si atoms and is fully consistent with the results of the DFT calculations.

**Table S13.** NPA charges for **1**,  $\mathbf{1}^+$ , Idipp and  $[\text{Si}_2(\text{Idipp})]^+$ .

	Si1	C1	Si2	C28	$\Sigma_{\text{carbene1}}^{\S}$	$\Sigma_{\text{carbene2}}^{\S}$
<b>1</b>	-0.10	0.12	-0.10	0.12	-0.46	-0.46
$\mathbf{1}^{+\#}$	0.24	0.04	0.22	0.03	-0.36	-0.36
Idipp		0.13			-0.49	
$[\text{Si}_2(\text{Idipp})]^+$	0.22	0.03	0.35		-0.29	

<sup>§</sup>  $\Sigma_{\text{carbene1}}$  and  $\Sigma_{\text{carbene2}}$  are the sums of the NPA charges of the atoms of the N-heterocyclic five-membered rings. <sup>#</sup> The NPA charges of both Idipp substituents are 0.27 in  $\mathbf{1}^+$ .

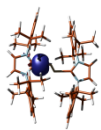
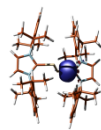
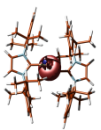
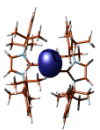
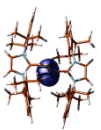
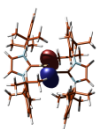
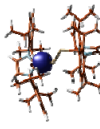
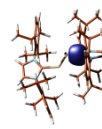
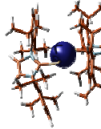
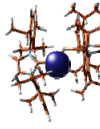
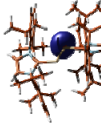
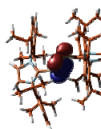
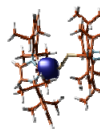
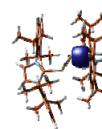
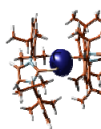
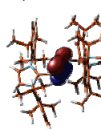
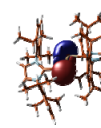
Bonding analysis of the  $C_1$  minimum structure of  $\mathbf{1}^+$  was carried out using the NBO method and the results were compared with those obtained for the  $C_T$ -symmetric **1** (Table S14). Due to the radical nature of  $\mathbf{1}^+$ , the NBOs are separated into  $\alpha$ - and  $\beta$ -spin orbitals.

The NBO analysis of  $\mathbf{1}^+$  indicates as for **1** highly carbon-polarized (ca. 80 %) Si–C<sub>carbene</sub> single bonds, which are formed from Si natural hybrid orbitals (NHOs) with a high p-character of 80% (average value of the  $\alpha$  and  $\beta$  spin orbital contributions) and natural sp-hybrid orbitals of the carbene carbon atoms (ca. 55% averaged p-contribution of the  $\alpha$  and  $\beta$  spin orbitals). The p-orbital contribution of the Si NHO employed in the Si–C<sub>carbene</sub> single bonds is in  $\mathbf{1}^+$  (ca. 80%) slightly lower than that in **1** (88%). Similarly, the p-orbital contribution of the Si NHO involved in the Si–Si  $\sigma$  bond (ca. 69% (averaged value of the p-

orbital contribution of the  $\alpha$  and  $\beta$  spin orbitals)) is slightly lower than that in **1** (82%). These results indicate an increase in the s-character of the Si natural hybrid orbitals used for the Si–C<sub>carbene</sub> and Si–Si  $\sigma$ -bonding in **1**<sup>+</sup>, and provide a rationale for the observed shortening of the Si–C<sub>carbene</sub> and Si–Si bonds, and the widening of the Si–Si–C<sub>carbene</sub> angles occurring upon oxidation of **1** to give **1**<sup>+</sup>.

In both cases (**1**<sup>+</sup> and **1**) a Si–Si  $\pi$ -bond NBO is found, which is formed from pure p NHOs of the two Si atoms. Notably, two  $\alpha$ -spin Si lone particle NBOs were found each occupied with roughly one electron. Both  $\alpha$ -spin Si lone particle NBOs are formed from Si NHOs, which have a high s-character (Si1: sp<sup>0.47</sup>, Si2: sp<sup>0.49</sup>), that is even larger than those used to form the lone-pair NBOs of **1** (sp<sup>0.38</sup>). In contrast, no lone particle orbital was found for the  $\beta$ -spin, but instead a Si–Si bonding orbital, which is occupied with 0.8699 e<sup>-</sup> (Table S14). This means, that a total number of approximately five electrons are involved in the Si–Si bond in **1**<sup>+</sup> leading to a higher Si–Si bond order than in **1**. This is also reflected in the increased Wiberg bond index (WBI) of **1**<sup>+</sup> (WBI = 2.046) compared to that of **1** (WBI = 1.703).

**Table S14.** Summary of the NBO analyses of **1** and **1<sup>+</sup>** divided into  $\alpha$ -spin NBOs and  $\beta$ -spin NBOs; WBI = Wiberg Bond Index.

<b>1</b>	<b>Si1-C1 <math>\sigma</math>-bond</b>		<b>Si2-C28 <math>\sigma</math>-bond</b>		<b>Si1-Si2 <math>\sigma</math>-bond</b>		<b>Lone Pair Si 1</b>	<b>Lone Pair Si 2</b>
<b>Occupancy</b>	1.9446 e <sup>-</sup>		1.9446 e <sup>-</sup>		1.7774 e <sup>-</sup>		1.8225 e <sup>-</sup>	1.8225 e <sup>-</sup>
<b>Contribution</b>	21 %	79 %	21 %	79 %	50 %	50 %	100 %	100 %
<b>Orbital contribution</b>	11 % s	48 % s	11 % s	48 % s	18 % s	18 % s	73 % s	73 % s
	88 % p	52 % p	88 % p	52 % p	82 % p	82 % p	28 % p	28 % p
								
					<b>Si1-Si2 <math>\pi</math>-bond</b>			
<b>Occupancy</b>					1.8472 e <sup>-</sup>			
<b>Contribution</b>					50 %	50 %		
<b>Orbital contribution</b>					100 % p	100 % p		
								
<b>WBI</b>	0.872		0.872		1.703			
<b>1<sup>+</sup> <math>\alpha</math>-Spin</b>	<b>Si1-C1 <math>\sigma</math>-bond</b>		<b>Si2-C28 <math>\sigma</math>-bond</b>		<b>Si1-Si2 <math>\sigma</math>-bond</b>		<b>Lone Particle Si1</b>	<b>Lone Particle Si2</b>
<b>Occupancy</b>	0.9764 e <sup>-</sup>		0.9768 e <sup>-</sup>		0.9562 e <sup>-</sup>		0.9548 e <sup>-</sup>	0.9589 e <sup>-</sup>
<b>Contribution</b>	20 %	79 %	20 %	79 %	49 %	50 %	100 %	100 %
<b>Orbital contribution</b>	12 % s	45 % s	12 % s	45 % s	21 % s	22 % s	68 % s	67 % s
	87 % p	55 % p	87 % p	55 % p	79 % p	78 % p	32 % p	33 % p
								
					<b>Si1-Si2 <math>\pi</math>-bond</b>			
<b>Occupancy</b>					0.8636 e <sup>-</sup>			
<b>Contribution</b>					50 %	50 %		
<b>Orbital contribution</b>					100 % p	100 % p		
								
<b>WBI</b>	0.757		0.763		1.630			
<b>1<sup>+</sup> <math>\beta</math>-Spin</b>	<b>Si1-C1 <math>\sigma</math>-bond</b>		<b>Si2-C28 <math>\sigma</math>-bond</b>		<b>Si1-Si2 <math>\sigma</math>-bond</b>			
<b>Occupancy</b>	0.9764 e <sup>-</sup>		0.9768 e <sup>-</sup>		0.8853 e <sup>-</sup>			
<b>Contribution</b>	22 %	78 %	22 %	78 %	52 %	48 %		
<b>Orbital contribution</b>	27 % s	44 % s	27 % s	44 % s	43 % s	38 % s		
	72 % p	56 % p	72 % p	55 % p	56 % p	61 % p		
								
					<b>Si1-Si2 <math>\pi</math>-bond</b>			
<b>Occupancy</b>					0.8474 e <sup>-</sup>			
<b>Contribution</b>					50 %	50 %		
<b>Orbital contribution</b>					100 % p	100 % p		
								
					<b>Si1-Si2 bond</b>			
<b>Occupancy</b>					0.8699 e <sup>-</sup>			
<b>Contribution</b>					48 %	52 %		
<b>Orbital contribution</b>					31 % s	35 % s		
					69 % p	64 % p		
								
<b>WBI</b>	0.197		0.199		0.416			

To evaluate the strength of the Si-C<sub>carbene</sub> bonds in **1** and **1**<sup>+</sup> the ZPVE (ZPVE = zero point vibrational energy) corrected bond dissociation enthalpies  $D^0(0)$  for the stepwise dissociation of the carbene groups to give the corresponding electronically and geometrically relaxed fragments at 0 K were calculated (Table S15). Both the heterolytic and homolytic Si-C<sub>carbene</sub> bond dissociation was considered, and the corresponding  $D^0(0)$  values are given in equations 1, 3, 6 and 9 (Si-C<sub>carbene</sub> heterolysis) and 2, 5, 7 and 11 (Si-C<sub>carbene</sub> homolysis), respectively. The total spin quantum number of each species is written in parentheses below the species and the term symbol of selected fragments is given in parentheses after the fragment.

The energy required to cleave the Si-C<sub>carbene</sub> bond without electronic and geometric relaxation of the corresponding fragments (BCE = bond cleavage energy) was calculated in each case for comparison reasons, and each BCE value obtained is given below the respective  $D^0(0)$  value (Table S15). In case the multiplicity of the fragment resulting from bond cleavage differs from that of the relaxed fragment, the bond cleavage energy is given in a separate equation (eqs. 4, 8 and 10). Two slightly different BCE were obtained for the heterolytic and homolytic cleavage of the first Idipp from **1**<sup>+</sup> respectively, depending on whether the Si2-bonded Idipp (torsion angle: 23.4°) or the Si1-bonded Idipp (torsion angle: 39.4°) was cleaved (eq. 6 and 8).

The calculated enthalpy for the dissociation of both Idipp groups from **1** ([Si<sub>2</sub>(Idipp)<sub>2</sub>] (S = 0) → Si<sub>2</sub> (S = 1, X<sup>3</sup>Σ<sub>g</sub><sup>-</sup>) + 2 Idipp (S = 0)), equals the sum of the  $D^0(0)$  values of equations 1 and 3 and amounts to 311.5 kJ mol<sup>-1</sup>. This value compares well with the calculated value of 80.9 kcal mol<sup>-1</sup> (= 338.7 kJ mol<sup>-1</sup>) obtained by Robinson et al. for the model system Si<sub>2</sub>L<sub>2</sub> (L = 1,3-dimethylimidazolin-2-ylidene) on the B3LYP/6-311+G\*\* level of theory.<sup>[1]</sup>

A comparison of the results reveals that the overall calculated enthalpy for the dissociation of both Idipp groups from **1**<sup>+</sup> ([Si<sub>2</sub>(Idipp)<sub>2</sub>]<sup>+</sup> (S = 0) → [Si<sub>2</sub>]<sup>+</sup> (S = 3/2, X<sup>4</sup>Σ<sub>g</sub><sup>-</sup>) + 2 Idipp (S = 0)) is considerably higher ( $D^0(0) = 674.4$  kJ mol<sup>-1</sup>) than that of **1** ( $D^0(0) = 311.5$  kJ mol<sup>-1</sup>). Remarkably, the mean Si-C<sub>carbene</sub> bond dissociation enthalpy of **1**<sup>+</sup> ( $D^0(0)_{av.} = 674.4/2$  kJ mol<sup>-1</sup> = 337.2 kJ mol<sup>-1</sup>) compares well with those of typical Si-C bonds in silanes (BDE = ca. 370 kJ mol<sup>-1</sup>) suggesting the presence of strong Si-C covalent bonds in **1**<sup>+</sup>.<sup>[24]</sup>

The structures of the electronically and geometrically relaxed fragments are depicted in Figure S16 and selected bonding parameters of these fragments are summarized in Table S16. The calculated bond lengths for Si<sub>2</sub> (S = 1, X<sup>3</sup>Σ<sub>g</sub><sup>-</sup>: 4σ<sub>g</sub><sup>2</sup>4σ<sub>u</sub><sup>2</sup>5σ<sub>g</sub><sup>2</sup>2π<sub>u</sub><sup>2</sup>) and [Si<sub>2</sub>]<sup>+</sup> (S = 3/2, X<sup>4</sup>Σ<sub>g</sub><sup>-</sup>: 4σ<sub>g</sub><sup>2</sup>4σ<sub>u</sub><sup>2</sup>5σ<sub>g</sub><sup>1</sup>2π<sub>u</sub><sup>2</sup>) compare well with those obtained by Dixon et al. from high level calculations using different basis sets.<sup>[25]</sup> The calculated bond lengths for [Si<sub>2</sub>]<sup>-</sup> (S = 1/2, X<sup>2</sup>Π<sub>u</sub>: 4σ<sub>g</sub><sup>2</sup>4σ<sub>u</sub><sup>2</sup>5σ<sub>g</sub><sup>2</sup>2π<sub>u</sub><sup>3</sup>) compare well with the previously experimentally and theoretically determined values.<sup>[26]</sup>

[24] R. Walsh, *Acc. Chem. Res.* **1981**, *14*, 246.

[25] D. A. Dixon, D. Feller, K. A. Peterson, J. L. Gole, *J. Phys. Chem. A* **2000**, *104*, 2326.

[26] H. Liu, D. Shi, J. Sun, Z. Zhu, *Spectrochim. Acta Mol. Biomol. Spectros.* **2013**, *108*, 295.



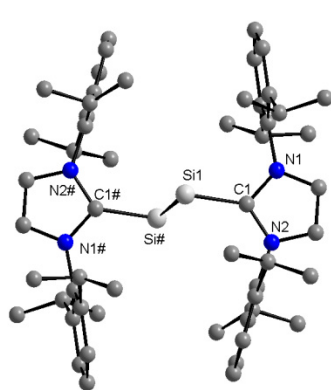
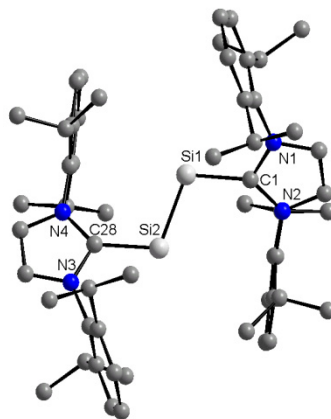
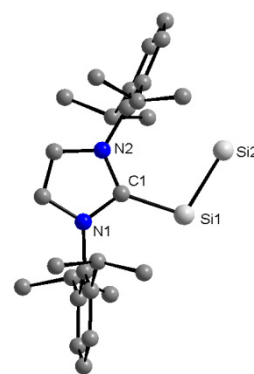
**Table S15.** Calculated bond cleavage energies (BCE) and bond dissociation energies at 0 K ( $D^0(0)$ ) for **1** and **1**<sup>+</sup>.

Resulting fragments				Calculated energies	Eq.
$[\text{Si}_2(\text{Idipp})_2]$ (S = 0)	→	$[\text{Si}_2(\text{Idipp})]$ (S = 0)	+ Idipp (S = 0)	$D^0(0) = 126.5 \text{ kJ mol}^{-1}$ BCE = 156.7 $\text{kJ mol}^{-1}$	(1)
$[\text{Si}_2(\text{Idipp})_2]$ (S = 0)	→	$[\text{Si}_2(\text{Idipp})]^-$ (S = 1/2)	+ Idipp <sup>+</sup> (S = 1/2)	$D^0(0) = 664.4 \text{ kJ mol}^{-1}$ BCE = 801.9 $\text{kJ mol}^{-1}$	(2)
$[\text{Si}_2(\text{Idipp})]$ (S = 0)	→	$[\text{Si}_2] (\text{X}^3\Sigma_g^-)^{\S}$ (S = 1)	+ Idipp (S = 0)	$D^0(0) = 185.0 \text{ kJ mol}^{-1}$	(3)
$[\text{Si}_2(\text{Idipp})]$ (S = 0)	→	$[\text{Si}_2] ({}^1\Delta_g)^{\S}$ (S = 0)	+ Idipp (S = 0)	BCE = 275.9 $\text{kJ mol}^{-1}$	(4)
$[\text{Si}_2(\text{Idipp})]$ (S = 0)	→	$[\text{Si}_2]^- (\text{X}^2\Pi_u)^{\#}$ (S = 1/2)	+ Idipp <sup>+</sup> (S = 1/2)	$D^0(0) = 673.7 \text{ kJ mol}^{-1}$ BCE = 713.4 $\text{kJ mol}^{-1}$	(5)
$[\text{Si}_2(\text{Idipp})_2]^+$ (S = 1/2)	→	$[\text{Si}_2(\text{Idipp})]^+$ (S = 1/2)	+ Idipp (S = 0)	$D^0(0) = 243.1 \text{ kJ mol}^{-1}$ BCE(Si1-C1) = 292.7 $\text{kJ mol}^{-1}$ BCE(Si2-C28) = 293.6 $\text{kJ mol}^{-1}$	(6)
$[\text{Si}_2(\text{Idipp})_2]^+$ (S = 1/2)	→	$[\text{Si}_2(\text{Idipp})]$ (S = 0)	+ Idipp <sup>+</sup> (S = 1/2)	$D^0(0) = 411.8 \text{ kJ mol}^{-1}$	(7)
$[\text{Si}_2(\text{Idipp})_2]^+$ (S = 1/2)	→	$[\text{Si}_2(\text{Idipp})]$ (S = 1)	+ Idipp <sup>+</sup> (S = 1/2)	BCE(Si1-C1) = 524.7 $\text{kJ mol}^{-1}$ BCE(Si2-C28) = 523.4 $\text{kJ mol}^{-1}$	(8)
$[\text{Si}_2(\text{Idipp})]^+$ (S = 1/2)	→	$[\text{Si}_2]^+ (\text{X}^4\Sigma_g^-)^*$ (S = 3/2)	+ Idipp (S = 0)	$D^0(0) = 431.3 \text{ kJ mol}^{-1}$	(9)
$[\text{Si}_2(\text{Idipp})]^+$ (S = 1/2)	→	$[\text{Si}_2]^+ ({}^2\Pi_u)^*$ (S = 1/2)	+ Idipp (S = 0)	BCE = 508.3 $\text{kJ mol}^{-1}$	(10)
$[\text{Si}_2(\text{Idipp})]^+$ (S = 1/2)	→	$[\text{Si}_2] (\text{X}^3\Sigma_g^-)^{\S}$ (S = 1)	+ Idipp <sup>+</sup> (S = 1/2)	$D^0(0) = 355.7 \text{ kJ mol}^{-1}$ BCE = 391.5 $\text{kJ mol}^{-1}$	(11)

<sup>§</sup> The valence electronic configuration of  $\text{Si}_2$  in the  $\text{X}^3\Sigma_g^-$  ground state and the  ${}^1\Delta_g$  state is  $4\sigma_g^2 4\sigma_u^2 5\sigma_g^2 2\pi_u^2$  ( $\text{X}^3\Sigma_g^-$ ) and  $4\sigma_g^2 4\sigma_u^2 5\sigma_g^2 2\pi_u^2$  ( ${}^1\Delta_g$ ), respectively.

<sup>#</sup> The valence electronic configuration of  $[\text{Si}_2]^-$  in the  $\text{X}^2\Pi_u$  ground state is  $4\sigma_g^2 4\sigma_u^2 5\sigma_g^2 2\pi_u^3$ .

<sup>\*</sup> The valence electronic configuration of  $[\text{Si}_2]^+$  in the  $\text{X}^4\Sigma_g^-$  ground state and the  ${}^2\Pi_u$  state is  $4\sigma_g^2 4\sigma_u^2 5\sigma_g^1 2\pi_u^2$  ( $\text{X}^4\Sigma_g^-$ ) and  $4\sigma_g^2 4\sigma_u^2 5\sigma_g^2 2\pi_u^1$  ( ${}^2\Pi_u$ ), respectively.

 $[\text{Si}_2(\text{Idipp})_2]$  (S = 0) $[\text{Si}_2(\text{Idipp})_2]^+$  (S = 1/2) $[\text{Si}_2(\text{Idipp})]$  (S = 0)

## S29

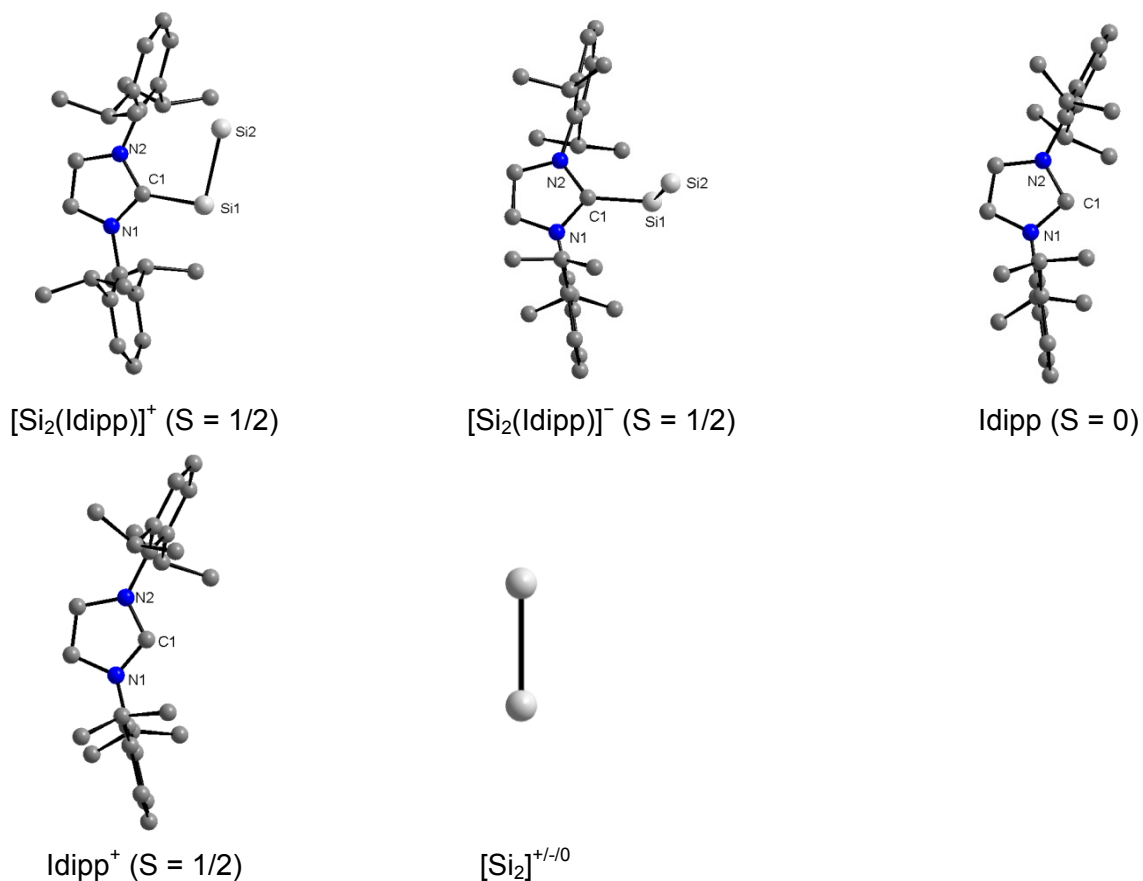


**Figure S16.** Illustration of the calculated optimized structures of of **1** and **1<sup>+</sup>** and their dissociation products.

**Table S16.** Selected calculated bonding parameters of the structures depicted in Figure S13. Bond lengths are given in [Å] and bond angles in [°].

	$d(\text{Si1-Si2})$	$d(\text{C1-Si1})$	$d(\text{Si2-C28})$	$d(\text{C1-N1})$	$d(\text{C1-N2})$	$\angle(\text{C1-Si1-Si2})$	$\angle(\text{C28-Si2-Si1})$	$\angle(\text{N2-C1-Si1-Si2})$
$[\text{Si}_2(\text{Idipp})_2]$ ( $S = 0$ )	2.247	1.954	1.954	1.379	1.379	98.8	98.8	87.8
$[\text{Si}_2(\text{Idipp})_2]^+$ ( $S = 1/2$ )	2.223	1.944	1.942	1.368	1.368	106.6	108.5	39.4
$[\text{Si}_2(\text{Idipp})]$ ( $S = 0$ )	2.206	1.910	-	1.378	1.379	102.8	-	0.2
$[\text{Si}_2(\text{Idipp})]^+$ ( $S = 1/2$ )	2.346	1.930	-	1.363	1.369	94.5	-	0.0
$[\text{Si}_2(\text{Idipp})]^-$ ( $S = 1/2$ )	2.249	1.919	-	1.396	1.396	99.3	-	94.0
$[\text{Si}_2]^+$ ( $S = 3/2$ )	2.303	-	-	-	-	-	-	-
$[\text{Si}_2]$ ( $S = 1$ )	2.281	-	-	-	-	-	-	-
$[\text{Si}_2]^-$ ( $S = 1/2$ )	2.198	-	-	-	-	-	-	-

**Cartesian atomic coordinates of calculated structures****Cartesian atomic coordinates of 1**

-2899.14186700

C	1.816480	0.112134	1.562631
C	-1.816480	-0.112134	-1.562631
C	0.257936	1.318706	4.289349
C	-0.257936	-1.318706	-4.289349
C	0.364291	1.051438	-3.945052
C	-0.364291	-1.051438	3.945052
C	-0.069650	-2.432159	3.367349
C	0.069650	2.432159	-3.367349
C	0.519621	3.744881	3.547277
C	-0.519621	-3.744881	-3.547277
C	0.477984	0.053761	3.705412
C	-0.477984	-0.053761	-3.705412
C	1.336438	3.175158	-2.913849
C	-1.336438	-3.175158	2.913849
C	0.723715	-3.290402	4.376142
C	-0.723715	3.290402	-4.376142
C	0.868375	-1.464722	-5.109365
C	-0.868375	1.464722	5.109365
C	1.217187	2.493037	4.109728
C	-1.217187	-2.493037	-4.109728
C	1.470150	0.848817	-4.779445
C	-1.470150	-0.848817	4.779445
C	1.942330	2.811521	5.433894
C	-1.942330	-2.811521	-5.433894
C	1.725577	-0.395443	-5.350634
C	-1.725577	0.395443	5.350634
C	2.889573	-0.459980	3.496775
C	-2.889573	0.459980	-3.496775
C	2.890773	-3.028363	-1.704454
C	-2.890773	3.028363	1.704454
C	3.498740	-2.333248	-0.476042
C	-3.498740	2.333248	0.476042
C	3.821817	-0.427596	2.516731
C	-3.821817	0.427596	-2.516731
C	3.776371	3.852331	0.233163
C	-3.776371	-3.852331	-0.233163
C	3.869737	0.140623	0.102580
C	-3.869737	-0.140623	-0.102580
C	4.039347	-0.941068	-0.785501
C	-4.039347	0.941068	0.785501
C	4.321958	2.560898	0.869319
C	-4.321958	-2.560898	-0.869319
C	4.598942	-3.212676	0.156180
C	-4.598942	3.212676	-0.156180
C	4.432533	1.413018	-0.131040
C	-4.432533	-1.413018	0.131040
C	4.781383	-0.708032	-1.949888
C	-4.781383	0.708032	1.949888
C	5.164160	1.588191	-1.312335
C	-5.164160	-1.588191	1.312335
C	5.333882	0.542406	-2.215080

C	-5.333882	-0.542406	2.215080
C	5.680357	2.816621	1.555189
C	-5.680357	-2.816621	-1.555189
H	-0.074528	-3.532342	-2.570727
H	0.074528	3.532342	2.570727
H	0.141994	-3.454243	5.291732
H	-0.141994	3.454243	-5.291732
H	1.054607	4.094692	-2.387816
H	-1.054607	-4.094692	2.387816
H	0.267044	-4.110381	-4.218135
H	-0.267044	4.110381	4.218135
H	1.235158	3.128138	6.209783
H	-1.235158	-3.128138	-6.209783
H	1.248622	4.554748	3.421108
H	-1.248622	-4.554748	-3.421108
H	0.549953	-2.291073	2.475736
H	-0.549953	2.291073	-2.475736
H	0.955324	-4.271210	3.943430
H	-0.955324	4.271210	-3.943430
H	1.921071	2.558823	-2.225351
H	-1.921071	-2.558823	2.225351
H	1.068191	-2.427043	-5.572339
H	-1.068191	2.427043	5.572339
H	1.971299	3.464757	-3.760447
H	-1.971299	-3.464757	3.760447
H	1.669830	-2.817985	4.661667
H	-1.669830	2.817985	-4.661667
H	1.978706	2.201690	3.381184
H	-1.978706	-2.201690	-3.381184
H	2.142582	1.675989	-4.981640
H	-2.142582	-1.675989	4.981640
H	2.485348	1.938955	5.815531
H	-2.485348	-1.938955	-5.815531
H	2.664578	3.623788	5.288233
H	-2.664578	-3.623788	-5.288233
H	2.124084	-2.400884	-2.166973
H	-2.124084	2.400884	2.166973
H	2.419566	-3.969841	-1.399400
H	-2.419566	3.969841	1.399400
H	2.592282	-0.528953	-5.993082
H	-2.592282	0.528953	5.993082
H	2.692363	-2.223740	0.255370
H	-2.692363	2.223740	-0.255370
H	2.789112	3.681195	-0.205813
H	-2.789112	-3.681195	0.205813
H	2.968663	-0.679596	4.549655
H	-2.968663	0.679596	-4.549655
H	3.610517	2.265548	1.645575
H	-3.610517	-2.265548	-1.645575
H	3.679816	4.633112	0.997400
H	-3.679816	-4.633112	-0.997400
H	3.648896	-3.272906	-2.458726
H	-3.648896	3.272906	2.458726
H	4.198687	-4.201655	0.410199
H	-4.198687	4.201655	-0.410199
H	4.443290	4.237849	-0.547184
H	-4.443290	-4.237849	0.547184

H	4.999885	-2.766350	1.073144
H	-4.999885	2.766350	-1.073144
H	4.883328	-0.617729	2.534420
H	-4.883328	0.617729	-2.534420
H	4.929935	-1.517503	-2.657273
H	-4.929935	1.517503	2.657273
H	5.435031	-3.355148	-0.539681
H	-5.435031	3.355148	0.539681
H	5.587008	3.610772	2.305775
H	-5.587008	-3.610772	-2.305775
H	5.611835	2.555357	-1.522689
H	-5.611835	-2.555357	1.522689
H	6.053963	1.917180	2.058341
H	-6.053963	-1.917180	-2.058341
H	5.907385	0.699545	-3.125136
H	-5.907385	-0.699545	3.125136
H	6.439136	3.129928	0.828078
H	-6.439136	-3.129928	-0.828078
N	1.671111	-0.132264	2.911888
N	-1.671111	0.132264	-2.911888
N	3.164530	-0.078701	1.343668
N	-3.164530	0.078701	-1.343668
Si	0.560096	0.924530	0.305759
Si	-0.560096	-0.924530	-0.305759

### Cartesian atomic coordinates of 1<sup>+</sup>

-2898.99052315			
C	-2.224829	1.140341	0.082820
C	-4.188467	2.094681	0.679921
H	-5.186247	2.123652	1.088732
C	-3.405994	3.066205	0.144608
H	-3.585625	4.117193	-0.017375
C	-3.956426	-0.347515	1.127066
C	-4.676764	-1.176459	0.240609
C	-5.190434	-2.370338	0.761716
H	-5.754209	-3.034665	0.114007
C	-5.003862	-2.713834	2.098542
H	-5.419556	-3.641734	2.481329
C	-4.299812	-1.866510	2.950390
H	-4.175938	-2.140719	3.993448
C	-3.759847	-0.659735	2.488790
C	-4.947827	-0.799554	-1.213215
H	-4.336942	0.075329	-1.459748
C	-6.426292	-0.400617	-1.404957
H	-6.710153	0.429997	-0.748701
H	-7.094163	-1.241174	-1.184504
H	-6.606662	-0.091554	-2.440747
C	-4.548435	-1.916417	-2.196311
H	-4.695106	-1.574452	-3.227276
H	-5.160420	-2.815365	-2.061171
H	-3.496676	-2.196739	-2.075596
C	-3.041214	0.273970	3.459272
H	-2.588297	1.086383	2.881825
C	-4.041004	0.908961	4.448123
H	-4.520846	0.146051	5.071670
H	-4.833468	1.457234	3.926147

H	-3.525420	1.610383	5.113872
C	-1.897796	-0.432474	4.211652
H	-1.376181	0.284019	4.856266
H	-1.168485	-0.857586	3.514275
H	-2.269495	-1.239996	4.852448
C	-1.138293	3.217037	-0.857865
C	-1.134894	3.293442	-2.265529
C	-0.110630	4.040596	-2.860947
H	-0.072879	4.126122	-3.942593
C	0.846021	4.693348	-2.088185
H	1.626583	5.274299	-2.571575
C	0.793089	4.626109	-0.697738
H	1.532482	5.160818	-0.110686
C	-0.202275	3.889004	-0.044185
C	-2.229474	2.673494	-3.131375
H	-2.840649	2.021816	-2.498254
C	-1.672168	1.799230	-4.269182
H	-1.041245	0.994709	-3.879261
H	-1.079206	2.383464	-4.981494
H	-2.497550	1.343582	-4.828124
C	-3.157562	3.772991	-3.690871
H	-3.971978	3.325451	-4.271883
H	-2.609340	4.454604	-4.351021
H	-3.602424	4.373705	-2.889459
C	-0.291291	3.895260	1.480239
H	-0.912020	3.046038	1.786390
C	-0.982656	5.185130	1.974644
H	-1.987947	5.299622	1.554656
H	-0.402198	6.070991	1.692335
H	-1.072978	5.175476	3.066940
C	1.074645	3.728317	2.169519
H	1.722142	4.597936	2.010703
H	1.600369	2.839829	1.805780
H	0.932068	3.625510	3.251272
C	2.233306	-1.146238	-0.093796
C	3.397852	-3.060999	-0.390545
H	3.553850	-4.079246	-0.710237
C	4.229216	-2.170907	0.209315
H	5.256909	-2.253318	0.526901
C	1.056642	-3.081361	-1.211576
C	0.185749	-3.854221	-0.415289
C	-0.861582	-4.510598	-1.073161
H	-1.552079	-5.120570	-0.499865
C	-1.027700	-4.402459	-2.452271
H	-1.845913	-4.924784	-2.940310
C	-0.136564	-3.648678	-3.211259
H	-0.263919	-3.594704	-4.288197
C	0.935737	-2.975631	-2.611800
C	0.395009	-4.044039	1.084998
H	1.061214	-3.248685	1.437014
C	-0.908688	-3.931182	1.895238
H	-1.597542	-4.755415	1.678896
H	-1.428811	-2.990869	1.688520
H	-0.683446	-3.971044	2.967091
C	1.085748	-5.395942	1.367641
H	1.264484	-5.516408	2.442245
H	2.049770	-5.478457	0.853714

H	0.459411	-6.231394	1.034403
C	1.946779	-2.229963	-3.479022
H	2.646987	-1.706857	-2.819399
C	1.284167	-1.161824	-4.367885
H	0.735974	-0.433836	-3.761883
H	0.585146	-1.606051	-5.085413
H	2.047511	-0.624113	-4.942158
C	2.769973	-3.221655	-4.328154
H	2.132283	-3.763709	-5.035474
H	3.277781	-3.964817	-3.702868
H	3.531658	-2.686585	-4.906557
C	4.066529	0.188174	0.992104
C	3.985318	0.327348	2.393405
C	4.583713	1.460990	2.957270
H	4.546230	1.603141	4.032995
C	5.235934	2.401703	2.164273
H	5.699556	3.269334	2.625321
C	5.308075	2.228577	0.784070
H	5.831360	2.963915	0.180622
C	4.727796	1.117174	0.160921
C	3.317479	-0.708052	3.293459
H	2.833044	-1.455131	2.655965
C	2.216134	-0.085006	4.172423
H	1.457471	0.413801	3.560018
H	2.624458	0.650027	4.875242
H	1.721049	-0.864690	4.762543
C	4.362846	-1.444644	4.156344
H	4.872803	-0.754615	4.837955
H	5.128622	-1.927293	3.538566
H	3.878812	-2.218102	4.763231
C	4.857495	0.935337	-1.348476
H	4.229528	0.088845	-1.645846
C	6.310548	0.592625	-1.737929
H	6.385094	0.420714	-2.817641
H	6.664795	-0.308943	-1.225344
H	6.993605	1.410393	-1.481257
C	4.352577	2.164837	-2.127847
H	4.971679	3.048648	-1.936493
H	3.318583	2.407286	-1.860707
H	4.390933	1.966002	-3.205055
N	-3.457310	0.921843	0.634641
N	-2.205836	2.474609	-0.216733
N	2.179199	-2.427432	-0.570162
N	3.508377	-1.004347	0.383892
Si	-1.054377	-0.368614	-0.282417
Si	1.029890	0.377644	-0.076201

### Cartesian atomic coordinates of [Si<sub>2</sub>(Idipp)]

-1739.03295287			
C	-0.111497	-0.003739	0.201090
C	0.520128	0.000242	-1.987642
H	1.213165	0.001927	-2.813932
C	-0.835740	0.000859	-1.958966
H	-1.564190	0.002883	-2.754855
C	2.354403	-0.000549	-0.316395
C	3.025241	1.242225	-0.217290

C	4.413306	1.210885	-0.032290
H	4.960468	2.145447	0.040854
C	5.102697	0.004021	0.052039
H	6.180501	0.005790	0.189940
C	4.416953	-1.205205	-0.029736
H	4.967032	-2.137819	0.045418
C	3.029033	-1.241168	-0.214618
C	2.297842	2.574838	-0.368593
H	1.224455	2.382284	-0.274750
C	2.669007	3.581944	0.735343
H	3.719665	3.888993	0.675394
H	2.489532	3.157616	1.728177
H	2.058058	4.486350	0.632569
C	2.550367	3.179127	-1.766387
H	1.996241	4.118164	-1.881220
H	2.233424	2.500187	-2.566301
H	3.614745	3.396670	-1.915353
C	2.304537	-2.575666	-0.363558
H	1.232204	-2.387388	-0.250647
C	2.697236	-3.589688	0.726414
H	2.542790	-3.170246	1.725518
H	3.744806	-3.901138	0.640284
H	2.080321	-4.491025	0.633224
C	2.536553	-3.169366	-1.769455
H	3.599857	-3.377351	-1.938565
H	2.199684	-2.488426	-2.559398
H	1.987918	-4.112141	-1.880045
C	-2.594292	0.000416	-0.197120
C	-3.242637	1.238835	-0.016844
C	-4.594255	1.210742	0.346575
H	-5.124517	2.146980	0.494552
C	-5.267518	0.005264	0.525542
H	-6.316831	0.007161	0.808348
C	-4.599263	-1.202622	0.344119
H	-5.133415	-2.136942	0.490202
C	-3.247733	-1.235634	-0.019295
C	-2.534744	2.576689	-0.205138
H	-1.479315	2.376406	-0.414309
C	-2.584512	3.432009	1.076011
H	-2.154232	2.889233	1.923991
H	-3.612066	3.714230	1.334097
H	-2.013072	4.356935	0.933322
C	-3.106697	3.347027	-1.412200
H	-4.164167	3.595017	-1.263062
H	-3.029674	2.762034	-2.336191
H	-2.561275	4.286802	-1.558610
C	-2.545349	-2.576033	-0.209944
H	-1.489320	-2.379642	-0.419790
C	-3.121344	-3.342679	-1.417401
H	-2.579507	-4.284250	-1.565577
H	-3.043151	-2.756786	-2.340725
H	-4.179549	-3.587041	-1.267488
C	-2.597709	-3.432640	1.070277
H	-3.626233	-3.711444	1.328262
H	-2.165343	-2.892336	1.918758
H	-2.029603	-4.359433	0.926415
N	0.957102	-0.002738	-0.670195



N	-1.213787	-0.001715	-0.625889
Si	1.936233	-0.005775	2.687105
Si	-0.192426	-0.008321	2.109812

**Cartesian atomic coordinates of [Si<sub>2</sub>(ldipp)]<sup>+</sup>**

-1738.83550248

C	0.141888	0.000008	0.182339
C	-0.509611	0.000114	-1.980151
H	-1.202201	0.000190	-2.807469
C	0.855029	-0.000023	-1.953099
H	1.579112	0.000005	-2.753664
C	-2.318116	0.000082	-0.256096
C	-2.998532	-1.251317	-0.162523
C	-4.387222	-1.209548	0.035366
H	-4.937606	-2.141644	0.106603
C	-5.074055	-0.000131	0.115145
H	-6.151252	-0.000200	0.250935
C	-4.387383	1.209390	0.035639
H	-4.937890	2.141403	0.107059
C	-2.998703	1.251356	-0.162253
C	-2.289392	-2.587859	-0.358760
H	-1.209362	-2.408404	-0.325905
C	-2.615906	-3.608863	0.748024
H	-3.674010	-3.890957	0.748986
H	-2.368719	-3.222925	1.743141
H	-2.035155	-4.523050	0.587238
C	-2.624585	-3.168297	-1.751234
H	-2.073461	-4.101200	-1.909964
H	-2.358809	-2.477480	-2.559045
H	-3.693642	-3.390723	-1.839638
C	-2.289627	2.587970	-0.358201
H	-1.209587	2.408606	-0.325008
C	-2.616640	3.608977	0.748421
H	-2.369798	3.223155	1.743663
H	-3.674784	3.890952	0.748954
H	-2.035962	4.523232	0.587764
C	-2.624450	3.168415	-1.750776
H	-3.693496	3.390783	-1.839456
H	-2.358400	2.477646	-2.558538
H	-2.073333	4.101353	-1.909327
C	2.621915	0.000006	-0.183662
C	3.259667	-1.242040	0.008031
C	4.597560	-1.208092	0.418932
H	5.128025	-2.141466	0.579606
C	5.259188	-0.000172	0.624374
H	6.297409	-0.000240	0.943112
C	4.597789	1.207836	0.418745
H	5.128429	2.141140	0.579252
C	3.259881	1.241962	0.007903
C	2.570184	-2.584524	-0.219041
H	1.524048	-2.395802	-0.487577
C	2.561748	-3.444708	1.060751
H	2.093004	-2.914424	1.897574
H	3.576756	-3.718903	1.367780
H	2.008051	-4.374384	0.887320
C	3.211100	-3.348619	-1.395611

H	4.258367	-3.593235	-1.187652
H	3.185313	-2.761732	-2.320892
H	2.678815	-4.289602	-1.573963
C	2.570619	2.584513	-0.219439
H	1.524469	2.395908	-0.487994
C	3.211747	3.348311	-1.396085
H	2.679655	4.289372	-1.574608
H	3.185902	2.761295	-2.321283
H	4.259052	3.592742	-1.188097
C	2.562220	3.444915	1.060216
H	3.577230	3.719194	1.367163
H	2.093501	2.914760	1.897133
H	2.008499	4.374547	0.886645
N	-0.932150	0.000171	-0.666132
N	1.236514	0.000081	-0.630387
Si	-2.172891	-0.000082	2.324137
Si	0.163135	0.000106	2.112581

### Cartesian atomic coordinates of [Si<sub>2</sub>(ldipp)]<sup>-</sup>

-1739.05421195

C	0.024515	0.255706	0.000000
C	1.354956	-0.042279	3.077537
C	-1.104494	-0.196789	3.227144
C	-2.466784	-0.428638	2.581936
C	3.469634	1.195341	2.417094
C	0.093240	-0.247792	2.480684
C	-3.539735	0.553886	3.080750
C	-2.932910	-1.886192	2.780034
C	1.396557	0.210682	4.454021
C	2.654797	-0.104217	2.282638
C	-1.004418	0.055450	4.600981
C	3.492106	-1.336733	2.679101
C	0.230363	0.257758	5.211842
C	0.064481	-1.945644	0.676065
C	-3.539735	0.553886	-3.080750
C	-2.466784	-0.428638	-2.581936
C	0.064481	-1.945644	-0.676065
C	3.469634	1.195341	-2.417094
C	0.093240	-0.247792	-2.480684
C	-1.104494	-0.196789	-3.227144
C	2.654797	-0.104217	-2.282638
C	-2.932910	-1.886192	-2.780034
C	1.354956	-0.042279	-3.077537
C	-1.004418	0.055450	-4.600981
C	1.396557	0.210682	-4.454021
C	0.230363	0.257758	-5.211842
C	3.492106	-1.336733	-2.679101
H	2.869376	2.049413	2.086408
H	-3.050324	-2.122103	3.846179
H	-4.461400	0.412319	2.504326
H	3.797022	1.367733	3.450556
H	3.795808	-1.293264	3.732917
H	4.367755	1.143716	1.788265
H	-2.356046	-0.242145	1.508908
H	-3.902390	-2.045610	2.291105
H	-3.214947	1.587586	2.929494

H	2.356961	0.375485	4.935693
H	-3.784272	0.401270	4.140602
H	-2.221113	-2.602664	2.354647
H	2.394816	-0.203332	1.225675
H	-1.909332	0.103869	5.199243
H	2.929019	-2.266321	2.532740
H	4.403878	-1.393083	2.070797
H	-3.214947	1.587586	-2.929494
H	-4.461400	0.412319	-2.504326
H	0.282700	0.455845	6.280253
H	-2.356046	-0.242145	-1.508908
H	2.869376	2.049413	-2.086408
H	0.076925	-2.759196	1.384810
H	2.394816	-0.203332	-1.225675
H	4.367755	1.143716	-1.788265
H	-3.784272	0.401270	-4.140602
H	-3.902390	-2.045610	-2.291105
H	3.797022	1.367733	-3.450556
H	-2.221113	-2.602664	-2.354647
H	0.076925	-2.759196	-1.384810
H	-1.909332	0.103869	-5.199243
H	-3.050324	-2.122103	-3.846179
H	4.403878	-1.393083	-2.070797
H	2.356961	0.375485	-4.935693
H	2.929019	-2.266321	-2.532740
H	0.282700	0.455845	-6.280253
H	3.795808	-1.293264	-3.732917
N	0.036289	-0.616260	1.090097
N	0.036289	-0.616260	-1.090097
Si	0.167888	2.168957	0.000000
Si	-2.017712	2.697927	0.000000

### Cartesian atomic coordinates of Idipp

-1160.05846392

C	-0.000002	-0.000002	-0.334777
C	0.678198	0.000022	1.869122
H	1.391645	-0.000009	2.679635
C	-0.678197	0.000124	1.869124
H	-1.391643	0.000209	2.679639
C	2.439060	-0.000172	0.094948
C	3.087372	-1.234312	-0.114274
C	4.421639	-1.206073	-0.539233
H	4.944797	-2.142146	-0.714401
C	5.085337	-0.000404	-0.749138
H	6.120442	-0.000493	-1.080934
C	4.422034	1.205386	-0.538664
H	4.945507	2.141366	-0.713382
C	3.087769	1.233860	-0.113728
C	2.378252	-2.571686	0.072827
H	1.383419	-2.370314	0.480045
C	3.111678	-3.481556	1.076620
H	3.226779	-2.992352	2.050651
H	4.112027	-3.756038	0.721806
H	2.549415	-4.410737	1.227533
C	2.178006	-3.281042	-1.281079

H	1.628532	-4.220317	-1.143135
H	3.138762	-3.521565	-1.752354
H	1.609439	-2.648684	-1.970492
C	2.379006	2.571362	0.073823
H	1.384246	2.370148	0.481299
C	3.112885	3.480957	1.077523
H	4.113163	3.755362	0.722450
H	3.228214	2.991593	2.051448
H	2.550805	4.410198	1.228748
C	2.178539	3.280939	-1.279945
H	1.629323	4.220328	-1.141738
H	1.609642	2.648798	-1.969283
H	3.139233	3.521283	-1.751439
C	-2.439068	0.000181	0.094963
C	-3.087714	-1.233867	-0.113780
C	-4.421971	-1.205435	-0.538752
H	-4.945389	-2.141435	-0.713533
C	-5.085327	0.000333	-0.749172
H	-6.120424	0.000395	-1.080998
C	-4.421693	1.206024	-0.539185
H	-4.944896	2.142079	-0.714312
C	-3.087432	1.234304	-0.114212
C	-2.378933	-2.571355	0.073800
H	-1.384113	-2.370106	0.481113
C	-2.178659	-3.281110	-1.279899
H	-1.609827	-2.649075	-1.969388
H	-3.139411	-3.521494	-1.751252
H	-1.629453	-4.220496	-1.141636
C	-3.112704	-3.480801	1.077717
H	-2.550654	-4.410057	1.228960
H	-4.113055	-3.755178	0.722826
H	-3.227856	-2.991321	2.051604
C	-2.378338	2.571696	0.072888
H	-1.383598	2.370360	0.480356
C	-3.111938	3.481736	1.076392
H	-3.227274	2.992678	2.050468
H	-4.112192	3.756242	0.721331
H	-2.549650	4.410905	1.227290
C	-2.177798	3.280841	-1.281091
H	-3.138467	3.521314	-1.752570
H	-1.609130	2.648349	-1.970296
H	-1.628319	4.220121	-1.143196
N	1.065125	-0.000048	0.529300
N	-1.065128	0.000102	0.529302

**Cartesian atomic coordinates of Idipp<sup>+</sup>**

-1159.79679053

C	-0.000013	0.000118	-0.170718
C	0.681659	0.013129	1.897188
H	1.401342	0.029416	2.701739
C	-0.681124	-0.019612	1.897342
H	-1.400544	-0.038361	2.702079
C	2.471618	0.056512	0.062494
C	3.140764	-1.171595	-0.106573
C	4.454696	-1.104165	-0.585318
H	5.014168	-2.022863	-0.730790

## S40

C	5.054345	0.117908	-0.879374
H	6.074009	0.141952	-1.252324
C	4.356417	1.309314	-0.698269
H	4.839197	2.252624	-0.933228
C	3.041019	1.314247	-0.218512
C	2.510757	-2.526991	0.201704
H	1.481698	-2.363793	0.543618
C	3.258437	-3.247382	1.341938
H	3.289696	-2.639443	2.253139
H	4.291829	-3.475979	1.059942
H	2.762005	-4.194113	1.580829
C	2.433825	-3.411625	-1.059019
H	1.928052	-4.355268	-0.827108
H	3.431542	-3.656533	-1.438663
H	1.882153	-2.916869	-1.866338
C	2.300536	2.636044	-0.037111
H	1.319954	2.428476	0.407944
C	3.042865	3.576216	0.933387
H	4.022013	3.869419	0.540241
H	3.203013	3.104570	1.909236
H	2.461891	4.491728	1.088223
C	2.049386	3.323053	-1.395148
H	1.475640	4.245368	-1.252891
H	1.490222	2.674135	-2.079239
H	2.991405	3.589631	-1.886399
C	-2.471426	-0.056736	0.062545
C	-3.041895	-1.313518	-0.220613
C	-4.357253	-1.306603	-0.700396
H	-4.840980	-2.249153	-0.936508
C	-5.053961	-0.114244	-0.880081
H	-6.073559	-0.136807	-1.253300
C	-4.453196	1.106813	-0.584177
H	-5.011631	2.026301	-0.728622
C	-3.139402	1.172230	-0.104651
C	-2.303367	-2.636486	-0.039844
H	-1.318640	-2.429750	0.396334
C	-2.064750	-3.330233	-1.396707
H	-1.510424	-2.685348	-2.088467
H	-3.011107	-3.598027	-1.878852
H	-1.491109	-4.252660	-1.254828
C	-3.040805	-3.570189	0.940609
H	-2.463493	-4.488639	1.091749
H	-4.025640	-3.858512	0.558168
H	-3.188326	-3.095327	1.916902
C	-2.507987	2.526665	0.205101
H	-1.482211	2.361450	0.555808
C	-3.262342	3.252633	1.337339
H	-3.303768	2.646771	2.249512
H	-4.292313	3.485174	1.046271
H	-2.763876	4.197753	1.578354
C	-2.418421	3.407179	-1.057684
H	-3.412404	3.651621	-1.447285
H	-1.859874	2.909240	-1.858297
H	-1.913832	4.351092	-0.824260
N	1.099415	0.023917	0.563053
N	-1.099187	-0.026112	0.563318

**Cartesian atomic coordinates of Si<sub>2</sub><sup>+</sup>**

-578.609943856

Si 0.000000 0.000000 1.151292

Si 0.000000 0.000000 -1.151292

**Cartesian atomic coordinates of Si<sub>2</sub>**

-578.900972557

Si 0.000000 0.000000 1.140304

Si 0.000000 0.000000 -1.140304

**Cartesian atomic coordinates of Si<sub>2</sub><sup>-</sup>**

-578.977834800

Si 0.000000 0.000000 1.098804

Si 0.000000 0.000000 -1.098804

# Appendix G

## The Si<sub>2</sub>H Radical Supported by Two N-heterocyclic Carbenes

Marius I. Arz,<sup>i</sup> Gregor Schnakenburg,<sup>i</sup> Andreas Meyer,<sup>ii</sup> Olav Schiemann,<sup>ii</sup> and Alexander C. Filippou<sup>i</sup>

Received 9th April 2016, published online 9th May 2016.

Reprinted with permission from  
M. I. Arz, G. Schnakenburg, A. Meyer, O. Schiemann, and A. C. Filippou, *Chemical Science* 2016, DOI: 10.1039/C6SC01569G.  
Copyright ©2016, Royal Society of Chemistry.

### Own contributions to the manuscript

- Conducting the EPR measurements.
- Interpretation of the EPR spectra.
- Writing parts of the manuscript.

---

<sup>i</sup> Institut für Anorganische Chemie, Universität Bonn, Gerhard-Domagk-Straße 1, 53121 Bonn, Germany.

<sup>ii</sup> Institut für Physikalische und Theoretische Chemie, Universität Bonn, Wegelerstr. 12, 53115 Bonn, Germany.

CrossMark  
click for updatesCite this: *Chem. Sci.*, 2016, 7, 4973

# The Si<sub>2</sub>H radical supported by two N-heterocyclic carbenes†

Marius I. Arz,<sup>a</sup> Gregor Schnakenburg,<sup>a</sup> Andreas Meyer,<sup>b</sup> Olav Schiemann<sup>b</sup>  
and Alexander C. Filippou<sup>\*a</sup>

Cyclic voltammetric studies of the hydridodisilicon(0,II) borate [(Idipp)(H)Si<sup>II</sup>=Si<sup>0</sup>(Idipp)][B(Ar<sup>F</sup>)<sub>4</sub>] (**1H**[B(Ar<sup>F</sup>)<sub>4</sub>], Idipp = C[N(C<sub>6</sub>H<sub>3</sub>-2,6-*i*Pr<sub>2</sub>)CH]<sub>2</sub>, Ar<sup>F</sup> = C<sub>6</sub>H<sub>3</sub>-3,5-(CF<sub>3</sub>)<sub>2</sub>) reveal a reversible one-electron reduction at a low redox potential ( $E_{1/2} = -2.15$  V vs. Fc<sup>+</sup>/Fc). Chemical reduction of **1H**[B(Ar<sup>F</sup>)<sub>4</sub>] with KC<sub>8</sub> affords selectively the green, room-temperature stable mixed-valent disilicon(0,I) hydride Si<sub>2</sub>(H)(Idipp)<sub>2</sub> (**1H**), in which the highly reactive Si<sub>2</sub>H molecule is trapped between two N-heterocyclic carbenes (NHCs). The molecular and electronic structure of **1H** was investigated by a combination of experimental and theoretical methods and reveals the presence of a  $\pi$ -type radical featuring a terminal bonded H atom at a flattened trigonal pyramidal coordinated Si center, that is connected *via* a Si–Si bond to a bent two-coordinated Si center carrying a lone pair of electrons. The unpaired electron occupies the Si=Si  $\pi^*$  orbital leading to a formal Si–Si bond order of 1.5. Extensive delocalization of the spin density occurs *via* conjugation with the coplanar arranged NHC rings with the higher spin density lying on the site of the two-coordinated silicon atom.

Received 9th April 2016

Accepted 29th April 2016

DOI: 10.1039/c6sc01569g

www.rsc.org/chemicalscience

## 1. Introduction

Open-shell silicon hydrides are of significant importance as transient intermediates in the chemical vapor deposition (CVD) of silicon or silicon-containing thin films, which are extensively used in the semiconductor industry.<sup>1</sup> Fundamental species in the gas phase include the SiH<sub>x</sub> ( $x = 1-3$ ) and Si<sub>2</sub>H<sub>x</sub> ( $x = 1-5$ ) molecules as well as higher aggregated Si<sub>n</sub>H<sub>m</sub> clusters, which are formed from silane (SiH<sub>4</sub>) or disilane (Si<sub>2</sub>H<sub>6</sub>) in a complex cascade of reactions.<sup>1</sup> These species, which are also of interest in astrochemistry,<sup>2</sup> are unstable under terrestrial conditions and can only be detected by spectroscopic or mass spectrometric techniques.<sup>3</sup> One scarcely studied species in this context is the Si<sub>2</sub>H molecule, which was so far only detected by vibrationally-resolved photoelectron spectroscopy of Si<sub>2</sub>H<sup>-</sup> anions.<sup>4</sup> Quantum chemical calculations of Si<sub>2</sub>H suggest two almost isoenergetic, C<sub>2v</sub>-symmetric H-bridged structures, in which the unpaired electron occupies either the Si–Si  $\pi$ -bonding

orbital (<sup>2</sup>B<sub>1</sub> state) or a  $\sigma$ -type molecular orbital corresponding to the in-phase combination of the Si lone pair orbitals (<sup>2</sup>A<sub>1</sub> state).<sup>5</sup>

Recently, N-heterocyclic carbenes (NHCs) were found to be particularly suitable Lewis bases for the thermodynamic and kinetic stabilization of highly reactive, unsaturated, low-valent Si species, leading to the isolation of a series of novel compounds with intriguing synthetic potential.<sup>6,7</sup> Several CAAC-stabilized open-shell silicon compounds (CAAC = cyclic alkyl(amino)carbene) were also reported, in which the unpaired electron is mainly located on the CAAC substituent.<sup>8</sup> Trapping of Si<sub>2</sub>H by NHCs appeared therefore an achievable, albeit very challenging goal, given the fact that isolable molecular hydrides of silicon in an oxidation state <2 are very rare<sup>9,10</sup> and open-shell congeners presently unknown. In comparison, three-coordinate Si<sup>II</sup> hydrides<sup>11</sup> and four-coordinate Si<sup>II</sup> hydrides of the general formula (LB)SiH(X)(LA) (LB = neutral Lewis base; LA = neutral Lewis acid; X = singly bonded substituent)<sup>12</sup> are meanwhile well documented.

## 2. Results and discussion

The hydridodisilicon(0,II) salt [(Idipp)(H)Si<sup>II</sup>=Si<sup>0</sup>(Idipp)][B(Ar<sup>F</sup>)<sub>4</sub>] (**1H**[B(Ar<sup>F</sup>)<sub>4</sub>], Idipp = C[N(C<sub>6</sub>H<sub>3</sub>-2,6-*i*Pr<sub>2</sub>)CH]<sub>2</sub>, Ar<sup>F</sup> = C<sub>6</sub>H<sub>3</sub>-3,5-(CF<sub>3</sub>)<sub>2</sub>), which was isolated recently in our group upon protonation of Si<sub>2</sub>(Idipp)<sub>2</sub> (**1**),<sup>9</sup> appeared to be a suitable starting material to tackle the problem of isolating an NHC-trapped Si<sub>2</sub>H radical. Quantum chemical studies revealed the same sequence of frontier orbitals in **1H**<sup>+</sup> and its isolobal phosphorus counterpart [R<sub>2</sub>P=PR]<sup>+</sup>, according to which the HOMO–1

<sup>a</sup>Institute of Inorganic Chemistry, University of Bonn, Gerhard-Domagk-Str. 1, D-53121, Bonn, Germany. E-mail: filippou@uni-bonn.de

<sup>b</sup>Institute of Physical and Theoretical Chemistry, University of Bonn, Wegelerstr. 12, D-53115, Bonn, Germany

† Electronic supplementary information (ESI) available: Cyclic voltammetric studies of **1H**[B(Ar<sup>F</sup>)<sub>4</sub>]; synthesis, analytical data and illustrations of the IR and UV-Vis spectra of **1H**; details of the magnetic susceptibility measurements and single crystal X-ray diffraction analysis of **1H**; details of the EPR spectroscopic measurements and illustrations of the EPR spectra of **1H**; details of the quantum chemical calculations. CCDC 1471165. For ESI and crystallographic data in CIF or other electronic format see DOI: 10.1039/c6sc01569g





corresponds to the lone-pair orbital at the two-coordinated E atom (E = Si, P), the HOMO is the E=E  $\pi$ -bonding orbital and the LUMO is the E=E  $\pi^*$  orbital.<sup>9</sup> This isolobal interrelationship suggested that  $1\mathbf{H}^+$  might be also reversibly reducible as the phosphanylphosphenium cation  $[\text{Mes}^*(\text{Me})\text{P}=\text{PMes}^*]^+$  ( $\text{Mes}^* = \text{C}_6\text{H}_2\text{-2,4,6-}t\text{Bu}_3$ ).<sup>13</sup> In fact, cyclic voltammetric (CV) studies of  $1\mathbf{H}[\text{B}(\text{Ar}^F)_4]$  in fluorobenzene at room temperature revealed a reversible one-electron reduction at a rather low half-wave potential ( $E_{1/2}$ ) of  $-1.63$  V as well as an irreversible oxidation at  $+0.67$  V versus the  $[\text{Fe}(\eta^5\text{-C}_5\text{Me}_5)_2]^{+1/0}$  reference electrode (Fig. 1 and ESI†).<sup>14</sup> The methyl analogue  $[(\text{Idipp})(\text{Me})\text{Si}^{\text{II}}=\text{Si}^{\text{II}}(\text{Idipp})][\text{B}(\text{Ar}^F)_4]$  ( $1\mathbf{Me}[\text{B}(\text{Ar}^F)_4]$ )<sup>9</sup> was found also to undergo a reversible one-electron reduction, albeit at a more negative potential ( $E_{1/2} = -1.85$  V) than  $1\mathbf{H}[\text{B}(\text{Ar}^F)_4]$ . Notably, reduction of  $1\mathbf{H}^+$  and  $1\mathbf{Me}^+$  occurs at much lower potentials than that of the cation  $[\text{Mes}^*(\text{Me})\text{P}=\text{PMes}^*]^+$  ( $E_{1/2} = -0.48$  V).<sup>13</sup> This marked difference in the redox potentials of the Si- and P-based cations can be rationalized with the large increase of the LUMO energy occurring upon replacement of the two  $\text{PMes}^*$  fragments by the much less electronegative isolobal Si(Idipp) fragments as suggested by quantum chemical calculations.<sup>9</sup>

The CV results prompted us to attempt a chemical one-electron reduction of  $1\mathbf{H}[\text{B}(\text{Ar}^F)_4]$ . Indeed, vacuum transfer of THF to a 1 : 1 stoichiometric mixture of  $1\mathbf{H}[\text{B}(\text{Ar}^F)_4]$  and  $\text{KC}_8$  at  $-196$  °C followed by warming to  $-40$  °C resulted in a distinct color change of the dark red solution of  $1\mathbf{H}[\text{B}(\text{Ar}^F)_4]$  to give an intensely dark green solution, which after work-up and crystallization from *n*-hexane at  $-60$  °C afforded  $\text{Si}_2(\text{H})(\text{Idipp})_2$  ( $1\mathbf{H}$ ) as a dark green, almost black crystalline solid in 55% yield (Scheme 1) (see ESI†). Compound  $1\mathbf{H}$  is extremely air-sensitive and immediately decolorizes upon contact with air, but can be stored under an atmosphere of argon at  $-30$  °C without any color change or signs of decomposition in its EPR spectrum. Thermal decomposition of  $1\mathbf{H}$  in a vacuum-sealed glass capillary was detected upon melting at  $147$  °C leading to a dark red mass. Analysis of the soluble part of the melting residue in  $\text{C}_6\text{D}_6$  by  $^1\text{H}$  NMR spectroscopy revealed the presence of Idipp (95%) and  $1$  (5%).

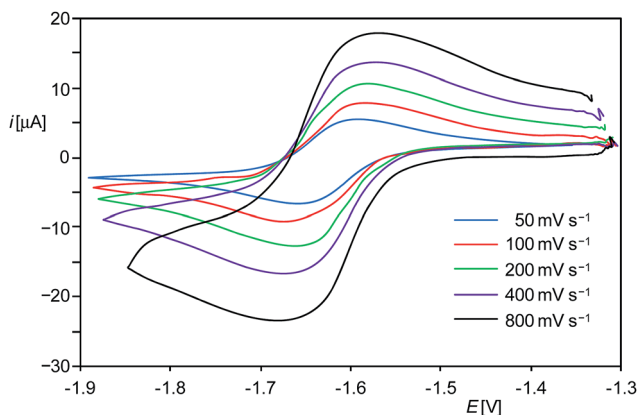
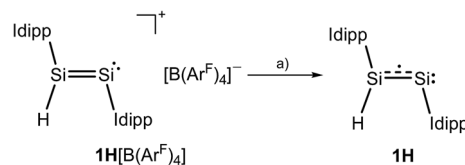


Fig. 1 Single-scan cyclic voltammograms of  $1\mathbf{H}[\text{B}(\text{Ar}^F)_4]$  from  $(-1.9)$  to  $(-1.3)$  V at different scan rates at room temperature in fluorobenzene/0.1 M  $(n\text{Bu}_4\text{N})\text{PF}_6$  solution; reference electrode: 4 mM  $[\text{Fe}(\eta^5\text{-C}_5\text{Me}_5)_2]^{+1/0}$ /0.1 M  $(n\text{Bu}_4\text{N})\text{PF}_6$  in fluorobenzene.



Scheme 1 Synthesis of  $1\mathbf{H}$  upon one-electron reduction of  $1\mathbf{H}[\text{B}(\text{Ar}^F)_4]$ ; (a)  $+\text{KC}_8$ ,  $-\text{K}[\text{B}(\text{Ar}^F)_4]$ ,  $-\text{8C}$ ; THF;  $-196$  °C  $\rightarrow$   $-40$  °C. Two dots indicate a lone pair of electrons and the dotted line indicates the population of the  $\text{Si}=\text{Si}$   $\pi^*$  orbital upon reduction; formal charges are omitted for clarity.

Notably, the redox potential of  $1\mathbf{H}$  [ $E_{1/2}$  in  $\text{C}_6\text{H}_5\text{F} = -2.15$  V vs.  $[\text{Fe}(\eta^5\text{-C}_5\text{H}_5)_2]^{+1/0}$  ( $\text{Fc}^+/\text{Fc}$ )]<sup>15</sup> lies in-between that of the benzophenone radical anion ( $E_{1/2}$  in THF =  $-2.30$  V vs.  $\text{Fc}^+/\text{Fc}$ )<sup>16</sup> and  $[\text{Co}(\eta^5\text{-C}_5\text{Me}_5)_2]$  ( $E_{1/2}$  in MeCN =  $-1.91$  V vs.  $\text{Fc}^+/\text{Fc}$ ),<sup>16</sup> indicating that the radical  $1\mathbf{H}$  is a very strong one-electron reducing agent. Consequently, the radical  $1\mathbf{H}$  is selectively oxidized back to  $1\mathbf{H}[\text{B}(\text{Ar}^F)_4]$  upon treatment with one equivalent of  $[\text{Fe}(\eta^5\text{-C}_5\text{Me}_5)_2][\text{B}(\text{Ar}^F)_4]$  in THF-*d*<sub>8</sub> (see ESI†). Thereby, the redox pair  $1\mathbf{H}^+/1\mathbf{H}$  provides a very rare example of a chemically reversible Si-based redox system.<sup>7c,17</sup>

Compound  $1\mathbf{H}$  is well soluble in *n*-hexane, benzene, diethyl ether or THF affording intensely dark-green solutions, even at low concentrations. The origin of this intense color was analyzed by UV-Vis-NIR spectroscopy of  $1\mathbf{H}$  in *n*-hexane (Fig. 2, left and ESI†), which revealed electronic absorptions in the whole spectral range from 220–1100 nm. Six absorption maxima were located at 254 (9970), 305 (8140), 436 (5170), 608 (7110), 704 (6860) and 958 (1440) nm, of which the intense absorptions at 608 and 704 nm are responsible for the green color of  $1\mathbf{H}$  (the values of the molar absorption coefficients  $\epsilon_\lambda$  are given in brackets in  $\text{L mol}^{-1} \text{cm}^{-1}$ ). The UV-Vis-NIR spectrum was also analyzed by time-dependent density functional theory (TDDFT) calculations (see ESI, Fig. S21†).<sup>18</sup>

Magnetic susceptibility measurements of solid  $1\mathbf{H}$  from 300.0–1.9 K suggest the presence of a paramagnetic compound with one unpaired electron following Curie's law. A plot of the reciprocal molar magnetic susceptibility ( $\chi_m^{-1}$ ) against the absolute temperature ( $T$ ) showed a linear correlation from which the effective magnetic moment  $\mu_{\text{eff}}$  was calculated after linear regression and found to be  $1.68 \mu_{\text{B}}$  (Fig. 2, right and ESI†). This value is slightly lower than the value derived from the spin-only formula for one unpaired electron ( $\mu_{\text{eff}} = 1.73 \mu_{\text{B}}$ ).

The molecular structure of  $1\mathbf{H}$  was determined by single crystal X-ray crystallography. The radical features a crystallographically imposed inversion symmetry (space group:  $P2_1/c$ ) in marked contrast to the  $C_1$ -symmetric structure of  $1\mathbf{H}^+$  in  $1\mathbf{H}[\text{B}(\text{Ar}^F)_4]$ .<sup>9</sup> The Si-bonded H atom was located in the difference Fourier map and anisotropically refined with a site occupancy of 1/2 at each Si atom. However, the exact position of this H atom could not be deduced by X-ray crystallography, since structural refinements with either a terminal (Si–H) or a bridging (Si–Si) position led to identical  $wR_2$  values.  $1\mathbf{H}$  features as  $1\mathbf{H}[\text{B}(\text{Ar}^F)_4]$  and  $1$  a *trans*-bent planar  $\text{C}_{\text{NHC}}\text{-Si-Si-C}_{\text{NHC}}$  core (Fig. 3). However, distinct structural differences become apparent upon comparing the three structures. For example, the Si–Si bond of



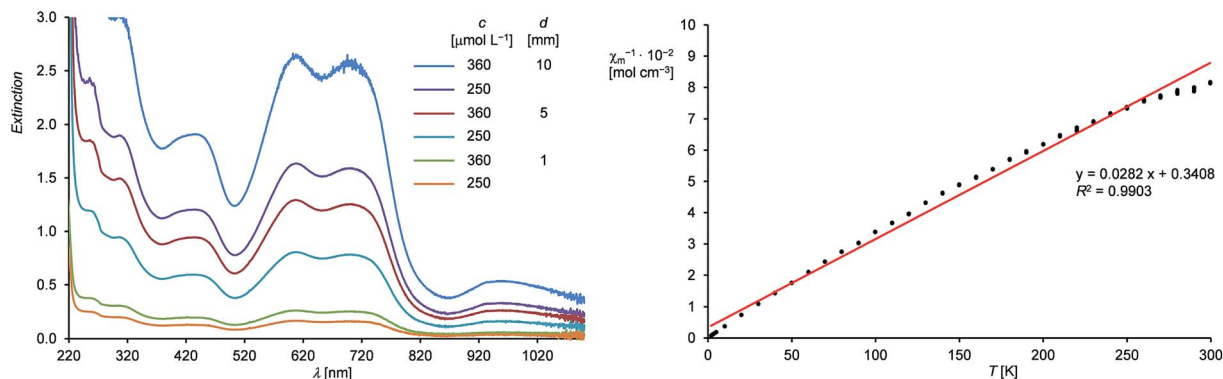


Fig. 2 Left: UV-Vis-NIR spectra of **1H** in *n*-hexane from 220–1100 nm at different concentrations ( $c$ ) and path lengths ( $d$ ). Right: Plot of the reciprocal molar magnetic susceptibility ( $\chi_m^{-1}$ ) against the absolute temperature ( $T$ ) (dotted black line) and the corresponding line (red) and line equation obtained by linear regression.

**1H** (2.281(3) Å) is considerably longer than that in **1H**[B(Ar<sup>F</sup>)<sub>4</sub>] (2.1873(8) Å)<sup>9</sup> or **1** (2.229(1) Å)<sup>19</sup> (Table 1), and lies in-between that of a typical Si=Si double bond (2.20 Å)<sup>20</sup> and a Si-Si single bond (e.g. 2.352 Å in  $\alpha$ -Si).<sup>21</sup> In comparison, the Si-C<sub>NHC</sub> bonds in **1H** (1.873(4) Å) are shorter than the Si-C<sub>NHC</sub> bonds of the dicoordinated Si atoms in **1H**[B(Ar<sup>F</sup>)<sub>4</sub>] (1.940(2) Å)<sup>9</sup> and **1** (1.927(1) Å)<sup>19</sup> (Table 1), and similar to that of the trigonal-planar coordinated Si atom in **1H**[B(Ar<sup>F</sup>)<sub>4</sub>] (1.882(2) Å).<sup>9</sup> Reduction of **1H**<sup>+</sup> results also in a distinct change of the conformation of the NHC substituents. Thus, both N-heterocyclic rings in **1H** are arranged coplanar with the *trans*-bent C<sub>NHC</sub>-Si-Si-C<sub>NHC</sub> core as evidenced by the dihedral angle  $\varphi_{\text{NHC}}$  of 3.3(2)° (Table 1), whereas in **1H**<sup>+</sup> one of the two N-heterocyclic rings (bonded to the two-coordinated Si atom) adopts an almost orthogonal orientation (Table 1). All these structural changes can be rationalized by quantum theory (*vide infra*). Thus, reduction of **1H**<sup>+</sup> leads to a population of the Si=Si  $\pi^*$  orbital with one electron, reducing thereby the formal Si-Si bond order from 2 in **1H**<sup>+</sup> to 1.5 in **1H** as nicely reflected in the computed Si-Si Wiberg bond indexes (WBI; WBI(Si-Si) of **1H**<sup>+</sup> = 1.70; WBI(Si-Si) of **1H** = 1.17) (see ESI, Tables S11 and S12†). The coplanar arrangement of the

N-heterocyclic rings allows for an optimal in-phase interaction ( $\pi$ -conjugation) of the Si=Si  $\pi^*$  orbital with  $\pi^*(\text{CN}_2)$  orbitals of the NHC substituents in the SOMO of **1H** (Fig. 6), providing a rationale for the shortening of the Si-C<sub>NHC</sub> bonds and the concomitant elongation of the C<sub>NHC</sub>-N<sub>NHC</sub> bonds of **1H** versus **1H**<sup>+</sup> (Table 1).

IR spectroscopy proved to be a very useful method to determine unequivocally the position of the Si-bonded H atom. In fact, the ATR FT-IR spectrum of **1H** displayed a  $\nu(\text{Si-H})$  absorption band at 2089 cm<sup>-1</sup>, which is characteristic for stretching vibrations of terminal Si-H bonds (see ESI, Fig. S4†). In comparison, the  $\nu(\text{Si-H-Si})$  band of Si<sub>2</sub>H is predicted at significantly lower wavenumbers (1592 cm<sup>-1</sup> (<sup>2</sup>A<sub>1</sub> state); 1491 cm<sup>-1</sup> (<sup>2</sup>B<sub>1</sub> state)),<sup>4</sup> and also the  $\nu(\text{Si-H-Si})$  absorption bands of H-bridged silylium ions are shifted to much lower wavenumbers (ca. 1750–1950 cm<sup>-1</sup>; e.g. 1900 cm<sup>-1</sup> in [Et<sub>3</sub>Si-H-SiEt<sub>3</sub>][CHB<sub>11</sub>Cl<sub>11</sub>]) compared with the  $\nu(\text{Si-H})$  bands of the corresponding silanes (ca. 2150 cm<sup>-1</sup>).<sup>22</sup> Notably, the  $\nu(\text{Si-H})$  absorption band of **1H** appears in-between that of **1H**[B(Ar<sup>F</sup>)<sub>4</sub>] containing a trigonal planar coordinated Si atom ( $\nu(\text{Si-H})$  = 2142 cm<sup>-1</sup>),<sup>9</sup> and the Si( $\eta$ )-hydride (IME<sub>4</sub>)SiH(Si<sup>t</sup>Bu<sub>3</sub>) containing a strongly pyramidal bonded Si atom (IME<sub>4</sub> = C[N(Me)CMe]<sub>2</sub>;  $\nu(\text{Si-H})$  in KBr = 1984 cm<sup>-1</sup>).<sup>11d</sup> Apparently, the  $\nu(\text{Si-H})$  frequency decreases with increasing pyramidalization of the Si atom, which according to the quantum chemical calculations can be traced back to the decreasing *s*-character of the Si hybrid orbital in the Si-H bond (see ESI, Tables S11 and S12†).

Further insight into the structure of **1H** was provided by continuous wave (cw) EPR spectroscopy at X-band frequencies. Spectra with a nicely resolved hyperfine coupling pattern could be obtained from samples of **1H** in *n*-hexane solution at 336 K (Fig. 4; see also ESI, Fig. S10† for EPR spectra at different temperatures). Notably, a similar EPR spectrum was obtained in diethyl ether solution at 298 K (see ESI, Fig. S12†), suggesting that solvent coordination effects are negligible. The EPR spectrum of **1H** displays a multiplet at a  $g_{\text{iso}}$  value of 2.00562, which could be well simulated assuming coupling of the unpaired electron to one <sup>1</sup>H ( $I = 1/2$ ) nucleus, two different <sup>29</sup>Si ( $I = 1/2$ ) and two pairs of two magnetically equivalent <sup>14</sup>N ( $I = 1$ ) nuclei, respectively (Fig. 4). These observations suggest that **1H** has

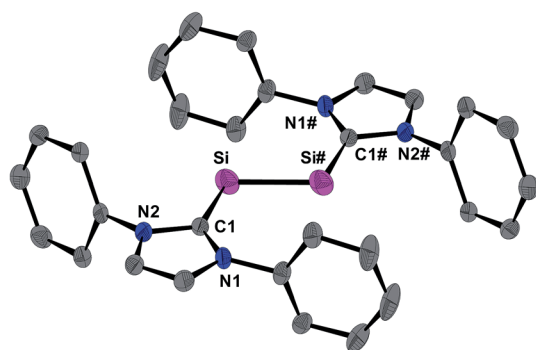


Fig. 3 DIAMOND plot of the molecular structure of **1H** in the single crystal at 123(2) K. Thermal ellipsoids are set at 30% electronic probability. The hydrogen atoms and the *iPr* groups are omitted for clarity. The Si-bonded H atom was omitted due to its uncertain position. Selected bond lengths [Å], bond angles [°] and torsion angles [°]: Si-Si# 2.281(3), Si-C1 1.873(4); C1-Si-Si# 109.5(1); C1-Si-Si#-C1# 180.0(3).



Table 1 Comparison of selected bonding parameters of **1H**, **1H**[B(Ar<sup>F</sup>)<sub>4</sub>] and **1**

	Si-Si [Å]	Si-C <sub>NHC</sub> [Å]	C <sub>NHC</sub> -N <sub>NHC</sub> [Å]	C <sub>NHC</sub> -Si-Si [°]	φ <sub>NHC</sub> <sup>c</sup> [°]
<b>1H</b>	2.281(3)	1.873(4)	1.381(4), 1.402(4)	109.5(1)	3.3(2)
<b>1H</b> [B(Ar <sup>F</sup> ) <sub>4</sub> ] <sup>a</sup>	2.1873(8)	1.882(2) (Si1-C <sub>NHC</sub> ) 1.940(2) (Si2-C <sub>NHC</sub> )	1.356(2), 1.358(2) 1.356(2), 1.358(2)	116.73(7) (C1-Si1-Si2) 95.34(6) (C28-Si2-Si1)	8.60(6) (φ <sub>NHC1</sub> ) 71.06(6) (φ <sub>NHC2</sub> )
<b>1</b> <sup>b</sup>	2.229(1)	1.927(2)	1.368(2), 1.372(2)	93.37(5)	87.11(5)

<sup>a</sup> Data taken from ref. 9. Connectivity: [(NHC1)(H)Si1=Si2(NHC2)]<sup>+</sup>. <sup>b</sup> Data taken from ref. 19. <sup>c</sup> φ<sub>NHC</sub> denotes the dihedral angles between the C<sub>NHC</sub>-Si-Si-C<sub>NHC</sub> least-square plane and the respective N-heterocyclic ring least-square planes.

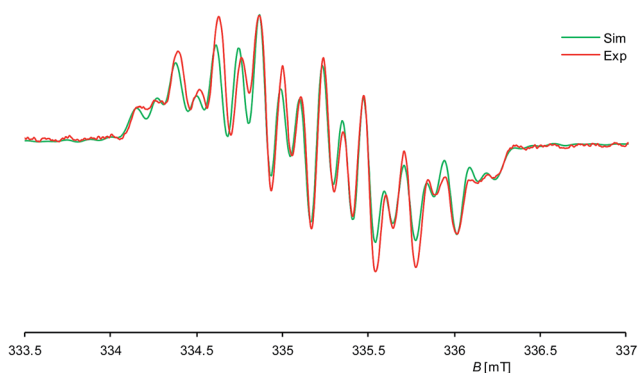


Fig. 4 Experimental (red curve) and simulated (green curve) X-band EPR spectra of **1H** in *n*-hexane at 336 K; the ordinate (dA/dB) is omitted for clarity.  $g_{\text{iso}} = 2.00562$ ,  $a(^{29}\text{Si}1) = 1.725$  mT,  $a(^{29}\text{Si}2) = 0.431$  mT,  $a(^{14}\text{N}1) = 0.246$  mT,  $a(^{14}\text{N}2) = 0.100$  mT,  $a(^1\text{H}) = 0.605$  mT.

a rigid structure and does not undergo a reversible 1,2-H-migration in solution in contrast to **1H**<sup>+</sup>.<sup>9</sup> Remarkably, two quite different  $a(^{29}\text{Si})$  hyperfine coupling constants (1.725 and 0.431 mT) were found, indicating an asymmetric spin density distribution over the Si atoms. Both values are smaller than those of other Si-based  $\pi$  type radicals, such as the disilene radical cation [Si<sub>2</sub>(Si*t*Bu<sub>2</sub>Me)<sub>4</sub>]<sup>+</sup> (2.30 mT)<sup>23</sup> or the disilene radical anions [Si<sub>2</sub>R<sub>4</sub>]<sup>-</sup> (2.45–4.83 mT, R = silyl substituent)<sup>24</sup> due to extensive delocalization of the spin density into the NHC substituents, and also significantly smaller than that of the  $\sigma$ -type radical cation in **1**[B(Ar<sup>F</sup>)<sub>4</sub>] (5.99 mT),<sup>7c</sup> indicating a localization of the unpaired electron in a molecular orbital of  $\pi$ -symmetry in agreement with the results of the quantum chemical calculations (*vide infra*). The two  $a(^{14}\text{N})$  hfcc's (0.246 and 0.100 mT) suggest a fast rotation of the magnetically different NHC substituents about the Si-C<sub>NHC</sub> bonds on the EPR timescale occurring even at low temperature (see ESI, Table S6†).

Quantum chemical calculations of **1H** were carried out using the B3LYP functional in combination with the 6-311G\*\* basis set for the Si, N, Si-bonded H and NHC ring C atoms and the 6-31G\* basis set for the peripheral C and H atoms or the B97-D3 functional in combination with RI-JCOSX approximations and the def2-TZVP basis set for all atoms.<sup>25</sup> The levels of theory are abbreviated in the following with B3LYP/I and B97-D3/II. Remarkably, calculations at the B3LYP/I level of theory yielded one minimum structure (**1H**<sub>calc</sub>), whereas two almost degenerate minimum structures were obtained at the B97-D3/II level

of theory (**1H**<sub>calc</sub> and **1H'**<sub>calc</sub>) (Fig. 5). All calculated minimum structures display a terminally bonded H atom bound to the Si1 atom. No minimum structure with a bridged H atom was found on the potential energy hypersurface of **1H** at both levels of theory. The geometrical parameters of the minimum structure calculated at the B3LYP/I level of theory and the global minimum structure at the B97-D3/II level of theory are almost identical (Table 2 and ESI, Table S8†). These structures (**1H**<sub>calc</sub>) contain a trigonal-pyramidal coordinated Si1 atom with a sum of angles of 335.51° (B3LYP/I) and 342.58° (B97-D3/II), respectively. Remarkably, the calculated structure of the diphosphanil radical P<sub>2</sub>(Me)Mes<sub>2</sub><sup>\*</sup>, which is isolobal to **1H**, displays a trigonal pyramidal geometry at the three-coordinated P atom (sum of angles: 337.5°),<sup>13</sup> as found for **1H**<sub>calc</sub>. In comparison, the second minimum structure obtained at the B97-D3/II level of theory (**1H'**<sub>calc</sub>) is only 5.5 kJ mol<sup>-1</sup> higher in energy than **1H**<sub>calc</sub> and contains the Si1 atom in a trigonal planar environment (sum of angles: 359.61°). A comparison of the structural parameters of **1H**<sub>calc</sub> and **1H'**<sub>calc</sub> with those obtained by single crystal X-ray diffraction reveals a good agreement of the calculated Si-Si, Si-C<sub>NHC</sub> and C<sub>NHC</sub>-N<sub>NHC</sub> bond lengths of both minimum structures (Table 2 and ESI, Table S8†). While the experimental results did not allow to clearly distinguish whether a flattened trigonal-pyramidal or a trigonal-planar geometry of the H-bound Si atom is present in **1H**, the theoretical studies suggest a flat energy hypersurface for the planarization of the three-coordinated Si atom.

The calculated quasi-restricted orbitals (QROs) of **1H**<sub>calc</sub> at the B3LYP/I level of theory and of **1H**<sub>calc</sub> and **1H'**<sub>calc</sub> at the B97-D3/II level of theory are almost identical (Fig. 6 and ESI, Fig. S17–S19†). The SOMO is the Si=Si  $\pi^*$  orbital, confirming

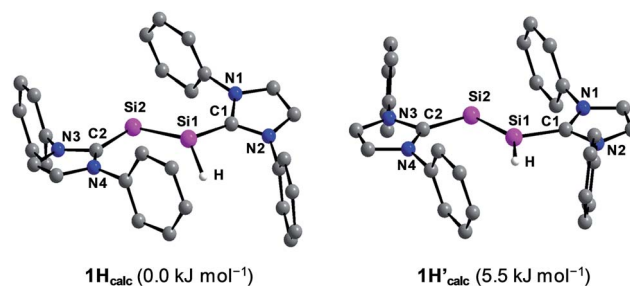


Fig. 5 Calculated minimum structures (**1H**<sub>calc</sub> and **1H'**<sub>calc</sub>) of Si<sub>2</sub>(H)(ldipp)<sub>2</sub> at the B97-D3/RI-JCOSX/def2-TZVP level of theory. The relative energies are given in brackets. The H atoms, except the H atom bonded to Si1, and the *i*Pr substituents are omitted for clarity.



Table 2 Comparison of selected experimental and calculated bonding parameters of **1H**, **1H<sub>calc</sub>** and **1H'<sub>calc</sub>**

	Si1-Si2 [Å]	Si1-C1 [Å]	Si2-C2 [Å]	$\sum_{\text{Si1}}^c$ [°]	C1-Si1-Si2-C2 [°]	$\varphi_{\text{NHC1}}^d$ [°]	$\varphi_{\text{NHC2}}^d$ [°]
<b>1H</b>	2.281(3)	1.873(4)	1.873(4)	—	180.0(3)	3.3(2)	3.3(2)
<b>1H<sub>calc</sub><sup>a</sup></b>	2.339	1.885	1.907	335.51	173.69	32.71	1.26
<b>1H<sub>calc</sub><sup>b</sup></b>	2.308	1.861	1.884	342.58	173.63	21.95	3.41
<b>1H'<sub>calc</sub><sup>b</sup></b>	2.289	1.841	1.886	359.61	179.32	6.68	3.24

<sup>a</sup> Calculated at the B3LYP/6-311G\*\*/6-31G\* level of theory. <sup>b</sup> Calculated at the B97-D3/RI-JCOSX/def2-TZVP level of theory. <sup>c</sup>  $\sum_{\text{Si1}}$  is the sum of angles around the Si1 atom. <sup>d</sup>  $\varphi_{\text{NHC1}}$  and  $\varphi_{\text{NHC2}}$  denote the dihedral angles between the least-square plane of the atoms C1, Si1, Si2, C2 and the least square plane of the heterocyclic ring atoms of the NHC substituent bonded to Si1 and Si2, respectively.

that reduction of **1H<sup>+</sup>** leads to a population of the empty Si=Si  $\pi^*$  orbital of **1H<sup>+</sup>** with one electron (see ESI, Fig. S16<sup>†</sup>). The SOMO reveals significant contributions of  $\pi^*$  NHC orbitals due to  $\pi$ -conjugation. The two lower lying doubly occupied molecular orbitals (DOMOs) are the Si=Si  $\pi$  and the  $n(\text{Si})$  lone pair orbital, respectively.

Notably, CASSCF(3,3)/def2-TZVP calculations<sup>26</sup> of **1H<sub>calc</sub>** revealed that the overall wave function is described by a major ground state configuration of [2-1-0] of the DOMO, SOMO and LUMO with 96% contribution, suggesting that static correlation can be neglected in the electronic description of **1H** (see ESI<sup>†</sup>).

The calculated spin densities of **1H<sub>calc</sub>** and **1H'<sub>calc</sub>** at the B97-D3/II level of theory are depicted in Fig. 7. Mulliken analyses<sup>27</sup> of the spin densities reveal that the highest spin density is located at the dicoordinated Si2 atom (37% in **1H<sub>calc</sub>**, 29% in **1H'<sub>calc</sub>**), whereas the spin density at the Si1 atom is quite small (9% in **1H<sub>calc</sub>**, 6% in **1H'<sub>calc</sub>**), which is in full agreement with the observation of one large and one small  $a(^{29}\text{Si})$  hfcc in the experimental EPR spectrum of **1H** (*vide supra*) (see ESI, Table S9<sup>†</sup>).<sup>28</sup> Remarkably, a significant amount of the spin density is delocalized into the C<sub>NHC</sub> and N<sub>NHC</sub> atoms of the Si1-bonded (17% in **1H<sub>calc</sub>**, 27% in **1H'<sub>calc</sub>**) and Si2-bonded (29% in **1H<sub>calc</sub>**, 30% in **1H'<sub>calc</sub>**) NHC substituents, which explains the EPR-spectroscopic detection of two  $a(^{14}\text{N})$  hfcc's. The calculated  $g_{\text{iso}}$  values of **1H<sub>calc</sub>** (2.00483) and **1H'<sub>calc</sub>** (2.00454) agree well with the experimentally obtained  $g_{\text{iso}}$  value (2.00562).

Further insight into the electronic structure of **1H** was provided by a natural bond orbital (NBO) analysis at the B3LYP/I level of theory (see ESI, Table S12<sup>†</sup>).<sup>25k</sup> The Si-Si bond is composed of a Si-Si  $\sigma$  bond and a Si=Si  $\pi$  bond with an occupancy of 1.95 and 0.82 electrons, respectively, which indicates indirectly a population of the Si=Si  $\pi^*$  orbital with one

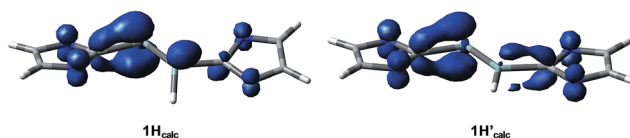


Fig. 7 Spin densities of the calculated minimum structures **1H<sub>calc</sub>** (left) and **1H'<sub>calc</sub>** (right) at the B97-D3/RI-JCOSX/def2-TZVP level of theory. The N-bonded 2,6-diisopropylphenyl substituents are omitted for clarity.

electron leading thereby to a decrease of the formal Si-Si bond order from 2 in **1H<sup>+</sup>** to 1.5 in **1H** (*vide supra*). The Si2 atom in **1H<sub>calc</sub>** bears a lone pair of high  $s$ -character (72%) as similarly found for **1H<sup>+</sup>** (75%). Remarkably, both Si-C<sub>NHC</sub> bonds in **1H<sub>calc</sub>** are composed of one doubly occupied Si-C<sub>NHC</sub>  $\sigma$  NBO and one singly occupied Si=C<sub>NHC</sub>  $\pi$  NBO, of which the latter is absent in **1H<sup>+</sup>**. These additional Si-C<sub>NHC</sub>  $\pi$  contributions rationalize the shortening and strengthening of the Si-C<sub>NHC</sub> bonds in **1H**, which is also reflected in the higher Si-C<sub>NHC</sub> WBI indexes (**1H**: WBI(Si-C<sub>NHC</sub>) = 1.01 and 0.95; **1H<sup>+</sup>**: WBI(Si-C<sub>NHC</sub>) = 0.86 and 0.74).

Comparative analyses of the charge by natural population analyses (NPA) of **1H<sub>calc</sub>** and **1H<sup>+</sup>** at the B3LYP/I level of theory reveal that the positive partial charges at the Si atoms of **1H<sup>+</sup>** ( $q(\text{Si1}) = 0.27e$ ,  $q(\text{Si2}) = 0.21e$ ) are decreased by the reduction (**1H**:  $q(\text{Si1}) = 0.14e$ ,  $q(\text{Si2}) = 0.03e$ ) (see ESI, Table S13<sup>†</sup>). Furthermore, the one-electron reduction leads to a significant decrease of the overall charges of the NHC substituents (**1H<sub>calc</sub>**:  $q(\text{NHC1}) = 0.36e$ ,  $q(\text{NHC2}) = 0.30e$ ; **1H**:  $q(\text{NHC1}) = 0.05e$ ,  $q(\text{NHC2}) = -0.04e$ ), whereas the hydridic character of the Si1-bonded H atom is retained (**1H<sup>+</sup>**:  $q(\text{H}) = -0.14e$ ; **1H**:  $q(\text{H}) = -0.18e$ ).

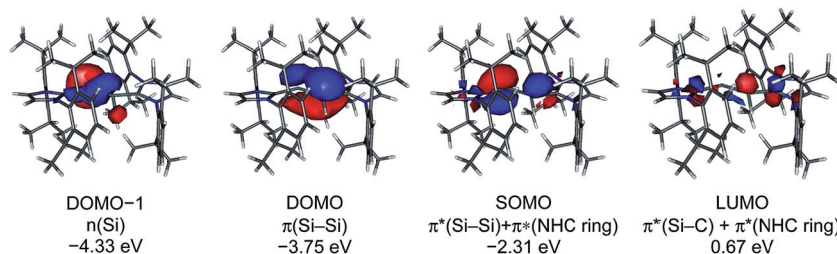


Fig. 6 Quasi-restricted orbitals (QROs) of **1H<sub>calc</sub>** (B97-D3/RI-JCOSX/def2-TZVP) and their corresponding energy eigenvalues; isosurface value: 0.04 e bohr<sup>-3</sup>; DOMO = doubly occupied molecular orbital, SOMO = singly occupied molecular orbital, LUMO = lowest unoccupied molecular orbital.





### 3. Conclusions

The isolation and full characterization of NHC-trapped  $\text{Si}_2\text{H}$  (**1H**) can be considered as a major advance in low-valent silicon hydride chemistry, given the intermediacy of  $\text{Si}_2\text{H}$  in the chemical vapor deposition of amorphous hydrogenated silicon that is widely used in solar cell and thin film transistors technology. Whereas  $\text{Si}_2\text{H}$  features a  $C_{2v}$ -symmetric H-bridged ground state structure and is a  $\sigma$ -type radical with a symmetric distribution of the spin density over the two silicon atoms, its NHC-trapped counterpart  $\text{Si}_2(\text{H})(\text{Idipp})_2$  (**1H**) features a terminal Si–H bond and is a  $\pi$ -type radical, in which the unpaired electron occupies the Si=Si  $\pi^*$  orbital (SOMO), leading to a formal Si–Si bond order of 1.5. Significant delocalization of the spin density into the NHC substituents occurs *via*  $\pi$ -conjugation of the Si=Si  $\pi^*$  orbital with the  $\pi^*$  orbitals of the coplanar arranged N-heterocyclic rings leading to a stabilization of the radical, in which the spin density is higher at the two-coordinated Si site. The mixed valent disilicon(0,I) hydride **1H** can be alternatively regarded as a H atom trapped in the closed shell compound  $\text{Si}_2(\text{Idipp})_2$ . Implications of this view in hydrogen atom transfer chemistry<sup>29</sup> are currently investigated.

### Acknowledgements

We thank the Deutsche Forschungsgemeinschaft (SFB813, "Chemistry at Spin Centers") for financial support of this study. We also thank Dr. Burhanshah Lewall for cyclic voltammetric studies, Martin Straßmann for recording the UV-Vis-NIR spectra and Norbert Wagner for the magnetic susceptibility measurements.

### Notes and references

- (a) J. M. Jasinski and S. M. Gates, *Acc. Chem. Res.*, 1991, **24**, 9; (b) M. Moravej, S. E. Babayan, G. R. Nowling, X. Yang and R. F. Hicks, *Plasma Sources Sci. Technol.*, 2004, **13**, 8.
- M. C. McCarthy, C. A. Gottlieb and P. Thaddeus, *Mol. Phys.*, 2003, **101**, 697 and refs. therein.
- (a) J. M. Jasinski, R. Becerra and R. Walsh, *Chem. Rev.*, 1995, **95**, 1203; (b) H. Stafast, G. Andrä, F. Falk and E. Witkowitz, in *Silicon Chemistry. From the Atom to Extended Systems*, ed. P. Jutzi and U. Schubert, Wiley-VCH, Weinheim, 2003, ch. 3, pp. 33–43.
- C. Xu, T. R. Taylor, G. R. Burton and D. M. Neumark, *J. Chem. Phys.*, 1998, **108**, 7645.
- (a) J. Kalcher and A. F. Sax, *Chem. Phys. Lett.*, 1993, **215**, 601; (b) B. Ma, N. L. Allinger and H. F. Schaefer III, *J. Chem. Phys.*, 1996, **105**, 5731; (c) C. Pak, S. S. Wesolowski, J. C. Rienstra-Kiracofe, Y. Yamaguchi and H. F. Schaefer III, *J. Chem. Phys.*, 2001, **115**, 2157; (d) Z. T. Owens, J. D. Larkin and H. F. Schaefer III, *J. Chem. Phys.*, 2006, **125**, 164322.
- Selected recent reviews: (a) R. S. Ghadwal, R. Azhakar and H. W. Roesky, *Acc. Chem. Res.*, 2013, **46**, 444; (b) E. Rivard, *Struct. Bonding*, 2014, **156**, 203; (c) Y. Wang and G. H. Robinson, *Inorg. Chem.*, 2014, **53**, 11815.
- (a) D. Geiß, M. I. Arz, M. Straßmann, G. Schnakenburg and A. C. Filippou, *Angew. Chem., Int. Ed.*, 2015, **54**, 2739; *Angew. Chem.*, 2015, **127**, 2777; (b) P. Ghana, M. I. Arz, U. Das, G. Schnakenburg and A. C. Filippou, *Angew. Chem., Int. Ed.*, 2015, **54**, 9980; *Angew. Chem.*, 2015, **127**, 10118; (c) M. I. Arz, M. Straßmann, A. Meyer, G. Schnakenburg, O. Schiemann and A. C. Filippou, *Chem.–Eur. J.*, 2015, **21**, 12509 and refs. therein; (d) M. I. Arz, D. Geiß, M. Straßmann, G. Schnakenburg and A. C. Filippou, *Chem. Sci.*, 2015, **6**, 6515 and refs. therein.
- (a) C. D. Martin, M. Soleilhavoup and G. Bertrand, *Chem. Sci.*, 2013, **4**, 3020; (b) M. Soleilhavoup and G. Bertrand, *Acc. Chem. Res.*, 2015, **48**, 256; (c) K. C. Mondal, S. Roy and H. W. Roesky, *Chem. Soc. Rev.*, 2016, **45**, 1080.
- M. I. Arz, M. Straßmann, D. Geiß, G. Schnakenburg and A. C. Filippou, *J. Am. Chem. Soc.*, 2016, **138**, 4589.
- R. Kinjo, M. Ichinohe and A. Sekiguchi, *J. Am. Chem. Soc.*, 2007, **129**, 26.
- (a) N. Wiberg, W. Niedermayer, H. Nöth and M. Warchhold, *Z. Anorg. Allg. Chem.*, 2001, **627**, 1717; (b) R. Rodriguez, D. Gau, Y. Contie, T. Kato, N. Saffon-Merceron and A. Baceiredo, *Angew. Chem., Int. Ed.*, 2011, **50**, 11492; *Angew. Chem.*, 2011, **123**, 11694; (c) T. Agou, Y. Sugiyama, T. Sasamori, H. Sakai, Y. Furukawa, N. Takagi, J.-D. Guo, S. Nagase, D. Hashizume and N. Tokitoh, *J. Am. Chem. Soc.*, 2012, **134**, 4120; (d) S. Inoue and C. Eisenhut, *J. Am. Chem. Soc.*, 2013, **135**, 18315.
- (a) A. Jana, D. Leusser, I. Objartel, H. W. Roesky and D. Stalke, *Dalton Trans.*, 2011, **40**, 5458; (b) M. Y. Abraham, Y. Wang, Y. Xie, P. Wei, H. F. Schaefer III, P. v. R. Schleyer and G. H. Robinson, *J. Am. Chem. Soc.*, 2011, **133**, 8874; (c) S. M. I. Al-Rafia, A. C. Malcolm, R. McDonald, M. J. Ferguson and E. Rivard, *Angew. Chem., Int. Ed.*, 2011, **50**, 8354; *Angew. Chem.*, 2011, **123**, 8504; (d) M. Stoelzel, C. Präsang, S. Inoue, S. Enthaler and M. Driess, *Angew. Chem., Int. Ed.*, 2012, **51**, 399; *Angew. Chem.*, 2012, **124**, 411; (e) S. M. I. Al-Rafia, A. C. Malcolm, R. McDonald, M. J. Ferguson and E. Rivard, *Chem. Commun.*, 2012, **48**, 1308; (f) S. M. I. Al-Rafia, R. McDonald, M. J. Ferguson and E. Rivard, *Chem.–Eur. J.*, 2012, **18**, 13810; (g) B. Blom, S. Enthaler, S. Inoue, E. Irran and M. Driess, *J. Am. Chem. Soc.*, 2013, **135**, 6703; (h) E. Rivard, *Chem. Soc. Rev.*, 2016, **45**, 989.
- S. Loss, A. Magistrato, L. Cataldo, S. Hoffmann, M. Geoffroy, U. Röthlisberger and H. Grützmacher, *Angew. Chem., Int. Ed.*, 2001, **40**, 723; *Angew. Chem.*, 2001, **113**, 749. The redox potential of  $[\text{Mes}^*(\text{Me})\text{P}=\text{PMes}^*]^+$  versus the saturated calomel electrode (SCE) was deduced from this work ( $E_{1/2}$  in MeCN =  $-0.57$  V) and converted to the  $[\text{Fe}(\eta^5\text{-C}_5\text{Me}_5)_2]^{+1/0}$  redox scale using the half-wave potential of the redox couple  $[\text{Fe}(\eta^5\text{-C}_5\text{Me}_5)_2]^{+1/0}$  versus SCE ( $E_{1/2}$  in MeCN =  $-0.09$  V) determined in our laboratory (see ESI†).
- The  $[\text{Fe}(\eta^5\text{-C}_5\text{Me}_5)_2]^{+1/0}$  was chosen as the reference standard for the CV experiments of **1H**[B(Ar<sup>F</sup>)<sub>4</sub>] owing to its favorable properties versus the  $[\text{Fe}(\eta^5\text{-C}_5\text{H}_5)_2]^{+1/0}$  redox couple: (a) I. Noviadri, K. N. Brown, D. S. Fleming, P. T. Gulyas, P. A. Lay, A. F. Masters and L. Phillips, *J. Phys. Chem. B*,



- 1999, **103**, 6713; (b) J. R. Aranzaes, M.-C. Daniel and D. Astruc, *Can. J. Chem.*, 2006, **84**, 288.
- 15 For comparison reasons, the half-wave potential of the  $[\text{Fe}(\eta^5\text{-C}_5\text{H}_5)_2]^{+1/0}$  (Fc<sup>+</sup>/Fc) redox couple was determined in C<sub>6</sub>H<sub>5</sub>F under the same conditions and found to be +0.520 V versus the redox couple  $[\text{Fe}(\eta^5\text{-C}_5\text{Me}_5)_2]^{+1/0}$ .
- 16 N. G. Connelly and W. E. Geiger, *Chem. Rev.*, 1996, **96**, 877.
- 17 (a) T. Matsuno, M. Ichinohe and A. Sekiguchi, *Angew. Chem., Int. Ed.*, 2002, **41**, 1575; *Angew. Chem.*, 2002, **114**, 1645; (b) H. Maruyama, H. Nakano, M. Nakamoto and A. Sekiguchi, *Angew. Chem., Int. Ed.*, 2014, **53**, 1324; *Angew. Chem.*, 2014, **126**, 1348.
- 18 The TdDFT calculations suggest that the absorption bands of **1H** centered at 608, 704 and 958 nm originate from several electronic transitions including those from the Si=Si  $\pi^*$  (HOMO( $\alpha$ )) and Si=Si  $\pi$  (HOMO-1( $\alpha$ )) orbitals into antibonding  $\pi^*$  orbitals of the N-bonded 2,6-diisopropylphenyl substituents (for details see ESI<sup>†</sup>). The SOMO → LUMO transition is predicted to give rise to a band at 1295 nm.
- 19 Y. Wang, Y. Xie, P. Wei, R. B. King, H. F. Schaefer III, P. v. R. Schleyer and G. H. Robinson, *Science*, 2008, **321**, 1069.
- 20 Si=Si bond lengths range between 2.118(1)–2.2700(5) Å: T. Iwamoto and S. Ishida, *Struct. Bonding*, 2014, **156**, 125.
- 21 A. F. Holleman, E. Wiberg and N. Wiberg, *Inorganic Chemistry*, Academic Press, San Diego/London, 2001; A. F. Holleman, E. Wiberg and N. Wiberg, *Lehrbuch der Anorganischen Chemie*, 102. Auflage, deGruyter, Berlin, 2007.
- 22 (a) S. P. Hoffmann, T. Kato, F. S. Tham and C. A. Reed, *Chem. Commun.*, 2006, 767; (b) A. Y. Khalimon, Z. H. Lin, R. Simionescu, S. F. Vyboishchikov and G. I. Nikonov, *Angew. Chem., Int. Ed.*, 2007, **46**, 4530; *Angew. Chem.*, 2007, **119**, 4614; (c) N. Kordts, C. Borner, R. Panisch, W. Saak and T. Müller, *Organometallics*, 2014, **33**, 1492.
- 23 S. Inoue, M. Ichinohe and A. Sekiguchi, *J. Am. Chem. Soc.*, 2008, **130**, 6078.
- 24 (a) M. Kira and T. Iwamoto, *J. Organomet. Chem.*, 2000, **611**, 236; (b) A. Sekiguchi, S. Inoue, M. Ichinohe and Y. Arai, *J. Am. Chem. Soc.*, 2004, **126**, 9626; (c) A. Tsurusaki and S. Kyushin, *Chem.–Eur. J.*, 2016, **22**, 134.
- 25 ORCA 3.0.0: (a) F. Neese, *Wiley Interdiscip. Rev.: Comput. Mol. Sci.*, 2012, **2**, 73; B3LYP functional: (b) C. Lee, W. Yang and R. G. Parr, *Phys. Rev. B*, 1988, **37**, 785; (c) A. D. Becke, *J. Chem. Phys.*, 1993, **98**, 5648; 6-311G\*\*/6-31G\* basis sets: (d) P. C. Hariharan and J. A. Pople, *Theor. Chim. Acta*, 1973, **28**, 213; B97-D3 functional: (e) S. Grimme, S. Ehrlich and L. Goerigk, *J. Comput. Chem.*, 2011, **32**, 1456; (f) S. Grimme, J. Antony, S. Ehrlich and H. Krieg, *J. Chem. Phys.*, 2010, **132**, 154104; RI-JCOSX approximation: (g) F. Neese, *J. Comput. Chem.*, 2003, **24**, 1740; (h) F. Neese, F. Wennmohs, A. Hansen and U. Becker, *Chem. Phys.*, 2009, **356**, 98; def2-TZVP basis set: (i) A. Schäfer, H. Horn and R. Ahlrichs, *J. Chem. Phys.*, 1992, **97**, 2571; (j) F. Weigend and R. Ahlrichs, *Phys. Chem. Chem. Phys.*, 2005, **7**, 3297; NBO 3.1 program: (k) E. D. Glendening, A. E. Reed, J. E. Carpenter and F. Weinhold, *NBO Version 3.1*.
- 26 B. O. Roos, P. R. Taylor and P. E. M. Siegbahn, *Chem. Phys.*, 1980, **48**, 157.
- 27 R. S. Mulliken, *J. Chem. Phys.*, 1955, **23**, 1833.
- 28 The higher spin density at the Si2 atom in **1H** can be rationalized considering the polarization of the Si=Si  $\pi$ -orbital in **1H**<sup>+</sup> towards the Si1 atom due to the hydride substituent. This leads to a reversed polarization of the Si=Si  $\pi^*$ -orbital in **1H**<sup>+</sup> with a higher contribution at the Si2 atom, which upon population with one electron gives rise to a higher spin density at Si2 in **1H**.
- 29 (a) A. Gansäuer, L. Shi, M. Otte, I. Huth, A. Rosales, I. Sancho-Sanz, N. M. Padial and J. E. Oltra, *Top. Curr. Chem.*, 2012, **320**, 93; (b) A. Simonneau and M. Oestreich, *Angew. Chem., Int. Ed.*, 2015, **54**, 3556; *Angew. Chem.*, 2015, **127**, 3626 and refs. therein.



## Electronic Supplementary Information

### Table of contents

1.	Experimental section – general part	S2
2.	Cyclic voltammetric studies of $[\text{Si}_2(\text{H})(\text{Idipp})_2][\text{B}(\text{Ar}^{\text{F}})_4]$ ( <b>1H</b> $[\text{BAr}^{\text{F}}]_4$ )	S3
3.	Synthesis of $\text{Si}_2(\text{H})(\text{Idipp})_2$ ( <b>1H</b> )	S5
3.1	Chemical one-electron oxidation of <b>1H</b>	S5
4.	UV-Vis-NIR spectroscopy of <b>1H</b>	S7
5.	Magnetic susceptibility measurement of <b>1H</b>	S9
6.	Single crystal X-ray diffraction analysis of <b>1H</b>	S10
7.	EPR spectroscopic analysis of <b>1H</b>	S11
8.	Quantum chemical calculations of <b>1H</b> <sup>+</sup> and <b>1H</b>	S14
8.1	Comparison of selected experimental and calculated bonding parameters	S15
8.2	Kohn-Sham orbitals of <b>1H</b> <sup>+</sup> <sub>calc</sub> and quasi-restricted orbitals of <b>1H</b> <sub>calc</sub> and <b>1H'</b> <sub>calc</sub>	S17
8.3	Spin densities of <b>1H</b> <sub>calc</sub> and <b>1H'</b> <sub>calc</sub>	S18
8.4	Comparison of experimental and calculated EPR parameters	S19
8.5	Results of the natural bond order (NBO) calculations	S19
8.6	Results of the TdDFT calculations	S20
8.7	Results of the CASSCF calculations	S24
8.8	Cartesian coordinates [Å] and SCF energies of the calculated structures	S25
9.	References	S33

## 1. Experimental section – general part

All experiments were carried out under an atmosphere of argon using Schlenk or glove box techniques. Argon was commercially received with a purity of  $\geq 99.999\%$  and passed through a gas purification system composed of two consecutive columns to remove traces of water and oxygen. The first column was filled with the BTS copper catalyst R3-11G from BASF and heated at  $\sim 80\text{ }^\circ\text{C}$  and the second column with 4 Å molecular sieves. The glassware was dried in an oven at approximately  $110\text{ }^\circ\text{C}$  and baked under vacuum prior to use.

THF and *n*-hexane were refluxed several days over sodium wire/benzophenone and sodium wire/benzophenone/tetraglyme (0.5 vol%), respectively, purged several times with argon during reflux and distilled off under argon. Fluorobenzene and acetonitrile for the cyclic voltammetric measurements was stirred several days over  $\text{CaH}_2$  and trap-to-trap condensed. Diethyl ether ( $\text{Et}_2\text{O}$ ) used for the EPR samples was stirred several days over  $\text{LiAlH}_4$  and trap-to-trap condensed. All solvents were degassed by three freeze-pump-thaw cycles and stored in the glove box.

The IR spectrum of **1H** ( $4000 - 400\text{ cm}^{-1}$ ) was recorded on a Bruker Alpha FT-IR spectrometer in the glovebox with a diamond single-reflection Platinum-ATR module at room temperature. The following abbreviations were used for the intensities of the absorption bands: vs = very strong, s = strong, m = medium, w = weak, vw = very weak.

The C, H, N analysis of **1H** was carried out in triplicate on an Elementar Vario Micro elemental analyzer. The individual C, H, N values did not differ by more than  $\pm 0.3\%$ . The mean C, H, N values are given below for compound **1H**.

The thermal behaviour of compound **1H** was studied on a Büchi melting point B-545 apparatus. The samples were sealed in glass-capillary tubes under vacuum and heated once with a gradient of  $5\text{ K min}^{-1}$  for a rough determination of the temperature of decomposition and twice with a gradient of  $2\text{ K min}^{-1}$  (starting 20 K below the roughly determined temperature) for a precise determination of the temperature of decomposition. The molten samples were cooled to room temperature and studied by  $^1\text{H}$  NMR spectroscopy verifying the decomposition of **1H**.

The compound  $[\text{Si}_2(\text{H})(\text{Idipp})_2][\text{B}(\text{Ar}^{\text{F}})_4]$  (**1H** $[\text{B}(\text{Ar}^{\text{F}})_4]$ ,  $\text{Idipp} = \text{C}[\text{N}(\text{C}_6\text{H}_3\text{-}2,6\text{-}i\text{Pr}_2)\text{CH}]_2$ ,  $\text{Ar}^{\text{F}} = \text{C}_6\text{H}_3\text{-}3,5\text{-(CF}_3)_2$ ) was prepared as described recently.<sup>[S1]</sup>  $\text{KC}_8$  was synthesized following the published procedure upon heating a 8:1 mixture of graphite and potassium to ca.  $450\text{ }^\circ\text{C}$  under vacuum.<sup>[S2]</sup>  $[\text{Fe}(\eta^5\text{-C}_5\text{Me}_5)_2][\text{B}(\text{Ar}^{\text{F}})_4]$  was synthesized as described in the literature and recrystallized from diethyl ether at  $-60\text{ }^\circ\text{C}$ .<sup>[S3]</sup>



## 2. Cyclic voltammetric studies of $[\text{Si}_2(\text{H})(\text{Idipp})_2][\text{B}(\text{Ar}^{\text{F}})_4]$ ( $1\text{H}[\text{B}(\text{Ar}^{\text{F}})_4]$ )

The cyclic voltammetric studies were performed with an Autolab Eco electrochemical workstation composed of an Autolab PGSTAT 20 potentiostat/galvanostat. The results were analyzed with the Autolab software version 4.9. The experiments were carried out in a glove box under argon in a gas-tight specially designed full-glass three-electrode cell at ambient temperature. A glass-carbon disk electrode ( $\text{Ø} = 2 \text{ mm}$ ) was used as working electrode, a Pt wire of 1 mm diameter as counter electrode and a 4 mM  $[\text{Fe}(\text{C}_5\text{Me}_5)_2]^{+1/0}$  / 0.1 M  $n\text{Bu}_4\text{NPF}_6$  solution as reference electrode, which was separated from the substrate/electrolyte solution with a Vycor frit (4 mm).<sup>1</sup> In all experiments fluorobenzene was used as solvent and tetra-*n*-butylammonium hexafluorophosphate ( $n\text{Bu}_4\text{NPF}_6$ ) as supporting electrolyte in a concentration of 0.1 M. The electrolyte was recrystallized twice from ethanol and dried for several hours at 150 °C before use. *iR*-drop compensation was applied for all experiments.

All potentials are reported relative to the reference electrode. For comparison reasons, the half-wave potential of the  $[\text{Fe}(\text{C}_5\text{H}_5)_2]^{+1/0}$  versus the  $[\text{Fe}(\text{C}_5\text{Me}_5)_2]^{+1/0}$  redox couple was determined under the same conditions by a separate cyclic voltammetric experiment and found to be  $E_{1/2} = 520 \text{ mV}$ .<sup>2</sup> For further comparison reasons, the half-wave potentials of the  $[\text{Fe}(\text{C}_5\text{H}_5)_2]^{+1/0}$  and the  $[\text{Fe}(\text{C}_5\text{Me}_5)_2]^{+1/0}$  redox couples in acetonitrile were determined versus the saturated calomel reference electrode (SCE), which was separated from the bulk solution by a salt bridge containing 0.1 M  $n\text{Bu}_4\text{NPF}_6$  in acetonitrile in order to modulate the SCE junction transport consequences,<sup>[S4]</sup> and found to be  $E_{1/2} = 406$  and  $-93 \text{ mV}$ , respectively.

The cyclic voltammograms of **1** are depicted in Figures S1 and S2, and show that the compound undergoes a reversible reduction in fluorobenzene at a half-wave potential  $E_{1/2}(1)$  of  $-1.626 \text{ V}$ . The following criteria were applied to verify the reversibility of this process (Table S1):<sup>[S4]</sup>

- the half-wave potential was found to be constant for several scan rates ( $\nu$ ) ranging from 50 – 800  $\text{mV s}^{-1}$ ;
- the anodic and cathodic peak currents were almost identical ( $i_{pc} / i_{pa} \approx 1$ ) independent of the scan rate;
- the difference between the cathodic and the anodic potentials  $\Delta E_p$  ranged from 62 – 80 mV at scan rates of 50 – 800  $\text{mV s}^{-1}$  and found to be slightly larger than the value for an

<sup>1</sup> The  $[\text{Fe}(\text{C}_5\text{Me}_5)_2]^{+1/0}$  redox couple was suggested to serve as a superior reference electrode compared to  $[\text{Fe}(\text{C}_5\text{H}_5)_2]^{+1/0}$ , see: a) I. Noviadri, K. N. Brown, D. S. Fleming, P. T. Gulyas, P. A. Lay, A. F. Masters, L. Phillips, *J. Phys. Chem. B* **1999**, 103, 6713; b) J. R. Aranzaes, M.-C. Daniel, D. Astruc, *Can. J. Chem.* **2006**, 84, 288.

<sup>2</sup>  $E_{1/2}$  corresponds to the thermodynamic standard redox potential of a redox pair, when the diffusion coefficients of the oxidized and reduced forms show little difference, which is often the case: J. Heinze, *Angew. Chem. Int. Ed. Engl.* **1984**, 23, 831; *Angew. Chem.* **1984**, 96, 823.

ideal Nernstian process (58 mV). The deviation of  $\Delta E_p$  from that of an ideal Nernstian process can be rationalized by an incomplete  $iR$  drop compensation;

d) a plot of the cathodic peak current  $i_{pc}$  against the square root of the scan rate confirmed an almost linear relationship (Figure S3).

One irreversible oxidation was also observed at  $E_{1/2(2)} = 0.665$  V at a scan rate of  $100 \text{ mV s}^{-1}$ , for which the cathodic peak could not be sufficiently resolved. The ratio of the cathodic and anodic peak currents was significantly smaller than 1 and the difference between the cathodic and the anodic potentials of 86 mV was significantly larger than 58 mV, thus indicating a rapid follow-up chemical reaction of a putative  $[\text{Si}_2(\text{H})(\text{Idipp})_2]^{2+}$  dication.

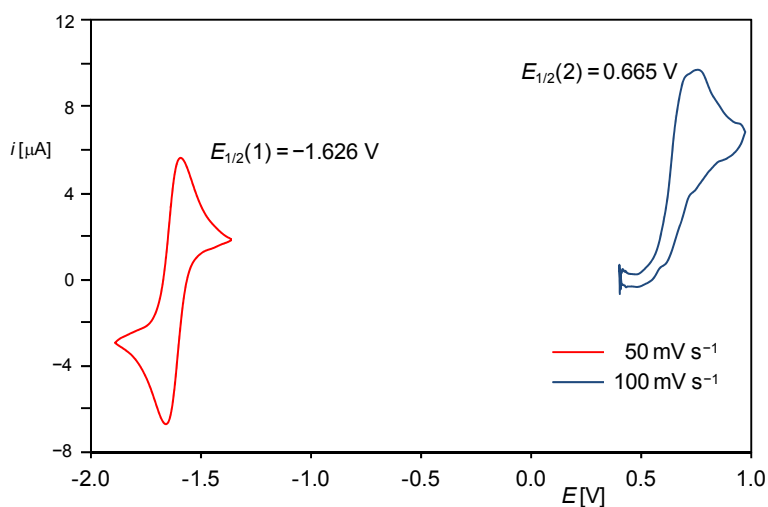


**Figure S1.** Single-scan cyclic voltammograms of  $1\text{H}[\text{B}(\text{Ar}^{\text{F}})_4]$  in fluorobenzene from  $(-2.000) - 1.000$  V at ambient temperature at scan rates of  $50$  and  $100 \text{ mV s}^{-1}$ ; reference electrode:  $4 \text{ mM } [\text{Fe}(\text{C}_5\text{Me}_5)_2]^{+1/0}$  /  $0.1 \text{ M } n\text{Bu}_4\text{NPF}_6$  in fluorobenzene; electrolyte:  $0.1 \text{ M } n\text{Bu}_4\text{NPF}_6$ .

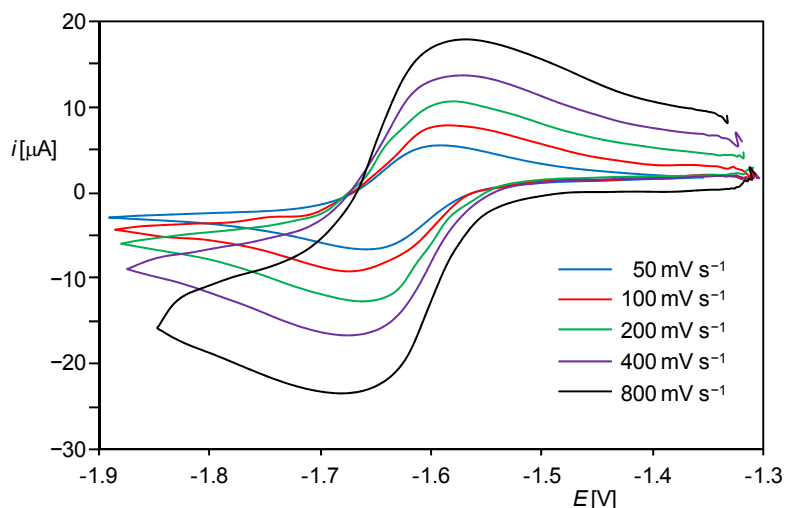


**Figure S2.** Single-scan cyclic voltammograms of  $1\text{H}[\text{B}(\text{Ar}^{\text{F}})_4]$  in fluorobenzene from  $(-1.900) - (-1.300)$  V at ambient temperature at different scan rates ( $50 - 800 \text{ mV s}^{-1}$ ); reference electrode:  $4 \text{ mM } [\text{Fe}(\text{C}_5\text{Me}_5)_2]^{+1/0}$  /  $0.1 \text{ M } n\text{Bu}_4\text{NPF}_6$  in fluorobenzene; electrolyte:  $0.1 \text{ M } n\text{Bu}_4\text{NPF}_6$ .

**Table S1:** Results of the cyclic voltammetric analysis of  $1\text{H}[\text{B}(\text{Ar}^{\text{F}})_4]$ .<sup>[a]</sup>

$\nu$ [ $\text{mV s}^{-1}$ ]	$\Delta E_p$ [mV]	$i_{pc} / i_{pa}$	$E_{1/2}$ [V]
50	62	1.00	-1.627
100	72	1.03	-1.628
200	76	1.00	-1.624
400	80	1.01	-1.624
600	66	1.03	-1.625
800	70	1.04	-1.627
100	86	0.20	0.665

[a]:  $\nu$  = scan rate;  $\Delta E_p = E_{pa} - E_{pc}$ , where  $E_{pa}$  is the anodic peak potential and  $E_{pc}$  the cathodic peak potential;  $i_{pc} / i_{pa}$  = ratio of cathodic and anodic peak current;  $E_{1/2} = (E_{pa} + E_{pc}) / 2$  = half-wave potential. Potentials are given versus the  $[\text{Fe}(\text{C}_5\text{Me}_5)_2]^{+1/0}$  redox pair.

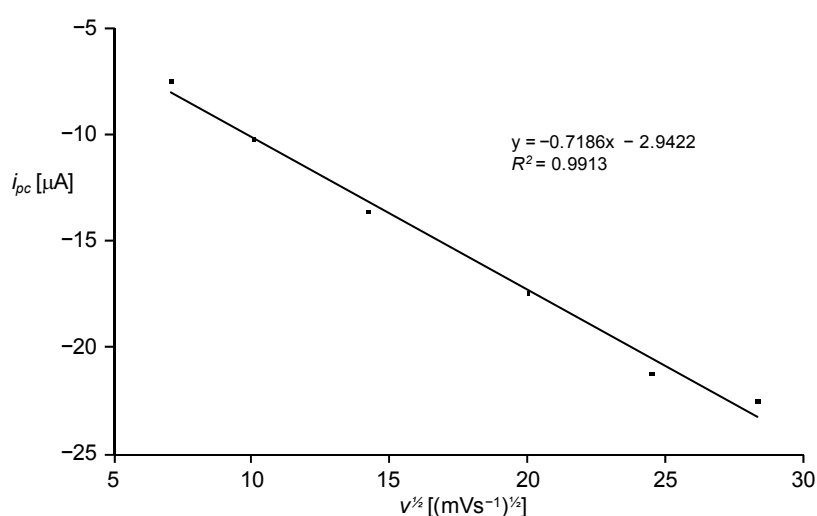


**Figure S3.** Plot of the cathodic peak current ( $i_{pc}$ ) against the square root of the scan rate ( $\nu^{1/2}$ ) for the reversible reduction of  $1\text{H}[\text{B}(\text{Ar}^{\text{F}})_4]$  at  $E_{1/2} = -1.626$  V.

### 3. Synthesis of $\text{Si}_2(\text{H})(\text{Idipp})_2$ ( $1\text{H}$ )

To a mixture of compound  $1\text{H}[\text{B}(\text{Ar}^{\text{F}})_4]$  (250 mg, 0.147 mmol) and  $\text{KC}_8$  (22 mg, 0.162 mmol, 1.1 eq.) were added 4 mL of THF by vacuum transfer at  $-196$  °C. The mixture was warmed to  $-40$  °C and a brownish suspension was obtained. Stirring for 10 minutes afforded a green solution with a black precipitate, which was further stirred at  $-40$  °C for 30 minutes. The suspension was warmed to room temperature and stirred for 1 h. Subsequent evaporation of the solvent under vacuum afforded a dark green-black residue, which was dried for 30 minutes under vacuum. The solid was extracted with  $3 \times 5$  mL and  $1 \times 2$  mL of *n*-hexane, of which the last extract had only a slightly greenish color. The combined dark green-blue extracts were concentrated under vacuum to ca. 3 mL (incipient precipitation of a dark green solid) and stored at  $-60$  °C for 48 h. The dark green solid was separated from the mother liquor with a filter cannula at  $-60$  °C and dried for 1 h at room temperature. Yield: 67 mg (0.08 mmol, 55 %). Elemental analysis calcd (%) for  $\text{C}_{54}\text{H}_{73}\text{N}_4\text{Si}_2$  (834.36): C 77.73, H

8.82, N 6.71; found: C 76.00 H 8.54 N 6.31 %. Melting point: 147 °C (decomposition upon melting to a dark red mass).<sup>3</sup>

IR (solid, RT, Figures S4 and S5):  $\nu$  [ $\text{cm}^{-1}$ ] = 409 (w), 460 (w), 495 (w), 521 (vw), 548 (w), 584 (vw), 638 (w), 670 (w), 694 (s), 714 (vw), 729 (vw), 750 (m), 757 (m), 794 (s), 839 (vw), 886 (vw), 930 (w), 958 (w), 1040 (s), 1074 (vs), 1083 (vs), 1113 (m), 1147 (vw), 1165 (vw), 1178 (w), 1200 (m), 1229 (vs), 1244 (vs), 1272 (m), 1292 (m), 1302 (m), 1315 (w), 1330 (w), 1360 (m), 1385 (m), 1457 (m), 1466 (m), 1496 (vw), 1553 (vw), 1590 (vw), 1609 (vw), 2089 (w) [ $\nu(\text{Si-H})$ ], 2864 (m), 2924 (m), 2958 (m), 3030 (vw), 3067 (vw), 3130 (vw).

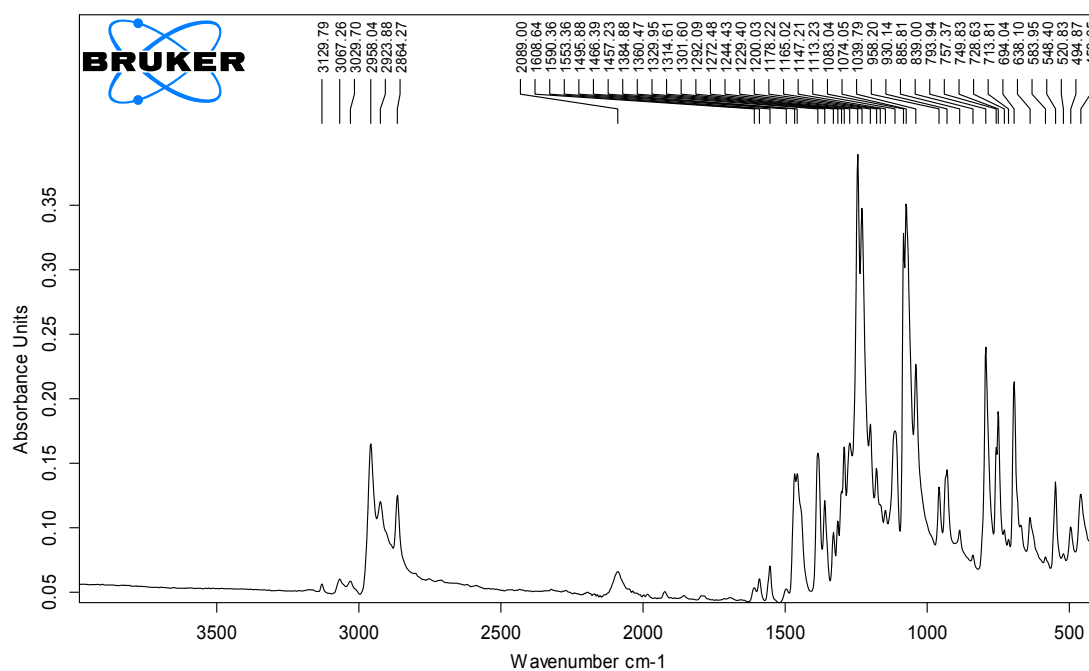


**Figure S4.** ATR FT-IR spectrum of a solid state sample of **1H**.

<sup>3</sup> A <sup>1</sup>H NMR spectrum of the red mass obtained after cooling of the molten sample to room temperature in C<sub>6</sub>D<sub>6</sub> showed the presence of Idipp and a small amount (ca. 5 %) of Si<sub>2</sub>(Idipp)<sub>2</sub>.

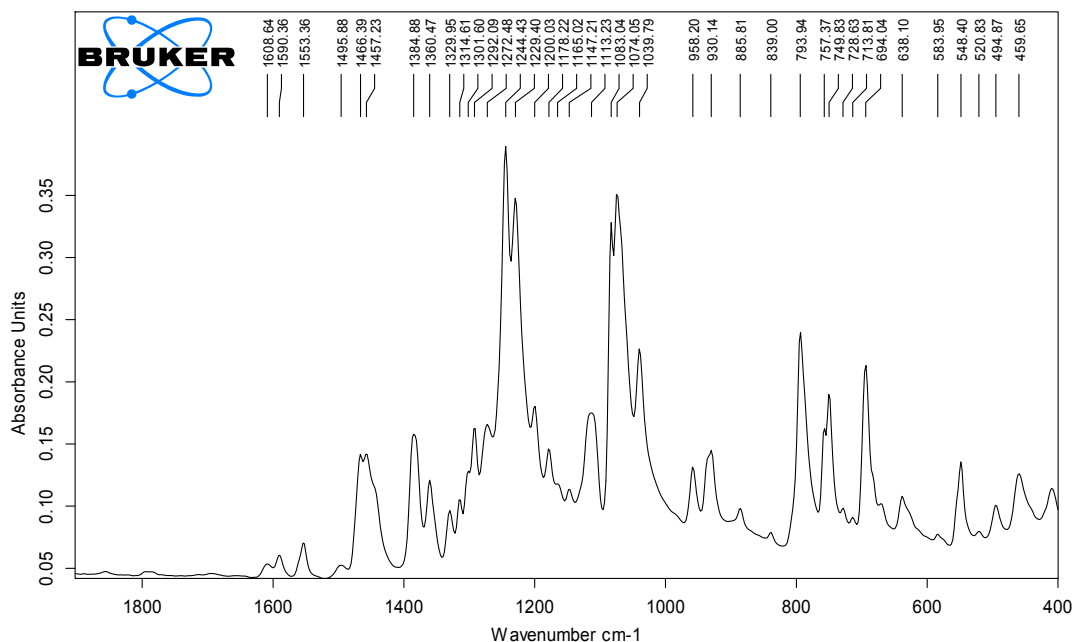


**Figure S5.** Excerpt of the ATR FT-IR spectrum of a solid state sample of **1H** from 400 – 1900  $\text{cm}^{-1}$ .

### 3.1 Chemical one-electron oxidation of **1H**

A J. Young NMR tube was charged with 10 mg (12  $\mu\text{mol}$ ) of **1H** and 14 mg (12  $\mu\text{mol}$ , 1.0 eq.) of  $[\text{Fe}(\eta^5\text{-C}_5\text{Me}_5)_2][\text{B}(\text{Ar}^{\text{F}})_4]$ . Upon addition of 0.5 mL of THF- $d_8$  a dark green solution was obtained, which rapidly turned dark red. The recorded  $^1\text{H}$  NMR spectrum showed the signals of  $\mathbf{1H}[\text{B}(\text{Ar}^{\text{F}})_4]$  and  $[\text{Fe}(\eta^5\text{-C}_5\text{Me}_5)_2]$ , indicating a selective one-electron oxidation of **1H** to  $\mathbf{1H}[\text{B}(\text{Ar}^{\text{F}})_4]$ .

### 4. UV-Vis-NIR spectroscopy of **1H**

The UV-Vis-NIR spectra of **1H** were recorded on a Thermo Scientific Evolution 300 spectrometer in a special designed quartz cuvette under inert conditions. The measurements were performed using three different path lengths ( $d = 1$  mm, 5 mm and 10 mm) and different concentrations ( $c = 360$   $\mu\text{mol L}^{-1}$  and 250  $\mu\text{mol L}^{-1}$ ) in *n*-hexane at ambient temperature. The UV-Vis-NIR spectra are depicted in Figure S6 and the absorption maxima and corresponding molar extinction coefficients  $\epsilon_\lambda$  are summarized in Table S2. The absorption bands were determined by means of band deconvolution assuming a Gaussian line profile. The corresponding deconvoluted absorption bands are displayed in Figure S7 and the parameters used for the band deconvolution are summarized in Table S3.<sup>4</sup>

<sup>4</sup> The measured spectrum was approximated as a convolution of different Gaussian functions, which represent the single absorption bands. The deconvolution operation was performed using Microsoft Excel 2007 following standard methods (see for example: E. J. Billo, *Excel for chemists - A comprehensive guide*, 3<sup>rd</sup> ed., Wiley-VCH, Weinheim, 2011, pp. 474–476).

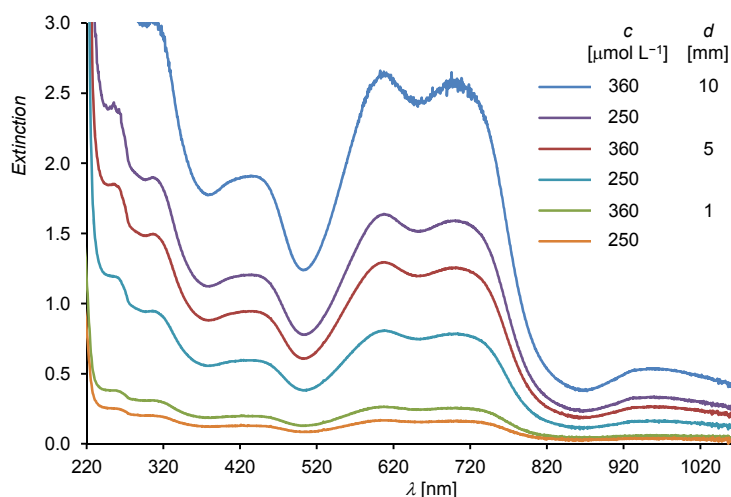


**Figure S6.** Experimental UV-Vis-NIR spectra of **1H** in *n*-hexane from 220 – 1100 nm at different concentrations *c* of **1H** and path lengths *d* of the cuvette.

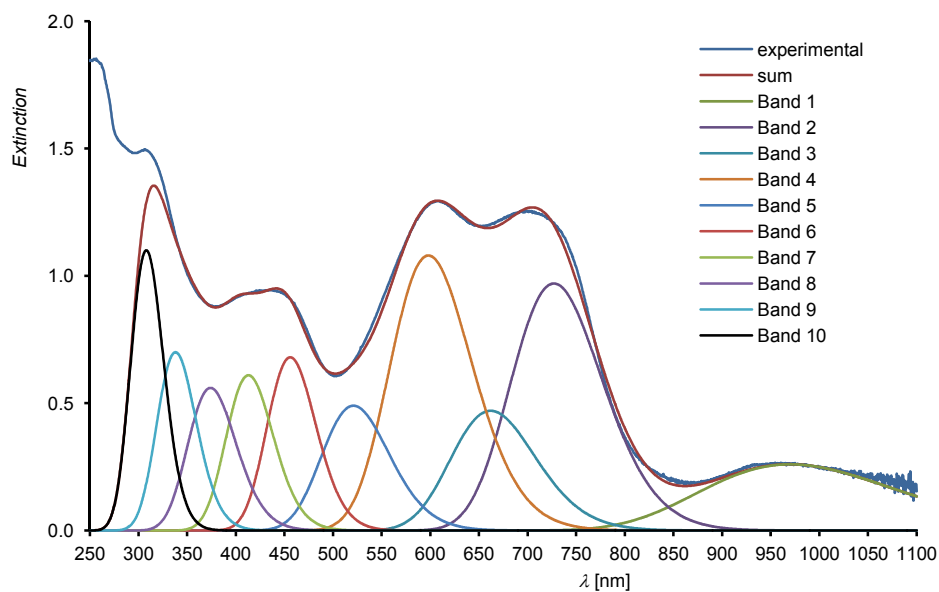


**Figure S7.** Deconvoluted and experimental UV-Vis-NIR spectra of **1H** in *n*-hexane at  $c = 360 \mu\text{mol L}^{-1}$  and  $d = 5 \text{ mm}$ .

**Table S2:** Absorption maxima of the UV-Vis-NIR spectra of **1H** depicted in Figure S6 and their corresponding molar extinction coefficients.

$\lambda$ [nm]	254	305	436	608	704	958
$\epsilon_{\lambda} \cdot 10^{-3} [\text{L mol}^{-1} \text{cm}^{-1}]$	9.97	8.14	5.17	7.11	6.86	1.44

**Table S3:** Parameters used for the band deconvolution of the UV-Vis-NIR spectrum depicted in Figure S7.<sup>[a]</sup>

	Band 1	Band 2	Band 3	Band 4	Band 5	Band 6	Band 7	Band 8	Band 9	Band 10
$\lambda$	970	727	662	598	521	456	413	374	338	308
$E$	0.26	0.97	0.47	1.08	0.49	0.68	0.61	0.56	0.70	1.10
$\sigma$	1500	1250	1400	1650	1800	1700	2000	2500	2500	2500

[a]:  $\lambda_{\text{max}}$  = wavelength [nm];  $E$  = extinction maximum;  $\sigma$  = linewidth [ $\text{cm}^{-1}$ ].

## 5. Magnetic susceptibility measurement of **1H**

The magnetic susceptibility measurement of **1H** was performed on a PPMS VLM-409p vibrating-sample magnetometer in a temperature range of 1.9 – 300 K and the obtained susceptibilities were diamagnetically corrected.<sup>[S5]</sup>

A plot of the reciprocal molar magnetic susceptibility against the absolute temperature (Figure S8) shows a linear correlation as expected for a paramagnetic compound following Curie's law.<sup>[S6]</sup> Calculation of the effective magnetic moment from the slope of the line obtained after linear regression ( $R^2 = 0.9903$ ) yielded  $\mu_{\text{eff}} = 1.68\mu_B$  ( $\mu_B = \text{Bohr magneton} = 9.27400968(20) \cdot 10^{-24} \text{ J T}^{-1}$ ). The value is slightly lower than the expected value derived from the spin-only formula for one unpaired electron ( $\mu_{\text{eff}} = 1.73\mu_B$ ).<sup>[S6]</sup> The difference might arise from a slight decomposition of the extremely air-sensitive compound **1H** during the measurement. A plot of the effective magnetic moment against the absolute temperature (Figure S9) revealed only a small temperature dependence of the effective magnetic moment of **1H**. The obtained data clearly suggest the presence of one unpaired electron in compound **1H**.

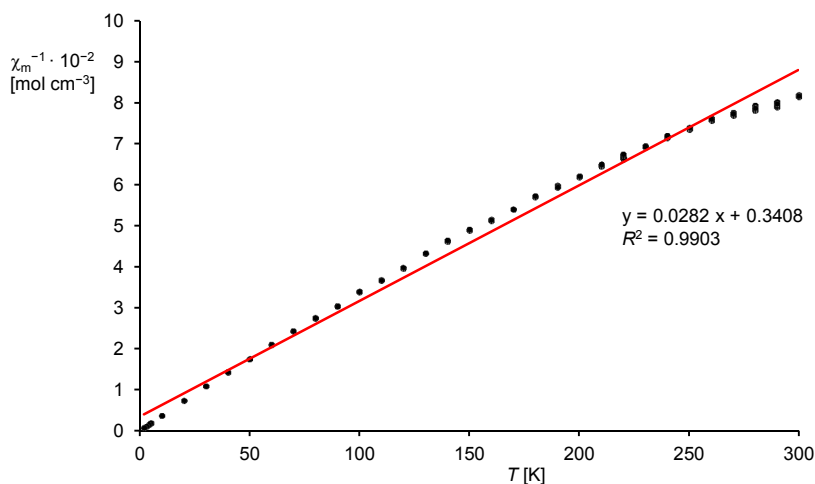


**Figure S8.** Plot of the reciprocal molar magnetic susceptibility  $\chi_m^{-1}$  against the absolute temperature  $T$  (dotted black line) and the corresponding line (red) and line equation obtained by linear regression.

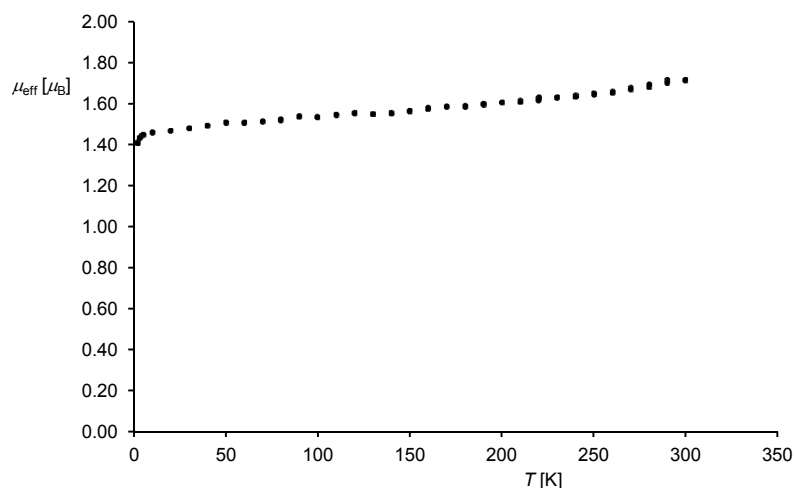


**Figure S9.** Plot of the effective magnetic moment  $\mu_{\text{eff}}$  against the absolute temperature  $T$ ;  $\mu_{\text{B}}$  = Bohr magneton =  $9.27400968(20) \cdot 10^{-24} \text{ J T}^{-1}$ .

## 6. Single crystal X-Ray diffraction analysis of 1H

Clear dark blue blocks of **1H** suitable for single crystal X-ray diffraction were obtained upon crystallization from a concentrated *n*-hexane solution at  $-60$  °C. The crystals were protected with Fomblin® Y during mounting on the goniometer.

The data collection was performed on a STOE IPDS-2T diffractometer using graphite monochromated Mo- $K_{\alpha}$  radiation ( $\lambda = 0.7107$  Å). The diffractometer was equipped with a low-temperature device (Oxford Cryostream 700er series, 123(2) K). Intensities were measured by fine-slicing  $\omega$  and  $\varphi$ -scans and corrected for background, polarization and Lorentz effects. An absorption correction by integration was applied for all data sets.<sup>[S7]</sup> The structures were solved by direct methods and refined anisotropically by the least-squares procedure implemented in the SHELX program system.<sup>[S8]</sup> Hydrogen atoms except the silicon-bonded hydrogen atom were included using the riding model on the bound carbon atoms. The silicon-bonded hydrogen atom was found on the difference Fourier map and anisotropically refined with an occupancy of 1/2, which results from the inversion centre of the space group  $P2_1/c$ . Due to the low electronic density, the position of the silicon-bonded hydrogen atom cannot be accurately determined by X-ray diffraction analysis. This was verified by changing the position of the hydrogen atom, including a bridged position between the silicon atoms, which resulted in no variation of the final  $R$  indices. Selected crystallographic refinement data are listed in Table S4.

CCDC-1471165 contains the supplementary crystallographic data for this paper, which can be obtained free of charge from the Cambridge Crystallographic Data Centre via [www.ccdc.cam.ac.uk/data\\_request/cif](http://www.ccdc.cam.ac.uk/data_request/cif).



**Table S4:** Crystal data and structure refinement of **1H**.

Empirical formula	C <sub>54</sub> H <sub>73</sub> N <sub>4</sub> Si <sub>2</sub>
Moiety formula	C <sub>54</sub> H <sub>73</sub> N <sub>4</sub> Si <sub>2</sub>
Formula weight	834.36 g mol <sup>-1</sup>
Temperature	123(2) K
Wavelength	0.71073 Å
Crystal system, space group	monoclinic, <i>P</i> 2 <sub>1</sub> / <i>c</i>
Unit cell dimensions	<i>a</i> = 12.9588(11) Å, $\alpha$ = 90° <i>b</i> = 13.5352(9) Å, $\beta$ = 126.432(5)° <i>c</i> = 18.2226(15) Å, $\gamma$ = 90°
Volume	2571.6(3) Å <sup>3</sup>
<i>Z</i>	2
$\rho_{\text{calc}}$	1.078 mg m <sup>-3</sup>
$\mu$	0.106 mm <sup>-1</sup>
<i>F</i> (000)	906.0
Crystal size	0.24 × 0.18 × 0.12 mm
2 $\theta$ -range for data collection	5.42 – 56°
Limiting indices	-17 ≤ <i>h</i> ≤ 17, -17 ≤ <i>k</i> ≤ 17, -24 ≤ <i>l</i> ≤ 24
Reflections collected	20621
Independent reflections	6197 ( <i>R</i> <sub>int</sub> = 0.1649, <i>R</i> <sub>σ</sub> = 0.2106)
Completeness to $\theta$	99.9 %
Absorption correction	integration
Min. and max. transmission	0.6417; 0.9185
Refinement method	Full-matrix least squares on <i>F</i> <sup>2</sup>
Data / restraints / parameters	6197 / 0 / 279
Goodness-of-fit on <i>F</i> <sup>2</sup>	0.754
Final <i>R</i> indices [ <i>I</i> ≥ 2σ( <i>I</i> )]	<i>R</i> <sub>1</sub> = 0.0754, <i>wR</i> <sub>2</sub> = 0.1719
Final <i>R</i> indices (all data)	<i>R</i> <sub>1</sub> = 0.1884, <i>wR</i> <sub>2</sub> = 0.2041
Largest diff. peak / hole	0.46 / -0.27 e Å <sup>-3</sup>

## 7. EPR spectroscopic analysis of **1H**

The samples used for the EPR experiments were prepared by dissolving a small amount of solid **1H** (approximately 1 mg) in 4 mL of *n*-hexane or diethyl ether in the glove box to afford a green colored solution (*c* ≈ 300 μmol L<sup>-1</sup>). The solution was transferred to a Wilmad® Suprasil EPR tube (Ø = 3.8 mm) with a syringe and the tube was sealed off under vacuum with an oxygen/hydrogen burner.

The continuous-wave (cw) EPR experiments were performed in *n*-hexane in the temperature range of 183 – 336 K at X-band microwave (MW) frequencies on a Bruker EMXmicro EPR spectrometer with the EMXmicro standard resonator. The sample temperature was adjusted using a liquid nitrogen evaporator and the ER 4131VT temperature control system.

The EPR experiment in diethyl ether was performed on a Bruker ELEXSYS E580 EPR spectrometer. A Super High-Q resonator and an Oxford ESR900 helium gas-flow cryostat was employed for the cw measurement at X-band MW frequency.

For each measurement it was validated that neither a saturation of the EPR signal occurred nor that the resolution could be further improved by varying the microwave power and the modulation amplitude, respectively.

The measurement parameters are given in Table S5. The spectra were simulated using the garlic routine of the EasySpin program package.<sup>[S9]</sup> The simulation parameters for all spectra are given in Tables S6 and S7.

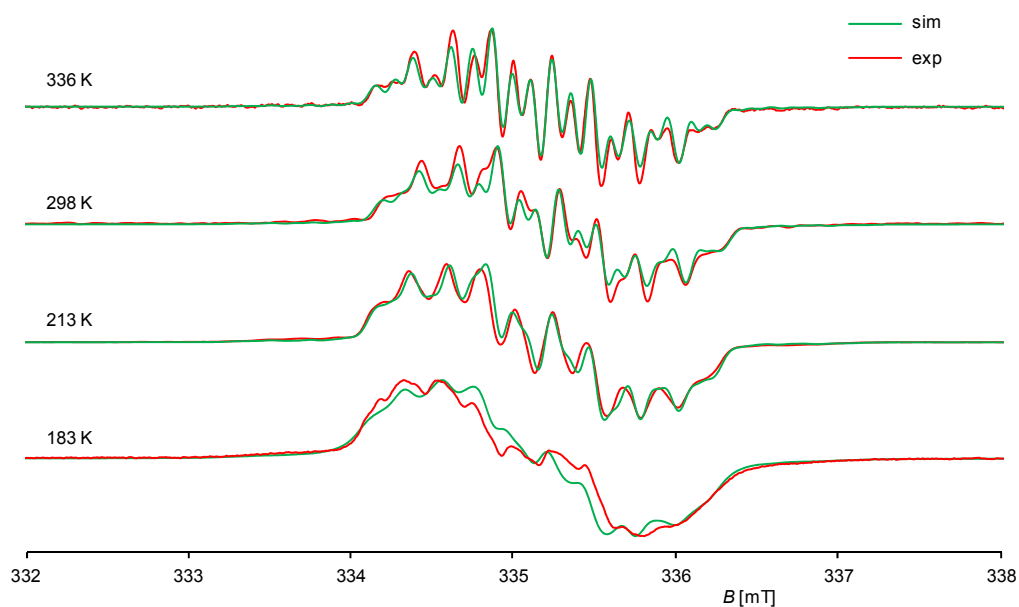


**Figure S10.** Experimental (red curves) and simulated (green curves) X-band EPR spectra of **1H** in *n*-hexane from 183 – 336 K; the ordinate ( $dA/dB$ ) is omitted for clarity.

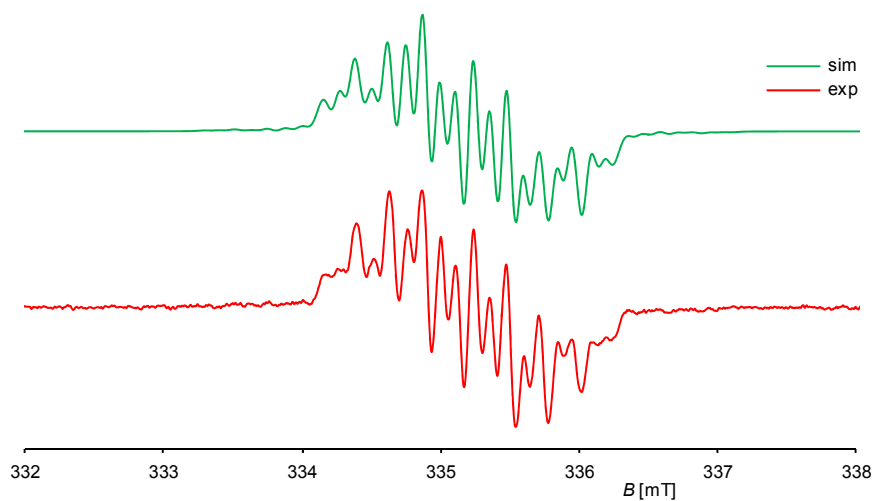


**Figure S11.** Experimental (bottom, red curve) and simulated (top, green curve) X-band EPR spectra of **1H** in *n*-hexane at 336 K; the ordinate ( $dA/dB$ ) is omitted for clarity.

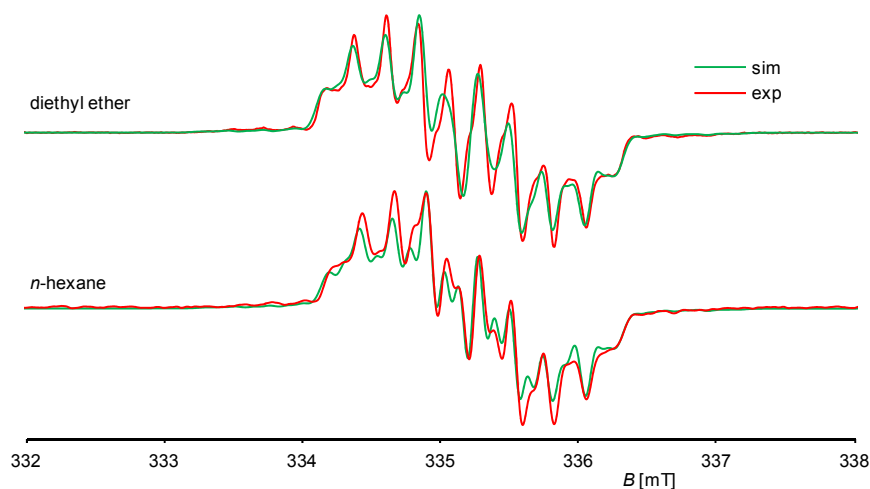


**Figure S12.** Experimental (red curves) and simulated (green curves) X-band EPR spectra of **1H** in diethyl ether (top) and *n*-hexane (bottom) at 298 K; the ordinate ( $dA/dB$ ) is omitted for clarity.

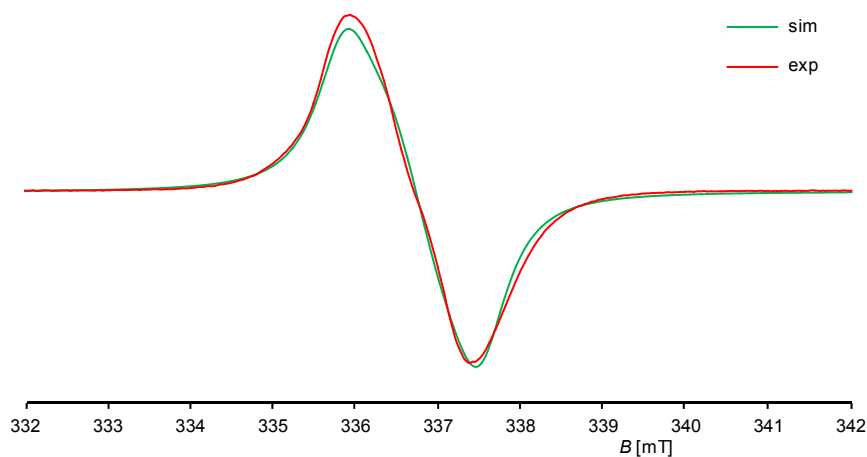


**Figure S13.** Experimental (red curve) and simulated (green curve) X-band EPR spectra of **1H** in frozen *n*-hexane solution at 153 K; the ordinate ( $dA/dB$ ) is omitted for clarity.

**Table S5:** Parameters used for the EPR measurements of **1H**.<sup>[a]</sup>

solvent	$T$ [K]	$\nu$ [GHz]	$MA$ [G]	$P$ [mW]	$RG$ [dB]	$CT$ [ms]	$TC$ [ms]	$CF$ [mT]	$SW$ [mT]	$NP$
<i>n</i> -hexane	153	9.4523	1.0	0.578	30	32.10	20.48	337.0	10.0	1902
<i>n</i> -hexane	183	9.4542	0.2	0.578	30	6.41	20.48	337.0	10.0	9509
<i>n</i> -hexane	213	9.4491	1.0	0.057	30	32.10	20.48	337.0	10.0	1902
<i>n</i> -hexane	298	9.4591	1.0	0.057	30	32.10	20.48	337.0	10.0	1902
<i>n</i> -hexane	336	9.4491	0.2	0.057	30	6.44	20.48	337.0	10.0	9509
diethyl ether	298	9.4094	0.5	1.262	40	21.00	20.48	335.5	10.0	1024

[a]:  $T$  = temperature,  $\nu$  = microwave frequency,  $MA$  = modulation amplitude,  $P$  = microwave power,  $RG$  = receiver gain,  $CT$  = conversion time,  $TC$  = time constant,  $CF$  = center field,  $SW$  = sweep width,  $NP$  = number of points on the field axis.

**Table S6:** Isotropic  $g$  values, hyperfine coupling constants ( $a$ ) and lineshape parameters used to simulate the spectrum of **1H** in liquid  $n$ -hexane and diethyl ether solution.<sup>[a]</sup>

solvent	$T$ [K]	$g$	$a(^{29}\text{Si}1)$ [mT]	$a(^{29}\text{Si}2)$ [mT]	$a(^{14}\text{N}1)$ [mT]	$a(^{14}\text{N}2)$ [mT]	$a(^1\text{H})$ [mT]	lwpp <sub>G</sub> [mT]	lwpp <sub>L</sub> [mT]
$n$ -hexane	183	2.00585	1.725	0.431	0.246	0.099	0.630	0.11	0.08
$n$ -hexane	213	2.00567	1.725	0.431	0.244	0.097	0.622	0.11	0.02
$n$ -hexane	298	2.00538	1.725	0.431	0.246	0.099	0.607	0.10	0.02
$n$ -hexane	336	2.00562	1.725	0.431	0.246	0.100	0.605	0.08	0.02
diethyl ether	298	2.00553	1.775	0.444	0.246	0.098	0.657	0.11	0.01

[a]:  $T$  = temperature; lwpp<sub>G</sub> = linewidth peak-to-peak for the Gaussian contribution; lwpp<sub>L</sub> = linewidth peak-to-peak for the Lorentzian contribution.

**Table S7:** Anisotropic  $g$  values and lineshape parameters used to simulate the spectrum of **1H** in frozen  $n$ -hexane solution.<sup>[a]</sup>

solvent	$T$ [K]	$g_{11}$	$g_{22}$	$g_{33}$	$g_{iso}$	lwpp <sub>G</sub> [mT]	lwpp <sub>L</sub> [mT]	HS <sub>11</sub> [mT]	HS <sub>22</sub> [mT]	HS <sub>33</sub> [mT]
$n$ -hexane	153	2.00110	2.00550	2.01070	2.00577	0.13	0.46	0.04	0.53	0.04

[a]:  $T$  = temperature; lwpp<sub>G</sub> = linewidth peak-to-peak for the Gaussian contribution; lwpp<sub>L</sub> = linewidth peak-to-peak for the Lorentzian contribution, HS = hyperfine strain parameter. The isotropic  $g$  value ( $g_{iso}$ ) was calculated according to  $g_{iso} = (g_{11} + g_{22} + g_{33})/3$ .

## 8. Quantum-chemical calculations of **1H<sup>+</sup>** and **1H**

The DFT calculations of the compounds **1H<sup>+</sup>** and **1H** were carried out using the B3LYP functionals<sup>[S10]</sup> in combination with the 6-311G\*\* basis set<sup>[S11]</sup> for the Si, N, Si-bonded H and heterocyclic ring C atoms and the 6-31G\* basis set for the peripheral C and H atoms or the B97-D3 functionals<sup>[S12]</sup> in combination with the RI-JCOSX approximations<sup>[S13]</sup> and the def2-TZVP basis sets<sup>[S14]</sup> for all atoms. The structure optimizations were performed without symmetry restraints using the ORCA 3.0.0 program package with its internal standard convergence criteria.<sup>[S15]</sup> The optimized geometries were verified as minima on the potential energy surface by two-sided numerical differentiation of the analytical gradients to obtain harmonic frequencies, which were also used to calculate the zero point vibrational energies (ZPVE). The calculations of the EPR parameters were carried out at the B97-D3/RI-JCOSX/def2-TZVP level of theory. The spin densities were obtained by a Mulliken spin density analysis at the B97-D3/RI-JCOSX/def2-TZVP level of theory.<sup>[S16]</sup> The natural bond orbital (NBO) analyses were performed using the NBO 3.1 program at the B3LYP/6-311G\*\*/6-31G\* level of theory.<sup>[S17]</sup>

## 8.1 Comparison of selected experimental and calculated bonding parameters

Calculations at the B3LYP/6-311G\*\*/6-31G\* level of theory revealed one optimized minimum structure for  $1\mathbf{H}_{\text{calc}}$  with a pyramidalized Si1 atom (Figure S14, Table S8). For comparison reasons, the bonding parameters of the optimized minimum structure of  $1\mathbf{H}^+_{\text{calc}}$  were also calculated at the B3LYP/6-311G\*\*/6-31G\* level of theory (Figure S14, Table S8). Calculations at the B97-D3/RI-JCOSX/def2-TZVP level of theory led to two structurally different minimum structures (Figure S15, Table S8). The first minimum structure ( $1\mathbf{H}_{\text{calc}}$ ) features a pyramidalized Si1 atom and shows similar bonding parameters as the minimum structure calculated at the B3LYP/6-311G\*\*/6-31G\* level of theory (Table S8). The second minimum structure ( $1\mathbf{H}'_{\text{calc}}$ ), which is  $5.5 \text{ kJ mol}^{-1}$  higher in energy compared to  $1\mathbf{H}_{\text{calc}}$ , consists of a trigonal-planar Si1 atom and a more coplanar orientation of the Si1-bonded NHC substituent, whereas the other bonding parameters are similar to those of  $1\mathbf{H}_{\text{calc}}$  (Table S8).

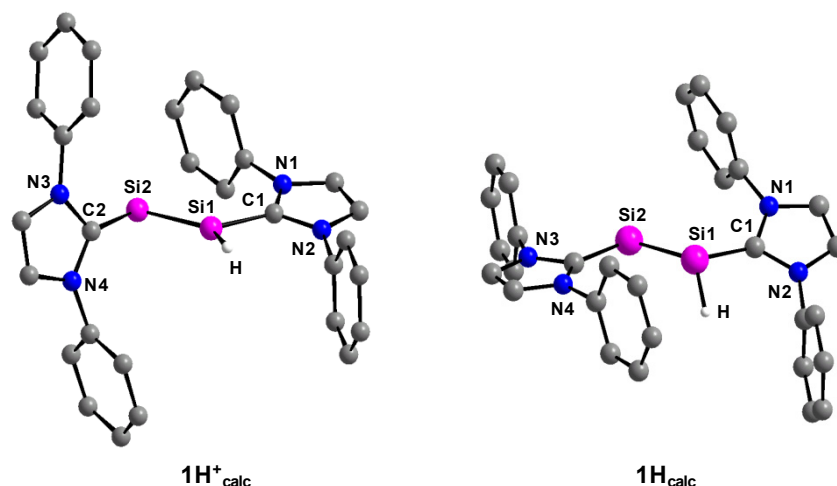


**Figure S14.** Calculated ( $1\mathbf{H}^+_{\text{calc}}$  and  $1\mathbf{H}_{\text{calc}}$ , B3LYP/6-311G\*\*/6-31G\*) structures of  $[\text{Si}_2(\text{H})(\text{Idipp})_2]^+$  and  $\text{Si}_2(\text{H})(\text{Idipp})_2$ . The H atoms, except the H atoms bonded to Si1, and the *i*Pr substituents are omitted for clarity.

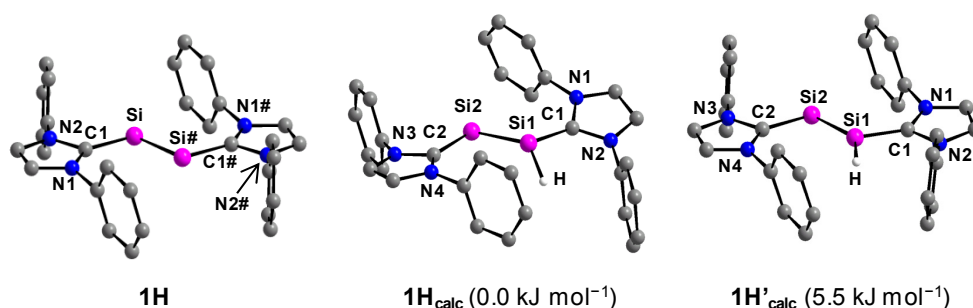


**Figure S15.** Experimental ( $1\mathbf{H}$ ) and calculated ( $1\mathbf{H}_{\text{calc}}$  and  $1\mathbf{H}'_{\text{calc}}$ , B97-D3/RI-JCOSX/def2-TZVP) structures of  $\text{Si}_2(\text{H})(\text{Idipp})_2$ . The relative energies of  $1\mathbf{H}_{\text{calc}}$  and  $1\mathbf{H}'_{\text{calc}}$  are given in brackets. The H atoms, except the H atom bonded to Si1 in  $1\mathbf{H}_{\text{calc}}$  and  $1\mathbf{H}'_{\text{calc}}$ , and the *i*Pr substituents are omitted for clarity.

**Table S8:** Comparison of selected experimental and calculated bonding parameters of  $\mathbf{1H}^+$  in  $\mathbf{1H}[B(Ar^F)_4]$ ,  $\mathbf{1H}^+$ <sub>calc.</sub>,  $\mathbf{1H}$ ,  $\mathbf{1H}$ <sub>calc.</sub> and  $\mathbf{1H}'$ <sub>calc.</sub>

	Si1–Si2 [Å]	Si1–C1 [Å]	Si2–C2 [Å]	Si1–H [Å]	C1–N1 [Å]	C1–N2 [Å]	C2–N3 [Å]	C2–N4 [Å]
$\mathbf{1H}^+$ <sup>[a]</sup>	2.1873(8)	1.882(2)	1.940(2)	1.32(2)	1.356(2)	1.358(2)	1.356(2)	1.358(2)
$\mathbf{1H}^+$ <sub>calc.</sub> <sup>[b]</sup>	2.209	1.896	1.972	1.481	1.369	1.366	1.366	1.366
$\mathbf{1H}$	2.281(3)	1.873(4)	1.873(4)	–	1.381(4)	1.402(4)	1.381(4)	1.402(4)
$\mathbf{1H}$ <sub>calc.</sub> <sup>[b]</sup>	2.339	1.885	1.907	1.496	1.392	1.389	1.400	1.397
$\mathbf{1H}$ <sub>calc.</sub> <sup>[c]</sup>	2.308	1.861	1.884	1.495	1.393	1.388	1.397	1.393
$\mathbf{1H}'$ <sub>calc.</sub> <sup>[c]</sup>	2.289	1.841	1.886	1.489	1.399	1.392	1.400	1.393
	C1–Si1–Si2 [°]	C2–Si2–Si1 [°]	C1–Si1–H [°]	Si2–Si1–H [°]	$\Sigma_{Si1}$ <sup>[d]</sup> [°]	C1–Si1–Si2–C2 [°]	$\varphi_{NHC1}$ <sup>[f]</sup> [°]	$\varphi_{NHC2}$ <sup>[f]</sup> [°]
$\mathbf{1H}^+$ <sup>[a]</sup>	116.73(7)	95.34(6)	106(1)	138(1)	360(1) <sup>[e]</sup>	177.61(9)	8.60(6)	71.06(6)
$\mathbf{1H}^+$ <sub>calc.</sub> <sup>[b]</sup>	120.12	97.94	103.60	136.11	359.83	–177.26	12.07	73.46
$\mathbf{1H}$	109.5(1)	109.5(1)	–	–	–	180.0(3)	3.3(2)	3.3(2)
$\mathbf{1H}$ <sub>calc.</sub> <sup>[b]</sup>	112.09	104.20	98.90	124.52	335.51	173.69	32.71	1.26
$\mathbf{1H}$ <sub>calc.</sub> <sup>[c]</sup>	111.88	102.40	99.87	130.83	342.58	173.63	21.95	3.41
$\mathbf{1H}'$ <sub>calc.</sub> <sup>[c]</sup>	116.55	102.87	101.90	141.16	359.61	179.32	6.68	3.24

[a]: Experimental structural parameters obtained from ref. [S1]. [b]: Calculated at the B3LYP/6-311G\*\*/6-31G\* level of theory.

[c]: Calculated at the B97-D3/RI-JCOSX/def2-TZVP level of theory. [d]:  $\Sigma_{Si1}$  is the sum of angles around the Si1 atom. [e]: The uncertainty ( $u$ ) of the sum of angles is given in parenthesis and was calculated from the individual uncertainties ( $u_i$ ) by error propagation using the formula  $u = (\Sigma(u_i)^2)^{1/2}$ . [f]:  $\varphi_{NHC1}$  and  $\varphi_{NHC2}$  denote the dihedral angles between the least-square plane of the atoms C1, Si1, Si2, C2 and the least square plane of the heterocyclic ring atoms of the NHC substituent bonded to Si1 and Si2, respectively.

## 8.2 Kohn-Sham orbitals of $1\mathbf{H}^+_{\text{calc}}$ and quasi-restricted orbitals of $1\mathbf{H}_{\text{calc}}$ and $1\mathbf{H}'_{\text{calc}}$

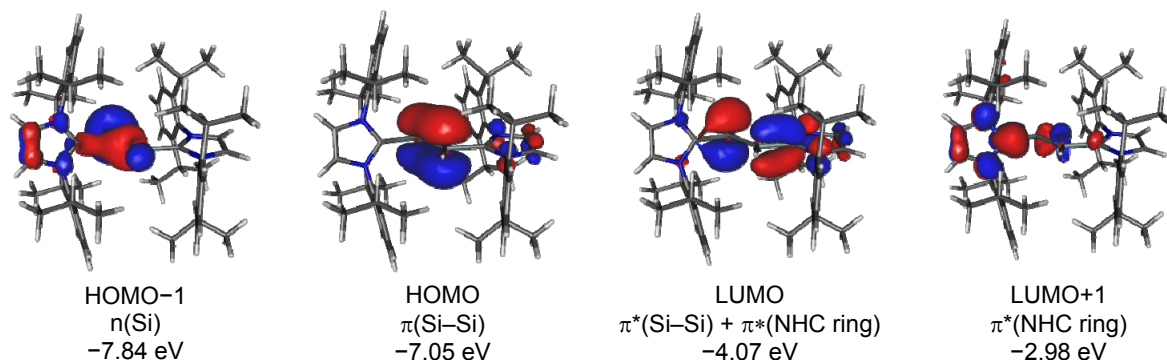


**Figure S16.** Kohn-Sham orbitals of  $1\mathbf{H}^+_{\text{calc}}$  (B3LYP/6-311G\*\*/6-31G\*) and their corresponding energy eigenvalues; isosurface value:  $0.04 \text{ e bohr}^{-3}$ ; HOMO = highest occupied molecular orbital, LUMO = lowest unoccupied molecular orbital.

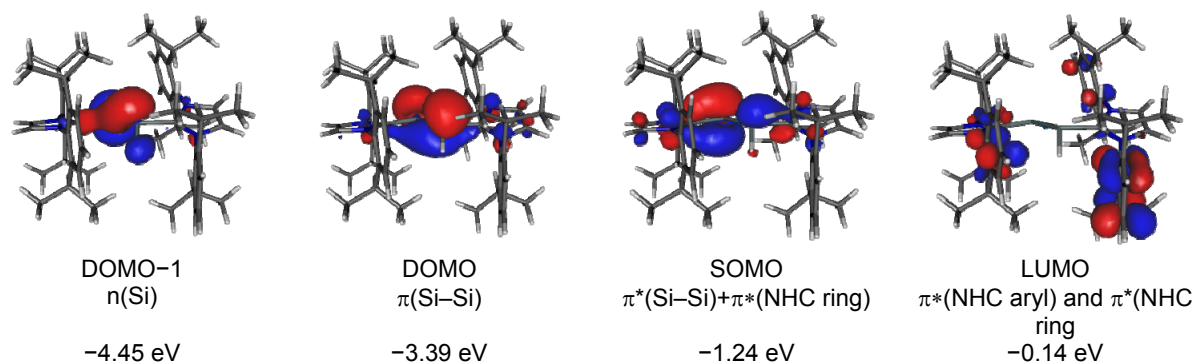


**Figure S17.** Quasi-restricted orbitals (QROs) of  $1\mathbf{H}_{\text{calc}}$  (B3LYP/6-311G\*\*/6-31G\*) and their corresponding energy eigenvalues; isosurface value:  $0.04 \text{ e bohr}^{-3}$ ; DOMO = doubly occupied molecular orbital, SOMO = singly occupied molecular orbital, LUMO = lowest unoccupied molecular orbital.

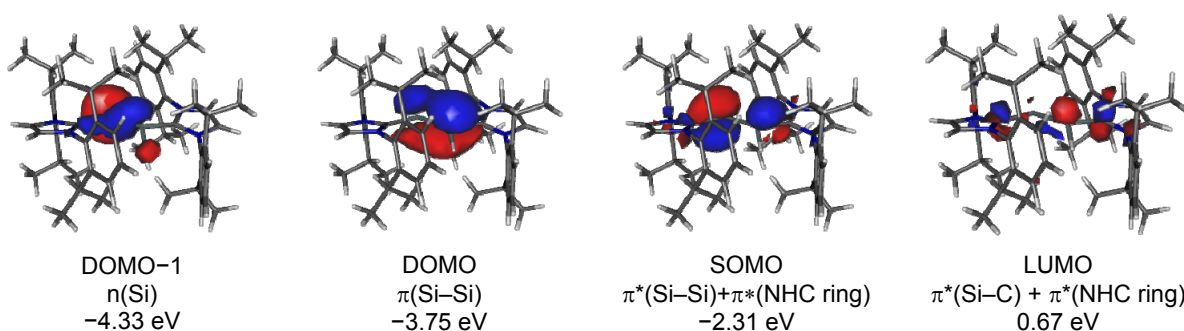


**Figure S18.** Quasi-restricted orbitals (QROs) of  $1\mathbf{H}_{\text{calc}}$  (B97-D3/RI-JCOSX/def2-TZVP) and their corresponding energy eigenvalues; isosurface value:  $0.04 \text{ e bohr}^{-3}$ ; DOMO = doubly occupied molecular orbital, SOMO = singly occupied molecular orbital, LUMO = lowest unoccupied molecular orbital.

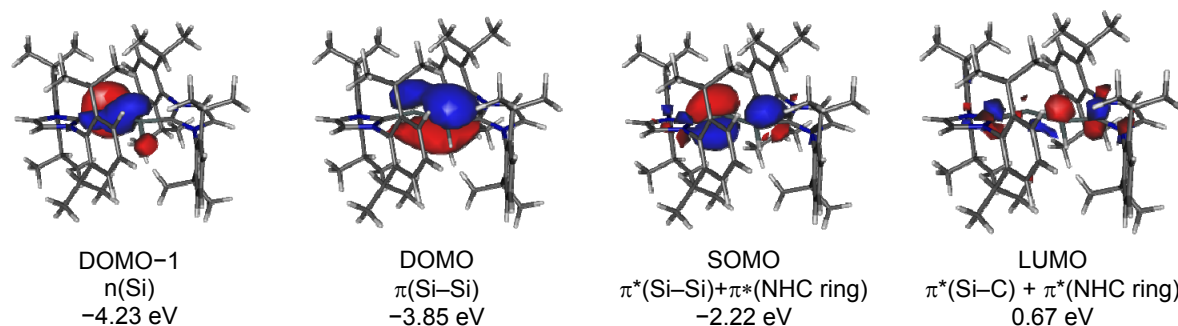


**Figure S19.** Quasi-restricted orbitals (QROs) of  $1\text{H}'_{\text{calc}}$  (B97-D3/RI-JCOSX/def2-TZVP) and their corresponding energy eigenvalues; isosurface value:  $0.04 \text{ e bohr}^{-3}$ ; DOMO = doubly occupied molecular orbital, SOMO = singly occupied molecular orbital, LUMO = lowest unoccupied molecular orbital.

### 8.3 Spin densities of $1\text{H}_{\text{calc}}$ and $1\text{H}'_{\text{calc}}$

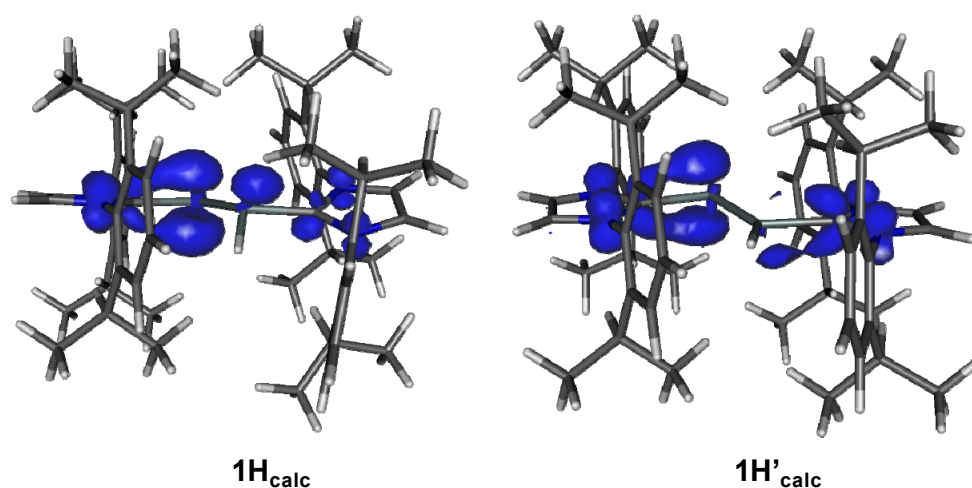


**Figure S20.** Spin densities of the calculated (B97-D3/RI-JCOSX/def2-TZVP) minimum structures  $1\text{H}_{\text{calc}}$  (left) and  $1\text{H}'_{\text{calc}}$  (right).

**Table S9:** Selected results of the Mulliken spin density analysis of the calculated (B97-D3/RI-JCOSX/def2-TZVP) minimum structures  $1\text{H}_{\text{calc}}$  and  $1\text{H}'_{\text{calc}}$ . For numbering of the atoms see Figure S15.

	Si1	C1	N1	N2	H	Si2	C2	N3	N4
$1\text{H}_{\text{calc}}$	0.09	0.10	0.04	0.03	0.00	0.37	0.17	0.05	0.07
$1\text{H}'_{\text{calc}}$	0.06	0.16	0.06	0.05	0.01	0.29	0.18	0.05	0.07



## 8.4 Comparison of experimental and calculated EPR parameters

**Table S10:** Comparison of selected calculated (B97-D3/RI-JCOSX/def2-TZVP) EPR parameters of  $1\mathbf{H}_{\text{calc}}$  and  $1\mathbf{H}'_{\text{calc}}$  with the experimentally determined values of  $1\mathbf{H}$ . For numbering of the atoms see Figure S15.

	$a(\text{Si1})$ [mT]	$a(\text{Si2})$ [mT]	$a(\text{N1})$ [mT]	$a(\text{N2})$ [mT]	$a(\text{N3})$ [mT]	$a(\text{N4})$ [mT]	$a(\text{H})$ [mT]	$g_{\text{iso}}$
$1\mathbf{H}_{\text{calc}}$	-1.314	-1.811	0.039	0.044	0.078	0.156	0.003	2.00483
$1\mathbf{H}'_{\text{calc}}$	-0.485	-1.380	0.065	0.092	0.093	0.100	-0.482	2.00454
$1\mathbf{H}^{[a]}$	0.431	1.725	0.099		0.246		0.607	2.00538

[a]: Experimental data given in *n*-hexane at 298 K. The absolute signs of the hyperfine coupling constants could not be determined experimentally.

## 8.5 Results of the natural bond order (NBO) calculations

The natural bond orbital (NBO) analysis of  $1\mathbf{H}_{\text{calc}}$  were carried out at the B3LYP/6-311G\*\*/6-31G\* level of theory. For comparison reasons, the NBO analysis of  $1\mathbf{H}'_{\text{calc}}$  was also carried out. Selected results of the NBO are summarized in Tables S11 and S12. The partial charges obtained by natural population analysis (NPA) are summarized in Table S13.

**Table S11:** Selected results of the natural bond orbital (NBO) analysis of  $1\mathbf{H}'_{\text{calc}}$  (B3LYP/6-311G\*\*/6-31G\*). For numbering of the atoms see Figure S14.<sup>[a]</sup>

	occ.	pol. [%]	hyb.	WBI
$\sigma(\text{Si1-Si2})$	1.94	61.2 (Si1) 38.8 (Si2)	$sp^{1.23}$ (Si1) $sp^{5.59}$ (Si2)	1.6966
$\pi(\text{Si1-Si2})$	1.80	60.8 (Si1) 39.2 (Si2)	p (Si1) p (Si2)	
$\sigma(\text{Si1-H})$	1.98	43.7 (Si1) 56.3 (H)	$sp^{2.22}$ (Si1) s (H)	0.9212
$\sigma(\text{Si1-C1})$	1.97	25.3 (Si1) 74.7 (C1)	$sp^{3.06}$ (Si1) $sp^{1.27}$ (C1)	0.8626
$\sigma(\text{Si2-C2})$	1.95	20.7 (Si2) 79.3 (C2)	$sp^{7.98}$ (Si2) $sp^{1.25}$ (C2)	0.7392
n(Si2)	1.87		$sp^{0.34}$	

[a]: occ. = occupancy, pol. = polarization, hyb. = hybridization, WBI = Wiberg bond index.

**Table S12:** Selected results of the natural bond orbital (NBO) analysis of  $1\mathbf{H}_{\text{calc}}$  (B3LYP/6-311G\*\*/6-31G\*). For numbering of the atoms see Figure S14.<sup>[a]</sup>

	$\alpha$ -spin			$\beta$ -spin			WBI
	occ.	pol. [%]	hyb.	occ.	pol. [%]	hyb.	
$\sigma(\text{Si1-Si2})$	0.97	58.9 (Si1) 41.1 (Si2)	$\text{sp}^{1.47}$ (Si1) $\text{sp}^{6.03}$ (Si2)	0.98	62.9 (Si1) 37.1 (Si2)	$\text{sp}^{1.28}$ (Si1) $\text{sp}^{6.87}$ (Si2)	1.1744
$\pi(\text{Si1-Si2})$	–	–	–	0.82	71.7 (Si1) 28.4 (Si2)	$\text{sp}^{32.05}$ (Si1) $\text{sp}^{34.08}$ (Si2)	
$\sigma(\text{Si1-H})$	0.99	41.6 (Si1) 58.6 (H)	$\text{sp}^{2.50}$ (Si1) s (H)	0.99	42.0 (Si1) 58.0 (H)	$\text{sp}^{2.36}$ (Si1) s (H)	0.8994
$\sigma(\text{Si1-C1})$	0.97	27.5 (Si1) 72.5 (C1)	$\text{sp}^{2.47}$ (Si1) $\text{sp}^{1.43}$ (C1)	0.98	24.1 (Si1) 75.9 (C1)	$\text{sp}^{3.15}$ (Si1) $\text{sp}^{1.13}$ (C1)	1.0114
$\pi(\text{Si1-C1})$	0.94	56.1 (Si1) 43.9 (C1)	$\text{sp}^{32.81}$ (Si1) $\text{sp}^{15.18}$ (C1)	–	–	–	
$\sigma(\text{Si2-C2})$	0.98	21.1 (Si2) 78.9 (C2)	$\text{sp}^{6.31}$ (Si2) $\text{sp}^{1.08}$ (C2)	0.98	21.0 (Si2) 79.0 (C2)	$\text{sp}^{5.46}$ (Si2) $\text{sp}^{1.08}$ (C2)	0.9475
$\pi(\text{Si2-C2})$	0.96	52.7 (Si2) 47.3 (C2)	p (Si2) p (C2)	–	–	–	
n(Si2)	0.95		$\text{sp}^{0.36}$	0.95		$\text{sp}^{0.42}$	

[a]: occ. = occupancy, pol. = polarization, hyb. = hybridization, WBI = Wiberg bond index.

**Table S13:** Comparison of selected partial charges [e] obtained by natural population analysis (NPA) of  $1\mathbf{H}^+$  and  $1\mathbf{H}_{\text{calc}}$  (B3LYP/6-311G\*\*/6-31G\*). For numbering of the atoms see Figure S14.

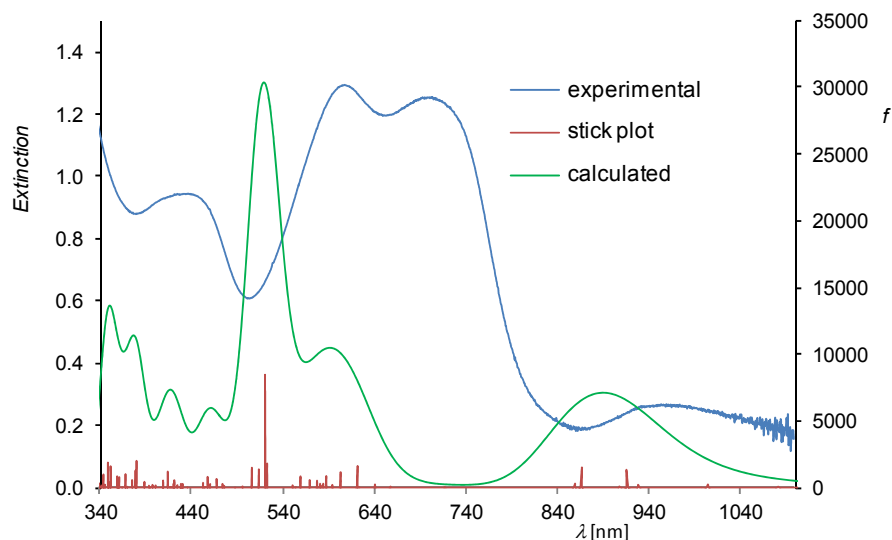
	Si1	Si2	H	C1	C2	$\Sigma(\text{NHC1 ring})^{[a]}$	$\Sigma(\text{NHC2 ring})^{[a]}$	$\Sigma(\text{NHC1})^{[b]}$	$\Sigma(\text{NHC2})^{[b]}$
$1\mathbf{H}^+$	0.27	0.21	-0.14	0.09	0.07	-0.22	-0.28	0.36	0.30
$1\mathbf{H}_{\text{calc}}$	0.14	0.03	-0.18	0.03	-0.04	-0.45	-0.53	0.05	-0.04

[a]:  $\Sigma(\text{NHC1 ring})$  and  $\Sigma(\text{NHC2 ring})$  are the sums of the partial charges of the heterocyclic ring atoms of the NHC substituents bonded to Si1 and Si2, respectively. [b]:  $\Sigma(\text{NHC1})$  and  $\Sigma(\text{NHC2})$  are the sums of the partial charges of all atoms of the NHC substituents bonded to Si1 and Si2, respectively.

## 8.6 Results of the TdDFT calculations

The electronic absorption spectrum of  $1\mathbf{H}$  was analyzed by time-dependent density functional theory (TdDFT). The first 75 dipole-allowed electronic excitations of  $1\mathbf{H}_{\text{calc}}$  were calculated at the B97-D3/RI-JCOSX/def2-TZVP level of theory. The calculated spectrum was simulated by convolution of the oscillator strengths with Gaussian functions applying a value of  $1500\text{ cm}^{-1}$  for the full linewidth at half maximum (FWHM), before the spectrum was converted to the nm scale for comparison with the experimental spectrum.

A comparison of the experimental UV-Vis-NIR spectrum of  $1\mathbf{H}$  with the simulated spectrum of  $1\mathbf{H}_{\text{calc}}$  and a stick plot of the oscillator strengths of the simulated spectrum is depicted in Figure S21. An overview of the calculated energies and assignments of the first electronic transition at 1295 nm and those electronic transitions of  $1\mathbf{H}_{\text{calc}}$ , which display a relative oscillator strength of >10 % with respect to the electronic transition with the highest oscillator strength at 521 nm, is given in Table S14. Selected  $\alpha$ - and  $\beta$ -spin Kohn-Sham orbitals of  $1\mathbf{H}_{\text{calc}}$  are depicted in Figures S22 and S23.

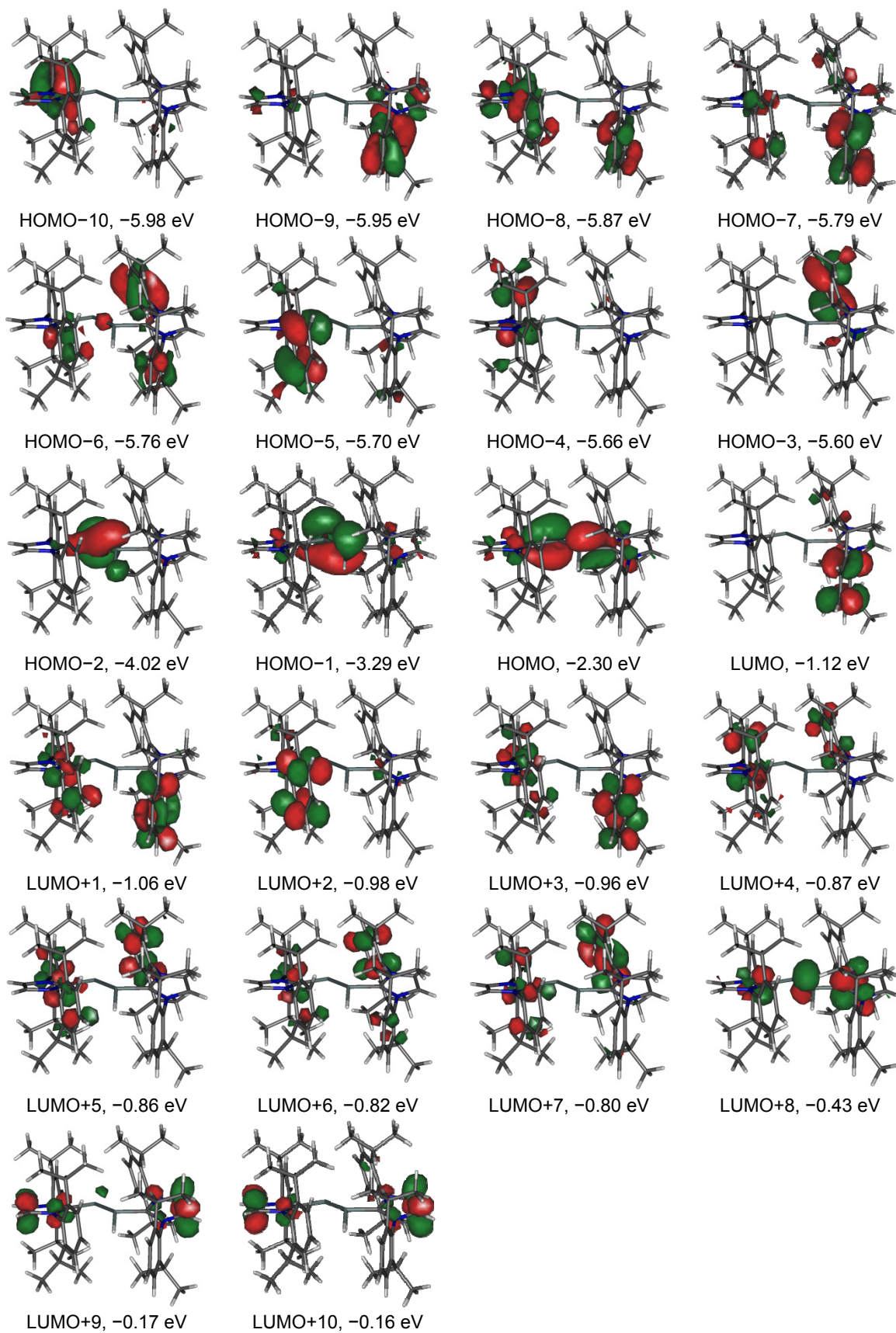


**Figure S21.** Experimental UV-Vis-NIR spectrum ( $c = 360 \mu\text{mol}$ ,  $d = 5 \text{ mm}$ , blue curve), calculated spectrum (green curve) and stick plot of the oscillator strengths (red curve) of  $1\mathbf{H}_{\text{calc}}$ ;  $f$  is the oscillator strength.

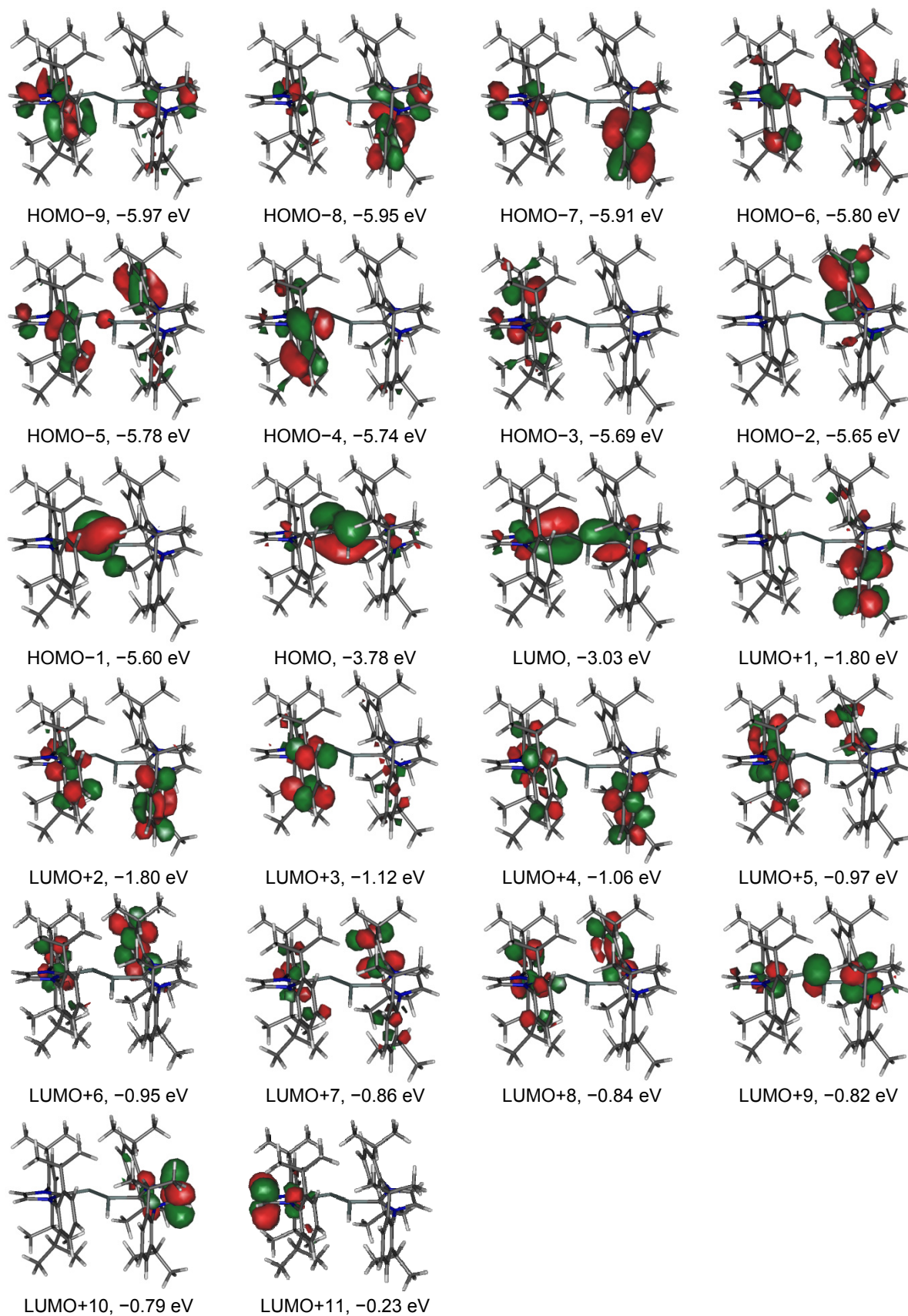
**Table S14:** Calculated energies and assignments of the electronic transitions of  $1\mathbf{H}_{\text{calc}}$ .<sup>[a]</sup>

Excited state	$\lambda$ [nm]	MO contributions <sup>[b]</sup>	Contribution [%]	$f$	$f_{\text{rel}}$ [%]
1	1295	HOMO( $\alpha$ ) $\rightarrow$ LUMO( $\alpha$ )	100	0.0004	0.3
5	916	HOMO( $\alpha$ ) $\rightarrow$ LUMO+2( $\alpha$ )	27	0.0215	15.8
		HOMO( $\alpha$ ) $\rightarrow$ LUMO+5( $\alpha$ )	20		
		HOMO( $\beta$ ) $\rightarrow$ LUMO( $\beta$ )	41		
8	868	HOMO( $\alpha$ ) $\rightarrow$ LUMO+5( $\alpha$ )	48	0.0242	17.8
		HOMO( $\alpha$ ) $\rightarrow$ LUMO+6( $\alpha$ )	29		
		HOMO( $\beta$ ) $\rightarrow$ LUMO( $\beta$ )	11		
13	622	HOMO-1( $\beta$ ) $\rightarrow$ LUMO( $\beta$ )	28	0.0261	19.1
		HOMO( $\beta$ ) $\rightarrow$ LUMO+3( $\beta$ )	54		
16	604	HOMO( $\alpha$ ) $\rightarrow$ LUMO+10( $\alpha$ )	50	0.0185	13.6
		HOMO( $\beta$ ) $\rightarrow$ LUMO+3( $\beta$ )	11		
26	521	HOMO-1( $\alpha$ ) $\rightarrow$ LUMO+2( $\alpha$ )	12	0.1361	1.00
		HOMO-1( $\alpha$ ) $\rightarrow$ LUMO+4( $\alpha$ )	13		
		HOMO( $\alpha$ ) $\rightarrow$ LUMO+8( $\alpha$ )	13		
		HOMO( $\alpha$ ) $\rightarrow$ LUMO+11( $\alpha$ )	25		
28	523	HOMO-1( $\alpha$ ) $\rightarrow$ LUMO+4( $\alpha$ )	15	0.0289	21.3
		HOMO-1( $\alpha$ ) $\rightarrow$ LUMO+5( $\alpha$ )	66		
29	514	HOMO-1( $\alpha$ ) $\rightarrow$ LUMO+6( $\alpha$ )	87	0.0219	16.1
30	507	HOMO-1( $\alpha$ ) $\rightarrow$ LUMO+7( $\alpha$ )	88	0.0240	17.6
56	415	HOMO-1( $\alpha$ ) $\rightarrow$ LUMO+9( $\alpha$ )	29	0.0192	14.1
		HOMO-1( $\alpha$ ) $\rightarrow$ LUMO+10( $\alpha$ )	20		
		HOMO-1( $\alpha$ ) $\rightarrow$ LUMO+11( $\alpha$ )	27		
59	380	HOMO( $\alpha$ ) $\rightarrow$ LUMO+18( $\alpha$ )	47	0.0322	23.7
60	379	HOMO( $\alpha$ ) $\rightarrow$ LUMO+18( $\alpha$ )	49	0.0206	15.1
62	368	HOMO( $\beta$ ) $\rightarrow$ LUMO+13( $\beta$ )	47	0.0161	11.9
68	352	HOMO( $\alpha$ ) $\rightarrow$ LUMO+22( $\alpha$ )	11	0.0257	18.9
		HOMO( $\alpha$ ) $\rightarrow$ LUMO+22( $\alpha$ )	12		
		HOMO( $\alpha$ ) $\rightarrow$ LUMO+23( $\alpha$ )	27		
69	349	HOMO( $\alpha$ ) $\rightarrow$ LUMO+23( $\alpha$ )	68	0.0301	22.1
71	344	HOMO( $\alpha$ ) $\rightarrow$ LUMO+12( $\alpha$ )	73	0.0158	11.6

[a]:  $\lambda$  is the wavelength of the excitation;  $f$  is the oscillator strength of the electronic transition;  $f_{\text{rel}}$  is the relative oscillator strength of the electronic transition with respect to the electronic transition with the highest oscillator strength at 521 nm. [b]: Only MO contributions  $>10\%$  are given.

$\alpha$ -Spin orbitals

**Figure S22.** Selected  $\alpha$ -spin Kohn-Sham orbitals of  $1\mathbf{H}_{\text{catc}}$  and their energy eigenvalues; isosurface value:  $0.04 \text{ e bohr}^{-3}$ .

$\beta$ -Spin orbitals

**Figure S23.** Selected  $\beta$ -spin Kohn-Sham orbitals of  $1\mathbf{H}_{\text{catc}}$  and their energy eigenvalues; isosurface value:  $0.04 \text{ e bohr}^{-3}$ .



## 8.7 Results of the CASSCF calculations

To find out whether a multiconfigurational wavefunction is necessary to describe compound **1H**, second-order Møller-Plesset (MP2) calculations<sup>[S18]</sup> were performed for **1H<sub>calc</sub>** to determine the relevant orbitals for a complete active space self-consistent field (CASSCF) calculation.<sup>[S19]</sup> This led to a CASSCF(7,8)/def2-TZVP calculation, which did not converge due to the presence of statically non-correlated orbitals. Successive removal of those orbitals from the active space gave rise to a CASSCF(3,3)/def2-TZVP calculation, which converged. The occupancies of the thereby derived CASSCF(3,3) orbitals (Figure S24) suggest, that static correlation effects can be neglected in the electronic description of **1H<sub>calc</sub>**. The overall wavefunction is described by a major contribution (96 %) from the electronic ground state configuration [2-1-0] and three minor contributions of electronically excited states with the configurations [0-1-2] (3 %), [1-1-1] (0.5 %) and [1-0-2] (0.5%), respectively. These results suggest that DFT methods are sufficient to analyse the electronic structure of compound **1H**.

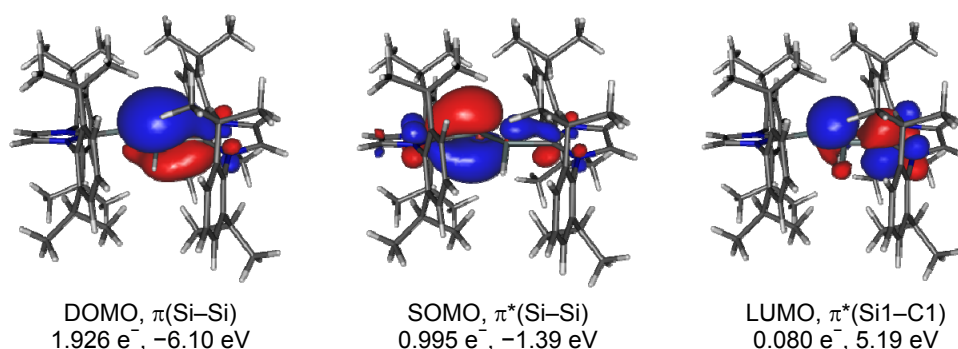


**Figure S24.** CASSCF(3,3)/def2-TZVP orbitals with their occupancies and energy eigenvalues of **1H<sub>calc</sub>**; iso surface value = 0.04  $e \text{ bohr}^{-3}$ ; DOMO = doubly occupied molecular orbital, SOMO = singly occupied molecular orbital, LUMO = lowest unoccupied molecular orbital.

## 8.8 Cartesian coordinates [Å] and SCF energies of the calculated structures

$1\text{H}^+$  <sub>calc</sub> (B3LYP/6-311G\*\*/6-31G\*)

Energy = -2899.60322742  $E_H$

Si	-1.190858	-0.283179	0.744687
N	-2.491430	2.215713	-0.391399
N	-3.280963	0.374417	-1.212966
C	-2.270707	0.867969	-0.437485
C	-3.620174	2.547879	-1.127105
H	-3.962835	3.566987	-1.204148
C	-4.112149	1.395625	-1.644525
H	-4.967042	1.202576	-2.272834
C	-1.734498	3.204580	0.354005
C	-2.082960	3.434513	1.701136
C	-1.367901	4.425697	2.385629
H	-1.605656	4.632748	3.424188
C	-0.371533	5.161952	1.752556
H	0.165447	5.930352	2.301726
C	-0.072631	4.931568	0.411841
H	0.691640	5.530960	-0.071886
C	-0.747561	3.950364	-0.324985
C	-3.238521	2.715701	2.394097
H	-3.520357	1.849760	1.786060
C	-4.471161	3.641556	2.478739
H	-4.256787	4.527199	3.087775
H	-5.314384	3.113318	2.938027
H	-4.787593	3.987859	1.488462
C	-2.864317	2.179812	3.787627
H	-1.992514	1.520157	3.739886
H	-3.701267	1.606877	4.202088
H	-2.643579	2.988573	4.492982
C	-0.454160	3.770409	-1.813366
H	-0.809941	2.777606	-2.111605
C	1.046778	3.838318	-2.148655
H	1.447122	4.849620	-2.016588
H	1.204145	3.565444	-3.198003
H	1.635265	3.155807	-1.529310
C	-1.223639	4.816512	-2.650269
H	-2.305582	4.756344	-2.494152
H	-1.029948	4.667691	-3.718666
H	-0.906397	5.832386	-2.388228
C	-3.515605	-1.021078	-1.531623
C	-4.328956	-1.780133	-0.663672
C	-4.579124	-3.109831	-1.024960
H	-5.201861	-3.726214	-0.384117
C	-4.058619	-3.649919	-2.197441
H	-4.273577	-4.681963	-2.460153
C	-3.275868	-2.867846	-3.042926
H	-2.891906	-3.297393	-3.962867
C	-2.985587	-1.533484	-2.733853
C	-4.978819	-1.201127	0.590537
H	-4.538070	-0.217784	0.784280
C	-4.720365	-2.061899	1.841113
H	-5.186542	-3.050272	1.759606
H	-5.147714	-1.572246	2.723487
H	-3.647898	-2.198838	2.012513
C	-6.491385	-0.990786	0.366999
H	-6.685694	-0.335056	-0.489320
H	-6.948668	-0.535932	1.252977
H	-6.999809	-1.943047	0.178235
C	-2.178986	-0.682131	-3.710215
H	-1.887109	0.241782	-3.199385
C	-0.881785	-1.374186	-4.165439
H	-0.261399	-1.660048	-3.309655
H	-0.300500	-0.694454	-4.798505
H	-1.083377	-2.274487	-4.756661

C	-3.040799	-0.287915	-4.928709
H	-3.360707	-1.174703	-5.487729
H	-2.469186	0.351940	-5.610616
H	-3.942425	0.257907	-4.629147
Si	0.762809	0.012569	-0.243010
H	1.256633	0.737380	-1.436521
N	2.365855	-1.951120	1.269096
N	3.585879	-0.689365	-0.011943
C	2.293490	-0.917545	0.378593
C	3.679293	-2.360817	1.423668
H	3.940664	-3.168499	2.088446
C	4.441175	-1.573750	0.623690
H	5.505121	-1.549616	0.450296
C	1.267367	-2.560256	1.993183
C	0.602403	-3.656113	1.405626
C	-0.417517	-4.255516	2.153499
H	-0.952367	-5.104350	1.739530
C	-0.748427	-3.790742	3.424099
H	-1.540361	-4.276138	3.987653
C	-0.058360	-2.718878	3.982963
H	-0.315315	-2.380663	4.982064
C	0.971369	-2.076481	3.284305
C	0.997548	-4.229215	0.047644
H	1.643689	-3.501151	-0.454425
C	1.813017	-5.527740	0.225913
H	1.216261	-6.301969	0.721475
H	2.128454	-5.918108	-0.748395
H	2.711539	-5.363308	0.831399
C	-0.212692	-4.465608	-0.873246
H	-0.801271	-3.552262	-1.000854
H	0.130954	-4.794586	-1.860645
H	-0.876750	-5.245778	-0.484632
C	1.760245	-0.951965	3.950642
H	2.418916	-0.502643	3.199878
C	0.854195	0.173504	4.481818
H	0.191418	-0.178198	5.280403
H	1.466901	0.981899	4.896728
H	0.233775	0.589145	3.681608
C	2.657048	-1.511115	5.075477
H	3.343497	-2.280189	4.703373
H	3.256359	-0.708717	5.520302
H	2.055477	-1.961913	5.872848
C	4.064131	0.364401	-0.887068
C	4.219793	0.083318	-2.259504
C	4.732160	1.107030	-3.065672
H	4.870628	0.930611	-4.127544
C	5.076308	2.344692	-2.528025
H	5.475267	3.122366	-3.173188
C	4.923901	2.584670	-1.165325
H	5.213173	3.548143	-0.756903
C	4.418987	1.599580	-0.306731
C	3.904495	-1.283348	-2.861424
H	3.300558	-1.842917	-2.138657
C	3.080116	-1.184722	-4.157671
H	3.648966	-0.720132	-4.970565
H	2.794114	-2.187431	-4.494212
H	2.166084	-0.602012	-4.006349
C	5.202240	-2.083957	-3.102301
H	5.774658	-2.218949	-2.177784
H	4.970281	-3.076856	-3.503849
H	5.850901	-1.572234	-3.822399
C	4.332203	1.872798	1.193058
H	3.806924	1.037069	1.666793
C	3.530625	3.147716	1.515061
H	2.515583	3.098463	1.108304
H	3.454531	3.275347	2.600794
H	4.015917	4.044489	1.113572
C	5.743513	1.940026	1.814152
H	6.322219	2.770314	1.393874



H 5.676506 2.092265 2.897281  
H 6.308533 1.018171 1.635721

**1H<sub>calc</sub>** (B3LYP/6-311G\*\*/6-31G\*)

Energy = -2899.72620651  $E_H$

Si	1.199453	0.444432	-0.176644
N	-0.089119	2.159375	-2.413457
N	2.088614	2.190880	-2.246855
C	0.954666	1.608877	-1.666670
C	0.397067	3.027448	-3.387481
H	-0.267485	3.542711	-4.062602
C	1.744794	3.042889	-3.283384
H	2.494129	3.576824	-3.846333
C	-1.499552	1.881830	-2.323780
C	-2.041939	0.878822	-3.153521
C	-3.432362	0.712899	-3.149618
H	-3.880692	-0.051348	-3.777535
C	-4.249144	1.514136	-2.357642
H	-5.326835	1.372824	-2.373145
C	-3.689481	2.496925	-1.544744
H	-4.339215	3.115273	-0.933226
C	-2.305052	2.702686	-1.506167
C	-1.173349	0.021188	-4.069066
H	-0.130414	0.164946	-3.771718
C	-1.309264	0.470344	-5.538671
H	-2.342010	0.360269	-5.891141
H	-0.666167	-0.137633	-6.186465
H	-1.021830	1.519740	-5.667718
C	-1.479182	-1.480577	-3.927275
H	-1.403299	-1.795191	-2.882497
H	-0.765599	-2.065800	-4.519626
H	-2.484857	-1.730131	-4.285860
C	-1.711482	3.818843	-0.651563
H	-0.651063	3.591639	-0.503417
C	-2.351981	3.907753	0.744196
H	-3.394744	4.244774	0.698535
H	-1.804922	4.633025	1.357872
H	-2.321729	2.937849	1.249932
C	-1.809629	5.176719	-1.378853
H	-1.284034	5.161015	-2.339711
H	-1.367432	5.972464	-0.767040
H	-2.856208	5.442193	-1.572400
C	3.458633	1.975554	-1.855921
C	4.199197	0.966805	-2.505002
C	5.554768	0.841826	-2.177001
H	6.152088	0.076003	-2.664088
C	6.149506	1.683835	-1.241629
H	7.204343	1.572084	-1.003621
C	5.395139	2.670582	-0.612034
H	5.869015	3.323666	0.115360
C	4.035953	2.838222	-0.901140
C	3.581546	0.042018	-3.548667
H	2.507513	0.246074	-3.584130
C	3.744892	-1.440816	-3.167179
H	4.799177	-1.742056	-3.142704
H	3.235594	-2.078167	-3.900235
H	3.309947	-1.635052	-2.181886
C	4.155213	0.321085	-4.952509
H	3.997411	1.364147	-5.250286
H	3.672166	-0.320952	-5.698899
H	5.233364	0.123816	-4.989759
C	3.239873	3.944940	-0.216982
H	2.183538	3.792842	-0.456437
C	3.363829	3.888674	1.316799
H	3.056303	2.909642	1.696604
H	2.720327	4.651896	1.771307
H	4.389947	4.084743	1.651227

C	3.649315	5.331508	-0.754314
H	4.705049	5.542866	-0.544626
H	3.049509	6.118774	-0.281778
H	3.504517	5.401490	-1.838605
Si	-0.966928	-0.239807	0.378594
H	-1.925594	-0.878399	-0.576650
N	-0.209559	-1.648646	2.881162
N	-1.955543	-2.527197	1.908404
C	-0.970334	-1.561451	1.722234
C	-0.730013	-2.609461	3.743746
H	-0.270251	-2.810029	4.698121
C	-1.810656	-3.152105	3.143304
H	-2.490786	-3.924927	3.464587
C	0.998522	-0.929271	3.203997
C	0.896202	0.304384	3.877891
C	2.086279	0.931057	4.265913
H	2.043345	1.881582	4.789124
C	3.324208	0.352744	3.998327
H	4.236114	0.855594	4.310050
C	3.397124	-0.867986	3.334532
H	4.368771	-1.307390	3.129766
C	2.239314	-1.536957	2.920986
C	-0.451813	0.925285	4.231406
H	-1.214586	0.444264	3.611836
C	-0.804352	0.660822	5.710007
H	-0.061258	1.111691	6.379104
H	-1.783479	1.090405	5.954824
H	-0.843126	-0.412359	5.929005
C	-0.508336	2.429336	3.914094
H	-0.232307	2.614840	2.871657
H	-1.525698	2.806104	4.071765
H	0.158990	3.013147	4.559495
C	2.347069	-2.893854	2.231253
H	1.364291	-3.136349	1.815577
C	3.343084	-2.880639	1.057433
H	4.373901	-2.727879	1.398513
H	3.311893	-3.842229	0.530714
H	3.095874	-2.084105	0.348879
C	2.711444	-3.998787	3.244843
H	1.972386	-4.069613	4.050915
H	2.762204	-4.974777	2.747004
H	3.688251	-3.805009	3.704251
C	-2.979368	-2.916830	0.974314
C	-4.247559	-2.308822	1.061658
C	-5.246913	-2.763876	0.192318
H	-6.236318	-2.317729	0.238428
C	-4.994201	-3.779584	-0.725511
H	-5.784354	-4.119342	-1.390357
C	-3.732513	-4.365773	-0.789762
H	-3.549814	-5.163862	-1.503754
C	-2.697841	-3.950701	0.057114
C	-4.558082	-1.220920	2.085297
H	-3.612185	-0.904828	2.534986
C	-5.186725	0.026955	1.439491
H	-6.170614	-0.189006	1.005181
H	-5.326558	0.808392	2.196054
H	-4.541795	0.425951	0.650850
C	-5.454255	-1.769270	3.214704
H	-4.986289	-2.621065	3.721529
H	-5.644295	-0.992472	3.965052
H	-6.423315	-2.104652	2.825634
C	-1.339910	-4.644611	0.005342
H	-0.643220	-4.062724	0.615237
C	-0.753881	-4.694872	-1.416448
H	-0.666780	-3.690285	-1.840039
H	0.246939	-5.142135	-1.393230
H	-1.368222	-5.300431	-2.093545
C	-1.425252	-6.059516	0.614668
H	-2.108947	-6.697347	0.041360

H	-0.438552	-6.537939	0.613424
H	-1.785394	-6.029822	1.649263

**1H<sub>calc</sub>** (B97-D3/RI-JCOSX/def2-TZVP)

Energy = -2899.073301627194  $E_H$

Si	7.654838	-6.199433	-0.025952
N	6.388366	-4.661857	-2.359323
N	8.546243	-4.502400	-2.116923
C	7.430271	-5.138075	-1.566646
C	6.850091	-3.766734	-3.320510
H	6.181300	-3.306553	-4.030209
C	8.194306	-3.668587	-3.165039
H	8.930343	-3.087205	-3.697162
C	5.049059	-5.163630	-2.350884
C	4.740468	-6.249427	-3.187775
C	3.420458	-6.714838	-3.181287
H	3.152294	-7.573400	-3.790878
C	2.449594	-6.096506	-2.399463
H	1.429607	-6.471980	-2.408414
C	2.782105	-5.012548	-1.591075
H	2.014807	-4.536748	-0.989313
C	4.096281	-4.539772	-1.526776
C	5.795862	-6.919171	-4.051809
H	6.709680	-6.322819	-3.986846
C	5.383393	-6.956599	-5.531283
H	4.499609	-7.585548	-5.685298
H	6.196195	-7.368297	-6.140517
H	5.151486	-5.952319	-5.902853
C	6.137056	-8.320293	-3.522643
H	6.499753	-8.261023	-2.492887
H	6.915248	-8.782052	-4.142635
H	5.257651	-8.973573	-3.534769
C	4.486426	-3.380091	-0.625791
H	5.558349	-3.481120	-0.423057
C	3.770562	-3.413460	0.729555
H	2.696590	-3.216844	0.632248
H	4.188617	-2.644069	1.388119
H	3.907394	-4.388714	1.208755
C	4.260448	-2.035060	-1.339310
H	4.830288	-1.979083	-2.271173
H	4.573886	-1.203070	-0.697223
H	3.199075	-1.899143	-1.578976
C	9.888206	-4.713330	-1.662476
C	10.610940	-5.799981	-2.190362
C	11.934992	-5.957482	-1.772114
H	12.524985	-6.781796	-2.160544
C	12.505213	-5.076229	-0.853875
H	13.536652	-5.216255	-0.539534
C	11.756997	-4.028121	-0.327787
H	12.206513	-3.360494	0.402399
C	10.426879	-3.828408	-0.715826
C	9.969630	-6.754121	-3.184419
H	8.891991	-6.726332	-2.999766
C	10.414514	-8.208944	-2.991410
H	11.464695	-8.357156	-3.269126
H	9.811314	-8.868605	-3.624021
H	10.285411	-8.521436	-1.951608
C	10.212388	-6.292917	-4.632092
H	9.831884	-5.280013	-4.799428
H	9.707073	-6.963969	-5.336485
H	11.283969	-6.294821	-4.863826
C	9.598696	-2.713988	-0.101074
H	8.577534	-2.811450	-0.482166
C	9.519051	-2.864763	1.425458
H	9.141193	-3.857835	1.683052
H	8.839809	-2.114118	1.846497
H	10.500810	-2.733736	1.896025

C	10.122833	-1.329256	-0.514004
H	11.143140	-1.167384	-0.146814
H	9.486274	-0.539895	-0.098131
H	10.137686	-1.221686	-1.604571
Si	5.516655	-6.982091	0.352548
H	4.519660	-7.591122	-0.579631
N	6.289169	-8.343091	2.844997
N	4.449627	-9.144619	1.991794
C	5.469324	-8.231457	1.730735
C	5.795884	-9.286446	3.738734
H	6.313520	-9.511798	4.656934
C	4.654345	-9.787208	3.208758
H	3.970648	-10.537457	3.571127
C	7.555711	-7.692051	3.006236
C	7.588400	-6.403547	3.565243
C	8.842171	-5.815646	3.755455
H	8.907010	-4.822084	4.186830
C	10.006456	-6.474521	3.370418
H	10.970883	-5.991571	3.506083
C	9.940605	-7.734935	2.785735
H	10.854239	-8.224518	2.461270
C	8.710924	-8.371428	2.587837
C	6.311689	-5.681330	3.959774
H	5.485183	-6.166663	3.430363
C	6.053194	-5.818771	5.469633
H	6.855683	-5.345178	6.047682
H	5.106931	-5.337019	5.744750
H	5.999640	-6.871695	5.766684
C	6.314317	-4.211873	3.519282
H	6.509229	-4.138505	2.444676
H	5.338474	-3.758155	3.726849
H	7.071238	-3.626044	4.051787
C	8.643531	-9.737290	1.924784
H	7.589535	-9.976368	1.756352
C	9.320410	-9.726848	0.546706
H	10.396211	-9.534572	0.627817
H	9.188492	-10.695588	0.049632
H	8.879470	-8.944464	-0.079149
C	9.227192	-10.826447	2.839738
H	8.701970	-10.857063	3.800228
H	9.140135	-11.812987	2.368098
H	10.288420	-10.641788	3.042690
C	3.383449	-9.435528	1.081572
C	2.237274	-8.620312	1.108760
C	1.241342	-8.877431	0.162607
H	0.345277	-8.264680	0.142337
C	1.388950	-9.904383	-0.768102
H	0.608282	-10.081506	-1.504585
C	2.523788	-10.709877	-0.756545
H	2.617396	-11.511539	-1.483556
C	3.546813	-10.496699	0.174805
C	2.093001	-7.527814	2.155817
H	3.101528	-7.157703	2.374007
C	1.267256	-6.330065	1.676976
H	0.205019	-6.581897	1.573110
H	1.339879	-5.512770	2.402933
H	1.634227	-5.965839	0.715807
C	1.501584	-8.101834	3.457643
H	2.113761	-8.917826	3.852976
H	1.439336	-7.321113	4.224973
H	0.491042	-8.488618	3.280470
C	4.798846	-11.359739	0.180905
H	5.285919	-11.226918	1.152460
C	5.795456	-10.893673	-0.892632
H	6.081729	-9.851279	-0.731460
H	6.700961	-11.510127	-0.866447
H	5.353256	-10.975409	-1.891844
C	4.482984	-12.855451	0.037583
H	4.094657	-13.097376	-0.957982

H 5.395230 -13.444813 0.181713  
 H 3.742109 -13.179581 0.777065

**1H'**<sub>calc</sub> (B97-D3/RI-JCOSX/def2-TZVP)

Energy = -2899.071227022923  $E_H$

Si	7.24284079667758	-6.25759931729236	-0.15224872866755
N	6.56785820632848	-4.90435577141306	-2.66043268322727
N	8.63483037991219	-4.53754749677159	-2.04236692603339
C	7.47993878892924	-5.22821439160652	-1.66023894833314
C	7.13324303226881	-4.04178286063014	-3.59247680500000
H	6.56974460770708	-3.68928979907850	-4.44121487459585
C	8.41003261722604	-3.80694697732009	-3.20674143499767
H	9.18031326625249	-3.18909341353486	-3.63824387965522
C	5.19624358424609	-5.31081822176705	-2.67427409918952
C	4.83388738782835	-6.44086250787783	-3.42306178012880
C	3.48344495793786	-6.80627132597069	-3.42738425234940
H	3.16901433805843	-7.68732594052281	-3.97953646681351
C	2.54289545628570	-6.07104785762583	-2.71379852335084
H	1.49964530703393	-6.37738386311601	-2.72013056588592
C	2.93277207548839	-4.95827280773812	-1.97258707204375
H	2.18933803655296	-4.40032451569761	-1.41174282457253
C	4.27202732945944	-4.56350718854963	-1.92171232092613
C	5.86333264537370	-7.25398528862655	-4.18789925914624
H	6.84594074072010	-6.81470193566439	-3.98951572677722
C	5.61815414804214	-7.17744265255827	-5.70311371944866
H	4.64968513780582	-7.61772860037698	-5.96734185107652
H	6.39647722416001	-7.72471421960759	-6.24710822544377
H	5.61962611875700	-6.13832977599925	-6.05160924827623
C	5.91303823569734	-8.70716679733646	-3.69403657740429
H	6.09034148898321	-8.73100488867555	-2.61418580631602
H	6.71907918949137	-9.25217317269684	-4.19917256471793
H	4.97305926324071	-9.23458371790065	-3.89498040612507
C	4.71254679568822	-3.36422203387089	-1.09964399541824
H	5.79432459659870	-3.44405687090341	-0.96209130877717
C	4.09550808831894	-3.35480973091924	0.30458916213341
H	3.01476023827150	-3.17577783793008	0.27485718062570
H	4.54873984455204	-2.55695523248560	0.90369373648133
H	4.27671082015067	-4.31073683213512	0.80594099327836
C	4.43148800031326	-2.05186857452690	-1.85132765029848
H	4.93018686074739	-2.04212821989335	-2.82536348756346
H	4.79405078315680	-1.19299597189591	-1.27323996892792
H	3.35597006411880	-1.92055443498368	-2.01837522976326
C	9.79372307585192	-4.39825478761720	-1.21590898668182
C	10.79731775271876	-5.38170593645867	-1.28023061640072
C	11.90566261098352	-5.22639108695261	-0.44371072576300
H	12.69910662603874	-5.96712855784844	-0.45992200377493
C	12.00150422108925	-4.14013188458175	0.42559462404166
H	12.86913453377272	-4.04301285074961	1.074190333587723
C	10.99358154229108	-3.18398574410339	0.46854712984233
H	11.07828293384926	-2.34152283958516	1.15012859251786
C	9.86419290908491	-3.29352618897629	-0.35251203280886
C	10.66729815004146	-6.55070086022082	-2.24306535687051
H	9.60614594364779	-6.82967714907320	-2.25971105945763
C	11.46183494873901	-7.78601564641451	-1.81021982334873
H	12.54306031020305	-7.62763842503403	-1.90635236450606
H	11.19743250199187	-8.63876131022989	-2.44434797005555
H	11.24129422348666	-8.05059387712619	-0.77434653721464
C	11.07109048716098	-6.13622370808873	-3.67087302804850
H	10.45891073283519	-5.31018318383310	-4.04238689870360
H	10.95100028019503	-6.98100454796317	-4.35965841434956
H	12.12184356575520	-5.82333718020028	-3.69363124991325
C	8.77784122701269	-2.23149660121061	-0.31456758400957
H	7.96970744475487	-2.55321265476060	-0.97638408150987
C	8.16875570061137	-2.08019501185120	1.08578286221205
H	7.72766588898049	-3.02477904446839	1.40964227356356
H	7.38126907229787	-1.31708305220432	1.07590144053606
H	8.92036067403308	-1.77965426110847	1.82461237590621

C	9.30680212036382	-0.89000977000075	-0.85029119021336
H	10.11539834791870	-0.50392646091462	-0.21843267947747
H	8.50437704126491	-0.14364134161723	-0.86946362667228
H	9.699117711258149	-0.99843202473424	-1.86727464050174
Si	5.25695975788060	-7.38344500347915	0.01609088280842
N	6.39092698217206	-8.48796651268054	2.64847375120460
N	4.35465289068701	-9.06117583273656	2.12565895316225
C	5.43365740230146	-8.30468711962809	1.65260290604657
C	5.90970883736586	-9.29814521446793	3.67362393657312
H	6.51400637510049	-9.53670873816113	4.53424473935947
C	4.64377882836254	-9.65468752690905	3.34347556221222
H	3.92592588552627	-10.27795487940381	3.85250185613879
C	7.74402540557555	-8.03514675608683	2.58489294186375
C	8.11284623458814	-6.89620772702242	3.31775252559167
C	9.45432443472155	-6.49979344705967	3.26759907806709
H	9.76961197608749	-5.60871077164544	3.80298053379345
C	10.38465800255247	-7.22078002600352	2.52649553995566
H	11.41990963248868	-6.89195928655123	2.49154421751249
C	9.99068508144474	-8.34909598549486	1.81042268760489
H	10.72762878657600	-8.90320204208381	1.23794371319584
C	8.65918883679456	-8.77210018626613	1.80810898004214
C	7.09895074311203	-6.10467783128377	4.12532030639053
H	6.12373669355930	-6.58336937079350	3.99533273516688
C	7.43337068003091	-6.13408376011535	5.62504397078002
H	8.39792209455846	-5.65280637590128	5.82446904848165
H	6.66668536068956	-5.60235197886619	6.19992158461649
H	7.49144576835729	-7.16261505475294	5.99844191788823
C	6.97018264577916	-4.66739528333616	3.60278444287297
H	6.70400217579092	-4.67854955130757	2.54124081447917
H	6.19113638348105	-4.12752332486649	4.15308157990218
H	7.90967509676203	-4.11460889629902	3.71645288211944
C	8.21652314180758	-9.99906756649595	1.02889163369287
H	7.13606449602101	-9.91729949147301	0.88599452670458
C	8.82985800198394	-10.07101637734751	-0.37383892914016
H	9.91112117607412	-10.24491900415584	-0.34172569122540
H	8.37786309553574	-10.89796154423941	-0.93266547580175
H	8.63811305835808	-9.14374245347611	-0.92242516102436
C	8.49230024513285	-11.28246096958846	1.83104932630395
H	7.99730685709540	-11.25246089518629	2.80640150356925
H	8.12143382007077	-12.16025112847452	1.28845369740021
H	9.56801220414695	-11.41366373617432	1.99807365493587
C	3.18205516866119	-9.33757896295845	1.35104388270920
C	2.09296374734763	-8.45348151196517	1.42513204736161
C	0.95842952065884	-8.76079259277206	0.66742289637536
H	0.09575062637360	-8.10175952121634	0.70302912448450
C	0.92110779399643	-9.89696142565525	-0.13803242478953
H	0.03030959873962	-10.11687434993044	-0.72171734538270
C	2.01902355978118	-10.75006846233872	-0.20039279292054
H	1.98068266816251	-11.63163795372959	-0.83476179349325
C	3.17643919366299	-10.48560670556063	0.54032473583814
C	2.13732686874112	-7.22596945453531	2.31685041728311
H	3.19015088016847	-7.02217315906465	2.53611386033588
C	1.57609787890467	-5.97963251217427	1.62127343365851
H	0.49356122688557	-6.05011522371393	1.46652757662430
H	1.76537236025599	-5.09076085431621	2.23397168301534
H	2.06026884453763	-5.83872461661843	0.65137942218163
C	1.42043040999954	-7.50207230149995	3.65018779154208
H	1.87390406683970	-8.35244643015086	4.17129912290890
H	1.47784280747041	-6.62660717476665	4.30811212735339
H	0.36172398219008	-7.73413326528185	3.48281601502633
C	4.37693258603583	-11.41192162342030	0.45057284006164
H	5.15956405065947	-11.01098658525102	1.09965365946088
C	4.94698211286188	-11.44630744996560	-0.97575044162508
H	5.19203268839233	-10.43454355893215	-1.30807959418817
H	5.85759722050403	-12.05527778270178	-1.00712025409520
H	4.22737018333511	-11.87649581436818	-1.68214497783616
C	4.03814355864529	-12.82158602674468	0.96122747859494
H	3.27172395692488	-13.29532904403956	0.33696433308989
H	4.92983354863312	-13.45829280796384	0.94295576167323

H 3.66062400016499 -12.78714578856175 1.98912400960849  
H 8.57393076995685 -6.14934735656170 0.50576060641518

## 9. References

- [S1] M. I. Arz, M. Straßmann, D. Geiß, G. Schnakenburg, A. C. Filippou, *J. Am. Chem. Soc.* **2016**, *138*, 4589.
- [S2] a) K. Fredenhagen, G. Cadenbach, *Z. Anorg. Allg. Chem.* **1926**, *158*, 249; b) W. Rüdorff, E. Schulze, *Z. Anorg. Allg. Chem.* **1954**, *277*, 156.
- [S3] I. Chávez, A. Alvarez-Carena, E. Molins, A. Roig, W. Maniukiewicz, A. Arancibia, V. Arancibia, H. Brand, J. M. Manríquez, *J. Organomet. Chem.* **2000**, *601*, 126.
- [S4] C. H. Hamann, W. Vielstich, *Elektrochemie*, 3., vollständig überarbeitete Auflage, Wiley-VCH, Weinheim, **1998**.
- [S5] G. A. Bain, J. F. Berry, *J. Chem. Educ.* **2008**, *85*, 532.
- [S6] H. Lueken, *Magnetochemie*, Teubner Studienbücher, Stuttgart, **1999**.
- [S7] SADABS, 2009/2, AXS, 2009.
- [S8] G. M. Sheldrick, *SHELXS97* and *SHELXL97*, University of Göttingen, Germany, **1997**.
- [S9] S. Stoll, A. Schweiger, *J. Magn. Reson.* **2006**, *178*, 42.
- [S10] a) C. Lee, W. Yang, R. G. Parr, *Phys. Rev. B* **1988**, *37*, 785; b) A. D. Becke, *J. Chem. Phys.* **1993**, *98*, 5648.
- [S11] P. C. Hariharan, J. A. Pople, *Theor. Chim. Acta* **1973**, *28*, 213.
- [S12] a) S. Grimme, S. Ehrlich, L. Goerigk, *J. Comp. Chem.* **2011**, *32*, 1456; b) S. Grimme, J. Antony, S. Ehrlich, H. Krieg, *J. Chem. Phys.* **2010**, *132*, 154104.
- [S13] a) F. Neese, *J. Comput. Chem.* **2003**, *24*, 1740; b) F. Neese, F. Wennmohs, A. Hansen, U. Becker, *Chem. Phys.* **2009**, *356*, 98.
- [S14] a) A. Schäfer, H. Horn, R. Ahlrichs, *J. Chem. Phys.* **1992**, *97*, 2571; b) F. Weigend, R. Ahlrichs, *Phys. Chem. Chem. Phys.* **2005**, *7*, 3297.
- [S15] F. Neese, *WIREs Comput. Mol. Sci.* **2012**, *2*, 73.
- [S16] R. S. Mulliken, *J. Chem. Phys.* **1995**, *23*, 1833.
- [S17] NBO Version 3.1, E. D. Glendening, A. E. Reed, J. E. Carpenter, F. Weinhold.
- [S18] M. Head-Gordon, J. A. Pople, M. J. Frisch, *Chem. Phys. Lett.* **1988**, *153*, 503.
- [S19] B. O. Roos, P. R. Taylor, P. E. M. Siegbahn, *Chem. Phys.* **1980**, *48*, 157.

# Appendix H

## Highly Active Titanocene-Catalysts for Epoxide Hydrosilylation – Synthesis, Theory, Kinetics, EPR

Dina Schwarz G. Henriques,<sup>i</sup> Katharina Zimmer,<sup>i</sup> Sven Klare,<sup>i</sup> Andreas Meyer,<sup>ii</sup> Elena Rojo-Wiechel,<sup>i</sup> Mirko Bauer,<sup>iii</sup> Rebecca Sure,<sup>iii</sup> Stefan Grimme,<sup>iii</sup> Olav Schiemann,<sup>ii</sup> Robert A. Flowers II<sup>iv</sup> and Andreas Gansäuer<sup>i</sup>

Received 3rd February 2016, published online 29th April 2016.

Reprinted with permission from

D. Schwarz G. Henriques, K. Zimmer, S. Klare, A. Meyer, E. Rojo-Wiechel, M. Bauer, R. Sure, S. Grimme, O. Schiemann, R. A. Flowers, and A. Gansäuer, *Angewandte Chemie International Edition* **2016**, *55*, 7671 – 7675.

Copyright ©2016, WILEY-VCH Verlag GmbH & Co. KGaA, Weinheim.

### Own contributions to the manuscript

- Conducting the EPR and ENDOR Measurements.
- Interpretation of the EPR and ENDOR spectra.
- Writing parts of the manuscript.

---

<sup>i</sup> Kekulé-Institut für Organische Chemie und Biochemie, Universität Bonn, Gerhard-Domagk-Straße 1, 53121 Bonn, Germany.

<sup>ii</sup> Institut für Physikalische und Theoretische Chemie, Universität Bonn, Wegelerstr. 12, 53115 Bonn, Germany.

<sup>iii</sup> Mulliken Center for Theoretical Chemistry, Universität Bonn, Berlingstr. 4, 53115 Bonn, Germany.

<sup>iv</sup> Department of Chemistry, Lehigh University, Bethlehem, PA 18015 USA.



## Homogeneous Catalysis

International Edition: DOI: 10.1002/anie.201601242  
German Edition: DOI: 10.1002/ange.201601242

## Highly Active Titanocene Catalysts for Epoxide Hydrosilylation: Synthesis, Theory, Kinetics, EPR Spectroscopy

Dina Schwarz G. Henriques<sup>+</sup>, Katharina Zimmer<sup>+</sup>, Sven Klare<sup>+</sup>, Andreas Meyer, Elena Rojo-Wiechel, Mirko Bauer, Rebecca Sure, Stefan Grimme, Olav Schiemann,\* Robert A. Flowers II,\* and Andreas Gansäuer\*

**Abstract:** A catalytic system for titanocene-catalyzed epoxide hydrosilylation is described. It features a straightforward preparation of titanocene hydrides that leads to a reaction with low catalyst loading, high yields, and high selectivity of radical reduction. The mechanism was studied by a suite of methods, including kinetic studies, EPR spectroscopy, and computational methods. An unusual resting state leads to the observation of an inverse rate order with respect to the epoxide.

Epoxide hydrosilylations are virtually unexplored reactions that offer a simple access to alcohols.<sup>[1]</sup> Epoxidation and titanocene-catalyzed<sup>[2]</sup> epoxide hydrosilylation (Scheme 1) provide a two-step approach to the formal anti-Markovnikov addition of H<sub>2</sub>O to olefins that circumvents hydroboration. However, it also highlights the difficulties associated with the reactive and relatively unstable titanocene(III) hydrides ([Cp<sub>2</sub>TiH] hereafter). Their generation is capricious and requires either harsh conditions<sup>[3]</sup> or the syntheses of sensitive complexes.<sup>[4]</sup> Herein, we report a reliable and easy procedure for catalyst generation from titanocene dichlorides, mechanistic key features of the reaction, and EPR data for the species involved.

Our starting point was the in situ generation of [Cp<sub>2</sub>TiH]. [Cp<sub>2</sub>TiR] complexes are attractive in this context because of the weak Ti–C bond.<sup>[5]</sup> We studied  $\sigma$ -bond metathesis of these complexes with PhSiH<sub>3</sub> and (EtO)<sub>3</sub>SiH computationally (Figure 1).<sup>[6]</sup>

[\*] D. S. G. Henriques,<sup>[a]</sup> K. Zimmer,<sup>[a]</sup> S. Klare,<sup>[a]</sup> E. Rojo-Wiechel, Prof. Dr. A. Gansäuer  
Kekulé-Institut für Organische Chemie und Biochemie  
Universität Bonn  
Gerhard-Domagk-Straße 1, 53121 Bonn (Deutschland)  
E-mail: andreas.gansaer@uni-bonn.de

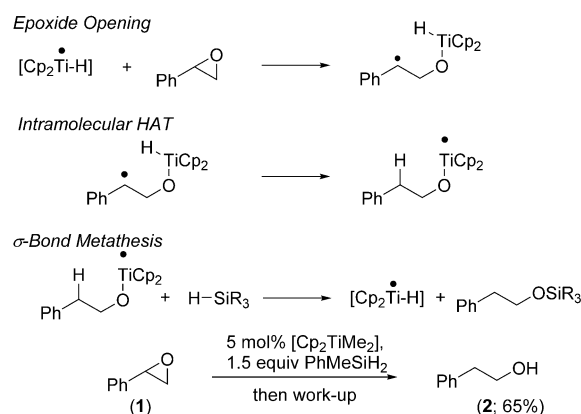
M. Bauer, Dr. R. Sure, Prof. Dr. S. Grimme  
Mulliken Center for Theoretical Chemistry  
Institut für Physikalische Chemie und Theoretische Chemie  
Universität Bonn  
Berlingstraße 4, 53115 Bonn (Deutschland)

A. Meyer, Prof. Dr. O. Schiemann  
Institut für Physikalische Chemie und Theoretische Chemie  
Universität Bonn  
Wegelerstraße 12, 53115 Bonn (Deutschland)

Prof. Dr. R. A. Flowers II  
Department of Chemistry, Lehigh University  
Bethlehem, PA 18015 (USA)

[†] These authors contributed equally.

Supporting information for this article can be found under:  
<http://dx.doi.org/10.1002/anie.201601242>.



Scheme 1. Titanocene-catalyzed epoxide hydrosilylation.<sup>[1a]</sup>

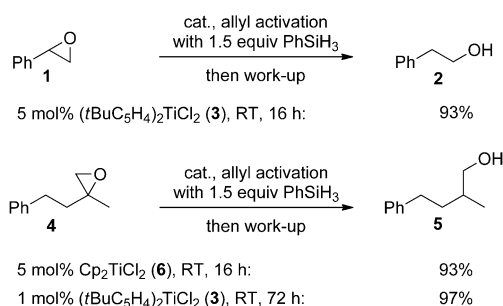
$\Delta G_{298}$  values for the  $\sigma$ -bond metathesis indicate that [Cp<sub>2</sub>TiH] formation is favorable for R = Me, thermoneutral for R = Allyl, and endergonic for R = Ph with PhSiH<sub>3</sub>. (EtO)<sub>3</sub>SiH was predicted to be inferior. In practice, [Cp<sub>2</sub>TiAllyl] is especially attractive since it can be prepared in situ by stirring Cp<sub>2</sub>TiCl<sub>2</sub> (1 equiv) and AllylMgBr (2.2 equiv) in THF (1–10 min, purple reaction mixture).<sup>[5]</sup> After the addition of PhSiH<sub>3</sub> (1.5 equiv with respect to the epoxide), the generation of [Cp<sub>2</sub>TiH] (the “allyl activation”) is complete in 1–10 min (green reaction mixture).

Examples of the hydrosilylation are shown in Scheme 2. The reaction of **1** with **3** leads to an excellent result. With 1 mol % **3**, 97 % **5** was obtained (86 % **5** with 0.5 mol % (Cp<sub>2</sub>TiOEt)<sub>2</sub>, that is 1 mol % of Ti, and 78 % **5** with 1 mol % Cp<sub>2</sub>TiMe<sub>2</sub>).<sup>[1a]</sup>

We then turned our attention to mechanistic issues and investigated whether EPR-active species<sup>[7]</sup> are present in the solution after “allyl activation”. To this end, the activation

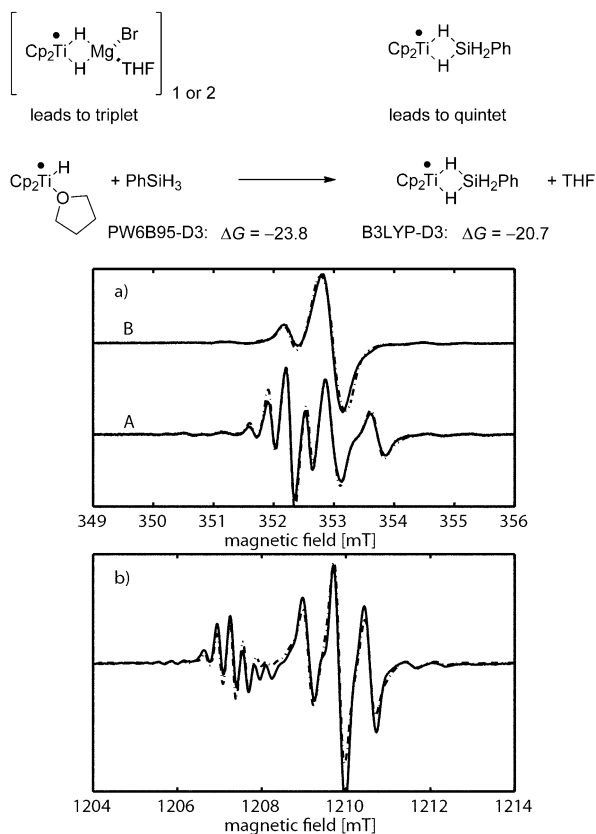
Cp <sub>2</sub> Ti–R*THF +	PhSiH <sub>3</sub>		PhSiH <sub>2</sub> R	
	or [(EtO) <sub>3</sub> SiH]		or [(EtO) <sub>3</sub> SiR]	
	R = Me	R = Ph	R = allyl	
PW6B95-D3	-4.2 (+4.3)	+2.5 (+15.0)	+0.6 (+9.7)	
B3LYP-D3	-3.8 (+5.2)	+3.2 (+16.4)	+0.6 (+10.1)	

Figure 1. Computed  $\Delta G$  at 298.15 K for [Cp<sub>2</sub>TiH] generation by  $\sigma$ -bond metathesis in THF in kcal mol<sup>-1</sup>. Values in parentheses refer to (EtO)<sub>3</sub>SiH. For comparison, data for two dispersion-corrected density functionals are given.



**Scheme 2.** Titanocene-catalyzed epoxide hydrosilylation after “allyl activation” (“allyl activation”: Titanocene dichloride (1 equiv) and AllylMgBr (2.2 equiv with respect to [Ti]) in THF for 1–10 min (purple reaction mixture), then PhSiH<sub>3</sub> (30–150 equiv with respect to [Ti], 1.5 equiv with respect to the epoxide) for 1–10 min (green reaction mixture).

was conducted under the standard reaction conditions with either PhSiH<sub>3</sub> or PhSiD<sub>3</sub>. The resulting X-band EPR spectra and their simulations are shown in Figure 2. Two dominating signals were observed when using PhSiH<sub>3</sub>. The first signal is centered at  $g_{\text{iso,quintet}} = 1.9970$  and shows a quintet hyperfine coupling (hfc) structure with an hfc constant of 8.75 MHz. We suggest that the observed quintet is the result of adduct formation between PhSiH<sub>3</sub> and Cp<sub>2</sub>TiH (Figure 2 and Sup-



**Figure 2.** Proposed structures present in solution and corresponding experimental (solid lines) and simulated (dashed lines) EPR spectra after “allyl activation” at X-band (a) and Q-band (b). At X-band, PhSiH<sub>3</sub> (A) and PhSiD<sub>3</sub> (B) were used during the activation. Free energies are given in kcal mol<sup>-1</sup>.

porting Information for details). Calculations show that this process is strongly exergonic. The calculated hfc constants are in qualitative agreement with the experimental values (see the Supporting Information). The other signal shows a triplet hfc structure with an hfc constant of 20.50 MHz and is centered at  $g_{\text{iso,triplet}} = 1.9930$ . The hfc structure of both signals is absent when PhSiD<sub>3</sub> is used. For the species resulting in the observed triplet, we propose a complex of solvated HMgBr with Cp<sub>2</sub>TiH or its dimer (see Figure 2 and the Supporting Information for details). The groups of Brintzinger and Mach have postulated, isolated, and characterized closely related complexes.<sup>[5b,8]</sup> Therefore, all species detected contain Ti–H bonds.

To understand the mechanism of this reaction, a series of rate experiments were performed on the hydrosilylation of **4** through “allyl activation” of **6** with PhSiH<sub>3</sub>. The reaction was monitored in real time through in situ IR Spectroscopy or Vis spectroscopy. Each experiment was repeated at least once. Initial experiments were designed to examine the stability of the catalyst under synthetically relevant conditions.<sup>[9,10]</sup> The conversion of **4** into **5** in the presence of 10 mol % catalyst was monitored by following [**5**] and subsequently plotting [**4**] as a function of time (Figure 3). A higher catalyst loading was

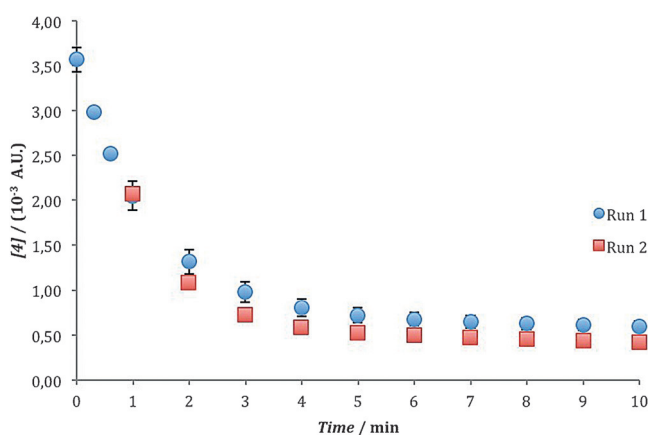


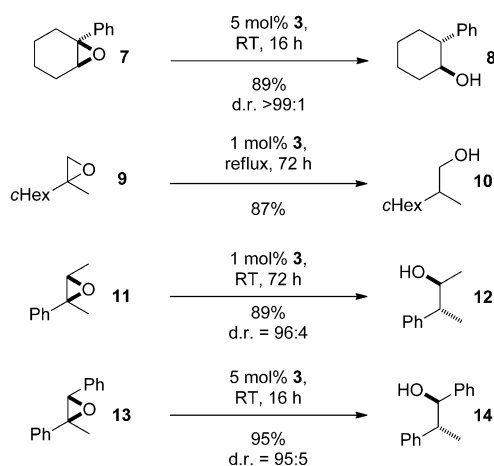
**Figure 3.** “Same excess” experiment. Profile of Run 1 plotted as [**4**] vs. time and the time-adjusted profile of Run 2 as [**4**] vs. adjusted time (see the Supporting Information for details).

employed to ensure reproducible detection of the titanocene species and to obtain fast turnover. When the reaction reaches the first half-life with respect to [**4**], an equivalent amount of PhSiH<sub>3</sub> should be consumed and [Ti] should remain constant under ideal conditions. A second run was initiated under identical conditions to the first half-life of the first reaction. When the concentration data for the second run are plotted versus time and time-adjusted accordingly, the overlay is good, showing only a very slight inhibition or deactivation at the early stages of the reaction.<sup>[11]</sup>

The rate orders with respect to the catalyst, **4**, and PhSiH<sub>3</sub> were determined by using the “initial rate” method. The reaction was approximately first order with respect to the catalyst, but surprisingly showed inverse order with respect to **4**.

The rate order with respect to the silane was established by varying  $[\text{PhSiH}_3]$  and monitoring  $[\text{Cp}_2\text{TiH}]$  through in situ Vis spectroscopy at 601 nm because of interfering silane bands in the IR spectrum. The overlap of the graphs was consistent with a rate order of zero with respect to the silane. To confirm these findings, two further sets of experiments were carried out. First, the rate order with respect to silane was additionally determined using “different excess” experiments (Supporting Information). The experiment examining the impact of  $[\text{PhSiH}_3]$  confirmed that the rate order with respect to the silane is indeed zero. Second, an experiment on the hydrosilylation of **7** (Scheme 3) also established an inverse rate order with respect to the epoxide (Table 1).

Clearly, the mechanism of epoxide hydrosilylation is rather intricate. Neither epoxide opening, nor the intramolecular hydrogen atom transfer (HAT), nor  $\sigma$ -bond metathesis can be the rate-determining step. The formation of a resting state of the catalyst that reversibly binds the epoxide substrate without inducing ring opening must thus be responsible for the observed reaction orders. A plausible scenario is epoxide binding by  $\text{Cp}_2\text{TiOR}$  (OR is formed through epoxide opening followed by HAT, Scheme 1).



**Scheme 3.** Titanocene-catalyzed epoxide hydrosilylation with **3** after “allyl activation” in the presence of 1.5 equiv (second example 2.3 equiv)  $\text{PhSiH}_3$ .

**Table 1:** Rate orders with respect to the different reactants for the titanocene-catalyzed hydrosilylation of **4** after “allyl activation”. Values in parentheses refer to **7**.

Reaction component	Rate order
$[\text{Ti}]$	$1.2 \pm 0.3^{[a]}$
$\text{PhSiH}_3$	$0.1 \pm 0.4^{[b]}$
Epoxide <b>4</b> (and <b>7</b> )	$-1.4 \pm 0.3^{[c]}$ ( $-1.3 \pm 0.2^{[d]}$ )

[a] Conditions: Initial rate method.  $[\text{Ti}]$  3.3–13 mM, 67 mM epoxide **4**, 103 mM  $\text{PhSiH}_3$ . [b] Owing to interfering silane bands in the IR spectrum, this rate order was determined by in situ monitoring of the  $[\text{Ti}]$  species through Vis spectroscopy. Conditions: Initial rate method.  $[\text{Ti}]$  2 mM, 37.5 mM epoxide **4**, 38.0–47.6 mM  $\text{PhSiH}_3$ . [c] Conditions: Initial rate method.  $[\text{Ti}]$  6.7 mM, 67–267 mM epoxide **4**, 103 mM  $\text{PhSiH}_3$ . [d] Conditions: Initial rate method.  $[\text{Ti}]$  6.7 mM, 67–183 mM epoxide **7**, 103 mM  $\text{PhSiH}_3$ .

Our calculations (Figure 4) show that  $[\text{Cp}_2\text{Ti-OEt}]$  forms a more stable epoxide complex than  $[\text{Cp}_2\text{Ti-H}]$ . The opening of the  $[\text{Cp}_2\text{Ti-OEt}]$  epoxide complex to the  $\beta$ -metalloxy radical is distinctly slower. In agreement with this prediction, we found that  $[\text{Cp}_2\text{TiOEt}]_2$  does not open **4** (see the Supporting Information). Therefore, it seems that an epoxide complex of titanocene(III) alkoxides is indeed the resting state of this catalyst.

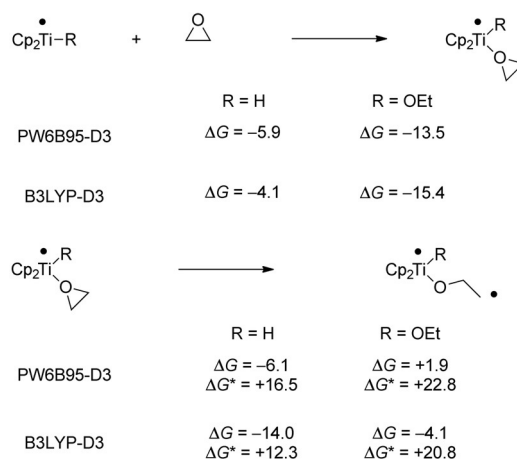


**Figure 4.** Computational analysis of epoxide complexation and opening by  $[\text{Cp}_2\text{Ti-H}]$  and  $[\text{Cp}_2\text{Ti-OEt}]$ . Free energies are given in  $\text{kcal mol}^{-1}$ .

To validate this conclusion, a solution of  $\text{Cp}_2\text{TiAllyl}$  was mixed with  $\text{PhSiH}_3$  and **4** and immediately shock-frozen with liquid  $\text{N}_2$  (Figure 5, black lines). Sample preparation was repeated using  $\text{PhSiH}_3$  and 2,2- $\text{D}_2$ -**4** (red lines),  $\text{PhSiD}_3$  and **4** (green lines), and  $\text{PhSiD}_3$  and 2,2- $\text{D}_2$ -**4** (blue lines). The frozen solutions were subjected to pulsed Q-band EPR and electron nuclear double resonance (ENDOR) spectroscopy (Figure 5 a).<sup>[12]</sup> The EPR spectra of the different samples are all similar and cover a field range of approximately 30 mT, with intense maxima at  $g$ -values of 1.9857 and 1.9651 (see the Supporting Information). The values are in the typical range for titanocenes.<sup>[4,13]</sup> The spectra are the result of the presence of several paramagnetic species.

ENDOR spectroscopy of these samples yielded the  $^1\text{H}$  hyperfine coupling patterns shown in Figure 5 a. When 2,2- $\text{D}_2$ -**4** was used instead of **4**, the proton resonance at an approximate hfc constant of 2.5 MHz was no longer observed. Similarly, resonances at an approximate hfc constant of 1.0 MHz were not detected with  $\text{PhSiD}_3$ , although the magnitude of the observed effect appeared to be weaker. The smaller hfc constant indicates a larger electron–nucleus separation. Finally, both resonances are suppressed when both reagents are deuterated. Additionally, deuteron resonances at corresponding hfc constants were observed when deuterated reagents were used (Figure 5 b). The observed effects in the ENDOR spectra indicate that one of the ligands at the  $\text{Ti}^{\text{III}}$  center is the alkoxide formed after epoxide opening and HAT. Whether or not an additional epoxide is also bound to the  $\text{Ti}^{\text{III}}$  center cannot conclusively be answered by using ENDOR spectroscopy. However, the obtained spectra do not

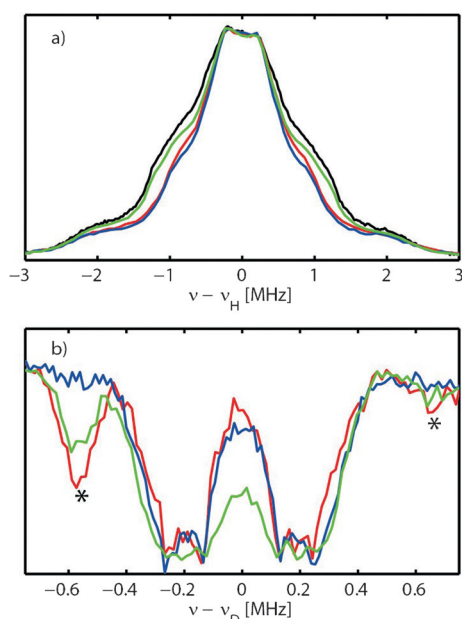


**Figure 5.** Q-band Davies ENDOR spectra of the protons<sup>[12b]</sup> (a) and Mims ENDOR spectra of the deuterons<sup>[12c]</sup> (b) of the reaction mixture using different degrees of deuteration. Black: no deuteration, red: 2,2-D<sub>2</sub>-4, green: PhSiD<sub>3</sub>, blue: 2,2-D<sub>2</sub>-4, PhSiD<sub>3</sub>. The asterisks in (b) indicate higher harmonics of the proton resonances.

contradict this interpretation. All of the computational and experimental data thus hint at the epoxide complex of the corresponding [Cp<sub>2</sub>TiOR] as the resting state of this catalyst.

Finally, we investigated the efficiency of our reaction for the substrates shown in Scheme 3. In all cases, we obtained high yields and diastereoselectivity (when applicable).

In summary, we have designed and developed an in situ method for the generation of [Cp<sub>2</sub>Ti-H] from Cp<sub>2</sub>TiCl<sub>2</sub> or substituted titanocenes, AllylMgBr, and PhSiH<sub>3</sub>. The system provides highly active and diastereoselective epoxide hydrosilylation and constitutes an atom-economical radical reaction.<sup>[14]</sup> By combining kinetic, EPR, and synthetic experi-

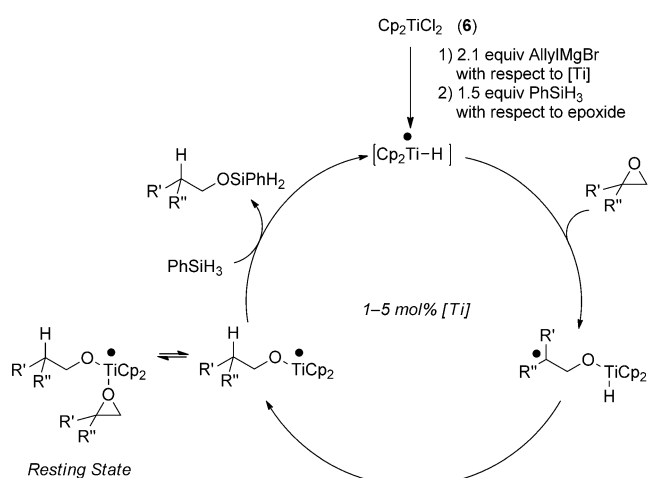


**Figure 6.** The catalytic cycle for epoxide hydrosilylation after “allyl activation” of 6.

ments with theoretical methods, we have shown that the catalytic cycle is rather unusual in having a resting state that leads to an inverse reaction order with respect to the epoxide (Figure 6).

## Acknowledgements

We thank the DFG (SFB 813 “Chemistry at Spin Centers” and Ga 619/11-1), the Jürgen Manchot Stiftung (fellowships to S.K. and D.S.G.H.), and the National Science Foundation (CHE-1123815, R.A.F.) for financial support.

**Keywords:** homogeneous catalysis · hydrogen-atom transfer · hydrosilylation · radicals · titanium

**How to cite:** *Angew. Chem. Int. Ed.* **2016**, *55*, 7671–7675  
*Angew. Chem.* **2016**, *128*, 7801–7805

- a) A. Gansäuer, M. Klatte, G. M. Brändle, J. Friedrich, *Angew. Chem. Int. Ed.* **2012**, *51*, 8891–8894; *Angew. Chem.* **2012**, *124*, 9021–9024; b) Y.-Q. Zhang, N. Funken, P. Winterscheid, A. Gansäuer, *Angew. Chem. Int. Ed.* **2015**, *54*, 6931–6934; *Angew. Chem.* **2015**, *127*, 7035–7038.
- Recent examples of titanocene(III)-catalysis: a) X. Zheng, J. He, H. H. Li, A. Wang, X. J. Dai, A. E. Wang, P. Q. Huang, *Angew. Chem. Int. Ed.* **2015**, *54*, 13739–13742; *Angew. Chem.* **2015**, *127*, 13943–13946; b) J. Streuff, M. Feurer, G. Frey, A. Steffani, S. Kacprzak, J. Weweler, L. H. Leijendekker, D. Krakert, D. A. Plattner, H. Dietmar, *J. Am. Chem. Soc.* **2015**, *137*, 14396–14405; c) J. Streuff, A. Gansäuer, *Angew. Chem. Int. Ed.* **2015**, *54*, 14232–14242; *Angew. Chem.* **2015**, *127*, 14438–14448.
- a) C. Aitken, J. F. Harrod, *J. Organomet. Chem.* **1985**, *279*, C11–C13; b) C. A. Willoughby, S. L. Buchwald, *J. Am. Chem. Soc.* **1994**, *116*, 11703–11714; c) C. A. Willoughby, S. L. Buchwald, *J. Am. Chem. Soc.* **1994**, *116*, 8952–8965; d) S. Xin, J. F. Harrod, *Can. J. Chem.* **1995**, *73*, 999–1002; e) K. Rahimian, J. F. Harrod, *Inorg. Chim. Acta* **1998**, *270*, 330–336; f) J. Yun, S. L. Buchwald, *J. Am. Chem. Soc.* **1999**, *121*, 5640–5644.
- E. Samuel, J. F. Harrod, D. Gourier, Y. Dromzee, F. Robert, Y. Jeannin, *Inorg. Chem.* **1992**, *31*, 3252–3259.
- a) H. A. Martin, F. Jellinek, *J. Organomet. Chem.* **1967**, *8*, 115–128; b) H. H. Brintzinger, *J. Am. Chem. Soc.* **1967**, *89*, 6871–6877; c) E. Klei, J. H. Teuben, *J. Organomet. Chem.* **1980**, *188*, 97–107; d) E. Klei, J. H. Teuben, H. J. de Liefde Meijer, E. J. Kwak, *J. Organomet. Chem.* **1982**, *224*, 327–339.
- The TURBOMOLE 7.0 program package<sup>[a]</sup> was employed for gas-phase geometry optimizations and calculations of thermo-statistical corrections at the TPSS<sup>[b]</sup>-D3<sup>[c,d]</sup>/def2-TZVP<sup>[e]</sup> level, as well as single-point energies at the PW6B95<sup>[f]</sup>-D3 or B3LYP<sup>[g,h]</sup>-D3 level with the def2-QZVP<sup>[e]</sup> basis set. Solvation contributions to  $\Delta G$  were included through the COSMO-RS<sup>[i,j]</sup> continuum solvation model. a) F. Furche, R. Ahlrichs, C. Hättig, W. Klopper, M. Sierka, F. Weigend, *WIREs Comput. Mol. Sci.* **2014**, *4*, 91–100; b) J. Tao, J. Perdew, V. Staroverov, G. Scuseria, *Phys. Rev. Lett.* **2003**, *91*, 146401; c) S. Grimme, J. Antony, S. Ehrlich, H. Krieg, *J. Chem. Phys.* **2010**, *132*, 154104; d) S. Grimme, S. Ehrlich, L. Goerigk, *J. Comput. Chem.* **2011**, *32*, 1456–1465; e) F. Weigend, R. Ahlrichs, *Phys. Chem. Chem. Phys.* **2005**, *7*, 3297–3305; f) Y. Zhao, D. G. Truhlar, *J. Phys. Chem. A* **2005**, *109*, 5656–5667; g) A. D. Becke, *J. Chem. Phys.* **1993**, *98*, 5648–5652; h) P. J. Stephens, J. Devlin, C. F. Chabalowski, M. J. Frisch, *J. Phys. Chem.* **1994**, *98*, 11623–11627; i) A. Klamt, *J. Chem. Phys.* **1995**, *99*, 2224–2235; j) F. Eckert, A. Klamt, *AIChE J.* **2002**, *48*, 369–385.



- [7] *Multifrequency Electron Paramagnetic Resonance, Theory and Applications* (Ed.: S. K. Misra), Wiley-VCH, Weinheim, **2011**.
- [8] a) H. Brintzinger, *J. Am. Chem. Soc.* **1966**, *88*, 4306–4307; b) V. Kupfer, U. Thewalt, M. Horáček, L. Petrusová, K. Mach, *Inorg. Chem. Commun.* **1999**, *2*, 540–544; c) S. I. Troyanov, V. Varga, K. Mach, *J. Organomet. Chem.* **1993**, *461*, 85–90; d) R. Gyepes, K. Mach, I. Císarová, J. Loub, J. Hiller, P. Sindelár, *J. Organomet. Chem.* **1995**, *497*, 33–41.
- [9] Selected reviews on RPKA: a) D. G. Blackmond, *Angew. Chem. Int. Ed.* **2005**, *44*, 4302–4320; *Angew. Chem.* **2005**, *117*, 4374–4393; b) D. G. Blackmond, *J. Am. Chem. Soc.* **2015**, *137*, 10852–10866.
- [10] Recent examples of RPKA in practice: a) A. J. Wagner, S. D. Rychnovsky, *Org. Lett.* **2013**, *15*, 5504–5507; b) M. Scott, A. Sud, E. Boess, M. Klussmann, *J. Org. Chem.* **2014**, *79*, 12033–12040; c) N. R. Patel, R. A. Flowers II, *J. Org. Chem.* **2015**, *80*, 5834–5841; d) Y. N. Ji, R. E. Plata, C. S. Regens, M. Hay, M. Schmidt, T. Razler, Y. P. Qiu, P. Geng, Y. Hsiao, T. Rosner, M. D. Eastgate, D. G. Blackmond, *J. Am. Chem. Soc.* **2015**, *137*, 13272–13281; e) P. Ruiz-Castillo, D. G. Blackmond, S. L. Buchwald, *J. Am. Chem. Soc.* **2015**, *137*, 3085–3092.
- [11] a) R. D. Baxter, D. Sale, K. M. Engle, J.-Q. Yu, D. G. Blackmond, *J. Am. Chem. Soc.* **2012**, *134*, 4600–4606; b) J. J. Devery III, J. J. Douglas, J. D. Nguyen, K. P. Cole, R. A. Flowers II, C. R. J. Stephenson, *Chem. Sci.* **2015**, *6*, 537–541.
- [12] a) A. Schweiger, G. Jeschke, *Principles of electron paramagnetic resonance*, Oxford University Press, Oxford, **2005**; b) E. R. Davies, *Phys. Lett. A* **1974**, *47*, 1–2; c) W. B. Mims, *Proc. R. Soc. London Ser. A* **1965**, *283*, 452–457.
- [13] a) W. W. Lukens, Jr., M. R. Smith III, R. A. Andersen, *J. Am. Chem. Soc.* **1996**, *118*, 1719–1728; b) A. Cangönlü, M. Behlendorf, A. Gansäuer, M. van Gastel, *Inorg. Chem.* **2013**, *52*, 11859–11866.
- [14] a) A. Gansäuer, A. Fleckhaus, M. A. Lafont, A. Okkel, K. Kotsis, A. Anoop, F. Neese, *J. Am. Chem. Soc.* **2009**, *131*, 16989–16999; b) A. Gansäuer, M. Behlendorf, D. von Laufenberg, A. Fleckhaus, C. Kube, D. V. Sadasivam, R. A. Flowers II, *Angew. Chem. Int. Ed.* **2012**, *51*, 4739–4742; *Angew. Chem.* **2012**, *124*, 4819–4823; c) A. Gansäuer, C. Kube, K. Daasbjerg, R. Sure, S. Grimme, G. D. Fianu, D. V. Sadasivam, R. A. Flowers II, *J. Am. Chem. Soc.* **2014**, *136*, 1663–1671; d) A. Gansäuer, D. von Laufenberg, C. Kube, T. Dahmen, A. Michelmann, M. Behlendorf, R. Sure, M. Seddiqzai, S. Grimme, D. V. Sadasivam, G. D. Fianu, R. A. Flowers II, *Chem. Eur. J.* **2015**, *21*, 280–289; e) A. Gansäuer, S. Hildebrandt, A. Michelmann, T. Dahmen, D. von Laufenberg, C. Kube, G. D. Fianu, R. A. Flowers II, *Angew. Chem. Int. Ed.* **2015**, *54*, 7003–7006; *Angew. Chem.* **2015**, *127*, 7109–7112.

Received: February 3, 2016

Published online: April 29, 2016

## Supporting Information

### **Highly Active Titanocene Catalysts for Epoxide Hydrosilylation: Synthesis, Theory, Kinetics, EPR Spectroscopy**

*Dina Schwarz G. Henriques<sup>+</sup>, Katharina Zimmer<sup>+</sup>, Sven Klare<sup>+</sup>, Andreas Meyer, Elena Rojo-Wiechel, Mirko Bauer, Rebecca Sure, Stefan Grimme, Olav Schiemann,\* Robert A. Flowers II,\* and Andreas Gansäuer\**

anie\_201601242\_sm\_miscellaneous\_information.pdf

## Table of Contents

<b>1</b>	<b>SYNTHETIC DETAILS</b>	<b>1</b>
1.1	General information	1
1.2	General procedure: 'allyl activation' and epoxide opening	1
1.3	Characterization of compounds	2
1.3.1	Synthesis of substrates	2
1.3.2	Synthesis of products	2
1.4	Stoichiometric Reaction of $\text{Cp}_2\text{TiOEt}$ and <b>4</b>	6
<b>2</b>	<b>KINETICS STUDIES DATA</b>	<b>7</b>
2.1	Reaction Progress Kinetic Analysis	7
2.1.1	Same Excess Experiments	7
2.1.2	Different Excess Experiments	11
2.2	Initial Rate Method IR	12
2.2.1	Titanocene Rate Order	12
2.2.2	Epoxide <b>4</b> Rate Order	16
2.2.3	Epoxide <b>7</b> Rate Order	17
2.3	Initial Rate Method Vis	19
<b>3</b>	<b>DETAILS FOR EPR MEASUREMENTS</b>	<b>22</b>
3.1	EPR sample preparation	22
3.2	EPR measurements and data analysis	23
3.2.1	General information	23
3.2.2	Pulse sequences	24
3.2.3	EPR parameters of the titanocene hydride species and discussion	25
3.2.4	Pulsed EPR measurements of the reaction solutions	28
<b>4</b>	<b>COMPUTATIONAL DETAILS</b>	<b>29</b>

<b>4.1 Computational Methods</b>	<b>29</b>
<b>4.2 References related to the Computational Details</b>	<b>30</b>



# 1 Synthetic Details

## 1.1 General information

All moisture- or oxygen-sensitive reactions were carried out under argon atmosphere in heat-dried flasks or Schlenk tubes. The solvents used were purified by distillation over the drying agents indicated and were transferred under argon: THF (K). All reactions were monitored by thin-layer chromatography (TLC) on Merck silica gel 60 F254 plates using UV light as visualizing agent (if applicable), and a solution of ammoniummolybdate tetrahydrate (25 g/L) and  $\text{Ce}(\text{SO}_4)_2 \cdot 4\text{H}_2\text{O}$  (10 g/L) in 10% aqueous  $\text{H}_2\text{SO}_4$  as developing agents followed by heating. The products were purified by flash column chromatography on Merck silica gel 50 or Macherey-Nagel silica gel 60.

$^1\text{H}$  NMR and  $^{13}\text{C}$  NMR spectra were recorded on a Bruker AMX 300 MHz or a Bruker AM 400 MHz instrument. Chemical shifts are denoted in ppm ( $\delta$ ), and calibrated by using residual undeuterated solvent [ $\text{CHCl}_3$  (7.26 ppm) or  $\text{C}_6\text{H}_6$  (7.16 ppm)] as internal reference for  $^1\text{H}$  NMR and the deuterated solvent [ $\text{CDCl}_3$  (77.0 ppm) or  $\text{C}_6\text{H}_6$  (128.1 ppm)] as internal standard for  $^{13}\text{C}$  NMR. Coupling constants reported in Hz constitute  $J(\text{H,H})$  coupling constants, unless otherwise noted.

## 1.2 General procedure: 'allyl activation' and epoxide opening

In a heat-dried Schlenk tube the corresponding titanocene dichloride (0.05 mmol, 5 mol%) was dissolved in THF (2 mL) under Ar. Then allylMgBr (0.10 mL, 0.11 mmol, 1.10 M in  $\text{Et}_2\text{O}$ , 11 mol%) was added and stirred for 2 min, while the color of the solution changed from red to deep purple (**Figure S 1**). Subsequently  $\text{PhSiH}_3$  (0.19 mL, 1.50 mmol, 1.5 eq.) was added. After 10 min the color had changed to green (**Figure S 1**) and the epoxide (1.00 mmol, 1.00 eq.) was added with THF (4 mL). The reaction mixture was stirred at room temperature for the indicated time, added to acetone (5 mL) and  $\text{K}_2\text{CO}_3$  (25 wt% in  $\text{H}_2\text{O}$ , 25 mL) and stirred for another 24 h. The mixture was then extracted with  $\text{Et}_2\text{O}$  (3x 20 mL), washed with brine (1x 20 mL) and dried over anhydrous  $\text{MgSO}_4$ . After removal of the solvent under reduced pressure, chromatography on  $\text{SiO}_2$  provided the desired alcohol.

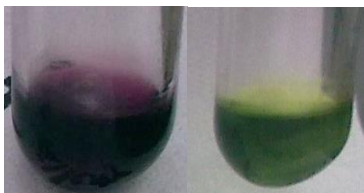


**Figure S 1.** Solution of [Cp<sub>2</sub>TiAllyl] in THF (on the left), followed by activation with PhSiH<sub>3</sub> to [Cp<sub>2</sub>TiH] (on the right).

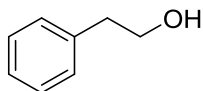
### 1.3 Characterization of compounds

#### 1.3.1 Synthesis of substrates

Styrene oxide (**1**) is commercially available. The following epoxides were prepared according to the literature: 2-Methyl-2-(2-phenylethyl)oxirane (**4**)<sup>[1]</sup>, 1-Phenyl-7-oxabicyclo[4.1.0]heptane (**7**)<sup>[2]</sup>, 2,2-Cyclohexylmethyloxirane (**9**)<sup>[3]</sup>, 2,3-Dimethyl-2-phenyloxirane (**11**)<sup>[4]</sup>, *trans*-2-Methyl-2,3-diphenyloxirane (**13**)<sup>[5]</sup>.

#### 1.3.2 Synthesis of products

##### 2-Phenylethanol (**2**):



According to GP: (tBuC<sub>5</sub>H<sub>4</sub>)<sub>2</sub>TiCl<sub>2</sub> (**3**) (18 mg, 0.05 mmol, 5 mol%) in THF (2 mL), allylMgBr (0.10 mL, 0.11 mmol, 1.10 M in Et<sub>2</sub>O, 11 mol%), PhSiH<sub>3</sub> (0.19 mL, 1.50 mmol, 1.5 eq.) and styrene oxide (**1**) (120 mg, 1.00 mmol, 1.00 eq.) in THF (4 mL) were stirred for 16 h. Work up and chromatography (SiO<sub>2</sub>, cyclohexane: ethyl acetate, hereafter denoted as CH:EA 90:10, R<sub>f</sub> = 0.1) yielded the desired alcohol (**2**) (114 mg, 0.93 mmol, 93 %) as a colorless oil.

<sup>1</sup>H-NMR (400 MHz; CDCl<sub>3</sub>): δ [ppm] = 7.34-7.30 (m, 2H), 7.26-7.22 (m, 3H), 3.87 (t, *J* = 6.6 Hz, 2H), 2.88 (t, *J* = 6.6 Hz, 2H).

[1] C. Molinaro, A.-A. Guilbault, B. Kosjek, *Org. Lett.* **2010**, *12*, 3772.

[2] M. Frohn, Z.-X. Wang, Y. Shi, *J. Org. Chem.* **1998**, *63*, 6425.

[3] T. Sone, A. Yamaguchi, S. Matsunaga, M. Shibasaki, *J. Am. Chem. Soc.* **2008**, *130*, 10078.

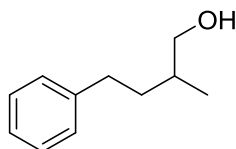
[4] P. Fristrup, B. B. Dideriksen, D. Tanner, P.-O. Norrby, *J. Am. Chem. Soc.* **2005**, *127*, 13672.

[5] M. Frohn, Z.-X. Wang, Y. Shi, *J. Org. Chem.* **1998**, *63*, 6425.

$^{13}\text{C}$ -NMR (100 MHz,  $\text{CDCl}_3$ ):  $\delta$  [ppm] = 138.4, 129.0, 128.5, 126.4, 63.6, 39.1.

In agreement with data of commercially available (Sigma-Aldrich) authentic sample.

**2-Methyl-4-phenylbutan-1-ol (5):**



a) According to GP:  $\text{Cp}_2\text{TiCl}_2$  (**6**) (12.5 mg, 0.05 mmol, 5 mol%) in THF (2 mL), allylMgBr (0.11 mL, 0.11 mmol, 1.0 M in  $\text{Et}_2\text{O}$ , 11 mol%),  $\text{PhSiH}_3$  (0.19 mL, 1.50 mmol, 1.5 eq.) and 2-Methyl-2-(2-phenylethyl)oxirane (**4**) (162 mg, 1.00 mmol, 1.00 eq.) were stirred for 16 h. Work up and chromatography ( $\text{SiO}_2$ , CH:EA 90:10,  $R_f = 0.2$ ) yielded the desired alcohol (**5**) (153 mg, 0.93 mmol, 93 %) as a colorless oil.

b) According to GP:  $(t\text{BuC}_5\text{H}_4)_2\text{TiCl}_2$  (**3**) (9 mg, 0.03 mmol, 1 mol%) in THF (1 mL), allylMgBr (0.05 mL, 0.06 mmol, 1.10 M in  $\text{Et}_2\text{O}$ , 2.2 mol%),  $\text{PhSiH}_3$  (0.48 mL, 3.75 mmol, 1.5 eq.) and 2-Methyl-2-(2-phenylethyl)oxirane (**4**) (405 mg, 2.50 mmol, 1.00 eq.) in THF (14 mL) were stirred for 72 h. Work up and chromatography ( $\text{SiO}_2$ , CH:EA 90:10,  $R_f = 0.2$ ) yielded the desired alcohol (**5**) (397 mg, 2.42 mmol, 97 %) as a colorless oil.

$^1\text{H}$ -NMR (300 MHz,  $\text{C}_6\text{D}_6$ ):  $\delta$  [ppm] = 7.26-7.11 (m, 5H), 2.66-2.45 (m, 2H), 2.66-2.45 (m, 2H), 1.98-1.78 (m, 2H), 1.41-1.28 (m, 1H), 0.91 (d, 3H,  $J = 6.9$  Hz).

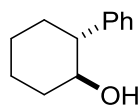
$^{13}\text{C}$ -NMR (75 MHz,  $\text{C}_6\text{D}_6$ ):  $\delta$  [ppm] = 143.0, 128.7, 128.6, 126.1, 67.9, 35.6, 35.4, 33.7, 16.7.

Data in agreement with the literature.<sup>[6]</sup>

---

<sup>[6]</sup> T. Tanaka, T. Inoue, K. Kamei, K. Murakami, C. Iwata, *J. Chem. Soc., Chem. Commun.* **1990**, 906.

### ***trans*-2-Phenylcyclohexanol (8):**



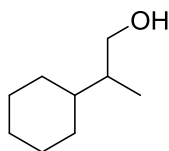
According to GP: (*t*BuC<sub>5</sub>H<sub>4</sub>)<sub>2</sub>TiCl<sub>2</sub> (**3**) (18 mg, 0.05 mmol, 5 mol%) in THF (2 mL), allylMgBr (0.10 mL, 0.11 mmol, 1.10 M in Et<sub>2</sub>O, 11 mol%), PhSiH<sub>3</sub> (0.19 mL, 1.50 mmol, 1.5 eq.) and 1-Phenyl-7-oxabicyclo[4.1.0]heptane (**7**) (174 mg, 1.00 mmol, 1.00 eq.) in THF (4 mL) were stirred for 16 h. Work up and chromatography (SiO<sub>2</sub>, CH:EA 90:10, R<sub>f</sub> = 0.2) yielded the desired alcohol (**8**) (157 mg, 0.89 mmol, 89 %, *trans:cis* >99:<1) as a colorless solid.

<sup>1</sup>H-NMR (300 MHz, CDCl<sub>3</sub>): δ [ppm] = 7.30-7.24 (m, 2H), 7.20-7.14 (m, 3H), 3.60 (ddd, *J* = 10.0, 10.0, 4.5 Hz, 1H), 2.37 (ddd, *J* = 12.2, 10.0, 3.5 Hz, 1H), 2.08-2.02 (m, 1H), 1.84-1.76 (m, 2 H), 1.73-1.66 (m, 1H), 1.45-1.23 (m, 4H).

<sup>13</sup>C-NMR (75 MHz, CDCl<sub>3</sub>): δ [ppm] = 143.4, 128.9, 128.0, 126.9, 74.6, 53.4, 34.6, 33.5, 26.2, 25.2.

Data in agreement with the literature.<sup>[7]</sup>

### **2-Cyclohexylpropanol (10):**



According to GP: (*t*BuC<sub>5</sub>H<sub>4</sub>)<sub>2</sub>TiCl<sub>2</sub> (**3**) (9 mg, 0.03 mmol, 1 mol%) in THF (1 mL), allylMgBr (0.05 mL, 0.06 mmol, 1.10 M in Et<sub>2</sub>O, 2.2 mol%), PhSiH<sub>3</sub> (0.72 mL, 5.63 mmol, 2.3 eq.) and 2,2-Cyclohexylmethyloxirane (**9**) (355 mg, 2.53 mmol, 1.00 eq.) in THF (13 mL) were stirred for 72 h at reflux. Work up and chromatography (SiO<sub>2</sub>, Eluent pentane: ethyl ether gradient from 100:0 to 80:20; R<sub>f</sub> = 0.2) yielded the desired alcohol (**10**) (314 mg, 2.21 mmol, 87 %) as a colorless oil.

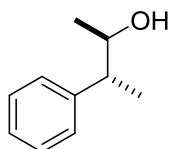
<sup>[7]</sup> C. Cadot, P. I. Dalko, J. Cossy, C. Ollivier, R. Chuard, P. Renaud, *J. Org. Chem.* **2002**, 67, 7193.

$^1\text{H}$  NMR (300 MHz,  $\text{CDCl}_3$ ):  $\delta$  [ppm] = 3.61 (dd,  $J$  = 10.5, 5.7 Hz, 1H), 3.46 (dd,  $J$  = 10.5, 6.8 Hz, 1H), 1.81-0.93 (m, 12H), 0.89 (d,  $J$  = 6.9 Hz, 3H).

$^{13}\text{C}$ -NMR (75 MHz;  $\text{CDCl}_3$ ):  $\delta$  [ppm] = 66.5, 41.1, 39.6, 31.1, 29.0, 27.0, 26.9, 26.8, 13.6.

Data in agreement with the literature.<sup>[8]</sup>

### 3-Phenylbutan-2-ol (**12**):



According to GP: ( $t\text{BuC}_5\text{H}_4$ ) $_2\text{TiCl}_2$  (**3**) (9 mg, 0.03 mmol, 1 mol%) in THF (1 mL), allylMgBr (0.05 mL, 0.06 mmol, 1.10 M in  $\text{Et}_2\text{O}$ , 2.2 mol%),  $\text{PhSiH}_3$  (0.48 mL, 3.75 mmol, 1.5 eq.) and 2,3-Dimethyl-2-phenyloxirane (**11**) (370 mg, 2.50 mmol, 1.00 eq. *trans:cis* 80:20) in THF (14 mL) were stirred for 72 h. Work up and chromatography ( $\text{SiO}_2$ , PE: $\text{Et}_2\text{O}$  80:20,  $R_f$  = 0.3) yielded the desired alcohol (335 mg, 2.23 mmol, 89 %, *anti:syn* 96:4) as a colorless oil.

$^1\text{H}$ -NMR (400 MHz;  $\text{CDCl}_3$ ):  $\delta$  [ppm] = 7.36-7.31 (m, 2H), 7.27-7.22 (m, 3H), 3.85 (dq,  $J$  = 7.4, 6.2 Hz, 1H), 2.68 (dq,  $J$  = 7.4, 7.2 Hz, 1H), 1.27 (d,  $J$  = 7.2 Hz, 3H), 1.23 (d,  $J$  = 6.2 Hz, 3H).

$^{13}\text{C}$ -NMR (101 MHz;  $\text{CDCl}_3$ ):  $\delta$  [ppm] = 143.7, 128.8, 128.2, 126.9, 72.5, 48.1, 20.8, 18.0.

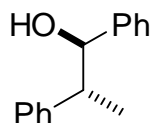
Diastereomeric ratio of the product were determined by integration of the  $^1\text{H}$ -Signals of  $\text{C}_\alpha$ -Me-Protons  $^1\text{H}$ -NMR (400 MHz;  $\text{CDCl}_3$ ):  $\delta$  = major: 1.23 (d,  $J$  = 6.2 Hz), minor: 1.09 (d,  $J$  = 6.3 Hz).

Data in agreement with the literature.<sup>[9]</sup>

<sup>[8]</sup> D. Strübing, P. Krumlinde, J. Piera, J.-E. Bäckvall, *Adv. Synth. Catal.* **2007**, 349, 1577.

<sup>[9]</sup> M. T. Reetz, S. Stanchev, H. Haning, *Tetrahedron* **1992**, 48, 6813.

### 1,2-Diphenylpropan-1-ol (**14**):



According to GP: (*t*BuC<sub>5</sub>H<sub>4</sub>)<sub>2</sub>TiCl<sub>2</sub> (**3**) (18.1 mg, 0.05 mmol, 5 mol%), allylMgBr (0.13 mL, 0.11 mmol, 0.88 M in Et<sub>2</sub>O, 11 mol%), PhSiH<sub>3</sub> (0.19 mL, 167 mg, 1.54 mmol, 1.54 eq.) and *trans*-2-Methyl-2,3-diphenyloxirane (**13**) (210 mg, 1.00 mmol, 1.00 eq.) were stirred in THF (1 mL) for 16 h. Work up and chromatography (SiO<sub>2</sub>, Eluent CH:EA gradient from 100:0 to 90:10; R<sub>f</sub> = 0.3) gave the desired alcohol (**14**) (200 mg, 0.95 mmol, 95%; *anti:syn* 95:5) as a colorless solid.

<sup>1</sup>H NMR (400 MHz, CDCl<sub>3</sub>): δ [ppm] = 7.40-7.27 (m, 10H), 4.82 (d, *J* = 5.8 Hz, *syn*) and 4.67 (d, *J* = 8.7 Hz, 1H, *anti*), 3.16-3.09 (m, *syn*) and 3.03 (dq, *J* = 14.2, 7.1 Hz, 1H, *anti*), 1.82 (br, 1H), 1.32 (d, *J* = 7.1 Hz, *syn*) and 1.09 (d, *J* = 7.1 Hz, 3H, *anti*).

<sup>13</sup>C NMR (75 MHz, CDCl<sub>3</sub>): δ [ppm] = 143.5, 142.7, 128.8, 128.4, 128.2, 128.0, 127.1, 127.1, 79.8, 48.3, 18.5.

Diastereomeric ratio of the product were determined by integration of the <sup>1</sup>H-Signals of C<sub>α</sub>-Me-Protons <sup>1</sup>H-NMR (400 MHz; CDCl<sub>3</sub>): δ = major: 1.09 (d, *J* = 7.1 Hz), minor: 1.32 (d, *J* = 7.1 Hz).

Data in agreement with the literature.<sup>[10]</sup>

#### 1.4 Stoichiometric Reaction of Cp<sub>2</sub>TiOEt and **4**

A heat-dried Schlenk tube was loaded with [Cp<sub>2</sub>TiOEt]<sub>2</sub> (223 mg; 0.50 mmol; 0.50 eq.), **4** (172 mg; 1.06 mmol) and 5 mL THF and stirred for 16 h at room temperature. Acetone (3 mL) was added and the mixture stirred for 30 min. The solvent was evaporated. The crude <sup>1</sup>H-NMR shows no conversion of epoxide **4**.

<sup>[10]</sup> C. Zhou, Z. Wang, *Synthesis* **2005**, 10, 1649.

## 2 Kinetics Studies Data

### 2.1 Reaction Progress Kinetic Analysis

All kinetic runs were carried out using a Mettler-Toledo's ReactIR 15 fitted with DiComp probe and running iCIR software 4.3 SP1. A flame dried two necked rbf attached to a reflux condenser was fixed to the ReactIR probe and flushed with argon. An air background (256 scans) was obtained and 9 mL of THF were added through a rubber septum into the rbf and heated to 60 °C for 15 min in a pre-heated oil-bath. The iCIR software was initiated to obtain data. IR spectra (with automatic no. of scans) were collected every minute or every 30 s till the completion of the reaction.

**Table S 1.** Summary of RPKA experiments. Values in parentheses correspond to the excess (XS).

Experiments	Run	[4]	[PhSiH <sub>3</sub> ]	[Ti]
Same XS	Run 1	67 mM	100 mM (78 mM)	6.6 mM
	Run 2	33 mM	89 mM (78 mM)	6.6 mM
Diff XS	Run 3	133 mM	100 mM (78 mM)	6.6 mM
	Run 4	133 mM	206 mM (162 mM)	6.6 mM

#### 2.1.1 Same Excess Experiments

A solution of Cp<sub>2</sub>TiCl<sub>2</sub> (**6**) (24.9 mg; 0.10 mmol) in 2.0 mL THF was added after 3.0 min of starting the data collection, after another 3.0-5.0 min a solution of allylMgBr (0.71 M in Et<sub>2</sub>O, 0.29 mL; 0.21 mmol; 2.10 eq. relative to [Ti]) was added and washed with 0.62 mL THF. The reaction mixture was refluxed until the color changes to a deep purple, at which point PhSiH<sub>3</sub> (Run 1: 0.19 mL; Run 2: 0.16 mL) was added and washed with THF (Run 1: 0.25 mL; Run 2: 0.28 mL). The reaction mixture was continued refluxing until the appearance of a dark green color indicative of formation of '[Cp<sub>2</sub>TiH]'. Epoxide **4** (Run 1: 162 mg; Run 2: 81.3 mg) in 2.0 mL THF was added and washed with THF (Run 1: 0.25 mL; Run 2: 0.35 mL; total volume: 15 mL). The contents were continued refluxing till the end of reaction as monitored by ReactIR.

Each experiment was repeated at least once. The growth curve for the formation of product, **5**, was monitored @ maximum absorbance 738-742 cm<sup>-1</sup>.

Conversion of raw data into epoxide concentration, **[4]**, and rate for the RPKA analysis:

1. The raw data as a plot of **[5]** (A.U. = Absorbance Unit) vs. time (min) was converted into decays with respect to the epoxide concentration (using Microsoft Excel 2007 and Origin software 8.5). This was fitted as a second order exponential decay for both runs (best fit).
2. The equations for the fit given as (a & b symbolizing the original and repeat experiments)

$$[4]_{a,b} = y_0 + A_1 \times \exp\left(-\frac{x}{t_1}\right) + A_2 \times \exp\left(-\frac{x}{t_2}\right) \quad (\text{Eq. 1})$$

were then converted to their derivatives to get rate, using **Eq. 2**:

$$\text{rate}_{a,b} = -\frac{d[4]_{a,b}}{dx} = -\frac{A_1 \times \exp\left(-\frac{x}{t_1}\right)}{t_1} - \frac{A_2 \times \exp\left(-\frac{x}{t_2}\right)}{t_2} \quad (\text{Eq. 2})$$

3. Since the experiments were repeated a second time, the RPKA was plotted as the average of both experiments:

$$[4] = \frac{[4]_a + [4]_b}{2} \quad (\text{Eq. 3})$$

$$\text{rate} = \frac{\text{rate}_a + \text{rate}_b}{2} \quad (\text{Eq. 4})$$

The deviation of the average was calculated according to the following equations (**Figure S 2**):



$$S_{[4]} = \sqrt{\frac{([4]_a - [4])^2 + ([4]_b - [4])^2}{2}} \quad (\text{Eq. 5})$$

$$S_{rate} = \sqrt{\frac{(rate_a - rate)^2 + (rate_b - rate)^2}{2}} \quad (\text{Eq. 6})$$

In order to compare the 100% (Run 1) and 50 % (Run 2) runs on the same scale and determine the catalyst stability, the runs were plotted as the decay of [4] over time (**Figure S 3**) and the 50 % run time adjusted accordingly (**Figure S 4**). The overlay is good with only a small difference, suggesting a very slight inhibition or deactivation at the early stages of the reaction (see main text).

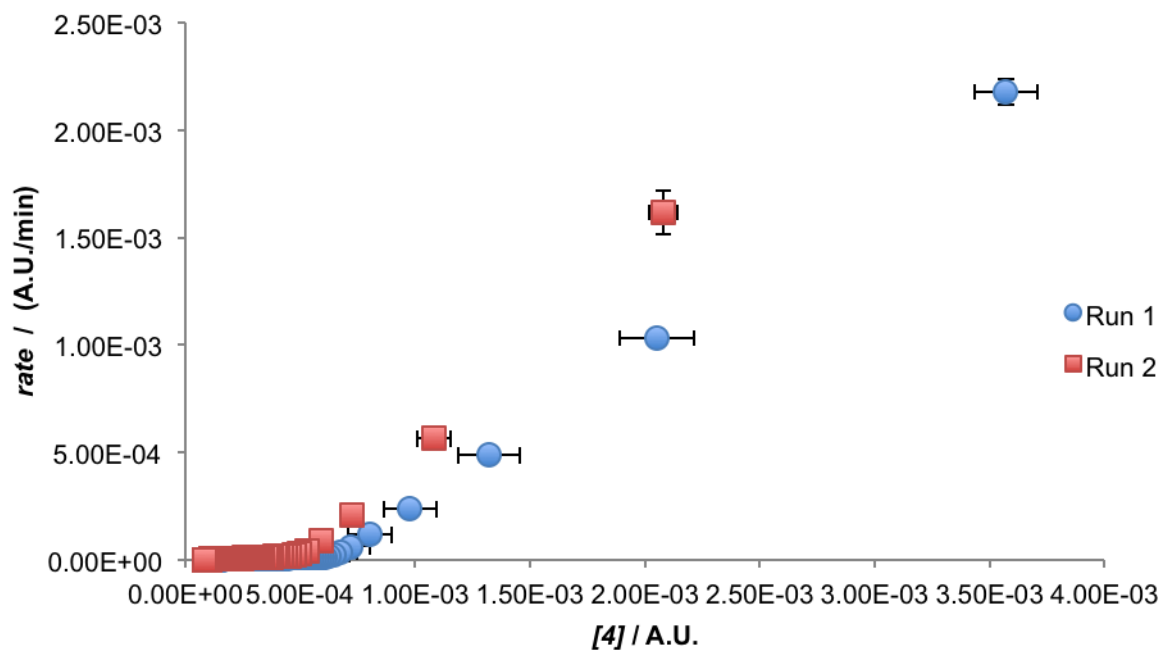


**Figure S 2:** Same Excess Experiment with 10 mol% catalyst loading. Run 1 – 100 % and Run 2 – 50 %.

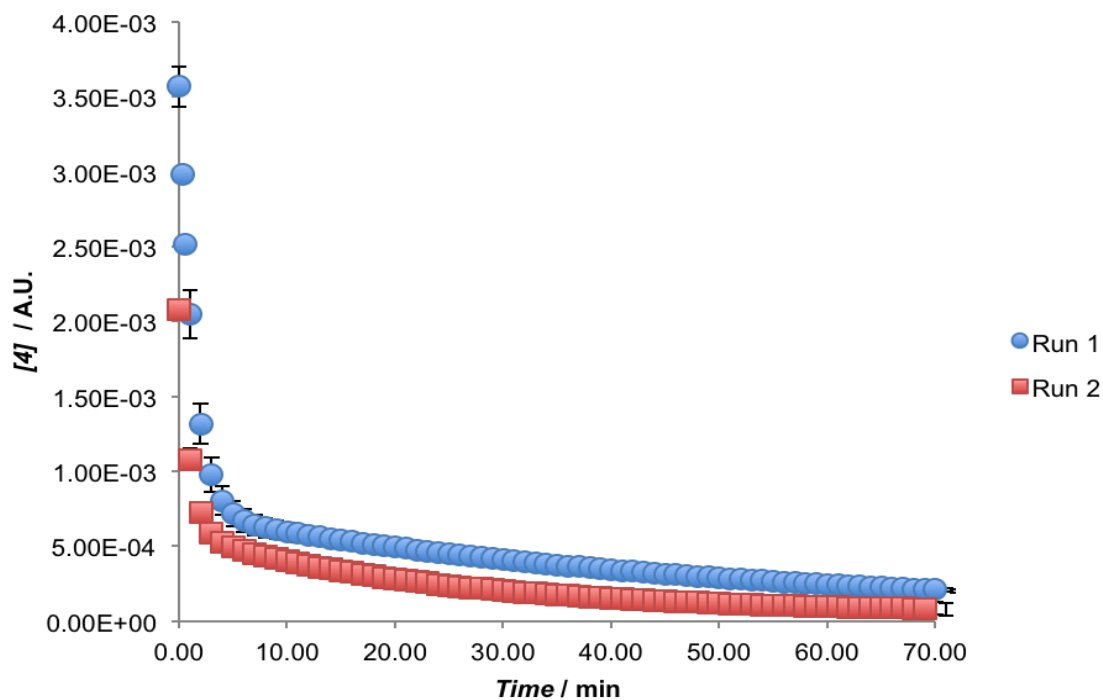


**Figure S 3.** Time Resolved Same Excess Experiment. Run 1 – 100 % and Run 2 – 50 %.

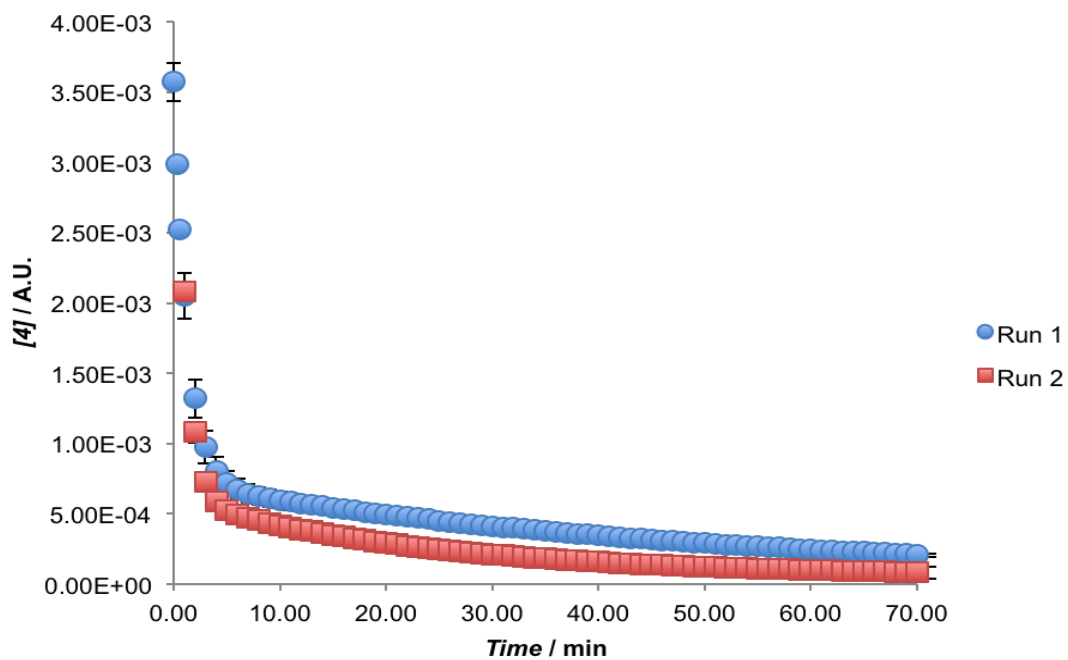


**Figure S 4.** Time Adjusted Same Excess Experiment. Run 1 – 100 % and Run 2 – 50 % (time adjusted  $t' = t + 0.99$  min).

### 2.1.2 Different Excess Experiments

These different excess experiments were carried out with twice the amount of substrate **4**, than in the same excess experiments, to avoid the overlap of the monitored product band with the interfering PhSiH<sub>3</sub> bands in the IR spectra at high [PhSiH<sub>3</sub>]. A solution of Cp<sub>2</sub>TiCl<sub>2</sub> (**6**) (24.9 mg; 0.10 mmol; 10 mol%) in 2.0 mL THF was added after 3 min of starting the data collection and washed with 0.25 mL THF, after another 3.0-5.0 min, a solution of allylMgBr (0.71 M in Et<sub>2</sub>O, 0.29 mL; 0.21 mmol; 2.10 eq. relative to [Ti]) was added and washed with (Run 3: 0.40 mL; Run 4: 0.25 mL) THF. The reaction mixture was refluxed until the color changes to a deep purple, at which point PhSiH<sub>3</sub> (Run 3: 0.19 mL; Run 4: 0.38 mL) was added and washed with THF (Run 3: 0.25 mL; Run 4: 0.26 mL). The reaction mixture was again refluxed until the appearance of a dark green color indicative of formation of '[Cp<sub>2</sub>TiH]'. Epoxide **4** (324 mg; 2.00 mmol) in 2.0 mL THF was added and washed with THF (Run 3: 0.30 mL; Run 4: 0.25 mL; total volume: 15 mL). The contents were continued refluxing till the end of reaction as monitored by ReactIR.

Each experiment was repeated at least once. The growth curve for the formation of product was monitored @ 738-742 cm<sup>-1</sup>.

Conversion of raw data was done according to the procedure described in the previous section (See 1.1.1. Same Excess Experiments). The plot rate vs. [**4**] overlap for both runs suggesting a rate order of zero for the silane (**Figure S 5**).

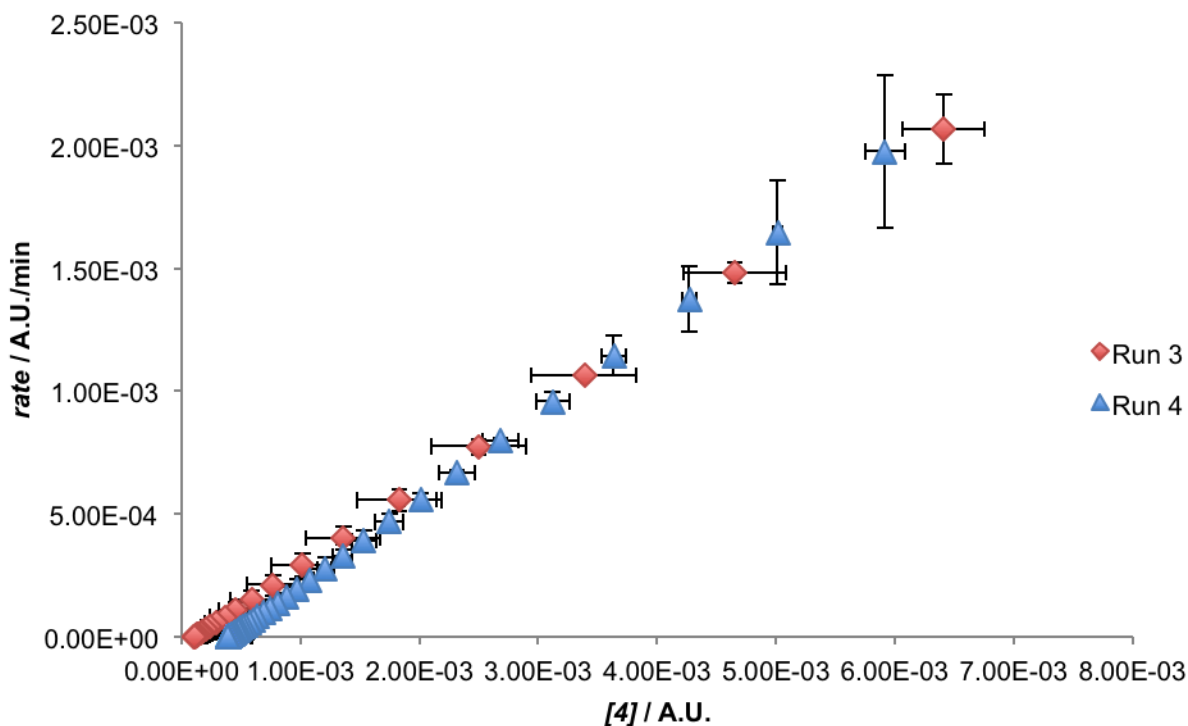


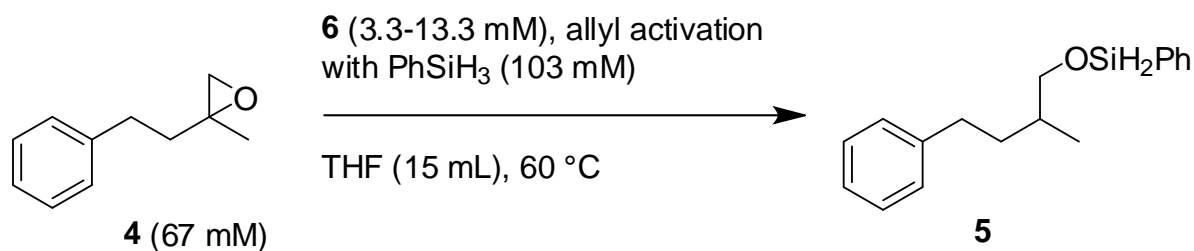
**Figure S 5.** Different Excess Experiment. 2.0 mmol epoxide **4**, 5 mol% [Cp<sub>2</sub>TiAllyl] (relative to epoxide amount); Run 3 - 1.5 eq PhSiH<sub>3</sub>; Run 4 - 3.0 eq PhSiH<sub>3</sub>.

## 2.2 Initial Rate Method IR

All kinetic runs were carried out using a Mettler-Toledo's ReactIR 15 fitted with DiComp probe and running iCIR software 4.3 SP1. A flame dried two necked rbf attached to a reflux condenser was fixed to the ReactIR probe and flushed with argon. An air background (256 scans) was obtained and 9 mL of THF was added through a rubber septum into the rbf and heated to 60 °C for 15 min in a pre-heated oil-bath. The iCIR software was initiated to obtain data. IR spectra (with automatic no. of scans) were collected every minute or every 30 s till the completion of the reaction.

### 2.2.1 Titanocene Rate Order

$$rate = k \times [Ti]^2 \times [epoxide]^2 \times [PhSH_3]^3 \quad (\text{Eq. 7})$$



To determine the rate order of the Ti-catalyst,  $z_1$  (see **Eq. 7**), the concentrations of the other components in the catalytic reaction were kept constant. The catalyst concentration **[6]** on the other hand was varied. The catalyst was always activated with 2.1 eq. of allylMgBr (0.71 M in  $\text{Et}_2\text{O}$ ). For each run 1.0 mmol **4** (67 mM in 15 mL THF) and 1.5 eq  $\text{PhSiH}_3$  (103 mM in 15 mL THF) were used. All experiments were carried out at 60 °C.

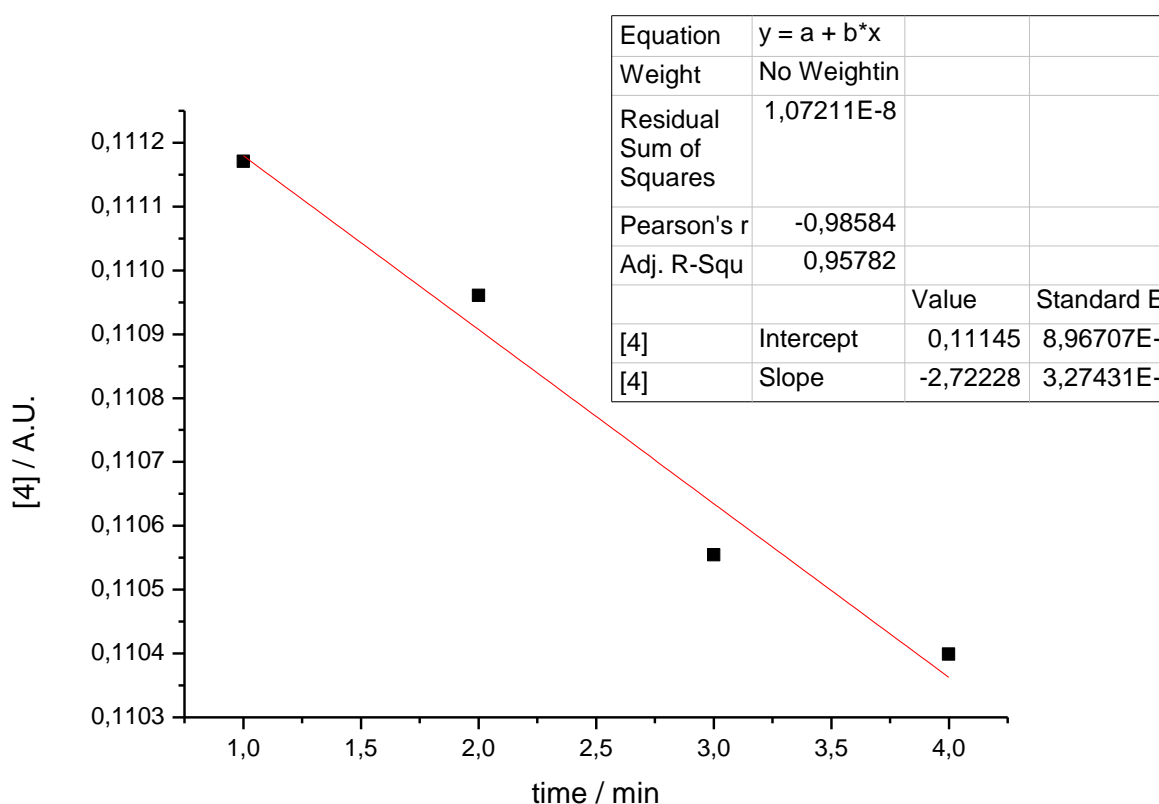


**Figure S 6.** Example plot for the decay of epoxide **4** vs. time at a catalyst loading of 5 mol% [Ti].

The initial rate for each run was determined by monitoring the initial formation of product, **5**, @738-742 cm<sup>-1</sup> vs. time in min. The plot is then converted into decay of **[4]** vs. time in min (**Figure S 6**). The slope obtained by at least 3 data points (with the higher catalyst loading the reaction was so fast, that points had to be extrapolated from a second order exponential fit, R<sup>2</sup>>0.91) is the desired initial rate -v<sub>0</sub> (**Eq. 8**). Each experiment was repeated at least once and an average v<sub>0</sub> calculated for each catalyst concentration (**Table S 2**).

**Table S 2.** Summary of results for the determination of catalyst rate order.

Cat.	[Ti] <sub>0</sub> in M	v <sub>0</sub> in A.U. min <sup>-1</sup>	ln([Ti] <sub>0</sub> )	ln(v <sub>0</sub> )
5 mol%	0,003325	0,000301	-5,70631	-8,11006
10 mol%	0,006668	0,001133	-5,01047	-6,78259
15 mol%	0,009988	0,001534	-4,60635	-6,47988
20 mol%	0,013335	0,001580	-4,31733	-6,45033

$$v_0 = k_{obs} \times [Ti]_0^{z_1} \quad (\text{Eq. 8})$$

By taking the natural log of **Eq. 8** we obtain the following simplified equation:

$$\ln(v_0) = \ln(k_{obs}) + z_1 \times \ln([Ti]_0) \quad (\text{Eq. 9})$$

The rate order of the catalyst can therefore be calculated by plotting ln(v<sub>0</sub>) versus ln([Ti]<sub>0</sub>). The slope gives the order of the catalyst, z<sub>1</sub> = 1.2 ± 0.3 (**Figure S 7**).

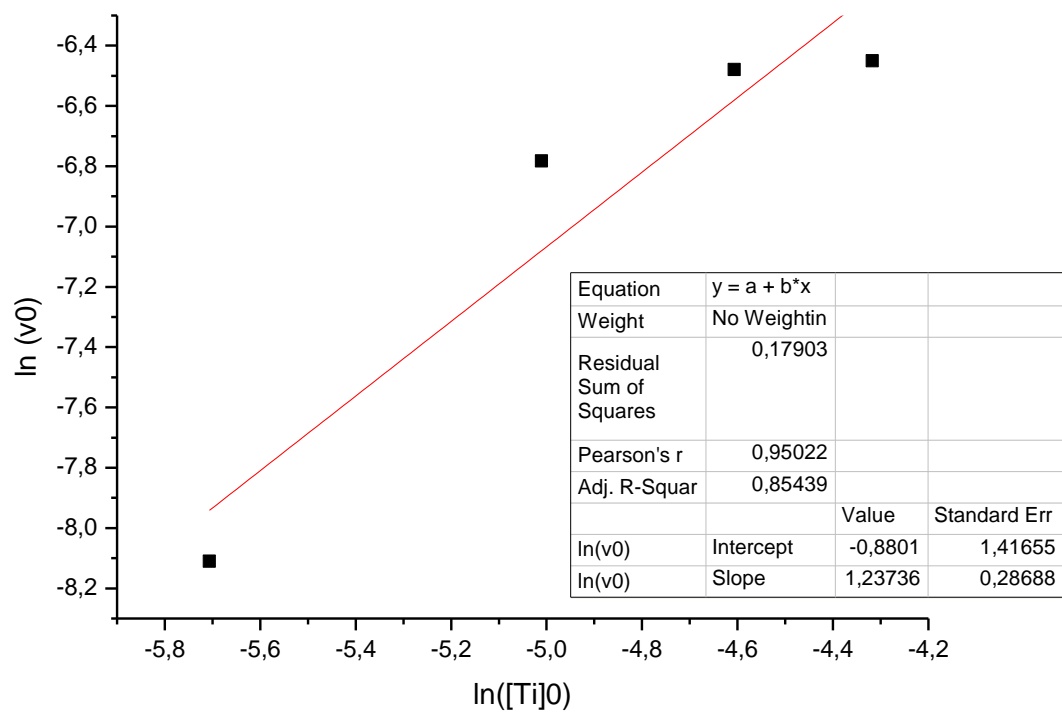
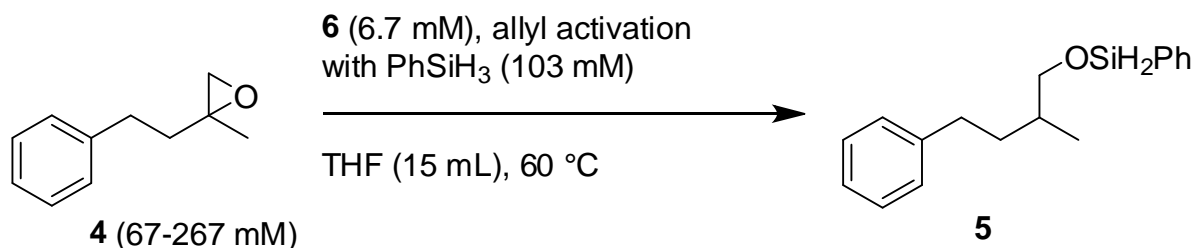


**Figure S 7.** The slope of the plot  $\ln(v_0)$  vs.  $\ln([Ti]_0)$  gives the rate order of the catalyst,  $z_1 = 1.2 \pm 0.3$ .

## 2.2.2 Epoxide **4** Rate Order



To determine the rate order of **4**,  $z_2$  (see **Eq. 7**), the concentrations of the other components in the catalytic reaction were kept constant, while varying the epoxide concentration. For each run 0.10 mmol **6** (6.7 mM in 15 mL THF), activated with 2.1 eq. allylMgBr solution (0.71 M in Et<sub>2</sub>O), and 1.5 mmol PhSiH<sub>3</sub> (103 mM in 15 mL THF) were used.

All experiments were carried out at 60 °C. Each experiment was repeated at least once and an average  $v_0$  calculated for each **[4]<sub>0</sub>**. The rate order of epoxide **4** was determined using the initial rate method as discussed in the previous section.

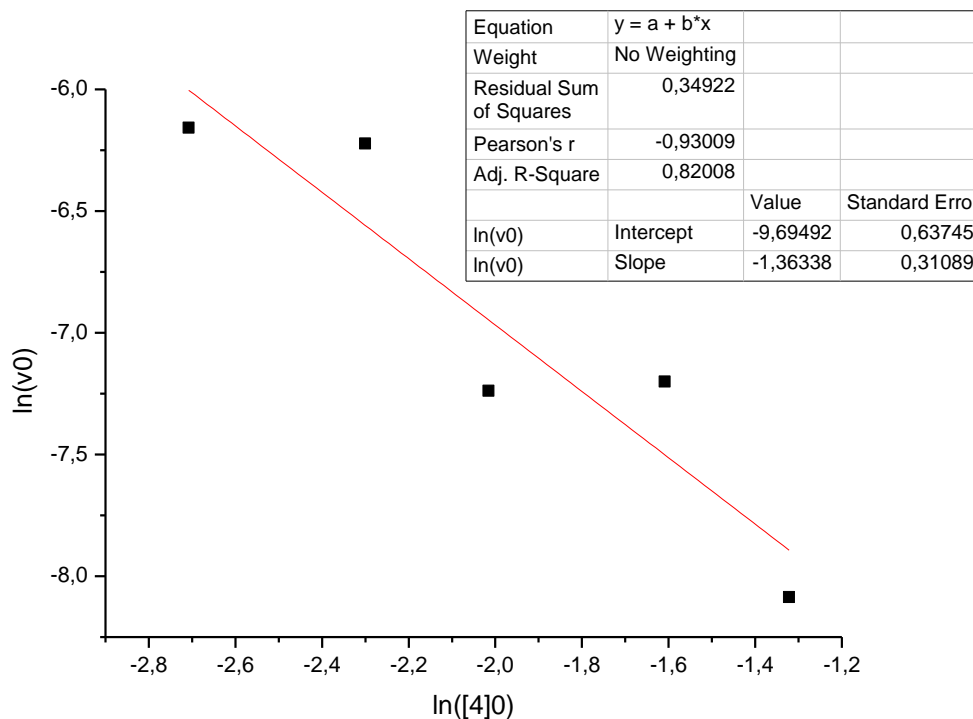


**Figure S 8.** The slope of the plot  $\ln(v_0)$  vs.  $\ln([4]_0)$  gives the rate order of **4**,  $z_2 = -1.4 \pm 0.3$ .

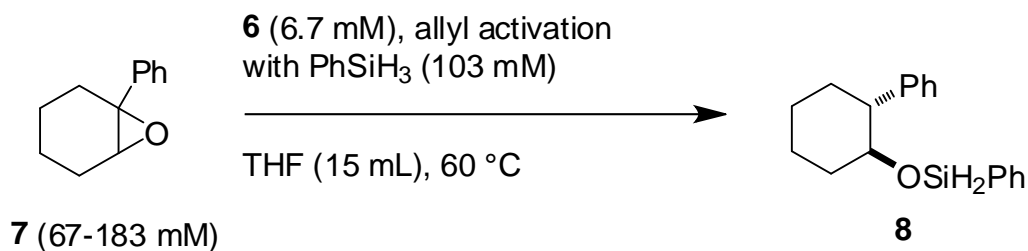


**Table S 3.** Summary of results for the determination of epoxide **4** rate order.

Molar Mass of <b>4</b>	[ <b>4</b> ] <sub>0</sub> in M	v <sub>0</sub> in A.U. min <sup>-1</sup>	ln([ <b>4</b> ] <sub>0</sub> )	ln(v <sub>0</sub> )
1.0 mmol	0,066695	-6,15752	-2,70762	-6,15752
1.5 mmol	0,100187	-6,22214	-2,30072	-6,22214
2.0 mmol	0,133268	-7,23834	-2,01540	-7,23834
3.0 mmol	0,200127	-7,20011	-1,60880	-7,20011
4.0 mmol	0,266741	-8,08541	-1,32148	-8,08541

The rate order of **4**, obtained by plotting ln(v<sub>0</sub>) versus ln([**4**]<sub>0</sub>), was z<sub>2</sub> = -1.4 ± 0.3 (**Figure S 8**).

### 2.2.3 Epoxide **7** Rate Order



To determine the rate order of **7**, z<sub>2'</sub> (see **Eq. 7**), the concentrations of the other components in the catalytic reaction were kept constant, while varying the epoxide concentration. For each run 0.10 mmol **6** (6.7 mM in 15 mL THF), activated with 2.1 eq. allylMgBr (0.71 M in Et<sub>2</sub>O), and 1.5 mmol PhSiH<sub>3</sub> (103 mM in 15 mL THF) were used. All experiments were carried out at 60 °C.

Each experiment was repeated at least once and an average v<sub>0</sub> calculated for each [**7**]. The rate order of epoxide **7** was determined using the initial rate method as discussed in the previous sections. Formation of product **8** was monitored @ 984 cm<sup>-1</sup>.

**Table S 4.** Summary of results for the determination of epoxide **7** rate order.

Molar Mass of <b>7</b>	[ <b>7</b> ] <sub>0</sub> in M	v <sub>0</sub> in A.U.min <sup>-1</sup>	ln([ <b>7</b> ] <sub>0</sub> )	ln(v <sub>0</sub> )
1.0 mmol	0,066651	3,83E-04	-2,70828	-7,86748
1.5 mmol	0,099480	1,81E-04	-2,30780	-8,61701
2.0 mmol	0,133150	1,31E-04	-2,01628	-8,94414
2.8 mmol	0,183272	1,07E-04	-1,69678	-9,14737

The rate order of **7**, obtained by plotting ln(v<sub>0</sub>) versus ln([**7**]<sub>0</sub>), was  $z_2' = -1.3 \pm 0.2$  (Figure S 9).

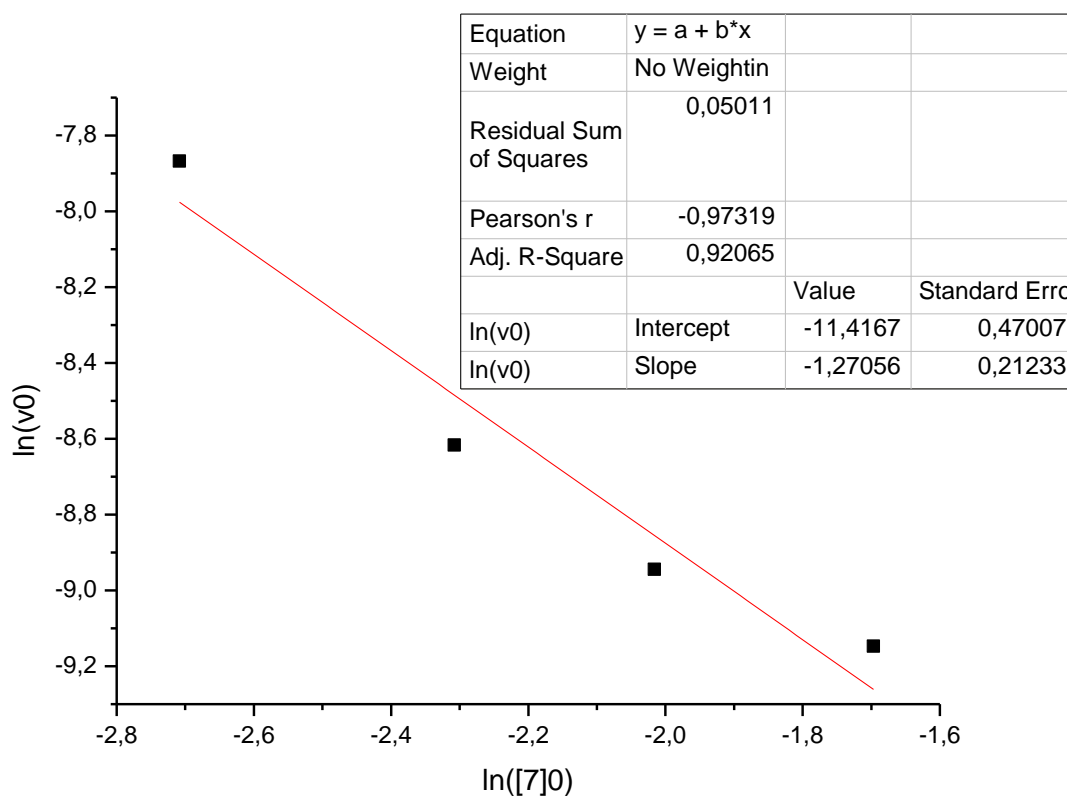


**Figure S 9.** The slope of the plot ln(v<sub>0</sub>) vs. ln([**7**]<sub>0</sub>) gives the rate order of **7**,  $z_2' = -1.3 \pm 0.2$ .

### 2.3 Initial Rate Method Vis

The absorbance maxima for the different Ti-species, [Cp<sub>2</sub>TiAllyl] and [Cp<sub>2</sub>TiH], were determined on a Shimadzu UV-1601 UV-Visible Spectrophotometer controlled by UV Probe (version 1.11) software (**Figure S 10**). An absorbance at 601 nm specific to [Cp<sub>2</sub>TiH] was established. All kinetics runs were carried out using a Vernier SpectroVis Plus and running Logger Lite 1.4 software. The following stock solutions were prepared inside an argon-filled glove box in volumetric flasks:

a) *green* [Cp<sub>2</sub>TiH] solution

Cp<sub>2</sub>TiCl<sub>2</sub> (12.4 mg; 0.05 mmol);  
allylMgBr (0.17 mL; 0.10 mmol; 0.61 M in Et<sub>2</sub>O);  
PhSiH<sub>3</sub> (0.12 mL; 0.97 mmol);  
THF (total volume: 25.0 mL);

b) *Epoxide 4* solution

**4** (487 mg; 3.00 mmol);  
THF (total volume: 2.0 mL)

c) *PhSiH<sub>3</sub>* solution

PhSiH<sub>3</sub> (0.12 mL, 0.97 mmol);  
THF (total volume: 5.0 mL)

A solvent background of dry THF was obtained and the wavelength fixed at 601 nm. A dry, air-tight cuvette with rubber septum and stirring bar was charged with 2.0-3.0 mL [Cp<sub>2</sub>TiH] solution (total concentration of [Ti] always: 2.0 mM) and varying amounts of PhSiH<sub>3</sub> solution (0 μL, 38.0 mM; 50 μL, 40.5 mM; 100 μL, 42.9 mM; 200 μL, 47.6 mM). This was taken out, inserted into the Vis spectrometer and stirred for a few minutes. The Logger Lite software was started. 50-75 μL of the epoxide solution (total concentration of epoxide always: 37.5 mM) was added to the cuvette through the septum and the contents were stirred till the end of reaction as monitored by SpectroVis. The absorbance at 601 nm was collected every second, till the regeneration of the catalyst starts.

Each run was repeated at least four times. In a few runs the first second of the measurement after epoxide addition had to be taken out of the raw data before analysis, due to a short induction period of the catalyst. This is recognizable in an extremely high value before the expected decay.

1. The raw data as a plot of '[Cp<sub>2</sub>TiH]' (A.U.) vs. time (s) was fitted as a second order exponential decay for all runs (best fit).
2. The fit (R<sup>2</sup>>0.94) was given as (a-e symbolizing the original and repeat experiments):

$$[Cp_2TiH]_{a-e} = y_0 + A_1 \times \exp\left(-\frac{x}{t_1}\right) + A_2 \times \exp\left(-\frac{x}{t_2}\right) \quad (\text{Eq. 10})$$

The constants  $k_1 = \frac{1}{t_1}$  and  $k_2 = \frac{1}{t_2}$  were calculated and  $k_{obs}$  was approximately equalized to the bigger of the two constants,  $k_{big}$ . ( $z_3$  being the rate order of PhSiH<sub>3</sub>):

$$-\frac{dt[Cp_2TiH]_{a-e}}{dx} \gg k' \times [PhSiH_3]_0^{z_3} = k_{obs} \times [Cp_2TiH]_{a-e} \gg k_{big} \times [Cp_2TiH]_{a-e} \quad (\text{Eq. 11})$$

3.  $k_{obs}$  average was calculated for each PhSiH<sub>3</sub> concentration.
4. The slope of the plot  $\ln(k_{obs})$  vs.  $\ln([PhSiH_3]_0)$ ,  $z_3 = 0.06 \pm 0.36$ , was determined by Origin 8.5, giving the order of PhSiH<sub>3</sub> (**Figure S 11**).

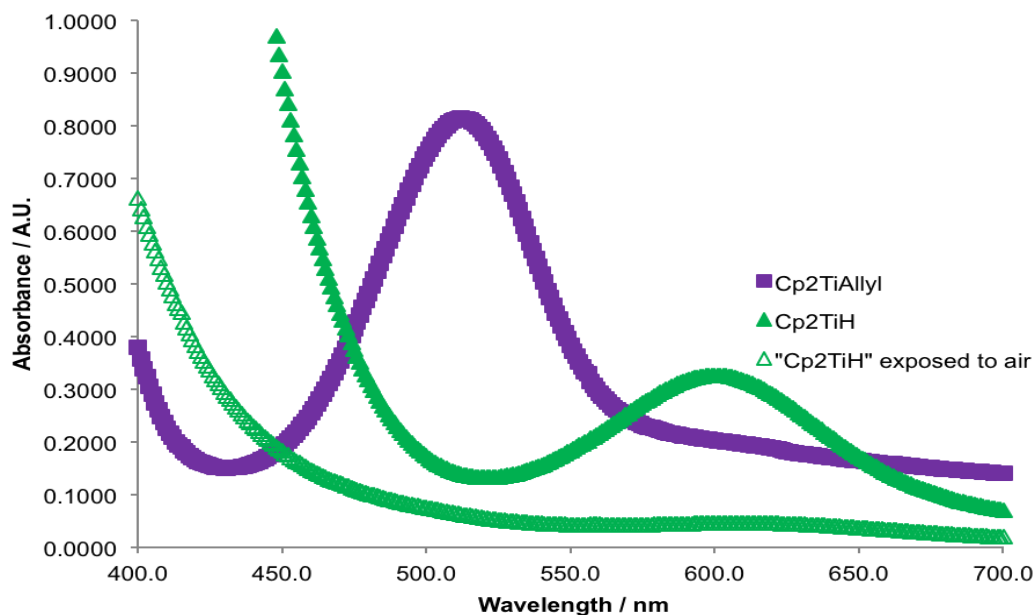


**Figure S 10.** UV/Vis spectra of [Cp<sub>2</sub>TiAllyl] (purple, max. absorbance @512 nm); [Cp<sub>2</sub>TiH] after 'allyl activation' and PhSiH<sub>3</sub> addition (green, max. absorbance @601 nm); and the [Cp<sub>2</sub>TiH] solution after exposing it to air.

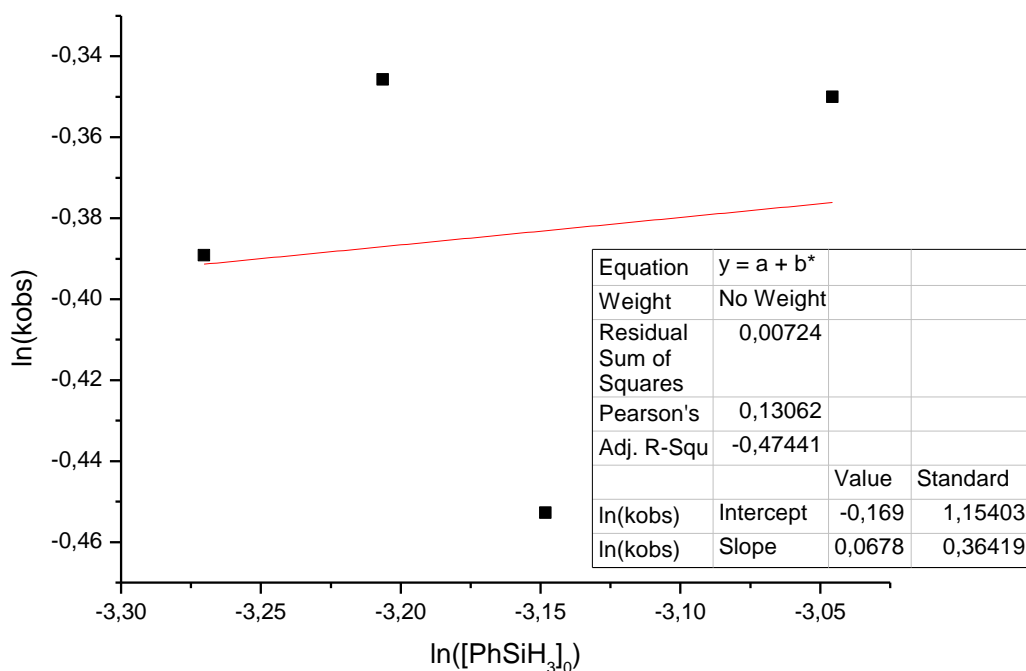


**Figure S 11.** Initial Rate Experiment monitored by SpectroVis. Plot  $\ln(k_{obs})$  vs.  $\ln([PhSiH_3]_0)$  for the titanocene catalyzed reductive opening of **4** after 'allyl activation'.

### 3 Details for EPR measurements

#### 3.1 EPR sample preparation

##### **General procedure (GP1):** preparation of 'allyl activated' solutions

A heat-dried Schlenk tube was charged with the corresponding titanocene halide (0.05 mmol, 1.0 eq.) under argon atmosphere. Freshly distilled THF (0.5 mL) was added, followed by allylMgBr (0.11 mmol, 2.2 eq). The mixture was stirred for 20 min at room temperature. Silane (1.00 mmol, 20 eq) was then added and the solution was stirred until the color changed to green. The solution was diluted with dry toluene (0.5 mL), resulting in a concentration of the catalyst of  $c(\text{catalyst}) = 0.05 \text{ M}$ . The activated solution was transferred via syringe into the EPR-tube under argon atmosphere. Then the sample was frozen in liquid nitrogen and the tube was flame sealed under vacuum ( $\text{H}_2/\text{O}_2$ -burner). Three samples for each solution were prepared according to this procedure.

**Table S 5.** Summary of EPR samples of 'allyl activation' (See Figure 2 in the main text).

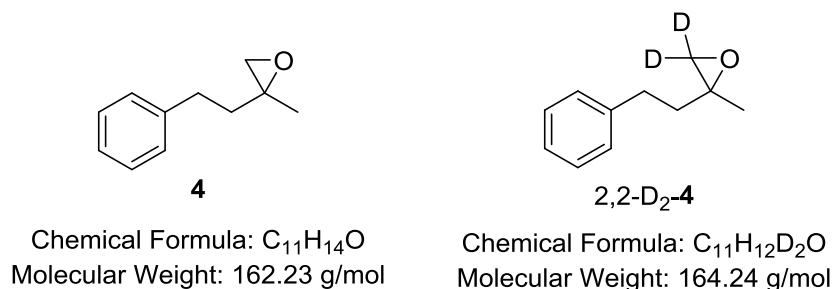
Entry	Sample	Titanocene	Silane
1	A	$\text{Cp}_2\text{TiCl}_2$ (12.4 mg)	$\text{PhSiH}_3$ (0.12 mL)
2	B	$\text{Cp}_2\text{TiCl}_2$ (12.4 mg)	$\text{PhSiD}_3$ (0.13 mL)

##### **General procedure (GP2):** preparation of 'allyl activated' solutions with epoxide

A heat-dried Schlenk tube was charged with the corresponding titanocene halide (0.05 mmol, 1.0 eq.) under argon atmosphere. Freshly distilled THF (0.5 mL) was added, followed by allylMgBr (0.11 mmol, 2.2 eq). The mixture was stirred for 20 min at room temperature. Silane (1.00 mmol, 20 eq) was then added and the solution was stirred until the color changed to green. The solution was diluted with dry toluene (0.5 mL), resulting in a concentration of the catalyst of  $c(\text{catalyst}) = 0.05 \text{ M}$ . Epoxide (0.5 mmol, 10 eq) was added and the color changed immediately from green to orange. The solution was transferred via syringe into the EPR-tube under argon atmosphere.

Then the sample was frozen in liquid nitrogen and the tube was flame sealed under vacuum ( $H_2/O_2$ -burner). Three samples for each solution were prepared according to this procedure.

**Table S 6.** Summary of EPR samples of 'allyl activated' solutions with epoxide (see main text).



Entry	Sample	Silane	Epoxide
1	a	PhSiH <sub>3</sub> (0.12 mL)	<b>4</b> (81 mg)
2	b	PhSiH <sub>3</sub> (0.12 mL)	2,2-D <sub>2</sub> - <b>4</b> (82 mg)
3	c	PhSiD <sub>3</sub> (0.13 mL)	<b>4</b> (81 mg)
4	d	PhSiD <sub>3</sub> (0.13 mL)	2,2-D <sub>2</sub> - <b>4</b> (82 mg)

## 3.2 EPR measurements and data analysis

### 3.2.1 General information

The continuous-wave (cw) X-band EPR experiments were all performed on a Bruker EMXmicro EPR spectrometer with the EMXmicro standard resonator.

All EPR experiments at Q-band frequency were performed on a Bruker ELEXSYS 580 EPR spectrometer using an ER 5106QD-2 resonator and an Oxford CF935 helium gas-flow cryostat. All Q-band cw EPR experiments were conducted at room temperature while all pulsed measurements were conducted at  $T = 30$  K. In pulsed measurements, the microwave pulses were amplified using a 150 W TWT amplifier manufactured by

Applied Systems Engineering. Typical  $\pi/2$  pulse lengths of 6 ns were obtained using this setup. The RF radiation for the ENDOR measurements were amplified using a 150 W Bruker EN 373 RF amplifier. Furthermore, a noise suppressor was used for the RF radiation. An attenuated MPFU was used for the inversion pulse  $\pi_{inv}$  in the Davies ENDOR experiments to allow for a selective inversion pulse. The length of the RF  $\pi$  pulse was optimized using a nuclear transient nutation experiment.

EPR spectra were simulated using the EasySpin program package.<sup>[11]</sup>

### 3.2.2 Pulse sequences

The pulse sequences used for the pulsed EPR measurements are summarized in **Figure S 12**.

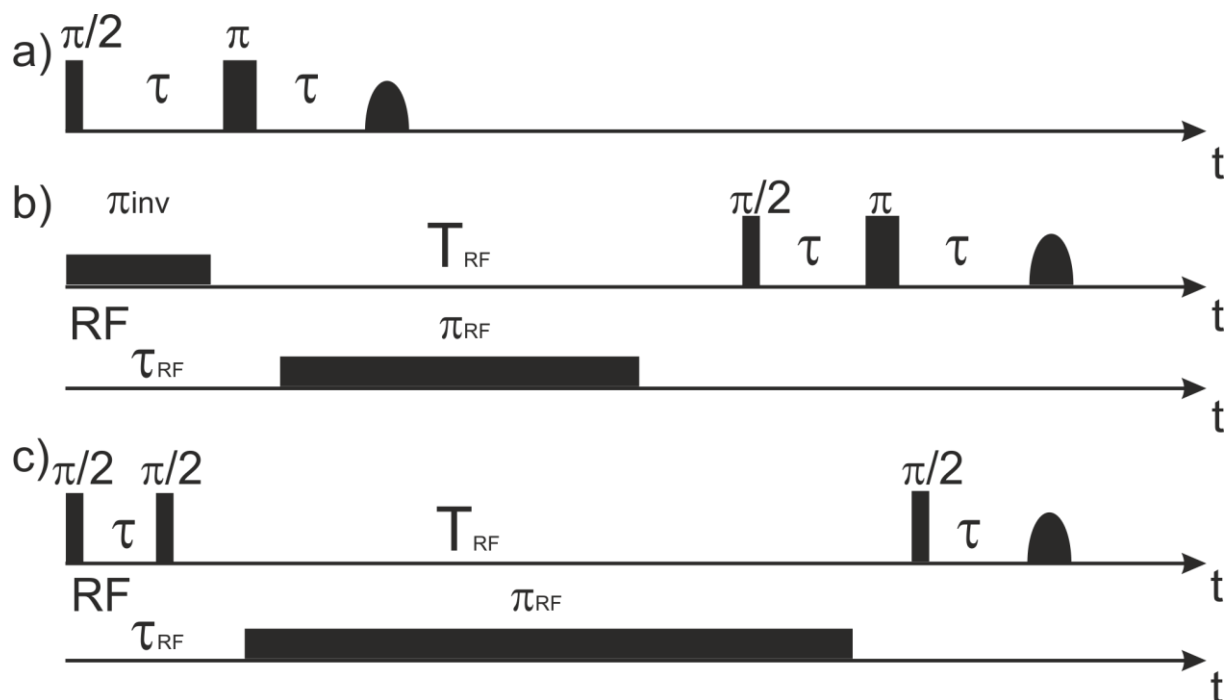


**Figure S 12.** Pulse sequences used for the pulsed EPR and ENDOR measurements. a) Hahn-Echo sequence. b) Davies ENDOR sequence. c) Mims ENDOR sequence.

The measurements parameters of all measurements are listed in **Table S 7 - S 9**.

<sup>[11]</sup> S. Stoll, A. Schweiger, *J. Magn. Reson.* **2006**, 178, 42.



**Table S 7.** Measurement parameters for the echo detected EPR spectra.

Parameter	$\pi/2$ [ns]	$\pi$ [ns]	$\tau$ [ns]	SRT <sup>a</sup> [ $\mu$ s]
Value	6	10	500	2000

a) SRT = Shot repetition time.

**Table S 8.** Measurement parameters of the Davies ENDOR measurements.

Parameter	$\pi_{inv}$ [ns]	$\pi/2$ [ns]	$\pi$ [ns]	$\tau$ [ns]	$\tau_{RF}$ [ $\mu$ s]	$T_{RF}$ [ $\mu$ s]	$\pi_{RF}$ [ $\mu$ s]	SRT <sup>a</sup> [ $\mu$ s]
Value	500	6	10	700	3	17	13.5	2000

a) SRT = Shot repetition time.

**Table S 9.** Measurement parameters of the Mims ENDOR measurements.

Parameter	$\pi/2$ [ns]	$\pi$ [ns]	$\tau$ [ns]	$\tau_{RF}$ [ $\mu$ s]	$T_{RF}$ [ $\mu$ s]	$\pi_{RF}$ [ $\mu$ s]	SRT <sup>a</sup> [ $\mu$ s]
Value	6	10	420	4	69	69	2000

a) SRT = Shot repetition time.

### 3.2.3 EPR parameters of the titanocene hydride species and discussion

The EPR spectra obtained after application of the 'allyl activation' of the catalyst are shown in **Figure S 13** along with their simulations. The EPR parameters used to simulate the spectra are listed in **Table S 10**.

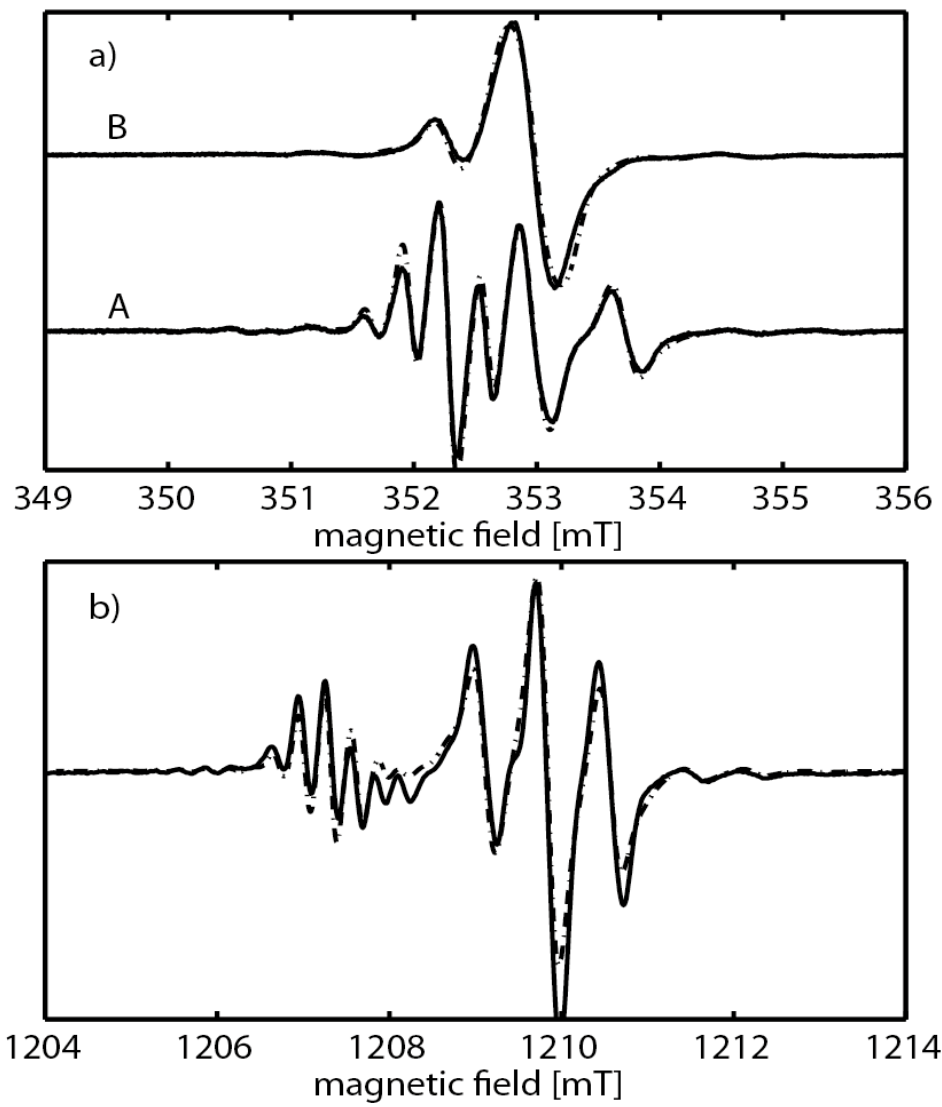


**Figure S 13.** EPR spectra (full lines) and their simulations (dashed lines) after 'allyl activation' at (a) X-band and (b) Q-band. At X-band, PhSiH<sub>3</sub> (**A**) and PhSiD<sub>3</sub> (**B**) were used during the activation.

**Table S 10.** EPR parameters used to simulate the EPR spectra, obtained after application of the 'allyl activation' compared to DFT calculations.

	X-band, PhSiH <sub>3</sub>	X-band, PhSiD <sub>3</sub>	Q-band, PhSiH <sub>3</sub>	Calc. <sup>d</sup> , PhSiH <sub>3</sub>
$g_{iso, quintet}$	1.9970	1.9970	1.9970	
$a_{iso, quintet} (^{1/2}H)^{a,b}$	8.75 (x4)	8.75 (x4)	8.75 (x4)	-7.07
$a_{iso, quintet} (^{47/49}Ti)^a$	15.50 (x1)	15.11 (x1)	15.75 (x1)	4.54
$g_{iso, triplet}$	1.9930	1.9930	1.9929	
$a_{iso, triplet} (^{1/2}H)^{a,b}$	20.50 (x2)	20.50 (x2)	20.50 (x2)	-22.10
$a_{iso, triplet} (^{47/49}Ti)^a$	18.90 (x1)	18.43 (x1)	18.69 (x1)	14.62
[quintet]/[triplet] <sup>c</sup>	1:3.5	1:12	1:13	

a) Values for the *hfc* constants  $a_{iso}$  are given in MHz, values in parentheses indicate the number of equivalent nuclei. The sign of the *hfc* constant cannot be determined experimentally. b) The value given for  $a_{iso} (^{1/2}H)$  was divided by 6.51 in the simulation to account for the different gyromagnetic ratio of deuterons as compared to protons. c) Ratio of approximate contributions of the quintet and triplet signal. d) For detailed information see Computational Details.

All spectra could be simulated with basically identical EPR parameters under all three experimental conditions. Only for the  $^{47/49}Ti$  *hfc* constant a variability of about  $\pm 2\%$  was found. The quintet species was found to be the minor species in all samples, albeit the exact ratios show some degree of variation. The ratio of the two signals does not change over time. The EPR parameters of the triplet signal agree nicely with those reported previously for  $[(Cp_2TiH_2MgBr(solvent))_2]$ .<sup>[12]</sup> For the quintet, no matching EPR spectrum was found in the literature. The quintet structure indicates the presence of four hydrogen nuclei, which are equivalent on the time scale of the EPR measurement. The adduct of PhSiH<sub>3</sub> and '[Cp<sub>2</sub>TiH]' appears to be a good candidate for the species responsible for the quintet for several reasons. First of all, similar species have been described before. The hydrogen nuclei of these species appear to be equivalent even at low temperatures as shown by NMR spectroscopy.<sup>[13]</sup> Furthermore, the adduct of

<sup>[12]</sup> J. G. Kenworthy, J. Myatt, M. C. R. Symons, *J. Chem. Soc.* **1971**, 1020.

<sup>[13]</sup> a) H. Sakaba, T. Hirata, C. Kabuto, K. Kabuto, *Organometallics* **2006**, 25, 5145; b) Y. Horbatenko, S. Vyboishchikov, *Organometallics* **2013**, 32, 514.

PhSiH<sub>3</sub> and '[Cp<sub>2</sub>TiH]' contains a titanium center which strongly resembles the titanium center in the species responsible for the triplet (formally [Cp<sub>2</sub>TiH<sub>2</sub>]<sup>+</sup>). Theory supports the assignment, as DFT calculations predict an exergonic formation of the adduct. Additionally, the *hfc* constants of the protons predicted by DFT calculations agree with those observed experimentally.

### 3.2.4 Pulsed EPR measurements of the reaction solutions

Pulsed EPR and ENDOR spectroscopy at Q-band frequency was used to investigate the structure of the resting state/intermediates after addition of the epoxide and silane. The echo detected EPR spectra of the reaction solution using different degrees of deuteration are shown in **Figure S 14**.

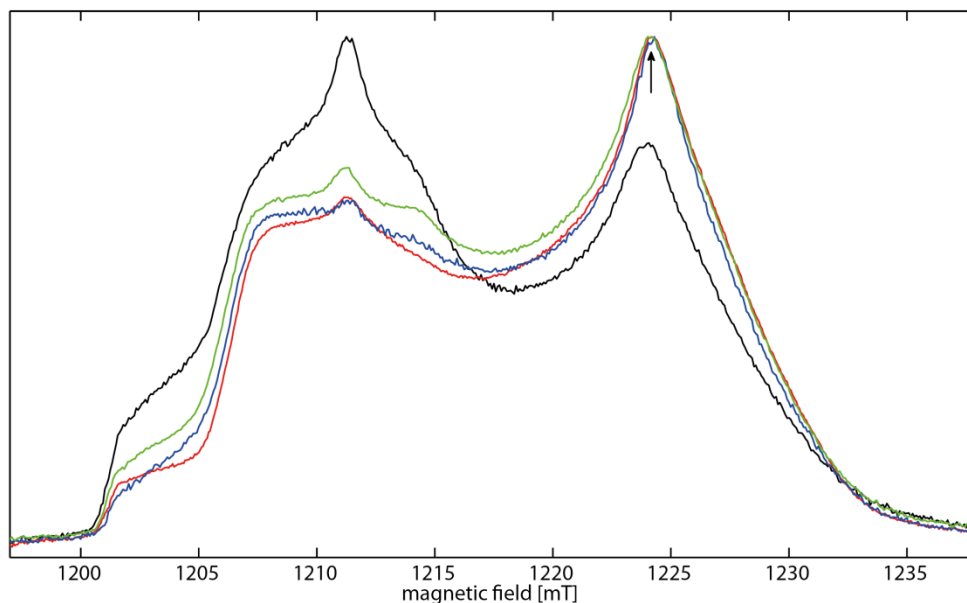


**Figure S 14.** Echo detected EPR spectra of the reaction solution. Black line: No deuteration. Red: 2,2-D<sub>2</sub>-**4**. Green: PhSiD<sub>3</sub>. Blue: 2,2-D<sub>2</sub>-**4** and PhSiD<sub>3</sub>. The arrow indicates the field position at which ENDOR spectra have been recorded.

As the spectrum shown in **Figure S 14** consists of several, overlapping EPR signals, a meaningful simulation of the spectrum was not possible.

## 4 Computational Details

### 4.1 Computational Methods

The quantum chemical calculations were performed with the TURBOMOLE 7.0 program package.<sup>[14]</sup> The geometries were optimized on the DFT level using the TPSS density functional<sup>[15]</sup> together with the polarized triple-zeta Gaussian AO basis set def2-TZVP<sup>[16]</sup>. This choice avoids major BSSE effects without employing counter-poise corrections.

For all DFT calculations the resolution-of-the-identity (RI) approximation for the Coulomb integrals<sup>[17]</sup> with matching default auxiliary basis sets<sup>[18]</sup> was applied. For geometry optimizations the numerical quadrature grid m4 was employed for integration of the exchange-correlation contribution. Default settings for convergence criteria of energy and gradients were not altered. For all geometry optimizations as well as single point calculations, the D3 dispersion correction scheme<sup>[19]</sup> together with the Becke-Johnson (BJ) damping<sup>[20]</sup> was used. For a detailed description of the dispersion correction, that is of great importance in studies of large molecules, see Ref. [21]; for recent chemical applications of this method, see e.g. Ref. [22].

The rovibrational corrections from energy to the free energy were obtained from a modified rigid-rotor-harmonic-oscillator statistical treatment<sup>[23]</sup> based on analytical harmonic frequencies calculated on the TPSS-D3/def2-TZVP level (see above). For the entropy calculation, frequencies with wavenumbers below  $100\text{ cm}^{-1}$  were treated as rigid rotors to avoid inherent errors in the harmonic approximation. Artificial small frequency imaginary modes of up to  $i30\text{ cm}^{-1}$  were inverted and thus included into the enthalpy and, more importantly, entropy calculations.

Solvent effects on the thermochemical properties were included by the COSMO-RS model<sup>[24]</sup> that was used as implemented in COSMOtherm<sup>[25]</sup> to obtain all solvation free energies. Single point calculations employing the default BP86<sup>[26]</sup>/def-TZVP<sup>[27]</sup> level of theory were executed on the optimized geometries. Solvation contributions to free energies at 298.15 K for THF were computed for these gas phase structures.

Single point energies were obtained in the gas phase on the PW6B95-D3<sup>[28]</sup> or B3LYP<sup>[29]</sup>-D3 level together with the large quadruple-zeta basis set def2-QZVP<sup>[16]</sup> and the larger grid m5 and m4, respectively. This setup ensures converged single-point energies.

EPR parameters were computed with the ORCA program package<sup>[30]</sup>, employing the PBE0 hybrid density functional in a large QZVP basis set. Integral evaluation was carried out on a large grid (Grid5, Finalgrid6) with tight SCF convergence criteria. Overall good agreement with experiment can be reached. However, the deviation of the Ti *hfc* in the quintet signal is due to the multi-reference character of the metal center in the given geometry, which can be observed in an FOD analysis<sup>[31]</sup>.

## 4.2 References related to the Computational Details

[14] R. Ahlrichs, K. M. Armbruster, M. Bär, H.-P. Baron, R. Bauernschmitt, N. Crawford, P. Deglmann, M. Ehrig, K. Eichkorn, S. Elliott, F. Furche, F. Haase, M. Häser, C. Hättig, A. Hellweg, H. Horn, C. Huber, U. Huniar, M. Kattannek, C. Kölmel, M. Kollwitz, K. May, P. Nava, C. Ochsenfeld, H. Öhm, H. Patzelt, D. Rappoport, O. Rubner, A. Schäfer, U. Schneider, M. Sierka, O. Treutler, B. Unterreiner, M. von Arnim, F. Weigend, P. Weis, H. Weiss, *TURBOMOLE 7.0*, Universität Karlsruhe: Karlsruhe, Germany, **2015**. See also <http://www.turbomole.com>.

[15] J. Tao, J. Perdew, V. Staroverov, G. Scuseria, *Phys. Rev. Lett.* **2003**, *91*, 146401.

[16] F. Weigend, R. Ahlrichs, *Phys. Chem. Chem. Phys.* **2005**, *7*, 3297.

[17] K. Eichkorn, O. Treutler, H. Öhm, M. Häser, R. Ahlrichs, *Chem. Phys. Lett.* **1995**, *242*, 652.

[18] F. Weigend, *Phys. Chem. Chem. Phys.* **2006**, *8*, 1057.

[19] S. Grimme, J. Antony, S. Ehrlich, H. J. Krieg, *Chem. Phys.* **2010**, *132*, 154104.

[20] a) S. Grimme, S. Ehrlich, L. Goerigk, *J. Comput. Chem.* **2011**, *32*, 1456; b) A. D. Becke, E. R. J. Johnson, *Chem. Phys.* **2005**, *123*, 154101; c) E. R. Johnson, A. D. J. Becke, *Chem. Phys.* **2005**, *123*, 24101.

[21] a) S. Grimme, J. Antony, T. Schwabe, C. Mück-Lichtenfeld, *Org. Biomol. Chem.* **2007**, *5*, 741; b) S. Grimme, *WIRE Comput. Mol. Sci.* **2011**, *1*, 211.

[22] a) A. Gansäuer, C. Kube, K. Daasbjerg, R. Sure, S. Grimme, G. D. Fianu, D. V. Sadasivam, R. A. Flowers, II, *J. Am. Chem. Soc.* **2014**, *136*, 1663; b) S. Grimme, H.

Kruse, L. Goerigk, G. Erker, *Angew. Chem.* **2010**, *122*, 1444; *Angew. Chem. Int. Ed.* **2010**, 1402; c) T. Schwabe, S. Grimme, J.-P. Djukic, *J. Am. Chem. Soc.* **2009**, *131*, 14156; d) H. Kruse, S. Grimme, *J. Phys. Chem. C* **2009**, *11*, 17006; e) M. Mömming, S. Frömel, G. Kehr, R. Fröhlich, S. Grimme, G. Erker, *J. Am. Chem. Soc.* **2009**, *131*, 12280.

[23] S. Grimme, *Chem. Eur. J.* **2012**, *18*, 9955.

[24] a) A. J. Klamt, *Chem. Phys.* **1995**, *99*, 2224; b) F. Eckert, A. Klamt, *AIChE J.* **2002**, *48*, 369.

[25] F. Eckert, A. J. Klamt, L. Pohler, COSMOtherm, Version C3.0, Release 14.01; COSMOlogic GmbH & Co. KG, Leverkusen, Germany, **2013**.

[26] a) A. D. Becke, *Phys. Rev. A* **1988**, *38*, 3098; b) J. P. Perdew, *Phys. Rev. B* **1986**, *33*, 8822.

[27] A. Schäfer, C. Huber, R. J. Ahlrichs, *Chem. Phys.* **1994**, *100*, 5829.

[28] Y. Zhao, D. G. Truhlar, *J. Phys. Chem. A* **2005**, *109*, 5656.

[29] A. D. Becke, *J. Chem. Phys.* **1993**, *98*, 5648; P. J. Stephens, J. Devlin, C. F. Chabalowski, M. J. Frisch, *J. Phys. Chem.* **1994**, *98*, 11623.

[30] F. Neese, ORCA: An ab Initio, Density Functional and Semiempirical Program Package, version 3.0.3 (Current Development Version); Max Planck Institute for Chemical Energy Conversion: Mülheim, Germany; F. Neese, *WIREs Comput. Mol. Sci.* **2012**, *2*, 73.

[31] S. Grimme, A. Hansen, *Angew. Chem. Int. Ed.* **2015**, *54*, 12308.

Listed below are the Cartesian coordinates of the optimized structures. Energies refer to the TPSS-D3/def2-TZVP level of theory and are given in au.

### **Cp<sub>2</sub>TiH + ethylene oxide opened**

29

Energy = -1391.402920888

C	0.5211603	-0.7121240	-1.9792317
C	-0.7460325	-0.0868530	-2.0550073
C	-0.5605816	1.3071057	-1.8886202
C	0.8326541	1.5430058	-1.7261376
C	1.5001123	0.2944817	-1.7730210
Ti	0.0875253	0.2820485	0.1502684
C	-1.0028344	2.2098651	1.0394815
C	-1.3188385	1.1273780	1.9005562
C	-0.1227126	0.6831061	2.5029567
C	0.9427033	1.4980092	2.0299009
C	0.3935303	2.4543116	1.1415375
O	-0.6829439	-1.3397864	0.6040663
C	-0.8963232	-2.6340531	0.1007884
C	0.3383742	-3.4639863	0.1462906
H	1.6782277	-0.1821239	0.5225346
H	-1.3372466	2.0582589	-1.9067333
H	1.3019060	2.5061279	-1.5878550
H	2.5643786	0.1367383	-1.6859616
H	0.7120657	-1.7761666	-2.0126391
H	-1.6983183	-0.5887333	-2.1670814
H	-0.0197987	-0.1795064	3.1455406
H	1.9803480	1.4164074	2.3168640
H	0.9443876	3.2227607	0.6186389
H	-1.7073585	2.7746805	0.4450184
H	-2.2928752	0.6719939	2.0156922
H	-1.6992231	-3.1114103	0.6932637
H	-1.2871849	-2.5808769	-0.9364427



H	1.2810032	-3.0044333	0.4229980
H	0.2938956	-4.5262260	-0.0776659

**Cp<sub>2</sub>TiH + ethylene oxide TS**

29

Energy = -1391.402920888

C	0.5211603	-0.7121240	-1.9792317
C	-0.7460325	-0.0868530	-2.0550073
C	-0.5605816	1.3071057	-1.8886202
C	0.8326541	1.5430058	-1.7261376
C	1.5001123	0.2944817	-1.7730210
Ti	0.0875253	0.2820485	0.1502684
C	-1.0028344	2.2098651	1.0394815
C	-1.3188385	1.1273780	1.9005562
C	-0.1227126	0.6831061	2.5029567
C	0.9427033	1.4980092	2.0299009
C	0.3935303	2.4543116	1.1415375
O	-0.6829439	-1.3397864	0.6040663
C	-0.8963232	-2.6340531	0.1007884
C	0.3383742	-3.4639863	0.1462906
H	1.6782277	-0.1821239	0.5225346
H	-1.3372466	2.0582589	-1.9067333
H	1.3019060	2.5061279	-1.5878550
H	2.5643786	0.1367383	-1.6859616
H	0.7120657	-1.7761666	-2.0126391
H	-1.6983183	-0.5887333	-2.1670814

H	-0.0197987	-0.1795064	3.1455406
H	1.9803480	1.4164074	2.3168640
H	0.9443876	3.2227607	0.6186389
H	-1.7073585	2.7746805	0.4450184
H	-2.2928752	0.6719939	2.0156922
H	-1.6992231	-3.1114103	0.6932637
H	-1.2871849	-2.5808769	-0.9364427
H	1.2810032	-3.0044333	0.4229980
H	0.2938956	-4.5262260	-0.0776659

### **Cp<sub>2</sub>TiH + ethylene oxide**

29

Energy = -1391.381186180

C	0.8041548	-0.0148999	-2.2635501
C	-0.6113965	-0.0627798	-2.2677781
C	-1.1097014	1.1895824	-1.8329157
C	0.0120445	2.0300372	-1.5879051
C	1.1956127	1.2855209	-1.8371985
Ti	0.1228852	0.2948700	-0.0090797
C	-0.2066475	2.1537952	1.3693704
C	-1.1137547	1.1527511	1.8117490
C	-0.3368511	0.0845293	2.3322741
C	1.0346409	0.4077599	2.1974637
C	1.1207961	1.6896319	1.5941645
O	-0.9733067	-1.6850109	0.1136324

C	-0.3898380	-2.7931693	0.8639765
C	-0.4505658	-2.8469983	-0.5974415
H	1.4466156	-0.8570464	0.0452397
H	-2.1512745	1.4615260	-1.7272110
H	-0.0281539	3.0618898	-1.2711327
H	2.2116403	1.6394944	-1.7316988
H	1.4758262	-0.8150734	-2.5375626
H	-1.2183475	-0.9238617	-2.5154614
H	-0.7325045	-0.8380295	2.7359316
H	1.8692276	-0.2130500	2.4873765
H	2.0330236	2.2168835	1.3502520
H	-0.4824408	3.1101854	0.9500666
H	-2.1936093	1.2068645	1.7860637
H	-1.2256371	-3.4285871	-1.0892049
H	0.4577291	-2.6330205	-1.1519169
H	0.5605931	-2.5395249	1.3235725
H	-1.1207603	-3.3342699	1.4589237

### **Cp<sub>2</sub>TiH + PhSiH<sub>3</sub>**

37

Energy = -1760.63549314200

C	-1.8759997	0.1828294	-3.0253621
C	-0.6923654	0.2695508	-2.2762436
C	0.0350211	1.4691030	-2.3338862

C	-0.3938670	2.5385968	-3.1180656
C	-1.5778333	2.4335309	-3.8521762
C	-2.3201926	1.2537436	-3.8033840
Si	-0.1075266	-1.2264141	-1.2670205
H	-0.2894717	-1.8298161	0.2388210
Ti	0.5072350	-0.6080498	1.3009554
C	2.7639799	-0.3932981	1.8759581
C	2.7032321	-1.3094342	0.7925717
C	1.9801729	-2.4535623	1.2193945
C	1.5858264	-2.2524242	2.5688178
C	2.0851231	-0.9843904	2.9771860
C	-0.6838155	0.2678608	3.1162360
C	-1.6035351	-0.4226449	2.2881963
C	-1.6544908	0.2662389	1.0411027
C	-0.7701554	1.3778679	1.1074752
C	-0.1616654	1.3741275	2.3825781
H	1.0182838	-2.9436628	3.1768915
H	1.7523360	-3.3191380	0.6131183
H	3.1136446	-1.1555701	-0.1951457
H	3.2490396	0.5731606	1.8664304
H	1.9658082	-0.5410670	3.9557696
H	-2.2743271	0.0048176	0.1934637
H	-0.5800533	2.0754301	0.3043187
H	0.5776752	2.0798501	2.7372276
H	-0.4199771	-0.0026914	4.1290970
H	-2.1712802	-1.3036112	2.5538392
H	0.8436150	-0.0906014	-0.3696210

H	1.1032457	-1.8776574	-1.8353425
H	-1.2266877	-2.1711358	-1.6355506
H	-2.4549222	-0.7382072	-2.9958934
H	-3.2438075	1.1682663	-4.3701762
H	-1.9201377	3.2692310	-4.4566959
H	0.1890382	3.4555111	-3.1556889
H	0.9488348	1.5636601	-1.7491964

### **Cp<sub>2</sub>TiH**

22

Energy = -1235.68625490082

C	-0.8089435	-1.6856291	-1.4311150
C	-1.1019053	-1.7837370	-0.0591571
C	-1.9450213	-0.7074006	0.2871420
C	-2.1753325	0.0578811	-0.8705713
C	-1.4683235	-0.5425413	-1.9369504
Ti	0.1265406	0.2227007	-0.4145039
C	0.9599092	1.9145143	1.0017359
C	0.5487769	0.8630558	1.8395559
C	1.3544269	-0.2603920	1.5598892
C	2.2662844	0.0953588	0.5488039
C	2.0208372	1.4419929	0.1966682
H	-1.4548951	-0.2039370	-2.9597441
H	-0.1879335	-2.3628191	-1.9983132
H	-0.7440337	-2.5490606	0.6131222
H	-2.3439582	-0.5071285	1.2702773

H	-2.7853888	0.9466585	-0.9335259
H	3.0224763	-0.5455612	0.1205986
H	1.2842566	-1.2243616	2.0411070
H	-0.2463501	0.9063868	2.5687387
H	0.5361965	2.9073538	0.9741132
H	0.5793939	1.0019350	-1.8803580
H	2.5629871	2.0147302	-0.5375131

### **Cp<sub>2</sub>TiOEt + ethylene oxide opened**

36

Energy = -1545.38471044665

C	-2.4293180	-0.5225664	-0.1439067
C	-2.3706714	-0.2561968	1.2501159
C	-2.1948730	1.1320485	1.4230008
C	-2.1160621	1.7288808	0.1339661
C	-2.2835869	0.7027407	-0.8278858
Ti	-0.1786236	0.2906996	0.3330968
C	1.7204564	0.4366309	1.8590774
C	0.7183642	1.3203374	2.3322681
C	0.5746210	2.3648485	1.3785000
C	1.4522253	2.1000481	0.3059157
C	2.1655094	0.9087719	0.6069684
O	0.4454021	0.1786814	-1.4357055
C	0.0430668	-0.6288195	-2.5226507
C	0.1116844	0.1683237	-3.8222419
O	0.0102074	-1.5440742	0.7331151

C	1.1520986	-2.3683515	0.6404389
C	1.5454562	-2.9293916	1.9615118
H	-2.2491612	0.8368221	-1.8996944
H	-2.5050540	-1.5021336	-0.5936082
H	-2.3962691	-0.9984247	2.0349944
H	-2.1092692	1.6501819	2.3676485
H	-1.9680875	2.7782762	-0.0799539
H	2.8747215	0.4206995	-0.0458140
H	2.0355548	-0.4761591	2.3478875
H	0.1718045	1.2184956	3.2597264
H	-0.1059801	3.2011502	1.4519740
H	1.5333772	2.6705882	-0.6085291
H	0.7206875	-1.4948702	-2.5756343
H	-0.9711675	-1.0294931	-2.3743353
H	-0.1608923	-0.4630201	-4.6763610
H	-0.5748094	1.0212821	-3.7874103
H	1.1244601	0.5525030	-3.9791176
H	2.4977455	-3.4401895	2.0789300
H	0.8092647	-2.9949731	2.7564217
H	0.9037293	-3.1934272	-0.0587966
H	2.0033881	-1.8399199	0.1760878

**Cp<sub>2</sub>TiOEt + ethylene oxide TS**

36

Energy = -1545.34318395472

C	-0.6173147	-1.3450797	-2.3419546
---	------------	------------	------------

C	0.7766601	-1.5949500	-2.2991463
C	1.4551095	-0.3466389	-2.2635480
C	0.4768068	0.6760939	-2.3330295
C	-0.7918350	0.0682153	-2.3785002
Ti	0.2082540	-0.5606539	-0.2076145
C	-0.5230874	-2.2848139	1.2711074
C	0.3440396	-2.9137021	0.3540839
C	1.6403939	-2.3531448	0.5209729
C	1.5780872	-1.4050332	1.5693137
C	0.2399203	-1.3474143	2.0275061
O	1.0330390	1.1166340	0.3165117
C	0.9340438	1.8116687	1.5277466
C	1.2910101	3.2849023	1.3273709
H	2.3940621	-0.7825870	1.9083960
H	-0.1449486	-0.6836478	2.7880162
H	-1.5863387	-2.4599595	1.3658601
H	0.0614785	-3.6578504	-0.3776617
H	2.5210983	-2.6014186	-0.0559428
H	0.6718881	1.7357871	-2.2616323
H	-1.7384526	0.5883432	-2.4398522
H	-1.4012433	-2.0905631	-2.3728364
H	1.2444051	-2.5688386	-2.2844515
H	2.5239066	-0.1988179	-2.1903464
H	-0.0838502	1.7317174	1.9527503
H	1.6147946	1.3726963	2.2820367
H	1.2432937	3.8317994	2.2775059
H	2.3036770	3.3765262	0.9213648



H	0.5970011	3.7531637	0.6203679
O	-1.5532141	0.2333280	0.5512211
C	-3.1779998	0.3236106	-0.0472907
C	-2.2391024	1.4267993	0.1805477
H	-3.2250338	-0.1661746	-1.0090182
H	-3.8354184	-0.0020031	0.7469799
H	-2.4220439	2.0860431	1.0305199
H	-1.8148429	1.9459854	-0.6785355

### **Cp<sub>2</sub>TiOEt + ethylene oxide**

36

Energy = -1545.36961183611

C	0.9414688	1.4016248	2.3106576
C	0.6841552	2.6034661	1.6101683
C	1.4407801	2.5883018	0.4067987
C	2.1957663	1.3850553	0.3907184
C	1.8758951	0.6430219	1.5544146
Ti	-0.0973404	0.7892993	0.2130127
C	-2.0035106	-0.0241028	1.3492620
C	-2.0815587	1.3946758	1.3531653
C	-2.2065066	1.8385908	0.0091888
C	-2.2492681	0.6854487	-0.8188742
C	-2.1227384	-0.4589032	0.0029481
O	0.5417083	-0.1753154	-1.2428103
C	0.1717366	-0.8623204	-2.4137574
C	0.3859088	0.0170757	-3.6429077

H	-2.3145201	0.6869898	-1.8989419
H	-2.0524725	-1.4869315	-0.3265695
H	-1.9121439	-0.6624696	2.2174900
H	-2.0313569	2.0275774	2.2276294
H	-2.2826627	2.8661466	-0.3208214
H	2.8333566	1.0512159	-0.4148613
H	2.2737105	-0.3272110	1.8211120
H	0.4920231	1.1026792	3.2486368
H	0.0020712	3.3849080	1.9159947
H	1.4616625	3.3672815	-0.3437767
H	0.7851590	-1.7728150	-2.4942286
H	-0.8802390	-1.1847084	-2.3575798
H	0.1166693	-0.5265281	-4.5561783
H	-0.2323024	0.9189161	-3.5770831
H	1.4338349	0.3249432	-3.7140254
O	-0.3580796	-3.3772571	0.6010437
C	0.4267097	-3.0104542	1.7508766
C	1.0556086	-3.1358586	0.4316309
H	0.2195543	-2.0149524	2.1423618
H	0.5521579	-3.8003758	2.4901726
H	1.6408186	-4.0249428	0.2012914
H	1.2939442	-2.2320716	-0.1261588

**Cp<sub>2</sub>TiOEt**

29

Energy = -1389.27898150571

C	-1.8683267	0.2332795	1.7845124
C	-2.1416352	0.8056126	0.5259301
C	-2.1334309	-0.2338915	-0.4260180
C	-1.8280366	-1.4353343	0.2365578
C	-1.6522816	-1.1476555	1.6053783
Ti	0.0904675	-0.0091334	0.4520739
C	0.9881266	1.7926977	1.7727376
C	1.8642479	1.5903718	0.6840790
C	2.4385180	0.3156208	0.8219302
C	1.9035242	-0.2870171	1.9786728
C	1.0283794	0.6420582	2.5797448
H	-2.3045923	-0.1204248	-1.4860944
H	-1.7230789	-2.4056711	-0.2255727
H	-1.4237439	-1.8626075	2.3815247
H	-1.8306966	0.7651401	2.7221134
H	-2.3619703	1.8447191	0.3327705
H	3.1211414	-0.1468858	0.1267948
H	2.1572139	-1.2632999	2.3639585
H	0.4780012	0.4865785	3.4946659
H	0.4031014	2.6809245	1.9596938
O	0.6443584	-0.5460650	-1.1864539
H	2.0550918	2.2889370	-0.1166231
C	0.3630784	-1.1044596	-2.4187178
C	0.3090007	-0.0492021	-3.5106197
H	1.1329322	-1.8448959	-2.6744398
H	-0.5923476	-1.6524439	-2.4045212
H	0.1081891	-0.5065818	-4.4805425

H	-0.4789753	0.6793546	-3.3126019
H	1.2537439	0.4902746	-3.5809334

### **ethylene oxide**

7

Energy = -153.45092472675

C	-0.0130812	0.1037100	-0.1258103
C	-0.1482305	-0.0506705	1.3192219
O	1.1127681	0.1312440	0.7195330
H	-0.5201218	0.7782116	1.9166677
H	-0.3428721	-1.0341951	1.7400374
H	-0.2850776	1.0465048	-0.5942212
H	-0.1076778	-0.7658347	-0.7717133

### **EtO<sub>3</sub>SiAllyl**

33

Energy = -870.67262508965

C	-0.0923711	-2.2554478	-1.6475131
Si	-0.3101198	-0.8191948	-0.4543445
O	0.9170763	0.2710122	-0.6543501
C	2.3030551	-0.0444945	-0.8579331
C	3.0003367	-0.4130520	0.4450417
O	-0.3992719	-1.4979824	1.0377134
C	-1.0038169	-0.8843094	2.1929963
C	-0.0917912	0.1586854	2.8245942

O	-1.6923767	0.0366643	-0.6709152
C	-1.8732508	1.0723746	-1.6523076
C	-1.8064355	2.4417623	-0.9936559
H	-1.9604540	-0.4364902	1.9000553
H	-1.2039892	-1.7003486	2.8951877
H	-1.1097824	0.9895936	-2.4370967
H	-2.8542297	0.9023733	-2.1100914
H	2.3960154	-0.8599539	-1.5886025
H	2.7567511	0.8496937	-1.2987180
H	-0.5661345	0.5752745	3.7209652
H	0.8647453	-0.2876820	3.1135755
H	0.1047011	0.9769212	2.1245767
H	-2.0019726	3.2283975	-1.7319865
H	-2.5543465	2.5179621	-0.1980467
H	-0.8146359	2.6047641	-0.5618356
H	4.0629165	-0.6087666	0.2595657
H	2.9174918	0.4043738	1.1675792
H	2.5526890	-1.3089323	0.8868331
H	0.0247273	-1.8571175	-2.6640421
H	0.8470655	-2.7656264	-1.3878846
C	-1.2381875	-3.2208694	-1.5849957
C	-2.1551450	-3.3913983	-2.5398392
H	-1.3242060	-3.7885054	-0.6589077
H	-2.9803222	-4.0863876	-2.4163949
H	-2.1139805	-2.8385975	-3.4762969

## EtO<sub>3</sub>SiH

26

Energy = -753.88114884641

Si	-0.4592050	-1.0215888	-0.7420544
O	-0.5697381	-1.7561352	0.7177674
O	0.8236416	-0.0006159	-0.9339809
O	-1.8058967	-0.1077164	-0.9393358
H	-0.3196111	-2.1273852	-1.7123978
C	-1.0989938	-1.1514268	1.9148178
C	-0.0966681	-0.2078907	2.5658141
H	-2.0268487	-0.6221941	1.6680439
H	-1.3425755	-1.9813423	2.5859875
C	-1.9078373	1.0636798	-1.7708581
C	-1.7540709	2.3246104	-0.9341124
H	-1.1465507	1.0333600	-2.5604016
H	-2.8956975	1.0234169	-2.2427062
C	2.1626262	-0.4459840	-1.2150737
C	2.9424108	-0.7094218	0.0658420
H	2.1291399	-1.3500690	-1.8398829
H	2.6345828	0.3500690	-1.8010135
H	-0.5160122	0.1985340	3.4936826
H	0.8316644	-0.7351547	2.8062592
H	0.1424857	0.6266825	1.8991822
H	-1.8940479	3.2137118	-1.5602044
H	-2.4988909	2.3438405	-0.1321550
H	-0.7549988	2.3643413	-0.4901016
H	3.9738716	-0.9927078	-0.1740103

H	2.9641020	0.1879943	0.6917411
H	2.4831195	-1.5206079	0.6391497

### EtO<sub>3</sub>SiMe

29

Energy = -793.23500896669

C	-0.0275608	0.1250807	2.7836925
C	-1.0548032	-0.7938297	2.1357185
O	-0.5300855	-1.4471668	0.9649368
Si	-0.4247765	-0.7641606	-0.5261776
O	-1.7778617	0.1478801	-0.7300671
C	-1.8710444	1.3357324	-1.5346019
C	-1.7573731	2.5790323	-0.6649789
O	0.8355720	0.2936112	-0.7089739
C	2.1998535	-0.0693443	-0.9670585
C	2.9278888	-0.4857975	0.3045169
C	-0.2768742	-2.1822786	-1.7248426
H	-1.9563702	-0.2334149	1.8607617
H	-1.3436410	-1.5954627	2.8238166
H	-1.0864601	1.3356181	-2.3019478
H	-2.8443555	1.2975569	-2.0370143
H	2.2362018	-0.8761489	-1.7122005
H	2.6727207	0.8141776	-1.4097422
H	-0.4456781	0.5679514	3.6954282
H	0.8755136	-0.4324088	3.0511839
H	0.2540598	0.9340226	2.1025301

H	-1.8897400	3.4816471	-1.2733401
H	-2.5252236	2.5703154	0.1152157
H	-0.7722551	2.6188555	-0.1908012
H	3.9751850	-0.7184408	0.0786702
H	2.9017548	0.3215705	1.0425519
H	2.4616701	-1.3714866	0.7476199
H	-0.1509119	-1.8244339	-2.7531592
H	0.5748711	-2.8285021	-1.4834851
H	-1.1802772	-2.8001749	-1.6882528

### **EtO<sub>3</sub>SiPh**

36

Energy = -982.76577285378

C	-0.0675149	-0.0547551	-0.0524859
C	0.1310218	0.3832514	1.3856450
O	1.4636880	0.2472208	1.8350157
Si	2.3137816	-1.1486457	1.9882286
O	1.2208776	-2.3308360	2.3203765
C	1.5162520	-3.6785335	2.6139725
C	1.4809316	-4.5511779	1.3747661
O	3.1130025	-1.6134853	0.6202807
C	4.2000344	-0.9337647	0.0287921
C	3.7506533	0.1742618	-0.9034400
C	3.5571366	-0.8883453	3.3480567
H	-0.5473562	-0.1762297	2.0369391
H	-0.1290821	1.4397008	1.4863337



H	2.4894151	-3.7752409	3.1114534
H	0.7701537	-4.0271978	3.3328329
H	4.8730138	-0.5233865	0.7914398
H	4.7775563	-1.6733559	-0.5320313
H	-1.0969528	0.1377446	-0.3582392
H	0.5902142	0.4907333	-0.7290535
H	0.1198028	-1.1213782	-0.1798353
H	1.6507491	-5.5943059	1.6459907
H	0.5111816	-4.4875918	0.8809240
H	2.2470069	-4.2573327	0.6584399
H	4.6148531	0.6191631	-1.3987401
H	3.0817443	-0.2093302	-1.6741159
H	3.2310077	0.9653151	-0.3629420
C	4.6782548	-1.7162896	3.4492801
C	5.5880134	-1.5690680	4.4858180
C	5.3930911	-0.5828054	5.4413189
C	4.2887395	0.2524286	5.3553178
C	3.3803442	0.0990650	4.3186050
H	4.8530042	-2.4857278	2.7056609
H	6.4499591	-2.2208039	4.5464130
H	6.1021898	-0.4633825	6.2502440
H	4.1363813	1.0261183	6.0966675
H	2.5262637	0.7616128	4.2613546

**PhSiH<sub>2</sub>Allyl**

22

Energy = -639.91352881113

C	-0.9656342	0.9212447	0.7692806
C	-1.0206468	-0.2067209	-0.0692733
C	-1.7849913	-0.1167842	-1.2455398
C	-2.4661002	1.0548975	-1.5757531
C	-2.3951418	2.1635083	-0.7315152
C	-1.6440607	2.0949381	0.4429616
Si	-0.0461502	-1.7543532	0.3351931
H	-0.0334628	-1.9671610	1.8049774
C	1.7528651	-1.5972148	-0.2599612
H	-0.6860607	-2.9190829	-0.3335489
H	-1.8540655	-0.9755669	-1.9102124
H	-3.0540200	1.1023691	-2.4884744
H	-2.9268502	3.0764338	-0.9854712
H	-1.5903800	2.9547926	1.1053450
H	-0.3858901	0.8807503	1.6888103
H	2.3026697	-2.4912206	0.0605235
H	1.7419552	-1.5877032	-1.3583771
C	2.3939129	-0.3518714	0.2730739
C	3.2806756	-0.3018686	1.2707177
H	2.0624049	0.5813787	-0.1824234
H	3.6803289	0.6429971	1.6266244
H	3.6386420	-1.2037645	1.7630444

**PhSiH<sub>2</sub>Me**

18

Energy = -562.47482143813

C	-0.6813873	0.8128920	1.0389568
C	-0.3248534	-0.1968659	0.1286405
C	-0.6208912	0.0098048	-1.2305255
C	-1.2435670	1.1792806	-1.6647067
C	-1.5854346	2.1706165	-0.7433975
C	-1.3044460	1.9853747	0.6104020
Si	0.5646621	-1.7460447	0.7019044
H	0.3080664	-1.9208627	2.1562610
C	2.4176020	-1.6309000	0.3898031
H	0.0190702	-2.9225014	-0.0269074
H	-0.3674847	-0.7560287	-1.9613264
H	-1.4656588	1.3169426	-2.7195995
H	-2.0728842	3.0817619	-1.0793573
H	-1.5736148	2.7520824	1.3320638
H	-0.4746470	0.6789778	2.0987993
H	2.9320018	-2.5397662	0.7225113
H	2.6231051	-1.4965187	-0.6782142
H	2.8503594	-0.7782430	0.9246933

### PhSiH<sub>2</sub>Ph

25

Energy = -752.60717122982

C	-2.0480744	0.7250043	3.2005929
C	-1.4605888	-0.3141110	2.4932625
C	-1.2008031	-0.1986758	1.1276691

C	-1.5422701	0.9958071	0.4899524
C	-2.1284962	2.0374746	1.1918877
C	-2.3832008	1.9022231	2.5494060
Si	-0.4298049	-1.6122454	0.1699662
C	0.8843094	-0.9758402	-1.0046438
H	0.1360401	-2.5700919	1.1562161
H	-1.4415436	-2.3436669	-0.6373028
H	-1.3417259	1.1212141	-0.5681418
H	-2.3850963	2.9565237	0.6811097
H	-2.8390887	2.7154015	3.0992030
H	-2.2405265	0.6170150	4.2601222
H	-1.1974410	-1.2256509	3.0174020
C	1.0403836	-1.5327533	-2.2741749
C	2.0281096	-1.0812890	-3.1374057
C	2.8769587	-0.0583662	-2.7426467
C	2.7339314	0.5114562	-1.4855391
C	1.7457785	0.0557623	-0.6264823
H	0.3796731	-2.3280206	-2.5998451
H	2.1330707	-1.5253507	-4.1187832
H	3.6471097	0.2971534	-3.4148747
H	3.3918425	1.3130241	-1.1755997
H	1.6414531	0.5180026	0.3486501

**PhSiH<sub>3</sub>**

15

Energy = -522.05675637754

C	-0.2617346	0.4403156	1.0884127
C	0.2701671	-0.4930637	0.1984845
C	0.1326245	-0.2524695	-1.1695711
C	-0.5107227	0.8842774	-1.6341223
C	-1.0307657	1.8031026	-0.7338266
C	-0.9063437	1.5796995	0.6289240
Si	1.1680905	-2.0134528	0.8225209
H	0.7695528	-2.2840085	2.2250328
H	2.6402183	-1.8271788	0.7841452
H	0.8379335	-3.1884039	-0.0203981
H	0.5274681	-0.9616856	-1.8882175
H	-0.6091330	1.0525261	-2.6986690
H	-1.5349426	2.6901694	-1.0945488
H	-1.3137644	2.2915360	1.3349913
H	-0.1786481	0.2786363	2.1568419

### **Cp<sub>2</sub>TiAllyl + THF**

42

Energy = -1586.87650488863

C	-1.9734774	-1.4108587	1.3201282
C	-2.1440591	-1.4489237	-0.0913984
C	-1.2713361	-2.4244784	-0.6202015
C	-0.5438817	-2.9976169	0.4514158
C	-0.9931665	-2.3819827	1.6525246
Ti	0.0939869	-0.7025989	0.3920547
C	1.5011252	1.0109478	1.3827216

C	2.2803920	0.2623818	0.4711173
C	2.3489145	-1.0767192	0.9431732
C	1.6065237	-1.1418161	2.1491137
C	1.0586813	0.1456752	2.4129738
H	-1.1560439	-2.6679801	-1.6661109
H	0.2152960	-3.7636175	0.3686460
H	-0.6595113	-2.6172924	2.6522612
H	-2.5211997	-0.7951758	2.0209127
H	-2.7905100	-0.8048824	-0.6725661
H	2.8673274	-1.8874191	0.4516359
H	1.4858866	-2.0197998	2.7662332
H	0.4457612	0.4166368	3.2629736
H	1.2477619	2.0588376	1.2859405
C	1.5276679	-1.7602693	-2.1743756
H	2.7448397	0.6323709	-0.4305410
O	-0.9552270	1.2059200	-0.1509229
C	-0.5912071	2.1510818	-1.2026375
C	-1.5045223	3.3504870	-0.9849588
C	-1.6563289	3.3668423	0.5430127
C	-1.7503654	1.8805596	0.8708119
H	0.4668427	2.4082773	-1.0778478
H	-0.7273380	1.6436354	-2.1570405
H	-1.0736561	4.2720111	-1.3847656
H	-2.4753091	3.1851583	-1.4644847
H	-0.7677587	3.8057231	1.0094716
H	-2.5342862	3.9203261	0.8855614
H	-1.3360076	1.6064320	1.8432051

H	-2.7767603	1.5038617	0.7947792
C	2.8548421	-1.7588826	-2.4117692
C	0.6835659	-0.6155426	-1.8226705
H	-0.2793287	-0.6347501	-2.3490768
H	1.1900092	0.3305624	-2.0415213
H	1.0286551	-2.7321059	-2.2009097
H	3.3999893	-2.6785713	-2.6039509
H	3.4332125	-0.8364469	-2.4229184

### **Cp<sub>2</sub>TiH + THF**

35

Energy = -1467.65896337458

C	-2.5092818	1.9779953	-0.5001849
C	-2.3927436	0.9594866	-1.4644137
C	-2.3505658	-0.2717916	-0.7865851
C	-2.4425258	-0.0231298	0.5993192
C	-2.5452225	1.3702896	0.7729385
Ti	-0.3967638	0.9528184	-0.1331041
C	0.6628194	3.0390963	0.1873574
C	1.6883309	2.1360254	-0.1682632
C	1.8002285	1.1873169	0.8612193
C	0.8363018	1.4785222	1.8474463
C	0.1487140	2.6396851	1.4344721
H	-2.2449930	-1.2399242	-1.2529217
H	-2.4710894	-0.7642563	1.3843336
H	-2.6585043	1.8795340	1.7172891

H	-2.5621147	3.0374406	-0.7009115
H	-2.3369012	1.0985487	-2.5312246
H	2.4954703	0.3605740	0.8807765
H	0.6897095	0.9504290	2.7779697
H	-0.6287781	3.1435121	1.9870321
H	0.3383915	3.8876782	-0.3953261
H	0.1209665	0.9714000	-1.7633133
H	2.2849508	2.1780436	-1.0643487
O	0.4071898	-1.0966315	-0.2570023
C	1.1470191	-1.5872615	-1.3800787
C	1.4459366	-3.0421401	-1.0525853
C	1.5209668	-3.0215964	0.4704432
C	0.4283324	-2.0258158	0.8228032
H	2.0596463	-0.9952113	-1.4865793
H	0.5497967	-1.4444013	-2.2787638
H	2.3636664	-3.3905557	-1.5249939
H	0.6339502	-3.6917141	-1.3867185
H	1.3563629	-3.9965973	0.9277074
H	2.4960665	-2.6582054	0.8027122
H	-0.5492954	-2.5126310	0.9006758
H	0.6139625	-1.4865328	1.7528232

### **Cp<sub>2</sub>TiMe + THF**

38

Energy = -1509.42685870462

C	-1.4907144	-1.8761881	1.2805089
---	------------	------------	-----------



C	-2.0683390	-0.9190377	0.4169924
C	-1.8373903	-1.3328088	-0.9196705
C	-1.1320083	-2.5687026	-0.8841545
C	-0.9268656	-2.9035863	0.4746022
Ti	0.3191875	-0.9230718	-0.0025841
C	1.7079069	-0.4873813	1.8687019
C	2.4034250	0.0224862	0.7363530
C	2.7280439	-1.0571363	-0.1133681
C	2.2354065	-2.2467229	0.4759807
C	1.6182602	-1.8949716	1.7090549
H	-2.1403361	-0.8068306	-1.8135063
H	-0.8051907	-3.1385423	-1.7424577
H	-0.4055726	-3.7784212	0.8379071
H	-1.4747668	-1.8327682	2.3615913
H	-2.5744933	-0.0127194	0.7236510
H	3.2278642	-0.9841739	-1.0677054
H	2.3136598	-3.2422508	0.0599034
H	1.1548145	-2.5797573	2.4051902
H	1.3535559	0.0805136	2.7185818
C	0.8095053	-0.6009107	-2.1643443
H	2.6026089	1.0653829	0.5281326
O	-0.1295114	1.2635651	-0.0756661
C	-0.4245099	1.9958880	1.1495215
C	-1.3551580	3.1285097	0.7289496
C	-0.8845718	3.4141980	-0.7049782
C	-0.6038142	2.0135067	-1.2347422
H	0.1728090	1.9585452	-1.9961329

H	-1.5100983	1.5234314	-1.6075975
H	0.0337702	4.0112999	-0.6941606
H	-1.6313492	3.9393577	-1.3061840
H	-1.2775145	3.9939178	1.3920583
H	-2.3959291	2.7867461	0.7262038
H	0.5240492	2.3683050	1.5535042
H	-0.8642337	1.2895294	1.8574644
H	-0.0705831	-0.3697822	-2.7809950
H	1.5370180	0.2122153	-2.3121080
H	1.2610674	-1.5116308	-2.5844958

### **Cp<sub>2</sub>TiPh + THF**

45

Energy = -1701.28635846893

C	-4.1409716	-1.5556298	0.8405555
C	-4.6141649	-0.9880611	-0.3621698
C	-4.1836056	-1.7958792	-1.4437709
C	-3.4630222	-2.8993654	-0.9005057
C	-3.4467179	-2.7510393	0.5066253
Ti	-2.1858808	-0.9804716	-0.4577370
C	-0.9459542	-0.0743720	1.3464895
C	-0.1681648	0.1388441	0.1725129
C	0.2218896	-1.1205042	-0.3409143
C	-0.3175353	-2.1219368	0.4995275
C	-1.0246471	-1.4743800	1.5507387
H	-4.3618659	-1.6117597	-2.4929478

H	-3.0196760	-3.7135947	-1.4551078
H	-2.9790378	-3.4299478	1.2051710
H	-4.2843530	-1.1569430	1.8363415
H	-5.1731187	-0.0649886	-0.4420068
H	0.7955618	-1.2873438	-1.2393316
H	-0.2160756	-3.1899351	0.3603200
H	-1.5415062	-1.9613022	2.3652326
H	-1.3579286	0.6852950	1.9967395
C	-1.5187653	-1.0113359	-2.5933870
H	0.0648843	1.0980064	-0.2698937
C	-1.7787439	-2.0292294	-3.5327945
C	-1.3105455	-1.9934153	-4.8507914
C	-0.5492097	-0.9150154	-5.2995328
C	-0.2637088	0.1178772	-4.4048739
C	-0.7364622	0.0565749	-3.0922238
H	-2.3701418	-2.8963262	-3.2454630
H	-1.5448435	-2.8122828	-5.5287570
H	-0.1828794	-0.8809391	-6.3222709
H	0.3332126	0.9693068	-4.7280477
H	-0.4854240	0.8856225	-2.4299115
O	-2.7532330	1.1202497	-1.0175876
C	-2.9825909	2.1255210	0.0169788
C	-3.7964593	3.2412642	-0.6478116
C	-3.5234429	3.0242481	-2.1449977
C	-3.4672051	1.5092098	-2.2305790
H	-2.9016893	1.1026915	-3.0667188
H	-4.4698842	1.0643946	-2.2095482

H	-2.5580816	3.4529131	-2.4339983
H	-4.3009484	3.4495649	-2.7849685
H	-3.4972668	4.2303395	-0.2919493
H	-4.8636650	3.1125725	-0.4392388
H	-1.9980544	2.4644525	0.3508689
H	-3.5001563	1.6457244	0.8528518

### THF

13

Energy = -231.94402244901

O	-1.1047634	0.5405904	-0.8010308
C	-1.2284996	0.0148721	0.4960097
C	0.1878485	0.0250083	1.0871273
C	1.0915516	0.0233156	-0.1608993
C	0.0878969	0.0113129	-1.3219515
H	-0.0632342	-1.0163862	-1.6835545
H	0.3968326	0.6203982	-2.1722691
H	1.7602895	-0.8364173	-0.1958130
H	1.7144189	0.9172200	-0.1903591
H	0.3617264	-0.8342739	1.7344530
H	0.3560069	0.9193130	1.6869818
H	-1.6216213	-1.0119690	0.4678964
H	-1.9384528	0.6270160	1.0534091

**Cp<sub>2</sub>TiH+PhSiH<sub>3</sub>**

37

Energy = -1760.63549314200

C	-1.8759997	0.1828294	-3.0253621
C	-0.6923654	0.2695508	-2.2762436
C	0.0350211	1.4691030	-2.3338862
C	-0.3938670	2.5385968	-3.1180656
C	-1.5778333	2.4335309	-3.8521762
C	-2.3201926	1.2537436	-3.8033840
Si	-0.1075266	-1.2264141	-1.2670205
H	-0.2894717	-1.8298161	0.2388210
Ti	0.5072350	-0.6080498	1.3009554
C	2.7639799	-0.3932981	1.8759581
C	2.7032321	-1.3094342	0.7925717
C	1.9801729	-2.4535623	1.2193945
C	1.5858264	-2.2524242	2.5688178
C	2.0851231	-0.9843904	2.9771860
C	-0.6838155	0.2678608	3.1162360
C	-1.6035351	-0.4226449	2.2881963
C	-1.6544908	0.2662389	1.0411027
C	-0.7701554	1.3778679	1.1074752
C	-0.1616654	1.3741275	2.3825781
H	1.0182838	-2.9436628	3.1768915
H	1.7523360	-3.3191380	0.6131183
H	3.1136446	-1.1555701	-0.1951457
H	3.2490396	0.5731606	1.8664304
H	1.9658082	-0.5410670	3.9557696
H	-2.2743271	0.0048176	0.1934637

H	-0.5800533	2.0754301	0.3043187
H	0.5776752	2.0798501	2.7372276
H	-0.4199771	-0.0026914	4.1290970
H	-2.1712802	-1.3036112	2.5538392
H	0.8436150	-0.0906014	-0.3696210
H	1.1032457	-1.8776574	-1.8353425
H	-1.2266877	-2.1711358	-1.6355506
H	-2.4549222	-0.7382072	-2.9958934
H	-3.2438075	1.1682663	-4.3701762
H	-1.9201377	3.2692310	-4.4566959
H	0.1890382	3.4555111	-3.1556889
H	0.9488348	1.5636601	-1.7491964

### **Cp<sub>2</sub>TiH+HMgBr+THF**

Energy = -4245.00788555675

C	0.0307110	-3.3024079	-0.2020864
C	1.3569365	-3.3153505	0.3202112
C	2.0632128	-2.2202767	-0.2305651
C	1.1695506	-1.5242662	-1.0966870
C	-0.0782044	-2.2067048	-1.0862921
Ti	0.3360118	-1.3398907	1.0922186
C	-0.0556086	-2.6650500	2.9568300
C	-1.2330138	-1.9024080	2.7293301
C	-0.9095787	-0.5360693	2.9614603

C	0.4610040	-0.4586233	3.3162955
C	0.9992402	-1.7706667	3.2989442
Mg	0.0824698	1.3632266	0.5702486
O	0.1718314	1.9890322	-1.3958355
H	1.4039736	0.1584167	0.9896624
H	2.0228802	-2.0415383	3.5192547
H	1.0006412	0.4500073	3.5441655
H	-1.5894567	0.3024338	2.8911411
H	-2.2039325	-2.2878443	2.4501874
H	0.0249474	-3.7403851	2.8800379
H	1.4066982	-0.6343309	-1.6630667
H	-0.9665355	-1.9193933	-1.6311232
H	-0.7572633	-4.0013500	0.0447319
H	1.7529294	-4.0324965	1.0260833
H	3.0884680	-1.9486825	-0.0221350
Br	-0.5220889	3.3607761	1.8000644
H	-0.9156362	-0.1859949	0.3857137
C	0.4559380	3.3943188	-1.7519525
C	-0.5804234	3.7732397	-2.8187406
C	-1.6588436	2.6825140	-2.6864203
C	-0.8296516	1.4623231	-2.3229984

H	0.3534024	3.9682576	-0.8279189
H	1.4860196	3.4370831	-2.1148448
H	-0.1341622	3.7452261	-3.8177336
H	-0.9777490	4.7765355	-2.6499964
H	-2.2318941	2.5411976	-3.6063713
H	-2.3500496	2.9182165	-1.8712582
H	-0.3091591	1.0381502	-3.1903329
H	-1.3636152	0.6727753	-1.7902218